Transactions of the ASME®

Journal of Turbomachinery

Published Quarterly by The American Society of Mechanical Engineers

VOLUME 118 • NUMBER 3 • JULY 1996

Technical Editor, **T. H. OKIISHI (1998)**
Associate Technical Editors
Aeromechanical Interaction
R. E. KIELB (1999)
Gas Turbine (Review Chair)
A. KIDD (1997)
Heat Transfer
M. G. DUNN (1999)
Nuclear Engineering
H. H. CHUNG (1996)
Power
D. LOU (1998)
Turbomachinery
R. A. DELANEY (1998)

BOARD ON COMMUNICATIONS
Chairman and Vice-President
R. MATES

OFFICERS OF THE ASME
President, **R. J. GOLDSTEIN**

Executive Director, **D. L. BELDEN**

Treasurer, **J. A. MASON**

PUBLISHING STAFF
Managing Director, Engineering
CHARLES W. BEARDSLEY

Director, Technical Publishing
PHILIP DI VIETRO

Managing Editor, Technical Publishing
CYNTHIA B. CLARK

Managing Editor, Transactions
CORNELIA MONAHAN

Production Coordinator
VALERIE WINTERS

Production Assistant
MARISOL ANDINO

Transactions of the ASME, Journal of Turbomachinery (ISSN 0889-504X) is published quarterly (Jan., Apr., July, Oct.) for $150.00 per year by The American Society of Mechanical Engineers, 345 East 47th Street, New York, NY 10017. Periodicals postage paid at New York, NY and additional mailing offices. POSTMASTER: Send address changes to Transactions of the ASME, Journal of Turbomachinery, c/o THE AMERICAN SOCIETY OF MECHANICAL ENGINEERS, 22 Law Drive, Box 2300. Fairfield, NJ 07007-2300.

CHANGES OF ADDRESS must be received at Society headquarters seven weeks before they are to be effective. Please send old label and new address.

PRICES: To members, $40.00, annually; to nonmembers, $150.00.

Add $24.00 for postage to countries outside the United States and Canada.

STATEMENT from By-Laws. The Society shall not be responsible for statements or opinions advanced in papers or . . . printed in its publications (B7.1, Par. 3).

COPYRIGHT © 1996 by The American Society of Mechanical Engineers. Authorization to photocopy material for internal or personal use under circumstances not falling within the fair use provisions of the Copyright Act is granted by ASME to libraries and other users registered with the Copyright Clearance Center (CCC) Transactional Reporting Service provided that the base fee of $3.00 per article is paid directly to CCC, 222 Rosewood Dr., Danvers, MA 01923. Request for special permission or bulk copying should be addressed to Reprints/Permission Department.

INDEXED by Applied Mechanics Reviews and Engineering Information, Inc.

Canadian Goods & Services
Tax Registration #126148048

TECHNICAL PAPERS

(Contents continued on p. 443)

Downloaded 01 Jun 2010 to 171.66.16.52. Redistribution subject to ASME license or copyright; see http://www.asme.org/terms/Terms_Use.cfm

(Contents continued)

ANNOUNCEMENTS

Z. Wang

P. T. Ireland

T. V. Jones

Department of Engineering Science,
University of Oxford,
Oxford, United Kingdom

R. Davenport

Rolls Royce plc,
Bristol, United Kingdom

A Color Image Processing System for Transient Liquid Crystal Heat Transfer Experiments

A color image processing system for liquid crystal heat transfer experiment has been developed. The system is capable of digitizing and processing the complete liquid crystal surface color (hue) change history in a transient test and, together with a calibration, can give the complete history of surface temperature over a full surface. Two methods for automatically processing the hue history to give heat transfer coefficient distributions are presented. Both methods raise the accuracy of the transient technique above other approaches by using the redundancy inherent in the multiple surface temperature measurements. The first regression approach applied to the determination of both h and T_{gas} is reported. The uncertainty in all measurements has been quantified and examples of applications of both techniques given.

Introduction

Thermochromic liquid crystals have been used in numerous experimental studies to measure detailed distributions of local heat transfer coefficient (Jones et al., 1992; Ireland et al., 1993). In transient heat transfer experiments, the surface temperature history is typically determined by analyzing the surface color change monitored by color video cameras and recorded on video tape. Often, the color video recording contains sufficient information to allow calculation of the complete history of the surface temperature over the entire observed surface. Early methods of digitally processing recorded information from transient heat transfer experiments concentrated on the monochrome intensity component of the color video signal (Davenport, 1989; Wang et al., 1990). The processing can be automated and very accurate, especially when the complete intensity history is utilized as reported by Wang et al. (1995). However, by processing a color attribute of the signal, it will be shown that it is possible to determine the model surface temperature over a much broader range than has been achieved with conventional intensity (not intensity history) based processing. This fact is responsible for the high accuracy of the new method even in situations where more than one thermal quantity is measured.

One important advantage over intensity history processing (Wang et al., 1995), is the removal of the need for the liquid crystal to reach the peak intensity temperature. In some cases, this makes the selection of experimental temperatures much easier. Since the crystals selectively reflect incident light, at any point on the model surface the signal obtained from an intensity processing approach is a function of the local illumination strength (which can be nonuniform over the model surface). The signal can only be processed to determine temperature by analyzing the change in intensity with time. Consideration of Fig. 1 shows that only the peak intensity is uniquely related to temperature. Thus, in order to be able to analyze the surface intensity change data, the crystal must pass through the peak intensity.

It has been shown by Camci et al. (1992) that the hue component of the color video signal from thermochromic liquid crystals recorded during heat transfer experiments can be accurately calibrated to the surface temperature. Importantly, this calibration is independent of the strength of illumination. However, to date, hue processing of liquid crystal video data has only been applied to individual frames.

In some experimental situations, either because the flow field is fluctuating or because the test conditions are changing, the full history of the surface temperature distribution is required. This paper describes a system that enables the complete hue history recorded during a transient heat transfer experiment to be captured and subsequently processed to give a continuous surface temperature history.

Liquid Crystal Color Signal Processing

The temperature-dependent color display of thermochromic liquid crystals is caused by the temperature sensitivity of the selective reflectivity of the component materials. At a particular temperature, the liquid crystal material selectively reflects incident light within a certain wavelength range. As the temperature increases from the lower limit of the color change temperature range, the dominant reflected wavelength shifts and the surface appears to change color from red to blue. It is therefore possible to determine the surface temperature by analyzing the spectrum of the reflected light. In a typical transient heat transfer experiment, the color change is recorded using domestic color video equipment. In such a system, the optical signal is detected by a color video camera, which generates a signal that can be considered to be made up of red, green, and blue (RGB) components defined by the following equations:

$$R = \int_{-\infty}^{\infty} E(\lambda)R(\lambda)r(\lambda)d\lambda \qquad (1)$$

$$G = \int_{-\infty}^{\infty} E(\lambda)R(\lambda)g(\lambda)d\lambda \qquad (2)$$

$$B = \int_{-\infty}^{\infty} E(\lambda)R(\lambda)b(\lambda)d\lambda \qquad (3)$$

Here $r(\lambda)$, $g(\lambda)$, and $b(\lambda)$ are filter transmissivities and $E(\lambda)$ is the lighting spectral distribution. In the case of the signal from a liquid crystal coated surface, the reflectance, $R(\lambda)$, is a function of the temperature. The color signal measured by the camera is then encoded into a composite video signal (e.g.,

---

Contributed by the International Gas Turbine Institute and presented at the 39th International Gas Turbine and Aeroengine Congress and Exposition, The Hague, The Netherlands, June 13–16, 1994. Manuscript received by the International Gas Turbine Institute February 25, 1994. Paper No. 94-GT-290. Associate Technical Editor: E. M. Greitzer.

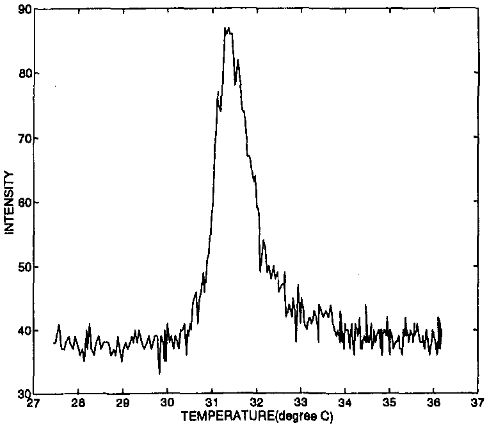

Fig. 1 Typical intensity temperature calibration

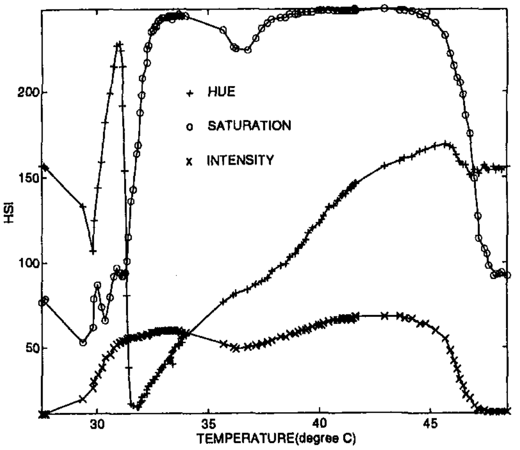

Fig. 2 HSI signals for a typical calibration (BM/R30C15W/S-33)

PAL or NTSC format) and recorded on video tape. When the video tape is played back, the composite video signal can be displayed directly by a video monitor. The separate RGB components can, however, be recovered by a signal decoder.

Although the values of the RGB signals can fully specify the temperature of a thermochromic liquid crystal, they are not used in the current study. This is partly because the amount of data to be processed from a video recording is three times that for monochromic processing and partly because the relationship between values of RGB and temperature is not simple. In addition, the R, G, and B signals, if considered in isolation, are dependent on the local illumination strength. The best solution is to use a processing approach that employs a *color index* that is based on the RGB signals and that satisfies the following conditions:

(i) It is a simple and monotonic function of the liquid crystal temperature.

(ii) It is independent of the local illumination strength.

The hue signal, H, in the HSI (hue, saturation, and intensity) color definition satisfies these conditions. It is defined as

$$H = \frac{1}{360}\left[90 - \arctan\left(\frac{F}{\sqrt{3}}\right) + \begin{matrix} 0, G > B \\ 180, G < B \end{matrix}\right] \quad (4)$$

where

$$F = \frac{2R - G - B}{G - B} \quad \text{for} \quad G \neq B$$

$$F = R \quad \text{for} \quad G = B \quad (5)$$

and saturation, S, and intensity, I, are defined as

$$I = \frac{R + G + B}{3} \quad (6)$$

and

$$S = 1 - \left[\frac{\min(R, G, B)}{I}\right] \quad (7)$$

The hue value for light reflected from liquid crystal coated surfaces changes smoothly and continuously from 0 to 240 when the temperature of the crystal is increased and the color passes through the entire visible spectrum. The hue signal thus satisfies requirement (i), Fig. 2. Furthermore, inspection of Eqs. (4) and (5) shows that since both $(2R - G - B)$ and $(G - B)$ are directly proportional to the strength of illumination, H is independent of the illumination strength. In the current study, the hue value defined above was chosen as the color index and has been calibrated to enable the temperature to be measured during a transient experiment.

Calibration of Wide Temperature Range Liquid Crystals

The application of color processing to liquid crystal video data allows temperature to be determined continuously over a calibrated range. When liquid crystal material that changes color over a broad temperature range is used, the full history of the surface temperature throughout a transient experiment can be obtained. In the current study, two wide-band liquid crystals, BM/R25C15W/S-40 and BM/R30C15W/S-33, were calibrated. The experimental equipment is shown in Fig. 3. It was arranged to be representative of the impinging jet heat transfer experiments that have since been performed (Van Treuren et al., 1994) at Oxford. First, a liquid crystal coating is applied to a 12-mm-thick perspex plate. A layer of black ink is applied on top of the liquid crystal to eliminate light transmitted through the perspex. A fine (0.0245 mm wire diameter) type-T thermocouple was glued to the surface before the liquid crystal was

Nomenclature

c = specific heat capacity, J/kgK
$E(\lambda)$ = illumination intensity spectrum
h = heat transfer coefficient, W/m^{2}K
H = hue
I = local lighting intensity
k = conductivity, W/mK
n = number of intensity samples
$r(\lambda)$, $g(\lambda)$, $b(\lambda)$ = red, green, and blue filter functions
$R(\lambda)$ = surface reflectance
R, G, B = red, green, and blue signals
t = time, s
T = surface temperature, °C
Y = intensity (or luminance) signal
β = Eq. (9)
λ = wavelength, m
ρ = density, kg/m^3
σ = standard deviation

Subscripts

gas = gas
initial = initial
1, 2 = measurement locations

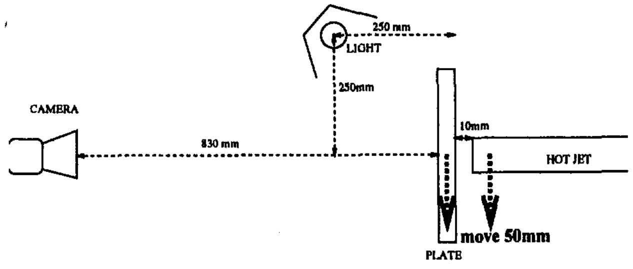

Fig. 3 Calibration setup

applied. A video camera was placed 830 mm from the calibration plate and the lens adjusted so that about 80 percent of the plate was presented in the field of view. A 2-m-long fluorescent strip light was placed 250 mm away and perpendicular to the axis of the camera and 250 mm from the plate. This arrangement and the composition of the liquid crystal, binder, and black ink system were identical to those used in the heat transfer experiment. The effect of illumination and observation angles on the color play from thermochromic liquid crystals has been considered by Jones et al. (1992). A hot air jet was directed to the liquid crystal coated surface of the plate by feeding air through a perspex tube, 1150 mm long, with inner diameter 21 mm. The exit of the pipe is 10 mm away from the plate. During a calibration, the temperature of the jet was slowly incremented and, when thermal equilibrium was reached, the temperature and the color attributes of the liquid crystal coated surface at the center of the plate were simultaneously measured. In this study, the hue, saturation, and intensity values were measured using a system that determines HSI values according to the equations above. Each hue, saturation, and intensity value is measured by averaging all the pixel values within a predefined window (typically 30 by 30 pixels) around the thermocouple. The temperature was measured by averaging a large sample of thermocouple readings to minimize the effect of random instrumentation noise.

The measured hue, saturation, and intensity values for liquid crystal BM/R30C15W/S-33 as functions of temperature are given in Fig. 2. It should be noted that in all of the following figures, the HSI values are plotted with 255 as the full-scale value. It can be seen that, starting from about 32°C, the hue value increases monotonically from around 30 (red) through 80 (green) and reaches 170 (blue) at 45°C. At higher temperatures the liquid crystal enters the isotropic phase and the color fades away as the crystal effectively melts. From 32°C, the saturation value increases steeply to a peak at 33.5°C and then decreases to a minimum at 36°C. At this temperature during the calibration, the liquid crystal appears green but significant hue fluctuations can be seen on the monitor showing the digitized image. After this point the saturation increases again and remains high until the isotropic phase. The intensity reaches a high value at 31°C and remains relatively flat until the isotropic phase at 45°C. The features described above were observed for the other calibrated liquid crystal but at different temperatures. One feature specific to liquid crystal BM/R30C15W/S-33 that has not previously been reported occurred between 30°C to 31°C. Here, the hue value shows a strong peak before dropping to the expected low value, which indicates the familiar red color at the start of colour play. Because the saturation is low, only a milky color can be observed by eye.

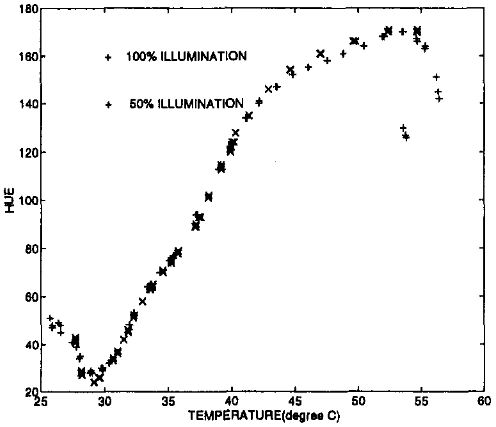

Fig. 4 Hue calibration for different illumination strengths

To investigate the effect of the strength of illumination on the hue calibration, the test was repeated with 50 percent of the fluorescent tube surface obscured. It can be seen from Fig. 4 that the change in illumination intensity does not alter the calibration apart from at the high-temperature end of the curve. It has been shown (Farina et al., 1993) that both the illumination angle and the viewing angle can influence the liquid crystal calibration. In the current study, this effect was quantified for a heat transfer test representative geometry (Fig. 3). At the center of the flat plate, the viewing angle is 90 deg and the illumination angle is 45 deg. From the center to the side of the plate, both the viewing angle and the illumination angle change. By moving the calibration thermocouple and the digitizing window off the centerline and repeating the calibration, the angle effect was assessed. The results are shown in Fig. 5. It can be seen that, for a typical flat plate test, the calibration obtained at the center of the plate can be used for other locations up to 50 mm from the center. It was also observed from subsequent experiments that the hue temperature calibration is a strong function of the camera used and of the illumination spectrum. It is clear that a calibration should be performed for each heat transfer experimental arrangement.

Repeat calibration of the crystal coating using the same hardware enabled the uncertainty in the calibration to be assessed. The uncertainty was found to be a function of temperature, but the maximum uncertainty from the averaged (calibration) curve was always less than 0.3°C.

Full Hue History Capture System

In the current study, the conversion from RGB to HSI is carried out on a commercially available frame grabber fitted to a PC, which is controlled by software developed in house. This frame grabber has two ASIC (application specific integrated circuit) chips, which convert the RGB color components to HSI components in real time according to Eqs. (4), (6), and (7). The HSI signals are then stored in the frame grabber on board memory bank, ready to be transferred to the PC's memory and

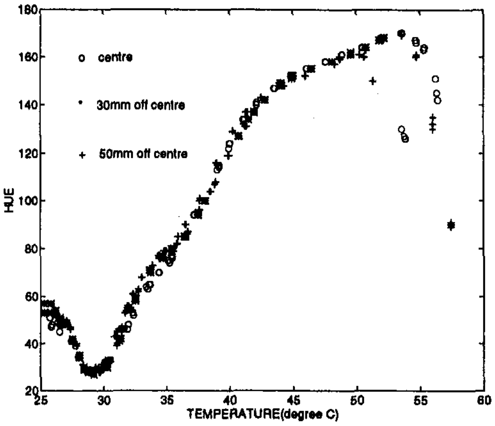

Fig. 5 Hue calibration at different locations on a flat plate

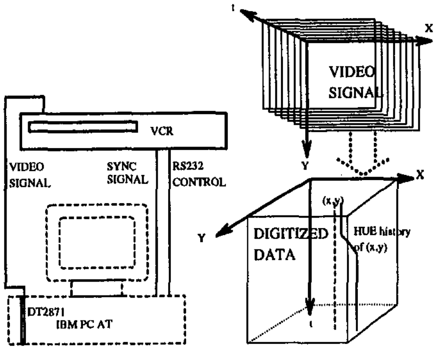

Fig. 6 Automated color video processing system

then to the hard disk. The challenge of implementing a full history capture system is in meeting the requirements of the system time response demanded by the data rate of the color video system. In PAL format, 25 frames of video images have to be processed per second. Although the frame grabber can digitize and display the video signal in real time, it is not possible to transfer this amount of data to the computer RAM or hard disk in time (512*512*25 = 6.55 Mbytes/s for a single color component). The processing speed of a typical microcomputer system normally allows only a fraction of these data to be processed and stored in digital form in real time.

Dedicated hardware systems that accomplish this task exist, but they are invariably very expensive. The solution adopted in this study is to implement an automated processing procedure in which the video tape from an experiment is processed repeatedly, analyzing a subwindow of the required image each time. The hardware system, consists of the above-mentioned color frame grabber in a 486 PC and digitally controlled video player, Fig. 6. Using the digitally controlled video player, the video tape can be played under the control of the program running on the PC. For accurate timing of the data capture, a frequency modulated timing signal is recorded onto the sound track of the video tape prior to video processing. When the tape is played, this timing signal is monitored so that the data captured from each pass through the tape can be accurately referenced to time. To optimize the throughput, the data from the frame grabber are first transferred to the RAM of the PC and whenever the CPU is not occupied by this process the data from the RAM are saved to the hard disk. In this way, RAM is released for more data.

With 10 Mbytes of RAM allocated as the buffer, hue data from a window of 256 × 144 can be saved for recorded times of up to 100 seconds. When the window size is reduced to 256 × 60 pixels, the data are saved to the hard disk at higher speed than the incoming data rate from the frame grabber. This means that there is no limit to the length of test that can be processed. A fully automated computer program has been implemented on the 486 PC so that, when necessary, the full hue history acquisition is repeated automatically in a succession of windows to cover the defined region of interest. A typical transient liquid crystal experiment needs a total window size of 512 × 300 and lasts 60 seconds. A tape from such an experiment can be completely digitized by replaying the tape four times. Using the calibration shown in Fig. (4), the complete temperature history can be obtained over the full surface.

Hue History Data Processing

The transient heat transfer method used previously (Jones et al., 1992) usually uses a single temperature determined from the liquid crystal color change to determine a single local unknown, the heat transfer coefficient. Once the complete hue history has been obtained, however, it can be used to determine more than one unknown thermal parameter. Two methods are presented of employing the information redundancy to achieve high accuracy and resolve more than one unknown. These methods are referred to as the "hue history time scaling" method and the "temperature history matching" method. The application and advantages of each method are discussed in a separate section below.

Hue History Time Scaling Method. The surface temperature history in a transient heat transfer experiment under a step change in gas temperature and constant heat transfer coefficient can be written as

$$T = (1 - \exp(\beta^2)\ \mathrm{erfc}\ (\beta)) * (T_{\mathrm{gas}} - T_{\mathrm{initial}}) + T_{\mathrm{initial}} \quad (8)$$

in which

$$\beta = \frac{h\sqrt{t}}{\sqrt{(\rho c k)}} \quad (9)$$

When temperature in the liquid crystal hue calibration $H(T)$ (e.g., Fig. 5) is replaced by Eq. (8), it can be seen that the hue history of every surface location can be expressed by

$$H(\beta, T_{\mathrm{gas}}, T_{\mathrm{initial}}) = H((1 - \exp(\beta^2)\ \mathrm{erfc}\ (\beta))(T_{\mathrm{gas}} - T_{\mathrm{initial}}) + T_{\mathrm{initial}}) \quad (10)$$

When the initial temperature and the gas temperature are uniform, the hue history for all surface locations can be collapsed onto a single curve when plotted as functions of β. It follows that the second measured hue history can be made to match the first one when the former time data are scaled by:

$$t_2' = \left(\frac{h_2}{h_1}\right)^2 t_2 \quad (11)$$

By minimizing the difference between the measured and reference curves, the heat transfer coefficient ratio can be obtained using all of the measured hue data. It should be noted that this processing method does not need a hue temperature calibration to allow matching of measured hue histories. Detailed explanation of the history scaling method applied to intensity data was first given by Wang et al. (1995). The heat transfer coefficient at the reference location is obtained by conventional processing. Uncertainty in this value can be reduced by multiple sampling over a small area. If possible, the reference site is chosen where h is known as a function of the flow Reynolds number. Otherwise, the correlation between Nusselt and Reynolds numbers can be used to process the data from numerous tests to reduce the uncertainty in reference h further. Alternatively, a foil thermocouple could be used at the reference location to provide a full record of surface temperature to enable the reference h to be determined very accurately.

Temperature History Matching Method. A method for calculating both the heat transfer coefficient and the local adiabatic wall temperature, T_{gas}, has been implemented, using the full history of the measured temperature. The surface temperature history is related to the heat transfer coefficient, the gas and initial temperatures by Eq. 8. The temperature history matching method employs the fact that, when the correct values are chosen for all the parameters in Eq. (8), the predicted temperature history should match the temperature history obtained from the hue measurement. Regression analysis is used to select values of the two parameters (h and T_{gas}) to minimize the sum of the squared differences between the measured surface temperature and that predicted by Eq. (8).

Results

Experimental results from two transient heat transfer tests are presented in the following. The first shows the heat transfer

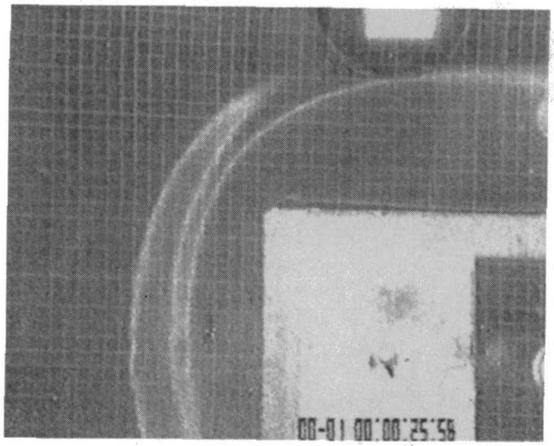

Fig. 7 Heat transfer around a rectangular obstacle

distribution on one wall of a high-aspect-ratio channel in the vicinity of a rectangular obstacle. In this case, a single narrow band liquid crystal was used with color play range of approximately 1°C, starting at 34.3°C. The color display at one time during the test is shown in Fig. 7. The influence of the main horseshoe vortex and a second upstream separation vortex on the heat transfer is evident. The complete hue history within a window of Fig. 7 was digitized and stored on the hard disk of the PC. Data at selected locations were extracted from this complete history data file and the hue history scaling method mentioned above was used to scale all the history data on to a selected hue history. Figures 8 and 9 show two hue histories before and after the scaling.

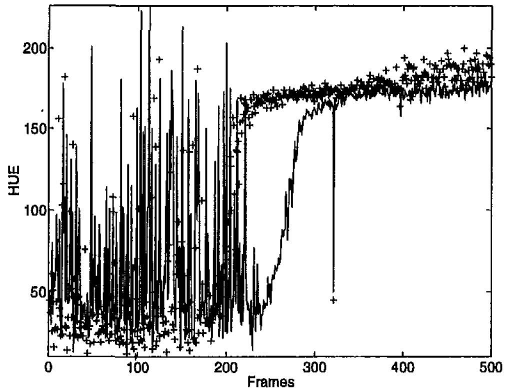

Fig. 8 Two hue histories

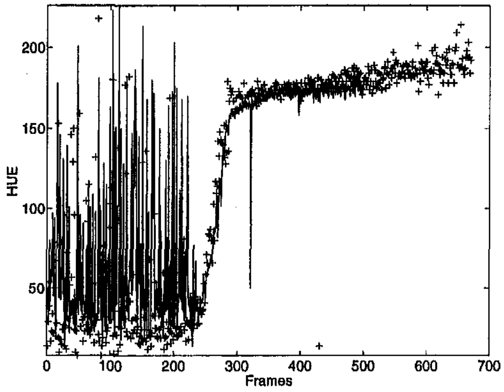

Fig. 9 Hue histories after time scaling

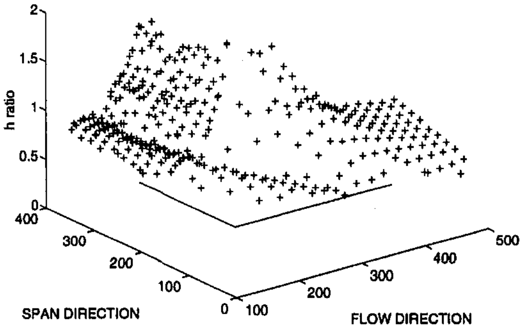

Fig. 10 Heat transfer ratio around a rectangular obstacle

By digitally filtering the noisy signal, it was possible to determine the standard deviation of the hue history before scaling was attempted. The noisy portion of the data was not used in the scaling. The criterion used rejected sections of the hue history when the standard deviation divided by the filtered signal exceeded 15 percent. In positions where the heat transfer was too low for color change to occur, the complete history was discarded. The heat transfer ratio obtained by this method at all locations where the hue value changed and are shown in Fig. 10. The data were then interpolated to a regularly spaced grid and plotted in Fig. 11. It should be noted that, once data is extracted from the complete hue history file, the subsequent processing was totally automatic and Fig. 10 shows the quality of the heat transfer ratio that can be obtained using this technique.

The experimental apparatus used to measure heat transfer to a plate under an array of impinging jet is specified by Van Treuren et al. (1994). A wide-band liquid crystal, BM/R25C15W/S-40, was used and an in situ calibration was carried out and applied. The color change of the plate under the first three rows of the jet array at a time during the transient test is shown in Fig. 12. The complete hue history was digitized by the above-mentioned hue history capturing system and an example of this captured data is shown in Fig. 13. This hue history data is then converted, using the in situ calibration, to temperature history data shown in Fig. 14. Using the temperature history matching method described above, for each measured temperature history, the adiabatic gas temperature and heat transfer coefficient can be found for each location. Figure 15 shows a measured temperature history directly under a jet and the matching result. The agreement between the measured and the predicted temperature histories justifies the assumptions used in the analysis. The calculated heat transfer coefficient and adiabatic wall temperature distributions are presented by Van Treuren et al. (1994).

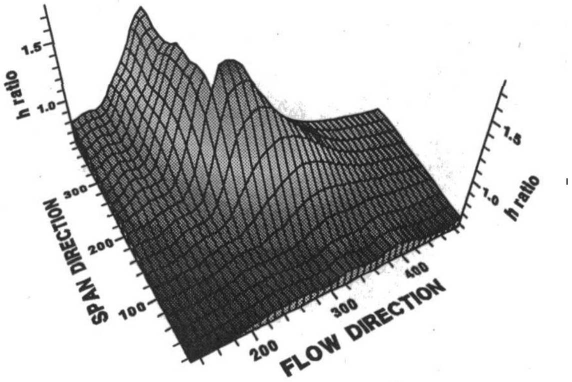

Fig. 11 Interpolated heat transfer ratio

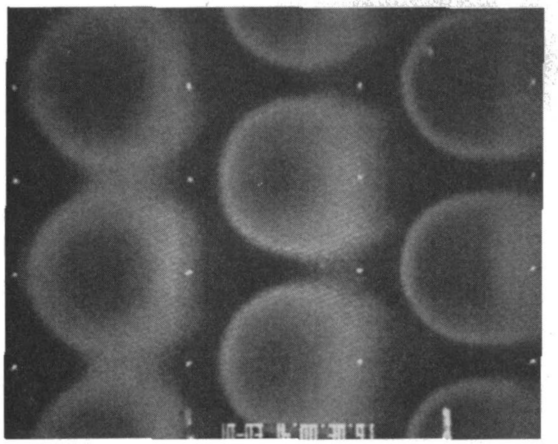

Fig. 12 Intensity map at a time in transient heat transfer experiment

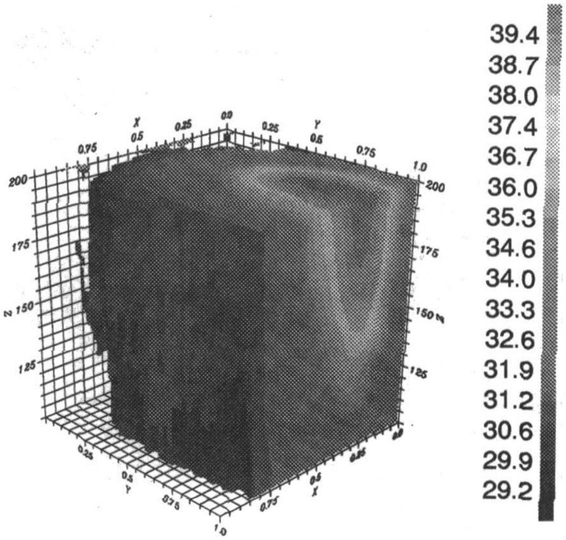

Fig. 14 Temperature distribution history (*z* axis indicates time)

Uncertainty Analysis

Hue History Time Scaling Method. In this approach, a hue versus temperature calibration is not required. Each hue time history is scaled to that from a reference location where the heat transfer coefficient is known and the heat transfer coefficient ratio determined from the square root of the scaling factor. Even with a relatively noisy hue signal, the absence of a uncertainties associated with calibration and the large number of points involved in the least-squares regression used to determine the best scale factor enable this technique to yield a very accurate time ratio. A typical scaling operation with 100 frames to be matched in the reference history and with a superposed (exaggerated) random signal of peak to peak extent 50 produces a value of h ratio with estimated standard deviation of less than 1 percent. In this analysis, the statistical properties of the time scaling factor are determined from the numerically determined covariance matrix (Seber and Gill, 1989). The standard deviation of the hue signal is estimated from the sum of the squared residuals between the reference and scaled hue signals. From the insignificant uncertainty in h ratio, it follows that the uncertainty in absolute value of h is sensibly the same as the uncertainty in the reference heat transfer coefficient.

Temperature History Matching Method. In the previous paragraph it was reported that random fluctuations in hue introduced by the video equipment cause an insignificant uncertainty in h ratio. This analysis route estimated uncertainty in the measured signal from the size of the fluctuations. In the temperature history method, however, a calibration is used to determine the surface temperature from hue, and when this calibration is performed, numerous hue and temperature samples are averaged to determine every point on the curve. Uncertainty in the calibration curve is caused by small changes in the experimental conditions as the points that are used to define the curve are measured. Such small changes in the calibration, brought about, for example by instrumentation drift, changes in background lighting or illumination power, etc., would thus cause the calibration line to deviate slightly. It is clear that it is not now possible to estimate uncertainty in the calibration from a particular measured signal. Repeat calibrations, referred to above, enable uncertainty in the calibration line to be estimated as less than 0.3°C.

The effect of deviation in the calibration was assessed by dividing the temperature range into n steps. The least-squares regression procedure was adapted to use the difference between a typical measured temperature signal at each step and values calculated from Eq. (8). As before, the parameters h and T_{gas} are chosen to minimize the sum of the squared differences but, this time, only at each step. The surface temperature history for a typical transient experiment was successively perturbed at each step boundary by 1°C and the partial derivatives of h and

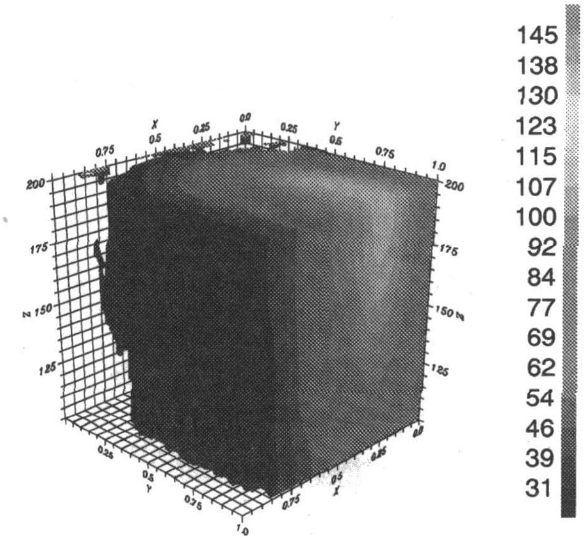

Fig. 13 Hue distribution history (*z* axis indicates time)

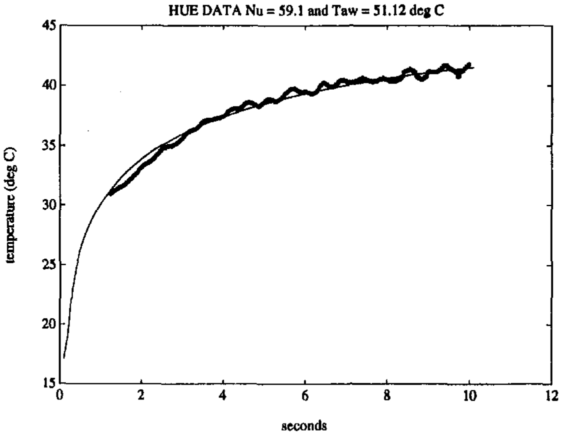

Fig. 15 Matching predicted temperature to temperature history obtained from the hue history

T_{gas}, calculated by the least-squares procedure described above, were then determined numerically. Each of the partial derivatives (n for both h and T_{gas}) is a measure of the sensitivity of these values to deviation in the calibration curve at each step. The standard deviation, σ, in h caused by surface temperature uncertainty then follows from

$$\sigma^2 = \sum_{i=1}^{i=n} \left(\frac{\partial h}{\partial T_i} \sigma_T \right)^2 \tag{12}$$

where σ_T, the standard deviation in the surface temperature, is taken to be the same at each step. Equation (12) can easily be extended to include the effect of errors in other measured quantities. Using estimated values for uncertainty in measurands of $T_{initial}$, 0.2°C, thermal product, 5 percent, and surface temperature, 0.3°C, values for a typical experiment were found to be:

Quantity	Uncertainty
h	7.5-8.5 percent
T_{gas}	1.5-2.1 percent

This uncertainty level in h shows an improvement from using only two surface temperature measurements in calculation where the uncertainty associated with h was estimated to be typically 10 percent.

Together with the magnitude in the uncertainty in surface temperature, the number of steps chosen to represent the calibration must be decided. Clearly, if many steps are chosen, the solution reverts to one representative of uncorrelated noise superposed on the temperature signal and the resulting uncertainties in h and T_{gas} become very small, as was the case for the hue time scaling method. The values at the ends of the ranges presented above were for five and ten steps, respectively. It can be seen that the uncertainties are sensibly insensitive to the number of steps when the number is representative of the deviation seen in Fig. 5.

Comparison of Methods and Conclusions

A new hue history processing system that is capable of producing the full surface temperature history during thermochromic liquid crystal transient heat transfer experiments has been developed. Two distinct methods have been applied to process the captured hue temperature history data with great success:

(*i*) The hue history time scaling method offers the advantage of not needing a liquid crystal calibration and, for typical test conditions, results in negligible errors in the h caused by hue signal noise. The time scaling technique is, however, dependent on the uniformity of T_{gas} over the test surface.

(*ii*) In cases where the gas temperature varies, the temperature history matching method should be employed. In this approach, determination of T from H requires a calibration that introduces extra uncertainty. With care, this additional error can be minimized to produce values of both T_{gas} and h at accuracies that compare favorably with other heat transfer methods.

The power of the latter method rests in its ability to determine more than one thermal quantity (in the examples given, both T_{gas} and h). With earlier processing methods that identify discrete temperatures at the peak values of intensity, the accuracy is improved if the peak is sharp because color play occurs over a narrow temperature range. The peak intensity temperature is thus less sensitive to angle of illumination and observation than for a wide band crystal.

It should be noted that hue time scaling is faster than intensity time scaling since hue is independent of strength of illumination and does not need strength of signal scaling. Hue time scaling of a narrow band crystal is thus the recommended approach for uniform T_{gas} models. However, for an experiment where the adiabatic wall temperature changes over the surface, the accuracy is improved if regression can be applied to numerous data points at appreciably different temperatures. This is most easily implemented by using a hue signal that changes monotonically with temperature, i.e., from a single, wide-band crystal coating. Regression processing of multiple crystal coatings is possible, but is a more complex procedure.

It has been shown above that the liquid crystal hue change can be calibrated accurately to temperature with high resolution. It is also evident, Fig. 14, that this method is capable of producing the full time history of surface temperature. There is no doubt that the technique will be invaluable in the study of heat transfer phenomenon that are transient by nature. The authors are currently using the system to investigate the formation of turbulent spots in a transitional boundary layer and the heat transfer under a bubble in a boiling process.

Acknowledgments

This work was carried out with the support of the UK Ministry of Defence and Rolls Royce plc. The technical assistance of Mr. P. J. Timms was also much appreciated. The liquid crystals were supplied by Hallcrest LCT.

References

Davenport, R., 1989, "Innovative Use of Thermochromic Liquid Crystals for Turbine Blade Internal Cooling Passage Flow Visualisation and Heat Transfer Measurements," *Proc. European Propulsion Forum, Modern Techniques and Developments in Engine and Component Testing,* Bath, Royal Aeronautical Society.

Camci, C., Kim, K., and Hippensteele, S. A., 1992, "A New Hue Capturing Technique for the Quantitative Interpretation of Liquid Crystal Images Used in Convective Heat Transfer Studies," ASME JOURNAL OF TURBOMACHINERY, Vol. 114, pp. 765–775.

Farina, D. J., Hacker, J. M., Moffat, R. J., and Eaton, J. K., 1993, "Illuminant Invariant Calibration of Thermochromic Liquid Crystals," presented at the ASME National Heat Transfer Conference, Atlanta, GA.

Ireland, P. T., Wang, Z., and Jones, T. V., 1993, "Liquid Crystal Heat Transfer Measurements," Measurement techniques Lecture series, von Kármán Institute for Fluid Dynamics, Belgium.

Jones, T. V., Wang, Z., and Ireland, P. T., 1992, "Liquid Crystals in Aerodynamic and Heat Transfer Testing," *Proc. Optical Methods and Data Processing in Heat and Fluid Flow,* IMechE, London.

Seber, G. A. F., and Gill, C. J., 1989, *Nonlinear Regression,* Wiley, New York.

Van Treuren, K. W., Wang, Z., Ireland, P. T., Jones, T. V., and Kohler, S. T., 1994, "Local Heat Transfer Coefficient and Adiabatic Wall Temperature Measurement Beneath Arrays of Staggered and Inline Impinging Jets," ASME Paper No. 94-GT-181.

Wang, Z., Ireland, P. T., and Jones, T. V., 1990, "A Technique for Measuring Convective Heat Transfer at Rough Surfaces," ASME Paper No. 90-GT-300.

Wang, Z., Ireland, P. T., and Jones, T. V., 1995, "An Advanced Method of Processing Liquid Crystal Video Signals From Transient Heat Transfer Experiments," ASME JOURNAL OF TURBOMACHINERY, Vol. 117, pp. 184–189.

J. R. Shen
Institute of Engineering
Thermophysics,
Chinese Academy of Sciences,
Beijing, China

Z. Wang

P. T. Ireland

T. V. Jones

Dept. of Engineering Science,
University of Oxford,
Oxford, United Kingdom

A. R. Byerley
Department of Mechanical Engineering,
Mercer University,
Macon, GA 31207

Heat Transfer Enhancement Within a Turbine Blade Cooling Passage Using Ribs and Combinations of Ribs With Film Cooling Holes

A transient heat transfer method using liquid crystals has been applied to a scale model of a turbine rotor blade passage. Detailed contours of local heat transfer coefficient are presented for the passage in which the heat transfer to one wall was enhanced first by ribs and then with ribs combined with holes. The hole geometry and experimental dimensionless flow rates were representative of those occurring at the entrance to engine film cooling holes. The results for the ribbed passage are compared to established correlations for developed flow. Qualitative surface shear stress distributions were determined with liquid crystals. The complex distributions of heat transfer coefficient are discussed in light of the interpreted flow field.

Introduction

High-pressure air from the compressor is used to cool the early stages of the turbine in modern propulsive jet engines in two distinct ways. Heat is passed to the coolant as it flows through intricate passages within the airfoils. The reduction in blade temperature caused by the internal flow is classified as *convective cooling.* In addition, the coolant is often bled from the cooling passages through holes that connect to the airfoil surface. The air forms an insulating layer of relatively cool gas between the blade external surface and the combustion products. This second cooling method is termed *film cooling.*

There are many examples in the literature of reports of research that has sought to quantify the performance of convective and film cooling. A comprehensive review of convective cooling research was given by Yeh and Stepka (1984). Comparatively little research has assessed the effect of drawing flow from the coolant passages (for film cooling) on the passage heat transfer coefficients. Byerley et al. (1988) were the first to measure distributions of local heat transfer coefficient in the vicinity of the entrance to a film cooling hole. They found that the local heat transfer coefficient, under certain conditions, could be increased by as much as a factor of six. A more recent report (Byerley et al., 1992) assessed the effect of hole inclination on the heat transfer distribution. Good qualitative agreement was demonstrated between heat transfer measurements and the results of a computational fluid dynamics study. The influence of upstream holes and hole diameter was assessed by Shen et al. (1991). They showed that the heat transfer coefficient level around the entrance to the holes was insensitive to the number of holes upstream.

The aim of the present work was to quantify the effect of flow through holes on heat transfer in a rib-roughened passage. Ribs are frequently used to promote heat transfer at the expense of increased pressure drop. It was not clear to what extent bleed through holes would increase heat transfer in a passage in which heat transfer promoters were already employed.

Experimental Apparatus and Method

The experimental apparatus used to represent the engine blade cooling passage at 15 times actual size is illustrated in Fig. 1. Air is drawn by a vacuum pump from heaters to a plenum upstream of the perspex duct. During the warm-up stage of the experiment, the heated air passes out of the plenum through the perforated section ahead of the test section. Once the air temperature is steady, the experiment is begun by triggering solenoid-operated valves, which divert the flow through the perspex section. The cross section of the first 338 mm of the perspex duct is square with side 76.5 mm. The following 466 mm, from the line AA, contracts with flat sides to an exit square cross section of 63 mm. In the engine, the uniform section passes through the blade root and the tapered section is within the blade. The abrupt edged inlet is also representative of the engine coolant feed system.

Before the experiment starts, the perspex test section temperature is uniform at room temperature. A heated steady flow is abruptly started through the wind tunnel and the internal surface temperature of the model is measured with temperature-sensitive liquid crystals. The use of these full surface thermometers in heat transfer experiments has been discussed in detail by Jones et al. (1992). The encapsulated type of crystal used passes through the full visible spectrum, from red to violet, with increasing temperature. The accuracy of the temperature measurement was kept high by using liquid crystals, which pass through the color play range in less than 1°C. A single color (yellow) was then used as the calibrated response.

The transient process of heat conduction from the surface into the perspex wall can be considered to be one dimensional since heat conducted laterally is negligible compared to heat flow normal to the surface. Under these conditions and when the gas temperature change is a simple step, the solution for the surface temperature, T_s, is

$$\frac{T_s - T_i}{T_g - T_i} = 1 - \exp \frac{h^2 t}{\sqrt{\rho c k}} \operatorname{erfc} \frac{h\sqrt{t}}{\sqrt{\rho c k}} \qquad (1)$$

The initial temperature and the gas temperature are measured for each experiment and the crystal color response is calibrated to a surface-mounted thermocouple. Hence, if the time required

---

Contributed by the International Gas Turbine Institue and presented at the 39th International Gas Turbine and Aeroengine Congress and Exposition, The Hague, The Netherlands, June 13–16, 1994. Manuscript received by the International Gas Turbine Institute February 15, 1994. Paper No. 94-GT-232. Associate Technical Editor: E. M. Greitzer.

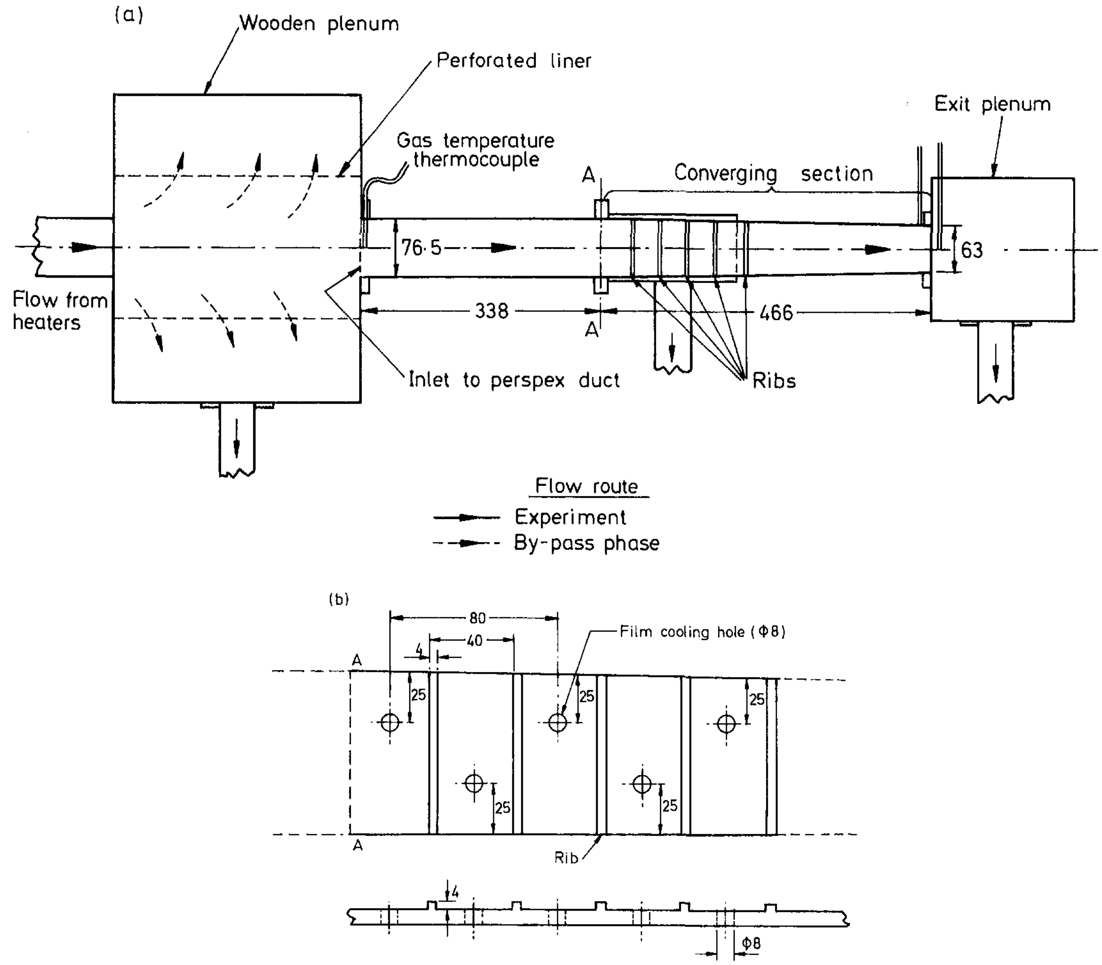

Fig. 1 Side view of the experimental apparatus; all dimensions in mm

for the crystal to change color at any location is known, the local heat transfer coefficient can be calculated. The surface color response during the experiment is recorded on video-tape using standard (PAL format) video equipment. The contours of heat transfer coefficient were obtained by identifying the location of the yellow contour at different times from flow initiation. The experimental method enables the distribution of local heat transfer coefficients to be measured over a full surface with an uncertainty of about 7 percent (Baughn et al., 1989). The method has been successfully applied to numerous other internal cooling ducts at Oxford. Previous work has shown that the measured heat transfer coefficients correspond closely to those measured under isothermal wall conditions for numerous flow fields.

The duct geometry is identical to that reported by Shen et al. (1991) except that ribs have been combined with the film cooling holes. The objective of the experiments was to obtain comparative enhancement factor data for this engine typical configuration at different massflows through the holes representing the film cooling holes.

Heat Transfer Measurements

Base Level Heat Transfer Coefficient. Figure 2 shows the measured variation in the static pressure through the duct. C_p

Nomenclature

a = tunnel side dimension at inlet = 76.5 mm
A = duct surface area between locations 1 and 2, m^2
c_p = specific heat capacity, J/kgK
C_p = pressure coefficient
e = rib size = 4 mm
EF = enhancement factor = h/h_d
h = heat transfer coefficient, W/m^{2}K
$\bar{h}$ = clean wall h, W/m^{2}K
h_d = duct h in the absence of holes, W/m^{2}K
h_{gap} = average h over the duct wall between the ribs
h_{mbi} = h based on mixed bulk temperature, i = 1, 2, W/m^{2}K
k = thermal conductivity, W/mK
$\dot{m}$ = mass flow rate, kg/s
Nu_{mbi} = Nusselt number based on mixed bulk temperature, i = 1, 2
Pr = Prandtl number
Re = Reynolds number = $\dot{m}/\mu a$
SR = suction ratio, average hole velocity divided by passage average velocity
t = time, s
T_g = gas temperature, °C
T_i = perspex initial temperature, °C
T_{mbi} = mixed bulk temperature at i (= 1, 2), °C
T_s = perspex surface temperature, °C
x = distance from start of boundary layer,
$\sqrt{\rho c k}$ = thermal product, Ws$^{0.5}$/m^{2}K
μ = dynamic viscosity, Ns/m^2

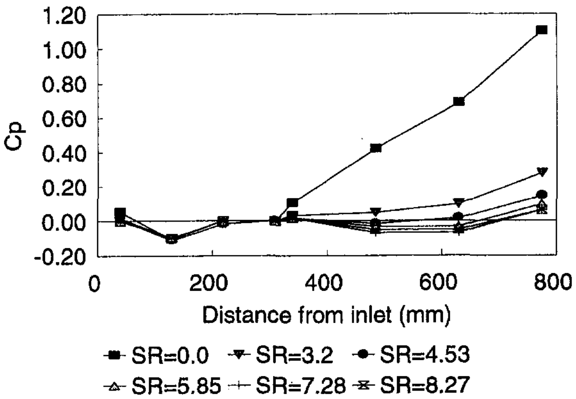

Fig. 2 Measured pressure coefficient (defined in text)

is defined as the difference between the static pressure at the measurement location and at a reference location 338 mm from the inlet divided by the dynamic head at the reference point. In the case of no suction, as expected, the pressure drops continuously from the start of the tapered section (the reference location). The local static pressure, together with the total pressure, measured on the duct centerline at the plane of the sharp edged inlet, was used to calculate the local duct velocity. Figure 3 shows the measured heat transfer data along the passage in the absence of heat transfer promoters. The theoretical line is calculated by applying an integral turbulent boundary layer analysis (Kays and Crawford, 1980) and using the measured pressure results to determine velocity. The high level of agreement between the measured results and the boundary layer analysis indicates that the flow is not developed for practically the whole of the passage. The interpreted flow field is illustrated in Fig. 4.

The Nusselt number just ahead of the converging section (338 mm from the duct inlet) is presented in Fig. 5. A double event liquid crystal coating was used and, for most of the experiments, the value presented is the average of two measurements. In the present work, the flow has not developed at this position so the temperature of the core flow is the same as the gas inlet temperature. The theoretical line is produced using the expression for Nusselt number beneath an external boundary layer:

$$\frac{h_d a}{k} = 0.0287 \, \mathrm{Re}^{0.8} \left(\frac{a}{x}\right)^{0.2} \mathrm{Pr}^{0.6} \tag{2}$$

The equation shows that the theoretical Nusselt number is a weak function of the boundary layer development length. However, allowance was made for the effect of the separation at the inlet by subtracting the measured distance between the attachment line from the inlet (20 mm) from the 338 mm distance between the measurement site and the inlet. The experimental values are, on the whole, slightly higher than the prediction. This is probably accounted for by turbulence shed into the flow from the entrance separation.

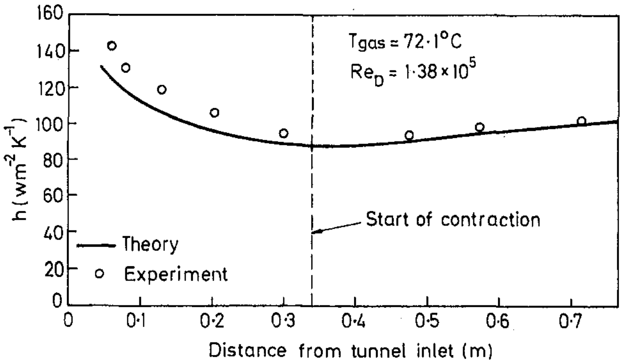

Fig. 3 *h* along the duct wall centerline for the no-rib, no-hole configuration

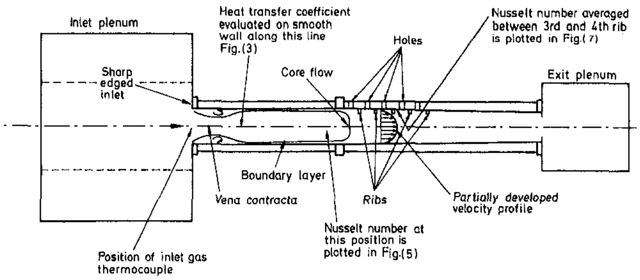

Fig. 4 Plan view of the apparatus showing the heat transfer measurement points and the interpreted flow field

Passage With Ribs. The large-scale rib dimensions relative to the passage size were engine representative and had a 4 mm square section, *e*. At 15 times engine size, the perspex ribs correspond to 0.27 mm engine ribs. The pitch was 10 rib dimensions and the rib positions and geometry are specified in Fig. 1(*b*). This figure also gives the locations of the film cooling holes discussed in the next section. The heat transfer data are presented in the form of contours of enhancement factor, *EF*. This is defined as local heat transfer coefficient divided by heat transfer coefficient at the start of the tapered section ahead of the ribs:

$$EF = \frac{h}{h_d} \tag{3}$$

The variation of the normalizing heat transfer coefficient has been discussed above and presented in Fig. 5. The form of the distribution in enhancement factor between the ribs, Fig. 6, is in agreement with the findings of other workers, such as Han (1988), with the local level peaking between the ribs. The reduction in level toward the smooth (top and bottom) walls is not surprising, but does not appear to have been reported before. The enhancement factor distributions were found to be a weak function of the Reynolds number. The distributions in Fig. 6 are at the limits of the Reynolds number range tested.

It is interesting to note that developed conditions are achieved almost straightaway. For this reason, it was thought worthwhile

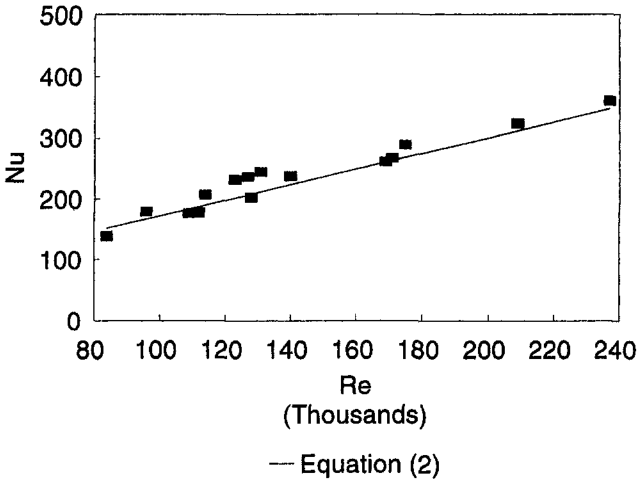

Fig. 5 Nusselt number, $h_d a/k$, in the duct at 338 mm from the plenum

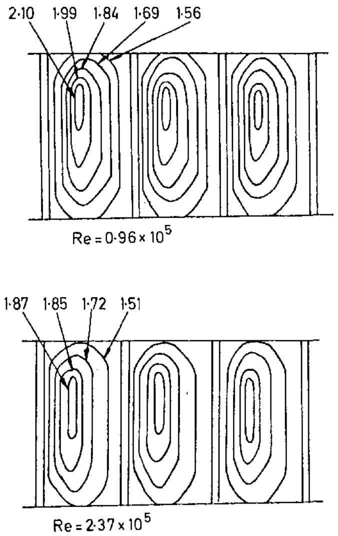

Fig. 6 Local value of the enhancement factor at the first three gaps between the ribs

to compare the data to a correlation for developed flow in rib roughened ducts. The average Nusselt number at the third gap (between the third and fourth ribs—Fig. 4) is shown as a function of the Reynolds number in Fig. 7. These values have been adjusted to account for the heat transfer over the surface of the rib as will be described below. The measured data have been compared to a theoretical line derived from the work of Webb et al. (1971) who correlated the developed heat transfer coefficient results for isothermal circular pipes. The average of the present data was determined along a line midway between the smooth walls and normal to the rib surface.

Webb's correlation is for Nusselt number based on the local mixed bulk gas temperature for developed conditions in pipes with complete annular ribs. It is possible to calculate the Nusselt number based on local mixed bulk temperature, T_{mb2}, for the present work by using an energy balance. This approach gives the following equation for the Nusselt number based on the local mixed bulk temperature, Nu_{mb2}, as

$$\frac{\mathrm{Nu}_{mb2}}{\mathrm{Nu}_{mb1}} = \frac{1}{1 - (hA/\dot{m}c_p)} \qquad (4)$$

where h is the average heat transfer coefficient based on the upstream gas temperature, and A is the passage area between the places at which the mixed bulk temperature is specified as T_{mb1} and T_{mb2}. The results are slightly lower than the theoretical line. The lower line is the best fit to the present results and is 5 percent less than the theory. Given the differences between the present experimental conditions and those used by Webb, the discrepancy is not great.

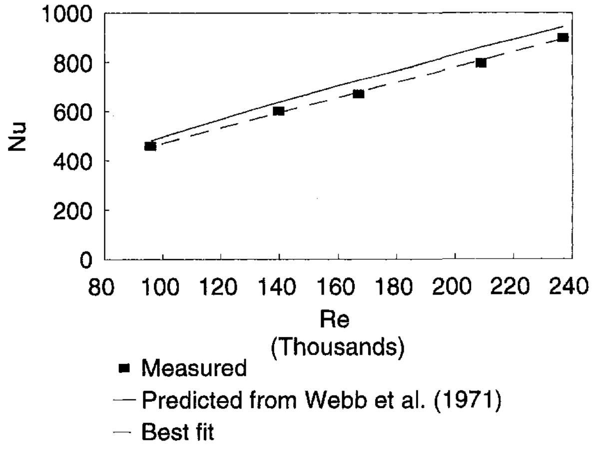

Fig. 7 Nusselt number, $h_{mb2}a/k$, between the third and fourth ribs and averaged along a line midway between the smooth walls

In the present work, the liquid crystal coating was only observable between the perspex ribs so that no values were obtained over the surface of the rib. Previously unpublished measurements by Byerley at Oxford showed that the heat transfer coefficient on the top of the rib surface is significantly higher than the average value between the ribs, Fig. 8. Here the heat transfer coefficient has been normalized by the peak value in the second and third gaps. These experiments were performed on 10 mm square ribs fixed to one wall of a channel with a high aspect ratio cross section. Ahead of the ribs the flow was two-dimensional channel flow and the rib pitch was $10e$. In processing the present results, the assumption has been made that values of heat transfer coefficient on the rib surface divided by the peak value between the ribs is the same as that measured by Byerley, i.e., the distribution of local normalized h is a weak function of the geometry and Reynolds number. On the top surface of the first rib, it can be seen that h increases in the flow direction. This is probably because the flow has separated from the leading edge of the rib. Over the top of the second rib, the flow appears to be attached with a very high value at the front edge of the rib and an ensuing reduction in level downstream. A more uniform distribution is apparent over the top of the third rib. Similar high levels over the rib top surface have been presented recently by Ristori et al. (1991) who computed the flow over ribs in a rectangular passage geometry tested previously by Han. The slight increase in level on the passage wall immediately ahead of all of the ribs is repeatable and is associated with the circulation that has been observed (Atli, 1988) ahead of two-dimensional obstacles immersed in boundary layers. The separation behind each rib is responsible for the region of low h, which extends approximately $0.6e$ from the rib rear face. Surface shear visualization showed that the attachment line occurs midway between the ribs. It is interesting to note that this is not the location of the peak h which in all of the liquid crystal results occurred slightly upstream of the attachment line. The same phenomenon was observed by Dunne (1983) in a different engine representative cooling passage.

In Byerley's experiments, the average heat transfer coefficient on the top of the third rib was 1.94 times the value averaged in the gap between the second and third ribs. The value on the front and the rear surface of the ribs is unknown but was estimated as being the same as the average value between the ribs. The average level over the faces of the ribs in terms of the average value between the ribs is shown in Fig. 9. Considering all rib surfaces and the gap between the ribs, we can tabulate the lengths and average heat transfer coefficients applicable to each surface.

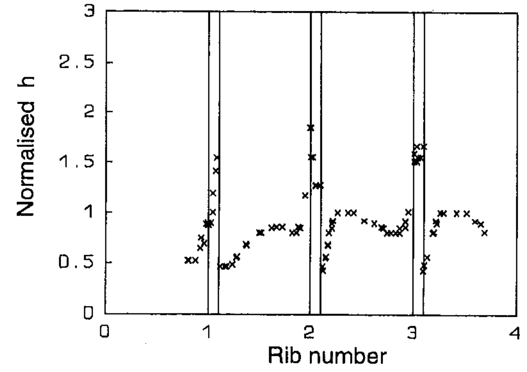

Fig. 8 Normalized heat transfer coefficients measured over the top surface and between large ribs

Surface	Length/e	h/h_{gap}
Front	1.00	1.00
Top	1.00	1.94
Rear	1.00	1.00
Gap	9.00	1.00

h_{gap} is the value averaged between the ribs, Fig. 9. The overall average heat transfer coefficient for a "clean wall" length of 10e is thus

$$\bar{h} = \frac{e\cdot h_{gap} + (1.94e)\cdot h_{gap} + e\cdot h_{gap} + (9e)\cdot h_{gap}}{10e} \tag{5}$$

A factor of 1.294 was applied to the average data measured between the ribs in the present converging passage to obtain the clean wall data presented in Fig. 7.

Passage With Combined Film-Cooling Holes and Ribs. Distributions of surface heat transfer coefficient between the ribs with five 8 mm diameter film cooling holes added are presented in Figs. 10(a)–10(h) for a range of suction ratios. The suction ratio is defined as

$$SR = \frac{\text{Mean hole velocity}}{\text{Mean duct velocity}} \tag{6}$$

where the mean duct velocity is evaluated ahead of the holes. The pressure coefficient at different suction ratios is presented in Fig. 2. It can be seen that the flow ceases to accelerate in the converging passage at the higher suction ratios as more air is drawn through the holes.

It was hoped that suction would draw flow from the separation behind the rib and produce a continuous flow from this zone into the hole. In this way the separation would be changed from two dimensional to three dimensional and the region of low heat transfer would be altered. This appears to have happened as shown by the surface shear measurements presented in Fig. 11 where an example of a heat transfer contour distribution is also included for comparison. A type of unencapsulated liquid crystal that changes color when subjected to an air flow was first used by Bonnett et al. (1989) to measure surface shear. Under the action of surface shear, the cholesteric liquid crystals change from the focal conic to the grandjean states. This texture change is associated with the onset of color play. Under optimal conditions, the time from flow initiation for the crystal to change color is a function of the local shear stress. The method was used in the present work to visualize the direction of the local shear. The viscosity of the crystal is a function of temperature and the inlet air heaters were adjusted to give the best visualization. Once established, the crystal color distribution did not change with time and it was recorded using color print film in an SLR camera.

It can be seen that the presence of the hole reduced the extent of the slow-moving fluid behind the rib. Away from the hole, the attachment line occurs at close to the midgap location, but flow that passes upstream (to the left in the figure), which would otherwise be trapped in a comparatively stagnant recirculation, is seen to be swept in the rib direction before passing into the hole. The accumulation of this fluid at the upstream

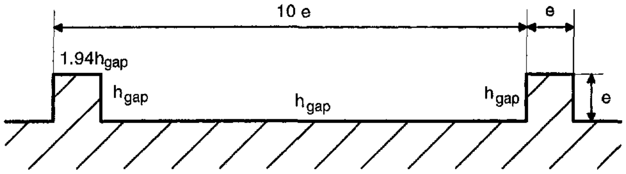

Fig. 9 Average heat transfer coefficient over the rib surfaces in terms of the average value between the ribs

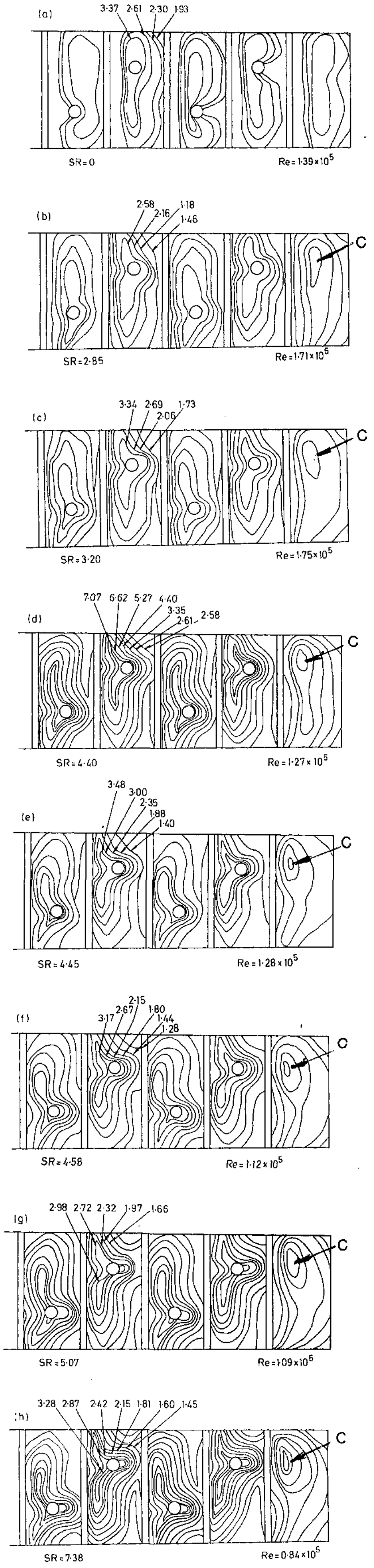

Fig. 10 Contours of enhancement factor for the combined ribs and film cooling holes

edge of the hole is responsible for the local reduction in heat transfer here, which is seen as a bump in the contours (marked *A*) between the hole and the preceding rib. The contour bump in the opposite direction immediately downstream of the hole, *B*, is due to the attachment of the flow in this location—the subsequent boundary layer development decreases the level in the downstream direction. Referring to Fig. 10, the local peak downstream of the last rib, *C*, is evidence of the influence of conditions upstream of a rib on the downstream enhancement. The removal of near-wall (slower moving and cooler than the core) fluid is seen to promote the heat transfer. The position of the peak heat transfer contour downstream of the last rib under the action of the upstream hole appears to move closer to the rib.

The zero suction ratio case is included only for interest as the holes were not blocked but communicated through the plenum external to the test section. The nonperiodic distribution is due to (an unmeasured) flow leaving the wind tunnel through the first hole and returning to the tunnel at the third and fourth holes. The distribution at the second gap is very close to the distribution in the absence of holes and this indicates that little flow passes through the second hole. The return of cooled gas at the third and fourth holes constitutes film cooling of the rough surface, as is clear from the reduction in the heat transfer behind the holes.

An automated image processing method devised by Wang et al. (1993) was used to average the heat transfer coefficient between the ribs. The enhancement factor over the plain wall case is presented in Fig. 12. The factor of 1.29 used in the preceding section to account for the heat transfer over the surface of the ribs has been applied to obtain the data presented. The position along the duct is specified in terms of the gap number. Since there are five ribs, there are only four gaps between the ribs. The data for the first and last abscissa coordinates are for the areas ahead of the first and downstream of the last ribs respectively. These end areas are 36 mm long in the streamwise direction.

Consideration of the lowest (but greater than zero) suction ratio data shows that developed conditions are achieved by the third hole. The heat transfer level for the first area is appreciably lower than the others. The heat transfer level is only increased by the presence of the (first) hole. The value of enhancement factor for the sixth station is also low since there is no hole in this area. In general, the heat transfer levels can be seen to increase with suction ratio over the no-hole value. Accounting for the rib surface heat transfer, the no-hole value is about 2.0.

The reduction in heat transfer through the passage at the two highest suction ratios is due to the decrease in duct Reynolds number as air leaves through the film cooling holes. Calculations showed that, at the highest suction ratio, the duct Reynolds number decreased by 6 percent between the third and fifth gaps.

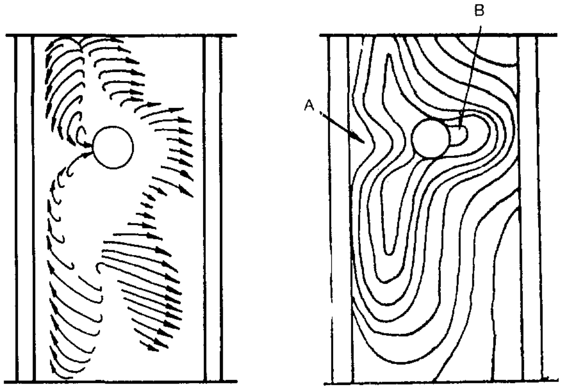

Fig. 11 Surface shear visualization using texture change liquid crystals (see Bonnett et al., 1989) for the combined ribs and film cooling holes

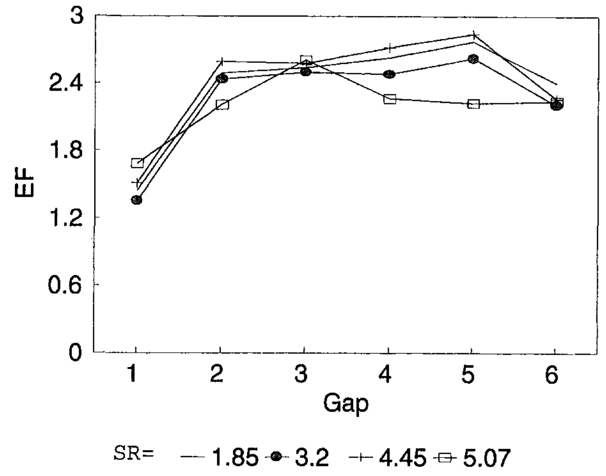

Fig. 12 Average clean wall enhancement factor for the combined ribs and film cooling holes. The abscissa specifies position along the duct and is given in terms of gap number (see text).

Conclusions

Detailed distributions of heat transfer coefficient have been measured over the surface of a turbine blade cooling passage wall where the heat transfer coefficient was enhanced by ribs and combinations of ribs with film cooling holes. The addition of holes has been shown to alter the familiar flow field between the ribs and, in particular, to reduce the extent of the separation downstream of each rib. The reduction in the extent of this region of low heat transfer and the addition of a zone of high heat transfer in the vicinity of each hole act to raise the average heat transfer coefficient from the ordinary ribbed wall value by approximately 25 percent. It should be noted however, that the reduction in the duct Reynolds number at high suction ratios was seen to reduce the heat transfer coefficient.

Acknowledgments

This work was carried out with the support of the UK Ministry of Defence and Rolls-Royce plc. The technical assistance of Mr. P. J. Timms was also much appreciated. The liquid crystals were supplied by Hallcrest LCT.

References

Atli, V., 1988, "Subsonic Flow Over a Two-Dimensional Obstacle Immersed in a Turbulent Boundary Layer on a Flat Surface," *Journal of Wind Engineering and Industrial Aerodynamics,* Vol. 31, pp. 225–239.

Baughn, J. W., Ireland, P. T., Jones, T. V., and Sanei, M., 1989, "A Comparison of the Transient and Heated-Coating Methods for the Measurement of Local Heat Transfer Coefficients on a Pin Fin," ASME *Journal of Heat Transfer,* Vol. 111, pp. 887–881.

Bonnett, P., Jones, T. V., and McDonnell, D. G., 1989, "Shear Stress Measurements in Aerodynamic Testing Using Cholesteric Liquid Crystals," *Liquid Crystals,* Vol. 6, No. 33, pp. 271–280.

Byerley, A. R., Ireland, P. T., Jones, T. V., and Ashton, S. A., 1988, "Detailed Heat Transfer Coefficient Measurements Near and Within the Entrance of a Film Cooling Hole," ASME Paper No. 88-GT-155.

Byerley, A. R., Jones, T. V., and Ireland, P. T., 1992, "Internal Cooling Passage Heat Transfer Near the Entrance to a Film Cooling Hole: Experimental and Computational Results," ASME Paper No. 92-GT-241.

Dunne, S. T., 1983, "A Study of Flow and Heat Transfer in Gas Turbine Blade Cooling Passages," D. Phil thesis, University of Oxford.

Han, J. C., 1988, "Heat Transfer and Friction Characteristics in Rectangular Channels With Rib Turbulators," ASME *Journal of Heat Transfer,* Vol. 110, pp. 321–328.

Jones, T. V., Wang, Z., and Ireland, P. T., 1992, "The Use of Liquid Crystals in Aerodynamic and Heat Transfer Experiments," *Proc. of Optical Methods and Data Processing in Heat and Fluid Flow,* Apr. 2–3, Institute of Mechanical Engineers.

Kays, W. M., and Crawford, M. E., 1980, *Convective Heat and Mass Transfer,* 2nd ed., McGraw-Hill, New York.

Mayle, R. E., 1991, "Pressure Loss and Heat Transfer in Channels Roughened on Two Opposite Walls," ASME JOURNAL OF TURBOMACHINERY, Vol. 113, pp. 60–66.

Ristori, A., Servouze, Y., Errera, M. P., Dutoya, D., and Perruchini, J., 1991, "Numerical Simulation of Flows Inside Internal Cavities of Turbine Blades," *Proc. Eurotherm Conference, Heat Transfer in Single Phase Flows* July 8–10.

Shen, J.-R., Ireland, P. T., and Jones, T. V., 1991, "Heat Transfer Coefficient Enhancement in Gas Turbine Blade Cooling Passage Due to Film Cooling Holes," *Proc. Turbomachinery: Latest Developments in a Changing Scene,* Institute of Mechanical Engineers, pp. 219–226.

Wang, Z., Ireland, P. T., and Jones, T. V., 1993, "An Advanced Method of Processing Liquid Crystal Video Signals From Transient Heat Transfer Experiments," ASME Paper No. 93-GT-282; ASME JOURNAL OF TURBOMACHINERY, Vol. 117, 1995, pp. 184–189.

Webb, R. L., Eckert, E. R. G., and Goldstein, R. J., 1971, "Heat Transfer and Friction in Tubes With Repeated Rib Roughness," *International Journal of Heat and Mass Transfer,* Vol. 14, pp. 601–618.

Yeh, F. C., and Stepka, F. S., 1984, "Review and Status of Heat-Transfer Technology for Internal Passages of Air-Cooled Turbine Blades," NASA Technical Paper 2232.

ERRATA

To the paper "The Combined Closed Form–Perturbation Approach to the Analysis of Mistuned Bladed Disks," by M. P. Mignolet and C.-C. Lin, published in the October 1993 issue of the JOURNAL OF TURBOMACHINERY, Vol. 115, pp. 771–780:

- The right-hand sides of Eqs. (45) and (56) should be multiplied by the probability $\Pr[-\tau \le k_1 \le \tau]$ that the random stiffness k_1 is in the interval $[-\tau, \tau]$.
- The right-hand sides of Eqs. (A.23) and (A.26) should be divided by the probability $\Pr[\sum_{f=1}^{n} b_f k_f \le b_0]$, which can be computed by relying on the technique described by Mignolet and Lin (1992).

Reference

Mignolet, M. P., and Lin, C. C., 1992, "Probability and Conditional Moments of Multivariate Uniform Random Variables Satisfying a Linear Inequality Constraint," *Probabilistic Engineering Mechanics*, Vol. 7, pp. 67–74.

S. Dutta
Department of Mechanical Engineering,
University of South Carolina,
Columbia, SC 29208

J.-C. Han

Y. Zhang

Department of Mechanical Engineering,
Turbine Heat Transfer Laboratory,
Texas A&M University,
College Station, TX 77843

C. P. Lee
General Electric Company,
Cincinnati, OH 45215

Local Heat Transfer in a Rotating Two-Pass Triangular Duct With Smooth Walls

Earlier heat transfer studies with orthogonal rotation were conducted mostly on ducts of square cross section. This paper reports a different cross section, a triangular duct. Unlike a square cross section, the triangular shape provides more restriction to the formation of the secondary flows. Moreover, the studied orientation of the right triangular duct avoids formation of symmetric vortex structures in the crossflow plane. This paper presents turbulent heat transfer characteristics of a two-pass smooth-walled triangular duct. One pass is for radial outward flow and the other for radial inward flow. With rotation the radial outward and inward flow directions show different surface heat transfer characteristics. Like a square duct, differences between the trailing and the leading Nusselt number ratios for the triangular duct increase with rotation number. However, the rate of change of Nusselt number ratios with rotation number varies for the two duct geometries. Standard $k-\epsilon$ model predictions for a radial outward flow situation show that the Nusselt number ratio variations with Reynolds number are not drastic for the same rotation number.

Introduction

With the increase of operating costs and sensitivity to environmental pollution, there is a growing need to increase the thermal efficiency of turbines. One way to improve thermal efficiency in turbines is to increase the inlet gas temperature. Hence, turbine blades with higher thermal load handling capabilities are in demand. No suitable material is presently available that can withstand the high level of mechanical stress in a hot operating environment of turbines. Therefore, standard metal blades with special cooling techniques are used. Sophisticated external and internal cooling techniques for turbine blades are needed to sustain the mechanical strength of the blades.

A two-pass rotating channel simulates the conditions of internal serpentine cooling passages of turbine blades. Earlier studies on cooling passages were primarily based on stationary models, which are easier to build and work on. Unlike a stationary-duct flow situation, rotation incorporates Coriolis and centrifugal buoyancy effects in the flow with an asymmetric distribution of velocity and turbulence. Heat transfer performance of the trailing side is superior to that of the leading side in radially outward rotating flow. The radially inward flow performs the opposite way. To understand and improve internal cooling techniques, it is necessary to investigate the heat transfer characteristics in a rotating frame.

There have been relatively fewer experimental studies in rotating channels than in stationary ducts with similar geometrical features. Han et al. (1994) covered the important published literature on turbulent heat transfer in ducts rotating perpendicular to its own axis. Most of the work has been on circular tubes and square or rectangular channels with radial outward flow (Mori et al., 1971; Guidez, 1989; Morris and Ghavami-Nasr, 1991). More complicated test cases were reported after the initial investigation. Taslim et al. (1991a, b) investigated heat transfer in a rotating square duct with opposite rib roughened walls. In a series of publications Wagner et al. (1991a, b, 1992) and Johnson et al. (1994) systematically explored the rotational effects on heat transfer in a serpentine square passage with and without ribs at uniform wall temperature condition. Yang et al. (1992) reported the effect of rotation on heat transfer in a serpentine square channel at constant wall heat flux condition. Han and co-workers studied the smooth and ribbed rotating two-pass square duct with different wall heating conditions (Han et al., 1993, 1994; Zhang et al., 1995; Parsons et al., 1994).

Besides the effects of surface roughness, effects of geometric features of rotating channels are also important. The curved shape of the turbine blade may prohibit the efficient use of square or circular cross-sectional coolant flow channels. Soong et al. (1991) listed experiments conducted in different duct types at different Reynolds numbers and rotation numbers. Based on their survey, the most popular channel geometry was circular followed by square, triangular, and rectangular. Earlier published experimental heat transfer results from a rotating triangular duct reported the total heat transfer characteristics (see Harasgama and Morris, 1988; Clifford et al., 1984). No information on heat transfer patterns from the individual surfaces were given.

This paper presents experimental and numerical results for an orthogonally rotating two-pass triangular duct. The experiment provides the turbulent heat transfer distribution of individual surfaces. Different wall heating conditions (constant wall temperature, constant wall heat flux, and engine condition) are imposed as boundary conditions to vary the centrifugal buoyancy levels. Numerical work is also carried out on a triangular duct with radial outflow and constant temperature walls. The predictions are based on the standard $k-\epsilon$ model. The numerical work is included to give insight to the three-dimensional turbulent flow and more detailed heat transfer patterns, which are difficult to achieve experimentally.

Unlike a square cross section, the triangular shape provides more restriction to the formation of the secondary flows. The right triangular duct used in our experiment avoids symmetric vortex formation and reduces the heat transfer disparities between the leading and trailing surfaces. The detailed heat transfer patterns given here will help strategic alignment of the right triangular duct in a turbine blade. The results obtained for several rotation numbers ($Ro = 0.22$, 0.11, 0.055, and 0.0275) and different wall heating conditions in combination provide a helpful guidance to the designers.

Contributed by the International Gas Turbine Institute and presented at the 39th International Gas Turbine and Aeroengine Congress and Exposition, The Hague, The Netherlands, June 13–16, 1994. Manuscript received by the International Gas Turbine Institute February 15, 1994. Paper No. 94-GT-337. Associate Technical Editor: E. M. Greitzer.

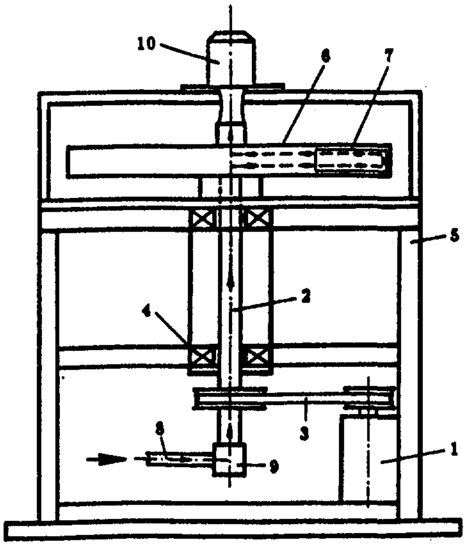

1. Electric Motor with Controller
2. Rotating Shaft
3. Belt Drive Pully System
4. Bearing Support System
5. Steel Table
6. Rotating Arm
7. Test Section
8. Compressor Air
9. Rotary Seal
10. Slip Ring

Fig. 1 Schematic of the rotating rig (from Han et al., 1993)

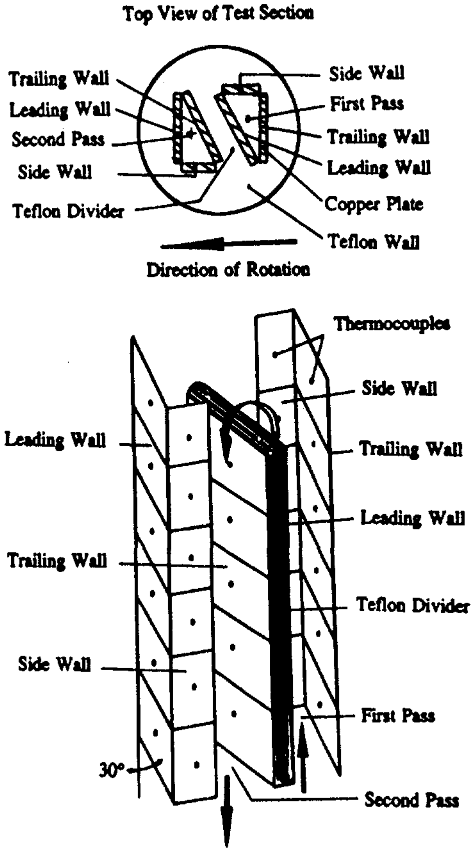
Top View of Test Section

Open view of the two-pass triangular duct

Fig. 2 Illustrative diagram of the two-pass triangular duct

Summary of Experimental Details

A brief description of the experimental setup, discussion on wall heating conditions, and data reduction procedure are included in this section. The experimental rig used by Han et al. (1993, 1994) for a rotating square duct is used here. Detailed illustrated descriptions were included in those two papers, so only a brief description is given here.

Experimental Facility. Regulated compressed air is used as the working fluid. An orifice meter measures the mean flow rate passing through the test section, which rotates in a horizontal plane as shown in Fig. 1. There are two sets of slip ring units. One is interfaced to a personal computer and maintains the connection between thermocouples and the data logger. The other connects power transformers to the heater modules built in the test section. The rotation speed is measured by a digital photo tachometer.

Schematics of the top and open views of the two-pass triangular duct are shown in Fig. 2. The short and medium sides of the triangular passage are 12.7 mm and 25.4 mm, respectively, with an inclusive angle of 90 deg. The heaters are divided into small isolated rectangular copper pieces to minimize wall conduction effect. Each copper piece is 25.4 mm long and is separated by 1.5 mm on all sides from the neighboring pieces. The group of copper elements, laid on one side, share the same input power but are equipped with individual thermocouples to provide local heat transfer coefficients. The two triangular passes are thermally isolated by teflon. The heated test section is preceded by an unheated starting duct, which has the same triangular shape of the test section and is made of teflon.

The hydraulic diameter of the triangular test section is 10.2 mm. The test section length to hydraulic diameter ratio is 30, while each pass is 15 hydraulic diameters long connected by a sharp 180 deg turn. The mean rotating arm length is 37.5 hydraulic diameters. Four Reynolds numbers (2500, 5000, 10,000, and 20,000) based on the hydraulic diameter of the channel are used for this experiment. The duct rotates at 800 rpm, resulting in four rotation numbers (0.22, 0.11, 0.055, 0.0275).

Nomenclature

C_p = specific heat of air
D = hydraulic diameter of the triangular or square duct
DR = coolant to wall density ratio = $(\rho_{bi} - \rho_w)/\rho_{bi} = (T_w - T_{bi})/T_w$
g = centrifugal acceleration
h = heat transfer coefficient
Nu = Nusselt number = hD/k
Nu_0 = Nusselt number in fully developed turbulent pipe flow
q''_{net} = net heat flux at wall
q'' = heat flux at wall
R = mean rotating radius of the heated test section
Re = Reynolds number = $\rho w_0 D/\mu$
Ro = Rotation number = $\Omega D/w_0$
T = local fluid temperature
T_b = bulk mean temperature
T_w = local wall temperature
w = axial velocity (in the z direction)
w_0 = average axial flow velocity through the triangular or square duct
z_0 = distance measured along the duct axis from the start of heating
β = volume expansion coefficient
μ = viscosity of air
ρ = density of air
ρ_0 = density of air at atmospheric pressure
Ω = rotational speed of the two-pass channel

Subscripts

b = bulk mean values
i = inlet values
w = wall values

Wall Heating Conditions. The wall heating conditions are listed in Table 1. The wall temperature profiles in Case A are uniform. The energy input to the heaters are adjusted so that at any cross section of the duct the surrounding walls are within 3°C of each other. Case B is similar to the uniform heat flux condition. The surfaces in Case B with higher Nusselt numbers are kept at a lower temperature than the sides with lower Nusselt numbers. The leading and trailing wall temperatures of Case B are reversed for Case C.

Data Reduction. The local heat transfer coefficient is calculated from the local heat flux, the local wall temperature, and the local bulk mean air temperature difference as

$$h = \frac{q''_{\text{net}}}{T_w - T_b} \tag{1}$$

Local net heat flux (q''_{net}) is obtained by subtracting heat loss for the power supplied to the heaters. Heat loss is estimated by running a separate test on the same test configuration but without air flow (no-flow condition) in the duct. Characteristic heat loss lines are obtained for each of the isolated rectangular copper pieces. The inlet and outlet openings for the rotating test section are located at more than 120 hydraulic diameters distance. This no-flow heat loss determination method was tested to be satisfactory on a similar rotating test rig. The local wall temperature (T_w) is obtained from the thermocouple reading of that heater section. A linear interpolation between measured inlet (one thermocouple) and outlet (two thermocouples) bulk temperatures is used for the local bulk temperature (T_b). The inlet temperature is observed to be higher than the ambient (9 to 16°C above ambient). Inlet temperature is higher for lower Reynolds number flow. This increase in inlet temperature is due to the transfer of heat by conduction to the unheated starting teflon duct of the test section and the exchange of heat with the outgoing heated air (17 to 31°C above ambient) from the second pass through the 13-mm-thick teflon divider wall. The calculated and measured outlet bulk mean temperatures are within 3°C and show satisfactory heat balance in the measurements.

To reduce the influence of flow Reynolds number on the heat transfer coefficient, the local Nusselt number is normalized by the Nusselt number for fully developed turbulent flow in smooth stationary pipe, correlated by Dittus–Boelter/McAdams (Rohsenow and Choi, 1961) as

$$\frac{\text{Nu}}{\text{Nu}_0} = \frac{hD}{k_{\text{air}}} \frac{1}{(0.023\ \text{Re}^{0.8}\ \text{Pr}^{0.4})} \tag{2}$$

The Prandtl number, Pr, for air is taken to be 0.72. The value of thermal conductivity of air, k_{air}, is taken at the average of the inlet and outlet bulk mean air temperatures.

Table 1 Coolant-to-wall density ratios (DR) applied to walls for different wall heating conditions

Density Ratio (T_w)	Case A	Case B	Case C
Side walls	0.12 (62°C)	0.1 (55°C)	0.1 (55°C)
Leading wall - Pass 1	0.12 (62°C)	0.14 (70°C)	0.1 (55°C)
Leading wall - Pass 2	0.12 (62°C)	0.1 (55°C)	0.14 (70°C)
Trailing wall - Pass 1	0.12 (62°C)	0.1 (55°C)	0.14 (70°C)
Trailing wall - Pass 2	0.12 (62°C)	0.14 (70°C)	0.1 (55°C)

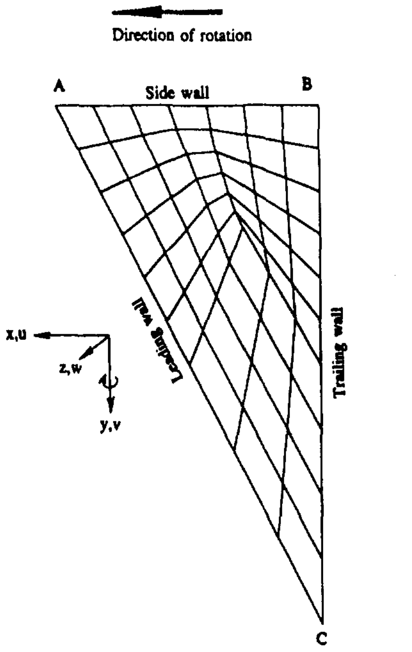

Fig. 3 Typical grid distribution for the triangular duct

Uncertainty. The uncertainty of the local heat transfer coefficient depends on the uncertainties in the local wall and bulk air temperature difference and the net heat input for each test section. This uncertainty increases with decreasing both the local wall to air temperature difference and the net heat flux. Based on the method described by Kline and McClintock (1953), the typical uncertainty in the Nusselt number is estimated to be less than 7 percent for Reynolds numbers larger than 5000. The maximum uncertainty, however, could be up to 20 percent for the lower heat transfer coefficient at the lowest Reynolds number tested (Re = 2500).

Summary of Numerical Details

A standard $k-\epsilon$ model of a commercial finite element analysis package, FIDAP (Version 6.01), is used for predictions. Galerkin formulation for the method of weighted residuals is used. The pressure and velocity interlinkage has been solved by the penalty function approach. The x, y, and z coordinates are shown in Fig. 3.

Governing Equations. The equations are based on a rotating coordinate system. The continuity equation is

$$\frac{\partial}{\partial x}(\rho u) + \frac{\partial}{\partial y}(\rho v) + \frac{\partial}{\partial z}(\rho w) = 0 \tag{3}$$

The momentum equations are

$$\begin{aligned} &\frac{\partial}{\partial x}(\rho uu) + \frac{\partial}{\partial y}(\rho uv) + \frac{\partial}{\partial z}(\rho uw) \\ &\quad = -\frac{\partial p}{\partial x} - 2\rho\Omega w + \frac{\partial}{\partial x}\left(\mu_e \frac{\partial}{\partial x} u\right) + \frac{\partial}{\partial y}\left(\mu_e \frac{\partial}{\partial y} u\right) \\ &\quad\quad + \frac{\partial}{\partial z}\left(\mu_e \frac{\partial}{\partial z} u\right) + S^u \end{aligned} \tag{4}$$

$$\begin{aligned} &\frac{\partial}{\partial x}(\rho uv) + \frac{\partial}{\partial y}(\rho vv) + \frac{\partial}{\partial z}(\rho vw) = -\frac{\partial p}{\partial y} + \frac{\partial}{\partial x}\left(\mu_e \frac{\partial}{\partial x} v\right) \\ &\quad + \frac{\partial}{\partial y}\left(\mu_e \frac{\partial}{\partial y} v\right) + \frac{\partial}{\partial z}\left(\mu_e \frac{\partial}{\partial z} v\right) + S^v \end{aligned} \tag{5}$$

$$\frac{\partial}{\partial x}(\rho u w) + \frac{\partial}{\partial y}(\rho v w) + \frac{\partial}{\partial z}(\rho w w) = -\frac{\partial\left(p - \frac{\rho\Omega^2 z^2}{2}\right)}{\partial z} + 2\rho\Omega u + \frac{\partial}{\partial x}\left(\mu_e \frac{\partial}{\partial x} w\right) + \frac{\partial}{\partial y}\left(\mu_e \frac{\partial}{\partial y} w\right) + \frac{\partial}{\partial z}\left(\mu_e \frac{\partial}{\partial z} w\right) + S^w - \rho\beta g(T - T_i) \quad (6)$$

The effective viscosity, μ_e, is modeled to account for both laminar and turbulent viscosities as

$$\mu_e = \mu + \mu_t; \quad \mu_t = \rho C_\mu \frac{k^2}{\epsilon} \quad (7)$$

The temperature, T, transport equation is

$$\frac{\partial}{\partial x}(\rho u T) + \frac{\partial}{\partial y}(\rho v T) + \frac{\partial}{\partial z}(\rho w T) = \frac{\partial}{\partial x}\left(\left(\frac{\mu}{\mathrm{Pr}}\right)_e \frac{\partial}{\partial x} T\right) + \frac{\partial}{\partial y}\left(\left(\frac{\mu}{\mathrm{Pr}}\right)_e \frac{\partial}{\partial y} T\right) + \frac{\partial}{\partial z}\left(\left(\frac{\mu}{\mathrm{Pr}}\right)_e \frac{\partial}{\partial z} T\right) + S^T \quad (8)$$

where S^T includes the heat source and viscous dissipation terms. The effective diffusivity, $(\mu/\mathrm{Pr})_e$, is given as

$$\left(\frac{\mu}{\mathrm{Pr}}\right)_e = \frac{\mu}{\mathrm{Pr}} + \frac{\mu_t}{\mathrm{Pr}_t} \quad (9)$$

The k and ϵ transport equations are

$$\frac{\partial}{\partial x}(\rho u k) + \frac{\partial}{\partial y}(\rho v k) + \frac{\partial}{\partial z}(\rho w k) = \frac{\partial}{\partial x}\left(\frac{\mu_t}{\sigma_k}\frac{\partial}{\partial x} k\right) + \frac{\partial}{\partial y}\left(\frac{\mu_t}{\sigma_k}\frac{\partial}{\partial y} k\right) + \frac{\partial}{\partial z}\left(\frac{\mu_t}{\sigma_k}\frac{\partial}{\partial z} k\right) + P + P_\beta - \rho\epsilon \quad (10)$$

$$\frac{\partial}{\partial x}(\rho u \epsilon) + \frac{\partial}{\partial y}(\rho v \epsilon) + \frac{\partial}{\partial z}(\rho w \epsilon) = \frac{\partial}{\partial x}\left(\frac{\mu_t}{\sigma_\epsilon}\frac{\partial}{\partial x} \epsilon\right) + \frac{\partial}{\partial y}\left(\frac{\mu_t}{\sigma_\epsilon}\frac{\partial}{\partial y} \epsilon\right) + \frac{\partial}{\partial z}\left(\frac{\mu_t}{\sigma_\epsilon}\frac{\partial}{\partial z} \epsilon\right) + C_1(P + (1 - C_3)P_\beta)\frac{\epsilon}{k} - C_2\rho\frac{\epsilon^2}{k} \quad (11)$$

The production term, P, is given as

$$P = \mu_t\left(2\left[\left(\frac{\partial u}{\partial x}\right)^2 + \left(\frac{\partial v}{\partial y}\right)^2 + \left(\frac{\partial w}{\partial z}\right)^2\right] + \left[\frac{\partial u}{\partial y} + \frac{\partial v}{\partial x}\right]^2 + \left[\frac{\partial u}{\partial z} + \frac{\partial w}{\partial x}\right]^2 + \left[\frac{\partial w}{\partial y} + \frac{\partial v}{\partial z}\right]^2\right) \quad (12)$$

The constants used above have the following values: $\mathrm{Pr} = 0.72$, $\mathrm{Pr}_t = 0.9$, $\sigma_k = 1.0$, $\sigma_\epsilon = 1.3$, $C_\mu = 0.09$, $C_1 = 1.44$, $C_2 = 1.92$, and $C_3 = 0.8$. The buoyancy-related turbulence production term is given as

$$P_\beta = \frac{\mu_t g \beta}{\mathrm{Pr}_t}\frac{\partial T}{\partial z} \quad (13)$$

The near-wall velocity and temperature are calculated from the universal logarithmic profiles. The k and ϵ equations are not solved in the near wall layer and in this region the Van Driest mixing length approach is adopted to model the turbulent viscosity. Detailed wall function treatments are available in the manuals of FIDAP. Initial calculation of wall heat flux as $q'' = k_{\mathrm{air}}(dT/dy)_{\mathrm{wall}}$ caused severe underprediction of Nusselt number from all three surfaces of the duct. Therefore, postprocessing of wall heat flux is done based on the effective wall diffusivity as

$$q'' = \frac{\mu C_p}{\mathrm{Pr}_t}\frac{y^+}{2.5\ln(9y^+) + P_{fn}}\left(\frac{dT}{dy}\right)_{\mathrm{wall}} \quad (14)$$

where P_{fn} is defined as (Jayatilleke, 1969)

$$P_{fn} = 9.24((\mathrm{Pr}/\mathrm{Pr}_t)^{0.75} - 1) \times [1 + 0.28\exp(-0.007\,\mathrm{Pr}/\mathrm{Pr}_t)] \quad (15)$$

The normalized distance from the wall, y^+, is computed as

$$y^+ = \frac{\rho y}{\mu} C_\mu^{0.25} k^{0.5} \quad (16)$$

Note that since the temperature gradient is calculated at the wall, a near-wall location is needed for proper evaluation of y^+. In this work, the Reynolds number has been varied by changing the density of air. The temperature gradient at the wall includes the effects of density variations and, therefore y is calculated as $y = (\rho_0/\rho)y_p$, to keep the near-wall diffusivity independent of density effects. y_p is the average distance of the near wall node from the wall.

Nusselt number calculations are performed as

$$\mathrm{Nu} = \frac{q'' D}{(T_w - T_b)k_{\mathrm{air}}} \quad (17)$$

where q'' is the average heat flux in the related surface at the desired radial location and k_{air} is the thermal conductivity of air. The bulk temperature, T_b, is calculated by the usual mass-average technique.

Features Added to the Standard $k-\epsilon$ Model. The standard $k-\epsilon$ model is expanded to include the rotational effects as shown in Eqs. (3) to (16). The one-pass rotating duct is modeled in a coordinate frame that rotates with the duct. The key features added to the standard three-dimensional $k-\epsilon$ model are:

- Coriolis effects in axial momentum and crossflow momentum equations,
- the centrifugal buoyancy effect, by assigning a gravitational acceleration of $\Omega^2 R$, and
- generation of turbulent kinetic energy from buoyancy effect.

Computation Domain and Boundary Conditions. The triangular duct cross section is discussed in an earlier section of this paper. Unlike the experimental setup, the duct modeled is one-pass with radially outward flow at Re = 5000 and Ro = 0.11. The duct modeled is 50 hydraulic diameters long. The results presented are for 30 to 45 hydraulic diameters corresponding to a mean rotating radius of 37.5 hydraulic diameters. Uniform axial velocity and zero cross-stream velocities are assigned at the inlet. The k and ϵ at the inlet are given as $k = 0.2$ percent of w_0^2 and $\epsilon = C_\mu k^{1.5}/D$. Due to an unheated starting length of 30 hydraulic diameters, the predictions are sufficiently independent of the inlet conditions. The three walls are maintained at DR = 0.12 (similar to Case A of the experiment) from 30 hydraulic diameters. Standard outflow conditions are given at the outlet.

Grid Independence and Convergence Criteria. Three grid densities with 450, 750, and 1700 nodal points are tested for grid independence. The axial velocities predicted by the three grid densities are within 8 percent of each other. Figure 3 shows a typical grid distribution. Three-dimensional brick elements with eight nodes are used. The results presented are with the densest grid distribution (1700 nodal points). The y^+ (normalized distance from the wall) values obtained are greater than 30 and less than 100 except for the corner region of the triangular duct, which signifies that most of the computational domain is in the turbulent flow regime. With rotational terms included in the momentum equations, the standard convergence criterion of mass residue fail to work with FIDAP (see manual of FIDAP, Version 6.01). This is related to the way the program handles pressure at the exit plane. Hence, spot values are monitored and less than 0.5 percent variation is observed for the flow related quantities at the region of interest (30 to 45 hydraulic diameters) in the last 10 iterations. Note that the finite element procedure takes fewer iterations to converge than required for the finite difference method. Therefore, almost no change in solution in the last ten iterations for a finite element formulation can be considered as a convergence criterion.

Results and Discussion

The experimental results on heat transfer are discussed first followed by the numerical predictions.

Experimental Results. Figure 4 presents the local Nusselt number ratios for rotation numbers of 0.22 and 0.0275 for Case A. Unlike a square duct (Han et al., 1992, 1993), at Ro = 0, because of the asymmetric shape of the triangular duct the three surfaces show different Nusselt numbers. In this figure the rotational heat transfer data are compared with the stationary duct results. For the first pass, at higher rotation number (Ro = 0.22) the Nusselt number ratio increases for the trailing side and decreases for the other two sides with rotation. The increase or decrease in Nusselt number is related to the changes in the axial velocity and turbulence distribution in the duct. The secondary velocities caused by rotation are of the order of one tenth of the mainstream velocity and have less direct effect (by convection) on heat transfer. The indirect effects of the secondary flow come through the asymmetric distribution of the axial velocity. With rotation, the core flow shifts toward the trailing side and away from the leading and side walls. Higher axial velocity near the trailing side increases heat transfer from this surface.

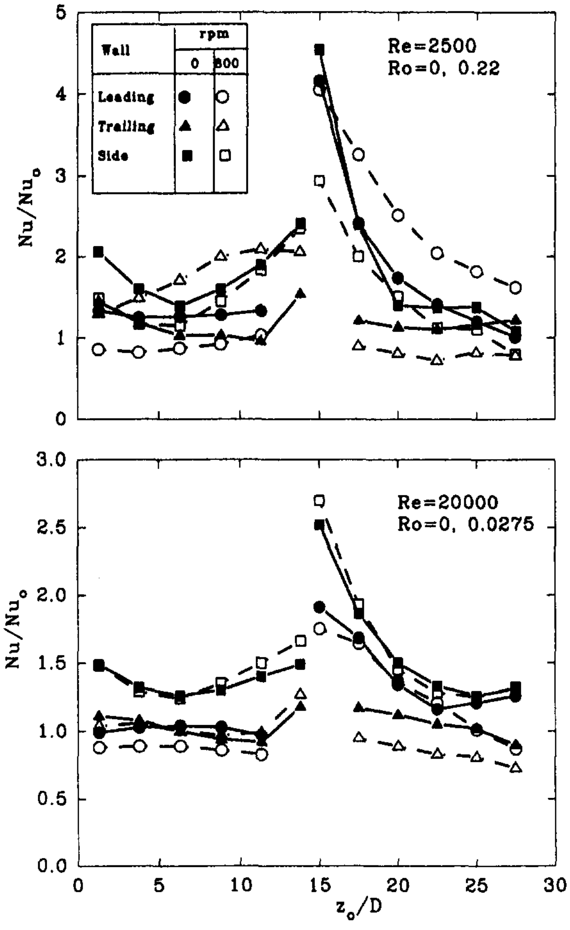

Fig. 4 Surface-averaged local Nusselt numbers at different locations of the triangular duct for Case A

In the second pass, due to radially inward flow, the core flow region shifts near the leading side. Thus the Nusselt number ratio for the leading side increases with rotation in the second pass and the other two surfaces show a decrease with rotation, as shown in Fig. 4. As expected, for a lower rotation number (Ro = 0.0275) the changes in Nusselt number ratios for the side walls and the first pass trailing and the second pass leading are much smaller than for the higher rotation number (Ro = 0.22). But the decrease in Nusselt number for the first pass leading and the second pass trailing are distinctly noticeable and are believed to be caused by the stabilization of the boundary layer with rotation (see Johnston et al., 1972).

Downstream of the sharp 180 deg turn, both stationary and rotating conditions show a sharp rise in Nusselt number (see Fig. 4). The alignment of the two-pass triangular duct (Fig. 2) is such that the wide side of the first pass triangular passage meets the narrow end of the second pass and the narrow end of the first pass expands to join the wide end of the second pass. Moreover, the turn direction is not perpendicular to the plane of rotation. Therefore, the secondary flows developed in the turn are in favorable direction to the secondary flows caused by rotation. The sudden change in duct geometry and favorable secondary flow developed in the turn together enhance the heat transfer at downstream locations of the bend. This enhancement of heat transfer decays rapidly as the flow develops through the second pass, as shown in Fig. 4.

Figure 5 shows the Nusselt number ratios for Case B at similar rotating flow conditions of Case A (Figure 4). Case A Nusselt number ratios with rotation are plotted for comparison with rotational data of Case B. The Coriolis effect, which is proportional to the rotation number, is of the same order for the two cases, Case A and Case B. But the centrifugal buoyancy effects are stronger in Case B. Stronger centrifugal buoyancy shifts the core flow to the corner of the trailing edge and side wall in the first pass (see predictions of Prakash and Zerkle, 1992, with higher density ratio). This shift in the core flow increases Nusselt numbers from the side wall and the trailing surface and decreases Nusselt number for leading surface at higher rotation number (Ro = 0.22) in Case B for radially outward flow condition of the first pass. In the second pass, the differences between Case A and Case B in leading and trailing surface heat transfer characteristics are opposite to the trend observed in the first-pass results. At lower rotation number (Ro = 0.0275) the changes in Nusselt numbers with heating conditions are insignificant.

Figure 6 illustrates the effect of rotation number at selected locations of the triangular duct for all three heating conditions. The square duct results for Case A from Han et al. (1993) at available nearby locations are included for comparison. Note that the lines are used as a visual aid to illustrate the experimental data and not to interpolate. It is observed that wall heating conditions (centrifugal buoyancy effect) can significantly alter the Nusselt number ratios. For the locations in the first pass (z_0/D = 6.25 and 11.25), the triangular duct Nusselt number

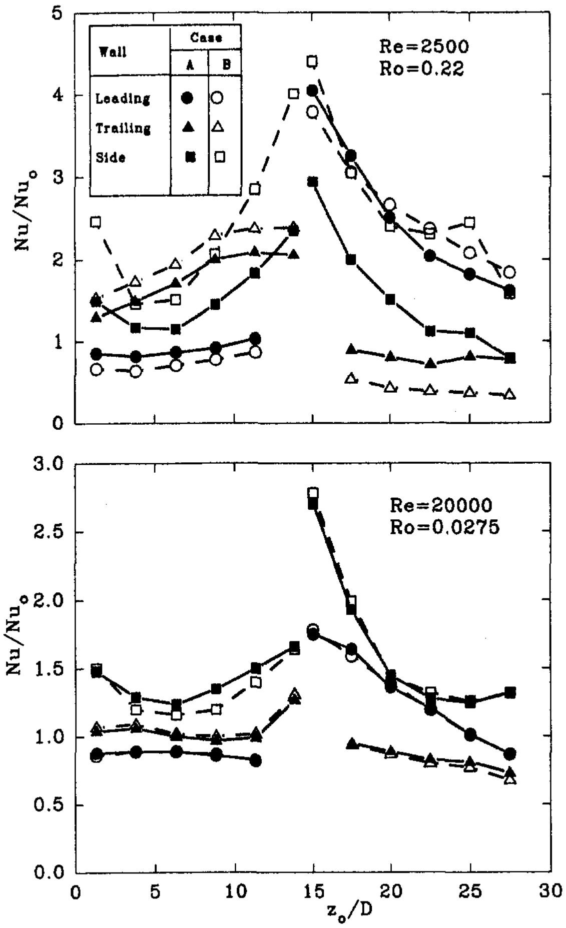

Fig. 5 Surface-averaged local Nusselt numbers at different locations of the triangular duct for Cases A and B

ratios for Case A are mostly contained within the limits imposed by the square duct. This is because in a triangular duct, there is less space for the fluid to form secondary flow. In the second pass, at $z_0/D = 17.5$ the leading side of triangular duct shows very high Nusselt number ratio compared to the square duct. An increase of up to 120 percent over the square duct results is noted at the second pass leading surface. This is due to more intense mixing and a favorable secondary flow in the 180 deg bend for the triangular duct configuration. Note that the bend for the square duct of Han et al. (1993) was in a plane perpendicular to the plane of rotation. Thus the secondary flow induced by the turn must have negated the rotational secondary flow. This reduction in secondary flow in the square duct brought the leading and trailing side Nusselt number ratios closer to each other downstream of the turn (entrance region of the second pass).

The Nusselt number ratio for other two heating conditions (Case B and Case C) are also shown in Fig. 6. The Nu/Nu_0 difference between the leading and trailing sides for Case B is slightly greater than Case A for the triangular duct. For a square duct, Han et al. (1993) observed the difference in Nusselt number ratio between the leading and trailing sides reduce for Case B than Case A. The reverse trend observed for the triangular duct may be due to the differences caused by the geometries of the ducts. Figure 6 shows that the Nusselt number ratio for Case C is least among the group for first-pass and second-pass leading surfaces.

Numerical Predictions. "The numerical predictions match well with the experimental data," has become a cliche in the technical papers, where authors try to establish the validity of their predictions. Duplication of exact data is pertinent to the studies that compare the model performances. For this work, only the standard $k-\epsilon$ model is included. Therefore, instead of repeating the experimental data by predictions for all the flow situations, the simplest flow condition has been selected. Besides the average heat transfer, other flow-related parameters and detailed distribution of Nusselt numbers are predicted to give more insight to the problem at hand. The flow with outward flow at rotation number Ro = 0.11 and Re = 5000 is selected for this numerical discussion. A higher rotation number signifies lower Reynolds number for the corresponding experimental data. Lower Reynolds number flows are difficult to predict with the standard $k-\epsilon$ model (high Reynolds number model). On the other hand, a lower rotation number with higher Reynolds number shows fewer effects of rotation. As mentioned earlier, the duct modeled is one pass with radial outward flow, which is similar to the first pass of the experiment. The walls are maintained at uniform temperatures like Case A.

Figure 7 compares the secondary flow vortex structure of the square duct with the triangular duct. Unlike the square duct, the triangular duct provides restricted flow area for the fluid to establish a secondary flow near the narrow corner. Therefore the triangular duct has one dominant circulation cell and one smaller cell compared to two symmetric vortex structures pres-

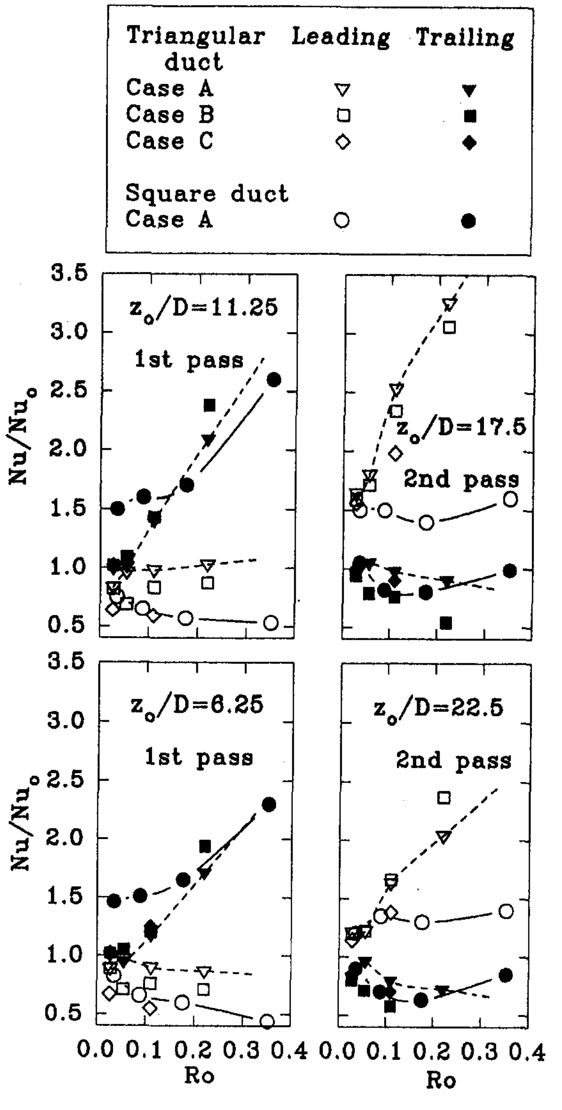

Fig. 6 Effect of rotation number on Nusselt number ratio at selected locations of the duct and comparison with the square duct results

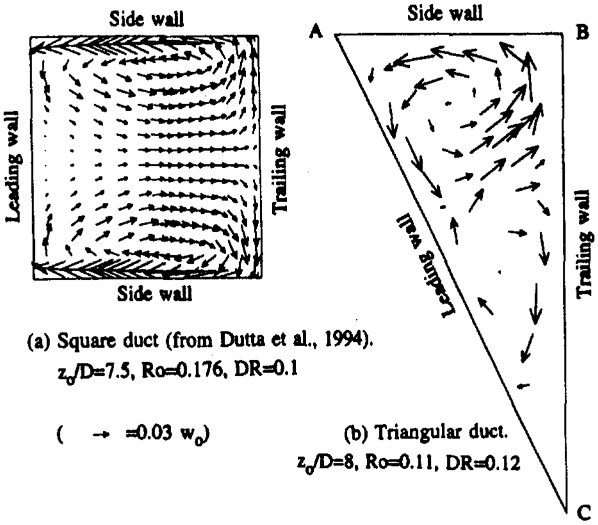

(a) Square duct (from Dutta et al., 1994). z_0/D=7.5, Ro=0.176, DR=0.1

(→ =0.03 w_0)

(b) Triangular duct. z_0/D=8, Ro=0.11, DR=0.12

Fig. 7 Vector plots of the secondary flow predicted by standard $k-\epsilon$ model

ent in the square duct (Dutta et al., 1994). However, the dominant vortex of the triangular duct is stronger than the vortex formed in a square duct. This is because unlike a square duct, in the triangular duct bulk of the flow is in the wider portion (toward side wall AB). Therefore, the source of the secondary flow momentum ($2\Omega w$) is stronger in the wider half of the triangular cross section than a square shape, where the w velocity is more uniformly distributed in the crossflow plane.

Figure 8 shows the contour plots for turbulent kinetic energy and mainstream velocity at $z_0/D = 8$. It is of interest to note that, though the axial velocities at the corners are less, the turbulence levels are higher near the corners than the core flow. The highest turbulence is observed near corner B of the triangular duct (junction of side and trailing walls). The peak axial velocity is nearer the trailing edge (BC) and farther from the side wall (AB) and the leading wall (AC). This explains the drop in Nusselt number for side and leading walls and the increases for trailing wall in the first pass (see Fig. 4) with rotation.

The prediction and experimental data of local surface averaged Nusselt number are shown in Fig. 9. Predictions for Re = 5000 and Ro = 0.11 compare satisfactorily with the experimental data. Predictions at two Reynolds numbers other than Re = 5000 are included in Fig. 9 for comparison. The Reynolds numbers of 25,000 and 50,000 are obtained by varying the density of the air. Hence, the average axial velocity and the rotation number remain the same for all three flow situations. Comparison of Nusselt number ratio (Fig. 9) shows that the effect of Reynolds number is not significant on the heat transfer patterns at Ro = 0.11 and DR = 0.12. Therefore, the experimental data obtained at atmospheric condition may infer the results for pressurized test condition at similar rotation numbers.

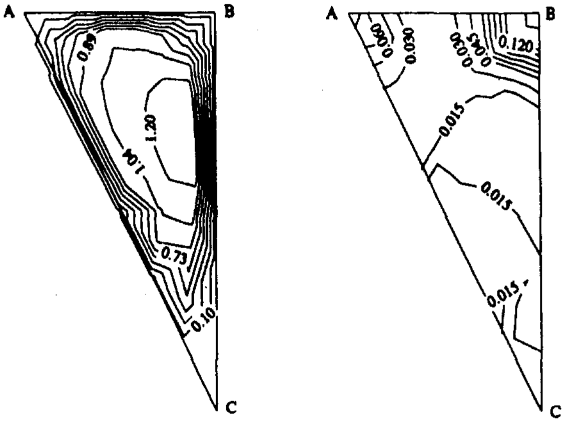

(a) Axial velocity, w/w_0 (b) Turbulent kinetic energy, k/w_0^2

z_0/D=8, Re=5000, Ro=0.11, DR=0.12.

Fig. 8 Contour plots of predicted flow-related quantities

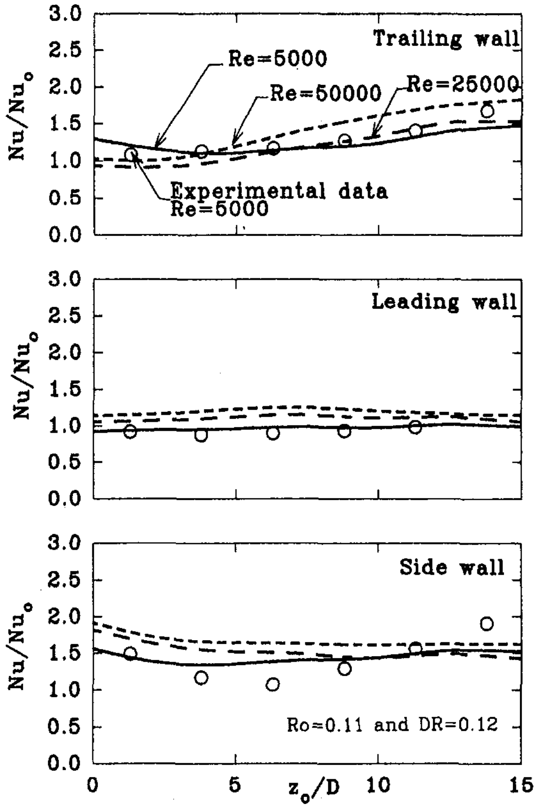

Fig. 9 Prediction of surface-averaged local Nusselt number ratios at R_o = 0.11

Figure 10 shows the isotherms in the fluid at the cross section of $z_0/D = 8$. The local distribution of Nusselt number for the three enclosure surfaces are also included. It is to be remembered that the Nusselt number results predicted here are for uniform wall temperature condition and therefore wall conduction effects are absent. The isotherms are similar to the axial velocity contour plot (Fig. 8(a)). Higher temperature correlates with lower axial velocity. The profile of local Nusselt number ratios for the three surfaces at $z_0/D = 8$ is also plotted in Fig. 10. All three corners show a reduction in Nusselt numbers. The peaks in Nusselt numbers on trailing and side walls correspond to the locations with higher turbulence (see Fig. 8(b)).

Figure 11 shows the contour plot of the Nusselt number ratios for the three surfaces of the triangular duct. The local Nusselt number predictions of the side wall do not show significant change along the duct. But the local Nusselt numbers increase in leading and trailing walls with z_0/D. In a stationary duct, the local Nusselt numbers will decrease gradually to a fully developed value as the thermal boundary layer thickens and reaches a stable profile. But in rotation, the centrifugal buoyancy redistributes the velocity and related quantities in the heated section of the duct and results are different from a stationary configuration. In a square duct, the centrifugal buoyancy tends to increase the Nusselt number at the trailing wall and decrease the Nusselt number in the leading wall with z_0/D (Dutta et al., 1994), whereas in a triangular duct both the leading and trailing surfaces show an increase in Nusselt number ratio with z_0/D. This is because, in the triangular duct, the fluid of the wider half is cooler than the fluid of the other half. The rotational buoyancy accelerates the cooler heavy fluid and the flow concentrates near the centroid of the triangle rather than toward the trailing edge, as is the case for a square duct. This increase in velocity near the middle of the triangular cross section helps to increase the Nusselt number ratio from both the leading and trailing sides of the triangular duct.

Conclusions

The following inferences are made from this experimental and numerical study. The sequence of highlighted observations presented is based on the sequence of discussion in this paper and does not conform to the hierarchy of importance. The square duct referred to in this section is the duct used by Han et al. (1993).

Conclusions Based on Experimental Data

- Nusselt number increases with rotation at the trailing side and reduces at the leading side. However, the Nusselt number difference between the trailing and leading sides in the triangular duct is smaller than that in the square duct in radially outward flow.
- For radially inward flow the changes in the Nusselt number at trailing and leading surfaces are reversed. The difference between the trailing and leading sides is greater than the square duct. This is because significant enhancement of Nusselt number ratio at the leading side occurs at immediate downstream locations of the 180 deg bend irrespective of the flow and heating conditions. The stationary duct results indicate that the 180 deg bend influences the downstream heat transfer results up to eight hydraulic diameters and beyond.
- The differences between the leading and trailing side Nusselt number ratios increase with the rotation number for both passes of the triangular duct, while the differences increase with rotation number only in the first pass for the square duct.
- Uniform wall heat flux (Case B) increases the differences between the local Nusselt number ratios of the trailing and leading walls over the differences observed for uniform wall temperature (Case A) at the same Reynolds numbers. However, the effect of heating condition, that is the changes in the local Nusselt number ratios of the trailing and leading walls with the two heating conditions (Cases A and B), in the triangular duct is relatively smaller than in the square duct.

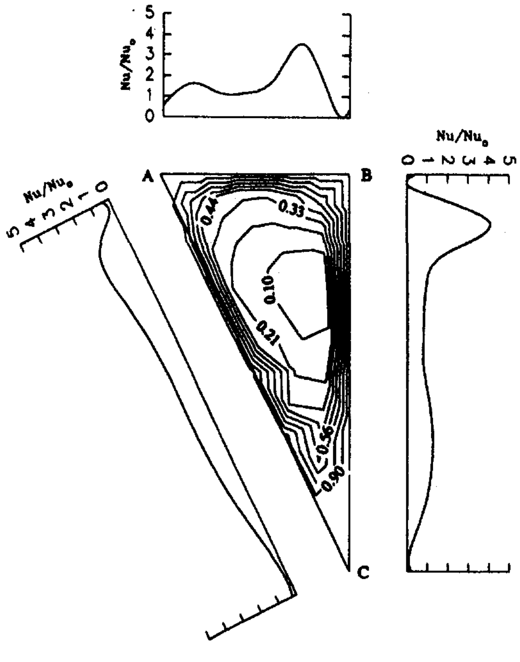

Fig. 10 Prediction of $(T - T_i)/(T_w - T_i)$ contours and local Nusselt number ratios

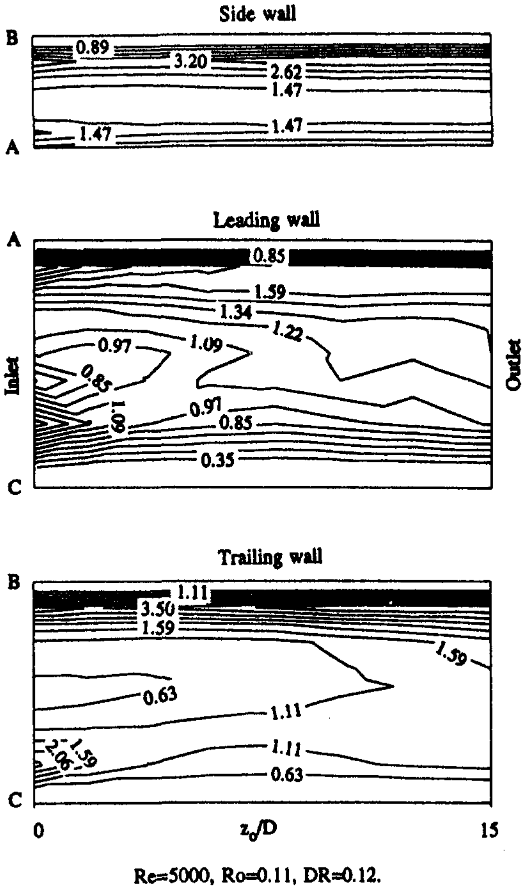

Fig. 11 Contour plots of predicted local Nusselt number ratios for three surfaces of the triangular duct

Conclusions Based on Standard $k-\epsilon$ Predictions.

- The triangular duct has one dominant vortex structure at the broad section and one smaller vortex at the narrow corner in the cross flow plane. However, the square duct has two symmetric counterrotating vortices.
- Predictions with standard $k-\epsilon$ model compare reasonably well with the experimental data. Effect of Reynolds number (with variation of density) on Nusselt number ratio is not appreciably large.
- The differences in Nusselt numbers between the trailing and leading surfaces are mainly due to the asymmetric distribution of the axial velocity.
- The Nusselt numbers at the three corners are less than the Nusselt numbers at the remaining areas. There are peaks in Nusselt number profiles associated with high turbulence in corresponding locations.

Acknowledgments

The experimental work was sponsored by General Electric Aircraft Engines. Research grant of computer time allocated by the Supercomputing Center, Texas A&M University, College Station, Texas was used for the numerical work. Their support is gratefully acknowledged.

References

Clifford, R. J., Morris, W. D., and Harasgama, S. P., 1984, "An Experimental Study of Local and Mean Heat Transfer in a Triangular-Sectioned Duct Rotating in the Orthogonal Mode," ASME *Journal of Engineering for Gas Turbines and Power*, Vol. 106, pp. 661–667.

Dutta, S., Andrews, M. J., and Han, J. C., 1994, "Numerical Prediction of Turbulent Heat Transfer in a Rotating Square Duct With Variable Rotational Buoyancy Effects," presented at the 6th AIAA/ASME Thermophysics and Heat Transfer Conference, Colorado Springs, CO, June 20–23.

Guidez, J., 1989, "Study of the Convective Heat Transfer in Rotating Coolant Channels," ASME JOURNAL OF TURBOMACHINERY, Vol. 111, pp. 43–50.

Han, J. C., Zhang, Y. M., and Kalkuehler, K., 1993, "Uneven Wall Temperature Effect on Local Heat Transfer in a Rotating Two-Pass Square Channel With Smooth Walls," ASME *Journal of Heat Transfer*, Vol. 115, pp. 912–920.

Han, J. C., Zhang, Y. M., and Lee, C. P., 1994, "Influence of Surface Heating Condition on Local Heat Transfer in a Rotating Square Channel With Smooth Walls and Radial Outward Flow," ASME JOURNAL OF TURBOMACHINERY, Vol. 116, pp. 149–158.

Harasgama, S. P., and Morris, W. D., 1988, "The Influence of Rotation on the Heat Transfer Characteristics of Circular, Triangular, and Square-sectioned Coolant Passages of Gas Turbine Rotor Blades," ASME JOURNAL OF TURBOMACHINERY, Vol. 110, pp. 44–50.

Jayatilleke, C. L. V., 1969, "The Influence of Prandtl Number and Surface Roughness on the Resistance of the Laminar Sub-layer to Momentum and Heat Transfer," *Progress in Heat and Mass Transfer*, Vol. 1, pp. 193–329.

Johnson, B. V., Wagner, J. H., Steuber, G. D., and Yeh, F. C., 1994, "Heat Transfer in Rotating Serpentine Passages With Trips Skewed to the Flow," ASME JOURNAL OF TURBOMACHINERY, Vol. 116, pp. 113–123.

Johnston, J. P., Halleen, R. M., and Lezius, D. K., 1972, "Effect of Spanwise Rotation on the Structure of Two-Dimensional Fully Developed Turbulent Channel Flow," *Journal of Fluid Mechanics*, Vol. 56, Part 3, pp. 533–557.

Kline, S. J., and McClintock, F. A., 1953, "Describing Uncertainties in Single-Sample Experiments," *Mechanical Engineering*, Jan., pp. 3–8.

Mori, Y., Fukada, T., and Nakayama, W., 1971, "Convective Heat Transfer in a Rotating Radial Circular Pipe (2nd Report)," *International Journal of Heat and Mass Transfer*, Vol. 14, pp. 1807–1824.

Morris, W. D., and Ghavami-Nasr, G., 1991, "Heat Transfer Measurements in Rectangular Channels With Orthogonal Mode Rotation," ASME JOURNAL OF TURBOMACHINERY, Vol. 113, pp. 339–345.

Parsons, J. A., Han, J. C., and Zhang, Y. M., 1994, "Wall Heating Effect on Local Heat Transfer in a Rotating Two-Pass Square Channel With 90° Rib Turbulators," accepted for publication in the *International Journal of Heat and Mass Transfer*.

Prakash, C., and Zerkle, R., 1992, "Prediction of Turbulent Flow and Heat Transfer in a Radially Rotating Square Duct," ASME JOURNAL OF TURBOMACHINERY, Vol. 114, pp. 835–846.

Rohsenow, W. M., and Choi, H., 1961, *Heat, Mass and Momentum Transfer*, Prentice-Hall, Inc., Englewood Cliffs, NJ, pp. 192–193.

Soong, C. Y., Lin, S. T., and Hwang, G. J., 1991, "An Experimental Study of Convective Heat Transfer in Radially Rotating Rectangular Ducts," ASME *Journal of Heat Transfer*, Vol. 113, pp. 604–611.

Taslim, M. E., Rahman, A., and Spring, S. D., 1991a, "An Experimental Investigation of Heat Transfer Coefficients in a Spanwise Rotating Channel With Two Opposite Rib-Roughened Walls," ASME JOURNAL OF TURBOMACHINERY, Vol. 113, pp. 74–82.

Taslim, M. E., Bondi, L. A., and Kercher, D. M., 1991b, "An Experimental Investigation of Heat Transfer in an Orthogonally Rotating Channel Roughened With 45 Degree Criss-Cross Ribs on Two Opposite Walls," ASME JOURNAL OF TURBOMACHINERY, Vol. 113, pp. 346–353.

Wagner, J. H., Johnson, B. V., and Hajek, T. J., 1991a, "Heat Transfer in Rotating Passages With Smooth Walls and Radial Outward Flow," ASME JOURNAL OF TURBOMACHINERY, Vol. 113, pp. 42–51.

Wagner, J. H., Johnson, B. V., and Kopper, F. C., 1991b, "Heat Transfer in Rotating Serpentine Passages With Smooth Walls," ASME JOURNAL OF TURBOMACHINERY, Vol. 113, pp. 321–330.

Wagner, J. H., Johnson, B. V., Graziani, R. A., and Yeh, F. C., 1992, "Heat Transfer in Rotating Serpentine Passages With Trips Normal to the Flow," ASME JOURNAL OF TURBOMACHINERY, Vol. 114, pp. 847–857.

Yang, W. J., Zhang, N., and Chiou, J., 1992, "Local Heat Transfer in a Rotating Four-Pass Serpentine Flow Passage With Throughflow," ASME *Journal of Heat Transfer*, Vol. 114, pp. 354–361.

Zhang, Y. M., Han, J. C., Parsons, J. A., and Lee, C. P., 1995, "Surface Heating Effect on Local Heat Transfer in a Rotating Two-Pass Square Channel With 60 deg Angled Rib Turbulators," ASME JOURNAL OF TURBOMACHINERY, Vol. 117, pp. 272–280.

J.-X. Chen

X. Gan

J. M. Owen

School of Mechanical Engineering,
University of Bath,
Claverton Down, Bath, United Kingdom

Heat Transfer in an Air-Cooled Rotor–Stator System

This paper describes a combined experimental and computational study of the heat transfer from an electrically heated disk rotating close to an unheated stator. A radial outflow of cooling air was used to remove heat from the disk, and local Nusselt numbers were measured, using fluxmeters at seven radial locations, for nondimensional flow rates up to $C_w = 9680$ *and rotational Reynolds numbers up to* $Re_\phi = 1.2 \times 10^6$*. Computations were carried out using an elliptic solver with a low-Reynolds-number* $k-\epsilon$ *turbulence model, and the agreement between the measured and computed velocities and Nusselt numbers was mainly good.*

1 Introduction

A rotor–stator system, as shown in Fig. 1, provides a simplified model for the flow and heat transfer that occurs in the wheel-space between an air-cooled turbine disk and an adjacent stationary casing. Air, admitted at the center of the stator, flows radially out and leaves the system via the clearance between the rotating and stationary shrouds or seals. In an engine, this cooling air is used to remove the heat that is conducted into the disk from the turbine blades and the heat that is generated by windage. Additional air, not shown in this figure, is usually supplied to the blade-cooling passages in the periphery of the turbine disk from preswirl nozzles in the stator. The effect of the preswirl flow is not considered in this paper and will be reported elsewhere.

Much of the work on rotor–stator systems has been concerned with the so-called "ingress problem" where hot mainstream gas is ingested into the wheel-space between the rotor and stator (see Owen and Rogers, 1989; Gan et al. 1993, for a review of work in this area), but less research effort has been devoted to measuring the heat transfer from the rotor to the cooling air. Millward and Robinson (1989) made heat transfer and windage measurements for an air-cooled disk, representative of that used in an engine, for rotational Reynolds numbers up to $Re_\phi = 1.7 \times 10^7$. Dibelius and Heinen (1990) made measurements in a rig with a heated isothermal rotor and a cooled stator for Re_ϕ up to 2×10^6, and their work will be discussed further below. Bunker et al. (1992a, b) used a transient thermochromic liquid crystal (TLC) technique to measure the Nusselt numbers on an air-cooled acrylic disk, at speeds up to $Re_\phi = 5 \times 10^5$, where the air was injected by a nozzle impinging on the disk. Staub (1992) also used the TLC technique to make steady-state measurements of the Nusselt numbers in a model of a turbine wheel-space for Re_ϕ up to 9×10^6.

This paper is concerned with a combined computational and experimental study of the heat transfer from the heated rotating disk in an air-cooled rotor–stator system. The computational method is described in Section 2, the apparatus in Section 3, and a comparison between the computations and measurements is given in Section 4.

2 Numerical Methods

2.1 Computational Procedure. The axisymmetric conservation equations (see appendix) were discretized using a finite-volume method with a hybrid-differencing for convection terms. The SIMPLE approach of Patankar and Spalding (1972) is adopted within a staggered grid arrangement, and the algebric equations were solved using a tridiagonal matrix algorithm (TDMA) iteratively in an ADI fashion. A Gosman et al. (1976) type damping function was used to improve convergence for the radial momentum equations.

2.2 Turbulence Modeling. Turbulent flow computations were made using a low Reynolds number $k-\epsilon$ (LR $k-\epsilon$) model described by Morse (1988), with some modifications (Morse, 1991), and turbulent heat fluxes were estimated from mean flow gradients using a turbulent Prandtl number. Details of the model are given in the appendix.

2.3 Grid Distribution. To satisfy the Ekman-layer characteristics and the LR $k-\epsilon$ model requirements, a varying geometric expansion/contraction parameter was used for the nonuniform grid distribution. A large number of grid points was packed near the walls and the grid in the core region was kept coarse. In the case of the centrally located shroud clearance, a dense grid was used in the middle of the wheel space. The expansion/contraction parameter varied from 1.0–1.2, where the maximum expansion occurred at three grid points away from the walls, and immediately adjacent to the walls the three points were uniformly distributed. The number of grid points within the boundary layer on the rotor was 23 for the enclosed system and 32 for the case with disk-cooling air.

Grid-independence tests were conducted by doubling the number of grid points and comparing the two solutions obtained. There was no graphic distinction between the velocity profiles of the two sets of solutions and the difference between the Nusselt numbers was within two percent. The coarser of the two sets of grids was 68×68 (radial × axial) for the enclosed rotor–stator case and 92×76 for the superposed flow case. It is important that for all the grids y^+ is kept less than unity at rotor/stator surfaces, and $y^+ < 0.5$ for all cases reported below.

2.4 Boundary Conditions. No-slip conditions were used for the velocity components on the solid surfaces. For the air at inlet and outlet, the radial component of velocity was calculated from the specified mass flow rate, assuming a uniform velocity; the radial derivative of the tangential component of velocity was taken to be zero at the outlet, and the tangential velocity itself was assumed to be zero at the inlet. For computations based on the rig described in Section 3, the stator and shrouds were assumed to be adiabatic; the measured temperature was used to provide the thermal boundary condition for the rotor.

For their experiments, Dibelius and Heinen (1990) measured the temperatures of the rotor and cooling air but not the temperature of the stator. For the computations of their data, presented

---

Contributed by the International Gas Turbine Institute and presented at the 39th International Gas Turbine and Aeroengine Congress and Exposition, The Hague, The Netherlands, June 13–16, 1994. Manuscript received by the International Gas Turbine Institute February 9, 1994. Paper No. 94-GT-55. Associate Technical Editor: E. M. Greitzer.

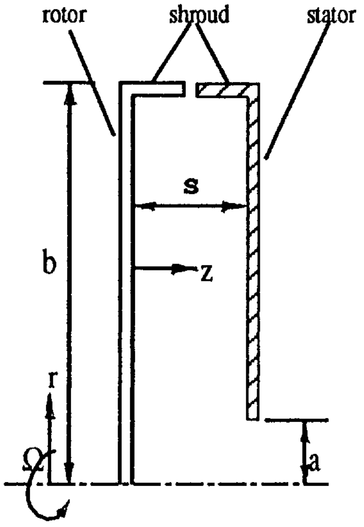

Fig. 1 Schematic diagram of rotor–stator system

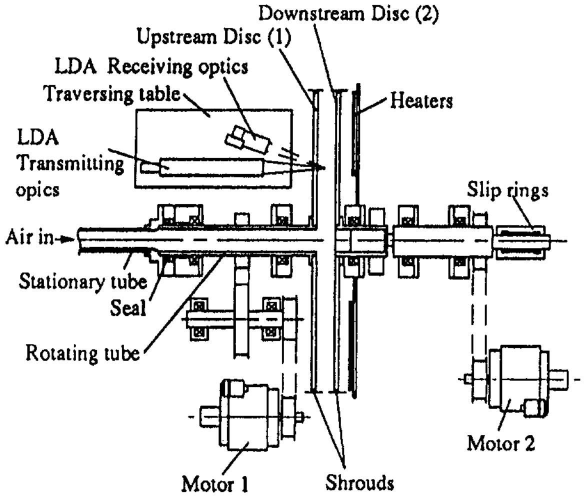

Fig. 2 Schematic layout of the rotating-disk rig and LDA system

below, the temperature of the stator was initially assumed and the temperature of the cooling air was computed. The temperature of the stator was then altered, in a sequence of iterations, until the temperature of the cooling air matched that specified by the authors.

3 Experimental Apparatus and Calibration of Fluxmeters

3.1 Apparatus. The apparatus, see Fig. 2, was the same as that used by Gan et al. (1995) for velocity measurements between contrarotating disks. The salient features are described below, together with details of the instrumentation used for the heat transfer measurements.

The rotating-disk rig comprised two disks of 762 mm diameter, which could be independently rotated at up to 1500 rpm in either direction. The internal diameter of the carbon-fiber shroud was 766 mm, and the 2 mm radial gap between each disk and the shroud was sealed with foam rubber, which also acted as a thermal insulator. The axial clearance between the two shrouds was less than 4 mm, and the axial gap ratio for the disks was $G = 0.12$. A radial outflow of air could be supplied through rotating gauze tubes, of 100 mm diameter, attached to the center of the disks, the air being supplied from a centrifugal fan via stationary tubes attached to the centre of the upstream disk. For the tests described below, the upstream disk was stationary.

The upstream disk was made from transparent polycarbonate, and a single-component TSI laser-Doppler anemometer, with an IFA 750 burst correlator, was used to measure the radial and tangential components of velocity. With the optical "probe-volume" of the LDA system inside the polycarbonate disk, the tangential component of velocity could be compared with the independently measured angular speed of the disk: The difference was typically less than 0.5 percent of the speed.

The back face of the downstream disk, which was made from steel, was heated by 30 stationary, radiant-heater elements located at an axial distance of approximately 30 mm from the disk. The electrical power, which was up to 22.5 kW, was regulated by a thyristor controller, and the disk was heated to a maximum temperature of around 100°C. A sheet, or "mat," of glass-fiber composite, 0.8 mm thick, was bonded to the front face of the steel disk, and thermocouples and fluxmeters were embedded in this "mat." Ten RDF fluxmeters (of which three were broken), made from a thermopile bonded to a thin Kapton film, were located at different radial positions, and ten copper-constantan thermocouples were embedded at the same radial locations but displaced tangentially from the fluxmeters. The thermal conductivity of the glass-fiber mat ($k \approx 0.27$ W/m K) was sufficiently close to that of the Kapton film to ensure that

Nomenclature

a = inner radius of disk
b = outer radius of disk
C_m = moment coefficient = $M/0.5\rho\Omega^2 b^5$
C_p = specific heat at constant pressure
C_w = nondimensional flow rate = $m/\mu b$
G = gap ratio = s/b
k = turbulent kinetic energy; thermal conductivity
m = mass flow rate
M = moment on rotating disk
Nu = Nusselt number = $q_o r/k(T_o - T_{\text{ref}})$
p = static pressure
P = production rate of turbulent kinetic energy
Pr = Prandtl number = $\mu C_p/k$
Pr_t = turbulent Prandtl number
r = radius
q_o = convective heat flux from disk to air
q_r = radiative heat flux from disk
R = recovery factor
Re_ϕ = rotational Reynolds number = $\rho\Omega b^2/\mu$
s = axial gap between disks
T = temperature
U_τ = friction velocity
V_r, V_ϕ = radial, tangential components of velocity
x = nondimensional radius = r/b
y = distance normal to wall
y^+ = wall-distance Reynolds number = $\rho U_\tau y/\mu$
z = axial coordinate
ϵ = turbulent energy dissipation rate, emissivity
λ_T = turbulent flow parameter = $C_w \text{Re}_\phi^{-0.8}$
μ, μ_t, μ_{eff} = dynamic, turbulent and effective viscosity
ρ = density
σ = Stefan–Boltzmann constant
τ_w = total wall shear stress
Ω = angular speed of disk

Subscripts

am = ambient value
I = inlet value
o = surface of rotating disk
ref = reference value

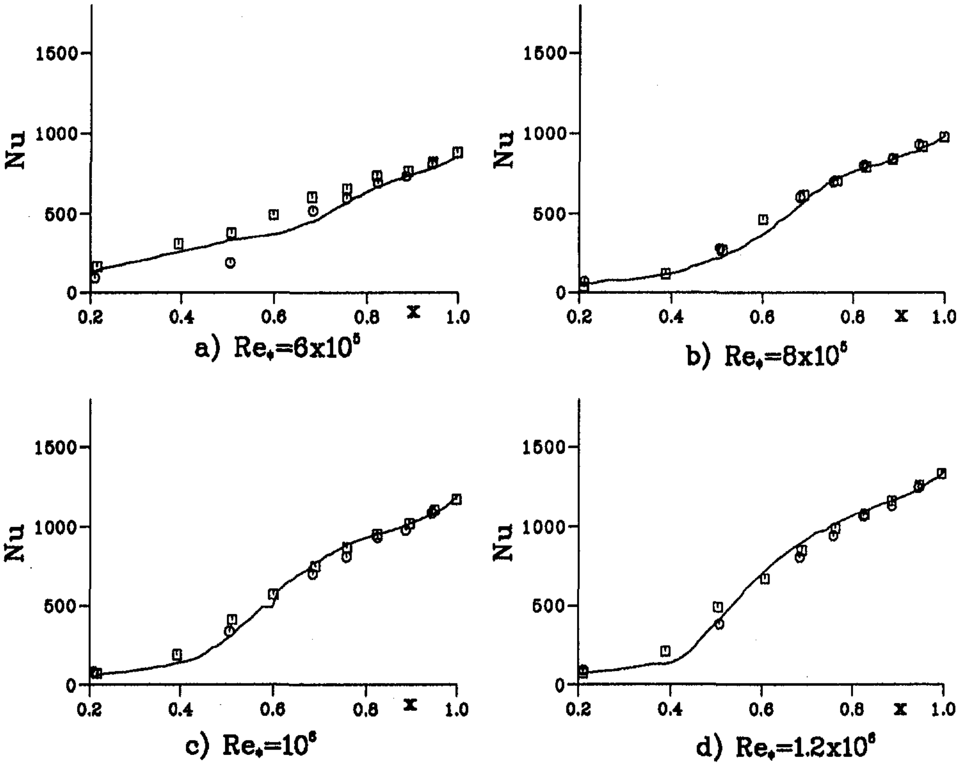

a) $Re_\phi=6x10^5$ b) $Re_\phi=8x10^5$

c) $Re_\phi=10^6$ d) $Re_\phi=1.2x10^6$

Fig. 3 Computed and measured Nusselt numbers for free-disk calibration tests: ○ current data; □Farthing (1988); —— computations

the "thermal disturbance errors" caused by the fluxmeters were small.

The voltages from the fluxmeters and thermocouples were taken out via a 52-way IDM silver slip-ring assembly to a computer-controlled Schlumberger Scorpio datalogger, capable of recording up to 120 channels/second with a resolution of 1 μV. Once steady conditions had been achieved, 100 sets of data were recorded for each channel; the ensemble average of each data set was then used for subsequent analysis. Typical 95 percent confidence intervals of the average of the thermocouple readings was ±0.03°C, and for the Nusselt numbers it was ±0.5 percent, but it should be emphasized that these figures relate to the uncertainty associated with random fluctuations of the signals; additional uncertainties relate to the fluxmeters, which are discussed below.

3.2 Calibration of Fluxmeters. The experimental rig was originally used at the University of Sussex and was rebuilt at the University of Bath in 1989. The fluxmeters had been calibrated at Sussex (see Farthing, 1988) using free-disk tests: The upstream disk was removed, the heated steel disk was operated by itself as a "free disk," and the fluxmeter readings were compared with the computation of a boundary-layer solver developed by Ong (1988). This solver had previously been tested on the experimental data of Northrop and Owen (1988), and the computed free-disk results are reported by Ong and Owen (1991).

Using the calibration procedure of Long (1991), the measured heat flux, q, was related to the voltage output of the fluxmeter, V, according to the relationship

$$q = A_o V[(A_1 + 4A_2T_o)^{1/2} + A_2 V] \tag{3.1}$$

where T_o is the temperature of the fluxmeter (measured by the adjacent thermocouple), and A_0, A_1, A_2 are empirical constants relating to the thermoelectric output of the thermopile and to the thermal conductivity and thickness of the Kapton film.

The heat flux, q, includes both the convective flux, q_o, from the surface of the disk to the air and the radiative flux, q_r, from the disk to the surroundings. The latter was calculated from

$$q_r = \sigma\epsilon(T_o^4 - T_{am}^4) \tag{3.2}$$

where σ is the Stefan–Boltzmann constant (5.67×10^{-8} W/m^2 K^4), ϵ is the emissivity of the surface, and T_o and T_{am} are the temperatures of the fluxmeter and the surroundings (or ambient), respectively. A value of $\epsilon = 0.95$ was obtained by Farthing (1988), and this was used in the radiation corrections made below. For the free-disk tests, T_{am} was taken to be the ambient temperature in the laboratory in which the rig was housed.

The local Nusselt number, Nu, is defined as

$$\mathrm{Nu} = \frac{q_o r}{k(T_o - T_{\mathrm{ref}})} \tag{3.3}$$

where $q_o = q - q_r$, k is the thermal conductivity of the ambient air, and T_{ref} is the adiabatic-disk temperature (see Owen and Rogers, 1989) where

$$T_{\mathrm{ref}} = T_{am} + R\frac{\Omega^2 r^2}{2C_p} \tag{3.4}$$

R being a recovery factor ($R \approx \mathrm{Pr}^{1/3}$, where Pr is the Prandtl number of the air) and C_p the specific heat at constant pressure.

Farthing carried out free-disk tests for $\mathrm{Re}_\phi = 0.6$, 0.8, 1.0, 1.2, 1.4, and 1.6×10^6, and used a regression analysis to determine the values of A_0, A_1, and A_2 that minimized the differences between Nu calculated from the experimental results and that computed using Ong's boundary-layer solver. After the rig had been operated at Bath, some of the wires of the fluxmeters and thermocouples broke and rewiring was necessary. Free-disk tests were carried out after the rewiring to check that the original calibrations were still valid.

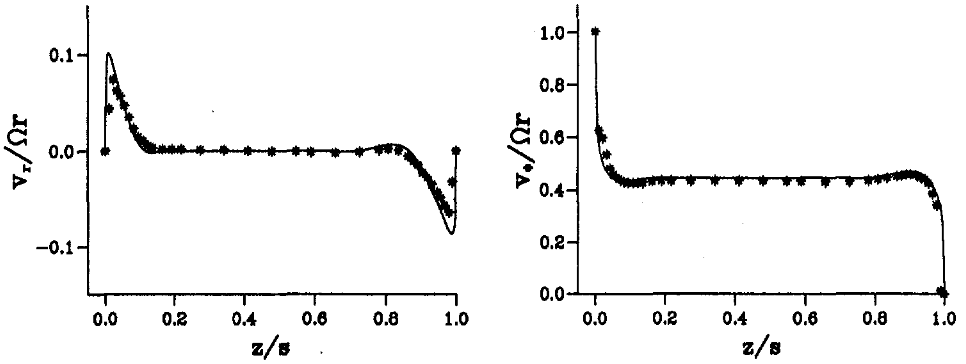

a) x=0.8

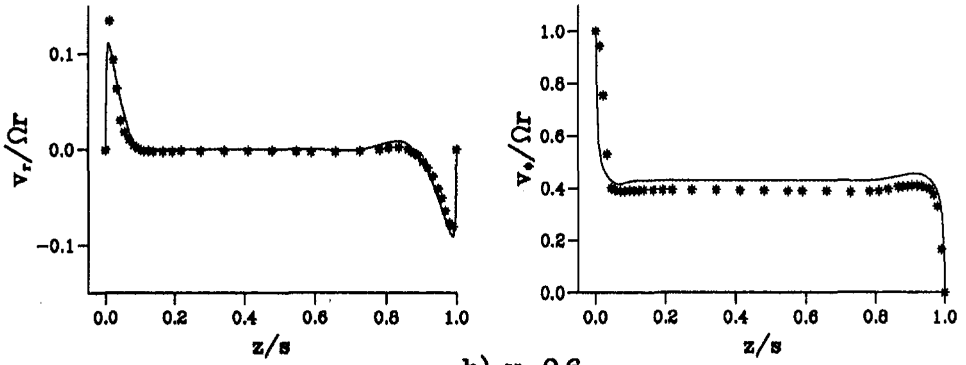

b) x=0.6

Fig. 4 Computed and measured velocity profiles for $Re_\phi = 10^6$, $G = 0.12$, $C_w = 0$: ——computations; * experimental data

Figure 3 shows the radial variation of the local Nusselt numbers, for $Re_\phi = 0.6$, 0.8, 1.0, and 1.2×10^6, showing the measurements of Farthing at Sussex and Gan at Bath together with the computed curve using Ong's solver. Although there were some small differences between the two data sets, the results were sufficiently close to give confidence in the continued use of the calibration of Farthing (1988).

4 Comparison Between Computations and Experiments

4.1 Velocity Profiles. Figure 4 shows a comparison between the measured and computed radial and tangential components of velocity for $C_w = 0$, $G = 0.12$, $Re_\phi = 10^6$, and $x = 0.6$ and 0.8. The flow structure is a turbulent version of that predicted for laminar flow between infinite disks by Batchelor (1951): There is radial outflow on the rotor ($z/s = 0$), inflow on the stator ($z/s = 1$), and between the boundary layers is an inviscid rotating core in which $V_r = 0$ and $V_\phi \approx 0.4\ \Omega r$. For these results, where $x^2\ Re_\phi \geq 3.6 \times 10^5$, the flow is completely turbulent, and agreement between the computed and measured results is mainly very good.

Figure 5 shows the comparison between the measured and computed velocities for $C_w = 6100$, $G = 0.12$, $Re_\phi = 1.25 \times 10^6$, and $x = 0.6, 0.7, 0.8$, and 0.85. The effect of the superposed flow is to reduce both the core rotation and the flow moving radially inward on the stator. The computed velocities tend to underestimate the core rotation and the inflow on the stator; as a consequence, the outflow on the rotor is overestimated. The flow in the source region is strongly affected by inlet conditions and, as a consequence, the differences between the measured and computed radial components of velocity tend to be larger at the smaller radii.

Computed velocity profiles for $0 \leq C_w \leq 9680$, $G = 0.12$, $Re_\phi = 1.25 \times 10^6$, and $x = 0.6$ and 0.8 are shown in Fig. 6. For $C_w > 0$, a source region is formed at the smaller radii in which both the core rotation and the inflow on the stator are zero. The radial extent of this source region increases as C_w increases, and for $C_w = 9680$ it appears to extend to $x \approx 0.6$. Radially outward of the source region, $V_\phi/\Omega r$ increases as x increases.

4.2 Thermal Measurements. The rig described in Section 3 was not suitable for making heat transfer measurements with $C_w = 0$. The polycarbonate stator was quasi-adiabatic, and without a superposed flow of air it was not practicable to cool the steel disk. For this case, the experimental results of Dibelius and Heinen (1990) are useful. In their rig, the rotor was 800 mm diameter and could be rotated up to 2000 rpm. It was of composite construction with a plastic slab housed inside a steel disk, the back face and tip of which were heated by stationary electric heaters. The outer surface of the slab was approximately isothermal, as was the cooled stator, which acted as a heat sink. The air temperature was measured at six locations in the wheel-space, and the heat flux at these locations was determined from a finite-element solution of Laplace's conduction equation for the plastic slab. Referring to Eq. (3.3), for the definition of Nu they based T_{ref} on the measured air temperature in the wheel-space.

Figure 7 shows a comparison between the computed Nusselt numbers, using the elliptic solver described in Section 2, and the data of Dibelius and Heinen for $G = 0.1375$, $C_w = 0$, and $Re_\phi = 1.93 \times 10^6$. It should be pointed out that the data points in this figure were obtained from the authors' graphic results, and the measured Nusselt numbers had an experimental uncertainty of ±15 percent. For these results, the average value of the temperature ratio $(T_o - T_{ref})/T_o$ was 0.09, and for the computations it was assumed that the (stationary) shroud was at the same temperature as the stator to which it was attached. In view of all these assumptions and uncertainties, agreement between the measured and computed results is good.

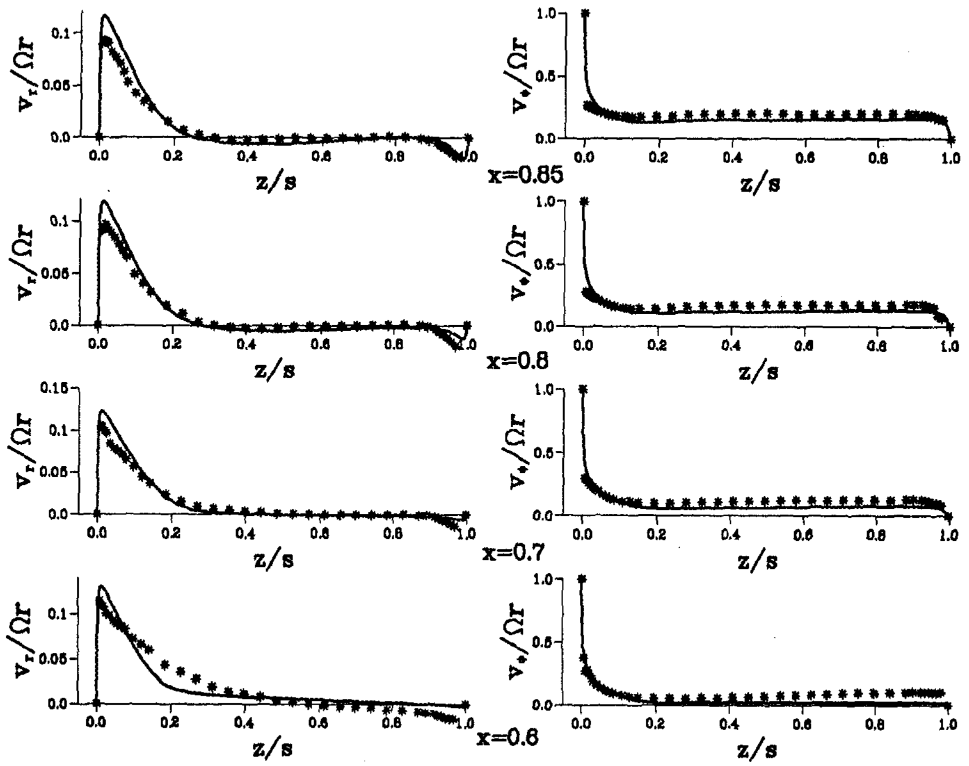

Fig. 5 Computed and measured velocity profiles for $Re_\phi = 1.25 \times 10^6$, $G = 0.12$, $C_w = 6100$: —— computations; * experimental data

Figure 8 shows computed temperature profiles, for the rig described in Section 3, for $G = 0.12$ and $Re_\phi = 1.25 \times 10^6$. Owing to the location of the radiant heaters, the radial distribution of temperature of the rotor is nonuniform and reaches a maximum value near the periphery. In the experiments, the maximum temperature was kept at approximately 100°C, but

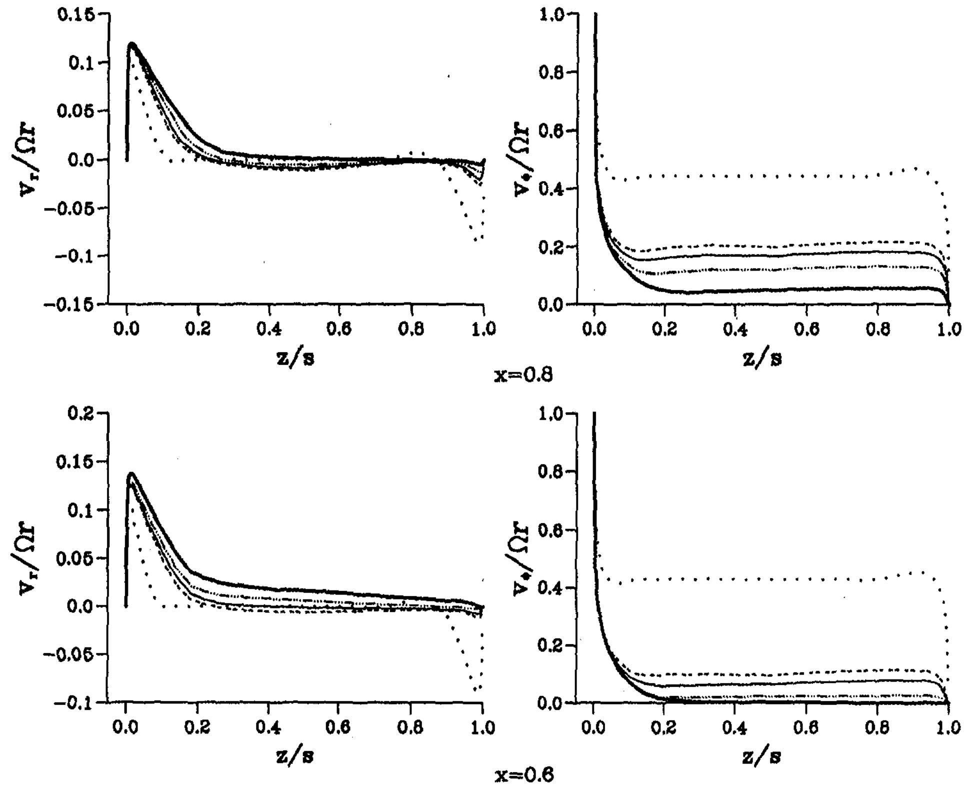

Fig. 6 Computed velocity profiles for $Re_\phi = 1.25 \times 10^6$, $G = 0.12$: .... $C_w = 0$; ---- $C_w = 2530$; —— $C_w = 3900$; — · · · — $C_w = 6100$; ▬ $C_w = 9680$

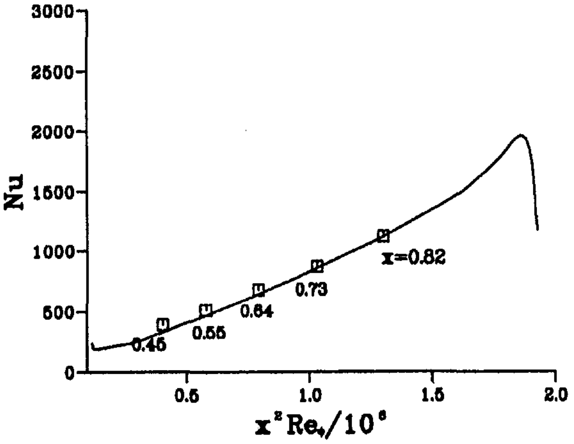

Fig. 7 Computed and measured Nusselt numbers for $Re_\phi = 1.93 \times 10^6$, $G = 0.1375$, $C_w = 0$: □ experimental data of Dibelius and Heinen (1990); —— computation

the radial distribution depended on both C_w and Re_ϕ; the air temperature was approximately 30°C at inlet to the system. It should also be noted that, as stated in Section 3, the shroud was separated from the disk by foam rubber of 2 mm thickness; for the computations, the foam rubber, the carbon-fiber shrouds and the polycarbonate stator were all assumed to be adiabatic.

The computed air temperature in the core (at $z/s = \frac{1}{2}$) is close to that of the (adiabatic) stator. In the source region, referred to above, the air temperature is equal to that at the inlet to the system. Outside the source region, where there is core rotation, some of the hot air leaving the periphery of the rotor flows radially inward on the stator before it moves axially across the wheel-space to be entrained by the boundary layer on the rotor. The amount of recirculation, and hence the extent to which the stator is heated, increases as C_w decreases, as can be seen in Fig. 8.

Figure 9 shows the comparisons between the computed and measured Nusselt numbers for $G = 0.12$, $Re_\phi \approx 1.2 \times 10^6$, and $2500 \le C_w \le 9700$ ($0.033 \le \lambda_T \le 0.127$). Both the computed and measured Nusselt numbers show the same trends, and both tend to increase with increasing C_w and, for $x < 0.8$, with increasing x.

Before commenting further, it is instructive to reconsider the radiation correction described in Section 3. T_{am} in Eq. (3.2) was based on the ambient temperature in the laboratory for the free-disk tests and on T_I for the rotor–stator tests. For the rotor–stator system, the shrouds are opaque and the polycarbonate disk, although transparent to radiation in the *visible* spectrum, is virtually opaque to infrared radiation. Although both the shrouds and the stator were assumed adiabatic for the computations, their temperatures were not measured and it is these temperatures that control the radiative heat transfer from the rotor. It can be seen from Fig. 8 that the computed temperature for the stator increases with radius and that this increase is greater at low flow rates. Also, although not shown here, the temperature of the adiabatic shrouds is virtually the same as that of the stator at $x = 1$. It therefore follows that the radiation correction based on $T_{am} = T_I$ should be an upper bound, and the true correction will decrease as C_w decreases. While, in principle, it is possible to evaluate a radiation correction based on the computed temperatures, this was not thought worthwhile, and both the corrected and uncorrected values are shown in Fig. 9. (As far as the authors are aware, the results of Dibelius and Heinen were not corrected for radiation, but this effect may have been small in their experiments.)

Again, despite (or because of!) all the assumptions and uncertainties, the agreement between the computed and the corrected Nusselt numbers shown in Fig. 9 is surprisingly good. In the main, the computed results are much closer to the corrected measurements than to the uncorrected ones, particularly at the large values of C_w where the corrections should be more accurate.

It is interesting to note that, for $C_w = 9680$, the corrected Nusselt numbers are similar to those shown in Fig. 3 for the free-disk at $Re_\phi = 1.2 \times 10^6$. For $x > 0.6$, the two sets of results are in reasonable agreement; for $x < 0.6$, the results in Fig. 9 are higher than those in Fig. 3. This is consistent with the observations made above that, for this flow rate, the source region extends to $x \approx 0.6$; inside the source region, the impinging flow will enhance the heat transfer from the rotor.

5 Conclusions

An experimental rotor–stator rig has been used to make LDA measurements of the radial and tangential components of velocity for an enclosed rotor–stator system and to make heat transfer measurements for the case of a radial outflow of cooling air. Fluxmeters used to measure the Nusselt numbers on the heated rotating disk were calibrated using free-disk tests, with corrections being made to account for radiation from the disk (which had a maximum temperature of around 100°C) to the surroundings (which were around 20°C). For the rotor–stator tests, the results showed that, for a given rotational speed ($Re_\phi \approx 1.2 \times 10^6$), the Nusselt numbers increase with both radius and with increasing flow rate. At the largest flow rate tested ($C_w = 9680$), the distribution of Nu on the rotating disk was similar to that for the free-disk case.

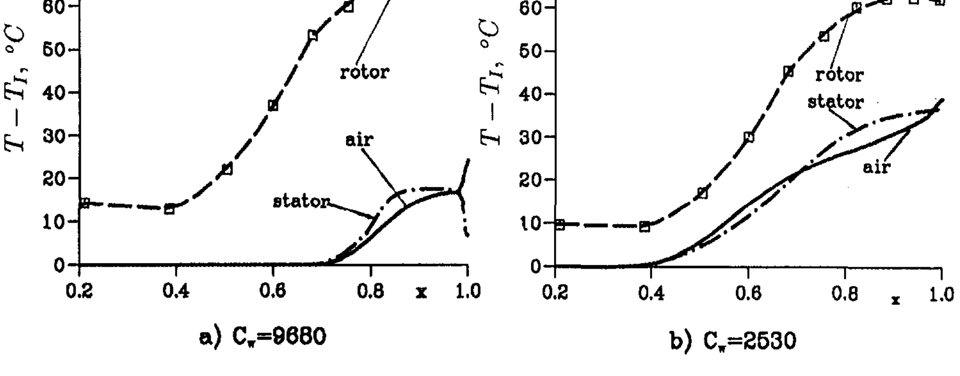

a) C_w=9680

b) C_w=2530

Fig. 8 Radial distribution of temperature for $Re_\phi = 1.25 \times 10^6$, $G = 0.12$: □ measured rotor temperature; -- fitted rotor temperature; —— computed air temperature ($z/s = \frac{1}{2}$); – · – computed stator temperature

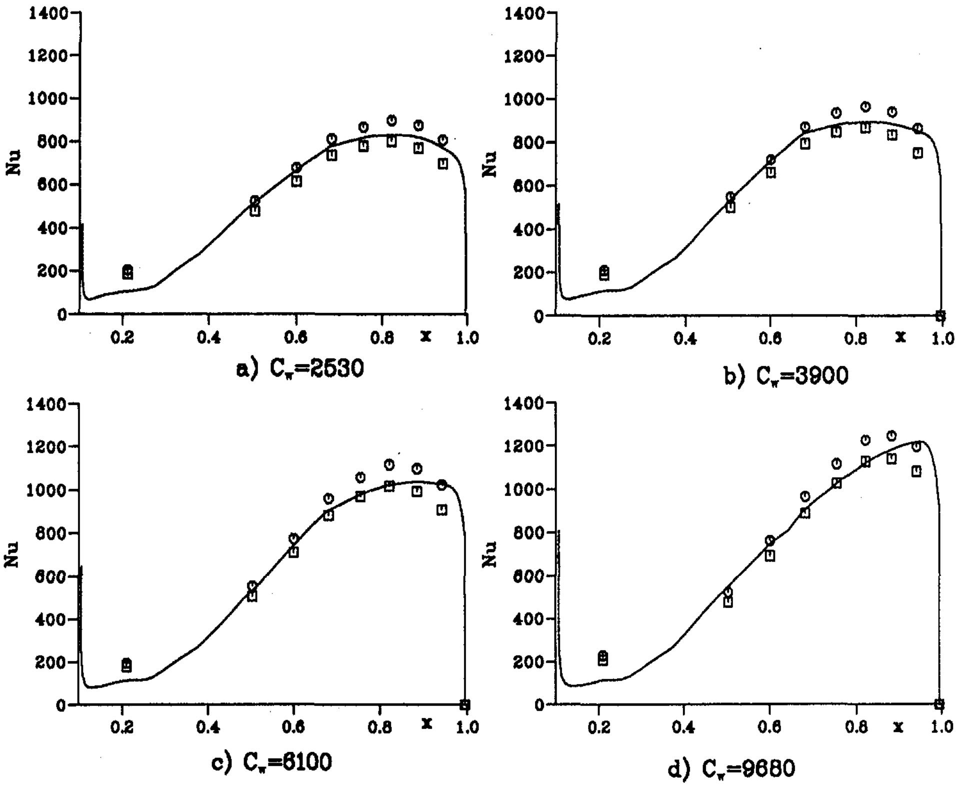

a) C_w=2530

b) C_w=3900

c) C_w=6100

d) C_w=9680

Fig. 9 Computed and measured Nusselt numbers for $Re_\phi = 1.25 \times 10^6$, $G = 0.12$: ○ uncorrected measurements; □ corrected measurements; —— computations

An elliptic solver, using a low-Reynolds-number $k-\epsilon$ turbulence model, has been used to compute the velocity distributions and the Nusselt numbers in rotor–stator systems with and without a radial outflow of cooling air. For the case of $C_w = 0$, the computations are in good agreement with LDA measurements and with the measured Nusselt numbers of Dibelius and Heinen (1990). For $C_w > 0$, the computations confirm the known effect that increasing C_w reduces both the rotation of the inviscid core of fluid in the wheel-space and the radial inflow on the stator. As a consequence, the temperature of an adiabatic stator, and of the air in the core, increases as C_w decreases. The radiation corrections made to the experimental measurements assumed that the (unmeasured) temperature of the stator was equal to the (measured) temperature of the cooling air at inlet to the system; as a consequence of the computed temperature on the stator, these corrections are believed to be an overestimate of the actual radiation from the rotor to the stator. Despite (or because of) the assumptions and uncertainties, the computed Nusselt numbers were in mainly good agreement with the corrected measurements, particularly at the larger values of C_w where the radiation corrections are believed to be more accurate.

Acknowledgments

The authors wish to thank the Engineering and Physical Sciences Research Council, UK, and the Defence Research Agency, UK, for funding the research described in this paper.

References

Batchelor, G. K., 1951, "Note on a Class of Solutions of the Navier–Stokes Equations Representing Steady Rotationally-Symmetric Flow," *Quart. J. Mech. Appl. Maths.*, Vol. 4, pp. 29–41.

Bunker, R. S., Metzger, D. E., and Wittig, S., 1992a, "Local Heat Transfer in Turbine Disk-Cavities. Part I: Rotor and Stator Cooling With Hub Injection of Coolant," ASME JOURNAL OF TURBOMACHINERY, Vol. 114, pp. 211–220.

Bunker, R. S., Metzger, D. E., and Wittig, S., 1992b, "Local Heat Transfer in Turbine Disk-Cavities. Part II: Rotor Cooling With Radial Location Injection of Coolant," ASME JOURNAL OF TURBOMACHINERY, Vol. 114, pp. 221–228.

Dibelius, G. H., and Heinen, M., 1990, "Heat Transfer From a Rotating Disc," ASME Paper No. 90-GT-219.

Farthing, P. R., 1988, "The Effect of Geometry and Heat Transfer in a Rotating Cavity," D. Phil Thesis, University of Sussex, United Kingdom.

Gan, X., Kilic, M., and Owen, J. M., 1993, "Flow and Heat Transfer Between Gas Turbine Discs," AGARD-CP-527, pp. 25.1 to 25.11.

Gan, X., Kilic, M., and Owen, J. M., 1995, "Flow Between Contrarotating Disks," ASME JOURNAL OF TURBOMACHINERY, Vol. 117, pp. 298–305.

Gosman, A. D., Koosinlin, M. L., and Spalding, D. B., 1976, "Transfer of Heat in Rotating Systems," ASME Paper No. 76-GT-25.

Long, C. A., 1991, "A Calibration Technique for Thermopile Heat-Flux Gauges," presented at the 5th Int. Exhibition and Congress for Sensors and Systems Technology, Nuremberg.

Millward, J. A., and Robinson, P. H., 1989, "Experimental Investigation Into the Effects of Rotating and Static Bolts on Both Windage Heating and Local Heat Transfer Coefficients in a Rotor–Stator Cavity," ASME Paper No. 89-GT-196.

Morse, A. P., 1988, "Numerical Prediction of Turbulent Flow in Rotating Cavities," ASME JOURNAL OF TURBOMACHINERY, Vol. 110, pp. 202–215.

Morse, A. P., 1991, private communication.

Northrop, A., and Owen, J. M., 1988, "Heat Transfer Measurements in Rotating-Disc Systems, Part I: The Free Disc," *Int. J. Heat Fluid Flow*, Vol. 9, pp. 27–36.

Ong, C. L., 1988, "Computation of Fluid Flow and Heat Transfer in Rotating-Disc Systems," D. Phil Thesis, University of Sussex, United Kingdom.

Ong, C. L., and Owen, J. M., 1991, "Computations of the Flow and Heat Transfer Due to a Rotating Disc," *Int. J. Heat Fluid Flow*, Vol. 12, pp. 106–115.

Owen, J. M., and Rogers, R. H., 1989, *Flow and Heat Transfer in Rotating Disc Systems, Vol. 1: Rotor-Stator Systems*, Research Studies Press, Taunton; Wiley, New York.

Patankar, S. V., and Spalding, D. B., 1972, "A Calculation Procedure for Heat, Mass and Momentum Transfer in Three-Dimensional Parabolic Flows," *Int. J. Heat Mass Transfer*, Vol. 15, pp. 1787–1806.

Staub, F. W., 1992, "Rotor Cavity Flow and Heat Transfer With Inlet Swirl and Radial Outflows of Cooling Air," ASME Paper No. 92-GT-378.

APPENDIX

Conservation Equations and Low-Reynolds-Number $k-\epsilon$ Turbulence Model

The axisymmetric equations for conservation of momentum, mass, energy, and turbulence quantities k and ϵ can be written in the following form using a cylindrical-polar coordinate system (r, ϕ, z) with velocity components (v_r, v_ϕ, v_z):

$$\frac{\partial}{\partial z}(\rho v_z \Phi) + \frac{1}{r}\frac{\partial}{\partial r}(r\rho v_r \Phi) = \frac{\partial}{\partial z}\left(\Gamma_z \frac{\partial \Phi}{\partial z}\right) + \frac{1}{r}\frac{\partial}{\partial r}\left(r\Gamma_r \frac{\partial \Phi}{\partial r}\right) + S_\Phi$$

where Φ represents the transported variables v_r, v_ϕ, v_z, k, ϵ, or T, and the continuity equation is recovered by setting $\Phi = 1$ and $S_\Phi = 0$. S_Φ contains all source terms (Table A.1). Γ_z and Γ_r are the effective diffusivities comprising both laminar and turbulent components, e.g., the effective viscosity is $\mu_{\text{eff}} = \mu + \mu_t$, where μ_t is determined from the computed turbulence quantities k and ϵ:

$$\mu_t = C_\mu f_\mu \rho k^2/\epsilon$$

Table A.1

Φ	Γ_z	Γ_r	S_Φ
v_z	$2\mu_{eff} - \mu$	μ_{eff}	$-\frac{\partial}{\partial z}(p + \frac{2}{3}\rho k)$ $+\frac{1}{r}\frac{\partial}{\partial r}(r\mu_t \frac{\partial v_r}{\partial z})$ $-\frac{2}{3}\frac{\partial}{\partial z}(\mu_{eff}\nabla \cdot \mathrm{v})$
v_r	μ_{eff}	$2\mu_{eff} - \mu$	$-\frac{\partial}{\partial r}(p + \frac{2}{3}\rho k)$ $-(2\mu_{eff} - \mu)\frac{v_r}{r^2}$ $+\frac{\rho v_\phi^2}{r} + \frac{\partial}{\partial z}(\mu_t \frac{\partial v_z}{\partial r})$ $-\frac{2}{3}\frac{\partial}{\partial r}(\mu_{eff}\nabla \cdot \mathrm{v})$
v_ϕ	μ_{eff}	μ_{eff}	$-\frac{\rho v_r v_\phi}{r} - \mu_{eff}\frac{v_\phi}{r^2}$ $-\frac{v_\phi}{r}\frac{\partial \mu_t}{\partial r}$
k	$\mu + \frac{\mu_t}{\sigma_k}$	$\mu + \frac{\mu_t}{\sigma_k}$	$P - \rho\epsilon - D$
ϵ	$\mu + \frac{\mu_t}{\sigma_\epsilon}$	$\mu + \frac{\mu_t}{\sigma_\epsilon}$	$\frac{\epsilon}{k}(c_{\epsilon 1}P - c_{\epsilon 2}\rho\epsilon)$ $+E - F$
T	$\frac{\mu}{Pr} + \frac{\mu_t}{Pr_t}$	$\frac{\mu}{Pr} + \frac{\mu_t}{Pr_t}$	$\frac{\mu_{eff}P}{\mu_t C_p}$

Table A.2

$D = 2\mu[(\frac{\partial k^{1/2}}{\partial z})^2 + (\frac{\partial k^{1/2}}{\partial r})^2]$
$E = \frac{2(1-f_\mu)\mu\mu_t}{\rho}[(\frac{\partial^2 v_r}{\partial z^2})^2 + (\frac{\partial^2 v_\phi}{\partial z^2})^2]$ $+\frac{2(1-f_\mu)\mu\mu_t}{\rho}[(\frac{\partial^2 v_z}{\partial r^2})^2 + (\frac{\partial^2 v_\phi}{\partial r^2})^2]$
$F = 2\mu[(\frac{\partial \epsilon^{1/2}}{\partial z})^2 + (\frac{\partial \epsilon^{1/2}}{\partial r})^2]$

where f_μ is a near-wall damping function,

$$f_\mu = [1 - \exp(-y^+/26.0)]^2$$

which forms part of the LR $k-\epsilon$ model described by Morse (1988). In Table A.2, D, E, and F are extra terms added to the high-Reynolds-number form of the model, to represent near-wall behavior. The production rate P of turbulent kinetic energy (k) is given by:

$$P = \mu_t\left[2\left(\left(\frac{\partial v_z}{\partial z}\right)^2 + \left(\frac{\partial v_r}{\partial r}\right)^2 + \left(\frac{v_r}{r}\right)^2\right) + \left(\frac{\partial v_z}{\partial r} + \frac{\partial v_r}{\partial z}\right)^2 + \left(\frac{\partial v_\phi}{\partial z}\right)^2 + \left(r\frac{\partial}{\partial r}\left(\frac{v_\phi}{r}\right)\right)^2\right]$$

The empirical coefficients appearing in the model are given by:

$$C_\mu = 0.09;\ C_{\epsilon 1} = 1.44;$$

$$C_{\epsilon 2} = 1.92 - 0.43\exp(\mathrm{Re}_t^2/36)$$

$$\sigma_k = 1.0;\ \sigma_\epsilon = 1.22;\ \mathrm{Pr}_t = 0.9$$

where $\mathrm{Re}_t = k^2/\nu\epsilon$ is the local turbulent Reynolds number.

Studies on Wake-Affected Heat Transfer Around the Circular Leading Edge of Blunt Body

K. Funazaki
Department of Mechanical Engineering,
Iwate University,
Morioka, Iwate, Japan

Detailed measurements are performed about time-averaged heat transfer distributions around the leading edge of a blunt body, which is affected by incoming periodic wakes from the upstream moving bars. The blunt body is a test model of a front portion of a turbine blade in gas turbines and consists of a semicircular cylindrical leading edge and a flat plate afterbody. A wide range of the steady and unsteady flow conditions are adopted as for the Reynolds number based on the diameter of the leading edge and the bar-passing Strouhal number. The measured heat transfer distributions indicate that the wakes passing over the leading edge cause a significant increase in heat transfer before the separation and the higher Strouhal number results in higher heat transfer. From this experiment, a correlation for the heat transfer enhancement around the leading edge due to the periodic wakes is deduced as a function of the Stanton number and it is reviewed by comparison with the other experimental works.

Introduction

Due to demands for more efficient and powerful aeroengines or gas turbines, turbine inlet temperature (TIT) has been constantly increasing during the last decade, and will become higher than 1800 K in the near future, as pointed out by Yoshida (1993). This high TIT can be attained by efficient blade cooling technologies as well as development of new materials for turbine blades. As for the blade cooling, an accurate prediction of a heat transfer distribution along the blade surface is indispensable and many efforts have been devoted to develop reliable prediction methods. They are based on, for example, rather simple correlations, boundary layer analyses with a turbulent model, or solvers of Navier–Stokes equations. Not a few efforts are directed to studies of turbine blade leading edge problems because the heat load around the leading edge where the flow stagnates is intrinsically very large; furthermore, incident mainstream turbulence increases the heat load to great extent. Frossling (1958) proposed an empirical correlation for the heat transfer distribution around the leading edge, $\mathrm{Nu}_D(\theta)$, such as

$$\frac{\mathrm{Nu}_D(\theta)}{\mathrm{Re}_D^{1/2}} = 0.9449 - \frac{0.510}{4}\theta^2 - \frac{0.596}{16}\theta^4, \tag{1}$$

where θ is an angle from the stagnation line; Re_D is Reynolds number based on the inlet velocity and the diameter of the leading edge. On the other hand, Lowry and Vachon (1975) showed the following equation for the stagnant heat transfer, $\mathrm{Nu}_{D,max}$:

$$\frac{\mathrm{Nu}_{D,\max}}{\mathrm{Re}_D^{1/2}} = 1.01 + 2.624\left[\frac{Tu\ \mathrm{Re}_D^{1/2}}{100}\right] - 3.07\left[\frac{Tu\ \mathrm{Re}_D^{1/2}}{100}\right]^2, \tag{2}$$

where Tu is a mainstream turbulence intensity.

Recently, effects of wake–blade interaction upon the heat transfer not only around the stagnation region of the leading edge but also on the blade surface have been collecting attention from a large number of researchers. Magari and LaGraff (1994) measured heat transfer distributions around the stagnation region of a circular cylinder that was immersed inside the wake from a stationary cylinder with smaller diameter, and found the importance of large vortical structures shed from the upstream cylinder (wake generator) in the heat transfer process around the leading edge. Likewise O'Brien (1990) conducted the measurement of the heat transfer distributions around the stagnation region of a circular cylinder that was under the influence of wake-passing generated from the upstream moving bars. He found an asymmetric heat transfer distribution about the geometrically determined stagnation line, especially at higher Strouhal number cases. Paxson and Mayle (1991), on the other hand, conducted unsteady velocity measurements of wake-affected laminar boundary layers around the stagnation region of a rounded bluff body, which can be regarded as a more appropriate model of a turbine blade than a circular cylinder. They discussed the validity of a perturbation approach to describe the unsteady disturbed flow. Furthermore, Dullenkopf and Mayle (1994) examined the effect of free-stream turbulence on augmenting heat transfer in accelerating flow regions such as a leading edge or aft portion of a turbine blade, and proposed a correlation that could fit with the experimental data as follows:

$$\mathrm{Nu}_a\,\mathrm{Pr}^{-0.37} = 0.571 + 0.0125Tu_a\left\{1 + \frac{2}{1 + (Tu_a/25)^3}\right\},$$

$$\mathrm{Nu}_a = \mathrm{Nu}_c/\sqrt{a_1\ \mathrm{Re}_c},\ Tu_a = Tu\sqrt{\mathrm{Re}_c/a_1} \tag{3}$$

where Nu_a is a local Nusselt number based on the blade chord length and a_1 is a coefficient of constant flow acceleration. They claimed that the above-mentioned correlation was able to apply to the prediction of the effect of periodically passing wakes on the heat transfer over the pressure surface of a turbine blade.

In this study, using a blunt test model with a semicircular leading edge similar to that of Mehendale et al. (1991) and a wake generator consisting of moving cylinders, detailed experiments are made to measure the influence of the periodically passing wakes on the heat transfer distribution over the surface. Much focus of the study is placed upon the wake effects on the

---

Contributed by the International Gas Turbine Institute and presented at the 39th International Gas Turbine and Aeroengine Congress and Exposition, The Hague, The Netherlands, June 13–16, 1994. Manuscript received by the International Gas Turbine Institute February 4, 1996. Paper No. 94-GT-25. Associate Technical Editor: E. M. Greitzer.

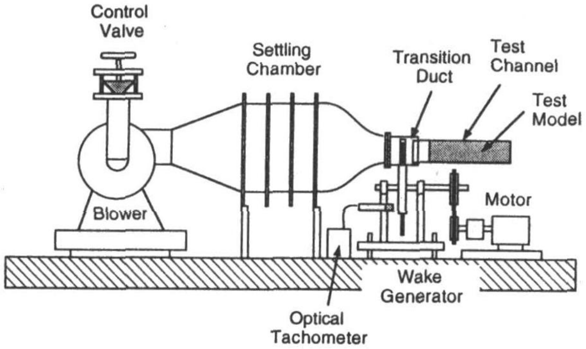

Fig. 1 Schematic layout of the test apparatus

heat transfer augmentation at the stagnation region, as well as upon the wake-induced peak value variations of the heat transfer at the reattachment point.

Test Apparatus

Outline. A schematic layout of the test apparatus is shown in Fig. 1. Air from the blower is led to contraction nozzle with the exit cross section of 240 mm × 350 mm, passing through the settling chamber. Flow rate is adjusted by the inlet valve of the blower. The acrylic resin transition duct attached to the nozzle has a slot through which circular cylinders on the rim of the rotating disk can move, generating wakes behind them. The front portion of the test channel containing the test model is inserted into the transition duct, removing the upstream boundary layer as a result of the transition duct, so that the boundary layer inside the test channel starts from the leading edge of the test channel.

Wake Generator. Six circular cylinders of 5 mm diameter and 250 mm length can be mounted on the disk rim. Since the disk is made of brass and its diameter is 400 mm, its inertia is large enough to maintain a nearly constant rotational speed. The rotational speed of the disk is controlled by the transmission gear box connected to the induction motor and it is monitored by an optical tachometer or a stroboscope. The range of rotational speed is 900–1500 rpm. A slight vibration of the cylinder probably due to the flow and the structural vibration was observed but it didn't seem to alter the wake characteristics drastically.

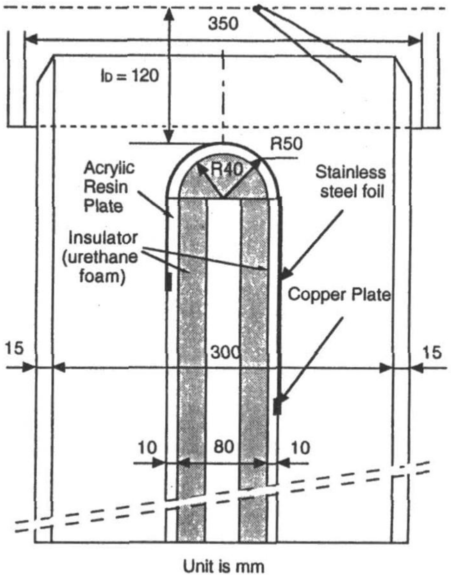

Fig. 2 Test model for heat transfer measurement

Test Channel. The cross section of the test channel is 200 mm height and 300 mm width and its length is 1000 mm. The front end of the channel is sharp-edged and is inserted into the transition duct with 10 mm clearance around it. On the one side of the test channel, there is a longitudinal slot for the measurement of the inlet velocity by a Pitot tube and incident wakes by a hot-wire probe. This slot is usually plugged with several blocks with great care paid to the air leakage during the test run.

Test Model

Test Model for Heat Transfer Measurement. The test model for the heat transfer measurement has exactly the same geometry with that for the pressure measurement, which is shown in Fig. 2. Along the midspan of the test model, 60 holes are shaped through the cylinder and the plate with equal surface wise distance. Each of the holes is plugged with small piece of urethane

Nomenclature

a_1 = acceleration parameter
C_D = drag coefficient
D = diameter of test model leading edge or drag
d = diameter of circular cylinder
h = heat transfer coefficient
f = wake-passing frequency = $nn_c/60$
l_D = axial distance between the moving bars and the test model
n, n_c = number of rotation, number of circular cylinder
$\mathrm{Nu}_D(x)$ = local Nusselt number based on the leading edge diameter
$\mathrm{Nu}_{D,\max}$ = maximum Nusselt number
p = static pressure
$\dot{q}_{\mathrm{wall}}$, $\dot{q}_{\mathrm{loss}}$ = wall heat flux, heat loss
R = radius of test model leading edge
Re_D = Reynolds number based on the leading edge diameter and inlet flow
Re_x = local Reynolds number = $U(x_{\mathrm{surf}})x_{\mathrm{surf}}/\nu$
S = Strouhal number = fD/U_{in}
St = local Stanton number = $\mathrm{Nu}_x/\mathrm{Re}_x\mathrm{Pr}$
t = pitch of wake-generating bars
T_{wall}, T_∞ = wall temperature, inlet flow temperature
Tu = turbulence intensity
U_{in}, $U(x_{\mathrm{surf}})$ = inlet velocity, local velocity along the model surface
W_1, W_2, W_∞ = relative inlet, outlet, and vector-averaged flow velocities
x, x_{surf} = axial length, surface length
β_1, β_2 = relative inlet and outlet flow angles in the frame of the moving bars
$\Delta\beta$ = turning angle
ϵ = emissivity
θ = angle measured from the stagnation point
λ = thermal conductivity
ν = kinematic viscosity
ρ = density
σ = Stefan–Boltzmann constant

Subscripts

0 = values free from the wake effect
1, 2 = inlet, outlet
max = maximum
w = wake-affected values

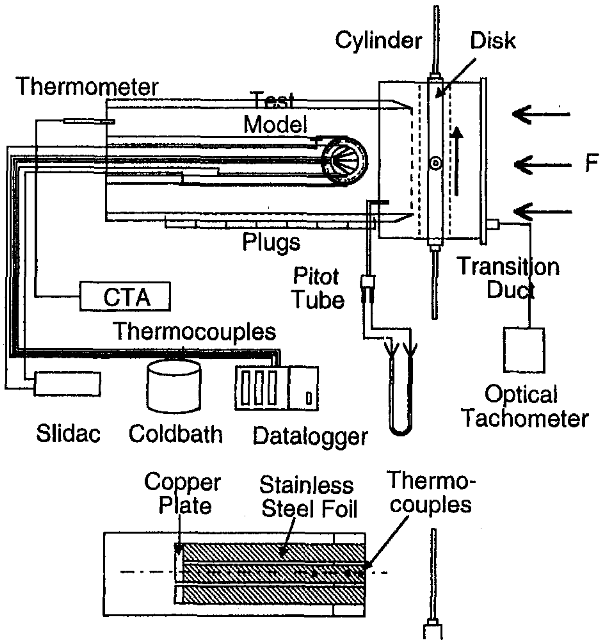

Fig. 3 Schematic of the measurement system

foam and then a hot junction of a K-type thermocouple is flush-mounted on the measurement surface penetrating back through the urethane foam. Lines of the thermocouples are then connected to a computer-controlled datalogger (Data Acquisition Controller, NEC San-ei) to convert the signals to digital ones, where 10 samples for each measuring point are acquired during one scan.

Very thin stainless steel adhesive tapes of 30 mm width and 700 mm length are pasted on the surface of the test model as a heater, one of which covers the hot junctions on the surface. Those tapes are connected through the copper plates in series to form an electric circuit and electric power is supplied to it from a power controller in order to obtain a constant heat flux condition on the measurement surface. To prevent the tapes from buckling due to thermal elongation, they are covered by transparent tapes (3M Booktape 845) of 90 μm thickness. Temperature drop through these tapes is estimated to be about 0.25°C.

Test Model for Pressure Measurement. The test model used for the the pressure measurement has the same geometry as the model of Fig. 2. It consists of a semicircular component and two flat plates, and at the midspan of the model several small holes of 1.1 mm diameter are dug through the plates for the wall static pressure measurement. Very small Teflon tubes are inserted through each of the holes, which are then connected to a Betz type manometer of ±0.49 Pa precision.

Experiments

A schematic of the measurement system is shown in Fig. 3. Setting the inlet velocity to specified values, i.e., 5 m/s, 10 m/s, 15 m/s, and 20 m/s, corresponding to $\mathrm{Re}_D = 3.4 \times 10^4$, 6.7×10^4, 10.0×10^4, and 13.3×10^4, respectively, the stainless steel foil on the test model is then heated for two or three hours in order to achieve thermal equilibrium on the test model. After confirmation of the thermal equilibrium condition by monitoring the surface temperature distribution T_{wall}, the surface temperature distribution is measured, which then yields heat transfer coefficient $h(x)$ and Nusselt number Nu_D on the test model as follows:

$$h(x) = \frac{\dot{q}_{\mathrm{wall}}}{T_{\mathrm{wall}}(x) - T_\infty} = \frac{\dot{q}_{\mathrm{supply}} - \dot{q}_{\mathrm{loss}}}{T_{\mathrm{wall}}(x) - T_\infty} \qquad (4)$$

$$\mathrm{Nu}_D(x) = \frac{h(x)D}{\lambda}, \qquad (5)$$

where heat flux $\dot{q}_{\mathrm{supply}}$ is an electrical power supply, $\dot{q}_{\mathrm{loss}}$ is heat flux that does not contribute to $\dot{q}_{\mathrm{wall}}$ (the convective heat flux from the surface), T_{wall} is an ambient temperature around the test model measured at the downstream of the test channel as seen in Fig. 4. The heat flux, $\dot{q}_{\mathrm{loss}}$, consists of radiation heat flux, $\dot{q}_{\mathrm{rad}}$, and conduction heat flux inside the plate, $\dot{q}_{\mathrm{cond}}$.

Radiation heat flux from the heated surface can be, in principle, evaluated with the Stefan–Boltzmann radiation equation (Benedict, 1969). In such a case precise information about the configuration factor as well as the emissivity of each of the heated surfaces is indispensable. However, such information, especially configuration factor, is not always easily available, so that a simplified approach is taken to assess the configuration factor. On the semicircular cylinder surface, its configuration factor is assumed to be unity, which yields the following expression as for the radiation heat flux around the leading edge of the test model:

$$\dot{q}_{\mathrm{rad}} = \sigma\epsilon_1(T^4_{\mathrm{wall},1} - T^4_{\mathrm{ambient}}), \qquad (6)$$

where σ is the Stefan–Boltzmann constant ($=5.67 \times 10^{-8}$ W/($\mathrm{m}^2\cdot\mathrm{K}^4$)), ϵ_1 is the emissivity of the stainless steel foil, estimated to be 0.22 according to Mehendale et al. (1991). On the other hand, the radiation heat flux on the flat plate is evaluated using a correlation for parallel infinite plates as follows:

$$\dot{q}_{\mathrm{rad}} = \sigma(T^4_{\mathrm{wall},1} - T^4_{\mathrm{ambient}})\frac{1}{\dfrac{1}{\epsilon_1} + \dfrac{1}{\epsilon_2} - 1}, \qquad (7)$$

where ϵ_2 is the emissivity of the acrylic resin plate opposite to the heated stainless steel foil and it is assumed to be 0.9.

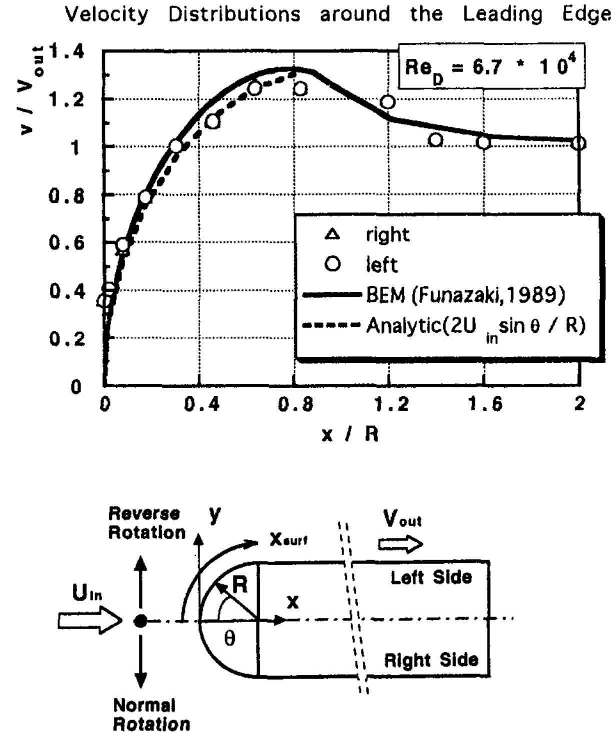

Fig. 4 Velocity distribution measured around the test model, with some incompressible flow calculations, and some notations about the coordinate system of the test model; $\mathrm{Re}_D = 6.7 \times 10^4$

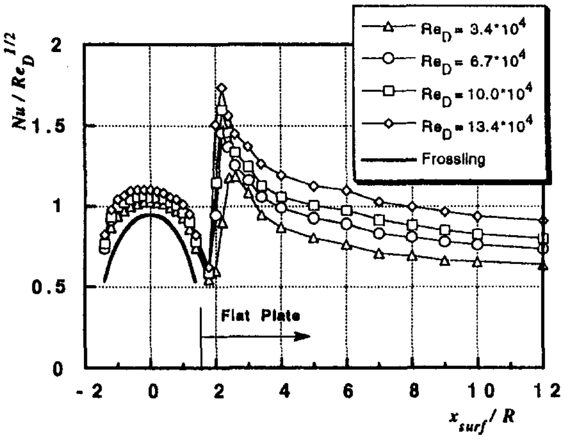

Fig. 5 Heat transfer distributions with no influences of incident wakes, which are represented in terms of the Frossling factor

A preliminary experiment was conducted in order to deduce a correlation for the conduction heat flux, where an averaged surface temperature and an ambient temperature were measured with small level of electric power being applied to the stainless steel foil for at least an hour. Note that a rather parasitic heat flux was inevitable around the copper electrodes due to its contact resistance with the stainless steel foils and it was found to be about 10 percent of the supplied electric power. The contribution of such heat flux to the total conduction heat flux was incorporated in the above-mentioned correlation.

Uncertainty

An uncertainty analysis was carried out using the method of Kline and McClintock (1953). The estimated uncertainties in h, Nu, and Re were 3.5, 4.1, and 3.6 percent, respectively.

Results

Velocity Distribution. The test model is placed at the center of the test channel so as to establish the symmetric flow field with respect to the centerline of the model. Such asymmetry is confirmed by the measurement of the velocity distribution along the model surface, as appeared in Fig. 5. This figure shows the normalized velocity distributions on the right and left sides of the model in the case of $Re_D = 6.7 \times 10^4$, where Re_D is Reynolds number based on the 100 mm diameter of the semicircular cylinder. Note that the right side of the test model when viewed from the inlet of the test channel is referred to as "right" and vice versa. Also shown in Fig. 4 are the calculations of the velocity distribution by BEM (Boundary Element Method) developed by Funazaki (1989) and the analytic solution for a circular cylinder. Measured velocity distributions on both sides of the test model coincide, which verifies the symmetric flow field. The calculations agree with the measured data fairly well, except around the junction between the semicircular cylinder and the flat plates. Close investigation has revealed that this discrepancy can be attributed to a small separation bubble existing around there. As the inlet velocity increases, the differences between the measured data and the calculation become larger and the measured distributions become flatter, which means an advancement of the separation point, i.e., a growth of the separation bubble. It was also identified in an oil-flow visualization.

Heat Transfer Distribution

Heat Transfer in Steady (No-Wake) Flow Conditions. Figure 5 presents local heat transfer distributions for four different cases of the inlet Reynolds number. Also shown in this figure is the curve of Eq. (1).

All these data expressed in terms of $Nu_D/Re_D^{1/2}$ tend to converge onto a single curve along the leading edge with a band of scatter. This scatter is probably due to uncertainty in the data and the effect of the inlet free-stream turbulence, which was about 0.8 percent. The local heat transfer decreases from the stagnation point down to the position just beyond the cylinder-flat plate junction ($x_{surf}/R \cong 1.8$), followed by the rapid increase and then the gradual decrease toward the aft portion of the flat plate. Apparently, such drastic changes in heat transfer around the junction are caused by the separation bubble existing there.

In order to examine an incoming wake effect on the heat transfer distribution over the surfaces of both the circular leading edge and the flat plate, it is convenient to express the distribution in terms of Stanton number against the local Reynolds number, Re_x. Figure 6 illustrates the Stanton number distributions for the no-wake flow conditions versus Re_x along the left surface of the test model. In this figure the following two lines are also plotted:

$$St = 0.57 Pr^{-0.6} Re_x^{-0.5}, \tag{8}$$

the laminar solution for the two-dimensional stagnation flow with a linear velocity distribution from the stagnation point, and

$$St = 0.0307 Pr^{-0.4} Re_x^{-0.2}, \tag{9}$$

a turbulent flow correlation over the flat plate given by Kays and Crawford (1980). The heat transfer data before the abrupt change in Stanton number in Fig. 6 follow the line of Eq. (8) very well for all cases of the inlet flow conditions. After the maximum points of the Stanton number, which correspond to the reattachment points, the data gradually follow the line of Eq. (9) for the turbulent flow correlation.

Wake-Affected Heat Transfer. Figure 7 shows wake-affected heat transfer distributions on the test model for the lowest Reynolds number case among the test conditions ($Re_D = 3.4 \times 10^4$). Unsteady flow parameter adopted here is a bar-passing Strouhal number, S, defined as

$$S = \frac{fD}{U_{in}}, \tag{10}$$

$$f = \frac{nn_c}{60}, \tag{11}$$

where n is a rotational speed of the wake generator, n_c is the number of the cylinders attached to it, and D is the diameter of the leading edge of the test model. Compared to the heat transfer

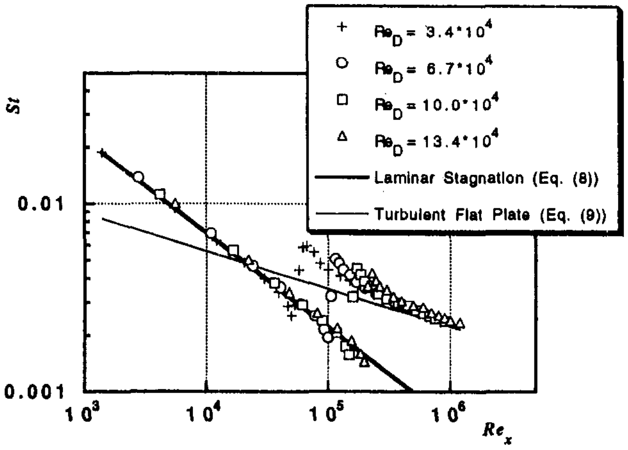

Fig. 6 Stanton number distributions against local Reynolds number under no-wake conditions

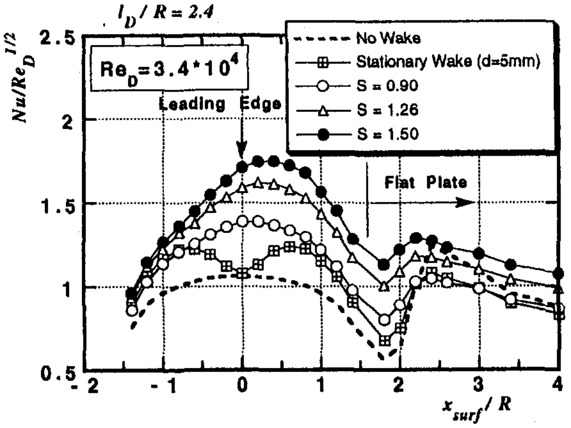

Fig. 7 Wake-affected heat transfer distributions on the test model for several unsteady flow conditions; $Re_D = 3.4 \times 10^4$

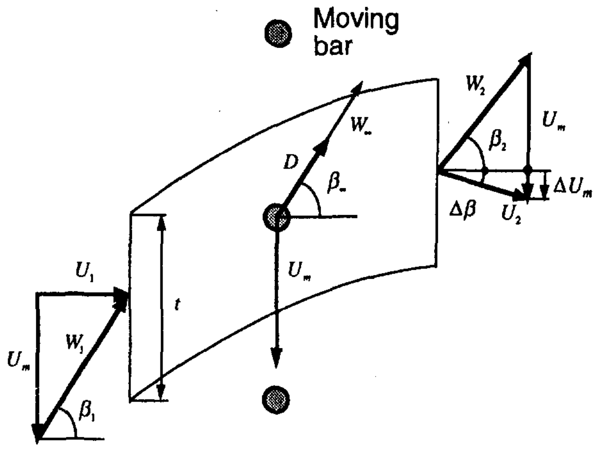

Fig. 9 The moving bars and the inlet/outlet velocity diagrams

data in the no-wake condition, overall levels of the heat transfer around the leading edge as well as on the flat plate increase considerably as the Strouhal number increases. Investigation into the data has revealed that the profiles of the heat transfer distributions along the leading edge are asymmetric with respect to the centerline of the test model and the peak positions shift toward the ''left'' side of the model. To inspect the mechanism of this phenomenon, additional experiments were conducted by rotating the wake generator in reverse, which results in the data of Fig. 8. It is very clear that the peak positions tend to move toward the ''right'' side of the model due to the reverse rotation, while the profiles of both cases are apparently a mirror image relationship. One of the possible explanations for the phenomenon is that the movement of the cylinders causes the flow to turn, which leads to nonzero incident angle of the inlet flow to the test model and consequently results in the shift of the actual stagnation line from the geometric one. Such supposition can be easily verified by applying the two-dimensional cascade theory to the present case as shown in Fig. 9. Note that the control volume of Fig. 9 has an unit depth of the cylinder. It follows that the flow turning angle measured from the geometric stagnation line, $\Delta\beta$, is given by

$$\Delta\beta = \tan^{-1}\frac{\Delta U_m}{U_1} \qquad (12)$$

$$\Delta U_m = W_2\sin\beta_2 - W_1\sin\beta_1$$
$$= \frac{D\sin\beta_\infty}{\rho t W_\infty\cos\beta_\infty\cdot 1} \cong \frac{D\sin\beta_1}{\rho t U_1}, \qquad (13)$$

$$t = \frac{2\pi R}{n_c},\ D = C_D d\frac{\rho}{2}W_\infty^2 \cong C_D d\frac{\rho}{2}W_1^2 \qquad (14)$$

The results are plotted in Fig. 10. This shows that the positions of the calculated stagnation line and the measured heat transfer peak positions coincide fairly well. It should be noted that the minimum values of the heat transfer data as well as the overall heat transfer levels after the separation are quite different between the normal and reverse rotation cases, probably because the growth rates of the boundary layers for those cases are significantly different.

Additional heat transfer data referred to as ''Stationary Wake'' are also plotted in Fig. 7. These were obtained by setting one of the circular cylinders on the wake generator just in front of the leading edge of the test model so that the wake from that cylinder constantly covered the surface of the test model. Twin peaks of the heat transfer appear at almost symmetric positions about $x_{\mathrm{surf}}/R = 0.0$ at which the minimum heat transfer is identified. These peaks can be attributed to the shear layers of the wake that impact upon the surface of the model front portion. Figure 11 expressed in a logarithmic form in Fig. 6, presents the curves of the wake-affected Stanton number distributions against the local Reynolds number. The Stanton number distribution before the separation bubble increases according to the Strouhal number as in the no-wake condition, being in a linear relation with respect to Nu_x in this diagram. Keep in mind that the data for the no-wake conditions are in good agreement with the correlation for the laminar stagnation flow (Eq. (8)). After

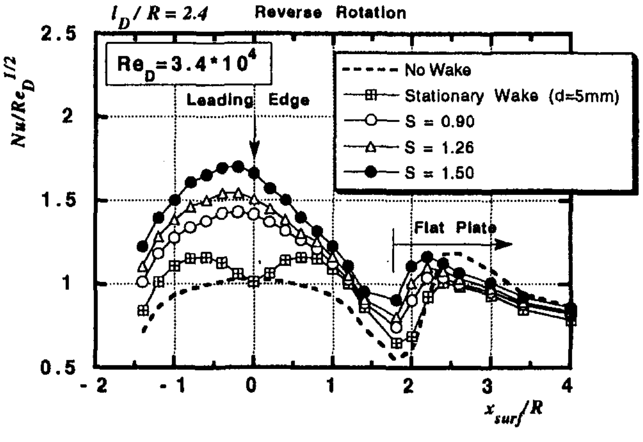

Fig. 8 Wake-affected heat transfer distributions on the test model obtained with the wake generator being rotated in reverse, while other flow conditions are the same with Fig. 7

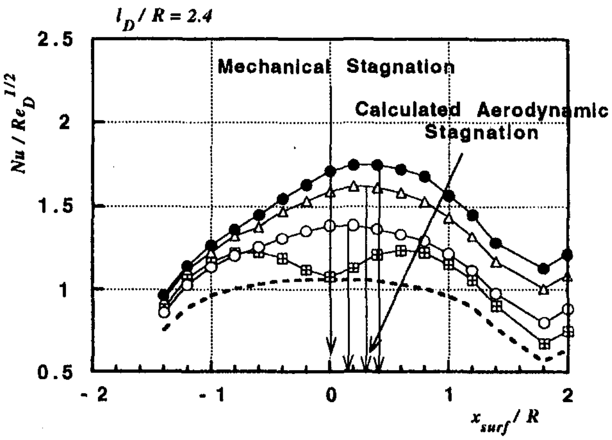

Fig. 10 Shift of the aerodynamic stagnation line due to the moving wake-generating bars; experimental data and predictions by the two-dimensional cascade theory

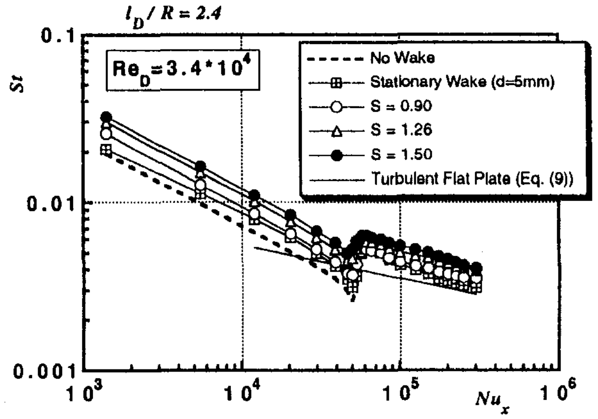

Fig. 11 Wake-affected Stanton number distributions against local Reynolds number; $Re_D = 3.4 \times 10^4$

the reattachment, the Stanton number distributions under the unsteady flow conditions look like those of the turbulent flow but the differences between the data and the correlation (Eq. (9)) are relatively large, while the heat transfer data for the stationary wake case tend to follow the correlation. These phenomena can also be attributed to the shift of the actual stagnation lines.

As the inlet Reynolds number increases, the profiles of the wake-affected heat transfer distributions around the semi-circular cylinder become almost symmetric about $x_{\mathrm{surf}}/R = 0.0$, as illustrated in Fig. 12. This is expected from Eq. (10), that is, even at the highest Strouhal number in this case ($S = 1.5$) the calculation yields the stagnation position to be $x_{\mathrm{surf}}/R = 0.22$, which almost corresponds to the measured peak position for the same condition. Likewise in the previous case, heat transfer along the test model surface is considerably enhanced due to the increase in the Strouhal number; Fig. 13 also confirms this situation. In this case the Stanton number after the reattachments is likely to follow the correlation for the turbulent flow, although slight deviations appear with the Strouhal number.

Both Figs. 14 and 15 show the case for the highest inlet Reynolds number among the present experiments. In this case the moving wake effect on the heat transfer distribution is seen to be like the previous cases, but the data under the influence of the stationary wake show some pronounced increase in their overall level compared to the data in Fig. 8 or Fig. 12. After the reattachment, on the other hand, the heat transfer data for the entire Strouhal numbers differ very little from one another.

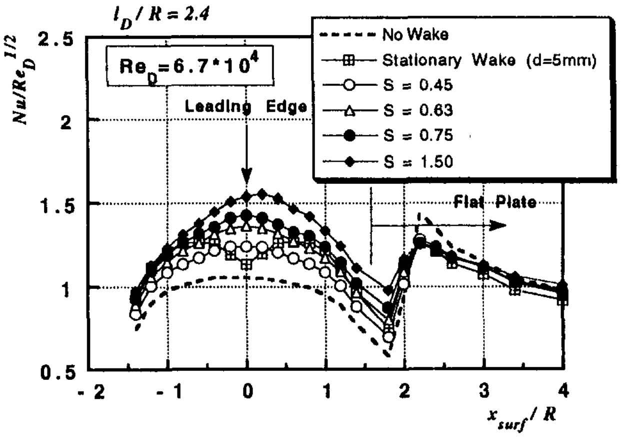

Fig. 12 Wake-affected heat transfer distributions on the test model for several unsteady flow conditions; $Re_D = 6.7 \times 10^4$

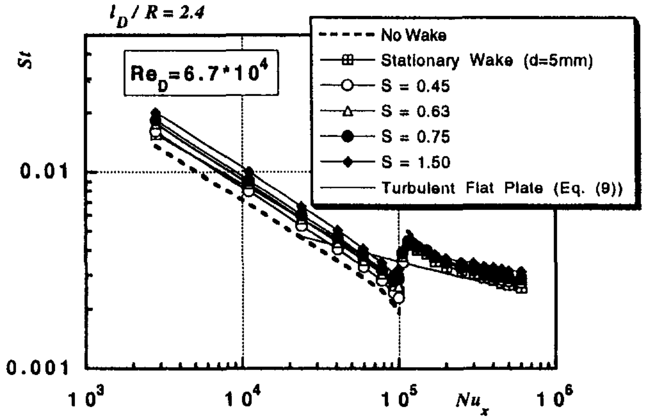

Fig. 13 Wake-affected Stanton number distributions against local Reynolds number; $Re_D = 6.7 \times 10^4$

In these observations, the distance between the rotation plane of the bars and the leading edge of the test model, l_D, was fixed to be $l_D/R = 2.4$. In order to examine an effect of such distance on the wake-affected heat transfer, the test model was moved downward by 100 mm so that l_D/R be 4.4, in which case it was expected that the extended distance could alter the wake characteristics. Figure 16 reveals the results for that case. Compared with the previous results in Fig. 14, one might notice that the minimum value of the heat transfer at the stagnation line

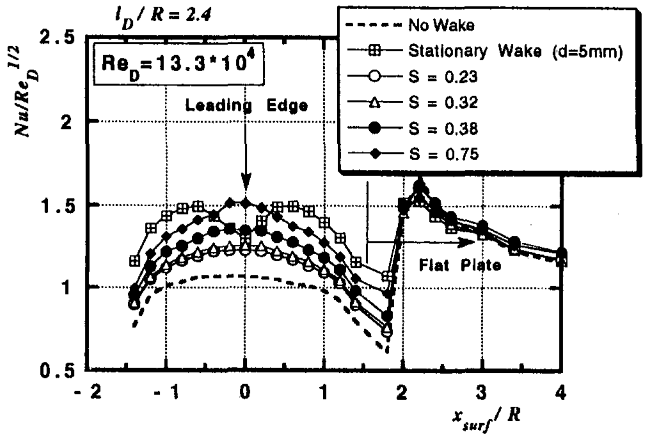

Fig. 14 Wake-affected heat transfer distributions on the test model for several unsteady flow conditions; $Re_D = 13.3 \times 10^4$

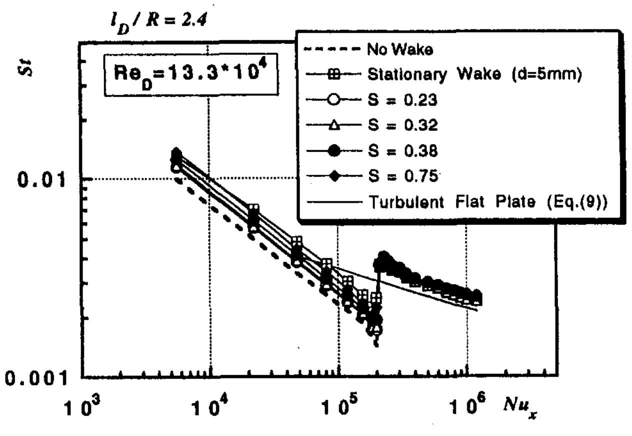

Fig. 15 Wake-affected Stanton number distributions against local Reynolds number; $Re_D = 13.3 \times 10^4$

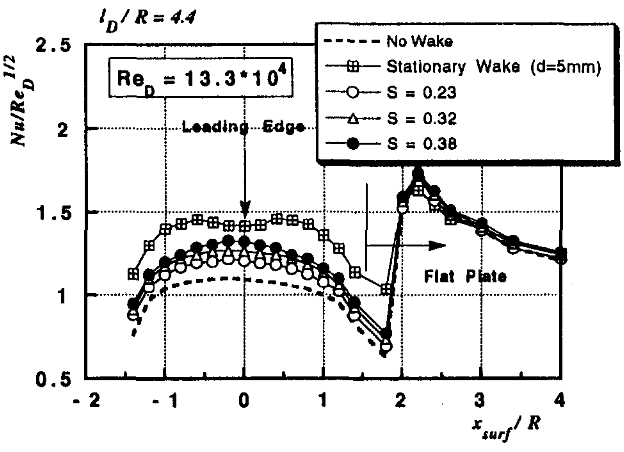

Fig. 16 Wake-affected heat transfer distributions on the test model with the distance between the bars and the test model being elongated; $l_D/R = 4.4$, $Re_D = 13.3 \times 10^4$

increases at the stationary wake condition and the protruding twin peaks identified in Fig. 14 almost disappear. This is obviously due to the decay of the shear layers in the wake. On the contrary, the heat transfer distributions at the unsteady flow conditions show very little change.

From those observations mentioned above, it appears that the wakes from the moving cylinders enhance the heat transfer around the leading edge of the test model to a great extent, the dependency of the Stanton number on the local Reynolds number being almost unchanged. Therefore the wake-affected heat transfer of the stagnant flow around the leading edge can be expressed from an analogy with Eq. (8) as follows:

$$\overline{\mathrm{St}}_w = C\ \mathrm{Pr}^{-0.6}\ \mathrm{Re}_x^{-0.5} \tag{14}$$

where C is a proportional factor, which could be a function of Strouhal number, incident wake characteristics, inlet Reynolds number, and so on. It seems natural to assume that the Strouhal number is a dominant parameter in the heat transfer enhancement, so that by calculating $\overline{\mathrm{St}}_w/\mathrm{Pr}^{-0.6}\ \mathrm{Re}_x^{-0.5}$ from the heat transfer data before the separation bubble, and then interpolating such results by a polynomial function of the Stanton number, the following expression for the factor C can be deduced, as shown in Fig. 17:

$$C(S) = 0.626 + 0.162S + 0.016S^2 \tag{15}$$

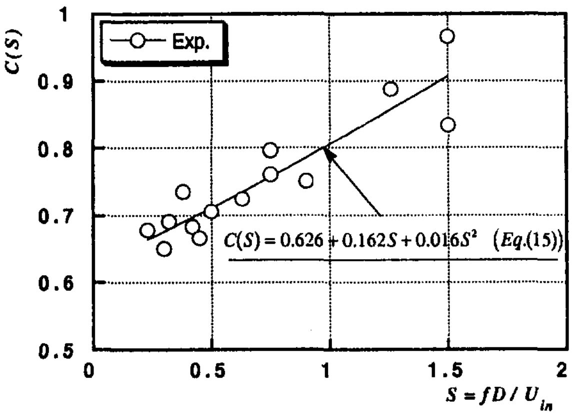

Fig. 17 Correlation for the enhancement factor of the wake-affected heat transfer averaged around the leading edge, which is a function of the bar-passing Strouhal number

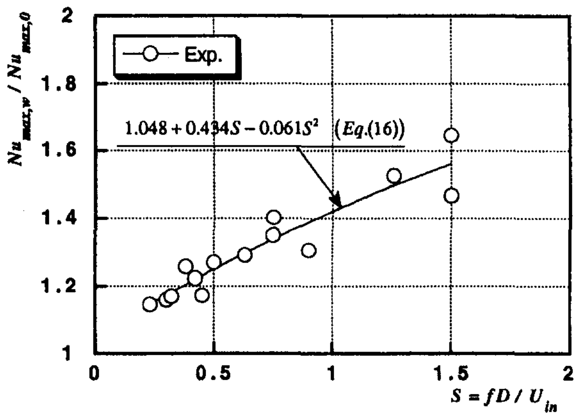

Fig. 18 Dependency of the maximum wake-affected Nusselt numbers on the bar-passing Strouhal number and its correlation

Despite some data scattering, Fig. 18 as well as the interpolated expression Eq. (15) reveal the clear dependency of the heat transfer enhancement around the leading edge upon the Strouhal number, which is rather in contrast to the case for the Stanton number after the reattachment.

Strictly speaking, Eq. (15) cannot hold on the stagnation line because of the definition of Stanton number. Hence, for the convenience of a later discussion, a correlation for heat transfer enhancement on the stagnation line, $\mathrm{Nu}_{\max,w}/\mathrm{Nu}_{\max,0}$, shown in Fig. 18, is given as

$$\frac{\mathrm{Nu}_{\max,w}}{\mathrm{Nu}_{\max,0}} = 1.048 + 0.434S - 0.061S^2. \tag{16}$$

It should be noted that the dependencies of $C(S)$ and $\mathrm{Nu}_{\max,w}/\mathrm{Nu}_{\max,0}$ on the Strouhal number are not the same. This is because, in contrast to the case of Fig. 18, each of the points in Fig. 17 is obtained from the average of the corresponding heat transfer data before the separation bubble.

Discussion

Effect of Negative Jet. In the previous section some discussion was made about the asymmetric profiles of the Nusselt number around the semicircular leading edge at the lowest inlet Reynolds number condition, which was also observed in the study by O'Brien (1990). Meanwhile, O'Brien, along with Paxson and Mayle (1991), has claimed that so-called negative jet effects appeared around the leading edge under the influence of the periodic passing wakes and such effects were detected in different fashions on the leeward and windward side of the leading edge, which correspond to the right and left side, respectively, in the present notation. Consequently one might suppose that the above-mentioned asymmetric profiles were caused by those asymmetric effects of the wakes to some extent. Such supposition is partially supported by the author's previous experiments about the wake-affected heat transfer on a flat plate instead of the present test model as shown in the upper portion of Fig. 19 (Funazaki et al., 1993). This figure also illustrates the results obtained in those experiments, where the symbols with "R" represent the data in the reverse rotation case. It is found that the heat transfer coefficients for the reverse rotation are meaningfully lower than those of the normal rotation case, though the differences in magnitude are not as large as 10 percent of the normal rotation data. Accordingly it is concluded that the rotation direction of the disk in the wake generator might affect the heat transfer around the circular leading edge, but its effect is a somewhat limited one.

Comparison With O'Brien's Experiment. From his experiment using a spoked-wheel wake generator in an annular-flow wind tunnel, O'Brien (1990) measured the time-averaged

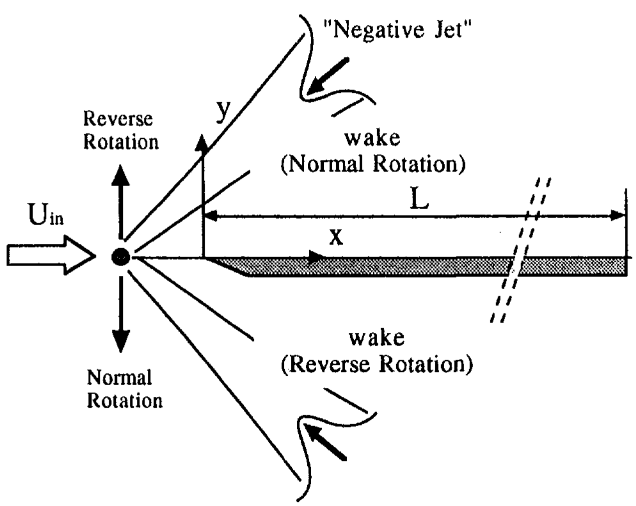

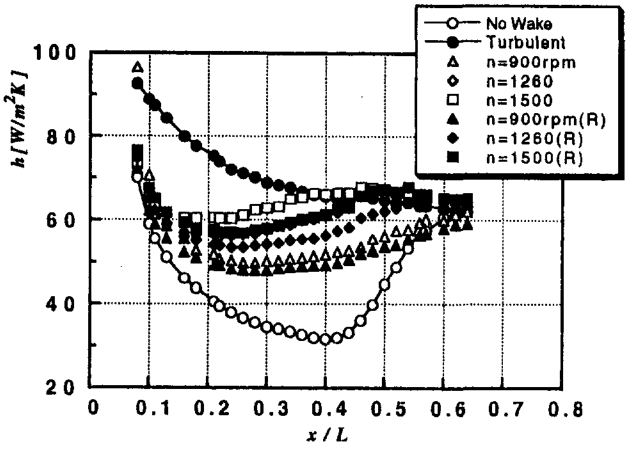

Fig. 19 Wake-affected heat transfer on the flat plate with the wake generator being rotated in the normal and the reverse directions (Funazaki et al., 1993)

heat transfer around the test cylinder with a 12.7 mm diameter; these results are shown in Fig. 21. In this figure, the ordinate is the ratio of wake-affected Nusselt number to the corresponding steady Nusselt number at the stagnation line against the Strouhal number. Note that the definition of Strouhal number in the O'Brien paper differs from the present definition, so that the data in Fig. 20 are reproduced from the original paper according to the present definition. Also shown in this figure is the correlation curve of Eq. (13), for comparison. The heat transfer ratio at the Strouhal number less than 0.1 is almost of constant value ($\cong$1.08), and at the higher Strouhal numbers the ratio tends to increase according to the Strouhal number in almost the same manner with the correlation. Agreement between the O'Brien data and the correlation at the higher Strouhal numbers surprising, considering the fact that the diameter ratios of wake-generating bar and test model (d/D) employed in the two studies are quite different, where $d/D = 0.29$ for the O'Brien's experiment and $d/D = 0.05$ for the present study.

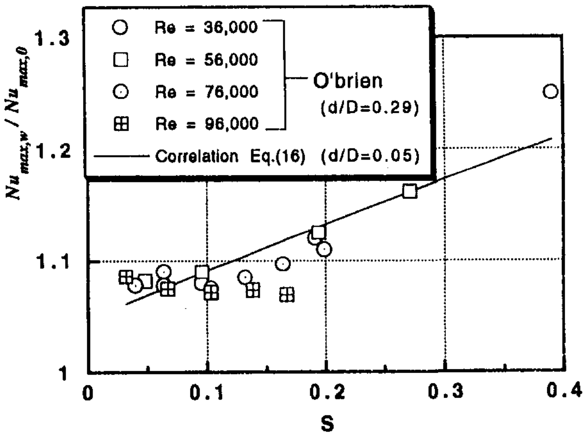

Fig. 20 Comparison between the present correlation (Eq. (15)) and the experimental data by O'Brien (1990)

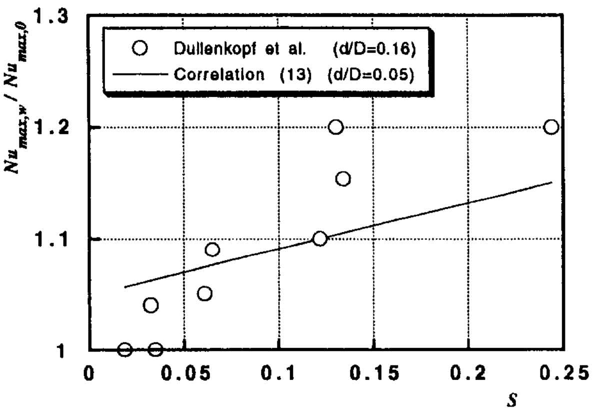

Fig. 21 Comparison between the present correlation (Eq. (16)) and the experimental data by Dullenkopf et al. (1990)

Comparison With the Cascade Test Data. Dullenkopf et al. (1990) conducted an experiment similar to the present one using the linear cascade as well as the rotating wake generator. From the wake-affected heat transfer distributions around the blade leading edge in their paper, the heat transfer enhancement at the stagnation line, $\mathrm{Nu}_{\max,w}/\mathrm{Nu}_{\max,0}$, are calculated and compared with the correlation (Eq. (16)), as shown in Fig. 21. Consequently, it is found that the present correlation yields results similar to the data derived from the cascade test. However, some quantitative differences between the two appear in a meaningful fashion, which can probably be attributed to the uncertainties involved in both experiments.

Conclusions

The influence of the periodic passing wakes on the heat transfer over the leading edge as well as the flat plate was investigated. Local heat transfer distributions along the test surface were measured under the several unsteady conditions of the bar-passing Strouhal number for four inlet Reynolds numbers. The findings in this study are summarized as follows:

1 The heat transfer along the surface of the test model is enhanced by the periodic passing wakes from the moving bars, and such enhancing effect becomes prominent as the bar-passing Strouhal number increases.

2 In the lowest Reynolds number case, the profiles of the wake-affected heat transfer around the stagnation region become considerably asymmetric about the geometric stagnation line, especially at the higher Strouhal number. This is mainly because of the flow being turned by the moving bars ahead of the test model.

3 The dependency of the wake-affected Stanton number around the stagnation region on the local Reynolds number is quite similar to that of the no wake condition. This means the Stanton number in the region is proportional to $\mathrm{Re}_x^{1/2}$. From this finding, a correlation is deduced for the enhancement factor due to the periodic wakes.

4 Comparisons are made between the correlations obtained in this study and the other experimental data, and it follows

that the present study yields similar results to those of the previous studies about the wake effect, despite the large difference in the geometric conditions.

Acknowledgments

The work reported in this paper is financially supported by Aero-engine Division of IHI, Ishikawajima-Harima Heavy Industries, under the supervision of S. Yamawaki. The author is greatly indebted to Freedrick P. Laing, a former student of Iwate University, for his valuable involvement in conducting the experiment, and to Y. Yamashita for his great help in manufacturing the test model.

References

Benedict, R. P., 1969, *Fundamental of Temperature, Pressure, and Flow Measurements,* Wiley, New York.

Dullenkopf, K., and Mayle, R. E., 1994, "The Effects of Incident Turbulence and Moving Wakes on Laminar Heat Transfer in Gas Turbines," ASME JOURNAL OF TURBOMACHINERY, Vol. 116, pp. 23–28.

Dullenkopf, K., Schulz, A., and Wittig, S., 1991, "The Effect of Incident Wake Conditions on the Mean Heat Transfer of an Airfoil," ASME JOURNAL OF TURBOMACHINERY, Vol. 113, pp. 412–418.

Frossling, N., 1958, "Evaporation Heat Transfer and Velocity Distribution in Two-Dimensional and Rotationally-Symmetric Laminar Boundary Layer," NACA TM-1432.

Funazaki, K., 1989, "Measuring Technique of Heat Transfer on Turbine Airfoils Using Boundary Element Method," *IHI Technical Report,* Vol. 28, pp. 327–332.

Funazaki, K., Meguro, T., and Yamawaki, S., 1993, "Studies on the Unsteady Boundary Layer on a Flat Plate Subjected to Incident Wakes (Forced Transition Models of the Boundary Layer)," *JSME International Journal,* Vol. 36, pp. 532–539.

Kays, W. M., and Crawford, M. E., 1980, *Convective Heat and Mass Transfer,* McGraw-Hill, New York, p. 140.

Kline, S. J., and McClintock, F. A., 1953, "Describing Uncertainties in Single Sample Experiments," *Mechanical Engineering,* Jan., pp. 3–8.

Lowry, G. W., and Vachon, R. I., 1975, "The Effect of Turbulence on Heat Transfer From Heated Cylinders," *International Journal of Heat and Mass Transfer,* Vol. 18, pp. 1229–1242.

Magari, P. J., and Lagraff, L. E., 1994, "Wake-Induced Unsteady Stagnation-Region Heat Transfer Measurements," ASME JOURNAL OF TURBOMACHINERY, Vol. 116, pp. 29–38.

Mehendale, A. B., Han, J. C., and Ou, S., 1991, "Influence of High Mainstream Turbulence on Leading Edge Heat Transfer," ASME *Journal of Heat Transfer,* Vol. 113, pp. 843–850.

O'Brien, J. E., 1990, "Effects of Wake Passing on Stagnation Region Heat Transfer," ASME JOURNAL OF TURBOMACHINERY, Vol. 112, pp. 522–530.

Paxson, D. E., and Mayle, R. E., 1991, "Laminar Boundary Layer Interaction With an Unsteady Passing Wake," ASME JOURNAL OF TURBOMACHINERY, Vol. 113, pp. 419–427.

Yoshida, T., 1993, "Progress in High Temperature Turbine Cooling Technology and Its Prospects," *Journal of the Gas Turbine Society of Japan,* Vol. 20, pp. 4–9.

DISCUSSION

R. E. Mayle[1] and K. Dullenkopf[2]

Even the simplest physical consideration concerning the effect of passing wakes in the free stream on heat transfer indicates that the correlations given in Eqs. (15) and (16) cannot be generally valid. In particular, neither correlation contains any quantity related to the individual wakes. To illustrate the wake's role, if Nu_0 is the Nusselt number for a position on the surface without passing wakes and Nu_w is a representative Nusselt number in the wake, then the time-averaged Nusselt number for a flow with periodically passing wakes is $\overline{\mathrm{Nu}} = \mathrm{Nu}_0 + (\mathrm{Nu}_w - \mathrm{Nu}_0)(\tau_w/\tau)$, where τ_w is a representative passing time for the wake over any point on the surface and τ is the period between wakes. For no wake, $\tau_w = 0$, or no augmentation caused by the wake, $\mathrm{Nu}_w = \mathrm{Nu}_0$, the time-averaged Nusselt number is, as expected, Nu_0. For a completely wake saturated flow, $\tau_w = \tau$, and $\overline{\mathrm{Nu}} = \mathrm{Nu}_w$ as expected.

Introducing your definition of the Strouhal number, $S = fD/U_{in}$, the above expression becomes $\overline{\mathrm{Nu}} = \mathrm{Nu}_0 + (\mathrm{Nu}_w - \mathrm{Nu}_0) \times (U_{in}\tau_w/D)S$, which clearly indicates that the coefficient of the Strouhal number (which you consider constant in Eqs. (15) and (16)) really depends on wake-related quantities. Such quantities are wake turbulence level and length scales, which affect Nu_w, and the wake width, which affect τ_w. Since different experiments have different wake characteristics, wake passing times, and periods, all which affect the coefficient of S in this simplest of models, the poor comparisons shown in Figs. 20 and 21 should not be surprising. For details regarding a more realistic model for the effect of passing wakes on laminar heat transfer, you are referred to Dullenkopf and Mayle (1994).

Author's Closure

The author would like to acknowledge the comment from Mayle and Dullenkopf. As described in their comment or in their paper (Dullenkopf and Mayle, 1992), it is necessary to take account of several factors of the wake characteristics in order to gain a thorough understanding of how the wake passage affects the heat transfer around stagnation regions. In particular, much attention must be paid to wake structure and its turbulence length. The author also agrees with the viewpoint of Dullenkopf and Mayle, which implies that wakes at higher turbulence levels would produce heat transfer enhancement, almost independent of the wake generation. The author believes this could be applied to the present case.

Although Dullenkopf and Mayle (1992) proposed a simple but useful method for predicting wake-affected heat transfer around the stagnation region, the author has not been fully contented with their method because there was no information given to evaluate the Nusselt number Nu_w or the wake duration τ_w. This situation directed the author to start the present study. Since effects of free turbulence are not included in his experiment, this paper does not provide a general correlation on the wake-affected heat transfer for the readers. Therefore, the author has proceeded with his research to investigate effects of free-stream turbulence upon the wake-affected heat transfer, which also discusses how Nu_w or τ_w should be specified (Funazaki, 1994; Funazaki et al., 1995). Despite this study, much remains to be done for further understanding of this complicated phenomenon.

References

Funazaki, K., 1995, "Studies on Wake-Affected Heat Transfer Around the Leading Edge of Turbine Blades (Modeling of Heat Transfer Enhancement)," *Journal of the Gas Turbine Society of Japan,* Vol. 22, pp. 83–90.

Funazaki, K., et al., 1995, "Studies on Wake-Affected Heat Transfer Around the Leading Edge of a Blunt Body," *Proc. ASME/JSME Thermal Engineering Conference,* Vol. 1, pp. 343–350.

---

[1] Professor Emeritus of Mechanical Engineering, Rensselaer Polytechnic Institute, Troy, NY 12180 USA.

[2] Dr.-Ingenieur, Institut für Thermische Strömungs Maschinen, Universität Karlsruhe, 76128 Karlsruhe, Germany.

that the present study yields similar results to those of the previous studies about the wake effect, despite the large difference in the geometric conditions.

Acknowledgments

The work reported in this paper is financially supported by Aero-engine Division of IHI, Ishikawajima-Harima Heavy Industries, under the supervision of S. Yamawaki. The author is greatly indebted to Freedrick P. Laing, a former student of Iwate University, for his valuable involvement in conducting the experiment, and to Y. Yamashita for his great help in manufacturing the test model.

References

Benedict, R. P., 1969, *Fundamental of Temperature, Pressure, and Flow Measurements,* Wiley, New York.

Dullenkopf, K., and Mayle, R. E., 1994, "The Effects of Incident Turbulence and Moving Wakes on Laminar Heat Transfer in Gas Turbines," ASME JOURNAL OF TURBOMACHINERY, Vol. 116, pp. 23–28.

Dullenkopf, K., Schulz, A., and Wittig, S., 1991, "The Effect of Incident Wake Conditions on the Mean Heat Transfer of an Airfoil," ASME JOURNAL OF TURBOMACHINERY, Vol. 113, pp. 412–418.

Frossling, N., 1958, "Evaporation Heat Transfer and Velocity Distribution in Two-Dimensional and Rotationally-Symmetric Laminar Boundary Layer," NACA TM-1432.

Funazaki, K., 1989, "Measuring Technique of Heat Transfer on Turbine Airfoils Using Boundary Element Method," *IHI Technical Report,* Vol. 28, pp. 327–332.

Funazaki, K., Meguro, T., and Yamawaki, S., 1993, "Studies on the Unsteady Boundary Layer on a Flat Plate Subjected to Incident Wakes (Forced Transition Models of the Boundary Layer)," *JSME International Journal,* Vol. 36, pp. 532–539.

Kays, W. M., and Crawford, M. E., 1980, *Convective Heat and Mass Transfer,* McGraw-Hill, New York, p. 140.

Kline, S. J., and McClintock, F. A., 1953, "Describing Uncertainties in Single Sample Experiments," *Mechanical Engineering,* Jan., pp. 3–8.

Lowry, G. W., and Vachon, R. I., 1975, "The Effect of Turbulence on Heat Transfer From Heated Cylinders," *International Journal of Heat and Mass Transfer,* Vol. 18, pp. 1229–1242.

Magari, P. J., and Lagraff, L. E., 1994, "Wake-Induced Unsteady Stagnation-Region Heat Transfer Measurements," ASME JOURNAL OF TURBOMACHINERY, Vol. 116, pp. 29–38.

Mehendale, A. B., Han, J. C., and Ou, S., 1991, "Influence of High Mainstream Turbulence on Leading Edge Heat Transfer," ASME *Journal of Heat Transfer,* Vol. 113, pp. 843–850.

O'Brien, J. E., 1990, "Effects of Wake Passing on Stagnation Region Heat Transfer," ASME JOURNAL OF TURBOMACHINERY, Vol. 112, pp. 522–530.

Paxson, D. E., and Mayle, R. E., 1991, "Laminar Boundary Layer Interaction With an Unsteady Passing Wake," ASME JOURNAL OF TURBOMACHINERY, Vol. 113, pp. 419–427.

Yoshida, T., 1993, "Progress in High Temperature Turbine Cooling Technology and Its Prospects," *Journal of the Gas Turbine Society of Japan,* Vol. 20, pp. 4–9.

DISCUSSION

R. E. Mayle[1] and K. Dullenkopf[2]

Even the simplest physical consideration concerning the effect of passing wakes in the free stream on heat transfer indicates that the correlations given in Eqs. (15) and (16) cannot be generally valid. In particular, neither correlation contains any quantity related to the individual wakes. To illustrate the wake's role, if Nu_0 is the Nusselt number for a position on the surface without passing wakes and Nu_w is a representative Nusselt number in the wake, then the time-averaged Nusselt number for a flow with periodically passing wakes is $\overline{Nu} = Nu_0 + (Nu_w - Nu_0)(\tau_w/\tau)$, where τ_w is a representative passing time for the wake over any point on the surface and τ is the period between wakes. For no wake, $\tau_w = 0$, or no augmentation caused by the wake, $Nu_w = Nu_0$, the time-averaged Nusselt number is, as expected, Nu_0. For a completely wake saturated flow, $\tau_w = \tau$, and $\overline{Nu} = Nu_w$ as expected.

Introducing your definition of the Strouhal number, $S = fD/U_{in}$, the above expression becomes $\overline{Nu} = Nu_0 + (Nu_w - Nu_0) \times (U_{in}\tau_w/D)S$, which clearly indicates that the coefficient of the Strouhal number (which you consider constant in Eqs. (15) and (16)) really depends on wake-related quantities. Such quantities are wake turbulence level and length scales, which affect Nu_w, and the wake width, which affect τ_w. Since different experiments have different wake characteristics, wake passing times, and periods, all which affect the coefficient of S in this simplest of models, the poor comparisons shown in Figs. 20 and 21 should not be surprising. For details regarding a more realistic model for the effect of passing wakes on laminar heat transfer, you are referred to Dullenkopf and Mayle (1994).

Author's Closure

The author would like to acknowledge the comment from Mayle and Dullenkopf. As described in their comment or in their paper (Dullenkopf and Mayle, 1992), it is necessary to take account of several factors of the wake characteristics in order to gain a thorough understanding of how the wake passage affects the heat transfer around stagnation regions. In particular, much attention must be paid to wake structure and its turbulence length. The author also agrees with the viewpoint of Dullenkopf and Mayle, which implies that wakes at higher turbulence levels would produce heat transfer enhancement, almost independent of the wake generation. The author believes this could be applied to the present case.

Although Dullenkopf and Mayle (1992) proposed a simple but useful method for predicting wake-affected heat transfer around the stagnation region, the author has not been fully contented with their method because there was no information given to evaluate the Nusselt number Nu_w or the wake duration τ_w. This situation directed the author to start the present study. Since effects of free turbulence are not included in his experiment, this paper does not provide a general correlation on the wake-affected heat transfer for the readers. Therefore, the author has proceeded with his research to investigate effects of free-stream turbulence upon the wake-affected heat transfer, which also discusses how Nu_w or τ_w should be specified (Funazaki, 1994; Funazaki et al., 1995). Despite this study, much remains to be done for further understanding of this complicated phenomenon.

References

Funazaki, K., 1995, "Studies on Wake-Affected Heat Transfer Around the Leading Edge of Turbine Blades (Modeling of Heat Transfer Enhancement)," *Journal of the Gas Turbine Society of Japan,* Vol. 22, pp. 83–90.

Funazaki, K., et al., 1995, "Studies on Wake-Affected Heat Transfer Around the Leading Edge of a Blunt Body," *Proc. ASME/JSME Thermal Engineering Conference,* Vol. 1, pp. 343–350.

---

[1] Professor Emeritus of Mechanical Engineering, Rensselaer Polytechnic Institute, Troy, NY 12180 USA.

[2] Dr.-Ingenieur, Institut für Thermische Strömungs Maschinen, Universität Karlsruhe, 76128 Karlsruhe, Germany.

Effect of Free-Stream Turbulence on Flat-Plate Heat Flux Signals: Spectra and Eddy Transport Velocities

R. W. Moss

M. L. G. Oldfield

Department of Engineering Science,
University of Oxford,
Oxford, United Kingdom

An experimental study of the eddy structure in a flat-plate turbulent boundary layer with significant levels of free-stream turbulence is presented. This is relevant to the enhancement of turbomachinery heat transfer by turbulence and should lead to more realistic CFD modeling. Previous measurements showed that Nusselt numbers may be increased by up to 35 percent, and that this increase depended on turbulence integral length scale as well as intensity. The new results described here provide an insight into the mechanism responsible. Thin film gages and hot wires were used to take simultaneous high-frequency measurements of fluctuating heat transfer rates to the flat plate and the fluctuating flow velocity in the free stream and boundary layer. Spectra and correlation analysis shows that the turbulent eddy structure of the boundary layer is dominated by the free-stream turbulence at intensities of 3 percent and above. Eddies in the boundary layer mimicked those in the free stream and convected at the free-stream velocity U, rather than the ~0.8U characteristic of boundary layers. The main heat transfer enhancing mechanism is due to the penetration of free-stream turbulent eddies deep into the boundary layer, rather than enhancement of existing boundary layer turbulence.

Introduction

This paper describes experiments that show that the eddy structure of a flat-plate turbulent boundary layer in a flow with significant levels of free-stream turbulence is dominated by the free-stream eddy structure. This is relevant to the understanding of the fundamental mechanisms that lead to the enhancement of heat transfer to turbomachinery blading due to upstream turbulence from either the combustion chamber or upstream blade rows.

Most previous studies of the effects of free-stream turbulence have either studied purely aerodynamic parameters (Hancock and Bradshaw, 1983; Castro, 1984), or have used time-mean heat flux measurements (Blair, 1983).

Hancock and Bradshaw (1983) measured the change in skin friction coefficient resulting from free-stream turbulence intensities of up to 6 percent and showed that this could be correlated against a function of turbulence intensity and length scale. They also measured the change in boundary layer profile, and found that the wake region, despite a change in profile resulting from the turbulence field, could still be described in terms of a polynomial wake function. Later work (Hancock and Bradshaw, 1989) measured rms levels of fluctuating velocity and Reynolds stresses through the boundary layer, and showed that a logarithmic ''law of the wall'' was valid in the presence of free-stream turbulence at intensities of up to 4 percent. They used a heated plate with conditional sampling to distinguish between free-stream and boundary layer fluid and, by considering intermittency profiles through the boundary layer, showed that free-stream turbulence greatly increases mixing in the wake region as well as increasing the outer extent of the boundary layer. They concluded that larger free-stream length scales penetrate further into the boundary layer than small-scale turbulence.

Blair (1983) used an electrically heated plate to measure turbulent heat flux under the influence of free-stream turbulence. He found that the resulting increase in Stanton number could be correlated using a similar function to that described by Hancock and Bradshaw (1983) for changes in the skin friction coefficient.

Zhou and Wang (1994) used a three-wire probe to make detailed transitional boundary layer measurements on a heated flat plate at turbulence intensities up to 7 percent. Boundary layer profiles of Reynolds shear stress and Reynolds heat flux were obtained; they found that the wake region of the turbulent boundary layer was depressed by the presence of free-stream turbulence, and that the v' distribution in the outer part of the boundary layer was controlled by the free-stream v' level.

MacMullin et al. (1989) used a turbulent free jet impinging on a flat plate to produce turbulence intensities between 7 and 18 percent, and measured increases in Stanton number of up to 100 percent above the predicted level for a turbulent boundary layer on a flat plate. In this type of facility it is difficult to distinguish between the free stream and the boundary layer, with the apparent boundary layer thickness being largest near the plate leading edge, and one cannot actually measure a datum, low free-stream turbulence Stanton number distribution.

Maciejewski and Moffat (1989) also used a turbulent free jet and studied the effects of very high (between 20 and 60 percent) turbulence intensities. They found that at these turbulence levels the Stanton number was not a function of Reynolds number and the heat transfer coefficient could best be described as $h \propto \rho C_p u'$. Boundary layer velocity profiles showed that the rms free-stream turbulence level was present down to $y^+ = 50$ above the surface. In these circumstances the boundary layer itself is unimportant, and the heat transfer is mainly caused by free-stream turbulent eddies.

This paper differs from such previous studies in that it actually describes the unsteady velocity and heat flux signals, and shows that these correlate even at turbulence intensities as low as 4 percent; such high-speed measurements of fluctuating heat flux are, at present, unique.

Contributed by the International Gas Turbine Institute and presented at the 39th International Gas Turbine and Aeroengine Congress and Exposition, The Hague, The Netherlands, June 13–16, 1994. Manuscript received by the International Gas Turbine Institute February 25, 1994. Paper No. 94-GT-205. Associate Technical Editor: E. M. Greitzer.

The work described here follows experiments (Moss and Oldfield, 1991) that showed that combustion chamber turbulence spectra were independent of combustion, and thus appeared to be due to dilution mixing. Further work (Moss and Oldfield, 1992) using a flat plate in a short-duration wind tunnel found that the turbulent heat transfer to the plate was a function of turbulence integral length scale as well as intensity. An empirical modification of the correlation by Blair (1983) was proposed that took into account the turbulence integral length scale as well as the turbulence level. With high free-stream turbulence the Nusselt number could be enhanced by as much as 35 percent.

In order to gain an insight into the physical mechanisms responsible for this large enhancement of turbulent thermal transport rates, high-frequency measurements of fluctuating heat transfer rates on the flat plate were carried out and are analyzed below. Spectra and correlation techniques were used to process both the gage signals and hot-wire measurements of flow velocity, and showed that the turbulent eddy structure of the boundary layer is dominated by high free-stream turbulence. This is felt to be the main heat transfer enhancing mechanism.

Apparatus

The experimental apparatus is described by Moss and Oldfield (1992). An existing high-speed (up to M = 0.5) wind tunnel in the Oxford University Turbomachinery Laboratories was used with a new working section built to allow transient heat transfer measurements. The experimental flat plate (150 mm span, 332 mm chord, 10 mm thick) was machined from a sheet of machinable glass ceramic (MACOR) and mounted on the centerline of the 150 × 150 mm tunnel working section. An 8:1 involute profile that blended smoothly onto the flat surface was chosen for the leading edge in order to reduce the risk of high turbulence levels causing transient separation. An array of 34 thin film heat transfer gages (4 mm × 0.25 mm, aligned transversely to the flow) was fired onto the plate surface and can be seen in Fig. 1. These were connected to a Heat Transfer Analogue (Oldfield et al., 1982) which produces an output voltage proportional to heat flux over a bandwidth of 0.2 Hz to 80 kHz; the resulting heat flux signals were sampled at 200 kHz by a 12-bit analogue to digital convertor with a 66 kHz second-order Butterworth anti-aliasing filter.

Although the thin film gage frequency responses are high (>100 kHz), the smallest turbulence dimension that can be measured is limited by the 0.25 mm streamwise gage width, corresponding to a maximum frequency of ~40 kHz for a 70 m/s velocity.

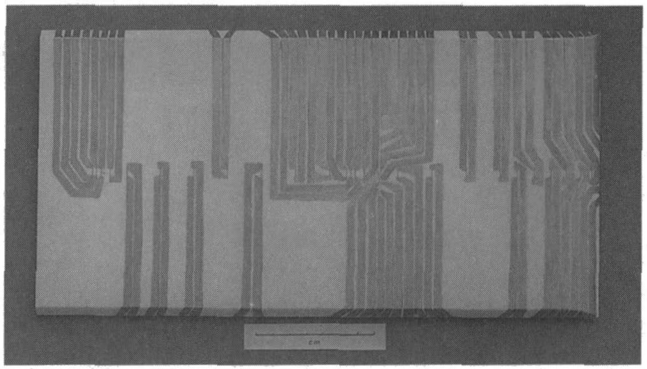

Fig. 1 MACOR plate showing thin film gages

The transient technique of using thin-film resistance gages to measure heat transfer requires a temperature difference between the plate surface and the free stream. This was provided by preheating the working section and plate with hot air. The tunnel flow started in 200 ms and measurements were then taken for a further 300 ms. A movable probe holder allowed a single transverse hot wire probe, measuring the mean plus fluctuating streamwise velocity $U + u'$, to be positioned anywhere above the plate.

A set of interchangeable grid boxes and spacers allowed turbulence generating grids of various sizes to be placed at any position from 90 mm to 1000 mm upstream of the plate leading edge. The grids referred to in this paper are shown in Fig. 2 and summarized in Table 1.

In Table 1, x is the distance from the leading edge of the plate, Tu is the measured free-stream turbulence intensity $\sqrt{\overline{u'^2}}/U \times 100$ percent and $\mathrm{Nu}/\mathrm{Nu}_0$ is the Nusselt number enhancement factor above the level in a turbulent boundary layer with zero free-stream turbulence. A measure of the size of the turbulent eddies is given by the integral length scale (Hinze, 1975), defined as $\Lambda_x = U \int_0^{R(\tau)=0} R(\tau)d\tau$ where $R(\tau) = \overline{u'(t)u'(t+\tau)}/\overline{u'^2}$ is the autocorrelation of the streamwise velocity fluctuation, the integration limit is $R(\tau) = 0$ as described by Moss and Oldfield (1992), and U is the free-stream mean velocity.

One can see that Grids D and E have high turbulence levels, but different length scales, while grids A and E have similar length scales but different Tu. Parallel bar grids were used as these allow larger bar diameters, and hence length scales, for a

Nomenclature

C_p = specific heat capacity of air, J/kgK
d = pitch of bar grids
D_f = "distance factor" = $-U\tau/\Delta x$
$\hat{D}_f$ = distance factor corresponding to peak in R_{qq}
f = frequency, Hz
h = heat transfer coefficient, W/m^{2}K
k = conductivity of air, W/mK
k = wavenumber $2\pi f/U$
M = Mach number
Nu = Nusselt number = hx/k
Nu_0 = datum Nusselt number distribution (tripped boundary layer, low Tu)
q = fluctuating component of surface heat flux
Q = time-mean component of surface heat flux
PSD = power spectral density = $(1/U^2)(d(u'^2)/dk)$ or $(1/Q^2)(d(q^2)/dk)$
$R(\tau)$ = correlation coefficient at time lag τ
$R_{qq}(\tau)$ = cross correlation between heat fluxes from two gages
$R_{qu}(\tau)$ = cross correlation between surface heat flux and velocity measured by hot wire
Re_x = Reynolds number based on distance from leading edge
Tu = fractional streamwise turbulence intensity = u'_{rms}/U
U = time-mean component of streamwise velocity, m/s
u' = fluctuating component of streamwise velocity, m/s
u^* = friction velocity = $\sqrt{\tau_w/\rho}$
V_e = event velocity ratio = $-1/\hat{D}_f$
v' = fluctuating component of crosswise velocity, m/s
x = streamwise distance from plate leading edge, mm
x_g = distance between grids and plate leading edge, mm
y^+ = nondimensional height above surface = yu^*/v
δ_{995} = predicted turbulent boundary layer thickness = $0.37x\ \mathrm{Re}_x^{-0.2}$
θ = predicted turbulent boundary layer momentum thickness = $0.036x\ \mathrm{Re}_x^{-0.2}$
ρ = density of air, kg/m^3
Λ_x = streamwise integral turbulence length scale
τ = correlation time lag, s
τ_w = shear stress at wall, N/m^2

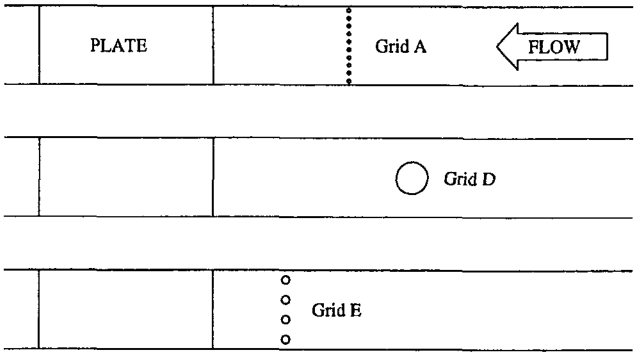

Fig. 2 Grid configurations, drawn to scale; working section width 150 mm

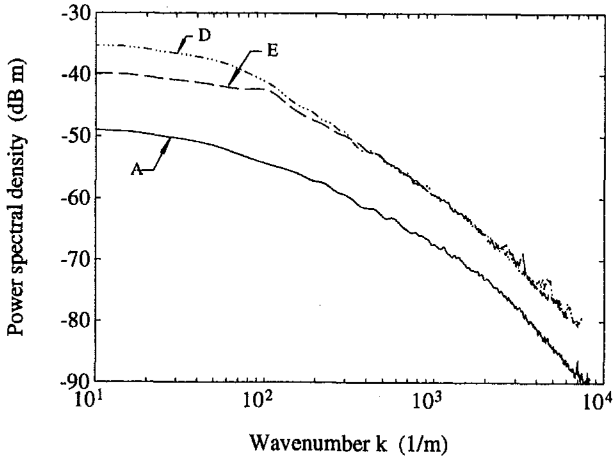

Fig. 3 Free-stream streamwise turbulence spectra at x = 100 mm

given blockage ratio than crossed-bar grids. Comparison of the free-stream spectra (Fig. 3) shows grids D and E to differ mainly in the low wavenumber ($k < 100\ \mathrm{m}^{-1}$) region. A similar comparison at a later station would show the turbulence from the high $(x + x_g)/d$ grids (A and E) decaying more rapidly than the single bar grid D.

The flowfield behind the single bar in grid D will inevitably suffer from some nonuniformity. Thermochromic liquid crystal studies of heat transfer over the whole plate, however, showed heat transfer coefficients to be roughly constant across the central third of the width of the plate. Turbulence levels as high as those produced by grid D are likely to occur in an engine on aerofoil pressure surfaces and it is essential that such conditions be investigated even if flowfield uniformity and isotropy of the turbulence cannot be guaranteed.

In general, the variables presented in this paper have been the physical parameters, for simplicity and to allow direct comparisons between data. The boundary layer variables x^+ and y^+ have not been used as they depend on knowing the friction velocity τ_w. The nondimensional variables y/δ_{995} and Re_x can be obtained by noting that $\mathrm{Re}_x = 5.26 \times 10^6 x = 7.89 \times 10^5$ at $x = 150$ mm, and $\delta_{995} = 0.37x\ \mathrm{Re}_x^{-0.2} = 3.67$ mm here. The appropriate nondimensional wavenumber is $k \times \delta_{995}$.

Table 1 Turbulence grid geometry and performance

GRID:	A	D	E
Bar diameter (mm)	6	60	15
Bar pitch (mm)	15	single	37.5
Distance to LE x_g (mm)	260	380	140
Tu (%) at x = 100 mm	4	16	12.1
180 mm	3.3	15	9.4
300 mm	2.9	11.7	6.9
Λ_x (mm) at x = 100 mm	9.4	14.6	8.5
180 mm	9.0	15.3	9.7
300 mm	10.0	16.6	12.1
Nu/Nu_0 at x = 100 mm	1.01	1.30	1.30
180 mm	1.06	1.39	1.30
300 mm	1.07	1.41	1.30

Comparison of Heat Flux With Velocity Characteristics in the Boundary Layer and Free-Stream

To understand the effects of the free-stream turbulent eddy structure on the turbulent boundary layer structure, various diagnostics were used.

Raw Heat Flux Signals. Figure 4 compares the signal from the gage at $x = 150$ mm ($\mathrm{Re}_x = 7.5 \times 10^5$) at Tu = 15 percent (grid D) with the low turbulence grid-out case. The high-turbulence signal shows Nusselt number fluctuations between a "low" level, which is very similar to that seen in a turbulent boundary layer with no free-stream turbulence, and a "high" level, which can be up to 100 percent higher. The transition between these levels occurs at a lower frequency than the turbulent fluctuations within them, and one may imagine that the large features are due to large free-stream turbulence vortices acting on the boundary layer while the smaller fluctuations may be a result of the turbulence within the boundary layer.

Boundary Layer Traverses. Figure 5 compares boundary layer mean velocity profiles, measured by a hot wire, under four different free-stream turbulence levels. y is the distance above the plate surface. The presence of free-stream turbulence

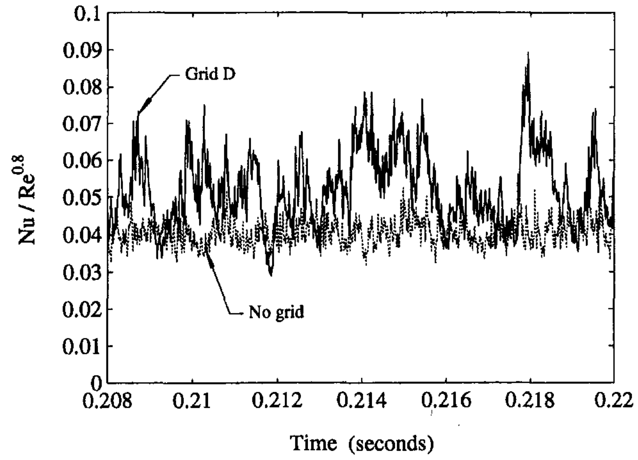

Fig. 4 Comparison of nondimensionalized heat flux signals with high and low free-stream turbulence

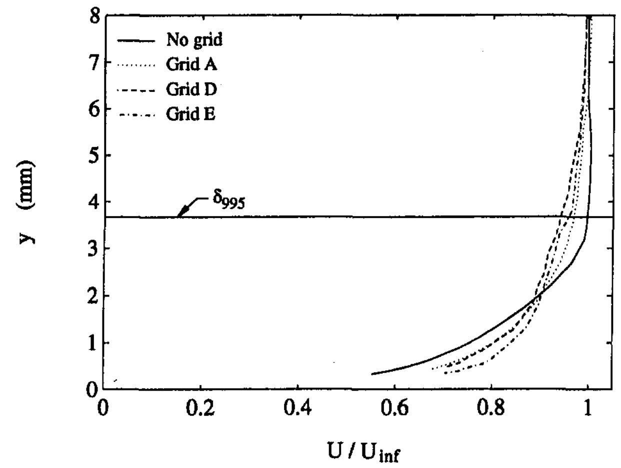

Fig. 5 Effect of free-stream turbulence on boundary layer velocity profile (x = 150 mm, tripped: $Re_x = 7.89 \times 10^5$, $\delta_{995} = 3.67$ mm, $\theta = 0.357$ mm)

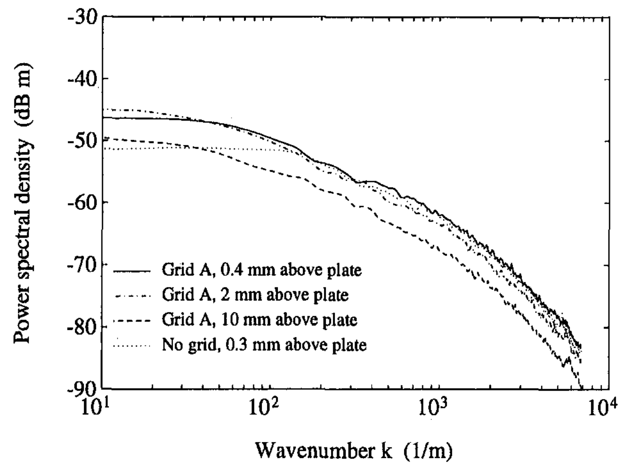

Fig. 7 Boundary layer turbulence spectra (Grid A, x = 150 mm, tripped) compared with grid-out case. 10 mm line is similar to freestream spectrum.

has changed the velocity profile by increasing the mixing in the outer part of the boundary layer (and giving a higher velocity gradient across the log-law region). This is consistent with the findings of Blair (1983) and Hancock and Bradshaw (1989). The boundary layer has increased in thickness from approximately 3.2 mm ($y/\delta_{995} = 0.9$) to 6 mm ($y/\delta_{995} = 1.6$); this effect is seen even at $Tu = 4$ percent with grid A. The difference between the three grids, in terms of the velocity profile, is surprisingly small when compared to the $Tu = 0$ case.

Turbulence Spectra Through the Boundary Layer. Figure 6 compares measurements of turbulence spectra in the boundary layer with no grid and with grid D. These are velocity measurements, taken using a hot wire in a continuous (cold plate) test, and they have been plotted against wavenumber defined using the free-stream (as opposed to local) velocity U.

The grid-out case shows turbulence levels that are highest close to the surface and fall to zero as one approaches the free stream. Grid D, however, produces turbulence spectra that are almost identical, whether measured in the free stream or 0.5 mm above the surface. Only at low wavenumbers ($k < 80$ m^{-1}) is there any noticeable variation with height; a slight increase in the (streamwise) velocity component is seen close to the surface, and is presumably associated with the attenuation of any vertical component here. The similarity of the spectra throughout the boundary layer is remarkable; it suggests that free-stream turbulent eddies are penetrating right through the velocity-defect part of the boundary layer. Grid E produces a similar effect.

With grid A the free-stream turbulence level is less than that produced at the bottom of the boundary layer in the grid-out case. Figure 7 shows that the spectrum within the boundary layer is not raised by the presence of the free-stream turbulence except at low wavenumbers. This suggests that the change in the velocity distribution (Fig. 5) and the increase in Nusselt number are a result of changes to the low wavenumber structure of the boundary layer.

Length Scales Within Boundary Layer. Table 2 shows the integral length scales derived from hot-wire measurements within the boundary layer. It can be seen that even as little as 3.5 percent Tu in the free stream makes a large difference to the integral scale within the boundary layer, and that the boundary layer length scale is similar to that in the free stream when the latter is highly turbulent (grids D and E).

Comparison of Heat Flux and Velocity Signals. Figures 8, 9, and 10 compare the hot-wire velocity signal 0.5 mm above the plate with the surface heat flux signal at x = 150 mm. The grid D heat flux measurements show much larger fluctuations than in the grid-out case (as expected from Fig. 4). The similarity of velocity and heat flux traces is evident even with the modest 3.5 percent free-stream turbulence intensity provided

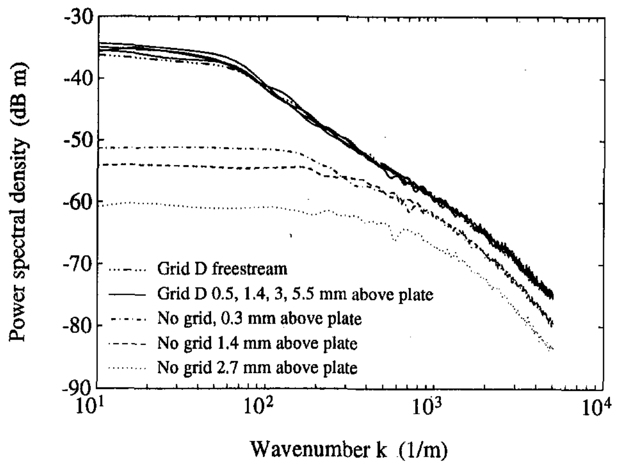

Fig. 6 Boundary layer and free-stream turbulence spectra (Grid D) compared with grid-out case. x = 150 mm.

Table 2 Integral length scales and turbulence intensities within the boundary layer at x = 150 mm, $Re_x = 7.89 \times 10^5$, $\delta_{995} = 0.37x\, Re_x^{-0.2}$ = 3.67 mm

	y = 0.6 mm, y/δ_{995} = 0.16	y = 3 mm, y/δ_{995} = 0.82	Freestream
No grid	3.3 mm, 5.4%	2.0 mm, 2.5%	64 mm, 0.07%
Grid A	8.2 mm, 6.4%	14.2 mm, 5.9%	9.1 mm, 3.5%
Grid D	12.0 mm, 15%	15.9 mm, 15.4%	15.0 mm, 14.5%
Grid E	10.4 mm, 10.5%	9.5 mm, 11.3%	9.3 mm, 11.7%

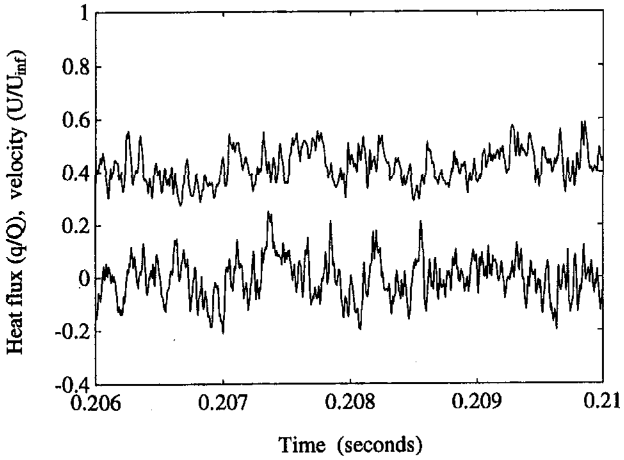

Fig. 8 Velocity and heat flux signals with hot wire 0.5 mm above gauge; no grid

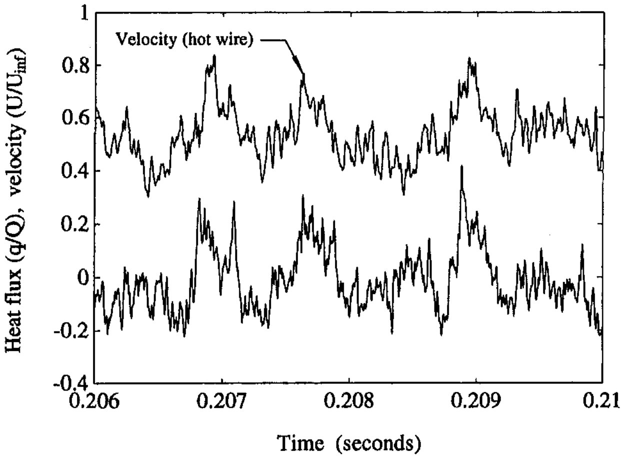

Fig. 9 Velocity and heat flux signals, wire 0.5 mm above plate; Grid A

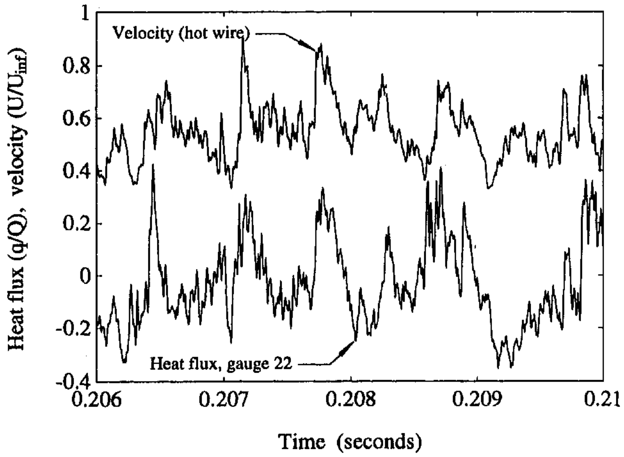

Fig. 10 Velocity and heat flux signals, wire 0.5 mm above plate; Grid D

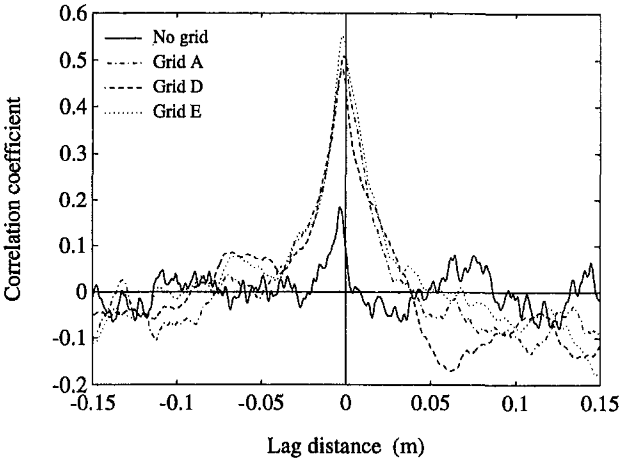

Fig. 11 Cross-correlation between heat flux signal and velocity from hot wire 0.5 mm above gage

by Grid A (Fig. 9), and one can see that the most significant components of the velocity signal correspond to the larger (low wavenumber) events. Cross-correlations R_{qv} between u' measured by the hot wire and heat flux q on the surface, Fig. 11, show a significant correlation factor for all grid-in cases, and the similarity in the shape of the correlation peaks indicates that the turbulence components responsible for the heat flux signal have a similar length scale in each case. The similarity of the high peak levels of R_{qv} with the grids in place is a consequence of the small spacing between the wire and the thin film gage relative to the turbulence length scale. The no-grid peak is lower as the length scale in this case is only 3.3 mm.

The correlation coefficients have been plotted against *lag distance* $U\tau$, defined as the free-stream velocity × the time lag used when correlating, instead of lag time. This should make the correlation shape independent of velocity for turbulence structures with a constant wavenumber spectrum. The grid-out case gives a lower correlation coefficient than the cases with free-stream turbulence, implying that in the absence of free-stream turbulence an appreciable proportion of the fluctuations in heat flux must be due to very small turbulence structures of wavelength < 1 mm.

Figure 12 shows heat flux spectra resulting from the differing free-stream turbulence conditions. At wavenumbers > 1000 m^{-1} the spectra are very similar. In this region there is little difference between the velocity spectra within the boundary layer (Figs. 6 and 7); the majority of the turbulence energy is due to the turbulent nature of the boundary layer itself. At longer wavenumbers, where the free-stream turbulence is much stronger than in a natural turbulent boundary layer, a large increase can be seen in the level of the heat flux spectra.

Cross Correlation of Heat Flux Gage Signals

Figure 13 shows cross-correlations between a gage at $x =$ 150 mm with upstream gages; as with Fig. 11, these are plotted

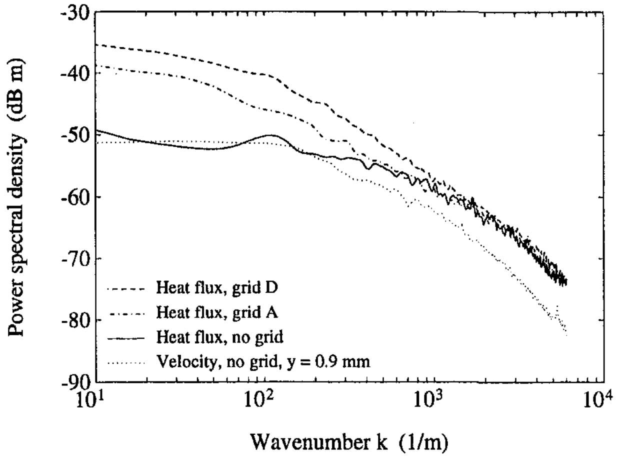

Fig. 12 Heat flux spectra compared with datum turbulent boundary layer velocity spectrum

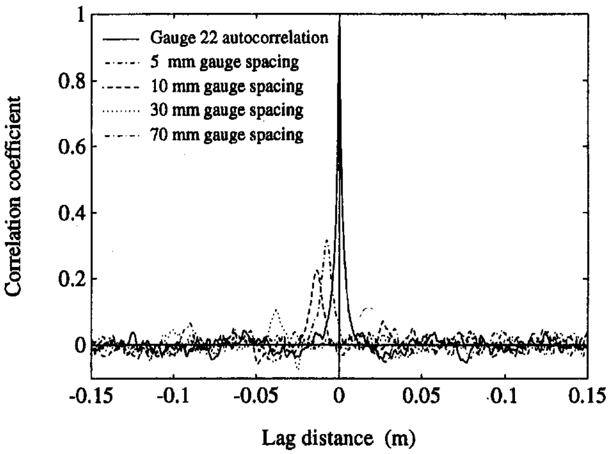

Fig. 13 Cross-correlation of gages at x = 80, 120, 140, 145, and 150 mm with the 150 mm heat flux signal; no grid

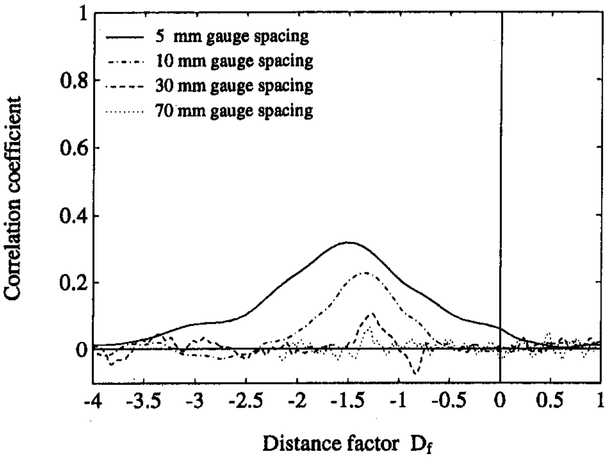

Fig. 14 Data from Fig. 13 with x-axis values divided by gauge spacing to show event transit time relative to time at free-stream velocity; no grid

against lag distance. As expected, the gages that are close together (5 and 10 mm spacings) give appreciable correlation peaks, while the 30 mm and 70 mm spacings give rather smaller peaks. The lag distance at which peaks occur is roughly proportional to the gage spacing.

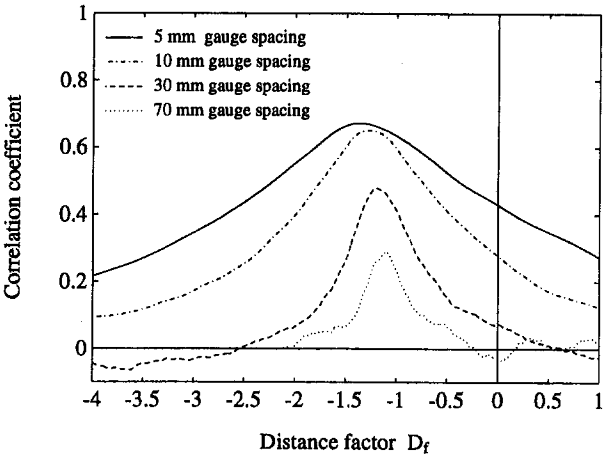

Fig. 15 Gage signal cross-correlation: transit time of events relative to time at free-stream velocity; Grid A

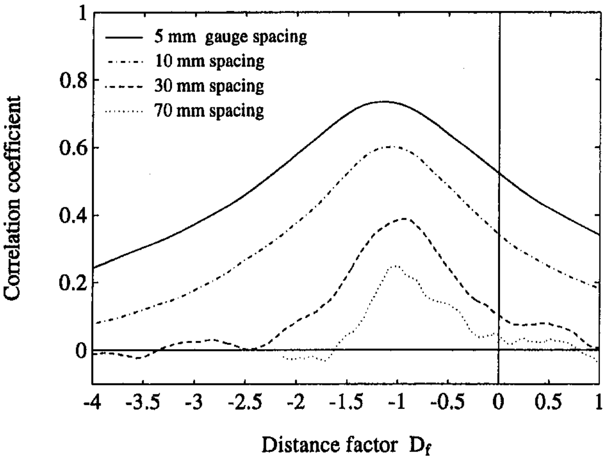

Fig. 16 Gauge signal cross-correlation: transit time of events relative to time at free-stream velocity; Grid D

These correlations may be used to infer a propagation velocity for heat flux events. This could be useful in showing whether, for instance, the periods of high Nusselt number seen in Fig. 4 are the immediate (local) effect of turbulence structures moving at free-stream velocity, or are due to the effect of the turbulence on the boundary layer at some point upstream producing boundary layer events that then propagate over the gages at a lower than free-stream velocity.

Figure 14 shows the same data as Fig. 13 replotted against a *Distance factor* defined as the distance that free-stream fluid would have moved during the correlation time lag, divided by the spacing of the two gages, i.e., *Distance factor* $D_f = -U\tau/\Delta x$. The propagation velocity ratio, V_e, of the events causing the correlation peak can then be calculated: $V_e = -1/\hat{D}_f$ where $\hat{D}_f$ is the distance factor at which the peak occurs.

It can be seen that, with no grid, the 5 mm gage separation gives a distance factor of 1.5, which falls to 1.3 as the spacing increases. Figures 15, 16, and 17 show cross correlations based on data from grids A, D, and E for comparison with the grid-out case; the peak correlation coefficient increases as the free-stream turbulence level is raised, and a correlation peak is easily seen even for a spacing of 70 mm.

The velocity ratios defined by these correlation peaks have been plotted in Fig. 17. The low turbulence case tends to a velocity ratio of 0.78 for large gage spacings, which must be due to structures within the boundary layer moving at less than

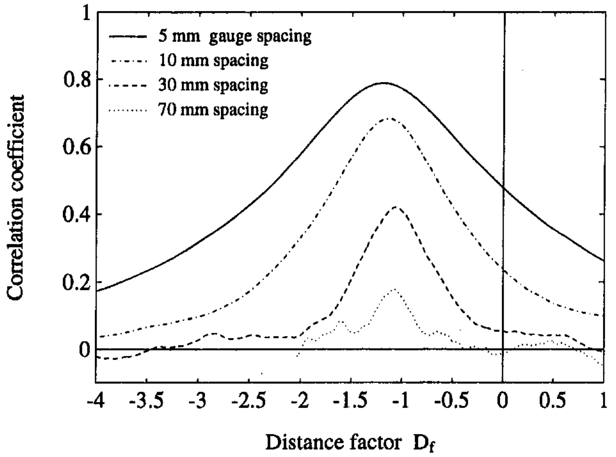

Fig. 17 Gage signal cross-correlation: transit time of events relative to time at free-stream velocity; Grid E

the free-stream velocity. (It is commonly believed that boundary layer events, e.g., turbulent spots, propagate at about $0.8 \times U_\infty$.)

As the turbulence level is increased, this value rises to approximately 1.0, which suggests that the peaks seen in Fig. 4 are produced by free-stream turbulence having an immediate effect on the boundary layer that is much more severe than effects due to turbulence structures developing within the boundary layer.

At small gage spacings (5 and 10 mm) the velocity ratio is less than the asymptotic value for large spacings. This suggests that the correlation here is mainly due to slower moving eddies close to the surface within the boundary layer. These damp out rapidly and so are not seen at large gage spacings.

Conclusions

A detailed examination of the unsteady heat flux signals on a flat plate with high levels of free-stream turbulence has suggested mechanisms for the process by which the mean heat transfer rate is enhanced. The enhancement was seen to be associated with periods of high heat transfer that lasted for 1 to 2 ms before dropping back to the undisturbed level typical of a turbulent boundary layer under a low turbulence free stream. The "high" level was approximately 60 percent higher than this datum level. Measurements of the boundary layer profile showed that free-stream turbulence results in a higher velocity gradient close to the wall and an increase in overall thickness.

The streamwise free-stream velocity spectrum from Grids D and E ($Tu > 9$ percent) exists unchanged down to 0.5 mm (i.e., $y/\delta_{995} = 0.14$) above the surface. The velocity signals at this height show similar features to the heat flux signals; correlation coefficients between the two signals can be as high as 50 percent. In general, at low ($k < 100$ m^{-1}) wavenumbers the heat flux spectra are similar to the velocity spectra, but at higher wavenumbers ($k > 1500$ m^{-1}) the heat flux spectrum is unaffected by free-stream turbulence. It appears in this case that the enhancement is produced mainly by turbulence structures that are larger than the boundary layer thickness and that originate in the free stream. The heat flux enhancement is caused by fluid being carried deep down into the boundary layer by large free-stream turbulence vortices. This is conceptually different to the alternative explanation of a simple increase in mixing within the boundary layer.

This hypothesis was tested by determining the propagation velocity of heat flux events by cross-correlating signals from gages spaced along the plate centreline. At high turbulence levels the propagation and free-stream velocities were equal. As the turbulence intensity was lowered to 4 percent the velocity ratio fell to 0.8. This further confirms that the eddy structure in the boundary layer is dominated by the free-stream turbulence structure.

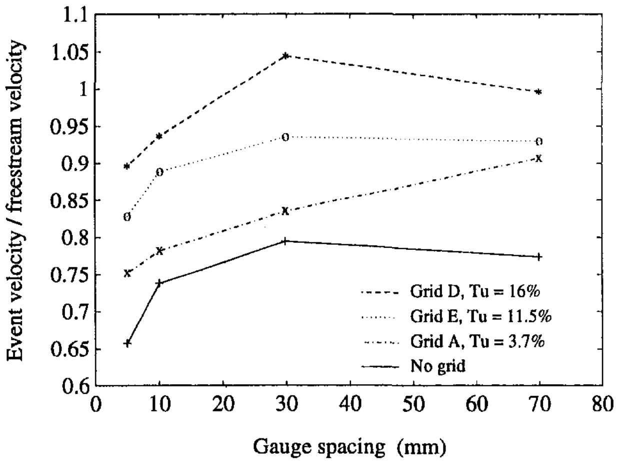

Fig. 18 Velocity relative to free stream of heat flux perturbations, as inferred from position of correlation peaks; *Tu* given at *x* = 125 mm

Acknowledgments

The authors wish to thank Rolls-Royce plc and the Defence Research Agency Royal Aerospace Establishment (Pyestock) for funding and supporting this work.

References

Blair, M. F., 1983, "Influence of Free-Stream Turbulence on Turbulent Boundary Layer Heat Transfer and Mean Profile Development, Part 2," ASME *Journal of Heat Transfer*, Vol 105, pp. 41–47.

Castro, I., 1984, "Effects of Free-Stream Turbulence on Low Reynolds Boundary Layers," ASME *Journal of Fluids Engineering*, Vol. 106, pp. 298–306.

Hancock, P. E., and Bradshaw, P., 1983, "The Effect of Free-Stream Turbulence on Turbulent Boundary Layers," ASME *Journal of Fluids Engineering*, Vol. 105, pp. 284–289.

Hancock, P. E., and Bradshaw, P., 1989, "Turbulence Structure of a Boundary Layer Beneath a Turbulent Free Stream," *Journal Fluid Mech.*, Vol. 205, pp. 45–76.

Hinze, J. O., 1975, *Turbulence*, McGraw-Hill, New York, pp. 42–44.

Maciejewski, P. K., and Moffat, R. J., 1989, "Effects of Very High Turbulence on Heat Transfer," Seventh Symposium on Turbulent Shear Flows, Stanford University.

MacMullin, R., Elrod, W., and Rivir, R., 1989, "Free-Stream Turbulence From a Circular Wall Jet on a Flat Plate Heat Transfer and Boundary Layer Flow," ASME JOURNAL OF TURBOMACHINERY, Vol. 111, pp. 78–87.

Moss, R. W., and Oldfield, M. L. G., 1991, "Measurements of Hot Combustor Turbulence Spectra," ASME Paper No. 91-GT-351.

Moss, R. W., 1992, "The Effects of Turbulence Length Scale on Heat Transfer," D. Phil Thesis, Department of Engineering Science, University of Oxford.

Moss, R. W., and Oldfield, M. L. G., 1992, "Measurements of the Effect of Free-Stream Turbulence Length Scale on Heat Transfer," ASME Paper No. 92-GT-244.

Oldfield, M. L. G., Bird, H. J., and Doe, N. G., 1982, "Design of Design of Wide-Bandwidth Analogue Circuits for Heat Transfer Instrumentation in Transient Tunnels," *16th Symposium of the International Centre for Heat and Mass Transfer*, D. E. Metzger and N. H. Afghan, eds.

Zhou, Dadong, and Wang, Ting, 1994, "Effects of Elevated Free-stream Turbulence on Flow and Thermal Structures in Transitional Boundary Layers," ASME JOURNAL OF TURBOMACHINERY, Vol. 117, pp. 407–417.

G. Wilfert
Dept. of Thermo- and Aerodynamics,
ABB Corporate Research Center,
Baden, Switzerland

L. Fottner
Institut für Strahlantriebe,
Universität der Bundeswehr München,
Neubiberg, Federal Republic of Germany

The Aerodynamic Mixing Effect of Discrete Cooling Jets With Mainstream Flow on a Highly Loaded Turbine Blade

For the application of film cooling to turbine blades, experimental investigations were performed on the mixing processes in the near-hole region with a row of holes on the suction side of a turbine cascade. Data were obtained using pneumatic probes, pressure tappings, and a three-dimensional subminiature hot-wire probe, as well as surface flow visualization techniques. It was found that at low blowing rates, a cooling jet behaves very much like a normal obstacle and the mixing mainly takes place in the boundary layer. With increasing blowing rates, the jet penetrates deeper into the mainstream. The variation of the turbulence level at the inlet of the turbine cascade and the Reynolds number showed a strong influence on the mixing behavior. The kidney-shaped vortex and as an important achievement the individual horseshoe vortex of each single jet were detected and their exact positions were obtained. This way it was found that the position of the horseshoe vortex is strongly dependent on the blowing rate and this influences the aerodynamic mixing mechanisms. A two-dimensional code for the calculation of boundary layer flows called GRAFTUS was used; however, the comparison with the measurements showed only limited agreement for cascade flow with blowing due to the strong three-dimensional flow pattern.

Introduction

The specific power as well as the specific fuel consumption of modern gas turbines can only be improved by an optimization of the thermodynamic cycle, i.e., by increasing the turbine entry temperature and the pressure ratio of the compressor in an optimal manner. However, the turbine entry temperature is limited by the blade material, and a further increase of this temperature is only allowable if the turbine blade is safeguarded against the hot gases. One very effective solution is film cooling, where cooling air is blown through slots or holes on the surface of the turbine blades and a cooling film is generated, which guards the blade against the hot gases (Fig. 1).

However, film cooling also has an unwanted effect. This blowing leads to changes in the aerodynamic behavior of the blade and mixing processes, which can noticeably decrease the efficiency of the turbine. Thus in order to improve the overall efficiency of the engine by increasing the turbine entry temperature, the blowing configuration has to be selected in such a way that the cooling effect is obtained with the least amount of cooling air and at the same time minimal aerodynamic losses in the flow. In order to optimize the cooling effect, the cooling air should change its direction as fast as possible, forming a film following the profile. It should also spread sidewise in order to guard the profile area between the blowing holes. In reality, however, the hot gas penetrates into the area between the blowing holes and is fed underneath the cooling jet. The processes described may be influenced by a number of parameters, i.e., the geometry of the blowing holes, the blowing rate, the profile geometry, the turbulence level, the Reynolds and Mach numbers, the condition of the boundary layer, etc.

This leads to the conclusion that a remarkable increase of the efficiency of cooled turbines can only be reached by a simultaneous optimization of the cooling configuration and the profile geometry. The "missing link" is in this case a good understanding of the flow in the mixing area of the blowing jets and the mainstream flow within the boundary layer, which could lead to improved computational methods, making unreliable mostly empirical methods unnecessary.

Mostly basic research concerning the aerodynamic behavior of film-cooled turbine blades was performed in the past because of the huge numbers of parameters and the complex experimental setup. In the last years studies of the effects of suction side film cooling upon the aerodynamic performance were carried out by Brown (1973), Goldstein et al. (1987), Haas et al. (1988), Haller (1980), Kiock et al. (1985), Manickam and Marugesam (1989), and McFarland (1976) using turbine cascades and Köllen and Koschel (1985) and Velazquez (1988) using turbine nozzle guide vanes. Most of these investigators used low-speed wind tunnels and investigated only the characteristics and the general loss behavior of the cascade. Three-dimensional measurements of the near-hole region are only available for flate plate investigations (López Péna and Arts, 1992). But to validate calculations and to optimize a cooling configuration, more information on the mixing processes at realistic Mach and Reynolds numbers in the near-hole region of a turbine blade with a correct profile pressure distribution is necessary. In order to obtain this detailed information, a highly loaded turbine cascade was equipped with holes on the suction sides of the profiles for the simulation of isothermal film cooling.

Experimental Setup

Turbine Cascade. The experimental and theoretical investigation is performed on a highly loaded turbine rotor section called T106-300 as shown in Fig. 2. Earlier both experimental and theoretical investigations on the turbine profile T106 referred to the boundary layer flow and especially the laminar/turbulent transition of the boundary layer on the suction side of the profile (Kiock, 1982; Römer, 1990).

Contributed by the International Gas Turbine Institute and presented at the 39th International Gas Turbine and Aeroengine Congress and Exposition, The Hague, The Netherlands, June 13–16, 1994. Manuscript received by the International Gas Turbine Institute February 26, 1994. Paper No. 94-GT-235. Associate Technical Editor: E. M. Greitzer.

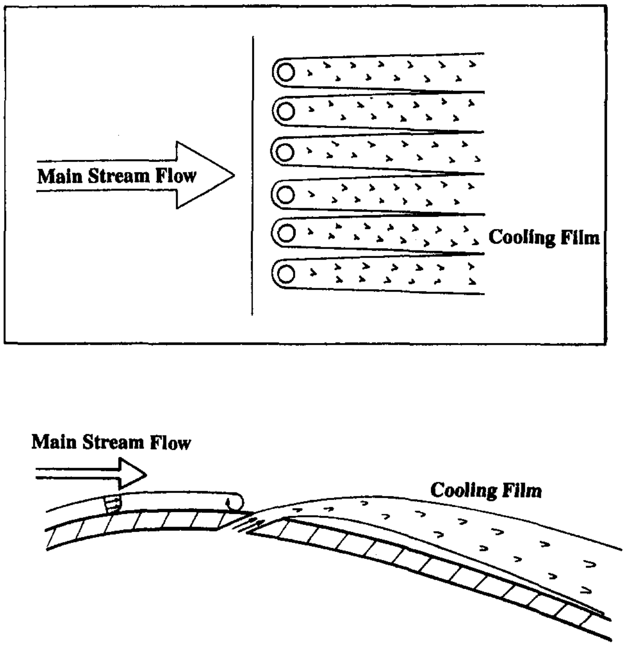

Fig. 1 Mixing process of mainstream flow and cooling jets

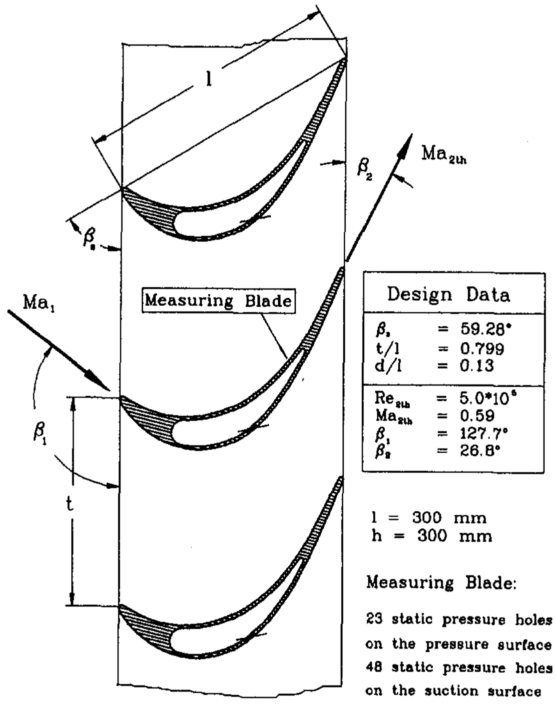

Fig. 2 Turbine cascade geometry T106-300

Since the experimental investigation requires an extensive spatial resolution, the turbine profile T106-300 was to be manufactured with a chord length as big as possible. From this requirement and the limiting condition of the test section area of the high-speed-cascade wind tunnel for a cascade with a minimum of three blades, a turbine blading with a chord length of 300 mm resulted. The instrumented blade with 71 static pressure tappings is located in the center of the test section of the wind tunnel while the blades located above and below this instrumented blade lead to realistic pressure distributions on the suction and pressure sides of the instrumented blade. In order to simulate the film cooling, all blades are hollow and connected with a supply of secondary air. Each blade suction side is fit with a row of 34 holes at 40 percent chord length ($x/l = 0.4$). The holes have a diameter of 3 mm, the relative distance between the holes is $s/d = 2.5$, and the injection angle is 30 deg with respect to the surface. The temperature of the air in the hollow blade is measured with a Pt-100 probe and the total pressure with two separate pitot probes. In order to obtain an equal blowing rate at every hole, air is supplied on both ends of the blades. This air is compressed by an external air supply cooled to the same temperature as the mainstream flow and regulating valves enable the exact setting of the desired blowing rate.

High-Speed Cascade Wind Tunnel. The high-speed cascade wind tunnel shown in Fig. 3 is contained in a huge tank and can operate continuously. Mechanical energy is supplied by a 1.3 MW three-phase motor, which runs essentially on constant rpm. The adjustment to the desired rpm of the compressor drive is accomplished by a hydraulic coupling and a gear transmission. Its drive shaft enters the tank and drives the six-stage axial compressor. The air is supplied from inside the tank. After leaving the compressor the air is cooled to a constant

Nomenclature

c_p = specific heat at constant pressure, J/kg/K
c_{p2th} = pressure distribution coefficient
d = cooling hole diameter, mm
h = blade height, mm
l = chord length, mm
M = blowing rate
Ma = Mach number
p = static pressure, hPa
p_t = total pressure, hPa
Re = Reynolds number
T = temperature, K
Tu = turbulence level, percent
u = velocity parallel to the surface, m/s
v = velocity perpendicular to the surface, m/s
w = velocity in lateral direction, m/s
x = coordinate (axial direction), mm
y = coordinate (perpendicular direction), mm
z = coordinate (lateral direction), mm
β = flow angle, deg
β_S = stagger angle, deg
δ = boundary layer thickness, mm
η = wall distance perpendicular to the surface, mm
ξ = kinetic loss coefficient
ω = pressure loss coefficient
Ω = vortex intensity, s^{-1}

Subscripts

ax = axial direction
c = cooling air
ex = exit of the cooling hole at the profile surface
h = referenced to the mainstream flow
is = isentropic
k = related to the pressure tank of the wind tunnel
l = local
max = maximum
t = total
1 = upstream conditions
2 = downstream conditions
$2th$ = isentropic downstream conditions

Abbreviations

3D-HFA = three-dimensional Hot-Film Anemometry
HGK = High-Speed Cascade Wind Tunnel
SMASH = Software for Measurement and Analytical Evaluation of Signals from Hot-Sensor Anemometry

UniBw München Institut für Strahlantriebe	**High-Speed Cascade Wind-Tunnel**	**1985**

test section data:

- Mach number : $0.2 \leq Ma \leq 1.05$
- Reynolds number : $10^6 m^{-1} \leq Re/l \leq 1.5 \cdot 10^7 m^{-1}$
- degree of turbulence : $0.3\% \leq Tu_1 \leq 6\%$
- upstream flow angle : $25° \leq \beta_1 \leq 155°$
- blade height : 300 mm

supply units:

- evacuating unit : $P_1 = 30$ kW, $P_2 = 20$ kW
- boundary layer suction (centrifugal compressor) : P = 155 kW
- additional air supply (screw compressor) : P = 1000 kW

wind-tunnel data:

- a.c. electric motor : P = 1300 kW
- axial compressor (six stages):
  - air flow rate : $\dot{V} = 30 m^3/s$ (max.)
  - total pressure ratio : $\Pi = 2.14$ (max.)
  - number of revolutions : n = 6200 rpm (max.)
- tank pressure : $0.05 bar \leq p_K \leq 1.2 bar$

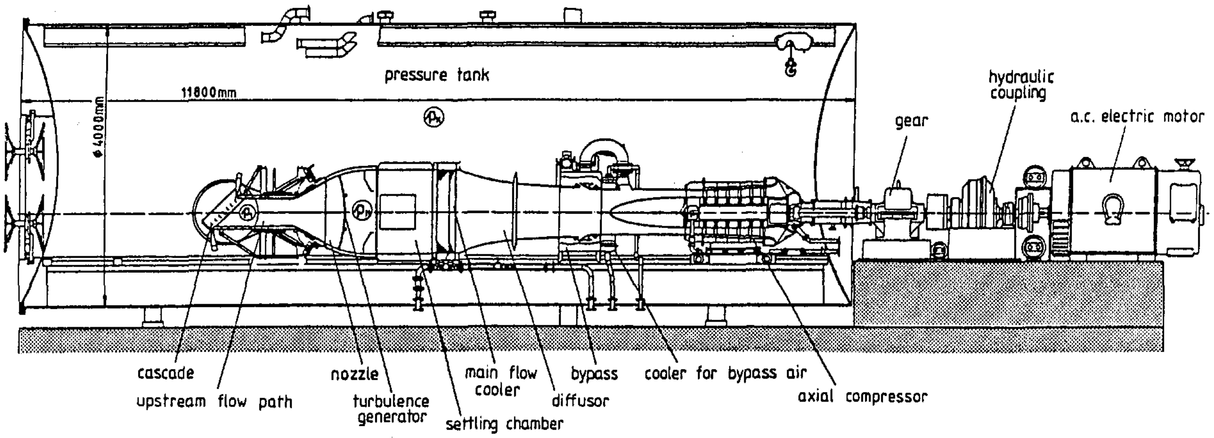

Fig. 3 Sectional view of the high-speed cascade wind tunnel

temperature. After the cooling process the air flow passes the nozzle whose exit height can be varied from 250 mm to 500 mm at a width of 300 mm, while turbulence generators supply turbulence levels of $Tu_1 = 0.8-8.0$ percent in the test section where the cascade is located. The air leaves the cascade into the tank losing its kinetic energy thus rendering the wind tunnel an open-loop system in a closed test facility.

The setup of the wind tunnel holds distinct advantages that otherwise could not be accomplished. By setting the exit area of the nozzle and the rpm of the compressor any desired Mach number between 0.2 and 1.05 can be obtained in the test section. At the same time the pressure inside the tank can be varied between 0.05 and 1.2 bar setting the Reynolds number for a profile length of 1 m between 10^6 and 1.5×10^7. These two variations can be applied independently so that the Mach number and the Reynolds number setting are not coupled. This facilitates the independent variation of the most important parameters in the testing of cascades.

Tests of film cooling need a secondary air supply. Due to the special conception of the wind tunnel, i.e., the test section inside a pressurized tank, the secondary air has to be supplied from the tank to a compressor and back through the blowing holes into the tank. This circuit has to be vacuum-tight since the pressure inside the tank will not change during a test run. The compressor is a screw-compressor with a maximum pressure ratio of 3 and a maximum mass flow rate of 6 kg/s at sea level inlet conditions.

Figure 4 shows how the T106-300 turbine cascade is installed in the test section. Deflecting sheet metals with integrated suction are used on the upper and lower channel walls in order to obtain periodic cascade flow in spite of the setup with only three blades. The turbulence level of the inlet flow Tu_1 is increased by built-in turbulence generators at the inlet of the nozzle and it was set between 3.9 and 6.5 percent for these experiments.

Three-Dimensional Hot-Film Anemometry

For the investigation of the mixing processes in the near-hole region, a measurement technique was necessary which could detect the three-dimensional character of the flow. Therefore the multidimensional hot sensor technique was set up at the high-speed cascade wind tunnel (see Wunderwald et al., 1992). The sensor of the three-dimensional hot-film anemometry (3D-HFA) consists of three spatially stretched wires or films. These sensors are used in various sizes depending on the measuring tasks (Fig. 5).

The setup of the 3D-HFA at the high-speed cascade wind tunnel is based on a "digital solution," which means that the analog output signal of the anemometer is digitized, filtered, and stored on a hard disk. After the measurement the stored data can be subsequently evaluated.

The hardware setup of the 3D-HFA can be divided into three parts:

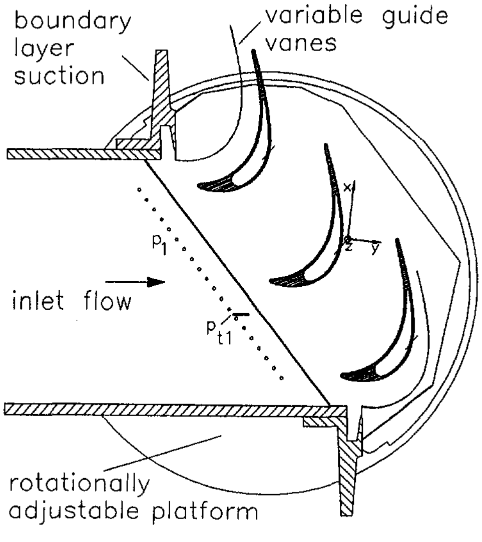

Fig. 4 Sectional view of the turbine cascade build-up

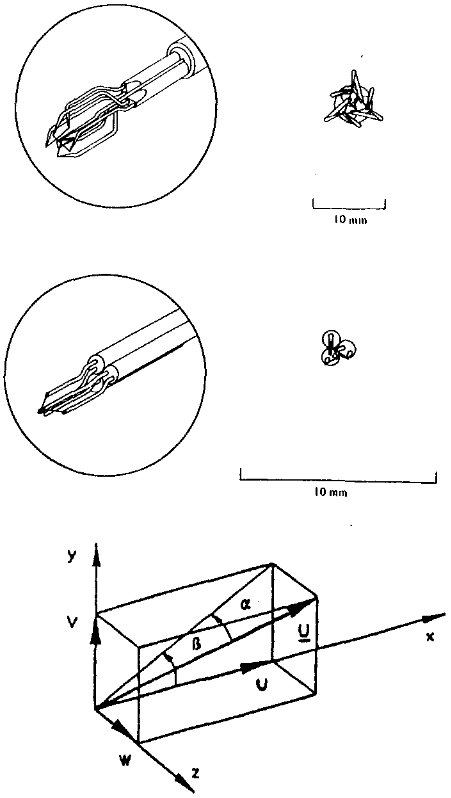

Fig. 5 Triple probes and coordinate system

- hot-film digitization with the direct storing on a fast hard disk (through-put-disk)
- peripheral data measurement controlled by an IEEE-Bus for temperatures, pressures, traversing coordinates, etc.
- monitoring of the anemometer output signal by using two voltmeters for AC and DC, an oscilloscope, and a Fast Fourier Analyzer.

In the first part the analog output signals of the three anemometers have to be digitized, filtered, and stored (Fig. 6). The hardware for this task is an optimized system of an A/D-converter with an anti-aliasing filter, which allows a converting frequency only 2.56 times higher than the cutoff frequency. In addition to the hot-film signals a lot of other data (peripheral data) have to be recorded, e.g., pressures, temperatures, traversing coordinates, etc. For these data, hard and software are used that were developed and tested for wake and profile pressure distribution measurements at the institute (see Wilfert et al., 1990).

Triple hot-film probes have to be calibrated not only for the velocity but also for the directional sensitivity. For the directional calibration the probe has to be rotated around the z axis (pitch angle) and the y axis (yaw angle) at the same flow conditions. A rotation of the probe around the z axis has been installed already. In order to prevent a complicated modification for the variation of the yaw angle, a simple method is to rotate the probe around its own axis (roll angle φ) and obtain the pitch and yaw angle by a coordinate transformation of the adjusted angles φ and β (Fig. 5).

In order to control the data acquisition system and to evaluate the signals of the hot-film anemometry, a program package was developed (SMASH). This software is highly modular and flexible for many different test applications. In one module a triple hot-film probe can be calibrated for velocity and directional sensitivity. The procedure to calculate the velocity and directional coefficients was developed at DLR-Göttingen. An advantage of this procedure is the possibility to calibrate the velocity and directional sensitivity separately. The evaluation can be performed on- or off-line to obtain the calibration coefficients. After reading configuration and calibration data a measurement can be carried out. For every test point of the traversing program, data are obtained that are written on the through-put-disk in a compressed binary mode. During the traversing to the next test point these data are reread and stored on a magneto-optical-disk together with the peripheral data to be evaluated off-line later. The evaluation module, also developed by the DLR, transforms the anemometer voltages to the velocity vector using the calibration coefficients. Fluctuations of the flow velocity with respect to time are measured with a sufficiently high frequency in order to calculate the degree of turbulence as well as the Reynolds stress tensor.

For boundary layer measurements with hot-film anemometry, a correction of the measured data is necessary because the wires very near the wall lose more energy and thus show a higher velocity. Furthermore the wires of a three-dimensional probe are at different positions to the wall and this leads to wrong flow angles and normally also to wrong velocities. For this investigation a subminiature boundary layer probe with 8 deg incidence was used. To find a correction method for the boundary layer behavior of this subminiature probe, tests were made on a flat plate and compared with measurements of a flattened pitot probe (see Ardey, 1993). These showed no differences for the mean velocity but for the pitch and yaw angles. In addition, the wall influence depends not only on the geometry of the probe but also on the boundary layer conditions and therefore on the mainstream flow conditions: Mach number, Reynolds number, and turbulence level.

This complex coordination could not be calculated yet so that the correction polynomials have to be calculated from the measurements (Fig. 7). This was done in the film cooling investigation by boundary layer measurements on the suction side of the turbine profile with a blowing rate of $M = 0$. This is

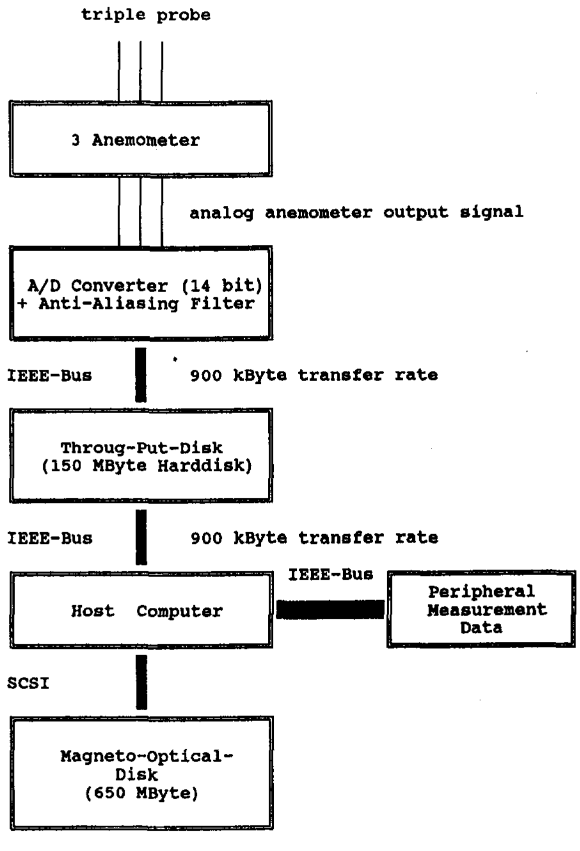

Fig. 6 Data flow of the three-dimensional-hot-film anemometry

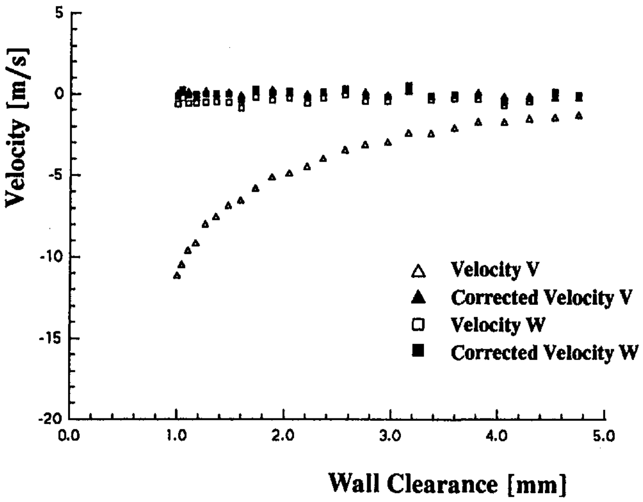

Fig. 7 Correction of 3D-HFA boundary layer measurements

possible because in the midspan section of the profile no velocity components in the lateral and perpendicular direction occur.

Analysis of Test Results

Test Program. The extensive test program can be divided into two main parts. In the first part the cascade characteristics were studied by wake and profile pressure distribution measurements for different blowing rates, Reynolds numbers, and turbulence levels. In the second part the near-hole region was analyzed for the same variation with the 3D-HFA and with the flow visualization technique (Table 1). Furthermore these tests were used to verify the calculations with the boundary layer program GRAFTUS.

Evaluation of Blowing Jet Measurements. In order to display the behavior of a film cooling configuration in general, it is necessary to introduce a few parameters of similarity and to know how they depend on each other. The blowing rate M describes the mass flux ratio of the cooling air (c) and the mainstream in the inlet area of the cascade (1):

$$M = \frac{\rho_c v_c}{\rho_1 v_1} \tag{1}$$

The local blowing rate M_l refers to the mainstream condition at the outlet of the cooling air (1):

$$M_l = \frac{\rho_c v_c}{\rho_l v_l} \tag{2}$$

The local impulse ratio I_l is defined in the same manner:

$$I_l = \frac{\rho_c v_c^2}{\rho_l v_l^2} \tag{3}$$

Thus, in order to obtain an impulse ratio $I_l = 1$, the local blowing rate has to be

$$M_l = \sqrt{\frac{T_{tl}}{T_{tc}}} \tag{4}$$

i.e., for blowing at equal temperature and $I_1 = 1$, $M_1 = 1$.

The aerodynamic performance of a film cooling configuration can be expressed in general form by a loss coefficient. For subsonic flow two different loss coefficients can be specified: the loss of kinetic energy and the total pressure loss parameter defined as

$$\omega = \frac{p_{t1} - p_{t2}}{p_{t1} - p_k} \tag{5}$$

Since the effect of the cooling air is not considered in the coefficient of the total pressure loss ω, there is little value in using this coefficient for the description of losses due to film cooling configurations. Thus the influence of the cooling air is taken into consideration by a correction of the total pressure at the inlet of the blading.

$$\omega_{ex} = \frac{p_{t1}^* - p_{t2}}{p_{t1}^* - p_k} \quad p_{t1}^* = \frac{\dot{m}_1}{\dot{m}_1 + \dot{m}_c} p_{t1} + \frac{\dot{m}_c}{\dot{m}_1 + \dot{m}_c} p_{t,ex} \tag{6}$$

The loss coefficient of the kinetic energy is defined as follows:

$$\xi_{kin} = 1 - \frac{(c_{pt2}T_{t2} - c_{ps2}T_2)(\dot{m}_1 + \dot{m}_c)}{(c_{pt2}T_{t2} - c_{p2,is}T_{2,is})\dot{m}_1 + (c_{pt2}T_{t2} - c_{p2c,is}T_{2c,is})\dot{m}_c} \tag{7}$$

leading to the following expression if adiabatic flow is assumed:

$$\xi_{kin} = 1 - \frac{\left(1 - \left(\frac{p_2}{p_{t2}}\right)^{(\kappa-1)/\kappa}\right)\left(1 + \frac{\dot{m}_c}{\dot{m}_1}\frac{c_{pc}}{c_{p1}}\frac{T_{tc}}{T_{t1}}\right)}{\left(1 - \left(\frac{p_2}{p_{t1}}\right)^{(\kappa-1)/\kappa}\right) + \frac{\dot{m}_c}{\dot{m}_1}\frac{c_{pc}}{c_{p1}}\frac{T_{tc}}{T_{t1}}\left(1 - \left(\frac{p_2}{p_{tc}}\right)^{(\kappa-1)/\kappa}\right)} \tag{8}$$

Using this formula the influence of the cooling air can be considered in different ways. In this paper only the so-called external loss coefficient is used. The kinetic energy of the blowing jet is included in this definition but losses arising in the blowing hole are not taken into account ($p_{tc} = p_{t,ex}$):

$$\xi_{ex} = 1 - \frac{\left(1 - \left(\frac{p_2}{p_{t2}}\right)^{(\kappa-1)/\kappa}\right)\left(1 + \frac{\dot{m}_c}{\dot{m}_1}\frac{c_{pc}}{c_{p1}}\frac{T_{tc}}{T_{t1}}\right)}{\left(1 - \left(\frac{p_2}{p_{t1}}\right)^{(\kappa-1)/\kappa}\right) + \frac{\dot{m}_c}{\dot{m}_1}\frac{c_{pc}}{c_{p1}}\frac{T_{tc}}{T_{t1}}\left(1 - \left(\frac{p_2}{p_{t,ex}}\right)^{(\kappa-1)/\kappa}\right)} \tag{9}$$

The corrected total pressure loss coefficient (6) and the external loss coefficient of the kinetic energy (9) should be used for future work, so that the additional mixing losses of different

Table 1 Measurement program

Re_{2th}	500000 and 900000				
Tu_1	3.9 % and 6.5 %				
M x/l	0.0	0.5	1.0	1.5	2.0
0.35	Y	X*	X	X*	X
0.41	Y	X*	X	X*	X
0.45	Y	X*	X	X*	X
0.50	Y	X*	X	X*	X

*: Only measured for Re_{2th} = 500000

X, Y: Wake and profile pressure distribution measurements

Y: Boundary layer measurements at z/d = 0.0

X: Boundary layer measurements at z/d=-1.25, -0.9375, -0.625, -0.3125, 0.0, 0.3125, 0.625, 0.9375, 1.25

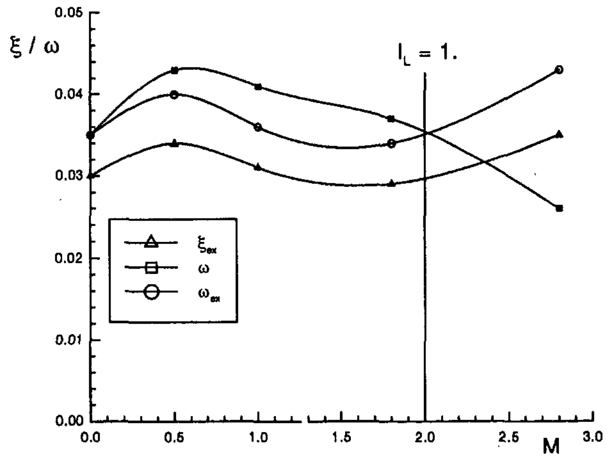

Fig. 8 Loss coefficients at design conditions

turbine blades can be compared. The losses of the blowing holes should not be added because only a slightly different hole geometry makes a comparison inaccurate.

Results. As mentioned before, various loss coefficients can be defined for turbine blading with film cooling. In order to obtain a measure for the energy transfer, the loss coefficient of the kinetic energy ξ is used. In Fig. 8 the loss coefficient ξ_{ex} is plotted where the losses in the blowing hole are neglected. At a turbulence level at the inlet of 3.9 percent and at Re_{2th} = 500,000, a strong decrease of the losses is observed at low blowing rates. This results from the fact that the blowing jet adds little energy to the mainstream flow; however, its interference with the boundary layer is extensive. Around a blowing rate of $M = 1.5$ a minimum of the losses is reached. For increasing blowing rates the losses increase also since the jet penetrates deeper into the mainstream flow while a strong kidney-shaped vortex with high lateral velocities arises from the deflection of the blowing jet. It seems as if the loss coefficient ω shows a contradictory behavior at high blowing rates but this results from the neglect of the kinetic energy of the blowing jet in the definition of the loss coefficient. If this kinetic energy is included by a correction of the total pressure at the inlet, the behavior of the loss coefficient ω_{ex} is similar to the curve of ξ_{ex}.

The influence of the cooling air on the midspan profile pressure distribution is presented in Fig. 9. In front of the hole the mainstream flow is retained and this is independent of the blowing rate. In the near-hole region a high acceleration can be seen with a minimum suction side pressure right in between the holes. About 10 hole diameters behind the blow-out the distributions with and without film cooling concur and no influence of different blowing rates can be seen in the downstream part of the distribution.

In order to study the mixing effects of the cooling air and the mainstream flow in detail, boundary layer measurements were performed with the three-dimensional hot-film anemometry subminiature probe, which enabled the measurement of the instantaneous speed components in the three spatial directions for every test location. A computation leads to the averaged mainstream velocity and its three components, to the flow angles α and β, to the local turbulence level Tu_l, and the turbulence level Tu_h, which is referenced to the mainstream flow, and to the Reynolds stresses.

Figure 10 shows the v-w-flow vectors in the tested x/d planes (1, 5, 10) at the highest blowing rate of $M = 2$ for Re_{2th} = 500,000 and $Tu_1 = 3.9$ percent. It is found that the jet blows up in the plane $x/d = 1$ leading to a strong deflection in the direction of the mainstream flow and thus the kidney-shaped vortex as expected. Its structure is well observed in the plane $x/d = 5$ and is still visible at $x/d = 10$. In Fig. 11 the v-w-vector diagram is shown for the lowest tested blowing rate of $M = 0.5$ at otherwise equal conditions (Re_{2th} = 500,000, Tu_1 = 3.9 percent). It is found that the jet does not blow up as before due to the small impulse ratio and that at the plane x/d = 5 the core of the jet is filled up by the mainstream flow. Thus the blowing jet can be looked at as a perturbation body. In spite of the small impulse ratio the jet is deflected toward the mainstream flow and is strongly accelerated.

Figure 12 shows the turbulence level referenced to the mainstream flow for both blowing rates $M = 0.5$ and 2 in the distance of 10 diameters behind the holes. For the lower blowing rate the jet remains within the boundary layer and mixes with the mainstream flow while strongly thickening the boundary layer. In the case of the highest blowing rate the shape is still clearly visible and that means the distinct jet is still found and penetrates deeply into the mainstream flow.

The rotation of the kidney-shaped vortex is not always clearly recognizable from the distributions of the lateral velocity components. Therefore the rotation was calculated in the respective planes perpendicular to the surface of the profile. The location and the shape of the kidney-shaped vortex is clearly visible from the distribution of the rotation shown in Fig. 13 (left) for the blowing rate $M = 0.5$. The right part of the vortex rotates in a positive direction (bright) while the left part rotates in a negative direction (dark) around the axis of the main flow (perpendicular to the displayed test plane). At the plane x/d = 10 the kidney-shaped vortex has almost disintegrated. This means that the jet has turned into the direction of the mainstream flow, and the mixing with the mainstream flow is largely completed.

The distribution of the rotational flow at the high blowing rate $M = 2.0$ is shown in Fig. 13 (right). The kidney-shaped vortex has a stronger intensity than at $M = 0.5$. But now it is interesting to see that at the plane $x/d = 1$ another strong pair of vortices is found rotating in the opposite direction to the kidney-shaped vortex and located just above the kidney-shaped

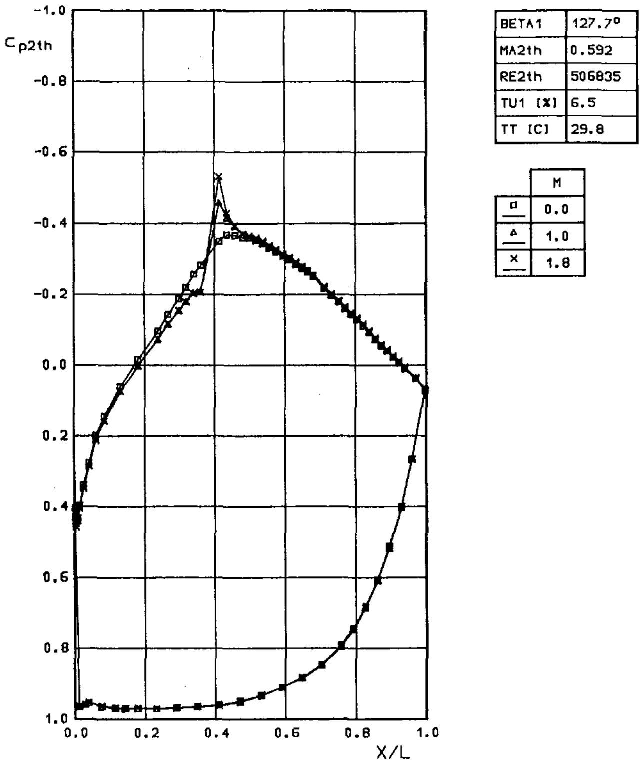

Fig. 9 Pressure distributions for different blowing rates

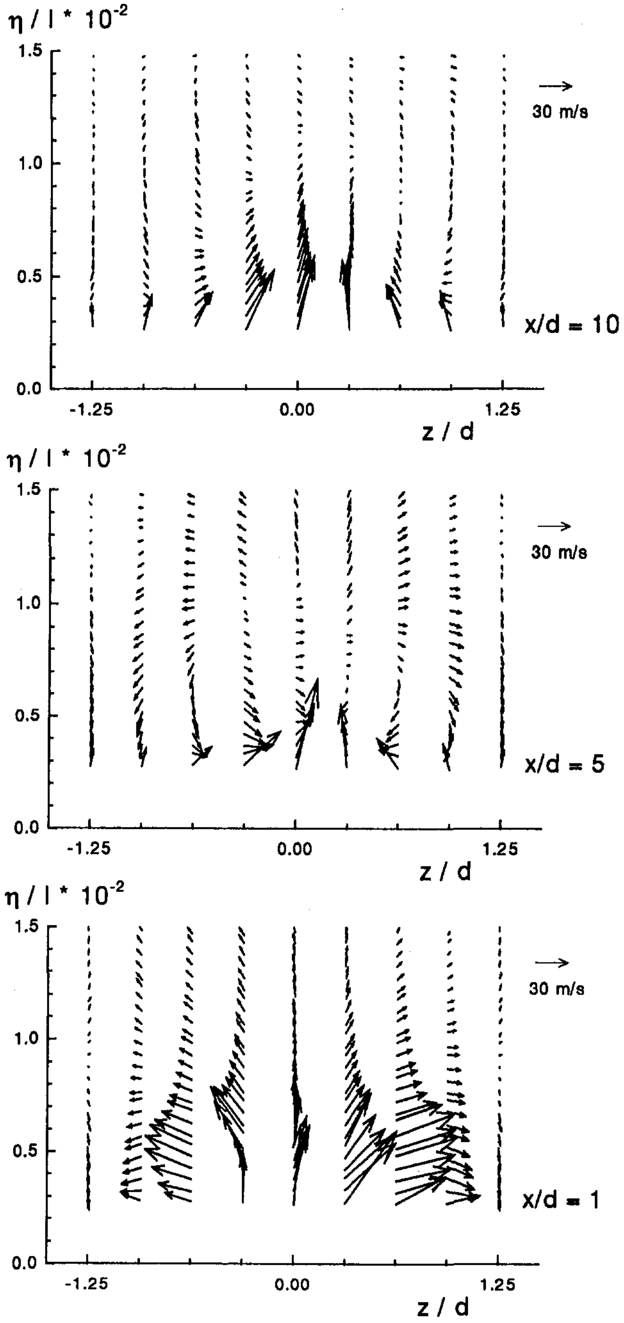

Fig. 10 Crossflow velocity vectors for $M = 2.0$

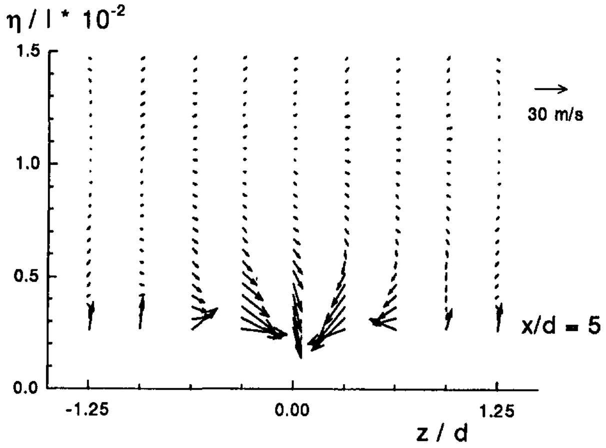

Fig. 11 Crossflow velocity vectors for $M = 0.5$ at $x/d = 5$

vortex. This new pair of vortices is the horseshoe vortex, which arises from the rollup of the boundary layer in front of each blowing hole. Contrary to the case of single jets or at low blowing rates where this horseshoe vortex is located sideways below the blowing jet, the vortices are now located above the cooling jet. In the case of a low blowing rate the horseshoe vortex is clearly visible sideways of the blowing jet (Fig. 13 (left)) and even in the plane $x/d = 10$ where the mixing has taken place extensively, the rotation of the horseshoe vortex still can be found.

Considering again the high blowing rate $M = 2.0$, it is found that the jet blows up at the blowing hole in such a way that the horseshoe vortex is pushed away from the surface just above the kidney-shaped vortex. It decomposes rather fast in the mainstream flow so that it cannot be found anymore at the plane $x/d = 5$. However, since this horseshoe vortex is located above the kidney-shaped vortex, it prevents the jet from penetrating deeper into the mainstream flow between the planes $x/d = 1$ and $x/d = 5$ at the high blowing rate of $M = 2$ compared to low blowing rates. This phenomenon is shown schematically in Fig. 13 (lower part).

Another possibility to investigate the flow behavior and to analyze mixing effects on the suction side of the profile is the comparison of the boundary layer measurements with flow visualization techniques on the basis of the surface oil-flow technique.

An enlargement of an oil-flow picture close to the blowing hole enables a good analysis of the mixing effects. Figure 14 (left) shows an oil-flow picture where the mainstream flow runs from top to bottom, for a blowing rate of $M = 0.5$. The region in front of the blowing hole is easily visible. It contains no paint, leading to the conclusion that material is transported away from the wall into the mainstream flow. The horseshoe vortex rolls up around the blowing hole, which can be recognized from the fact that no material is in front of the hole and at the very edge of the blowing hole material is still visible (see Jabbari and Goldstein, 1992). Between the blowing holes the horseshoe vortices of two adjacent jets rotate upward, which is shown by a region of no paint in the oil-flow picture. Directly behind the blowing hole a so-called jet wake vortex arises with two single vortices rising from the surface into the cooling jet shown by a region without paint. These two vortices rotate in the same direction as the kidney-shaped vortices and are therefore not detected further downstream. All the way downstream of the hole the oil-flow picture does not change. This shows that the horseshoe vortex stays very stable in the boundary layer, which is also visible in Fig. 13 (left) at $x/d = 10$.

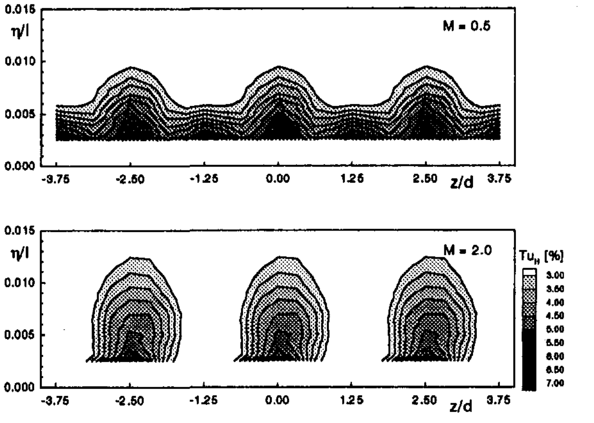

Fig. 12 Turbulence intensity at $x/d = 10$

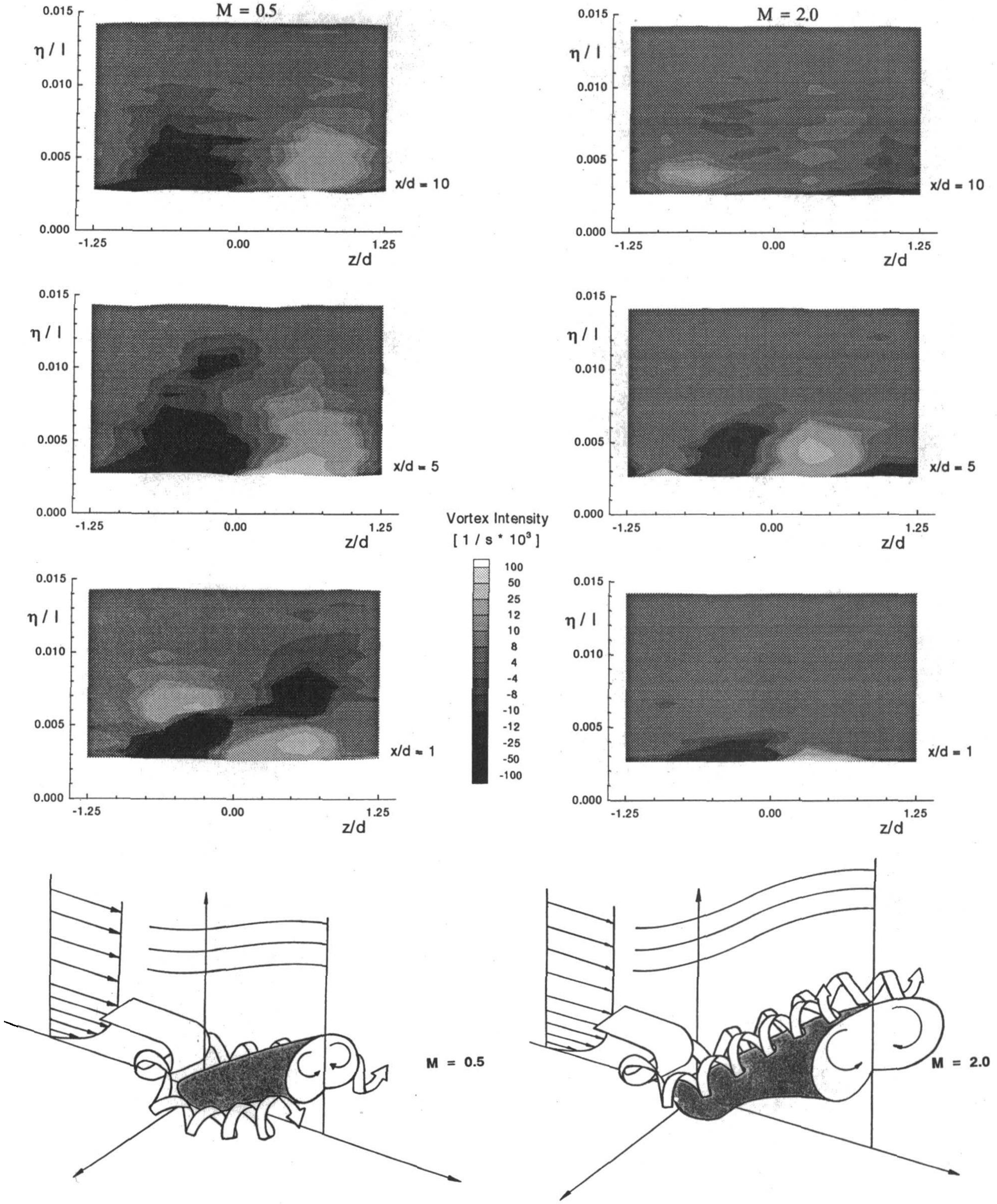

Fig. 13 Vortex intensity and schematic view of the vortices

Increasing the blowing rate to $M = 2$ leads to a completely different flow behavior as shown in the oil-flow picture in Fig. 14 (right). As already mentioned the jet blowing up forces the horseshoe vortex to withdraw from the surface. This is shown by a paintless region in front of the blowing hole up to the throat between the holes formed by the jets. The jet wake vortex is better visible in this oil-flow picture. Behind this vortex traces are recognizable on the surfaces between $z/d = 1.25$ and $z/d = 0$ where the two adjacent vortices of the kidney-shaped vortices rotate parallel to the surface. At all positions downstream of the hole the jet had penetrated so deeply into the mainstream that the material on the surface cannot be completely absorbed by the velocity components in the y direction at $z/d = 0$. Thus only regular uniform lines are observed in the oil-flow picture.

After looking at the high and the low blowing rates an intermediate blowing rate of $M = 1.0$ is considered by comparing

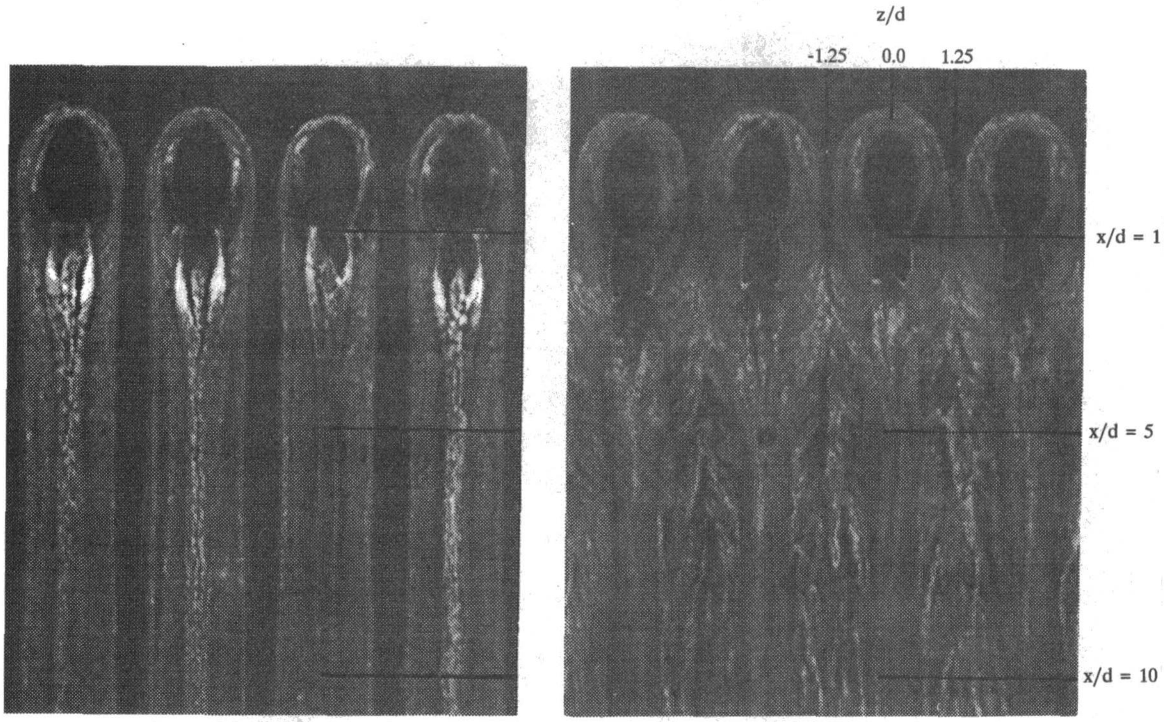

M = 0.5 M = 2.0

Fig. 14 Flow visualization at the near-hole region

distributions of the turbulence levels for various turbulence levels at the inlet of the cascade and various Reynolds numbers. Figure 15 shows these distributions for the plane $x/d = 5$ where the turbulence of the mainstream flow is subtracted. Increasing the turbulence level at the inlet leads to a more turbulent region in the core of the jet, which can be explained by the filling of the jet by the mainstream flow with its higher turbulence level. It seems that the very high turbulence level in the core of the

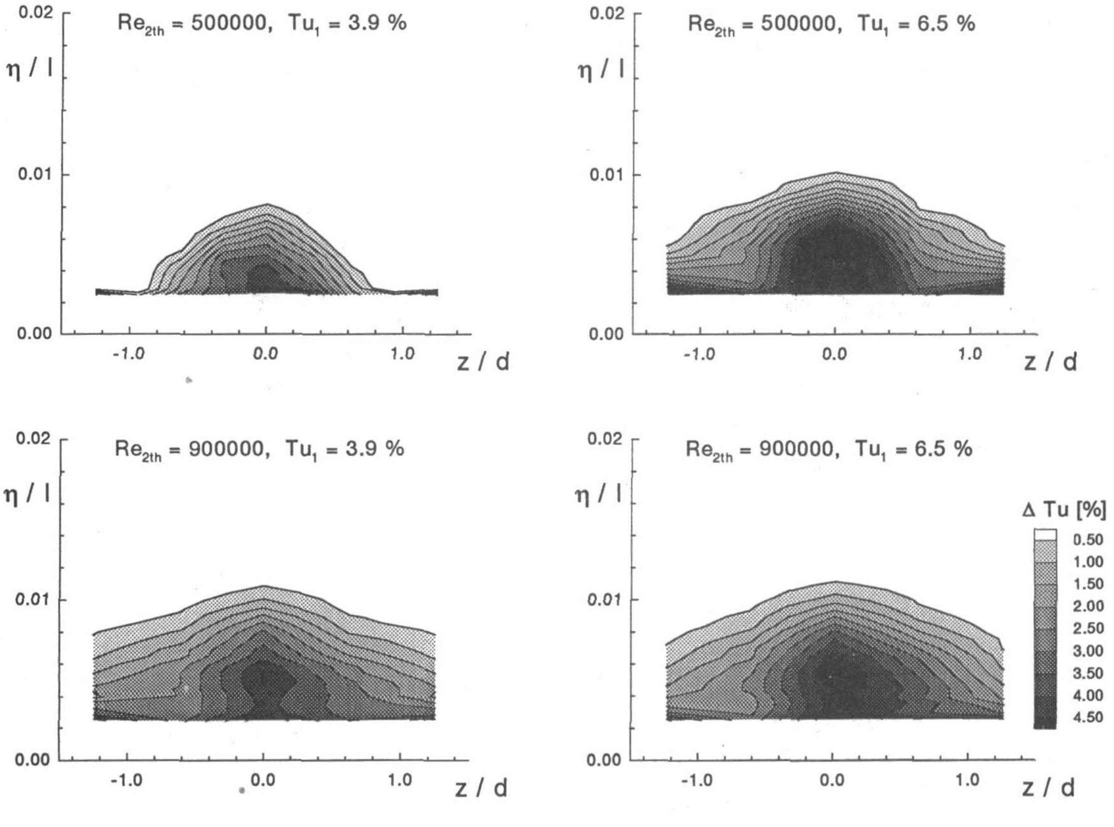

Fig. 15 Turbulence intensity for Re and Tu_1 variation ($M = 1$, $x/d = 5$)

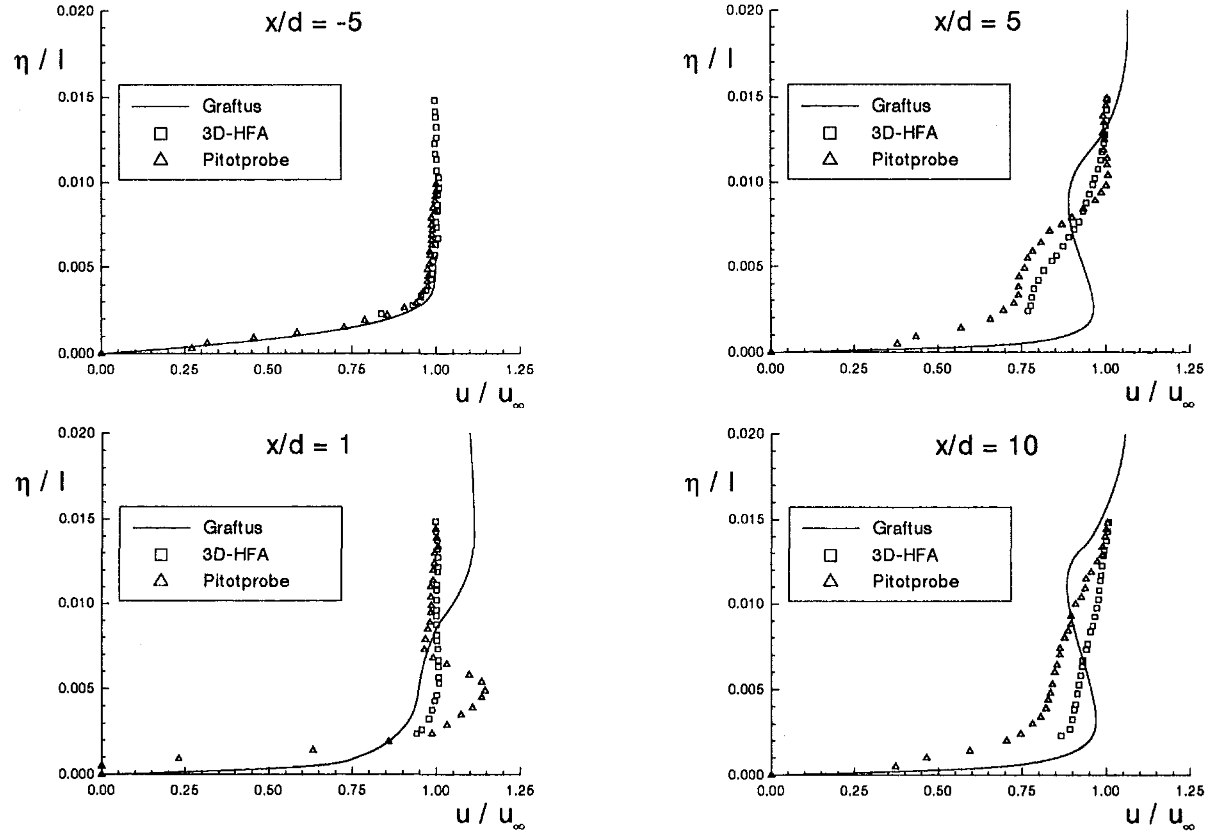

Fig. 16 Comparison of calculated and measured velocity profiles at design conditions and $M = 1$

jet results not only from transportation but also from diffusion and this leads to a kind of explosion limited to this region. Other results show that this phenomenon intensifies with decreasing cooling velocity. At a velocity ratio of one there is no increase of the turbulence intensity in the core of the jet at different turbulence levels at the inlet. Furthermore this phenomenon is limited to the area at $x/d = 5$ because at $x/d = 10$ the turbulence levels of the cores are similar. The mixing between the jet and the boundary layer flow has proceeded further at the turbulence level $Tu_1 = 6.5$ percent, and the boundary layer is thickened between the blowing jets. As the Reynolds number is increased, the behavior of the flow stays similar but without a further increase of the turbulence level in the core of the jet. In conclusion it can be mentioned that an increase of the turbulence level at the inlet of a turbine cascade or an increase of the Reynolds number both lead to a faster mixing but only for higher turbulence levels can a big increase of turbulence intensities in the core of the jet be recognized.

Boundary Layer Calculations

GRAFTUS is a two-dimensional boundary layer calculation program, which can evaluate flow separations by an inverse and interactive computation routine (Rodi et al., 1986). Furthermore it provides features for simulating film cooling phenomena like film cooling effectiveness, surface heat transfer coefficients, and boundary layer velocity profiles. Three-dimensional effects of film-cooling are allowed for by a correcting model containing the so-called dispersion terms.

The two-dimensionally averaged results of GRAFTUS cannot be directly collated to the fully three-dimensional measurements. Laterally the behavior of the boundary layer is most distinct in the trail of the cooling holes. Therefore the experimental results at a lateral position of $z/d = 0.0$ were chosen to be compared with the calculations taking into account that the computations will show averaged and accordingly less marked boundary layer profiles. Input data for GRAFTUS, which are normally obtained by a potential flow calculation program, are gained from pressure distribution measurements on the profile surface at zero blowing rate. With no flow separation, this is an admissable approach.

Without film cooling ($M = 0.0$) a high conformity of experimental and numerical results was observed, taking into account that similar to a locally increased surface roughness the film cooling holes induce a transition from laminar to turbulent flow. Figure 16 shows GRAFTUS boundary layer profiles together with measurements of a three-dimensional hot-wire probe and a flattened pitot probe at design point conditions ($\mathrm{Re}_{2th} = 500{,}000$, $Tu_1 = 3.9$ percent) with a blowing rate of $M = 2.0$. At $x/d = -5$, i.e., five hole diameters in front of the coolant injection, laminar boundary layer profiles can be identified. Numerical and experimental data show only slight discrepancies of the boundary layer thickness. Directly behind the film cooling hole at $x/d = 1$, measurements differ dramatically because the flattened pitot probe blocks the upward component of the cooling jet whereas the wire construction of the subminiature three-dimensional hot-wire probe allows the flow to pass easily. GRAFTUS and three-dimensional hot-wire probe results correspond well inside the cooling jet up to $\eta/l = 0.005$. But above the coolant layer GRAFTUS predicts a strong acceleration in the flow field due to the displaced flow, which could not be detected experimentally.

Further downstream at $x/d = 5$ and $x/d = 10$ the flattened pitot probe results are identical to the three-dimensional hot-wire probe measurements while the GRAFTUS calculations show distinct differences. In addition to the overrated displacement effect GRAFTUS indicates an increased velocity level inside the cooling jet whereas the experiments prove a reduced streamwise flow speed. Obviously the dispersion terms fail to simulate the substantial vertical and lateral velocity components in the vortex field around a jet in a crossflow, which cause a loss of kinetic energy in the streamwise direction.

Correspondence between the GRAFTUS calculations and the measurements was observed in relation to the position of the jet and the weakening of the coolant influence downstream. GRAFTUS proved to have the same problems for reduced blowing rates although the disparity lessens due to decreased vortex intensities and a smaller amount of displaced flow.

Summary

The influence of cooling jets on the mainstream flow at a turbine blade was investigated in the past only for very simplified conditions. However, in order to understand the mixing processes between the cooling jets and the mainstream flow more in detail and in order to obtain a database for the improvement of correlations used in calculations experimental tests were carried out at the high-speed cascade wind tunnel.

High gradients require an improved spatial resolution of the measuring devices. Due to the size of the test area in the wind tunnel a turbine cascade with three blades (chord length 300 mm) was designed and equipped with 34 holes on the suction sides of the profiles at $x/l = 0.4$.

For the investigation of the mixing processes between the cooling jets and the mainstream flow, three-dimensional hot-film anemometry was used. Employing a subminiature probe facilitates a rather good spatial resolution and in addition the influence of the probe on the flow is negligible if the probe is rather small. Measurements of the direction of the flow, which can be impaired by heat conduction close to the wall, can be corrected with a relatively simple procedure so that reliable data can be obtained in the boundary layer also in close proximity of the wall.

In order to measure the influence of the cooling air on the characteristics of the blading, wake and profile pressure distribution measurements were performed. The loss coefficients obtained from the test data show a minimum for blowing rates near $M = 1.5$. The three-dimensional hot-film anemometry results investigating film cooling show the kidney-shaped vortex, which in general arises from flows with a speed component perpendicular to the main flow. In addition, the horseshoe vortex is found, which arises from the rolling-up boundary layer on the front edge of each blowing jet. This horseshoe vortex is located in general below the blowing jet, but at a blowing rate $M = 2.0$ it is found above the blowing jet, contrary to the results for small blowing rates. The location and the strength of the vortices located in the boundary layer play an important role for the cooling effectiveness since the vortices direct hot gas to the surface of the profile. Increasing the turbulence level of the mainstream flow or the Reynolds number leads to a faster mixing between the blowing jet and the main flow, as can be expected. However, the Reynolds number or turbulence level variation showed no significant change of the vortices arising from those at the design condition.

The boundary layer behavior with film cooling calculated with the computer code GRAFTUS showed discrepancies from the measurements for all investigated configurations. A reason could be that the strongly three-dimensional processes arising from the blowing of cooling air through holes perpendicular to the main flow cannot be predicted well enough. The comparison made in this investigation refers to blowing jets at equal temperature as the main flow so that no evidence can be found of the thermal effects that are also taken into account in the computer code GRAFTUS.

Acknowledgments

This research project in the scope of which the reported work was performed is part of the joint research program of Forschungsvereinigung Verbrennungskraftmaschinen e.V. (FVV). The project has been supported by the Bundesministerium für Wirtschaft represented by Arbeitsgemeinschaft Industrieller Forschungsvereinigungen e.V. (AIF 8640), and has been supervised by a FVV working group chaired by Dipl.-Ing. H.-J. Dietrichs, MTU Munich. The support and permission for publication are gratefully acknowledged.

References

Ardey, S., 1993, "Vergleich dreidimensionaler Heißfühler-Messungen mit Ergebnissen von Grenzschichtmessungen an einem filmgekühlten Turbinenschaufelgitter," Diplomarbeit No. 93/4.15 Institut für Strahlantriebe, UniBw München, Germany.

Brown, D. B., 1973, "Cold-Air Aerodynamic Study in a Two-Dimensional Cascade of a Turbine Stator Blade With Suction-Surface Film Cooling," NASA TM X-2685.

Goldstein, B. J., Eckert, E. R. G., and Ito, S., 1987, "Film Cooling in a Plane Turbine Cascade," *Proc. First International Symposium on Transport Phenomena,* Honolulu, pp. 37–43.

Haas, W., Rodi, W., and Schönung, B., 1988, "Filmkühlung von Turbinenschaufeln durch Ausblasung aus einer Lochreihe," ZFW 12, pp. 159–172.

Haller, B. R., 1980, "The Effects of Film Cooling Upon the Aerodynamic Performance of Transonic Turbine Blades," Ph.D. Thesis, Cambridge.

Jabbari, M. Y., and Goldstein, R. J., 1992, "Vortex Structure and Mass Transfer Near the Base of a Cylinder and a Turbine Blade," AGARD CP-527 Paper No. 2.

Kiock, R., 1982, "Experimentelle Ermittlung des Grenzschichtumschlags am Turbinengitter T106," Institut für Entwurfsaerodynamik, DLR Braunschweig, IB 129-82/3.

Kiock, R., Hoheisel, H., and Dietrichs, H. J., 1985, "The Boundary Layer Behavior of an Advanced Gas Turbine Rotor Blade Under the Influence of Simulated Film Cooling," AGARD CP-390.

Köllen, O., and Koschel, W., 1985, "Effect of Film Cooling on the Aerodynamic Performance of a Turbine Cascade," AGARD CP-390, Paper No. 39.

López Péna, F., and Arts, T., 1992, "On the Development of a Film Cooling Layer," AGARD CP-527 Paper No. 36.

Manickam, M. D., and Murugesan, K., 1989, "Effect of Discrete Hole Film Cooling on Aerodynamic Performance of a Turbine Cascade," ISABE 89-7040, Bangalore, pp. 397–404.

McFarland, E. R., 1976, "An Investigation of the Aerodynamic Performance of Film Cooled Turbine Blades," Ph.D. Thesis, Cincinnati, OH.

Römer, N., 1990, "Untersuchungen zum Umschlagverhalten der Profilgrenzschicht an Verdichter- und Turbinengittern," Ph.D. Thesis, UniBw München, Germany.

Rodi, W., Haas, W., and Schönung, B., 1986, "Untersuchungen des Grenzschichtverhaltens an Turbinenschaufeln unter Berücksichtigung von Filmkühlung und von lokalen Ablöseblasen," FVV Forschungsbericht GRAFTUS Heft 310.

Velazquez, M., 1988, "Untersuchungen zur aerodynamischen Simulation der Filmkühlung von Gasturbinenschaufeln," Ph.D. Thesis, Universität Hannover, Germany.

Wilfert, G., Ladwig, M., and Fottner, L., 1990, "PANDA—A New Data Accquisition System for Wake and Profile Pressure Distribution Measurement at the High-Speed Cascade Wind Tunnel," 10th Symposium on Measuring Techniques for Transonic Flows in Cascades and Turbomachines.

Wunderwald, D., Wilfert, G., and Fottner, L., 1992, "The Experimental Setup of a Triple-Sensor Anemometry and Its Controlling System at the High-Speed Cascade Wind Tunnel," 11th Symposium on Measuring Techniques for Transonic Flows in Cascades and Turbomachines.

Design of a Low Aspect Ratio Transonic Compressor Stage Using CFD Techniques

N. L. Sanger
NASA Lewis Research Center,
Cleveland, OH 44135

A transonic compressor stage has been designed for the Naval Postgraduate School Turbopropulsion Laboratory. The design relied heavily on CFD techniques while minimizing conventional empirical design methods. The low aspect ratio (1.2) rotor has been designed for a specific head ratio of 0.25 and a tip relative inlet Mach number of 1.3. Overall stage pressure ratio is 1.56. The rotor was designed using an Euler code augmented by a distributed body force model to account for viscous effects. This provided a relatively quick-running design tool, and was used for both rotor and stator calculations. The initial stator sections were sized using a compressible, cascade panel code. In addition to being used as a case study for teaching purposes, the compressor stage will be used as a research stage. Detailed measurements, including nonintrusive LDV, will be compared with the design computations, and with the results of other CFD codes, as a means of assessing and improving the computational codes as design tools.

Introduction

The Naval Postgraduate School axial transonic compressor stage and test facility were designed in 1968 by Prof. Michael H. Vavra. The purpose of the stage was to provide an advanced test vehicle for operational and research experience for naval officers. The completed design, aerodynamic and mechanical, was performed manually by Prof. Vavra, a notable accomplishment. However, in almost the last step in the design calculations, an error in sign occurred, which resulted in an erroneous radial distribution of blade setting angle. This distribution was built into the rotor. A second inaccuracy arose from an assumption made for the through flow into the rotor. These, and other aspects of the Vavra design are described by Erwin (1983).

The major effect of the design errors occurred over the outer 25 percent of span, where the rotor blade setting angles were more open than the design intent, and over the inner 25 percent of span where the incidence was again too high because axial velocities were lower than had been assumed. The higher resulting incidence angles toward the tip increased supersonic expansion around the leading edge, producing larger shock losses and lower pressure rise than design intent. This, and the higher incidence angles toward the hub, led to a radial distribution of flow angle from the rotor, which was not matched to the distribution used in the design of the stator. Experimental results for the stage, and for the rotor only, were reported by Neuhoff (1985a, b) and Neuhoff et al. (1986).

While the Vavra stage design was not a correct one, it was quite successful in that it facilitated the development of a transonic compressor test capability at the Naval Postgraduate School, and of the development of high response instrumentation techniques to determine flow behavior in transonic stages (Shreeve and Neuhoff, 1984; Neuhoff et al., 1986). However, a new stage design was sought, one for which detailed measurements would provide a meaningful evaluation of current design and analysis methods. NASA Lewis Research Center agreed to perform the aerodynamic and mechanical design of such a stage. This provided the opportunity to use the newly emerging CFD tools, supplemented by traditional methods and, later, to have the procedure tested against experimental results. The purpose of the present paper is to present the design that was obtained, with a description of the design/analysis process that was used to arrive at the final geometry.

Test Facility

The open-loop test facility and present compressor stage are shown in Fig. 1. Air enters through filters in a housing surrounding the inlet piping. Within the housing an intake throttle valve is attached to a settling chamber. The throttle valve consists of two plates having identical hole patterns; the plates rotate with respect to each other and are driven by an hydraulic actuator. The flow then passes through perforated plates in the 0.813-m (32-in.) diameter settling chamber; following the settling chamber, the flow passes into a 0.457-m (18-in.) diameter pipe in which there is a calibrated nozzle. The flow enters the compressor through a 0.279-m (11-in.) diameter inlet pipe and exits radially. A honeycomb section following the stator removes any circumferential velocity component from the flow. Thus the torque supplied to the rotor is equal to the torque experienced by the stator and honeycomb section. The stator section is mounted on ball races and is free to rotate against flexures instrumented with strain gages. The strain gage reading is then a measure of the torque supplied to the rotor.

The compressor rotor is driven by an opposed-rotor single-stage air turbine supplied by air from the laboratory compressed air supply. The compressed air is supplied to the laboratory by a 12-stage Allis-Chalmers axial compressor.

Design Procedure

Preliminary Design. Design goal was to achieve as high a loading and specific weight flow as was practical, while keeping rotor tip Mach number at a moderate level. Chief constraint was power available from the drive turbine. The results of a parametric study are shown in Fig. 2. Specific head-rise was calculated for a series of tip speeds and pressure ratios ($\Psi = c_p T_{01}(PR^{((\gamma-1)/\gamma)} - 1)/U_t^2$). After consideration of various configurations, a target design was specified that has higher loading and lower tip speed than the original Vavra design. The loading is also slightly higher than the NASA Rotor 67, which is also plotted on Fig. 2.

Contributed by the International Gas Turbine Institute and presented at the 39th International Gas Turbine and Aeroengine Congress and Exposition, The Hague, The Netherlands, June 13–16, 1994. Manuscript received by the International Gas Turbine Institute February 18, 1994. Paper No. 94-GT-236. Associate Technical Editor: E. M. Greitzer.

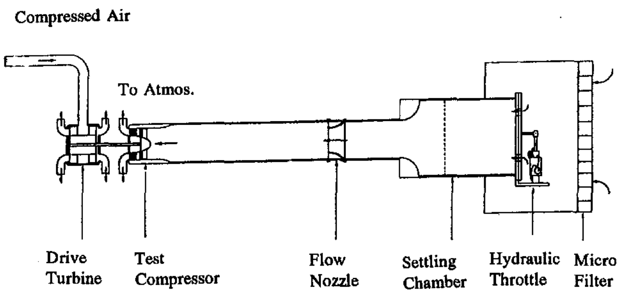

Fig. 1 (*a*) Test facility and piping (not to scale)

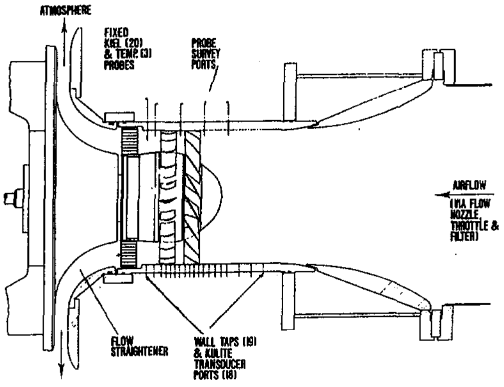

Fig. 1 (*b*) Existing transonic stage (Vavra design)

Fig. 1 Naval Postgraduate School transonic compressor test facility

Table 1 Design parameters

Rotor Pressure Ratio	1.61
Stage Pressure Ratio	1.56
Tip Speed	396.2 m/sec (1300 ft/sec)
Design Weight Flow	7.75 kg/sec (17.09 lb-m/sec)
Specific Weight Flow	170.9 kg/sec-m^2 (35 lb-m/sec-ft^2)
Specific Head Rise	0.246
Tip Inlet Relative Mach Number	1.28
Aspect Ratio	1.2
Hub/Tip Radius Ratio	0.51
Number of rotor blades	22
Number of stator blades	27
Tip Solidity - Rotor	1.3
Tip Solidity - Stator	1.0
Outside Diameter	27.94 cm (11.0 in)
Rotor Diffusion Factor - tip	0.4
Rotor Diffusion Factor - hub	0.47
Stator Diffusion Factor - tip	0.52
Stator Diffusion Factor - hub	0.58

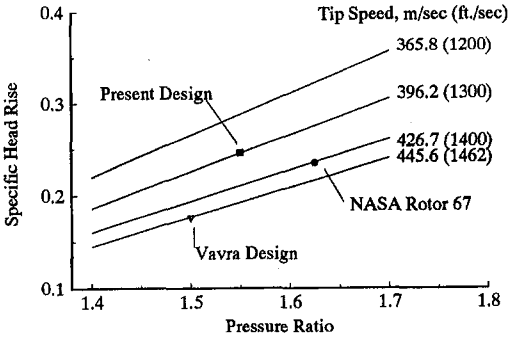

Fig. 2 Specific head rise

The power required by the target design (341 kW) was set very near the available (limiting) power available from the turbine drive (354 kW). To minimize fabrication expenses, the external flow path and stator mechanical design were retained. This restricted aerodynamic design choices, but was considered necessary for economic reasons. A new conical spinner for the rotor was designed having a constant 28-deg ramp angle. This angle is effectively set by the choice of pressure ratio and aspect ratio.

A review of in-house and contractor designs led to the choice of an approximately constant radial distribution of exit total pressure; exit total temperature (energy addition) was chosen to be nearly radially constant, but higher in the tip region to compensate for shock losses (see Fig. 16 later). These distributions of total pressure and temperature, the overall pressure and temperature ratio, flow rate and the new flow path were entered into a streamline curvature design program. During the preliminary design process, before final design parameters were chosen, various combinations of parameters were assessed until detailed distributions of parameters such as diffusion factor ($D = 1 - V'_2/V'_1 + \Delta V'_\theta/2\sigma V'_1$) and loss appeared reasonable in light of contemporary experience. Specific empirical loss sets or deviation angle distributions were not used. Deviation angle estimates for the controlled-diffusion stator were based on experimental results from the controlled-diffusion stator designed by Sanger (1983) and tested at the Naval Postgraduate School cascade facility.

A summary of the design parameters is given in Table 1.

Nomenclature

c_p = specific heat at constant pressure
D = diffusion factor
P = pressure
PR = pressure ratio, total-to-total
R = gas constant
s = entropy
T = temperature
U = rotor wheel speed
V = velocity

$\bar{W}$ = specific weight flow = ρV
β = flow angle
γ = ratio of specific heats
δ = deviation angle = $\beta_2 - \kappa_2$
i = incidence angle = $\beta_1 - \kappa_1$
κ = blade metal angle
ρ = gas density
σ = blade solidity, chord/blade spacing
Ψ = specific headrise
$\bar{\omega}$ = total pressure loss coefficient

Superscripts

$'$ = relative

Subscripts

0 = total
1 = inlet
2 = outlet
is = isentropic process value
t = tip

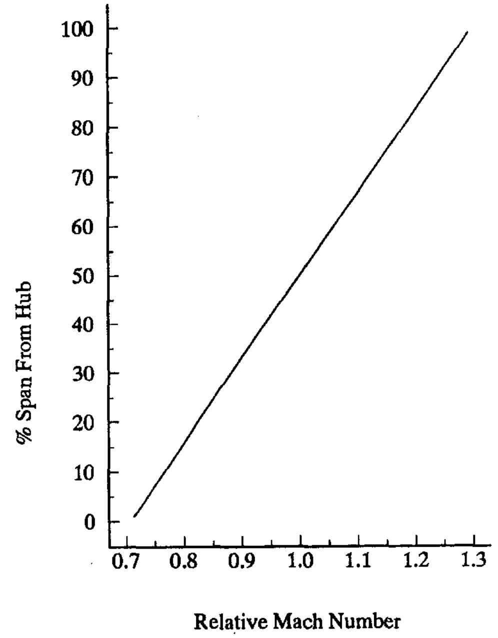

Fig. 3 (*a*) Radial distribution of rotor inlet relative Mach number

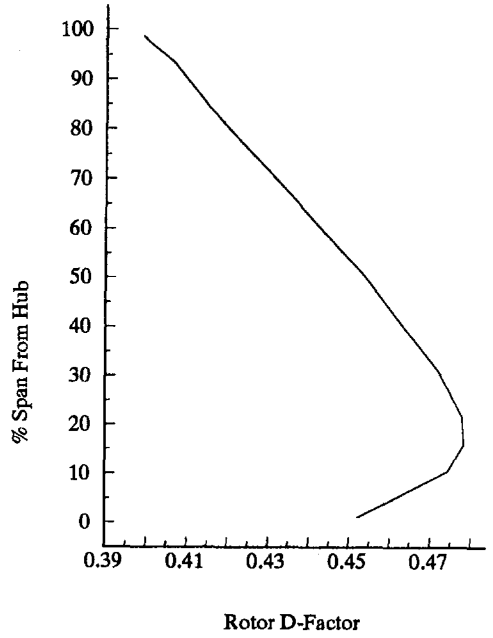

Fig. 3(*b*) Radial distribution of rotor *D*-factor

Computer Codes. Several computer codes were used in the design process.

Streamline-Curvature: The NASA in-house streamline-curvature code was used for preliminary calculations and production of fabrication coordinates. The main-frame version of the code was documented in NASA TP-1946 (Crouse and Gorrell, 1981). An improved PC version, available from and supported by James E. Crouse, was used in this design. This version has shown less sensitivity to blade section stacking in high hub ramp angle cases as encountered in this design. Steady, axisymmetric flow is assumed, thus reducing the problem to solving the two-dimensional flow in the meridional plane. The full radial equilibrium equation forms the basis of the code. The aerodynamic solution gives velocity diagrams on selected streamlines of revolution at the blade edges. There are no calculation stations inside the blade row. There are numerous options

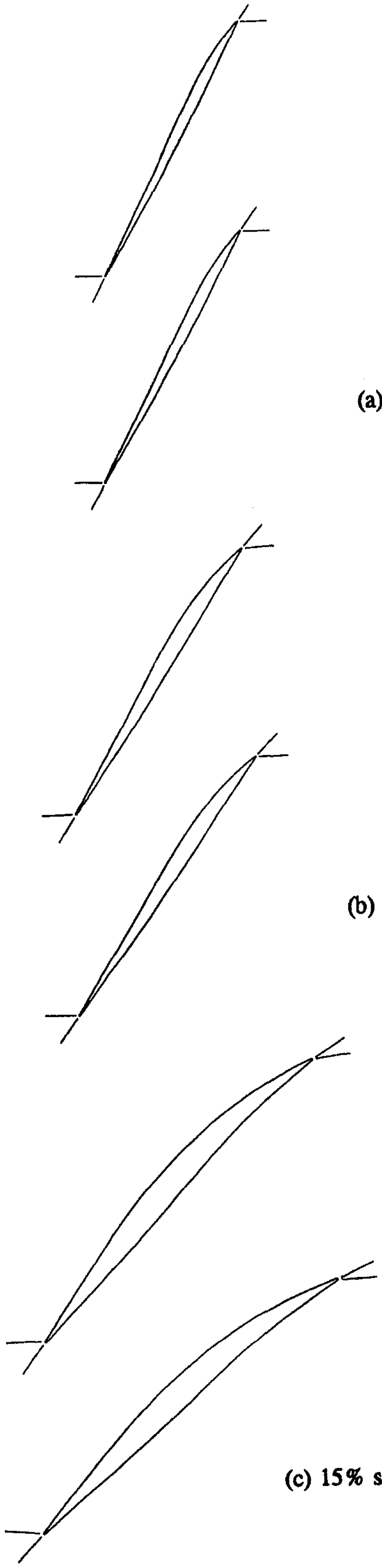

(a) 85% span from hub

(b) 50% span from hub

(c) 15% span from hub

Fig. 4 Rotor blade sections

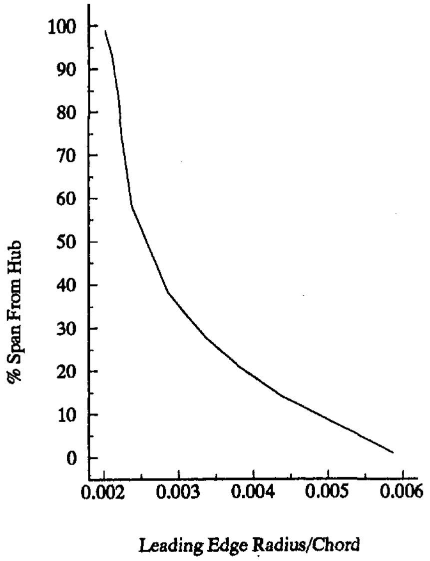

Fig. 5 Rotor leading edge radius/chord

for controlling the form of input and for specifying the amount of output.

Blade-Element Code: The geometry portion of the streamline-curvature code has been extracted and combined with in-house graphics to run on the Lewis mainframe computer. This short code affords a convenient means for designing individual blade sections according to the criteria established in the streamline-curvature code. The meanline of the blade is described by two polynomial segments, each of which can be specified by up to a quartic polynomial. The polynomial is a fit of local blade angle against mean-line distance. The distribution of blade thickness about the mean-line is also specified by two polynomials, each of which may be quartics. The thickness is added symmetrically on either side of the mean-line. A more complete description of this process is given by Sanger (1983).

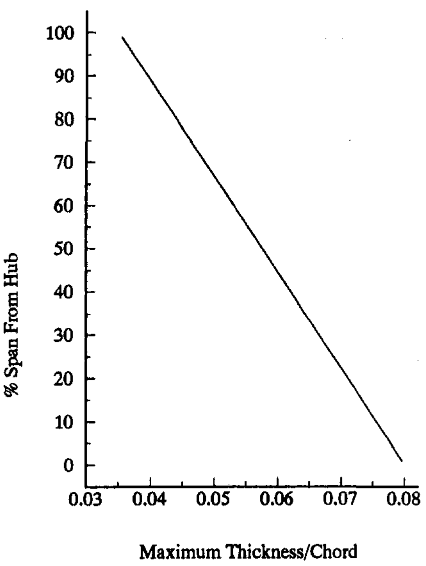

Fig. 6 Rotor maximum thickness/chord

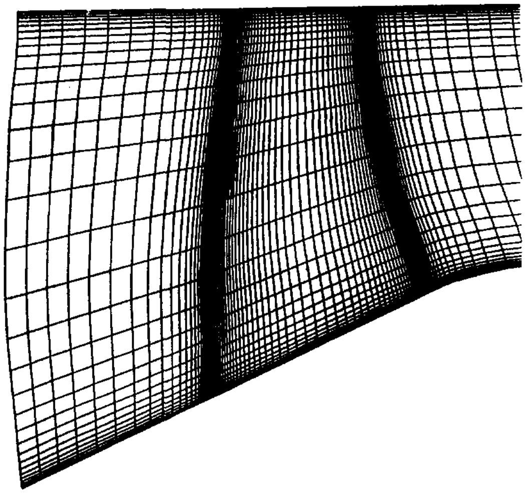

Fig. 7 Computational grid in the meridional plane

Denton TIP3D: The three-dimensional analysis code employed was a hybrid code developed by Denton and named TIP3D. It was originally reported in 1986 (Denton, 1986), but has since been expanded and upgraded. It uses the original Denton Euler code as a base (Denton, 1983), but couples it with a relatively simple viscous approximation in order to account for blockage and secondary flow effects. In the approximation, viscous effects are taken into account by including a body force term in the momentum equation and a source term in the energy equation. Wall shear stress is approximated by an empirical equation. The distribution of shear stress from the wall is obtained from the Boussinesq eddy viscosity model. The viscous effects can be "cut off" at some fraction of passage width by providing that fraction as input. With sufficient grid points within the boundary layer, one can obtain a reasonably good

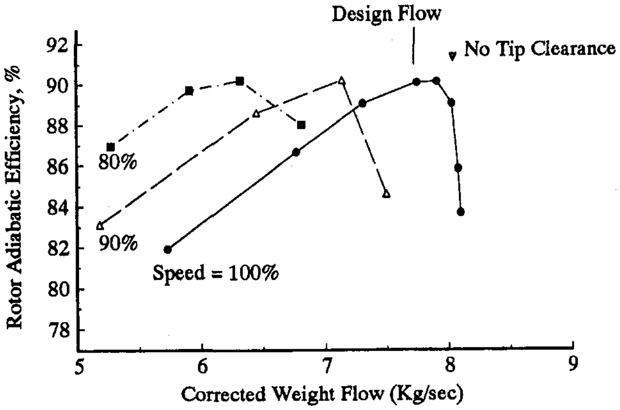

Fig. 8(*a*) Rotor adiabatic efficiency

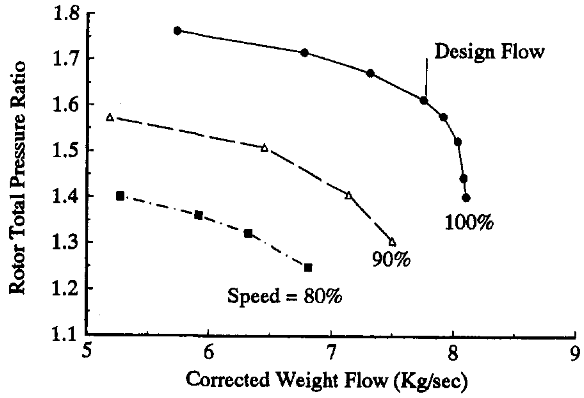

Fig. 8(*b*) Rotor total pressure ratio

Fig. 8 Rotor performance map calculated with Denton TIP3D code

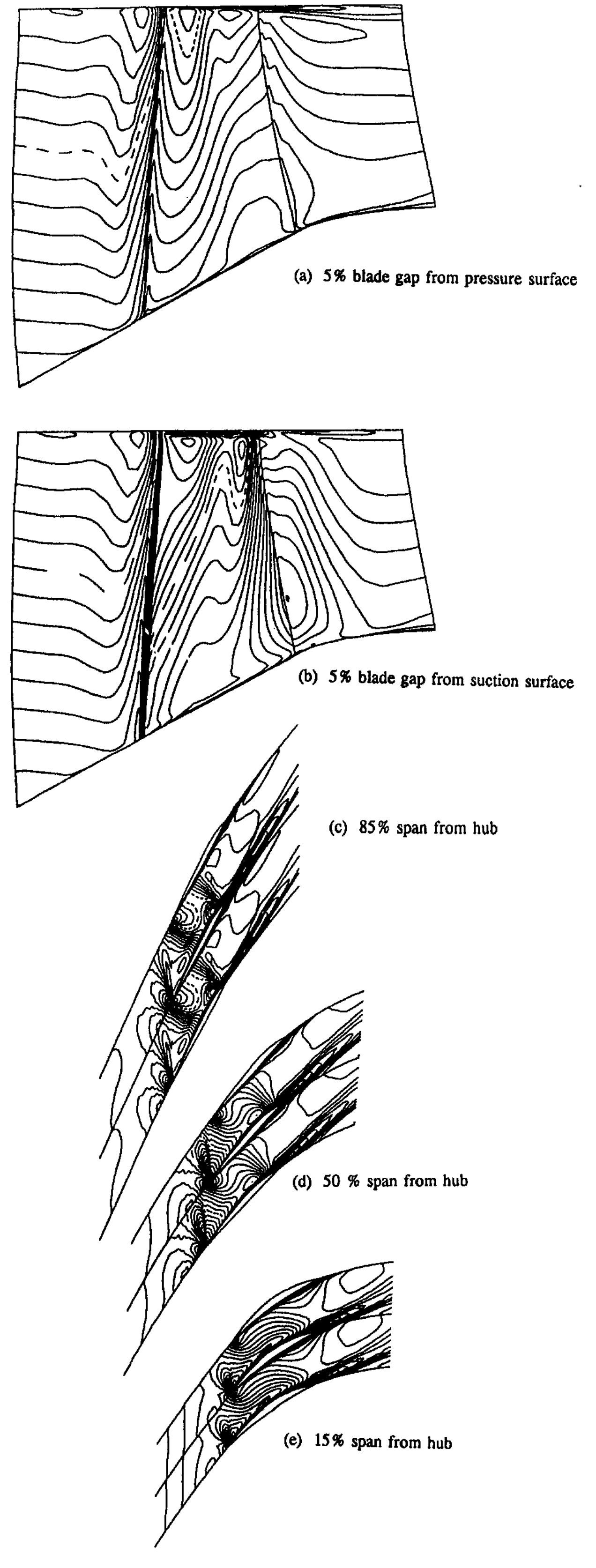
(a) 5% blade gap from pressure surface

(b) 5% blade gap from suction surface

(c) 85% span from hub

(d) 50 % span from hub

(e) 15% span from hub

Fig. 9 Rotor relative Mach number at design flow; Mach No. increments: (*a*) and (*b*), 0.05, (*c*)–(*e*), 0.025, M′ = 1.0 - - - - - - - -

prediction of the flow in a real turbulent boundary layer, and at a considerable saving in computing time and cost.

An additional improvement to the original code is the inclusion of tip clearance flow. The code is not capable of calculating the details of the flow in a tip clearance region, but is capable of including the effect on the primary flow and on the overall performance. The leakage is predicted simply by reducing the blade thickness to zero in the clearance gap, and by applying a periodicity condition within the gap in exactly the same way periodicity is applied upstream

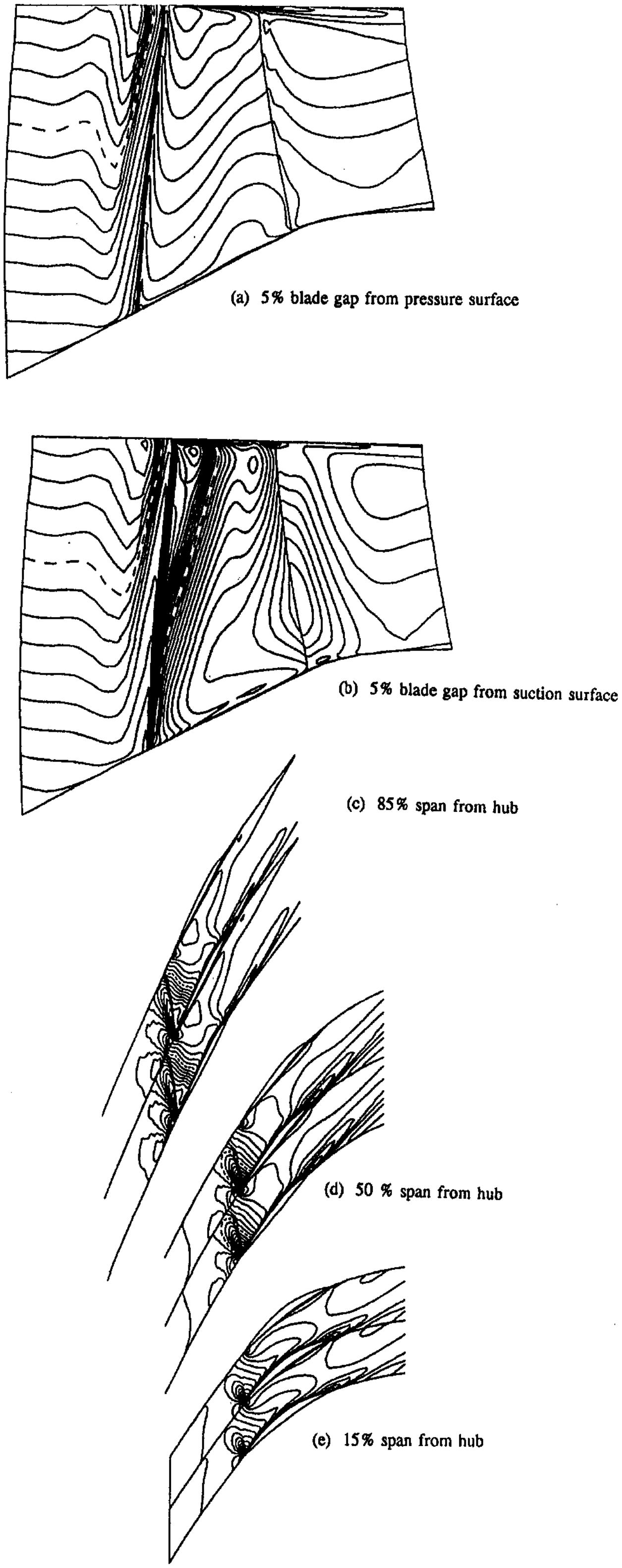
(a) 5% blade gap from pressure surface

(b) 5% blade gap from suction surface

(c) 85% span from hub

(d) 50 % span from hub

(e) 15% span from hub

Fig. 10 Rotor relative Mach number at near-stall flow; Mach number increments = 0.05, M′ = 1.0 - - - - - - - -

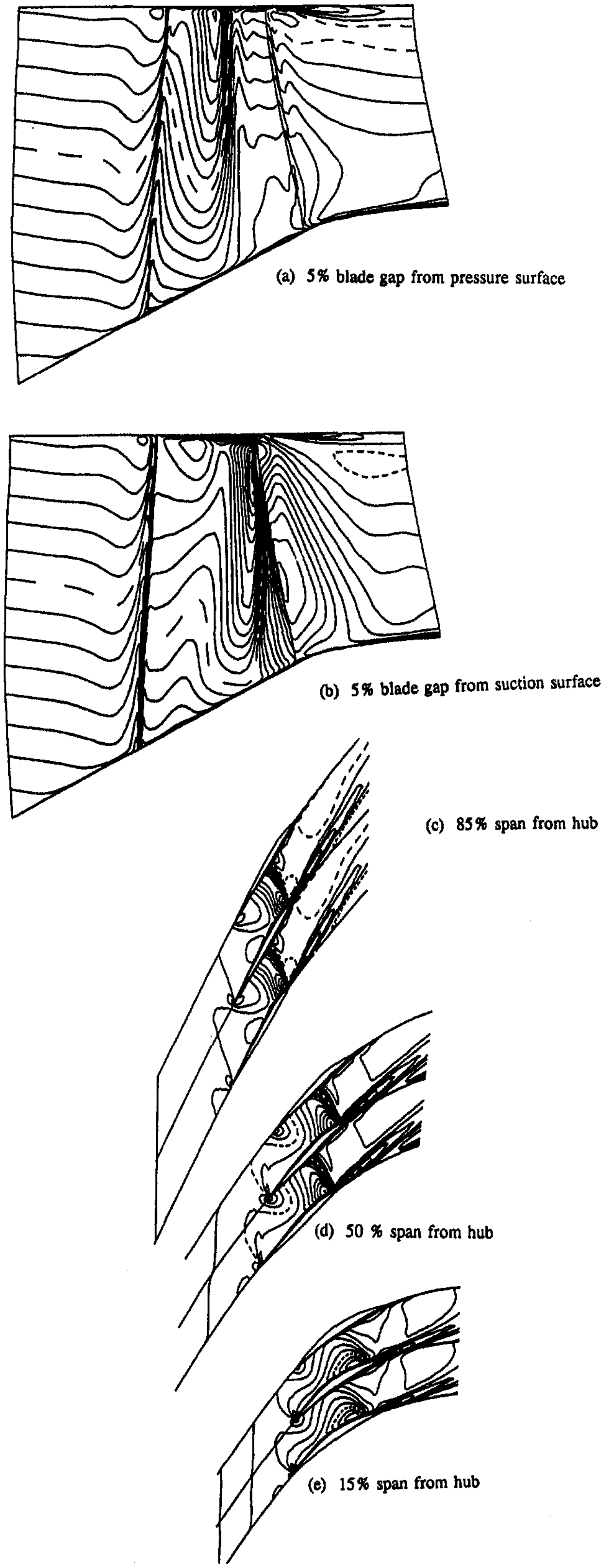

(a) 5% blade gap from pressure surface

(b) 5% blade gap from suction surface

(c) 85% span from hub

(d) 50 % span from hub

(e) 15% span from hub

Fig. 11 Rotor relative Mach number at near-choke flow; Mach number increments = 0.05, M′ = 1.0 - - - - - - - -

and downstream of the blade row. This enables flow to pass over the blade tip, and ensures that no load is carried within the gap. A typical run time for a transonic rotor blade row was 20 minutes on a Cray YMP.

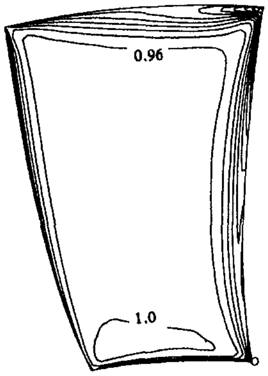

Fig. 12 Entropy function at 99.2 percent of rotor chord; design flow; entropy increments, 0.04

Panel Code: Because the stator flow field is subsonic, a subsonic two-dimensional panel code was used to screen blade sections. The entire stacked three-dimensional stator was then analyzed by the TIP3D code. The panel code (McFarland, 1984) employs a surface singularity method, which solves the inviscid, irrotational, compressible blade-to-blade flow equations on a surface of revolution. Streamsheet thickness can be incorporated as a function of meridional distance. The governing equations are linearized by approximating compressibility effects, and solved using an integral technique (panel method).

Blade sections were created with the blade geometry code and analyzed with the panel code and an integral boundary layer code (described below). This provided a quick screening method and allowed development of a series of blade sections, which showed no boundary layer separation at the design point. A typical run time on a 386 PC (25 MHz CPU) is 30 seconds.

Boundary Layer Code: An integral boundary layer code (McNally, 1970) was used in conjunction with the panel code to screen the two-dimensional blade sections. The design point surface velocity distributions calculated by the panel code were entered into the boundary layer code and the condition of the turbulent boundary layer was monitored. No blade section was accepted that indicated that turbulent separation had occurred (incompressible form factor must be less than 2.0).

The McNally code uses integral methods to solve the two-dimensional, compressible laminar and turbulent boundary layer equations in an arbitrary pressure gradient. Cohen and Reshotko's (1956) method is used for the laminar boundary layer, transition is predicted by the Schlichting–Ulrich–Granville (Schlichting, 1979) method, and Sasman and Cresci's (1966) method is used for the turbulent boundary layer. A typical run time on the Lewis Amdahl 5870 main-frame running under the VM operating system is 10 seconds.

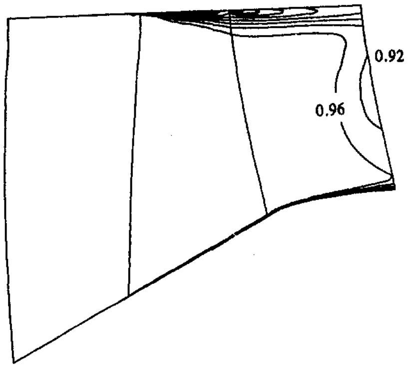

Fig. 13 Entropy function on mean meridional surface of rotor at design flow; entropy increments, 0.04

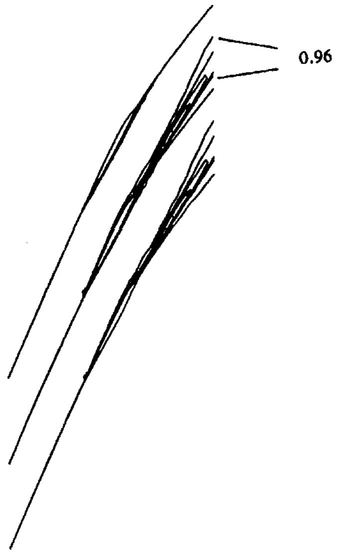

Fig. 14(*a*) 85 percent span from hub

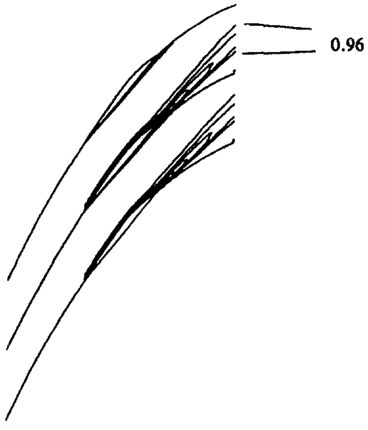

Fig. 14(*b*) 50 percent span from hub

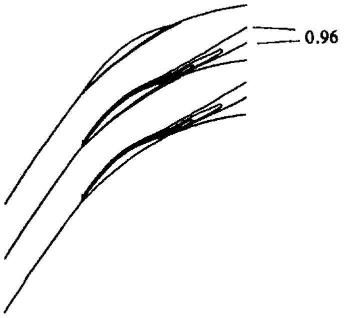

Fig. 14(*c*) 15 percent span from hub

Fig. 14 Entropy function on rotor blade-to-blade surfaces at design flow; entropy increments, 0.04

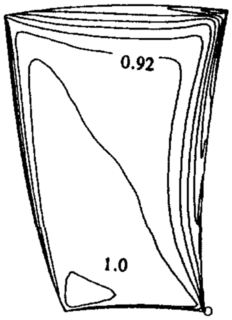

Fig. 15 Entropy function at 99.2 percent of rotor chord; near-stall flow; entropy increments, 0.04

Rotor Design. Velocity triangles were set with the streamline curvature code. Blade shapes were then fitted to the triangles using both quasi-three-dimensional and full-three-dimensional calculations. Rotor tip solidity was set at 1.3. At that solidity and a tip inlet Mach relative number of 1.3, it was verified that the leading edge oblique shock would be contained in the blade passage, striking the suction surface at about 80 to 90 percent of chord. The radial distributions of inlet relative Mach number and of *D*-Factor for the rotor are shown in Fig. 3.

Initially, rotor blade sections were screened using a quasi-three-dimensional version of the Denton Euler code, which had a transpiration model to simulate the boundary layer blockage. Surface boundary layer condition was checked using the McNally integral boundary layer code. Criteria used for design were to minimize supersonic acceleration on the uncovered portion of the blade to reduce shock strength, and then to control diffusion in the covered portion to prevent or delay boundary layer separation.

This procedure provided a quick, initial screening of blade shapes, but with the advent of the full-three-dimensional code with body forces, it probably would be more effective to use the three-dimensional code and develop a three-dimensional geometry package to fit and stack tentative blade designs. Although a quasi-three-dimensional code is quick, the result may be inaccurate because transonic sections are quite sensitive to streamtube height, a user-specified quantity.

When the three-dimensional body force code became available, the blade sections originally defined using the quasi-three-dimensional code were used as a base design; subsequent alterations to the geometry were made based on the three-dimensional calculations. Three blade sections from the final design are shown in Fig. 4. Leading edge radii nondimensionalized by chord varied from 0.002 at the tip to 0.0058 at the hub (Fig. 5). Trailing edge radius to chord had a similar distribution. Maximum thickness followed a linear variation from 3.5 percent of chord at the tip to 8 percent of chord at the hub. The rotor leading edge wedge angles in the supersonic region of the blade were minimized by positioning the maximum thickness location well back on the blade. The maximum thickness location was varied from 76 percent of chord at the tip to 50 percent at the hub (Fig. 6).

A meridional view of the grid used in the full-three-dimensional calculations is shown in Fig. 7. Slightly more than 100,000 points were used, with 97 points in the meridional direction and 33 each in the radial and circumferential planes. The grid points were packed close to the blade surfaces, hub, and casing, and meridionally from the leading and trailing edges of the blades using a geometric packing scheme. Expansion factors were 1.25 in the spanwise direction, 1.3 in the blade-to-blade direction, 1.25 in the meridional direction upstream and downstream of the blades, and 1.1 from the blade leading and trailing edges in the meridional direction inside the blade passage.

A complete calculated rotor map is presented in Fig. 8. The calculated performance projects a pressure ratio of 1.61 at design flow and an adiabatic efficiency of 90.1 percent. At the best efficiency flow point the pressure ratio was 1.58 and efficiency was 90.3 percent. Recalculating the performance with no tip clearance (at a different flow rate) raised the efficiency by about 2 points. Performance was calculated for decreasing flow (approaching stall). As the flow decreased, the number of time steps required for the solution to converge increased until the solution failed to converge. The nearest-stall points plotted in Fig. 8 are for converged or nearly converged points. Whether

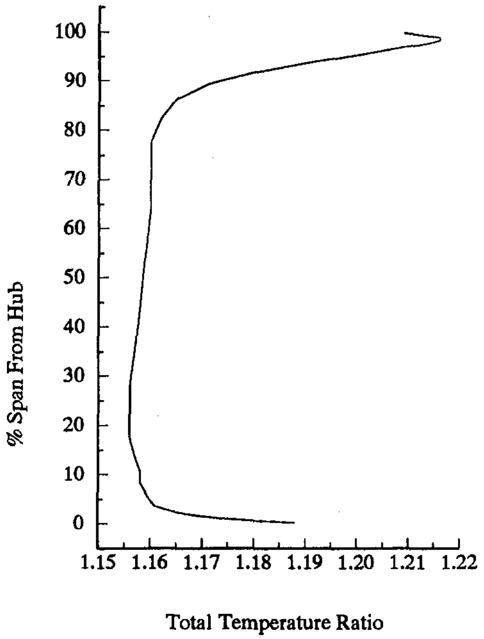

Fig. 16(*a*) **Rotor exit total temperature**

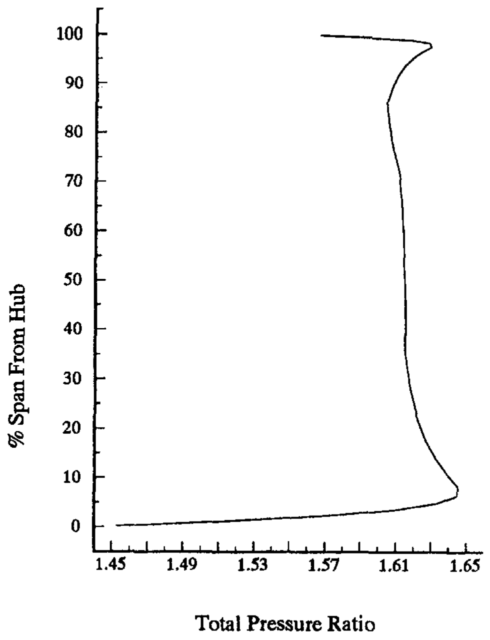

Fig. 16(*b*) **Rotor exit total pressure**

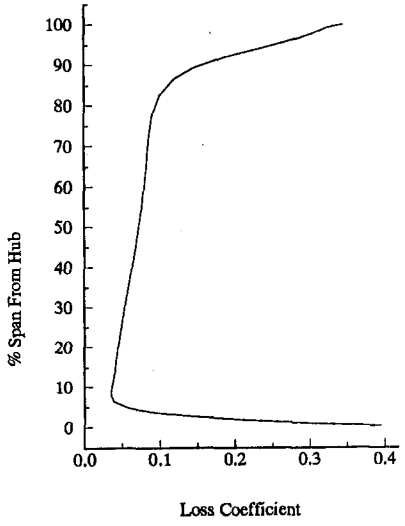

Fig. 16(*c*) **Rotor loss coefficient**

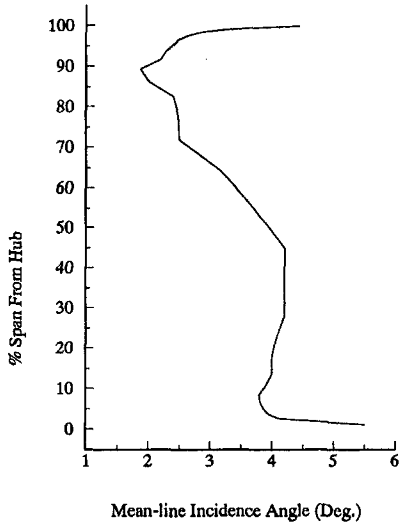

Fig. 16(*d*) **Rotor incidence angle**

these points correspond to actual stall is open to question, and must await experimental investigation. All that can be said is that numerically convergent solutions were obtained (albeit at increased numbers of time steps).

Relative Mach number contours are presented in Fig. 9 for the design flow point. Meridional planes 5 percent of passage width from the pressure and suction surfaces are shown in Figs. 9(*a*) and 9(*b*) respectively, and blade-to-blade planes at 15, 50 and 85 percent span from tip are shown in Figs. 9(*c*), 9(*d*), and 9(*e*), respectively. A weak oblique shock reflects from the suction surface as a strong normal shock at about 85 percent chord (Fig. 9(*c*)). The shock becomes weaker and disappears as the hub is approached. The tip clearance flow is evident (Fig. 9(*b*)). The spacing between the casing and the first gridline represents a distance of 0.18 percent of blade span, which is equivalent to an average tip clearance of 0.0114 cm (0.0045 in.). The cold clearance of the existing Vavra rotor is 0.0254 cm (0.010 in.). If built to the same specifications, the subject rotor should be expected to have a hot, running clearance reasonably close to the value used in the three-dimensional calculations.

At the near-stall point the normal shock is pushed forward in the passage and stands in front of the leading edge, intersecting the suction surface at about 30 percent chord near the tip. The three-dimensional spanwise sweep of the normal shock is clear from the meridional view near the suction surface (Fig. 10(*b*)).

At the near-choke point the normal passage shock has moved to the rear of the passage and extends to within 15 percent of the hub plane. There is still some sweep to the shock, but less than was present at the other flow conditions (Fig. 11(*b*)).

Losses are well behaved at the design point. Entropy function contours, $\exp(-\Delta s/R)$, are presented in Fig. 12 for the cross-channel plane just upstream of the trailing edge. The losses on the suction surface are higher than the losses on the pressure surface due to the combined effect of shock losses and higher diffusion. The considerable effect of the tip clearance flow is evident from Fig. 13, which shows losses on a meridional plane midway between blade surfaces. Entropy contours on the blade surfaces are shown in Fig. 14. Losses are high in the wakes as expected, with some indication of limited boundary layer separation near the trailing edge.

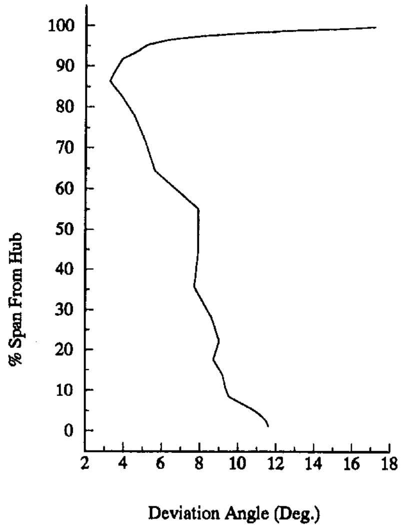

Fig. 16(*e*) Rotor deviation angle

Fig. 16 Radial distributions of rotor performance parameters at design flow

At the near-stall flow, the suction surface boundary layer is quite thick (Fig. 15) and tip clearance effects have penetrated into the core flow. Losses are higher, but are concentrated mainly in blade wakes and near the casing.

Aerodynamic quantities were mass-averaged in the blade-to-blade plane. Selected parameters are plotted in Fig. 16 as conventional radial distributions of performance quantities. The radially constant design energy addition and total pressure are clear from Figs. 16(*a*) and 16(*b*). Losses ($\bar{\omega} = (P'_{02is} - P'_{02})/(P'_{01} - p_1)$), as expected, are concentrated in the endwall regions with the casing having the greatest concentration of losses due to tip clearance flow and shock losses. Deviation angle distribution was initially set using Carter's Rule, but evolved to the final distribution (Fig. 16(*e*)) as a result of engineering judgments made in the course of analyzing the computations. Incidence angle distributions (Fig. 16(*d*)) evolved similarly. Area margin considerations were not ignored, but results of the computations drove the choice of setting angle and mean camber distribution rather than empirical rules. For reference, tip region throat area margins ($(A/A^*) - 1$) were about 3 percent.

At near stall, energy addition and losses are high in the tip region because high incidence angles lead to high supersonic expansion and shock losses. Exit total pressure is also higher over the outer portion of the span.

Stator Design. The stator poses some special problems. At design flow, inlet Mach number at the hub is 0.7 and diffusion factors are greater than 0.5 over the entire span, reaching 0.58 at the hub (Fig. 17). Camber angles range from 51 to 57 deg. Chord was kept radially constant to permit exchanging the new stator for the old. Twenty-seven blades were selected, giving a hub solidity of 1.5. A controlled-diffusion blade shape with elliptical leading and trailing edges was used. The maximum thickness distribution is shown in Fig. 18; the position of maximum thickness is constant from hub to tip at a value of 47 percent of chord. The blade section at midspan is shown in Fig. 19, and is typical of blade shapes at other sections. A typical surface velocity distribution is given in Fig. 20. Because the stator is free to rotate in order to measure torque supplied to the rotor, there is a clearance region between the tip and the casing; this region was accounted for in the three-dimensional computations.

Velocity triangles were set using a combination of the streamline curvature calculations and rotor exit profiles from three-dimensional computations. A screening process was followed

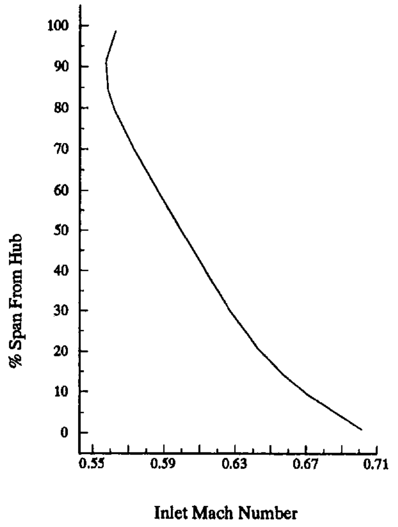

Fig. 17(*a*) Stator inlet Mach number

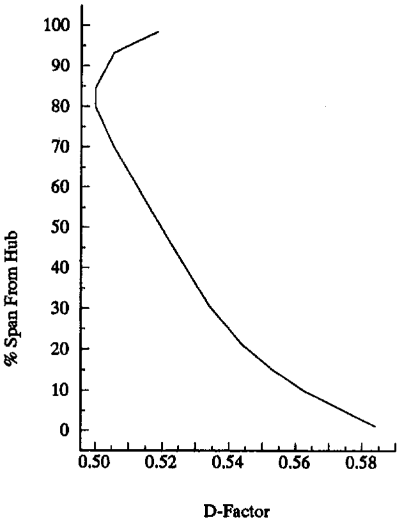

Fig. 17(*b*) Stator *D*-factor

Fig. 17 Stator radial distributions of inlet Mach number and *D*-factor

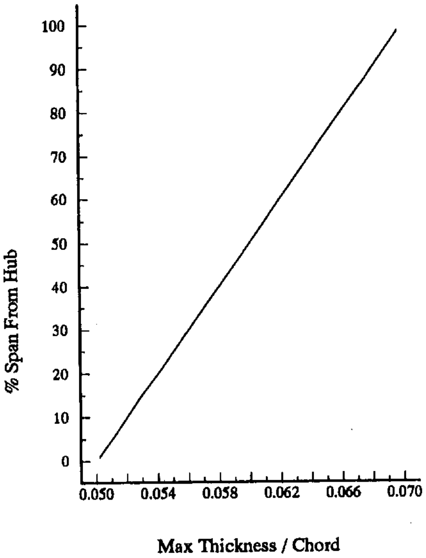

Fig. 18 Stator maximum thickness/chord

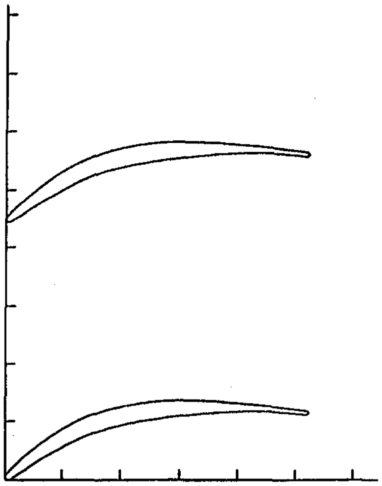

Fig. 19 Stator blade section at midspan

that aimed to produce a blade that was separation-free. The blade-element code was used to define a blade, surface Mach numbers were computed with McFarland's quasi-three-dimensional panel code, and the boundary layer was computed with the McNally integral boundary layer code. Adjustments were made to the geometry and the process was repeated until no separation of the suction surface boundary layer was predicted (incompressible form factor less than 2.0). A controlled diffusion shape was used, which strives for an acceleration to a peak Mach number on the suction surface, followed by a rapid deceleration, which reduces in magnitude as the trailing edge is approached. In highly loaded blades such as these, it is necessary to control the deceleration from the leading edge on the pressure surface of the blade as well. The midspan blade section was sized first and then a similar process was applied to blade sections at 15, 30, 70, and 85 percent of span. The blade was stacked in the streamline curvature code and geometric coordinates generated for the Denton three-dimensional computation. Because of time considerations, the Denton code was used only for post-design analysis. A "conventional" controlled diffusion stator was designed. That is, no attempt was made to customize it for end-wall flows (end bends) nor for high Mach numbers at the hub (leading edge sweep). Such customizing will be left for a future design, if attempted.

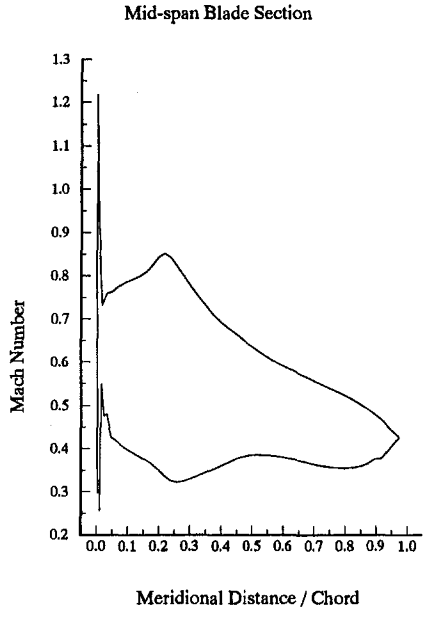

Fig. 20 Typical stator surface Mach number distribution

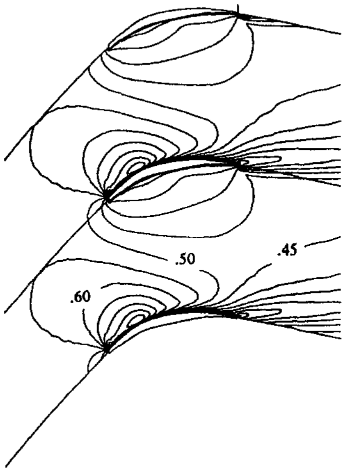

Fig. 21(*a*) 85 percent span from hub

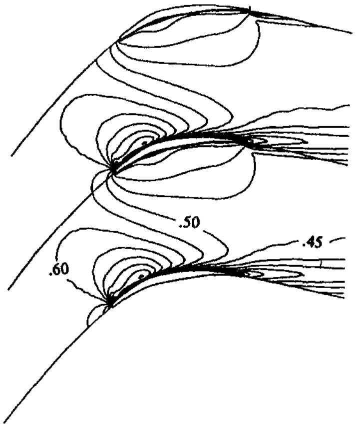

Fig. 21(*b*) 50 percent span from hub

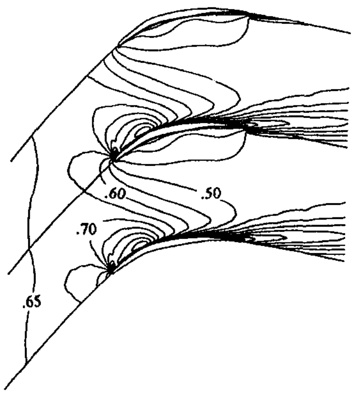

Fig. 21(*c*) 15 percent span from hub

Fig. 21 Absolute Mach numbers in the stator blade-to-blade planes at design flow; Mach number increments, 0.05

A three-dimensional grid identical to that applied to the rotor (Fig. 7) was generated for the stator. The tip clearance flow passes between the casing and the first grid line, amounting to a tip clearance gap of 0.18 percent of span. This is equivalent to an average clearance of 0.00838 cm (0.0033 in.). The present Vavra stator has a cold clearance of 0.0229 to 0.0254 cm (0.009 to 0.010 in.). If the subject stator is built to the same specifications, the actual tip clearance (accounting for thermal expansion) may be twice the value used in the three-dimensional calculations.

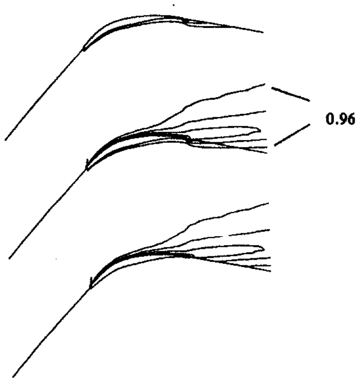

Fig. 22(*a*) 85 percent span from hub

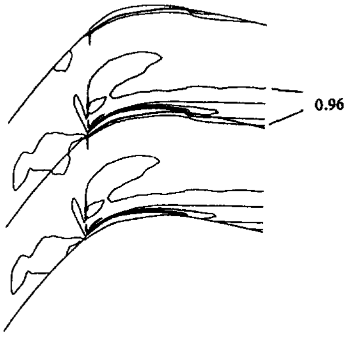

Fig. 22(*b*) 50 percent span from hub

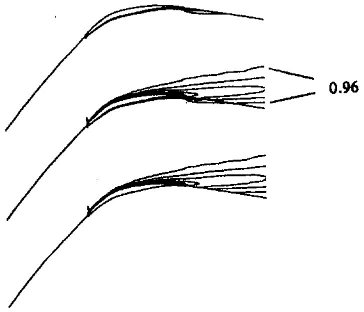

Fig. 22(*c*) 15 percent span from hub

Fig. 22 Entropy function in the stator blade-to-blade planes at design flow; entropy increments, 0.04

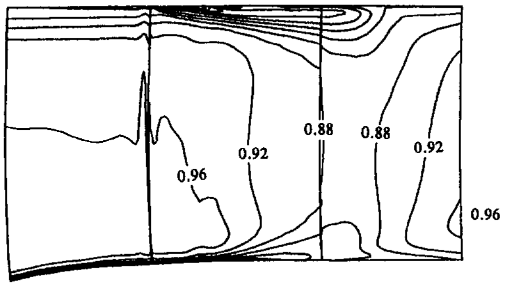

Fig. 24 Entropy function on the stator meridional plane at 5 percent blade gap from the suction surface; design flow; entropy increments, 0.04

Absolute Mach number contours in the blade-to-blade plane are presented in Fig. 21 at the design point flow for cascade sections at 15, 50, and 85 percent span from the hub. Peak Mach numbers occur, as expected, about one-third of chord from the leading edge, and diffuse rapidly. Mach number levels are the highest in the hub region. The entropy plots (Fig. 22) show a thickening of the boundary layer and perhaps some separation of the boundary layer at the hub and tip elements. The cross-plane entropy plots (Fig. 23) show the development of the surface boundary layers to be relatively well behaved. However, the stator must accept flow with high loss in the tip region and, due to its own tip clearance flow, contributes further losses near the suction surface extending inward over 15 to 20 percent of span. Secondary flow in the hub region places an accumulation of low-energy flow near the trailing edge adjacent to the suction surface, and the high loss region extends over 10 to 15 percent of span. Figure 24 provides another perspective on the distribution of loss, showing losses on a meridional plane 5 percent of blade gap from the suction surface. The effect of the tip clearance flow is evident.

At the near-stall point the entropy contours in the blade-to-blade planes (not shown) indicate blade suction surface boundary layers are separated from the leading edge. Losses are concentrated along the suction surface and in the corners between the suction surface and the endwalls (Fig. 25). The tip clearance flow interacting with the separated surface boundary layer provides a large concentration of losses. From the results of this calculation it would be expected that the stator will control the stall margin of the stage.

As with the rotor, aerodynamic quantities were mass-averaged in the blade-to-blade plane. Parameters of interest are plotted in Fig. 26 for the design flow condition. The calculated performance nearly achieves the intended constant radial distribution of total pressure. The combination of low energy inlet flow from the rotor plus the effect of stator tip clearance flow act to increase the losses over the outer span and reduce the exit total pressure in this region. The net effect of these losses is to reduce stage efficiency to 83 percent at design flow. A

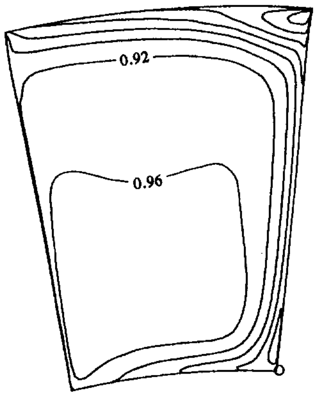

Fig. 23 Entropy function at 99.2 percent of stator chord; design flow; entropy increments, 0.04

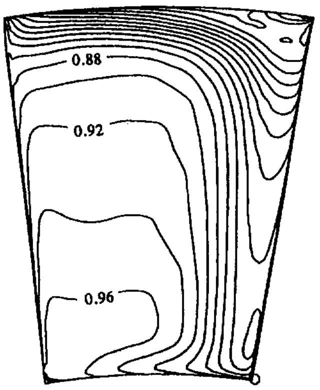

Fig. 25 Entropy function at 99.2 percent of stator chord; near-stall flow; entropy increments, 0.02

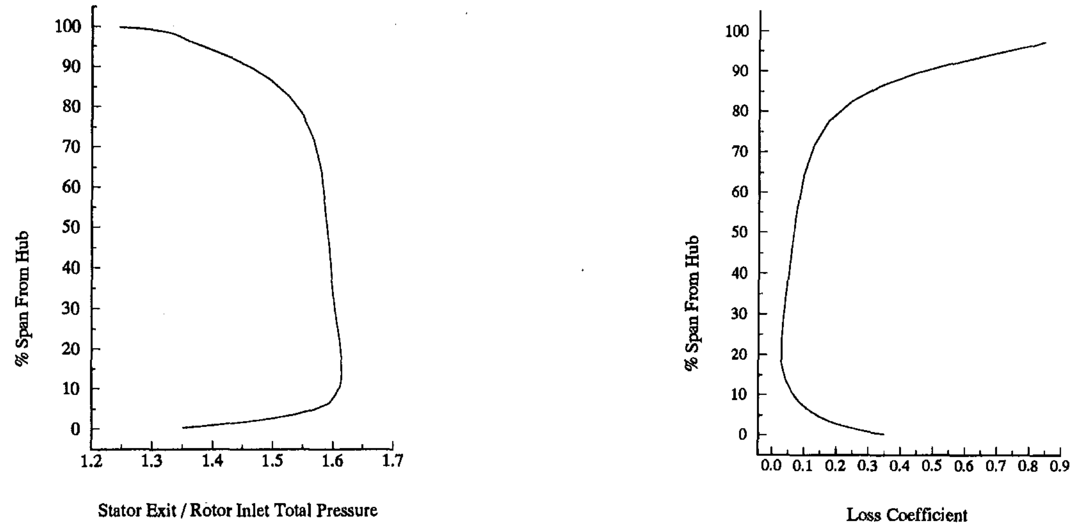

Fig. 26(*a*) Stator exit total pressure

Fig. 26(*b*) Stator loss coefficient

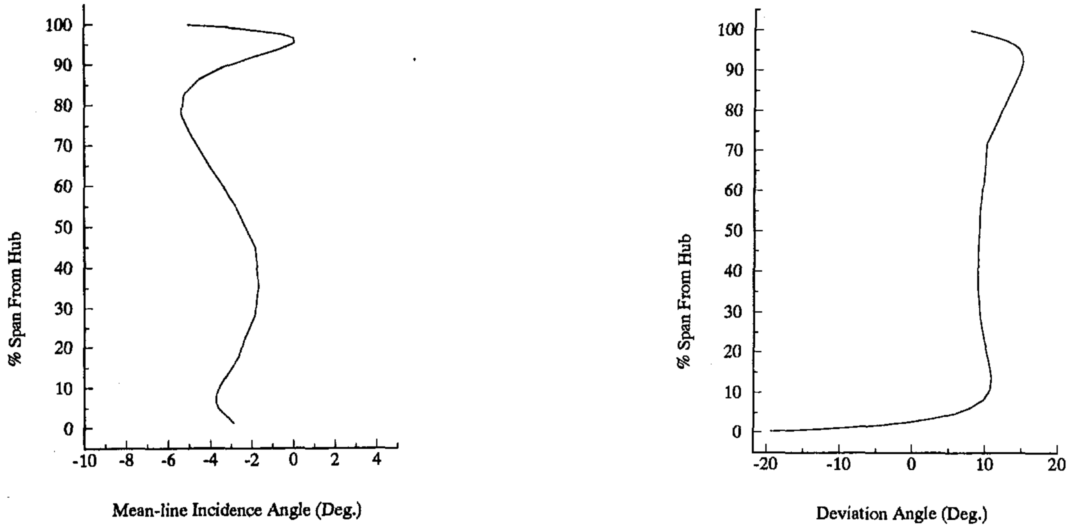

Fig. 26(*c*) Stator incidence angle

Fig. 26(*d*) Stator deviation angle

Fig. 26 Radial distribution of stator performance parameters at design flow

recalculation with zero stator tip clearance flow resulted in a stage efficiency gain of only 0.4 points to 83.4 percent. The combined effect of shock losses, boundary layer growth, and tip clearance in the rotor significantly affects the inlet flow to the stator in the tip region. Obviously, some form of restaggering should have been employed in the outer span region of the stator.

At near stall the mass-averaged losses are significant over the outer half of the flow path and reduce the exit total pressure correspondingly. Incidence angle is elevated in the outer region by the deficit in flow velocity in this high loss region. Deviation does not appear to change much between design flow and near stall—a worthy subject area for experimental confirmation.

Mechanical Design. The mechanical adequacy of the rotor, stator, and new nose cone was evaluated. Material chosen for the rotor was a high strength aluminum alloy, 7050-T7651, and for the stator a slightly lower strength aluminum alloy, 7075-T7351. Combined stress from centrifugal and bending loads for the rotor was calculated with NASTRAN. A maximum stress under combined loads was found to be 281.4 megaPa, which is below the allowable stress of 322 megaPa (obtained by applying a 1.5 safety factor to the ultimate stress). A maximum untwist of 1.5 deg was calculated, and the cold coordinates were corrected to account for this.

NASTRAN was also used to determine mode shapes and natural frequencies over a speed range of 0 to 35,000 rpm. Results are shown in a Campbell diagram (Fig. 27). The only resonances of significance occur in first bending mode at third and fourth engine orders. The engine orders and the speeds involved (less than 70 percent of design speed) are unlikely to be a source of forced vibration problems. A rotor high cycle fatigue analysis was performed and plotted as a Modified Goodman Diagram. The outcome indicated acceptability of the material at design speed and marginal acceptance at 110 percent design speed. The use of generous safety factors in the analysis, coupled with a clean inlet flow environment would suggest no cause for concern. The rotor was also analyzed for subsonic stall flutter in bending and torsional modes by a reduced velocity parameter analysis. In each case the reduced velocity parameter was less than the allowable limit (0.8 versus 1.25 in torsion and 2.3 versus 6.6 in bending).

The stator was also subjected to a NASTRAN blade stress analysis. Deflection was small and the maximum stress of 124.8 megaPa was well below the allowable stress of 303.4 megaPa. Mode shapes and natural frequencies were determined for the

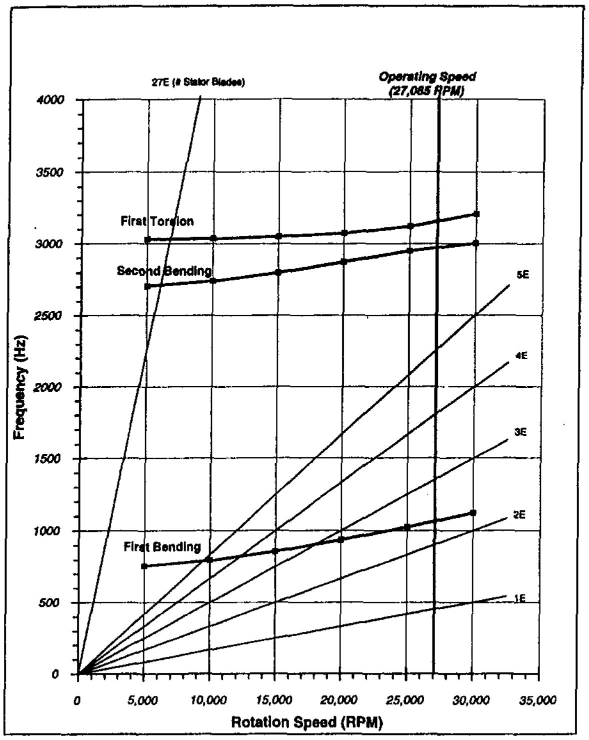

Fig. 27 Campbell diagram for rotor blades

stator by a NASTRAN analysis. A Campbell diagram was prepared and showed no excitations below the fifth engine order, but the 22nd engine order (rotor blade count) did show a third mode crossing (a combined bending and torsion) at 85 percent of design speed, and may bear watching. A subsonic stall flutter analysis was also performed on the stator; the reduced velocity parameter in torsion was 0.4, well below allowable of 1.25. (There were no pure bending modes indicated for the stator.) A finite element stress analysis was conducted on the new nose cone and on the rotor hub. Maximum stress on the nose cone was 88.95 megaPa and on the rotor hub, 79.3 megaPa, well below allowable stress levels. Finally, a shaft critical speed analysis was performed on the shaft assembly with the new nose cone. The first rigid shaft critical speed of the system was 37,358 rpm, well above the design speed of 27,085 rpm.

Summary of Results

1 A transonic compressor stage has been designed for the Naval Postgraduate School Turbopropulsion Laboratory. The low aspect ratio (1.2) rotor has a specific head-rise of 0.25 and a tip relative Mach number of 1.3. Overall stage pressure ratio is 1.56. The design relied heavily on CFD techniques rather than conventional empirically based methods.

2 An Euler code augmented by a distributed body force model to account for viscous effects was used heavily in the rotor design. Predicted total pressure ratio at design flow is 1.61 at an efficiency of 90.1 percent. At the best efficiency flow the pressure ratio is predicted to be 1.58 at an efficiency of 90.3 percent. Losses at design flow were concentrated in the end wall regions, particularly at the tip where shock loss and tip clearance effects were significant.

3 The stator was designed with controlled-diffusion blade shapes using a two-dimensional panel method and integral boundary layer method. Three-dimensional analysis indicates that the design could have benefitted from restaggering in the tip region (end bends) because of the low-energy flow ingested from the rotor. At design flow predicted stage pressure ratio is 1.56 at an efficiency of 83 percent. Diffusion factors are greater than 0.5 over the entire stator span. The three-dimensional calculations at off-design suggest that the stator will control stalling flow for the stage.

4 Although tip clearance effects are not modeled in detail in the three-dimensional calculation method, tip clearance flow and its effect on performance is modeled. For the rotor, the effect of tip clearance was demonstrated to cost 2 points in efficiency. The stator is free to rotate in order to measure torque supplied to the rotor and, therefore, also has a tip clearance. In the case of the stator, clearance flow is driven only by the pressure gradient across the blade (no scraping flow and associated vortex), and the calculated deficit in performance was only 0.4 points in efficiency.

5 High-strength aluminum alloys were chosen for rotor and stator, and both blade rows were analyzed using NASTRAN. Calculated stresses were all within allowable limits; a Campbell diagram for the rotor indicated the only significant resonance occurs in first bending mode at third and fourth engine orders, and at speeds below 70 percent of design speed; the stator Campbell diagram shows a third mode crossing at 22nd engine order (rotor blade count) at 85 percent design speed. This is not considered serious, but will bear watching. Subsonic stall flutter analyses indicated both rotor and stator to be within safe limits.

Acknowledgments

The author would like to thank Mr. Donald Sandercock (NASA-Lewis, retired) for his advice and counsel, Dr. Lonnie Reid (NASA-Lewis) for his support, Mr. Tony Herrmann (NASA-Lewis) for overseeing the mechanical design activities, and Mr. James E. Crouse (Dresser-Rand) for his assistance and counsel.

References

Cohen, C. B., and Reshotko, E., 1956, "The Compressible Laminar Boundary Layer With Heat Transfer and Arbitrary Pressure Gradient," NACA TR-1294.

Crouse, J. E., and Gorrell, W. T., 1981, "Computer Program for Aerodynamic and Blading Design of Multistage Axial-Flow Compressors," NASA TP-1946.

Denton, J. D., 1983, "An Improved Time-Marching Method for Turbomachinery Flow Calculation," ASME *Journal of Engineering for Power*, Vol. 105, pp. 514–524.

Denton, J. D., 1986, "The Use of a Distributed Body Force to Simulate Viscous Effects in 3D Calculations," ASME Paper No. 86-GT-144.

Erwin, J. R., 1983, "A Review of the Design of the NPS/TPL Transonic Compressor," Contractor Report No. NPS67-83-004CR, Naval Postgraduate School, Monterey, CA.

McFarland, E. R., 1984, "A Rapid Blade-to-Blade Solution for Use in Turbomachinery Design," ASME *Journal of Engineering for Gas Turbines and Power*, Vol. 106, pp. 376–382.

McNally, W. D., 1970, "Fortran Program for Calculating Compressible Laminar and Turbulent Boundary Layers in Arbitrary Pressure Gradients," NASA TN D-5861.

Neuhoff, F., 1985a, "Modifications to the Inlet Flow Field of a Transonic Compressor Rotor," Contractor Report NPS67-85-008CR, Naval Postgraduate School, Monterey, CA.

Neuhoff, F., 1985b, "Investigation of the Interaction Between the Rotor and Stator of a Transonic Compressor," Contractor Report No. NPS67-85-011CR, Naval Postgraduate School, Monterey, CA.

Neuhoff, F., Shreeve, R. P., and Fottner, L., 1986, "Evaluation of the Blade-to-Blade Flow From a High Speed Compressor Rotor," ASME Paper No. 86-GT-117.

Sanger, N. L., 1983, "The Use of Optimization Techniques to Design Controlled-Diffusion Compressor Blading," ASME *Journal of Engineering for Power*, Vol. 105, pp. 256–264.

Sasman, P. K., and Cresci, R. J., 1966, "Compressible Turbulent Boundary Layer With Pressure Gradient and Heat Transfer," *AIAA Journal*, Vol. 4, No. 1.

Schlichting, H., 1979, "Origin of Turbulence II," *Boundary Layer Theory*, 7th ed., McGraw-Hill, New York.

Shreeve, R. P., and Neuhoff, F., 1984, "Measurements of the Flow From a Compressor Rotor Using a Dual-Probe Digital Sampling (DPDS) Technique," ASME *Journal of Engineering for Gas Turbines and Power*, Vol. 106, pp. 366–375.

S. Kang

C. Hirsch

Department of Fluid Mechanics,
Vrije Universiteit Brussel,
Brussel, Belgium

Numerical Simulation of Three-Dimensional Viscous Flow in a Linear Compressor Cascade With Tip Clearance

A Navier–Stokes solver is applied to investigate the three-dimensional viscous flow in a low-speed linear compressor cascade with tip clearance at design and off-design conditions with two different meshes. The algebraic turbulence model of Baldwin–Lomax is used for closure. Relative motion between the blades and wall is simulated for one flow coefficient. Comparisons with experimental data, including flow structure, static and total pressures, velocity profiles, secondary flows and vorticity, are presented for the stationary wall case. It is shown that the code predicts well the flow structure observed in experiments and shows the details of the tip leakage flow and the leading edge horseshoe vortex.

1 Introduction

Wind tunnel experiments are particularly important in discovering new phenomena or structures of the three-dimensional viscous flow in turbomachines. However, the detailed analysis of the highly three-dimensional flow structures in the flow passages and tip clearances can benefit strongly from the support of reliable Navier–Stokes solvers. Hah (1986) and Perrin et al. (1992), by solving the Reynolds-averaged Navier–Stokes equations, predicted the overall effects of tip clearance in axial compressor rotors. Pouagare and Delaney (1986) using a SIMPLE-based algorithm reinforced some assumptions on compressor endwall flow phenomena, such as leading edge separation, leakage flow, separation line of tip leakage vortex, etc. The effects of Reynolds number on tip leakage flow in turbines were investigated by Moore et al. (1989) through laminar flow calculations for an idealized two-dimensional tip gap geometry. Choi (1992), by taking a much finer mesh inside the tip gap, captured some fine-scale leakage flow structures. Basson and Lakshminarayana (1995) captured accurately the tip clearance flow in a turbine nozzle through optimization of grid size and artificial dissipation. Adamczyk et al. (1993) and Copenhaver et al. (1993), with their numerical experiment, simulated well the interaction of the tip leakage vortex and the in-passage shock. Yet, many aspects, such as the nature of the three-dimensional flow and energy loss inside the tip clearance, remain unclear.

The present authors have presented a series of experimental investigations on the three-dimensional viscous flow in a low-speed, large-scale, linear compressor cascade with and without tip clearance, as referenced in Kang and Hirsch (1991, 1993a, b, 1994). In these investigations, some new flow phenomena were observed, such as a concentrated shed vortex in the wake and a multiple vortex structure around the blade tip in the cases with tip clearance. To confirm the experimental observations and to gain further insight into the complex three-dimensional flow phenomena, a three-dimensional Navier–Stokes solver, recently developed by Hirsch et al. (1992), has been applied to the compressor cascade under the experimental conditions with two different meshes. In this paper, the predicted data and their comparisons with the experimental results are reported for the case with tip clearance and stationary wall. The influence of relative motion between blades and the endwall is also studied through the numerical simulation.

2 Numerical Calculation Method

Brief Description of the Code. The Navier–Stokes code, developed by Hirsch et al. (1992), solves the time-dependent Reynolds-averaged Navier–Stokes equations, with the algebraic turbulence model of Baldwin–Lomax or the two-equation $k-\epsilon$ turbulence model for closure. It is based on a multiblock/multigrid approach and incorporates various numerical schemes, based on either central or upwind discretization.

For the present calculation, the algebraic turbulence model of Baldwin–Lomax is selected. A first calculation was done on a coarse mesh, with a second-order upwind symmetric TVD scheme and Minmod limiter. However, further calculations were performed with a central scheme with second-order dissipation coefficient set to 0. and the fourth-order to 0.1. All the calculations were performed with a **V**-cycle multigrid technique. The numerical procedure applied a four-stage Runge–Kutta scheme with standard coefficients ($\frac{1}{4}$, $\frac{1}{3}$, $\frac{1}{2}$, 1) for the upwind scheme and a five-stage Runge–Kutta scheme with coefficients of ($\frac{1}{4}$, $\frac{1}{6}$, $\frac{3}{8}$, $\frac{1}{2}$, and 1) for the central scheme. Incorporating implicit residual smoothing, the fine mesh calculations were performed at a CFL number of 7, requiring close to 300 interactions for a residual reduction of three orders of magnitude. It has been confirmed in the cases without tip clearance that the accuracy of the converged solutions, such as pressure distribution computed with the upwind and central schemes, is identical under the same mesh size.

Computational Grid. The cascade blades are NACA 65-1810 with a chord of 20 cm. Pitch and span of the cascade are respectively 18 cm and 20 cm, and the stagger angle is 10 deg. See Kang and Hirsch (1991) for the details of the cascade geometry.

Body-fitted grids with two calculation domains, shown in Fig. 1, were made by the Interactive three-dimensional Geometry Modeling and Grid Generation System (IGG) developed by Dener and Hirsch (1992), to represent the cascade geometry. The first domain with an *H-H* mesh is limited in the region with one pitch in tangential direction and half span in height,

---

Contributed by the International Gas Turbine Institute and presented at the 39th International Gas Turbine and Aeroengine Congress and Exposition, The Hague, The Netherlands, June 13–16, 1994. Manuscript received by the International Gas Turbine Institute March 4, 1994. Paper No. 94-GT-364. Associate Technical Editor: E. M. Greitzer.

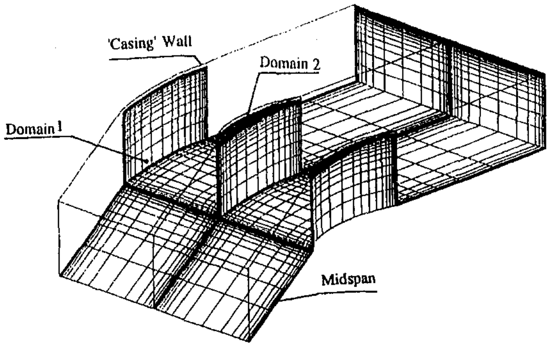

Fig. 1 Coarse mesh with tip clearance, two domains included, 49 × 21 × 37 for domain 1 and 49 × 13 × 17 for domain 2

since the existence of the tip gap produces little influence on the midspan flow field based on the experimental observations in Kang and Hirsch (1993a). In the axial direction, the mesh extends from 1.5 chord upstream to 1.5 chord downstream. The second domain occupies the space in the tip gap with an *O-H* mesh.

Two different grids were calculated. One consists of 49 × 21 × 37, in the axial (*I*), blade-to-blade (*J*), and spanwise (*K*) directions, in domain 1 and 49 × 13 × 17 in domain 2, as shown in Figs. 1–3. This mesh has 48,902 points and is called "coarse mesh" hereafter. For increasing the grid points under the limitation of the computer (HP workstation), a fine mesh of 97 × 41 × 45 in domain 1 and 97 × 13 × 13 in domain 2 was created. This mesh has 195,358 points and is called "fine mesh" hereafter. In both meshes, there are 13 *O*-lines leading to 25 points across the blade profile in the gap. Over the gap, however, there are 17 points for the coarse mesh and 13 points for the fine mesh. Hence, it was expected that the fine mesh would produce high accuracy inside the passage, but the coarse one would show more details of the gap flow.

Boundary Conditions. In the inlet plane, three velocity components and static pressure are given. At this location the flow is collateral and the spanwise velocity is zero. The profiles of the pitchwise and axialwise velocity components employed in the calculation were calculated from the measured velocity (Kang and Hirsch, 1993a) at 40 percent chord upstream of the leading edge and from the flow angles around midspan. The pressure in the inlet plane is considered uniform and also taken from the measured data at midspan. Riemann boundary treatment is employed for the inlet boundary. Hence the real imposed parameters in the inlet are entropy (first characteristic variable), axial velocity (second characteristic variable), and pitchwise and spanwise velocity components.

No-slip boundary conditions are used on the blade surfaces and the endwalls. Periodic conditions are enforced along the boundaries upstream and downstream of the passage, and also in the gap. A symmetric (or mirror) boundary condition is used at the midspan. In the outlet plane, uniform static pressure is imposed with the averaged midspan value, measured at 25 percent chord downstream.

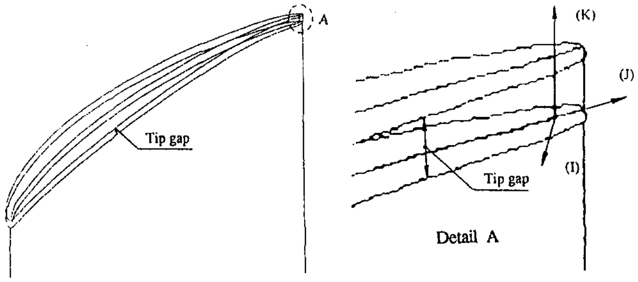

Fig. 2 Details of the domain 2 in Fig. 1, with its coordinate system

3 Calculation Conditions

In the calculation, only one clearance level with 4 mm, or 2.0 percent chord, is run for two experimental inlet flow angles, β_1 = 29.3 deg (design condition) and 36.5 deg (off-design condition). Other inlet flow conditions are the same as the experiments. The inlet flow velocity V_1 = 23.5 m/s, the Reynolds number, based on the velocity and blade chord, is about 3.0×10^5. The inlet boundary layer is turbulent with a shape factor of about 1.22 and a displacement thickness of 0.014 chord. The inlet Mach number was increased in the computations by four times for improving the convergence.

Although the blade surface boundary layer may have laminar and transition states, as observed in the experiments (Kang and Hirsch, 1991), the calculations will be undertaken with the supposition that all the boundary layers of the blade surfaces and endwall are in a turbulent state.

4 Review of the Flow Structure

Before discussing the calculated data, a brief review on the experimental observations of the three-dimensional flow may be necessary. Figures 4 and 5 show the endwall flow pattern and the multiple vortex structure around the tip.

Around the tip gap, the flow in the pressure side corner will in general diverge along the line L_r in Fig. 4. One part of the flow turns toward the suction side and joins with the passage vortex motion. The other part, however, passes through the tip gap toward the suction side corner in the adjacent passage and forms the tip leakage flow. Correspondingly, a separation line will be formed in the endwall flow pattern, as the line L_L in Fig. 4. Due to the tip leakage flow, a multiple vortex structure, with three vortices, will appear around the tip. One is the tip leakage vortex (TLV); the other two small-size vortices are the tip separation vortex (TSV) and the tip secondary vortex (SV) respectively, as shown in Fig. 5.

With the rotation of the tip leakage vortex, the blade sections close to the tip are strongly reloaded. The vortex core is quasi-circular after roll-up downstream of midchord, as observed from the contours of total pressure in the traverse sections and secondary velocity vector lines. Around the core the coefficient of total pressure loss reaches its higher value. The axial velocity profile along a line passing through the core shows a wake-like shape.

Generation of the tip separation vortex makes the flow inside the tip gap very complex. The limiting streamlines on the blade

Nomenclature

c = blade chord
C_p = static pressure coefficient
C_{pt} = total pressure coefficient
I, J, K = indices in axial, pitchwise, and spanwise
LE = leading edge
L_z = coordinate from tip vortex core to suction side
PS = pressure side
s = pitch
SS = suction side
TE = trailing edge
u, v, w = velocity components
u_a, v_a, w_a = averaged velocity
u_t = endwall moving speed
V_1 = inlet velocity

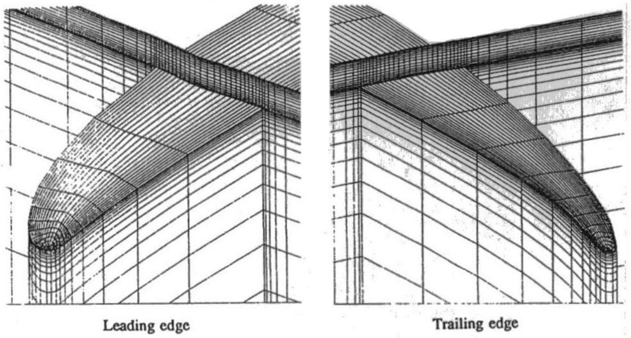

Fig. 3 Close view of the domain 2 in Fig. 1, near the leading and trailing edges

tip surface normally exhibit a divergence pattern. The vortex increases in size and strength along the chord. Due to the contracted area of the tip gap, the fluid moving toward the gap is accelerated. This acceleration continues a short distance inside the gap, affected by the vortex motion. After the vortex, the wall pressure tends to recover with the leakage flow mixing. In the present blade geometry and flow conditions, the mixing process is not fully completed at the gap exit, especially behind the midchord, as the gap exit velocity shows a wakelike profile close to the tip. Near the blade leading edge, the wall static pressure inside the gap is normally uniform because the leakage flow here is dominated by the streamwise pressure gradient, and the gap exit flow is fully developed.

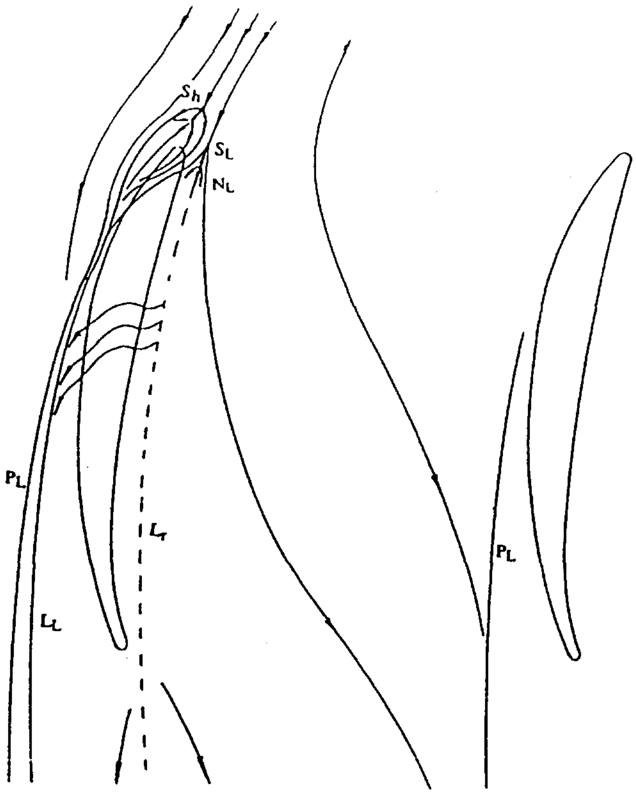

Fig. 4 Schematic of the flow pattern on the wall for 2.0 percent clearance, from Kang and Hirsch (1993a)

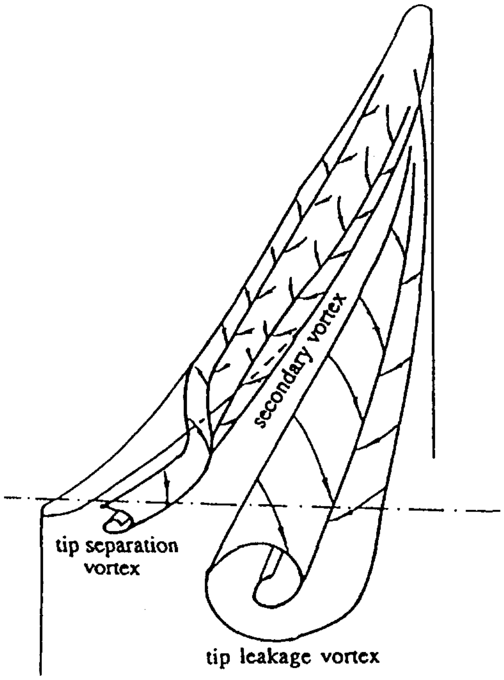

Fig. 5 Schematic of the vortex structure around the tip, from Kang and Hirsch (1993a)

5 Discussions on Computational Data

Surface Flow Visualization. At first, the predicted surface flow pattern, or limiting streamline patterns, are shown in Figs. 6 and 7 at the off-design condition, compared with the experimental observations. Streamlines passing through the mesh points close to a solid wall are considered limiting streamlines in this study. It is seen from Fig. 6(*b*), calculated with the coarse mesh, that the code predicts the endwall flow phenomena observed in the visualizations, such as the reattachment line in the pressure side and the separation line of the tip leakage vortex in the suction side. However, the predicted separation line L_L in Fig. 6(*b*) is closer to the midpassage downstream of the midchord than in the experiments. At the trailing edge, for example, the separation line in Fig. 6(*a*) is located at about 26 percent pitch from the suction side, compared to 36 percent pitch in Fig. 6(*b*). In addition, the calculated streamlines under the blade are almost straight over the whole chord, there are no turns as in Fig. 6(*a*) before midchord. No apparent difference was found from the endwall flow patterns between the fine and coarse mesh calculations.

Figure 7 presents the predicted limiting streamline patterns on the tip surface at the design and off-design condition, compared with the ink-trace visualization picture of the blade tip. It is seen that the main features of the flow, observed in the visualization, are reproduced in Fig. 7(*b*, *c*, *d*) with both meshes. The reattachment line of the tip separation vortex coincides well with the experiments. It is located near the mean line of the blade profile and disappears at about 70 percent downstream of the leading edge in the coarse mesh case (more points over the tip gap). With the fine mesh (less points over the gap), however, the reattachment line is closer to the pressure side edge and disappears near the trailing edge.

With a decreasing inlet flow angle, this line (Fig. 7*d*) tends to shift toward the pressure side, which implies a reduction of the tip separation vortex core. It is also observed from the calculations that the separation line of the tip separation vortex is not along the pressure side edge but a short distance inside the gap entrance.

Figure 8 shows the predicted flow structure around the tip and near the trailing edge with the coarse mesh. It includes the tip separation vortex, the tip leakage vortex, and the trailing edge separation vortex. The streamlines, indicated in the figure as tip leakage flow, pass through the midgap of the pressure side.

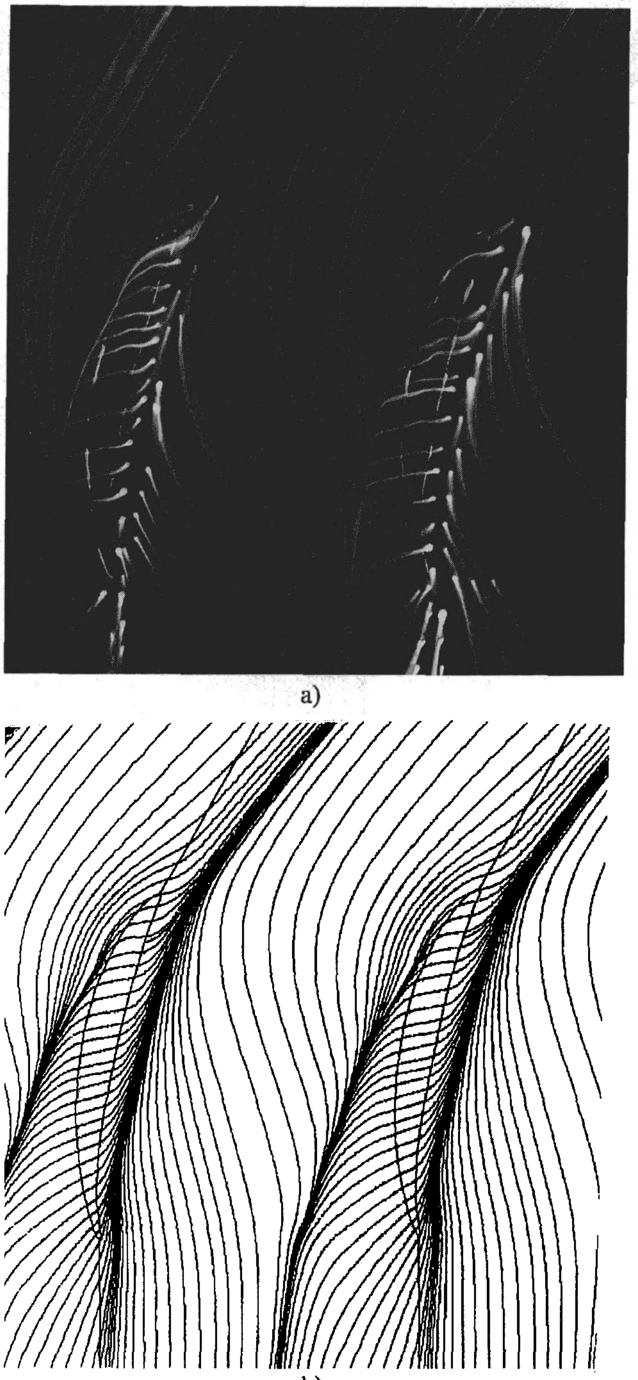

Fig. 6 (*a*) Paint-trace visualization and (*b*) limiting streamlines on the endwall, predicted with coarse mesh, at the off-design condition

However, the tip secondary vortex in Fig. 5 is not confirmed in this calculation. It will be seen later from the secondary flow plots that this vortex is well reproduced in the fine mesh calculation.

Static Pressure Distributions. Figure 9 shows the comparisons of the measured and calculated blade static pressure at midspan and close to the tip (1.5 percent span) at off-design conditions. It can be seen that at midspan, the calculation data are very comparable to the experimental data, but a large difference occurs close to the tip on the suction surface, on which strong reloading was observed around the midchord in the experimental data but not in the calculations. The difference may be related to the limitation of the simple algebraic turbulence model/Baldwin–Lomax model. This model, developed for two-dimensional calculation, would underpredict the flow approaching separation (Stock and Haase, 1987) and the strength of the tip leakage vortex. The underprediction of the tip leakage vortex will in turn effect the reloading around the midchord, as it is tightly correlated with the vortex motion.

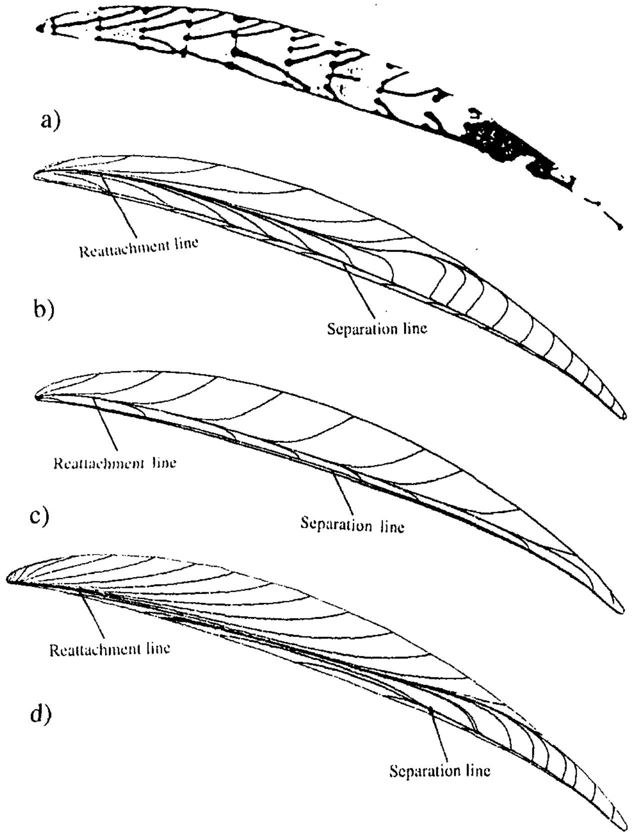

Fig. 7 (*a*) Ink-trace visualization on tip surface, (*b*), (*c*), and (*d*) calculated limiting streamlines of the tip surface. (*b*) coarse mesh (17 points over the gap) at off-design condition; (*c*) fine mesh (13 points over the gap) at off-design condition; (*d*) coarse mesh (17 points over the gap) at design condition.

Comparing between the fine and coarse mesh computations, there is almost no difference in midspan pressures. But differences do exist close to the tip. The fine mesh predicts better the unloading in the leading edge region, even though the down-

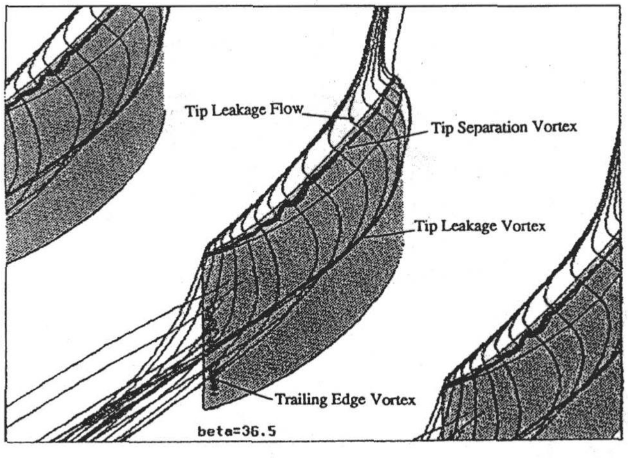

Fig. 8 Streamline pattern around the tip and trailing edge over half span at off-design condition, calculated with coarse mesh

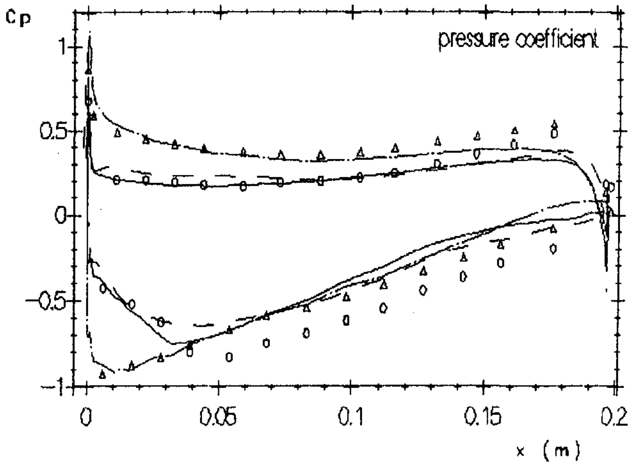

Fig. 9 Comparisons of blade static pressures at midspan and close to the tip at off-design condition. Δ: Exp., midspan; ○: Exp., 1.5 percent span; – · –: fine mesh cal., midspan; – – –: fine mesh cal. 1.5 percent span; – – –: coarse mesh cal., 1.5 percent span.

stream reloading is still underpredicted. The difference of endwall static pressures between the fine and coarse mesh computation can also be found from Fig. 10, which shows the static pressure isolines at the off-design condition. Due to the tip leakage vortex motion, the contours of wall static pressure just under the vortex core should exhibit a pressure trough, as shown by Inoue et al. (1991) and Moyle et al. (1992). It is seen clearly that the pressure trough is predicted with the fine mesh calculation but not with the coarse mesh. Under the blade, however, the pressure trough related to the tip separation vortex is well predicted in both meshes.

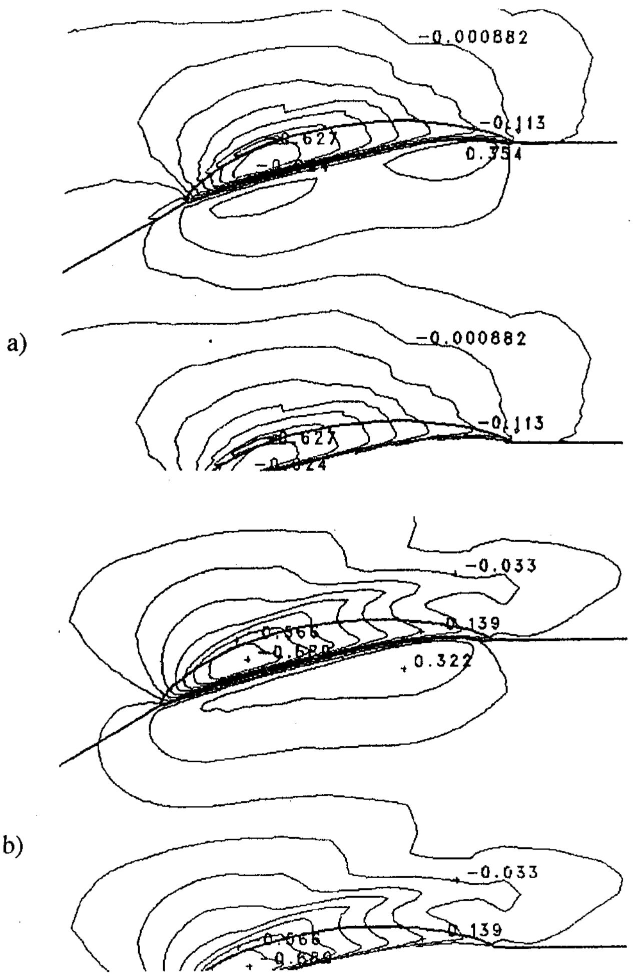

Fig. 10 Contours of static pressures on the endwall, calculated with (*a*) coarse and (*b*) fine meshes

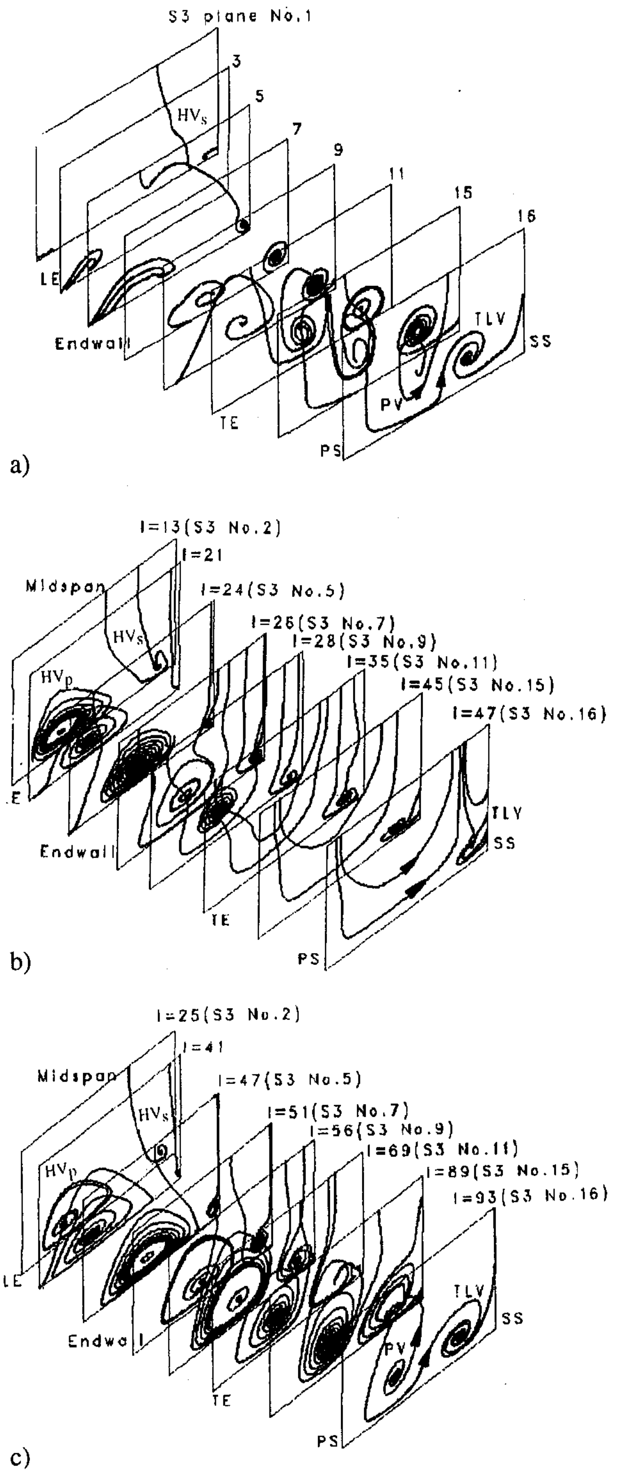

Fig. 11 Comparison of secondary flow vector lines: (a) experimental, (b) computational with coarse mesh, and (c) computational with fine mesh at off-design condition

Secondary Flows and Total Pressure Losses. Figure 11 shows a comparison of the vector lines of secondary flow velocity in selected traverse (S_3) planes, in which S_3 plane No. 2 is at the leading edge and S_3 plane No. 11 is located at 1 percent

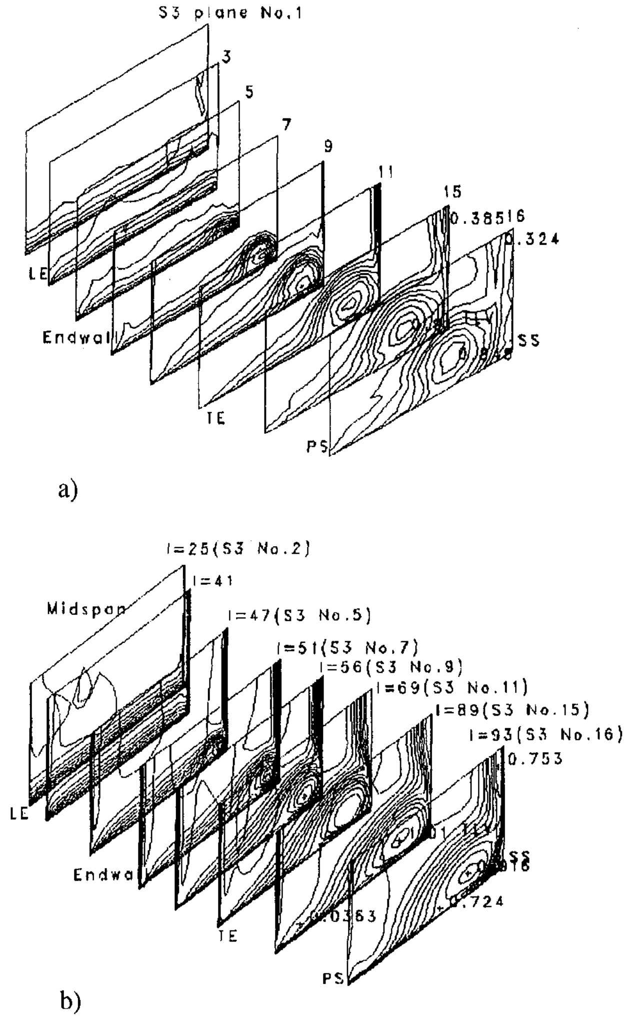

Fig. 12 Comparison of total pressure loss contours: (*a*) experimental and (*b*) computational with fine mesh at off-design condition

chord before the trailing edge. The secondary flow vectors are obtained by projecting the velocities on the plane normal to the flow direction at midspan at the same pitch coordinate. For presentation, the secondary flow vector is turned around the y-axis until it lies in the measuring plane (Kang and Hirsch, 1991). The spiral nodes occurring in the planes denote respectively the horseshoe vortex (HV), passage vortex (PV), and tip leakage vortex (LTV). Figure 12(*a*) shows the contours of total pressure loss in the measured traverse planes from the leading edge to downstream of the exit for off-design conditions, compared to calculated total pressure losses, with the fine mesh, in the corresponding planes in Fig. 12(*b*).

Since the clearance allows a certain amount of fluid to pass through the gap, a leading edge horseshoe vortex may be weakened or even not occur, especially when the clearance is great. At present condition, i.e., 2.0 percent clearance, one can see a node of the suction side horseshoe vortex (HV_s) from the experimental results (Fig. 11*a*) in the suction side of plane No. 1 (7.5%c upstream of the leading edge). In the calculations, both pressure and suction side legs of the horseshoe vortex can be seen from the secondary flowfield, denoted as HV_p and HV_s respectively in Figs. 11(*b*, *c*). The pressure side leg is merged into the passage vortex immediately inside the passage. The suction side leg, however, dissipates with its stretching into the passage due to both the fluid viscosity and the traverse pressure gradient, and completely disappears at about 11 percent chord (S_3 plane No. 3, or I = 21 in Fig. 11*b*) downstream of the leading edge. The apparent rotation of the tip leakage vortex starts from about S_3 plane No. 5 (32 percent chord), which compares well with the experimental results. In the coarse mesh calculations, the tip leakage vortex (TLV) and the passage vortex (PV) are diffusing toward the cascade exit. However, the fine mesh calculations predict well the TLV and PV vortices downstream of the cascade. The secondary vortex (SV) around the suction side tip (Fig. 5) deduced from experiments is well reproduced in the fine mesh calculation, as seen from Fig. 11(*c*) and Fig. 13 for details in the suction side corner of section I = 51 (around midchord) and I = 69 (near the trailing edge). This small vortex starts before S_3 No. 5 and evolves downstream along the tip suction side. Near the trailing edge, it wraps around the tip leakage vortex (TLV). The interaction between the tip leakage vortex and the secondary vortex (SV) may cause some instability, since the convergence history of residuals indicates the appearance of some unsteadiness. The maximum and mini-

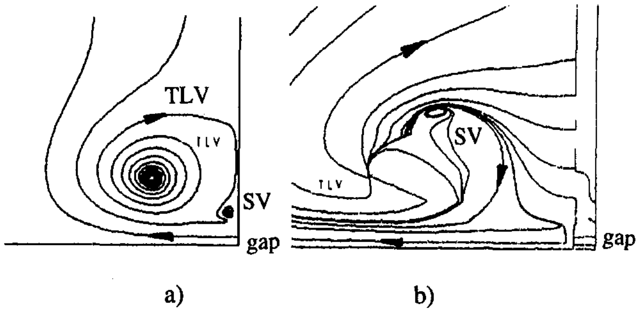

Fig. 13 Details of the secondary flow in the suction side corner: (*a*) I = 51 (around midchord) and (*b*) I = 69 (near trailing edge)

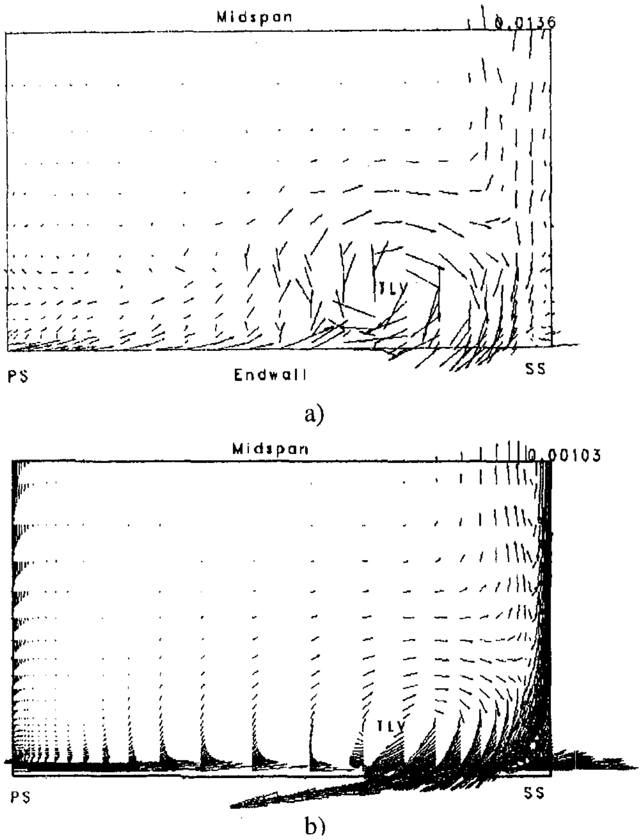

Fig. 14 Comparison of vorticity vectors in a section of 25%c behind the trailing edge at off-design condition; (*a*) experimental and (*b*) computational with coarse mesh

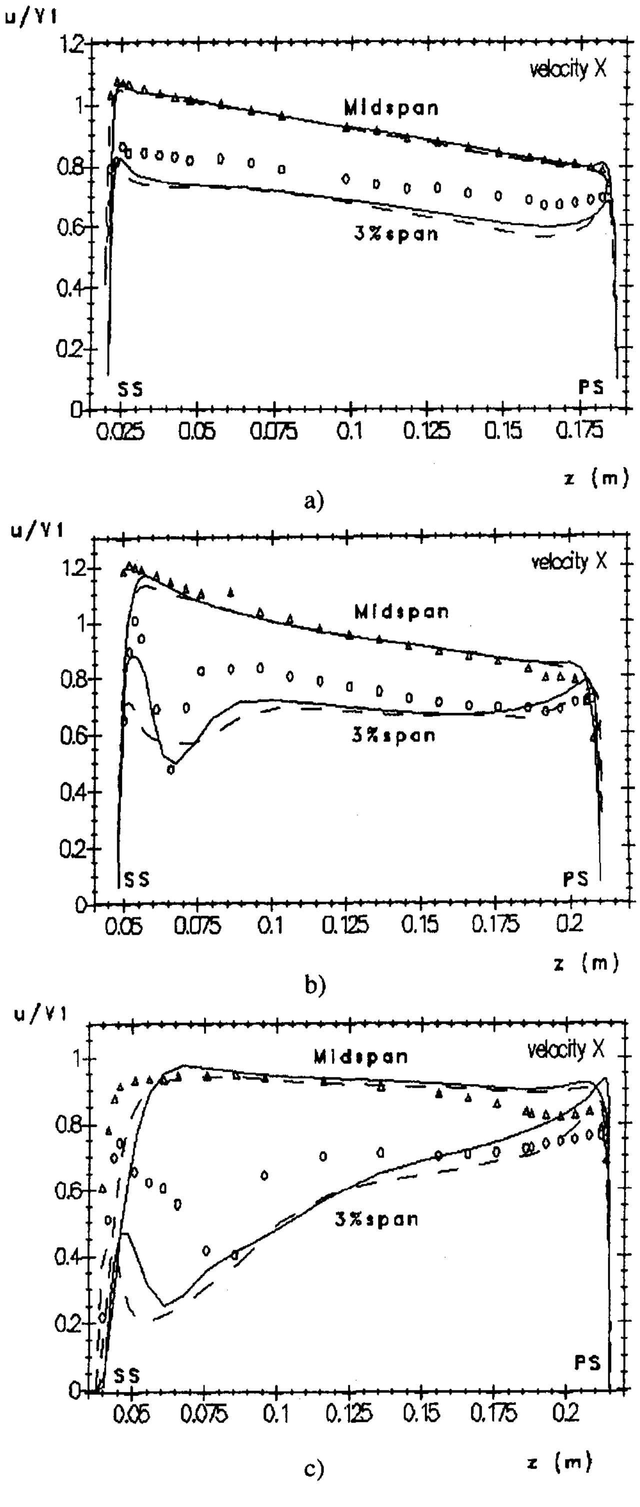

Fig. 15 Comparison of blade to blade profiles of axial velocity near tip (3 percent span) and at midspan at three chordwise locations: (*a*) 11%c, (*b*) 55%c, and (*c*) 98%c for design condition. Δ: Exp., midspan; ○: Exp., 3 percent span; ---: fine mesh cal.; ---: coarse mesh cal.

mum residuals occur in the suction side corner before 30%c, where the TLV and SV start.

It is noticed that the spiral nodes, as appearing in Fig. 11, can be constructed as a combination of a source and a free vortex or a sink and a free vortex. In the former, streamlines move outward from the nodes; in the latter, streamlines move inward towards the nodes. A more detailed discussion on this behavior goes beyond the range of the present paper.

In the total pressure contours (Fig. 12), the generation and development of the tip leakage vortex can be seen from the high loss values in the suction side corner. It is seen that the isolines in the corner, predicted with the fine mesh (Fig. 12*b*), compare well to the experimental ones (Fig. 12*a*) and are very consistent with the rotation center of the tip vortex shown in Fig. 11(*a*) and 11(*c*). The predicted loss values in the tip vortex core are also consistent with the experiments, as in S_3 plane No. 16, where the maximum losses for calculation and experiments are respectively 0.92 and 0.85. In the wake, however, the predicted loss is much larger than the experimental data since the predicted boundary layers of the blade surface are higher than the experiments. These discrepancies might again require calculations with finer meshes or different turbulence models and/or suitable laminar–turbulent transition models.

Figure 14 shows the cross-sectional vorticity plots of the fine mesh computation, compared with the experimental vorticities in the S_3 plane No. 15 (25%c behind the trailing edge). It is observed that the vorticity field is dominated by the tip leakage vortex (TLV).

Velocity Profiles. Comparisons of the measured and calculated blade to blade profiles of axial velocity are made at each S_3 plane near the blade tip (at $y/l = 0.03$) and at midspan for 2.0 percent clearance at the design condition. As a selection, Fig. 15 shows the profiles in three axial locations, i.e., S_3 plane No. 3 (11%c), 7 (55%c), and 11 (98%c). Figure 16 presents the spanwise velocity profiles at 3 percent span in S_3 plane No. 7 (55%c).

A good agreement can be found everywhere except for the region close to the suction surface where the tip leakage vortex core is present. In the suction side (Fig. 15), the profiles at 3 percent span close to the leading edge (S_3 plane No. 3) show similar distributions as midspan, since in this axial location the suction side horseshoe vortex has disappeared and the tip leakage vortex has not been generated yet (Fig. 11). Downstream of S_3 plane No. 3, however, the profiles exhibit the tip leakage vortex core clearly, around which the axial velocity takes lower values (or wakelike profile) and the total pressure loss is high. Comparing the axial velocity profile around midchord (Fig. 15*b*), it is found that the tip leakage vortex, predicted with the coarse mesh, diffuses much faster than the experimental one and the fine mesh computational one. Approaching the trailing edge (Fig. 15*c*), the predicted core is closer to the suction surface than the experiments, especially for the calculation with the coarse mesh. Moreover, the vortex predicted with the coarse mesh is weaker than the experimental and the fine mesh one, as the amplitude of the spanwise velocity profile (Fig. 16)

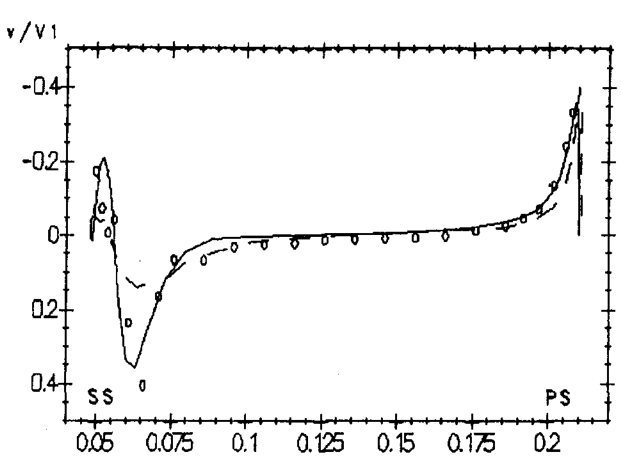

Fig. 16 Comparison of blade-to-blade profile of spanwise velocity near tip (3 percent span) at 55%c at design condition. ○: exp., 3 percent span; ---: fine mesh cal.; ---: coarse mesh cal.

around the vortex core is smaller in the coarse mesh case. The spanwise velocity near the pressure side is always directed to the blade tip over the whole chord, i.e., it is negative in the present coordinate system. Approaching the blade pressure surface, the spanwise velocity increases rapidly and shows a very thin boundary layer on the pressure surface.

Figure 17 shows comparisons of the pitchwise distributions of axial velocity at 2, 8.5, 21, and 50 percent span in S_3 plane No. 14 (12.5%c behind the trailing edge) for design condition. In this figure, the coordinate z increases from the suction side to the pressure side. It is seen that the prediction is reasonable over the pitch at all the spanwise locations. The wake and the core of the tip leakage vortex, both with high loss and low axial velocity values, are predicted at 8.5 and 21 percent height. However, the predicted vortex core is apparently shifted toward the suction side, as observed from Fig. 15 near the trailing edge. Near the wall at 2 percent span (Fig. 17*a*), the experimental data show the wake and the vortex, but in the prediction, these two regions have been mixed. The predicted wake around midspan is apparently sharper and thicker than the experiment, especially in the fine mesh calculation. This could result from the assumption of mirror symmetry at midspan in the computations.

Figure 18 presents the spanwise distributions of calculated axial velocity profiles, close to the centers of passage and tip leakage vortices, in S_3 plane No. 14 (12.5%c behind the trailing edge) together with the section streamlines, calculated with the fine mesh, to indicate the location of the profiles. The experimental data closest to the locations 1 and 2 are also presented in Fig. 18. The wakelike shape in the profiles at section 1 around the tip leakage vortex center is observed in the calculation. The calculated position of the center, however, is closer to the endwall than the experimental data, which explains part of the discrepancies between the experimental and calculated profiles at section 1. The profiles close to the passage vortex (PV) do not show any wakelike shape either but appear as normal boundary layers. Good agreement between the experimental and predicted data close to the passage vortex, or around the midpassage, can also be seen.

Tip Leakage Flow. The tip leakage flow is mainly characterized by the gap inlet and exit velocities, and the static pressure distributions along the tip surface and the endwall under the blade. It is highly three dimensional, as seen from the surface flow visualizations in Figs. 6 and 7.

Comparisons of the wall pressure distributions between the calculations and the experiments are presented in Fig. 19 for off-design flow conditions. In this figure, the z axis extends from the pressure to suction side, with the zero point at the suction side. It is seen that, over most of the chord, the calculated data are reasonable. A large difference between the experimental and the calculated results occurs behind the midchord and under the blade profile, due to an underprediction of the mass flow through the tip gap, as seen from Fig. 20. This may imply that the strength of the predicted tip separation vortices

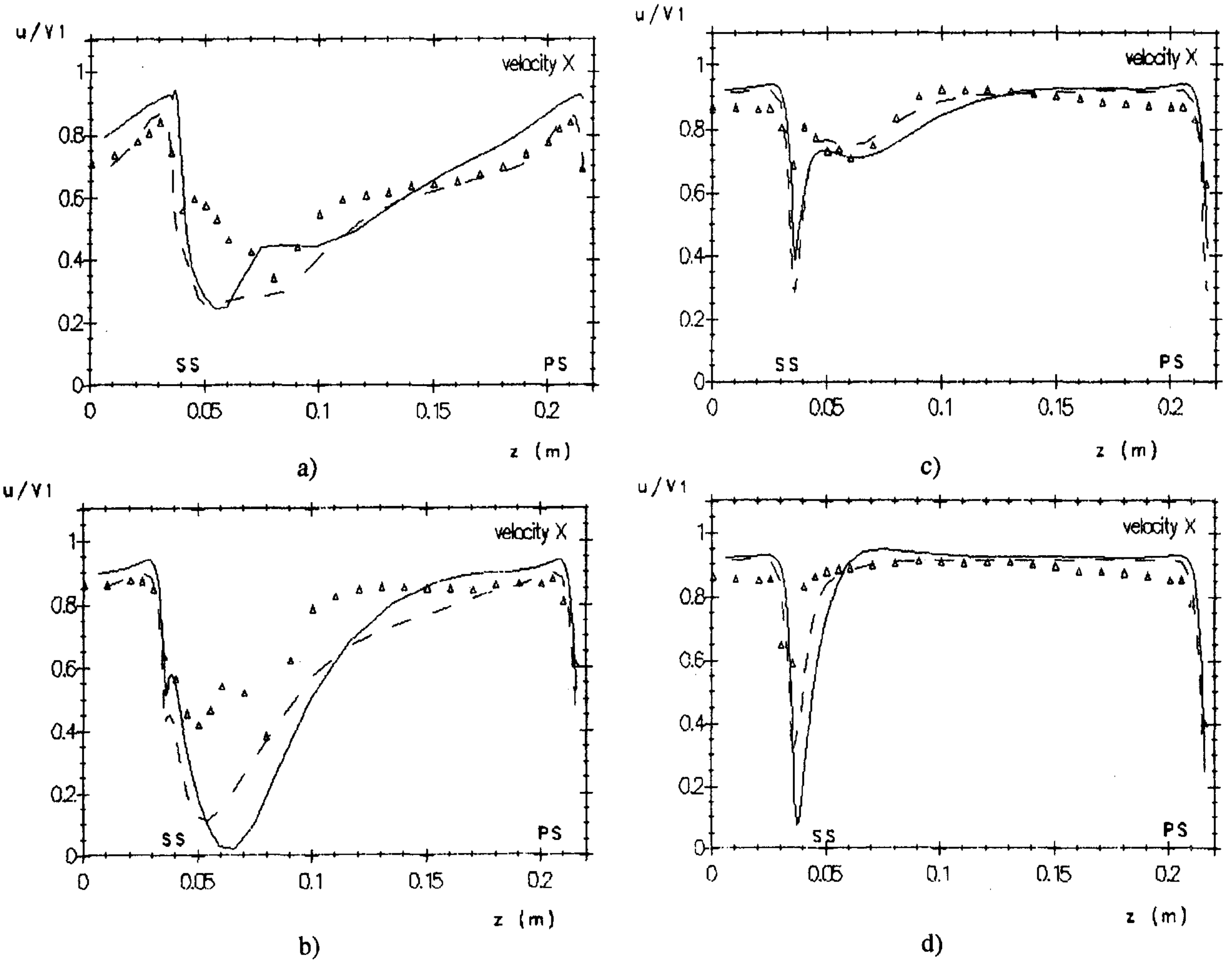

Fig. 17 Comparison of pitchwise distributions of axial velocity at (*a*) 2 percent, (*b*) 8.5 percent, (*c*) 21 percent, and (*d*) 50 percent span in a section of 12.5%c behind the trailing edge at design condition. Δ: Exp; ---: fine mesh cal.; ---: coarse mesh cal.

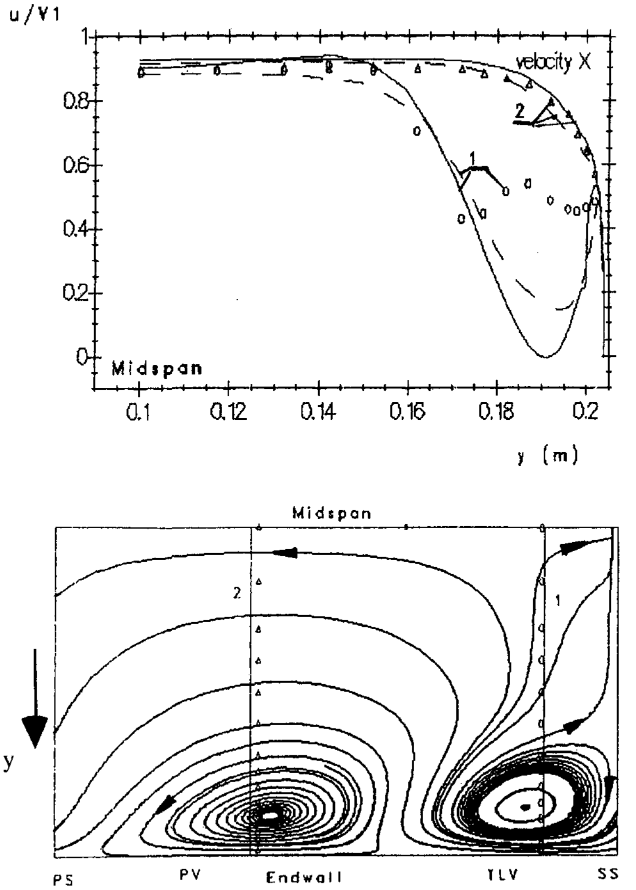

Fig. 18 Comparison of axial velocity profiles along lines 1 and 2, close to the centers of tip leakage vortex (TLV) and passage vortex (PV), in a section at 12.5%c behind the trailing edge at design condition. ○: Exp., section 1; △: Exp., section 2; ---; fine mesh cal.; ---: coarse mesh cal.

is weaker than the experimental, in connection with the underestimated blade loading near the tip (Fig. 9).

Comparisons of the calculated gap exit velocity with the experimental data are presented in Fig. 20 for the off-design condition, in which $y = 0.2$ m corresponds to the blade tip and $y = 0.204$ m to the "casing wall." It is seen that the calculated data at all the sections are reasonable. It is to be recalled here that the "coarse" mesh has 17 point over the gap, while the "fine" mesh has 13 points over the gap. Although at 22%c, Fig. 20(*a*), the "coarse" mesh calculation is clearly more accurate, the remaining sections are less conclusive. In both calculations, the predicted boundary layers are much thicker than the experimental.

Figure 21 shows the chordwise distribution of the area-averaged gap inlet (solid line) and exit (dashed line) velocities and static pressures, obtained by the coarse mesh computation at the off-design condition. The experimental data of the resultant velocity, static pressure difference, and the internal total pressure loss from Kang and Hirsch (1994) are also presented in the figures.

It is seen from Fig. 21 that the resultant and pitchwise velocities achieve their maximum values and the static pressures achieve their minimum values around 20%c, where the leakage flow reads its maximum value, as can also be seen from Fig. 22(*b*). Compared to the inlet (pressure side) resultant velocity, the exit value (the suction side) is larger near the leading edge but is smaller over the other portion of chord. The spanwise velocities (Fig. 21*c*) at both the inlet and exit are almost uniform except close to the leading and trailing edges. The large negative values in the inlet are due to the convergence of the passage flow toward the gap. At the exit, the nearly zero spanwise velocity indicates that the flow leaving the gap is similar to a jet. The averaged static pressure of the gap exit is similar to that of the blade suction surface near the tip (Fig. 9) in both distribution profile and value. The pressure of the gap inlet, however, has been significantly reduced due to the flow acceleration. It is found that the difference of the averaged static pressures between the inlet and exit is quite small with maximum difference of about 10 percent. The difference of the inlet and the exit total pressure coefficients, or internal loss, is presented in Fig. 22(*a*). In Fig. 22(*b*), the difference of the maximum static pressure in the pressure side endwall and the exit static

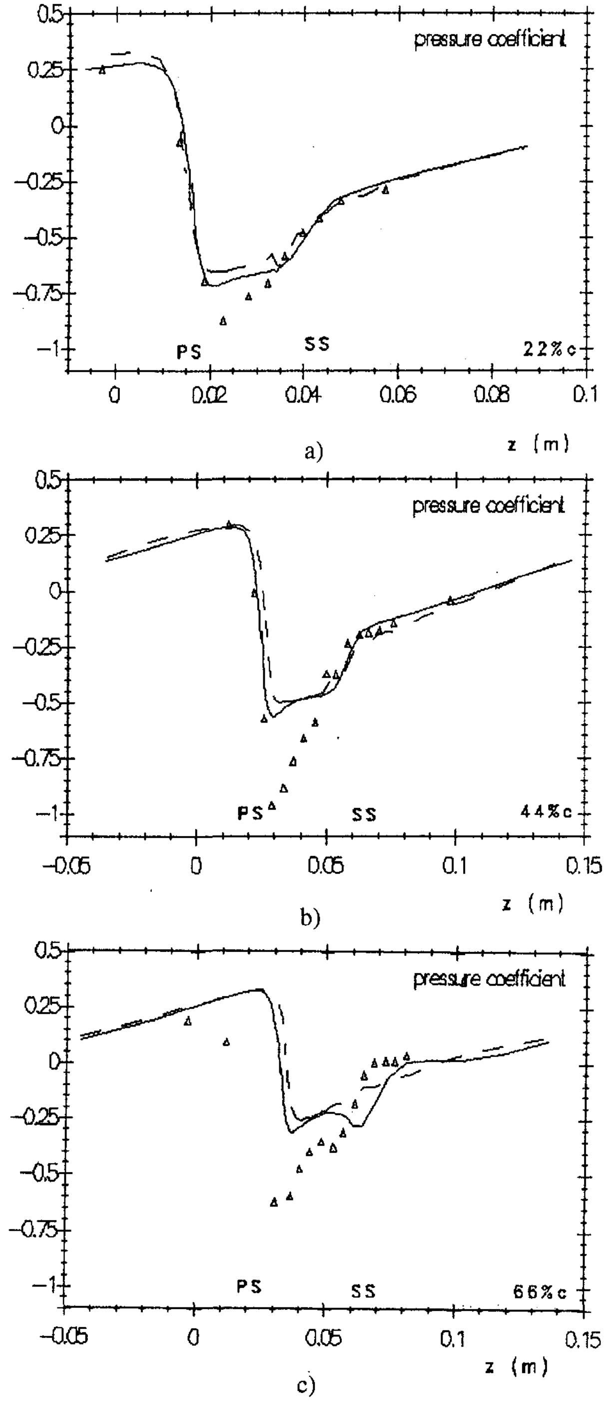

a)

b)

c)

Fig. 19 Comparison of wall static pressures under the blade at off-design condition at (*a*) 22%c, (*b*) 44%c, and (*c*) 66%c. △: Exp.; ---: fine mesh cal.; ---: coarse mesh cal.

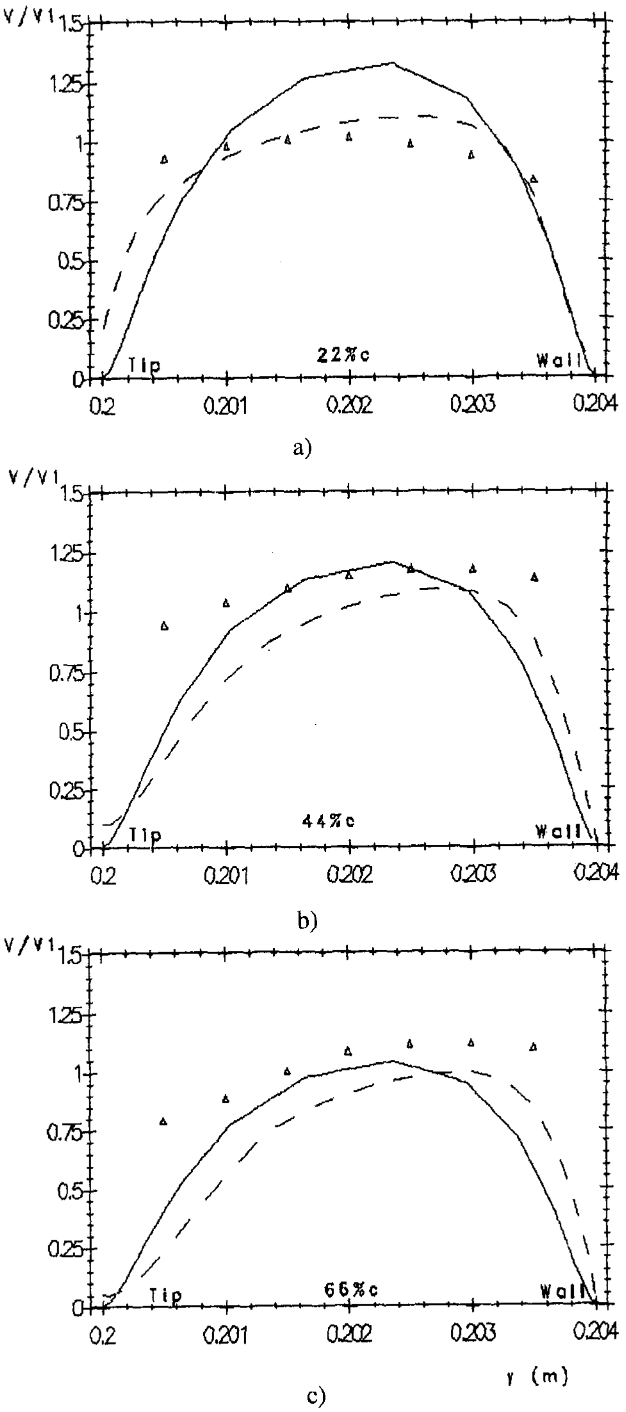

a) b) c)

Fig. 20 Comparison of gap exit velocities at (*a*) 22%c, (*b*) 44%c, and (*c*) 66%c. Δ: Exp.; ---: fine mesh cal.; ---: coarse mesh cal.

pressures is presented. This maximum value should be normally close to the reattachment line L_r in Fig. 4. The difference of the exit and the maximum static pressure of the pressure side endwall are significant. Hence, it is concluded that, to balance the pressure at the suction side corner, or the gap exit, most of the pressure drop occurs in front of the gap inlet.

Influence of Relative Motion. In real machines, one has to take into account the influence of the relative motion between wall and blade on the secondary flow field. A numerical simulation, which corresponds to a flow coefficient of 0.5 has been performed on the fine mesh. The flow condition imposed to the inlet boundary is the same as the design condition. Figure 23(*a*, *b*) shows the secondary flow plots at the trailing edge for moving and stationary walls, respectively. It is seen that the moving wall pulls the tip leakage vortex significantly from the suction side corner to the pressure side corner and pushes the passage vortex far away from the wall towards the suction side.

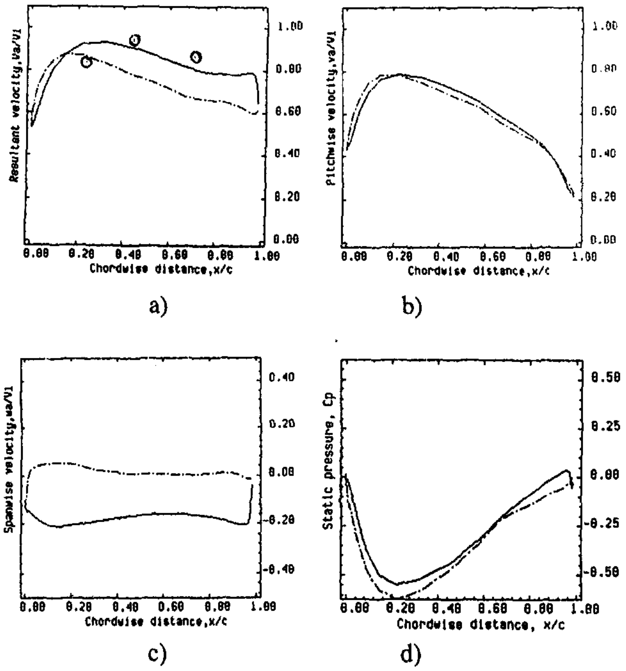

a) b)

c) d)

Fig. 21 Area-averaged gap inlet (solid line) and exit (dashed line) velocities and static pressures, (*a*) resultant, (*b*) pitchwise and (*c*) spanwise velocities, and (*d*) static pressure coefficient, calculated with coarse mesh at off-design condition. O: Exp. (Kang and Hirsch, 1994).

To answer the questions raised by N. Cumpsty and E. Greitzer in the discussion of our previous paper (Kang and Hirsch, 1993*b*), the present authors proposed a plot of tip vortex locus Lz/s at rotor exit, against flow coefficient, to indicate how the relative motion effects the tip leakage vortex trajectory. The experimental data were from Inoue et al. (1991) and Moyle et al. (1992). This plot is again shown here in Fig. 24, where the points from the present calculations have been added. The present computations again show the strong influence of relative motion on the tip leakage vortex trajectory, and the present simulation appears to show the correct trend.

6 Conclusions

Comparisons of the results predicted with a three-dimensional Navier–Stokes solver, with a Baldwin–Lomax turbulence

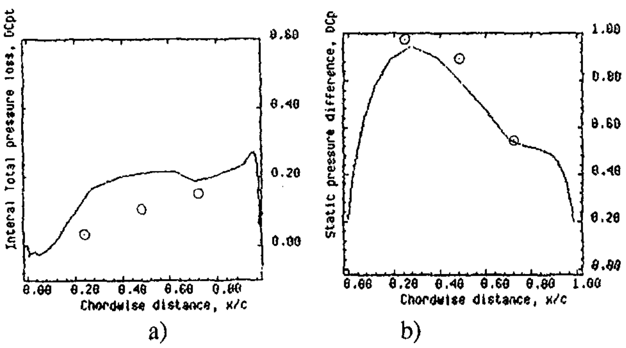

a) b)

Fig. 22 (*a*) Area-averaged total pressure coefficient difference between gap inlet and exit, and (*b*) area-averaged static pressure coefficient difference between gap exit and the maximum at the pressure side endwall, calculated with coarse mesh at off-design condition. O: Exp. (Kang and Hirsch, 1994).

model on two different mesh levels, with the experimental data are presented. It is seen that the code predicts well the very complex three-dimensional flow in a linear compressor cascade with tip clearance. The tip separation vortex inside the gap deduced from ink-trace visualization on the tip surface in the previous experimental study is reproduced. Increasing grid points greatly improves the predicted results. However, the tip leakage flow is still underestimated, which may be attributed to insufficient mesh resolution and/or to the simple turbulence model. Significant influence of relative motion on the tip leakage vortex is confirmed through a simulation under the same flow condition.

The present validations show that:

- the overall three-dimensional flow structure can be globally reproduced with a coarse mesh of close to 50,000 points, including the tip clearance gap.
- in order to capture the tip separation vortex, a minimum of 13 points over the clearance height appears necessary; earlier computation with 7 points did not allow us to capture this vortex.
- more detailed comparisons with the experimental data, especially the viscous and turbulent dominated effects, require finer meshes.
- the present fine mesh calculations, with close to 200,000 points, may still not be fine enough to ensure mesh independence and to reproduce quantitatively all the details of the flow.
- in addition to the above, the influence of turbulence modeling and/or transition effects should also be assessed. However, this can only be done, without ambiguity, on fine enough meshes.

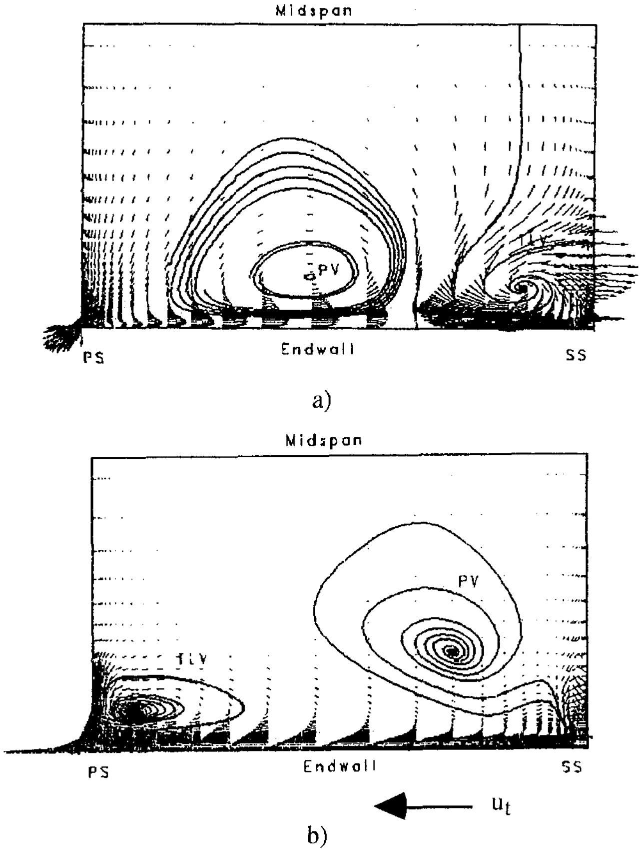

Fig. 23 Secondary flows near trailing edge at design condition: (*a*) stationary endwall, and (*b*) moving wall at a flow coefficient of 0.5

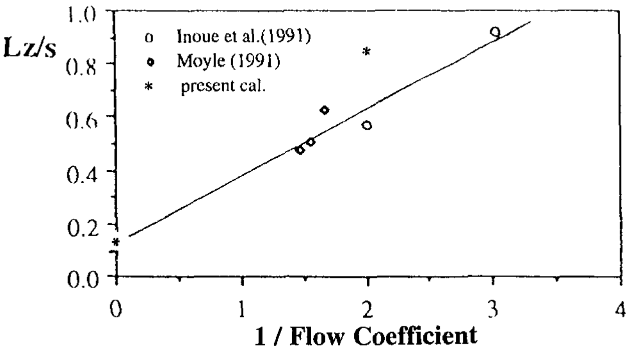

Fig. 24 Variation of tip vortex loci with flow coefficient, from Kang and Hirsch (1993b)

References

Adamczyk, J. J., Celestina, M. L., and Greitzer, E. M., 1993, "The Role of Tip Clearance in High-Speed Fan Stall," ASME JOURNAL OF TURBOMACHINERY, Vol. 115, pp. 28–39.

Basson, A., and Lakshminarayana, B., 1995, "Numerical Simulation of Tip Clearance Effects in Turbomachinery," ASME JOURNAL OF TURBOMACHINERY, Vol. 117, pp. 348–359.

Choi, D., 1992, "3D Navier–Stokes Analysis for a Tip Leakage Flow in a Low Aspect Ratio Turbine," AIAA Paper No. 92-0395.

Copenhaver, W. W., Hah, C., and Puterbaugh, S. L., 1993, "Three-Dimensional Flow Phenomena in a Transonic, High-Throughflow, Axial-Flow Compressor Stage," ASME JOURNAL OF TURBOMACHINERY, Vol. 115, pp. 240–248.

Dener, C., and Hirsch, Ch., 1992, "IGG—An Interactive 3D Surface Modeling and Grid Generation System," AIAA Paper No. 92-0073.

Hah, C., 1986, "A Numerical Modeling of Endwall and Tip-Clearance Flow of an Isolated Compressor Rotor," ASME *Journal of Engineering for Gas Turbines and Power,* Vol. 108, pp. 15–21.

Hirsch, Ch., Lacor, C., Dener, C., and Vucinic, D., 1992, "An Integrated CFD System for 3D Turbomachinery Applications," AGARD-CP-510.

Inoue, M., Kuroumaru, M., Iwamoto, T., and Ando, Y., 1991, "Detection of a Rotating Stall Prediction in Isolated Axial Flow Compressor Rotors," ASME JOURNAL OF TURBOMACHINERY, Vol. 111, pp. 281–289.

Kang, S., and Hirsch, Ch., 1991, "Three-Dimensional Flows in a Linear Compressor Cascade at Design Conditions," ASME Paper No. 91-GT-114.

Kang, S., and Hirsch, Ch., 1993a, "Experimental Study on the Three Dimensional Flow Within a Compressor Cascade With Tip Clearance: Part I—Velocity and Pressure Fields," ASME JOURNAL OF TURBOMACHINERY, Vol. 115, pp. 435–443.

Kang, S., and Hirsch, Ch., 1993b, "Experimental Study on the Three Dimensional Flow Within a Compressor Cascade With Tip Clearance: Part II—The Tip Leakage Vortex," ASME JOURNAL OF TURBOMACHINERY, Vol. 115, pp. 444–452.

Kang, S., and Hirsch, Ch., 1994, "Tip Leakage Flow in Linear Compressor Cascade," ASME JOURNAL OF TURBOMACHINERY, Vol. 116, pp. 657–664.

Moore, J., Moore, G. J., Henry, G. S., and Chaudhry, U., 1989, "Flow and Heat Transfer in Turbine Tip Gaps," ASME JOURNAL OF TURBOMACHINERY, Vol. 111, pp. 301–309.

Moyle, I. N., Walker, G. J., and Shreeve, R. P., 1992, "Stator-Averaged, Rotor Blade-to-Blade Near-Wall Flow in a Multistage Axial Compressor With Tip Clearance Variation," ASME JOURNAL OF TURBOMACHINERY, Vol. 114, pp. 668–674.

Perrin, G., Leboeuf, F., and Dawes, W. N., 1992, "Analysis of Three-Dimensional Viscous Flow in a Supersonic Axial Flow Compressor Rotor With Emphasis on Tip Leakage Flow," ASME Paper No. 92-GT-388.

Pouagare, M., and Delaney, R. A., 1986, "Study of Three-Dimensional Viscous Flows in an Axial Compressor Cascade Including Tip Leakage Effects Using a SIMPLE-Based Algorithm," ASME JOURNAL OF TURBOMACHINERY, Vol. 108, pp. 51–58.

Stock, H. W., and Haase, W., 1987, "The Determination of Turbulent Length Scales in Algebraic Turbulence Models for Attached and Slightly Separated Flows Using Navier–Stokes Methods," AIAA Paper No. 87-1302.

DISCUSSION

N. A. Cumpsty[1] and E. M. Greitzer[2]

The authors continue to provide detailed information about the flow in the clearance region of compressors in cascade. We

---

[1] Whittle Laboratory, Cambridge University, Cambridge, CB3 ODY United Kingdom.

[2] Gas Turbine Laboratory, Massachusetts Institute of Technology, Cambridge, MA 02139.

model on two different mesh levels, with the experimental data are presented. It is seen that the code predicts well the very complex three-dimensional flow in a linear compressor cascade with tip clearance. The tip separation vortex inside the gap deduced from ink-trace visualization on the tip surface in the previous experimental study is reproduced. Increasing grid points greatly improves the predicted results. However, the tip leakage flow is still underestimated, which may be attributed to insufficient mesh resolution and/or to the simple turbulence model. Significant influence of relative motion on the tip leakage vortex is confirmed through a simulation under the same flow condition.

The present validations show that:

- the overall three-dimensional flow structure can be globally reproduced with a coarse mesh of close to 50,000 points, including the tip clearance gap.
- in order to capture the tip separation vortex, a minimum of 13 points over the clearance height appears necessary; earlier computation with 7 points did not allow us to capture this vortex.
- more detailed comparisons with the experimental data, especially the viscous and turbulent dominated effects, require finer meshes.
- the present fine mesh calculations, with close to 200,000 points, may still not be fine enough to ensure mesh independence and to reproduce quantitatively all the details of the flow.
- in addition to the above, the influence of turbulence modeling and/or transition effects should also be assessed. However, this can only be done, without ambiguity, on fine enough meshes.

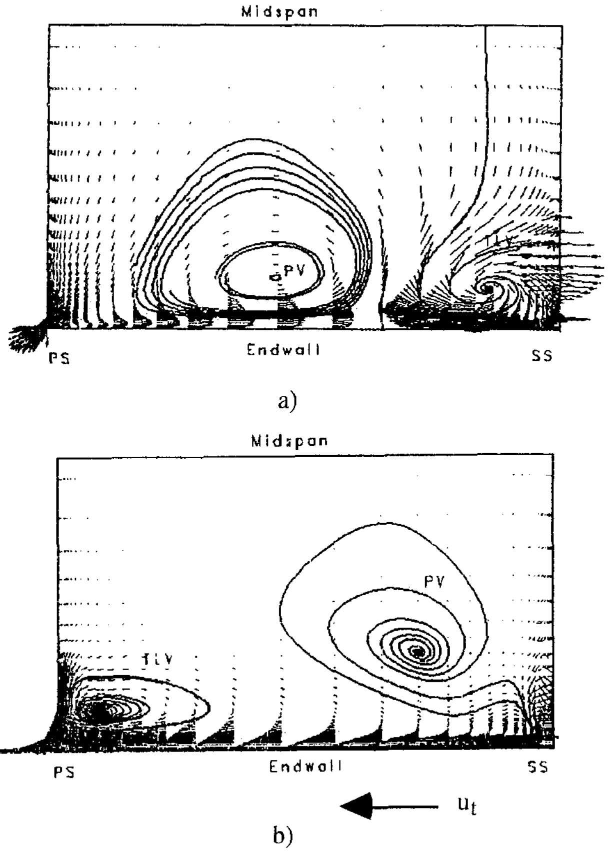

a)

b)

Fig. 23 Secondary flows near trailing edge at design condition: (*a*) stationary endwall, and (*b*) moving wall at a flow coefficient of 0.5

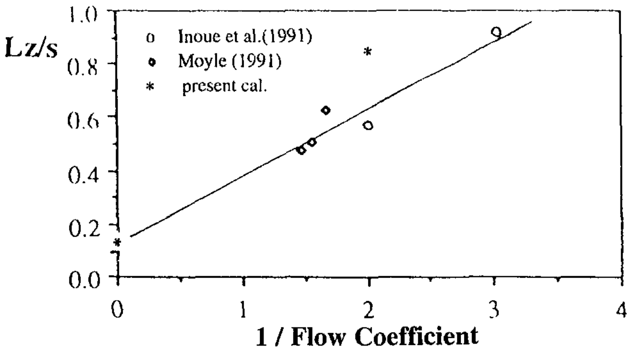

Fig. 24 Variation of tip vortex loci with flow coefficient, from Kang and Hirsch (1993b)

References

Adamczyk, J. J., Celestina, M. L., and Greitzer, E. M., 1993, "The Role of Tip Clearance in High-Speed Fan Stall," ASME JOURNAL OF TURBOMACHINERY, Vol. 115, pp. 28–39.

Basson, A., and Lakshminarayana, B., 1995, "Numerical Simulation of Tip Clearance Effects in Turbomachinery," ASME JOURNAL OF TURBOMACHINERY, Vol. 117, pp. 348–359.

Choi, D., 1992, "3D Navier–Stokes Analysis for a Tip Leakage Flow in a Low Aspect Ratio Turbine," AIAA Paper No. 92-0395.

Copenhaver, W. W., Hah, C., and Puterbaugh, S. L., 1993, "Three-Dimensional Flow Phenomena in a Transonic, High-Throughflow, Axial-Flow Compressor Stage," ASME JOURNAL OF TURBOMACHINERY, Vol. 115, pp. 240–248.

Dener, C., and Hirsch, Ch., 1992, "IGG—An Interactive 3D Surface Modeling and Grid Generation System," AIAA Paper No. 92-0073.

Hah, C., 1986, "A Numerical Modeling of Endwall and Tip-Clearance Flow of an Isolated Compressor Rotor," ASME *Journal of Engineering for Gas Turbines and Power,* Vol. 108, pp. 15–21.

Hirsch, Ch., Lacor, C., Dener, C., and Vucinic, D., 1992, "An Integrated CFD System for 3D Turbomachinery Applications," AGARD-CP-510.

Inoue, M., Kuroumaru, M., Iwamoto, T., and Ando, Y., 1991, "Detection of a Rotating Stall Prediction in Isolated Axial Flow Compressor Rotors," ASME JOURNAL OF TURBOMACHINERY, Vol. 111, pp. 281–289.

Kang, S., and Hirsch, Ch., 1991, "Three-Dimensional Flows in a Linear Compressor Cascade at Design Conditions," ASME Paper No. 91-GT-114.

Kang, S., and Hirsch, Ch., 1993a, "Experimental Study on the Three Dimensional Flow Within a Compressor Cascade With Tip Clearance: Part I—Velocity and Pressure Fields," ASME JOURNAL OF TURBOMACHINERY, Vol. 115, pp. 435–443.

Kang, S., and Hirsch, Ch., 1993b, "Experimental Study on the Three Dimensional Flow Within a Compressor Cascade With Tip Clearance: Part II—The Tip Leakage Vortex," ASME JOURNAL OF TURBOMACHINERY, Vol. 115, pp. 444–452.

Kang, S., and Hirsch, Ch., 1994, "Tip Leakage Flow in Linear Compressor Cascade," ASME JOURNAL OF TURBOMACHINERY, Vol. 116, pp. 657–664.

Moore, J., Moore, G. J., Henry, G. S., and Chaudhry, U., 1989, "Flow and Heat Transfer in Turbine Tip Gaps," ASME JOURNAL OF TURBOMACHINERY, Vol. 111, pp. 301–309.

Moyle, I. N., Walker, G. J., and Shreeve, R. P., 1992, "Stator-Averaged, Rotor Blade-to-Blade Near-Wall Flow in a Multistage Axial Compressor With Tip Clearance Variation," ASME JOURNAL OF TURBOMACHINERY, Vol. 114, pp. 668–674.

Perrin, G., Leboeuf, F., and Dawes, W. N., 1992, "Analysis of Three-Dimensional Viscous Flow in a Supersonic Axial Flow Compressor Rotor With Emphasis on Tip Leakage Flow," ASME Paper No. 92-GT-388.

Pouagare, M., and Delaney, R. A., 1986, "Study of Three-Dimensional Viscous Flows in an Axial Compressor Cascade Including Tip Leakage Effects Using a SIMPLE-Based Algorithm," ASME JOURNAL OF TURBOMACHINERY, Vol. 108, pp. 51–58.

Stock, H. W., and Haase, W., 1987, "The Determination of Turbulent Length Scales in Algebraic Turbulence Models for Attached and Slightly Separated Flows Using Navier–Stokes Methods," AIAA Paper No. 87-1302.

DISCUSSION

N. A. Cumpsty[1] and E. M. Greitzer[2]

The authors continue to provide detailed information about the flow in the clearance region of compressors in cascade. We

---

[1] Whittle Laboratory, Cambridge University, Cambridge, CB3 ODY United Kingdom.

[2] Gas Turbine Laboratory, Massachusetts Institute of Technology, Cambridge, MA 02139.

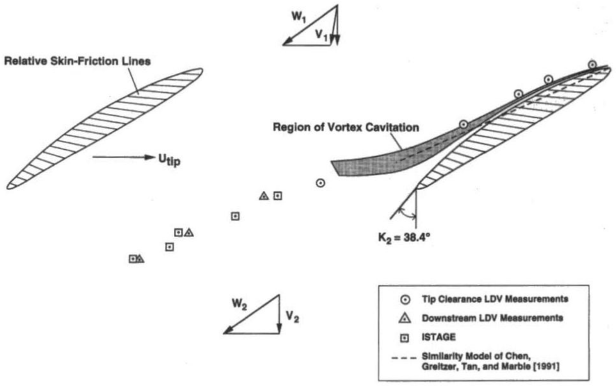

Fig. 25 Trajectory of rotor tip clearance vortex core

have been concerned for some time about a difference that appears in the authors' estimates for a parameter A in a simple model for predicting the locus of the clearance vortex by Chen et al. (1991). Chen et al. suggested a value of 0.46, whereas Kang and Hirsch (1993b) suggested 0.19; the two values imply a difference of more than a factor of two in the circumferential displacement of the vortex from the suction side of the blade. In our discussion we emphasized the importance of endwall motion and a non-collateral inlet boundary layer, as would occur in a rotor.

In the authors' response (Kang and Hirsch, 1993b) they introduced speed of the blade tip (relative to the wall) as an independent variable. We have to admit to being unable to follow the process leading from Eq. (4) to Eq. (6) in the paper and by the subsequent treatment of Inoue's data. As regards the latter, reducing the flow coefficient from 0.5 to 0.33 does more than just alter the speed of the wall (assuming the axial velocity is held constant)—it alters the pressure distribution around the whole blade.

In the final part of section 5 of the present paper the authors return to our discussion of the earlier paper (Kang and Hirsch, 1993b), and the effect of a moving endwall. This time they are presenting numerical results with a moving endwall. As far as we can understand the calculations with a moving endwall refer to the condition of flow coefficient equal to 0.5. With an axial inlet flow to the rotor a flow coefficient of 0.5 means the axial velocity outside the boundary layer is equal to half the blade speed, so the inlet flow direction is $\cot^{-1} 0.5 = 63.4$ deg. The blade inlet direction is, however, 32.5 deg, so the specified flow coefficient would correspond to an incidence of almost 30 deg. It may be that we have misunderstood what was done, but it is clearly important that the conditions chosen be physically plausible if the effect of relative motion of the endwall is to be assessed.

At the conference at which this paper was presented there was a two-part paper by Zierke et al. [later consolidated and published as Zierke et al. (1985)], who examined clearance flows in a high-Reynolds-number axial pump. With Dr Zierke's permission, Fig. 4 is reproduced here as Fig. 25. This shows how well the model of Chen et al. fits the observations of the vortex position; it also shows how well it fits the predictions of Navier–Stokes solver, ISTAGE.

References

Chen, G. T., Greitzer, E. M., Tan, C. S., and Marble, F. E., 1991, "Similarity Analysis of Compressor Tip Clearance Flow Structure," ASME JOURNAL OF TURBOMACHINERY, Vol. 113, pp. 260–271.

Zierke, W. C., Farrell, K. J., and Straka, W. A., 1995, "Measurements of the Tip Clearance Flow for a High-Reynolds-Number Axial-Flow Rotor," ASME JOURNAL OF TURBOMACHINERY, Vol. 117, pp. 522–531.

Authors' Closure

The authors would like to thank N. Cumpsty and E. Greitzer for their discussion and for raising the question of the range of validity of the simplified model, developed by Chen et al. (1991), for the prediction of the tip vortex trajectory, which is represented as follows:

$$\frac{L_z/s}{x/c} = A \cdot \sqrt{\frac{c(\tan \beta_1 - \tan \beta_2)}{s \cos \beta_m}} \tag{1}$$

This discussion provides an opportunity for a more critical analysis of this model, based on inviscid considerations and on a number of assumptions, some of which deserve particular attention:

(*i*) It is fair to assume, following Chen et al., that the basic mechanism for the creation of the tip vortex is of inviscid nature, since it is mainly pressure driven;

(*ii*) It is also acceptable to consider that the influence of the tip clearance height is not a first-order effect, although a certain dependence of the tip vortex trajectory on clearance height, especially for small values, is clearly observed by Inoue et al. (1986), Fig. 9 in Chen et al. (1991);

(*iii*) The influence of the entrainment effect of the end wall is totally ignored, which is clearly the main weakness of the model of Chen et al.

Due to the small values of tip clearance gap heights, the viscous effects from the end wall tangential motion, leading in addition to the end wall boundary layer skewness upstream of the blade, reinforces the tip vortex and drags it away from the suction surface. A rigorous analysis of the data of Fig. 15 of Chen et al. clearly indicates the nonnegligible effect of the flow coefficient. With higher flow coefficients, that is for smaller end wall entrainment at fixed axial velocity, the experimental position of the tip vortex is shifted toward the suction surface and the correspondence with the simplified model seen on this figure is, at best, qualitative. This appears, both from numerical simulations and from experimental data of Inoue et al. (1991) and Moyle et al. (1992) to be an important effect. In high-speed axial compressors, Adamczyk et al. (1993) and Jennions and Turner (1993) observed from their numerical results on NASA Rotor67 that with reducing mass flow the tip vortex inclined more toward the tangential direction.

On the other hand, the calibration of the constant in the model of Chen et al. to the value of 0.46 is based on data corresponding mostly to flow coefficients around 0.5, as seen from Table 1 in their paper. Only one set of data, from Smith, refers to a lower flow coefficient of 0.29. As seen from Fig. 5 in the paper of Chen et al., reproduced here as Fig. 26, the corresponding points (open diamonds) are off the main line of slope 0.46 and fit quite well to a slope of 0.55, indicated with a dashed line.

The assumptions made in our response to a previous discussion by the same authors on our paper (Kang and Hirsch, 1993b), are based on the following considerations:

(*i*) The quasi-linear variation of tip vortex position with the square root of main loading is well confirmed by experimental and numerical data;

(*ii*) The nearly linear variation of tip vortex position L_z with axial distance is also well validated, at least over the range about 70 to 80 percent chord from the leading edge. The position L_z is measured normal to the camber line as defined by Chen et al. (1991), even though a measurement from the chord is more convenient and may be even closer to a linear relation at certain conditions;

(*iii*) A linear variation of the entrainment effect due to the end wall relative motion, scaled by the axial velocity, is the simplest assumption. Based on our experimental and numerical data for a fixed end wall and the data of Inoue et al. (1991) and Moyle et al. (1992) for axial compressor rotors, measured at the trailing edge section, we tentatively calibrated the constant A in the model of Chen et al. as

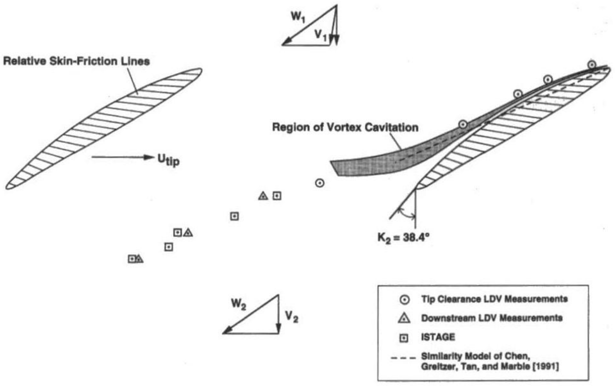

Fig. 25 Trajectory of rotor tip clearance vortex core

have been concerned for some time about a difference that appears in the authors' estimates for a parameter A in a simple model for predicting the locus of the clearance vortex by Chen et al. (1991). Chen et al. suggested a value of 0.46, whereas Kang and Hirsch (1993b) suggested 0.19; the two values imply a difference of more than a factor of two in the circumferential displacement of the vortex from the suction side of the blade. In our discussion we emphasized the importance of endwall motion and a non-collateral inlet boundary layer, as would occur in a rotor.

In the authors' response (Kang and Hirsch, 1993b) they introduced speed of the blade tip (relative to the wall) as an independent variable. We have to admit to being unable to follow the process leading from Eq. (4) to Eq. (6) in the paper and by the subsequent treatment of Inoue's data. As regards the latter, reducing the flow coefficient from 0.5 to 0.33 does more than just alter the speed of the wall (assuming the axial velocity is held constant)—it alters the pressure distribution around the whole blade.

In the final part of section 5 of the present paper the authors return to our discussion of the earlier paper (Kang and Hirsch, 1993b), and the effect of a moving endwall. This time they are presenting numerical results with a moving endwall. As far as we can understand the calculations with a moving endwall refer to the condition of flow coefficient equal to 0.5. With an axial inlet flow to the rotor a flow coefficient of 0.5 means the axial velocity outside the boundary layer is equal to half the blade speed, so the inlet flow direction is $\cot^{-1} 0.5 = 63.4$ deg. The blade inlet direction is, however, 32.5 deg, so the specified flow coefficient would correspond to an incidence of almost 30 deg. It may be that we have misunderstood what was done, but it is clearly important that the conditions chosen be physically plausible if the effect of relative motion of the endwall is to be assessed.

At the conference at which this paper was presented there was a two-part paper by Zierke et al. [later consolidated and published as Zierke et al. (1985)], who examined clearance flows in a high-Reynolds-number axial pump. With Dr Zierke's permission, Fig. 4 is reproduced here as Fig. 25. This shows how well the model of Chen et al. fits the observations of the vortex position; it also shows how well it fits the predictions of Navier–Stokes solver, ISTAGE.

References

Chen, G. T., Greitzer, E. M., Tan, C. S., and Marble, F. E., 1991, "Similarity Analysis of Compressor Tip Clearance Flow Structure," ASME JOURNAL OF TURBOMACHINERY, Vol. 113, pp. 260–271.

Zierke, W. C., Farrell, K. J., and Straka, W. A., 1995, "Measurements of the Tip Clearance Flow for a High-Reynolds-Number Axial-Flow Rotor," ASME JOURNAL OF TURBOMACHINERY, Vol. 117, pp. 522–531.

Authors' Closure

The authors would like to thank N. Cumpsty and E. Greitzer for their discussion and for raising the question of the range of validity of the simplified model, developed by Chen et al. (1991), for the prediction of the tip vortex trajectory, which is represented as follows:

$$\frac{L_z/s}{x/c} = A \cdot \sqrt{\frac{c(\tan \beta_1 - \tan \beta_2)}{s \cos \beta_m}} \tag{1}$$

This discussion provides an opportunity for a more critical analysis of this model, based on inviscid considerations and on a number of assumptions, some of which deserve particular attention:

(*i*) It is fair to assume, following Chen et al., that the basic mechanism for the creation of the tip vortex is of inviscid nature, since it is mainly pressure driven;

(*ii*) It is also acceptable to consider that the influence of the tip clearance height is not a first-order effect, although a certain dependence of the tip vortex trajectory on clearance height, especially for small values, is clearly observed by Inoue et al. (1986), Fig. 9 in Chen et al. (1991);

(*iii*) The influence of the entrainment effect of the end wall is totally ignored, which is clearly the main weakness of the model of Chen et al.

Due to the small values of tip clearance gap heights, the viscous effects from the end wall tangential motion, leading in addition to the end wall boundary layer skewness upstream of the blade, reinforces the tip vortex and drags it away from the suction surface. A rigorous analysis of the data of Fig. 15 of Chen et al. clearly indicates the nonnegligible effect of the flow coefficient. With higher flow coefficients, that is for smaller end wall entrainment at fixed axial velocity, the experimental position of the tip vortex is shifted toward the suction surface and the correspondence with the simplified model seen on this figure is, at best, qualitative. This appears, both from numerical simulations and from experimental data of Inoue et al. (1991) and Moyle et al. (1992) to be an important effect. In high-speed axial compressors, Adamczyk et al. (1993) and Jennions and Turner (1993) observed from their numerical results on NASA Rotor67 that with reducing mass flow the tip vortex inclined more toward the tangential direction.

On the other hand, the calibration of the constant in the model of Chen et al. to the value of 0.46 is based on data corresponding mostly to flow coefficients around 0.5, as seen from Table 1 in their paper. Only one set of data, from Smith, refers to a lower flow coefficient of 0.29. As seen from Fig. 5 in the paper of Chen et al., reproduced here as Fig. 26, the corresponding points (open diamonds) are off the main line of slope 0.46 and fit quite well to a slope of 0.55, indicated with a dashed line.

The assumptions made in our response to a previous discussion by the same authors on our paper (Kang and Hirsch, 1993b), are based on the following considerations:

(*i*) The quasi-linear variation of tip vortex position with the square root of main loading is well confirmed by experimental and numerical data;

(*ii*) The nearly linear variation of tip vortex position L_z with axial distance is also well validated, at least over the range about 70 to 80 percent chord from the leading edge. The position L_z is measured normal to the camber line as defined by Chen et al. (1991), even though a measurement from the chord is more convenient and may be even closer to a linear relation at certain conditions;

(*iii*) A linear variation of the entrainment effect due to the end wall relative motion, scaled by the axial velocity, is the simplest assumption. Based on our experimental and numerical data for a fixed end wall and the data of Inoue et al. (1991) and Moyle et al. (1992) for axial compressor rotors, measured at the trailing edge section, we tentatively calibrated the constant A in the model of Chen et al. as

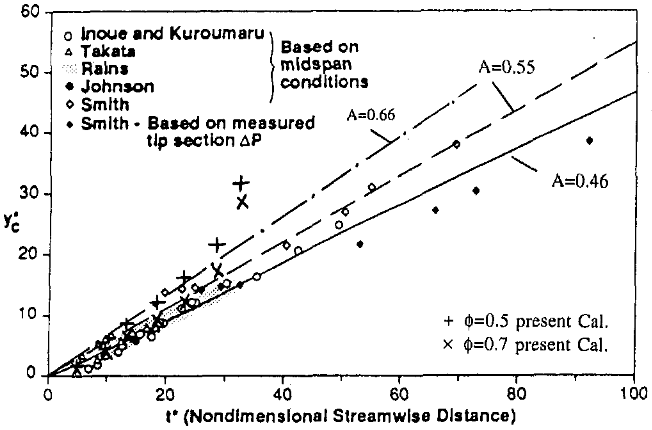

Fig. 26 Representation of Fig. 5 in the paper of Chen et al. (1991), with the data of present computations

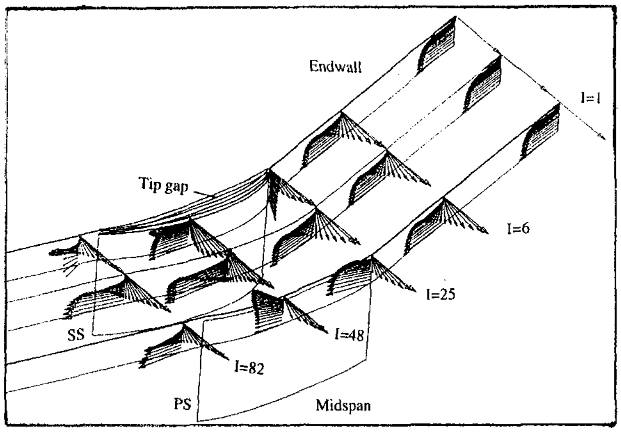

Fig. 27 Three-dimensional velocity vectors near the moving endwall at some axial sections from the inlet of computation domain, $I = 1$ (150%c upstream), to $I = 28$ (12%c behind trailing edge), for $\phi = 0.7$

$$A = A_0 + Au/\phi = 0.19 + 0.27/\phi \qquad (2)$$

where ϕ is the flow coefficient. For $\phi = 0.5$ and 0.29, the factors A calculated with this formula are respectively 0.73 and 1.12. These data are apparently larger than what one reads from Fig. 26 since the calibration was based only on the data at the exit section. Behind the exit of a compressor blade row, the slope of tip leakage vortex trajectory is generally greater than inside the blade passage. This variation may be even stronger at higher tip clearance and lower flow coefficient, as one can observe from Fig. 9 in the paper of Chen et al. (1991). Due to blade stagger, the entrainment effects on the vortex trajectory should be related to the projection of the wall speed along the normal to the blade. Hence, with a factor cos (γ), the coefficient A may be assumed as

$$A = A_0 + Au \cos(\gamma)/\phi \qquad (3)$$

Table 1 shows the calculated A for some of the experiments in Fig. 26, for which both the flow coefficient and stagger angle are known, with a suggestion of $Au = 0.24$ and $A_0 = 0.19$.

With regard to the conditions of our numerical simulations, it has to be specified that they are performed at fixed *relative* flow inlet angles and hence correspond to a nonaxial absolute flow field. It is true, as indicated by the discussors, that in an actual axial compressor changing the flow coefficient will modify the blade loading. Our simulations, however, allow variations of the flow coefficient independently of blade loading, enabling us to separate the effects. In addition, as seen from Fig. 27, which shows the three-dimensional velocity vectors near the endwall at $\phi = 0.7$, our simulation is performed with a relative motion of the end wall and represents the inlet end wall flow skewness, typical of compressor flows.

Table 1 Factor A for different cases ($A_u = 0.24$)

Author	Stagger Angle	ϕ	A
Inoue	56.2	0.33	0.59
Inoue	56.2	0.50	0.46
Rains	57.4	0.45	0.48
Katana	48.0 *	0.50	0.51
Katana	48.0 *	0.53	0.49
Katana	48.0 *	0.62	0.45
Zierke	58.1	0.74	0.36
Present Cal.	10.0	0.50	0.66
Present Cal.	10.0	0.70	0.53

* This stagger angle is measured from Fig.15 in Chen et al's paper.

Figure 28 presents the computed three-dimensional streamlines, issuing from the tip gap near the leading edge, and the

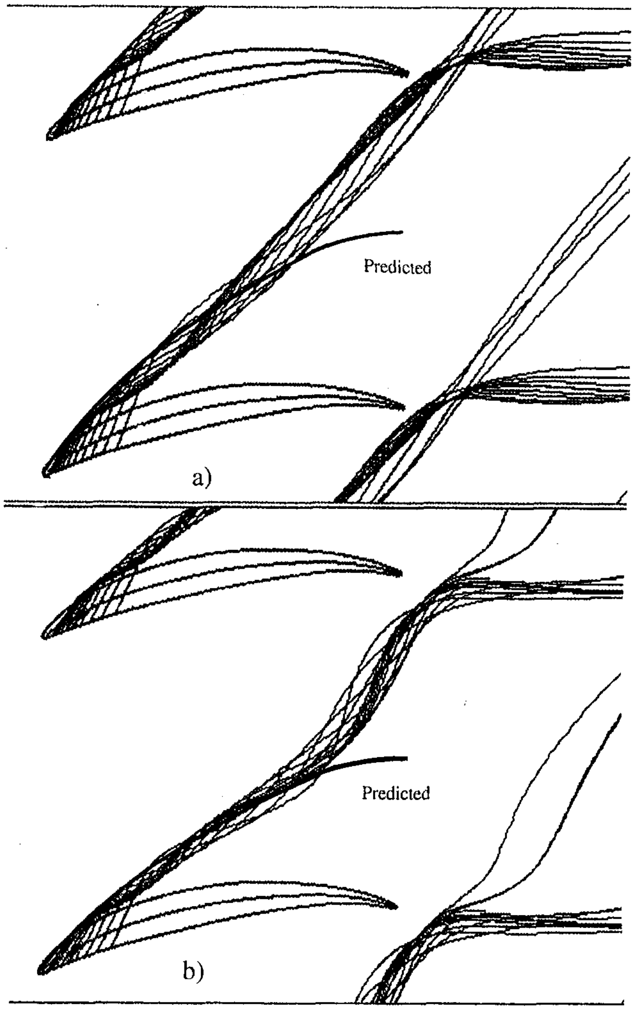

Fig. 28 Computed leakage vortex trajectories, compared with the predictions of the modified model: (*a*) $\phi = 0.5$; (*b*) $\phi = 0.7$

predicted leakage vortex trajectories with the modified model Eq. (3), for $\phi = 0.5$ and 0.7. The computed vortex trajectories are also presented in Fig. 26. The computations clearly show the good correspondence between the Navier–Stokes results and the corrected model of Chen et al., except near the trailing edge section. At $\phi = 0.7$, a strong variation of the trajectory slope is observed behind 70 percent chord. Behind the trailing edge the vortex follows the mainstream direction. Due to the entrainment effect, the streamlines closer to the wall move tangentially away from the vortex. It is seen that near the trailing edge (with large t^* in Fig. 26) the computed vortex trajectories are off the linear model, even though they are on a linear line in Fig. 28(*a*), as the vortex trajectories are measured perpendicularly to the camber line.

The discussors also refer to the difference between cascade and turbomachinery blade row data, raising doubts as to the validity of cascade data and computations for assessing real life phenomena. It appears that under this general statement, the discussors refer essentially to the effects of the presence of the inlet boundary layer skewness. As pointed out by Storer in his discussion of the paper of Chen et al., the main effect on the tip vortex is to shift its origin toward the leading edge of the blade, as a consequence of the high leading edge loading created by the relative motion of the end wall. This is indeed seen also from Fig. 28. It should be noted that the simulated cascade is characterized by a low stagger angle (10 deg), high blade camber, and thick blade profile. The computed flow is then close to a stator blade row with a hub clearance, rather than the tip flow in an unshrouded rotor.

Finally, we would like to emphasize, if needed, that the development of reliable CFD tools and of powerful computer hardware opens the way to a more systematic use of numerical simulations of complex phenomena, such as tip clearance flows, in order to gain a better understanding, particularly of flow behavior not accessible to experiments. This should allow also, when coupled to reliable experimental data, to establish limits and range of validity of simplified models, which are still necessary and useful for design purposes.

References

Adamczyk, J. J., Celestina, M. L., and Greitzer, E. M., 1993, "The Role of Tip Clearance in High-Speed Fan Stall," ASME JOURNAL OF TURBOMACHINERY, Vol. 115, pp. 28–39.

Inoue, M., Kuroumaru, M., and Fukuhara, M., 1986, "Behavior of Tip Leakage Flow Behind an Axial Compressor Rotor," ASME *Journal of Engineering for Gas Turbines and Power,* Vol. 108, pp. 7–14.

Hirsch, Ch., and Kang, S., 1996, "The 3D Flow in Krain's Centrifugal Impeller," ERCOFTAC Workshop on 3D Turbomachinery Flow Prediction, Jan. (unpublished).

Jennions, I. K., and Turner, M. G., 1993, "Three-Dimensional Navier–Stokes Computations of Transonic Fan Flow Using an Explicit Flow Solver and an Implicit *k–e* Solver," ASME JOURNAL OF TURBOMACHINERY, Vol. 115, pp. 261–272.

Development of Two-Dimensional Wakes Within Curved Channels: Theoretical Framework and Experimental Investigation

M. T. Schobeiri

J. John

K. Pappu

Turbomachinery Performance Laboratory,
Texas A&M University,
College Station, TX 77843

The development of a wake flow downstream of a cylindrical rod within a curved channel under zero streamwise pressure gradient is theoretically and experimentally investigated. The measured asymmetric wake quantities such as the mean velocity and turbulent fluctuations in longitudinal and lateral directions as well as the turbulent shear stress are transformed from the probe coordinate system into the curvilinear wake eigen-coordinate system. For the transformed non-dimensionalized velocity defect and the turbulent quantities, affine profiles are observed throughout the flow regime. Based on these observations and using the transformed equations of motion and continuity, a theoretical frame work is established that generally describes the two-dimensional curvilinear wake flow. The theory also describes the straight wake as a special case, for which the curvature radius approaches infinity. The comparison of the theory with the experimental data pertaining to the curvilinear and straight wakes demonstrate the general validity of the theory.

1 Introduction

The wake flow constitutes a special case of free turbulent flows with a broad range of general scientific and engineering applications. In the field of turbomachinery aerodynamics and heat transfer, the wake flow generated by the blades influences the boundary layer transition behavior and, particularly, the heat transfer characteristics of the blades positioned downstream of the wake. Because of its significant impact on turbomachinery efficiency and performance, the wake development associated with the inherent unsteadiness induced by mutual interaction between stator and rotor has attracted the interest of the scientific and engineering community, resulting in an increased number of publications in the turbomachinery performance area.

Considering the significance of the wake flow to the turbomachinery flow physics, in 1988 the principal author of this paper initiated the corresponding research program at Texas A&M University. One of the tasks of the research program was to develop a research facility capable of generating experimental information essential for better understanding the phenomenon of steady and unsteady wake development in curved channels under zero, negative, and positive longitudinal pressure gradients. These channels simulate the turbomachinery blade channels, where curvature and pressure gradient are the predominant parameters. This experimental task was necessary because the major part of the experimental data available in the literature, among others, by Schlichting (1930), Ermshaus (1970), Townsend (1947), Eifler (1975), and Pfeil and Eifler (1975a, b) deal with the development of wakes past a cylinder in straight channels, where the wake characteristics preserve their symmetric character throughout the flow regime. The few available results concerning the wake flow within curved channels, among others, by Savill (1983) and particularly by Nakayama (1987), have contributed to better understanding the wake development phenomena under different boundary conditions. However, they are not comprehensive enough to draw conclusions transferable to turbomachinery flow environment.

Taking into account the situation described above, systematic experimental investigations were carried out on the research facility mentioned previously to generate a consistent set of experimental data necessary for further theoretical treatment. Based on these data and using the transformed equations of motion and continuity, a theoretical framework is established that generally describes the development of wake flows through two-dimensional curvilinear channels. The theory also describes the wake flow through a straight channel as a special case, for which the curvature radius approaches infinity. The experimental investigation presented in this paper is focused on the development of steady wakes in a curved channel under zero-longitudinal pressure gradient. The wake is generated by utilizing a circular cylinder to simulate the wake by a cascade. The use of cylinder instead of blade cascade is appropriate, since the turbulence characteristics and the wake velocity defect of the cylinder wake flows are similar to those of turbomachinery blade wakes (for details see Eifler, 1975; Trost, 1975; Kiok, 1973). This is particularly true for relative distances $x/d > 80$ ("far wake").

The theoretical investigations, including the flow model, the corresponding governing equations, and the detail of solution procedures are described in section 2 of the paper. Sections 3 and 4 provide the necessary information about the research facility and the corresponding instrumentation, data acquisition, and data reduction. Detailed experimental results and their comparison with the theory are presented in section 5. To demonstrate the general validity of the presented approach, the theory is applied to the straight wake as a classical special case and the results are briefly discussed. This section is followed by a selected reference list. For detailed literature review, we refer to NASA Reports by Schobeiri and John (1994) and Schobeiri and Pappu (1994).

2 Theoretical Framework

For the following theoretical considerations we assume an incompressible turbulent flow through a two-dimensional

---

Contributed by the International Gas Turbine Institute and presented at the 39th International Gas Turbine and Aeroengine Congress and Exposition, The Hague, The Netherlands, June 13–16, 1994. Manuscript received by the International Gas Turbine Institute March 4, 1994. Paper No. 94-GT-367. Associate Technical Editor: E. M. Greitzer.

curved channel. We further assume that the velocity vector has a temporal and spatial dependency and can be decomposed into a time-independent mean and a time-dependent turbulent fluctuation vector. Based on the experimental observations, the flow regime under investigation can be divided into three distinct zones: first, the wake zone characterized by strongly asymmetric (about the wake centerline) mean velocity components, turbulent intensities, and shear stress distributions; second, the wake external zone, where the velocity distribution approximately corresponds to that of a potential flow, even though it is rotational and thus the assumption of a potential flow character is, strictly speaking, not correct; the third zone is the boundary layer at the convex and the concave channel walls where the viscosity effect is predominant and the boundary layer approximations can be applied. Based on our own experimental results and in accordance with the investigation of several other researchers, among others, Reichardt (1950), Pfeil and Eifler (1975a, b), Lakshminarayana and Raj (1976), and Nakayama (1987), we further assume that for free turbulent flow, the viscosity effect can practically be neglected. Under these assumptions the conservation equations of fluid mechanics in a coordinate invariant form are treated by transforming from a coordinate invariant form into an orthogonal curvilinear coordinate system by using tensor analytical tools. To analytically treat the problem, the contravariant velocity components V^i in ξ_i direction are substituted with the instantaneous physical ones by utilizing the metric coefficients and Christoffel symbols Γ_{ij}^k (for tensor analytical details, see Schobeiri, 1976, 1990).

2.1 Transformation of Conservation Laws. Conservation laws are first presented in coordinate invariant form and then are transformed to the special curvilinear coordinate system under investigation. Starting with the conservation law of mass, the equation of continuity in coordinate invariant form is:

$$\nabla \cdot \vec{V} = 0 \tag{1}$$

Under the assumption that the molecular viscosity can be neglected in comparison with the turbulent eddy viscosity, the equation of motion in coordinate invariant form is:

$$\vec{V} \cdot \nabla \vec{V} = -\frac{1}{\rho} \nabla p \tag{2}$$

Combining Eqs. (1) and (2) results in an appropriate version:

$$\nabla \cdot (\vec{V}\vec{V}) = -\frac{1}{\rho} \nabla p \tag{3}$$

This version is particularly useful for comparing the order of magnitude of individual terms and their contributions.

For further treatment of conservation laws, the velocity vector is decomposed into a time-averaged mean and a time-dependent fluctuation as:

$$\vec{V} = \bar{\vec{V}} + \tilde{\vec{V}} \tag{4}$$

Using this decomposition, the corresponding index notation for

Nomenclature

b = wake width = $1/2\Gamma \int_{-\infty}^{+\infty} (\bar{U}_1 \bar{U}_{1m}) d\xi_2$
c = integration constant
d = diameter of wake generating cylinder = 2 mm
C_w = momentum defect ratio = $2\delta_2/d$
f = frequency
g_{ij} = covariant metric coefficients
g^{ij} = contravariant metric coefficients
H_{12} = wake shape factor = δ_1/δ_2
N = total number of samples per channel of hot-film data for time averaging
p = static pressure
r = radial position of probe from the center of the convex wall
r_i = radius of convex wall = 500 mm
R = radius of wake centerline
T_u = turbulence intensity = $\sqrt{\overline{u}^2}/\bar{U}_{\text{local}} \times 100$
u = time-dependent physical component in longitudinal direction, ξ_1
$\overline{u^2}$ = mean longitudinal turbulent fluctuation impulse
$\overline{u_0^2}$ = mean longitudinal turbulent fluctuation impulse at the wake center
$\overline{uv}$ = Reynolds shear stress
$\bar{U}$ = mean velocity component in the longitudinal (ξ_1) direction of curvilinear coordinates
U_p = hypothetical potential velocity distribution of longitudinal component of velocity
$\bar{U}_1$ = mean velocity defect = $U_p - \bar{U}$
$\bar{U}_{1m}$ = maximum velocity defect at the wake center, $\xi_2 = 0$
$\bar{U}_1^2$ = wake momentum defect = $2U_p\bar{U}_1 - \bar{U}_1^2$
$\bar{U}_{1m}^2$ = maximum wake momentum defect
U_{p0} = hypothetical potential velocity at wake center, $\xi_2 = 0$
$\overline{UV}$ = total impulse
$\bar{U}\bar{V}$ = partial impulse
v = time-dependent physical component in lateral direction
$\overline{v^2}$ = mean lateral turbulent fluctuation impulse
$\overline{v_0^2}$ = mean lateral turbulent fluctuation impulse at the wake center
$\vec{V}$ = velocity vector
$\bar{\vec{V}}$ = time-averaged mean velocity vector
$\tilde{\vec{V}}$ = time-dependent fluctuating velocity vector
$\bar{V}$ = time-averaged physical component in ξ_2 direction
V^i = contravariant velocity component in ξ_i direction
V = velocity component in the lateral (ξ_2) direction of curvilinear coordinates
V_x = velocity component along x direction of probe coordinate system
V_y = velocity component along y direction of probe coordinate system
V_{in} = average inlet velocity
V_{xp} = hypothetical potential velocity component along x direction of probe
∇ = $\vec{g}^i(\partial/\partial\xi_i)$ = differential operator in ξ_i coordinate system
α = angle between resultant velocity vector and x axis
Γ = integral of the Gaussian curve = $\int_0^{+\infty} e^{-\zeta^2} d\zeta = \sqrt{\pi}/2$
δ_1 = displacement thickness = $1/U_{p0} \int_{-\infty}^{+\infty} (U_p - \bar{U}) d\xi_2$
δ_2 = momentum thickness = $1/U_{p0}^2 \int_{-\infty}^{+\infty} \bar{U}(U_p - \bar{U}) d\xi_2$
ζ = nondimensional coordinate = ξ_2/b
θ = angular position of the probe location from the inlet
ν = kinematic viscosity of air
ξ_1 = longitudinal direction of curvilinear coordinates
ξ_2 = lateral direction of curvilinear coordinates
ρ = density of air
ϑ = angle between probe and curvilinear coordinates
φ_1 = nondimensional velocity defect = $\bar{U}_1/\bar{U}_{1m} = e^{-\zeta^2}$
φ^2 = dimensionless wake momentum defect

Subscripts

in = inlet
x = x direction
y = y direction

Superscripts

$^{-}$ = time-averaged value

the two-dimensional orthogonal curvilinear coordinate system, Eqs. (1)–(3) in time-averaged sense can be written as:

$$\bar{V}^i_{,i} + \bar{V}^i\Gamma^j_{ij} = 0 \tag{5}$$

$$\bar{V}^j\bar{V}^i_{,j} + \bar{V}^j\bar{V}^k\Gamma^i_{kj} = -\frac{1}{\rho}g^{ij}\bar{p}_{,j} - (\overline{\tilde{V}^m\tilde{V}^i})_{,m} - \overline{\tilde{V}^m\tilde{V}^i}\Gamma^j_{mj} - \overline{\tilde{V}^m\tilde{V}^n}\Gamma^i_{mn} \tag{6}$$

$$(\bar{V}^m\bar{V}^j)_{,m} + \bar{V}^m\bar{V}^j\Gamma^i_{mi} + \bar{V}^m\bar{V}^n\Gamma^j_{mn} = -\frac{1}{\rho}g^{ji}\bar{p}_{,i} - (\overline{\tilde{V}^m\tilde{V}^j})_{,m} - \overline{\tilde{V}^m\tilde{V}^j}\Gamma^i_{mi} + \overline{\tilde{V}^m\tilde{V}^n}\Gamma^j_{mn} \tag{7}$$

Inserting the metric coefficients and Christoffel symbols:

$$g_{ij} = \begin{pmatrix} \left(\dfrac{R+\xi_2}{R}\right)^2 & 0 \\ 0 & 1 \end{pmatrix}; \quad g^{ij} = \begin{pmatrix} \left(\dfrac{R}{R+\xi_2}\right)^2 & 0 \\ 0 & 1 \end{pmatrix} \tag{8}$$

$$\Gamma^1_{ij} = \begin{pmatrix} 0 & \left(\dfrac{1}{R+\xi_2}\right) \\ \left(\dfrac{1}{R+\xi_2}\right) & 0 \end{pmatrix};$$

$$\Gamma^2_{ij} = \begin{pmatrix} -\left(\dfrac{R+\xi_2}{R^2}\right) & 0 \\ 0 & 1 \end{pmatrix} \tag{9}$$

and introducing $\bar{U}$ and $\bar{V}$ for the time-averaged physical components of V^i and $\bar{u}^2, \bar{v}^2, \overline{uv}$ for the time-averaged physical components of fluctuation impulse $\tilde{V}^i\tilde{V}^j$, the time-averaged version of continuity equation (Eq. (5)) is written as:

$$\bar{U}_{,1} + \left[\left(1 + \frac{\xi_2}{R}\right)\bar{V}\right]_{,2} = 0. \tag{10}$$

Equation (6) is decomposed in longitudinal direction ξ_1:

$$\frac{R}{R+\xi_2}\bar{U}\bar{U}_{,1} + \bar{V}\bar{U}_{,2} + \frac{\bar{U}\bar{V}}{R+\xi_2} = -\frac{1}{\rho}\frac{R}{R+\xi_2}\bar{p}_{,1} - \frac{R}{R+\xi_2}(\bar{u}^2)_{,1} - (\overline{uv})_{,2} - \frac{2}{R+\xi_2}\overline{uv} \tag{11}$$

and lateral direction ξ_2:

$$\frac{R}{R+\xi_2}\bar{U}\bar{V}_{,1} + \bar{V}\bar{V}_{,2} - \frac{\bar{U}^2}{R+\xi_2} = -\frac{1}{\rho}\bar{p}_{,2} - \frac{R}{R+\xi_2}(\overline{uv})_{,1} - (\bar{v}^2)_{,2} - \frac{\bar{v}^2}{R+\xi_2} + \frac{\bar{u}^2}{R+\xi_2} \tag{12}$$

Similarly Eq. (7) decomposed into ξ_1, ξ_2 components is written as:

$$\frac{R}{R+\xi_2}\left(\frac{\bar{p}}{\rho} + \bar{U}^2 + \overline{u^2}\right)_{,1} + (\bar{U}\bar{V} + \overline{uv})_{,2} + \frac{2}{R+\xi_2}(\bar{U}\bar{V} + \overline{uv}) = 0 \tag{13}$$

$$\frac{R}{R+\xi_2}(\bar{U}\bar{V} + \overline{uv})_{,1} + \left(\frac{\bar{p}}{\rho} + \bar{V}^2 + \overline{v^2}\right)_{,2} - \frac{1}{R+\xi_2}(\bar{U}^2 - \bar{V}^2 + \overline{u^2} - \overline{v^2}) = 0 \tag{14}$$

Equations (13) and (14) are of practical interest for estimating the order of magnitude of each individual term compared to the others. For the special case of zero longitudinal pressure gradient, presented in this paper, the changes in static pressure in longitudinal direction is set equal to zero. Furthermore, as the experimental results show, the longitudinal fluctuation velocity $|u|$ is considerably smaller than the mean velocity $\bar{U}$. The lateral fluctuation velocity $|v|$, however, has the same order of magnitude as the mean lateral velocity $\bar{V}$, while it is negligible compared to $\bar{U}$. This comparison leads to the conclusion that the contributions of the fluctuation velocity momenta are negligibly small compared to the contribution of the longitudinal mean velocity momentum $\bar{U}^2$.

2.2 Nondimensional Parameters. Eqs. (10), (13), and (14) describe the wake development phenomenon through a curved channel. To solve these equations for the required wake characteristics, we assume that from a definite distance downstream of the wake origin the velocity as well as the momentum defect profiles are similar. This assumption implies that for arbitrary points located on the wake center with the longitudinal coordinate ξ_1, corresponding length scale $b = b(\xi_1)$ on the lateral coordinate ξ_2 can be found to generate the dimensionless variable:

$$\zeta = \frac{\xi_2}{b} \tag{15}$$

Furthermore, the wake velocity and momentum defects are defined as:

$$\bar{U} = U_p - \bar{U}_1 \tag{16}$$

$$\bar{U}^2 = U_p^2 - \bar{U}_1^2 \tag{17}$$

In Eq. (16), U_p represents the hypothetical velocity distribution, which is an extension of the undisturbed wake-external velocity into the wake. In the vicinity of the wake center, it can be shown by employing the equation of motion (Eq. (11)) for potential flow that the velocity U_p can be approximated as:

$$U_p = U_{p0}\left(1 - \frac{\xi_2}{R}\right) \tag{18}$$

with U_{p0} as the hypothetical velocity at the wake center, $\xi_2 = 0$. Thus for the zero pressure gradient case presented in this paper, U_p is a function of ξ_2 only. The time-averaged velocity and momentum defects within the wake region are represented by $\bar{U}_1$ and $\bar{U}_1^2$.

The similarity assumption, stated previously, requires the following dimensionless wake velocity as well as the momentum defect functions:

$$\varphi_1 = \frac{\bar{U}_1}{\bar{U}_{1m}}, \quad \varphi^2 = \frac{\bar{U}_1^2}{\bar{U}_{1m}^2} \tag{19}$$

Here $\bar{U}_{1m}$, $\bar{U}_{1m}^2$ represent the maximum wake velocity and momentum defects at the wake center.

2.3 Expressions for Wake Characteristics. Introducing the wake velocity defect, Eq. (19), in connection with Eq. (16) into the continuity equation (Eq. (10)), separating the variables and integrating the resulting equation, we obtain:

$$\left(1 + \frac{\xi_2}{R}\right)\bar{V} = -\int\frac{d}{d\xi_1}\left[U_{p0}\left(1 - \frac{\xi_2}{R}\right) - \bar{U}_{1m}\varphi_1\right]bd\zeta + c \tag{20}$$

After some rearrangement of terms, Eq. (20) leads to:

$$\left(1+\frac{\xi_2}{R}\right)\bar V = \frac{d(\bar U_{1m}b)}{d\xi_1}\int \varphi_1 d\zeta - \frac{db}{d\xi_1}\bar U_{1m}\varphi_1\zeta$$

$$-\frac{dU_{p0}}{d\xi_1}b\int\left(1-\frac{\zeta b}{R}\right)d\zeta + c \quad (21)$$

Equation (21) shows that the lateral velocity is determined by the turbulent mixing and the decay process in longitudinal direction characterized by the longitudinal changes of the velocity-width product $\bar U_{1m}b$. Experimental investigations by Reichardt (1950), Eifler (1975), and Pfeil and Eifler (1975a, b) show that for the wake development downstream of a single cylinder under zero longitudinal pressure gradient, this product remains constant. As we will discuss later, our experimental results also show that the changes of the product above can be set equal to zero if the streamwise pressure gradient is approximately zero. However, for positive and negative streamwise pressure gradients, respectively it was found that the product $\bar U_{1m}b$ exhibits a pronounced dependency in longitudinal direction ξ_1. Also for the case of zero longitudinal pressure gradient, the variations in U_{p0} with streamwise distance can be neglected. Since the lateral velocity component $\bar V$ is zero at the wake center, the integration constant in Eq. (21) must identically vanish. Implementing these approximations, Eq. (21) simplifies to:

$$\bar V = -\frac{R}{R+\xi_2}\frac{db}{d\xi_1}\bar U_{1m}\varphi_1\zeta \quad (22)$$

With Eq. (22) the distribution of the lateral velocity component can be found provided the wake velocity defect function φ_1, the distribution of the wake width $b = b(\xi_1)$, and the distribution of $\bar U_{1m}$ are known.

From the assumption of similarity in wake velocity defect profiles, it follows that for an appropriately chosen length and velocity scales, wake width, and maximum wake velocity defect in this case, nondimensional wake velocity defect will be a function of ξ_2/b, i.e.,

$$\frac{\bar U_1}{\bar U_{1m}} = f\left(\frac{\xi_2}{b}\right) = f(\zeta) \quad (23)$$

From the experimental investigations by Reichardt (1950), Eifler (1975), and others it was concluded that the nondimensional wake velocity defect distribution in the case of a straight channel with zero streamwise pressure gradient follows the Gaussian distribution. Similar solution for the dimensionless wake velocity defect function, in Eq. (23), in case of curved channel wake flow can be obtained by using the equation of motion (Eq. (11)) with earlier specified order of magnitude analysis. The derivation involves the use of the expressions for mean longitudinal and lateral velocities, i.e., Eqs. (16) and (22), and also of shear stress. The analytical treatment with suitable approximations results in an ordinary second-order differential equation in φ_1, which can be solved by numerical integration. It has been found that the numerical solution of the ordinary differential equation follows the Gaussian distribution presented below.

$$\varphi_1 = e^{-\zeta^2} \quad (24)$$

Comprehensive experimental measurements in a curved channel with and without streamwise pressure gradient are also found to follow the Gaussian distribution given by Eq. (24) as well. Thus, it can be concluded that the effects of curvature and pressure gradient are not significant on dimensionless wake velocity defect distribution and assumption of similarity in wake velocity defect profiles is valid.

From the time-averaging procedure, it is obvious that shear stress is the difference of total and partial impulses, i.e., $\overline{uv} = \overline{UV} - \bar U\bar V$. Thus, knowing the expressions for total and partial impulses would lead to an expression for shear stress. Since the expressions for both the mean velocities are known from Eqs. (16) and (22), the partial impulse can be obtained as:

$$\bar U\bar V = -(U_p - \bar U_{1m}\varphi_1)\bar U_{1m}\frac{db}{d\xi_1}\zeta\varphi_1\frac{R}{R+\xi_2} \quad (25)$$

Substituting the approximation for U_p from Eq. (18) into Eq. (25) and nondimensionalizing the resulting equation with $\bar U_{1m}^2$, the final expression for nondimensional partial impulse is written as:

$$\frac{\bar U\bar V}{\bar U_{1m}^2} = -\frac{R}{R+\xi_2}\frac{db}{d\xi_1}\frac{U_{p0}}{\bar U_{1m}}\left(1-\frac{\zeta b}{R}\right)\zeta\varphi_1$$

$$+\frac{R}{R+\xi_2}\frac{db}{d\xi_1}\zeta\varphi_1^2 \quad (26)$$

The expression for total impulse can be obtained by using the equation of motion (Eq. (13)) in the ξ_1 direction and following the earlier specified order of magnitude analysis as:

$$\frac{R}{R+\xi_2}(\bar U^2 + \overline{u^2})_{,1} + (\overline{UV})_{,2} + \frac{2}{R+\xi_2}(\overline{UV})$$

$$= -\frac{1}{\rho}\frac{R}{R+\xi_2}\bar p_{,1} \quad (27)$$

Assuming that the mean longitudinal turbulent fluctuation is negligible in comparison with the mean velocity of the flow and also the variation of the potential velocity at the wake center in ξ_1 direction is very small for the case of zero longitudinal pressure gradient, Eq. (27) in connection with Eqs. (16) and (17) can be simplified as:

$$\frac{R}{R+\xi_2}\frac{\partial}{\partial\xi_1}(-\bar U_1^2) = -(\overline{UV})_{,2} - \frac{2}{R+\xi_2}(\overline{UV}) \quad (28)$$

Further rearrangement of terms, the following assumption $\overline{UV}/R \ll (\partial/\partial\xi_2)[(1+\xi_2/R)\overline{UV}]$, and integration of the resulting equation yield an expression for total impulse as:

$$\left(1+\frac{\xi_2}{R}\right)\overline{UV} = \int\frac{d}{d\xi_1}(\bar U_1^2)bd\zeta + c$$

$$= \int\frac{d}{d\xi_1}(\bar U_{1m}^2\varphi^2)bd\zeta + c \quad (29)$$

where $\bar U_{1m}^2 = 2U_p\bar U_{1m} - \bar U_{1m}^2$.

The approximate equality of dimensionless wake velocity and momentum defects, i.e., $\varphi^2 \cong \varphi_1$, has been verified experimentally for different locations downstream of the wake-generating body. Using this approximation and further rearrangement of some terms modify Eq. (29) to:

$$\left(1+\frac{\xi_2}{R}\right)\overline{UV} = \int\left(-2U_p\bar U_{1m}\frac{db}{d\xi_1} + \bar U_{1m}^2\frac{db}{d\xi_1}\right)\frac{d}{d\zeta}(\zeta\varphi_1)d\zeta$$

$$+\int 2\bar U_{1m}b\left(1-\frac{\xi_2}{R}\right)\varphi_1\frac{dU_{p0}}{d\xi_1}d\zeta + \int 2U_p\varphi_1\frac{d}{d\xi_1}(\bar U_{1m}b)d\zeta$$

$$-\int\varphi_1\frac{d}{d\xi_1}(\bar U_{1m}^2 b)d\zeta + c \quad (30)$$

This equation can further be simplified from the already stated approximations for zero streamwise pressure gradient case, which are based on the experimental results, that $\bar U_{1m}b$ is constant and the changes in U_{p0} in ξ_1 direction are quite small. Simplification, evaluation of the integrals, and finally nondimensionalizing with $\bar{U}_{1m}^2$ result in an expression for total impulse as:

$$\frac{\overline{UV}}{\bar{U}_{1m}^2} = \frac{R}{R+\xi_2}\frac{U_{p0}}{\bar{U}_{1m}}\frac{db}{d\xi_1}\left[-2\zeta\varphi_1 + \frac{b\varphi_1}{R}(1+2\zeta^2)\right] + \frac{R}{R+\xi_2}\frac{db}{d\xi_1}\zeta\varphi_1 + \frac{c}{\bar{U}_{1m}^2} \quad (31)$$

Now the expression for Reynolds shear stress can be obtained from the difference of total impulse and partial impulses, i.e., Eqs. (26) and (31), as:

$$\frac{\overline{uv}}{\bar{U}_{1m}^2} = \frac{R}{R+\xi_2}\frac{U_{p0}}{\bar{U}_{1m}}\frac{db}{d\xi_1}\left[-\zeta\varphi_1 + \frac{b\varphi_1}{R}(1+\zeta^2)\right] \quad (32)$$

$$+ \frac{R}{R+\xi_2}\frac{db}{d\xi_1}\zeta\varphi_1(1-\varphi_1) + \frac{c}{\bar{U}_{1m}^2}$$

The constant of integration in this expression is a function of ξ_1 and needs to be evaluated from the experimental results at $\zeta = 0$. For the case of straight channel with no streamwise pressure gradient, it is known from experimental results that shear stress is zero at the wake center with the distribution being symmetric about the wake center. In that case, the constant of integration is evaluated to be zero. But for the case of curved channel flow, the shear stress distribution is strongly asymmetric with its value being nonzero at the wake center, thus bringing out the influence of curvature. As a result, the constant of integration is no longer zero and needs to be evaluated from experimental measurements to incorporate the asymmetry.

3 Experimental Research Facility

The experimental facility described below enables the simulation of steady and unsteady wake development in a two-dimensional curved channel with positive, zero, and negative longitudinal pressure gradients. The wake is generated by a circular cylinder. As stated in the introduction, the use of cylinder instead of blade cascade is appropriate, since the turbulence characteristics of the cylinder wake flows, in terms of Reynolds stress components, are similar to those of rotor blade wakes.

The test facility shown in Fig. 1 consists of a large centrifugal fan, a settling chamber, a nozzle, a wake generator, a test section, and an exit duct. For detailed information about the design description and performance tests we refer to a report and a paper by Schobeiri (1988) and Schobeiri and Pardivala (1992). Thus only a brief description of facility and its components is given in the following paragraphs.

At the test section, the centrifugal fan generates a maximum mean velocity of 36 m/s and a maximum Reynolds number (based on the test section height) of 8.8×10^5. A Prandtl probe is permanently located in the straight pipe, upstream of the diffuser, to sense any fluctuations in the mean velocity resulting from fluctuations in the fan speed.

A short diffuser, designed using optimum design criteria (see Schobeiri, 1979), is located downstream of the straight pipe and decelerates the flow before it enters the settling chamber. With this diffuser-settling chamber configuration it was possible to establish a very uniform velocity profile and a free-stream turbulence intensity of 1.2 percent at the inlet of the test section. Downstream of the settling chamber is a nozzle with an area ratio 4:1, to accelerate the flow to the required velocity and to establish a smooth transition of the flow from the settling chamber to the wake generator.

The test section shown in Fig. 2 is located downstream of the wake generator and consists of a convex top wall, a concave bottom wall, and two vertical plexiglass side walls. The concave bottom wall is designed to slide horizontally within two T-slots in the bottom wall of the wake generator. This allows the creation of adverse or favorable longitudinal pressure gradients within the test section.

In addition to simulating convex curvature, the convex wall assembly is designed to allow precise radial and circumferential traversing of the probes. Figure 2 shows the mounting of the traversing system within the convex wall assembly. A D.C. stepper motor, providing the required drive for the slider of the traversing probe, receives signals from a computer and is driven by a FORTRAN code. An optical encoder connected to the traversing system provides a continuous feedback to the stepper motor for accurate positioning of the probes. Software stops and mechanical stops are used to prevent the probes from traversing beyond the desired limits.

The slider of the traversing system is designed to allow the simultaneous positioning of two probes. The first probe is a hot-film X-probe while the second probe is a pneumatic probe (Kiel probe). Angular positioning of the probes is achieved by rotating the entire convex wall assembly about its center of curvature. A rotary vernier is mounted on one of the triangular supporting walls for precise angular positioning of the probes.

4 Instrumentation, Data Acquisition, and Data Reduction

The data acquisition system is completely automated and is controlled by a 386 personal computer. The mean velocity and turbulent stress components are obtained using a three-channel, constant temperature anemometer (TSI, IFA 100) system. Each channel of the anemometer system has a signal conditioner with variable low and high pass filters, dc offset, and adjustable gain. All the measurements in the present study are made with platinum hot-film sensors 25 μm in diameter. Preliminary measurements are made using a standard single-film probe (TSI 1210-10) and the two component measurements are made using a specially designed X-film probe (TSI 1241-XX-10). The X-film probe is designed to allow the sensors to remain along the axis of the probe support. The first channel of the anemometer is connected to a single-film probe and the second and third channels are connected to a X-film probe. The fourth and fifth channels of the A/D board are connected with two high-precision differential pressure transducers (MKS 220CD, range: 0–10 mm Hg and 0–100 mm Hg) with a two-channel digital readout. A Prandtl probe (pitot-static probe), placed upstream of the diffuser, is connected to one of the pressure transducers to monitor a reference velocity at a fixed location. The second pressure transducer is used to measure the total pressure from a Kiel probe positioned at the same radial and longitudinal location as the X-probe. To monitor the flow temperature constantly, a further channel of the A/D board is connected to a thermocouple with a digital readout, which is placed just downstream of the test section.

The frequency spectra are measured to determine the desired cut-off frequency of the low pass filter of the anemometer system. One-dimensional frequency spectra, obtained from single sensor hot-film probe by performing a Fast Fourier Transform (FFT), at the inlet ($\theta = 0$ deg) for the zero pressure gradient case at three lateral locations is shown in Fig. 3. The location corresponding to the dotted line spectrum is in the potential flow region outside the wake. The thick solid line corresponds to a location almost near the center of the wake and the thin solid line corresponds to a location slightly away from the center of the wake. The peaks at 2.28 kHz observed in the solid line spectra clearly indicate the Kármán vortex shedding with a Strouhal number $S = f.d/V_{in} = 0.21$ and match with the data of Roshko (1953).

Accurate measurement of the wake characteristics presented in this paper requires extensive calibration of the hot-film sensors. In order to ensure a high level of accuracy and accelerate

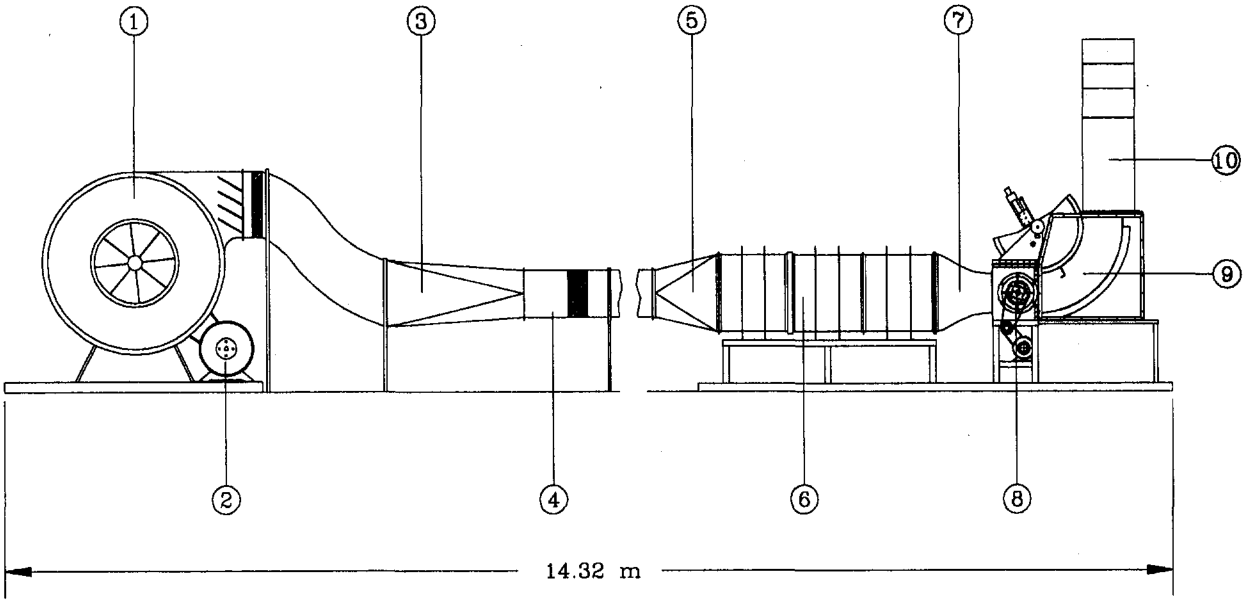

Fig. 1 Overall layout of the test facility: 1—fan; 2—motor; 3—transition duct; 4—straight pipe; 5—diffuser; 6—settling chamber; 7—nozzle; 8—wake generator; 9—test section; 10—exit duct

the calibration procedure, the simple calibration method by John and Schobeiri (1993) was used. For the data reduction and analysis, the characteristic response of X-film probe is stored in the form of calibration coefficients. The velocity components are obtained in the probe coordinates, which in the present measurements coincide with the radial and tangential directions to the convex wall. The instantaneous velocity component in the tangential direction is denoted by V_x and in the radial direction is denoted by V_y. The radial velocity V_y is taken as positive if its direction is toward the convex wall. The instantaneous velocity components can be represented in the following form:

$$V_x = \bar{V}_x + v_x; \quad V_y = \bar{V}_y + v_y \tag{33}$$

with $\bar{V}_x$ and $\bar{V}_y$ as the mean velocity components in the x and y directions (tangential and radial directions), respectively. The turbulent fluctuation components are denoted by v_x and v_y. The mean velocity components, also known as time average or global mean, are given by:

$$\bar{V}_x = \frac{1}{N}\sum_{j=1}^{N} V_{x_j} \tag{34}$$

$$\bar{V}_y = \frac{1}{N}\sum_{j=1}^{N} V_{y_j} \tag{35}$$

where N (=32,768) is the total number of samples per sensor

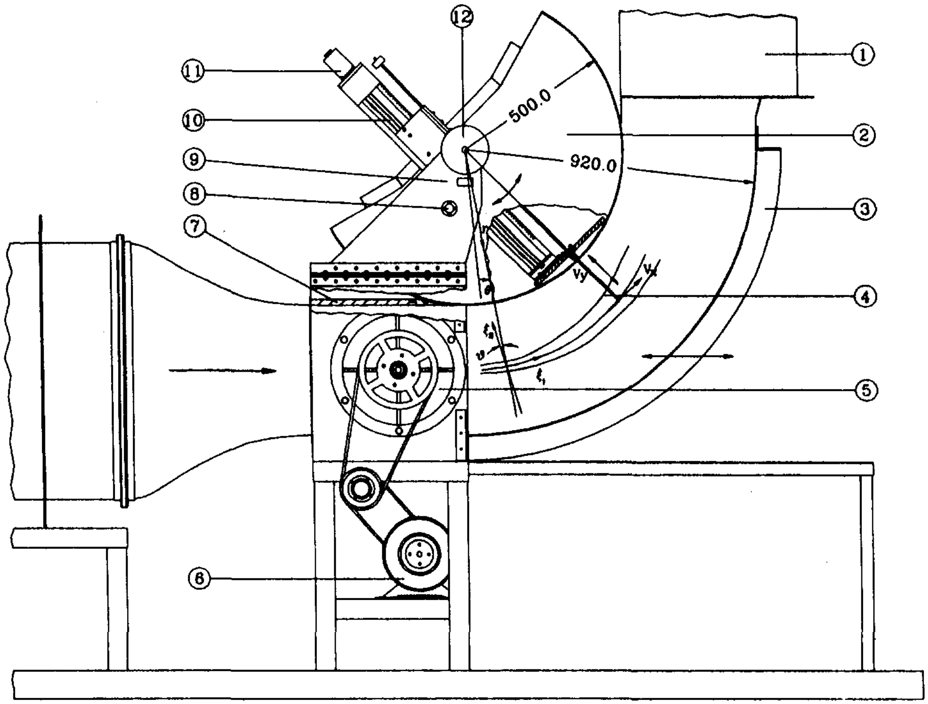

Fig. 2 Test section: 1—exit duct; 2—convex wall assembly; 3—concave wall; 4—probe; 5—unsteady wake generator (not used in this investigation); 6—motor; 7—top wall; 8—safety pin; 9—rotary vernier; 10—traversing system; 11—stepper motor; 12—locking wheel

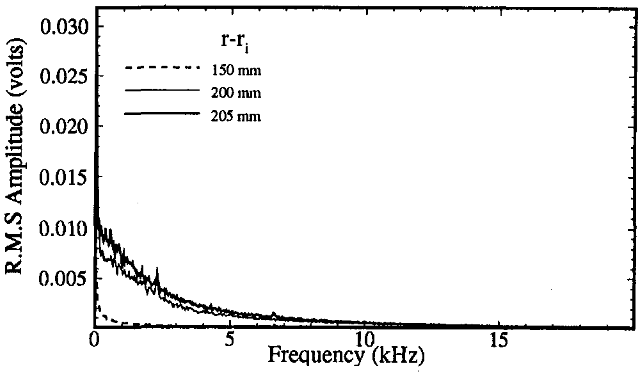

Fig. 3 Frequency spectra for different radial locations at the inlet of test section with θ = 0 deg and V_{in} = 21.5 m/s

of the X-film probe at one probe location. At the sampling rate of 2 kHz, employed in the investigation of steady wakes, 32,768 samples per sensor provided good convergence for the mean velocities and Reynolds stresses. The mean square values of the components of turbulent velocity fluctuations are obtained from the instantaneous and mean velocities as:

$$\overline{v_x^2} = \frac{1}{N}\sum_{j=1}^{N}(V_{x_j} - \bar{V}_x)^2 \tag{36}$$

$$\overline{v_y^2} = \frac{1}{N}\sum_{j=1}^{N}(V_{y_j} - \bar{V}_y)^2 \tag{37}$$

and the percentage turbulence intensity is defined as:

$$T_u = \frac{\sqrt{\overline{v_x^2}}}{\bar{V}_x} \times 100 = \frac{1}{\bar{V}_x}\sqrt{\frac{1}{N}\sum_{j=1}^{N}(V_{x_j} - \bar{V}_x)^2} \times 100 \tag{38}$$

The Reynolds shear stress is calculated by:

$$\overline{v_xv_y} = \frac{1}{N}\sum_{j=1}^{N}(V_{x_j} - \bar{V}_x)(V_{y_j} - \bar{V}_y) \tag{39}$$

The measurements are made in the probe coordinates (x, y), shown in Fig. 2, giving the tangential velocity component $\bar{V}_x$ and radial velocity component $\bar{V}_y$. In order to compare experimental results with the developed theory, the results have to be represented in a curvilinear coordinate system (ξ_1, ξ_2). In accordance with the definitions used in section 2, ξ_1 is defined as the direction along a streamline near the center of wake and ξ_2 the direction normal to it. The maximum inclination between these two orthogonal coordinate systems was found to be less than 7.5 deg for the data presented here, and hence, the distance taken radially from the wake center to a measuring point was approximated as ξ_2 and for all the measuring points at an angular position θ, the ξ_1 coordinate was assumed constant. The errors due to this approximation will be even small considering the fact that for most longitudinal locations the inclination between the two coordinate systems was less than 4 deg.

The instantaneous velocity components in the (ξ_1, ξ_2) can be represented by the instantaneous velocity components in (x, y) coordinates as:

$$U = V_x \cos\vartheta + V_y \sin\vartheta \tag{40}$$

$$V = V_y \cos\vartheta - V_x \sin\vartheta \tag{41}$$

where ϑ is the angle between ξ_1 and x direction. Also, the mean velocity component in (ξ_1, ξ_2) is obtained from mean velocities in the (x, y) coordinates by:

$$\bar{U} = \bar{V}_x \cos\vartheta + \bar{V}_y \sin\vartheta \tag{42}$$

$$\bar{V} = \bar{V}_y \cos\vartheta - \bar{V}_x \sin\vartheta \tag{43}$$

where $\bar{U}$ and $\bar{V}$ are the mean velocities in ξ_1 and ξ_2 directions, respectively. The mean Reynolds stress components in (ξ_1, ξ_2) coordinates are obtained by taking the product of the fluctuating velocities and time averaging, and are given by:

$$\overline{u^2} = \overline{v_x^2}\cos^2\vartheta + \overline{v_y^2}\sin^2\vartheta + \overline{v_xv_y}\sin 2\vartheta \tag{44}$$

$$\overline{v^2} = \overline{v_x^2}\sin^2\vartheta + \overline{v_y^2}\cos^2\vartheta - \overline{v_xv_y}\sin 2\vartheta \tag{45}$$

$$\overline{uv} = (\overline{v_y^2} - \overline{v_x^2})\frac{\sin 2\vartheta}{2} + \overline{v_xv_y}\cos 2\vartheta \tag{46}$$

The velocity defect distribution is determined from the wake velocity data and hypothetical potential velocity distribution. In order to obtain the location of maximum velocity defect accurately, a smoothing cubic spline function is used to fit the tangential component of velocity defect, $\bar{V}_{x1}$ ($\bar{V}_{x1} = \bar{V}_{xp} - \bar{V}_x$). The edges of the wake were determined by an integral method developed by Schobeiri and Pardivala (1992). The locations of wake edges are sensitive to the initial selection of the potential region used to determine the hypothetical potential velocity distribution. However, the integral parameters such as wake width are much less sensitive to the location of wake edges, especially if the location of the wake edges are in the potential flow region.

The components of mean velocity and Reynolds stresses in curvilinear coordinate system are calculated from Eqs. (42)–(46). The velocity defect distribution, maximum value of velocity defect, and the location of maximum velocity defect are calculated for the longitudinal component $\bar{U}$. Figure 4 shows the schematic diagram of the velocity defect distribution for the longitudinal velocity. The component of velocity defect in longitudinal direction $\bar{U}_1$, defined as $\bar{U}_1 = U_p - \bar{U}$, is calculated in a manner exactly identical to the determination of tangential component of velocity defect. Here U_p represents the hypothetical potential velocity distribution obtained by curve fitting the longitudinal velocity $\bar{U}$ outside the wake. The location of the maximum velocity defect obtained from $\bar{U}$ was almost the same as the one obtained from $\bar{V}_x$.

The maximum velocity defect $\bar{U}_{1m}$ is used as the velocity scale to nondimensionalize the mean velocity defect $\bar{U}_1$, lateral velocity component $\bar{V}$, and the Reynolds shear stress while the wake width is used to nondimensionalize the lateral coordinate ξ_2.

5 Results and Discussion

To demonstrate the general validation of the developed theory, the wake development under zero-pressure gradient within a curved channel as well as a straight channel are investigated. For the curved channel, the experimental results on the curved channel discussed previously is presented and compared with the theory. For a straight channel, the results from literature are taken and compared with the theory. To carry out the compari-

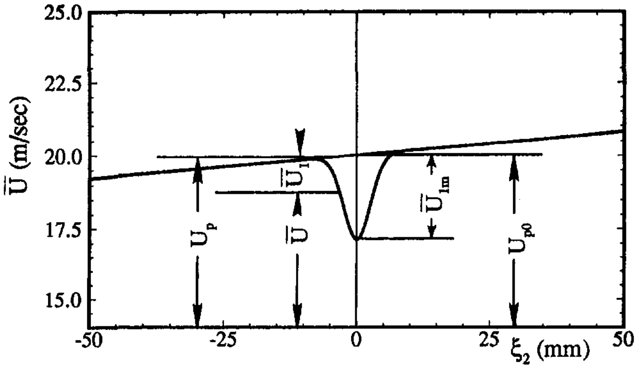

Fig. 4 Schematic velocity distribution, definitions: U_p: potential mean velocity, $\bar{U}$: mean velocity, $\bar{U}_1$: mean velocity defect = $U_p - \bar{U}$

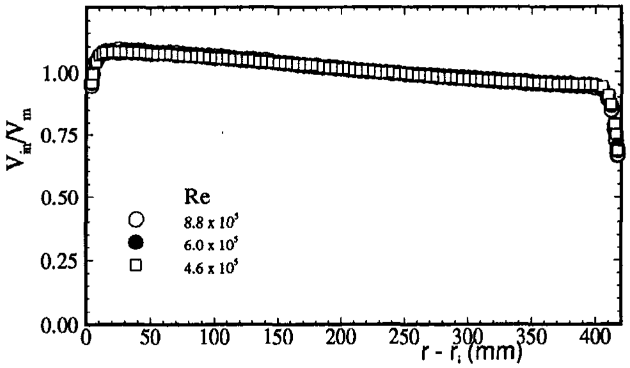

Fig. 5 Lateral distribution of dimensionless inlet velocity profiles at three different Reynolds numbers

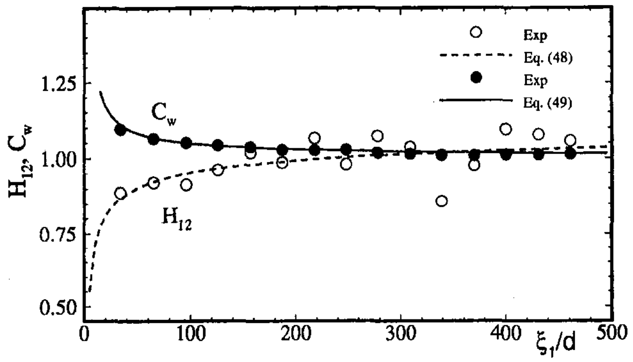

Fig. 7 Momentum thickness ratio and shape factor at different streamwise positions

son with theory, information regarding the wake width, maximum wake velocity defect, and hypothetical potential flow velocity at the wake center are taken from the experimental measurements.

5.1 Curved Channel Wake Flow

Inlet Flow Profile. To define the inlet flow condition of the test section without the wake generation rod clearly, the velocity and turbulence intensity distributions were measured immediately at the inlet to the curved test section, where the curvature starts. The velocity distribution obtained in radial direction for three different Reynolds numbers Re $= 4.6 \times 10^5$, 6.0×10^5, and 8.8×10^5 is nondimensionalized with the mass-averaged velocity (V_m). As shown in Fig. 5, this nondimensionalization causes the typical asymmetric distribution of the velocity profiles to collapse together indicating the negligible effect of the Reynolds number. Further information concerning the inlet flow profile is provided by measuring the turbulence intensity distribution. Figure 6 shows the local longitudinal turbulence intensity distribution with a freestream value of 1.2 percent.

Wake Development. The wake behind a stationary cylinder, with the diameter $d = 2$ mm located at midheight of the wake generating section, was measured using an X-hot-film probe. The curved channel test section had an inlet to exit area ratio of approximately 1 and an average inlet velocity of 20 m/s. The wake profiles were obtained at 15 angular positions (also referred to as longitudinal positions) from $\theta = 0$ deg to 70 deg in 5 deg intervals. The first measuring station $\theta = 0$ deg corresponds to the inlet of the curved test section, and is at a distance of 67 mm downstream of the wake generating cylinder. Based on the results of theoretical and experimental investigations of wake flows through straight channels, presented in section 5.2, it was found unnecessary to vary the cylinder diameter as a parameter for the wake flow through curved channels. As shown in section 5.2, the wake development in longitudinal direction depends primarily upon the ratio ξ_1/d (x/d for straight wake) regardless of the separate variation of the parameters involved in this ratio.

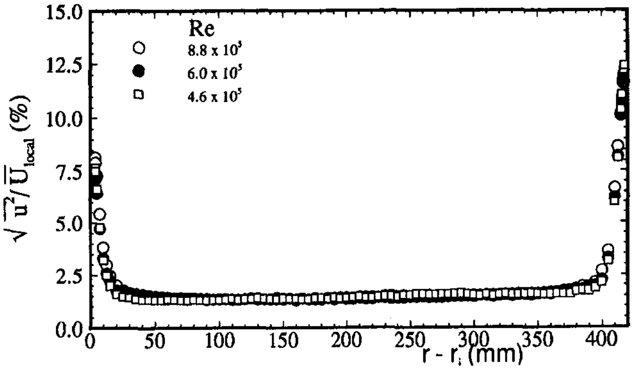

Fig. 6 Lateral distribution of local turbulence intensity at three different Reynolds numbers

The wake center is defined as the location of maximum velocity defect, as shown in Fig. 4. The path of wake center represents the direction of curvilinear coordinate ξ_1 at $\xi_2 = 0$. As the wake propagates through the channel, the trajectory of the wake center gradually moves toward the convex wall up to a longitudinal location $\xi_1/d = 240$ ($\theta = 33.66$ deg), and from there onward it moves away from the convex wall. The maximum inclination between the trajectory of the wake center and the tangential direction x was less than 5 deg. The maximum velocity defect and the potential velocity are sketched in Fig. 4.

For the estimation of the influence region of the wake generating cylinder, which in the literature frequently referred to as the "near and far wake regions," the nondimensional momentum defect ratio $C_w = 2\delta_2/d$ and the wake shape factor $H_{12} = \delta_1/\delta_2$ are utilized, where the velocity defect function φ_1 is introduced:

$$\delta_2 = b\,\frac{\bar{U}_{1m}}{U_{p0}}\left(1 - \frac{1}{\sqrt{2}}\,\frac{\bar{U}_{1m}}{U_{p0}}\right) \tag{47}$$

$$C_w = 2\,\frac{b}{d}\,\frac{\bar{U}_{1m}}{U_{p0}}\left(1 - \frac{1}{\sqrt{2}}\,\frac{\bar{U}_{1m}}{U_{p0}}\right) \tag{48}$$

$$H_{12} = \frac{\delta_1}{\delta_2} = \frac{1}{1 - \dfrac{1}{\sqrt{2}}\,\dfrac{\bar{U}_{1m}}{U_{p0}}} \tag{49}$$

As shown in Fig. 7, for a wide range of ξ_1/d, the C_w distribution does not exhibit any major changes that may suggest the existence of a pronounced near-wake region similar to that for straight wakes investigated by Reichardt (1950) and Pfeil and Eifler (1975a, b). However, considering the wake shape factor H_{12}, Fig. 7 as an alternative indicator, a transition zone $\lambda_{tr} = \xi_1/d < 40$ may be defined, for which the nondimensional wake velocity defect φ_1 indicates a certain dependency upon ξ_1/d. This dependency diminishes for $\lambda_{tr} = \xi_1/d \gtrsim 40$. Compared to the near-wake region of straight wake ($x/d < 100$), the relatively short transition zone suggested above may be attributed to the asymmetric velocity distribution associated with a lateral pressure gradient resulting in a stronger longitudinal and lateral mixing, and thus shorter transition zone.

The decay of the maximum velocity defect $\bar{U}_{1m}$ normalized by the potential velocity at the wake center U_{p0} is shown in Fig. 8(a). The solid line represents a power law fit with $\bar{U}_{1m}/U_{p0} \sim (\xi_1/d)^m$. The experimental results suggest that the exponent m is, among others, a function of pressure gradient and

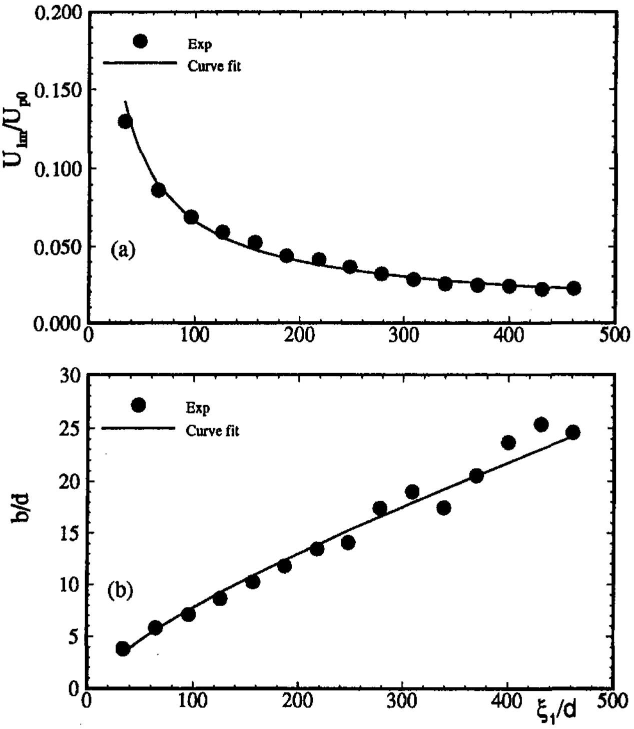

Fig. 8 Nondimensional (*a*) maximum velocity defect and (*b*) wake width as a function of ξ_1/d

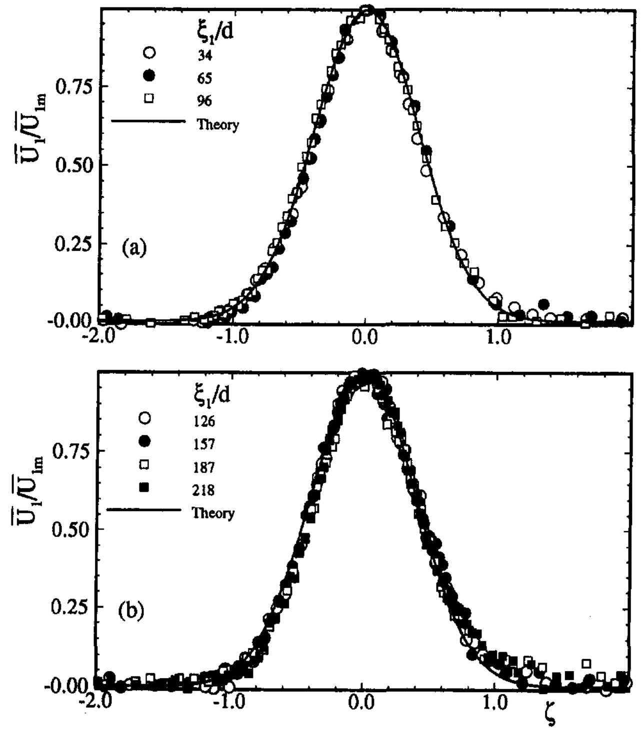

Fig. 9 Nondimensional mean velocity defect distribution in curved channel with ξ_1/d as parameter, comparison of theory (solid lines) and experiment (symbols)

may assume different values. In the present study m can be approximated as being equal to -0.71. For comparison, the straight wake decay process follows the relationship $\bar{U}_{1m}/U_\infty \sim (x/d)^{-0.5}$ for near wake ($x/d < 100$) and $\bar{U}_{1m}/U_\infty \sim (x/d + x_0/d)^{-0.5}$ for far wake ($x/d > 100$) (see Reichardt, 1950; Pfeil and Eifler, 1975a, b). The value of the virtual origin x_0 reported by different researchers varies from 40 to $100d$. It is evident that the decay of wake centerline velocity defect for the present curved wake is faster than the straight wake. This is mainly due to the asymmetric character of wake velocity distribution mentioned above.

The wake growth characterized by b/d as a function of ξ_1/d is shown in Fig. 8(*b*), the solid line being the power law fit with $b/d \sim (\xi_1/d)^m$ with the exponent m being equal to 0.74. For comparison, for a zero-pressure gradient straight wake b/d is proportional to $(x/d)^{0.5}$ for near wake and $(x/d + x_0/d)^{0.5}$ for far wake. This results in a higher growth rate b for curved wake compared to that of the straight wake. Considering the relationships for $\bar{U}_{1m}$ and b/d, the product of $\bar{U}_{1m}b$ leads to almost a constant value, which is characteristic for turbulent wake flow at zero pressure gradient.

Mean Velocity Distribution. The distribution of the mean velocity defect function $\varphi_1 = \bar{U}_1/\bar{U}_{1m} = f(\zeta)$ for different longitudinal locations is shown in Fig. 9. The lateral distance ξ_2 is nondimensionalized by the wake width b. Considering the asymmetric behavior of the velocity distribution, the introduction of the velocity defect has resulted in a fully symmetric defect function.

In Fig. 9 the experimental results (symbols) are compared with the developed theory (solid line). The solid lines are based on the velocity defect function, $\varphi_1 = e^{-\zeta^2}$, which is proved to be a general representation of the wake defect for curved and straight wakes (see also section 5.2). The mean velocity defect profiles are symmetric and almost identical to the straight wake (discussed in section 5.2) except for the fact that they are slightly wider on the inner side (concave side of the trajectory of the wake centerline) of the wake. This small deviation from the straight wake data is clearer at higher longitudinal locations. In general, it may be considered that the effect of curvature on mean velocity defect distribution is small.

The distributions of the experimental and theoretical mean longitudinal velocity components are shown for different longitudinal locations in Figs. 10 and 11, where experimental and

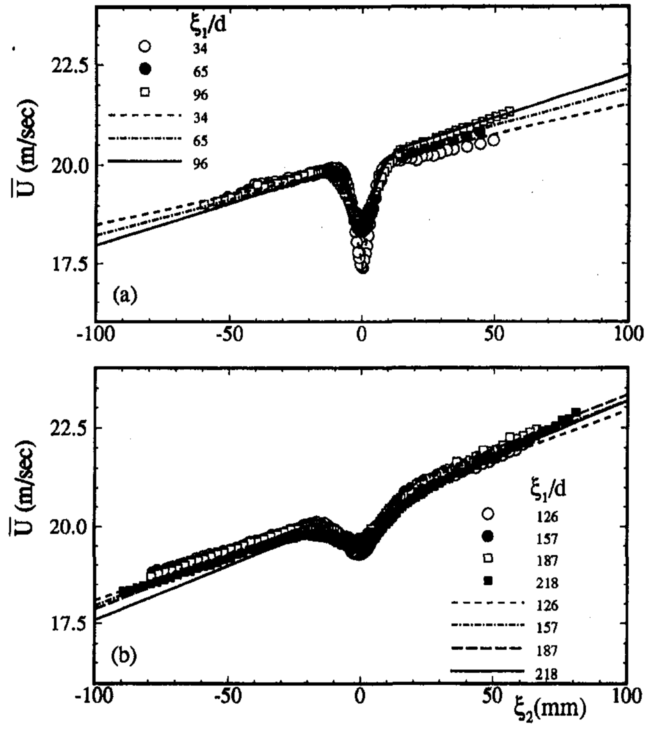

Fig. 10 Mean longitudinal velocity distribution in curved channel with ξ_1/d as parameter, comparison of theory (lines) and experiment (symbols)

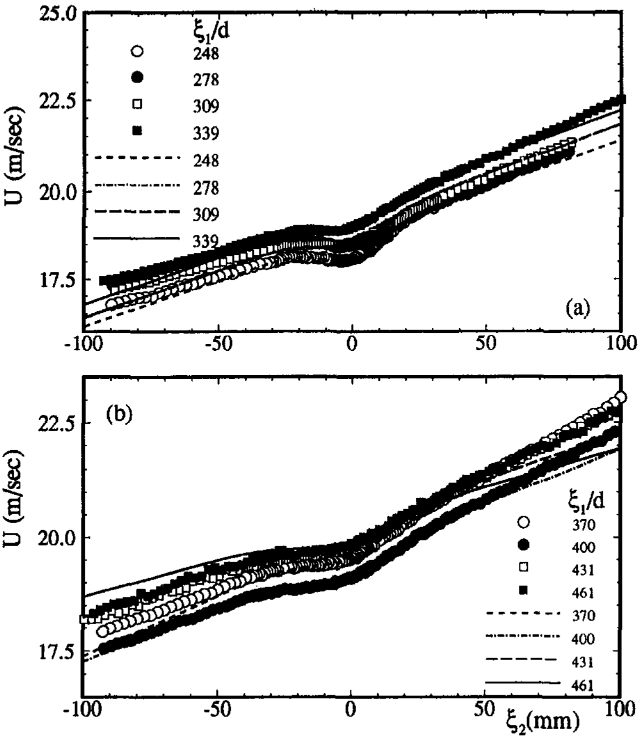

Fig. 11 Mean longitudinal velocity distribution in curved channel with ξ_1/d as parameter, comparison of theory (lines) and experiment (symbols)

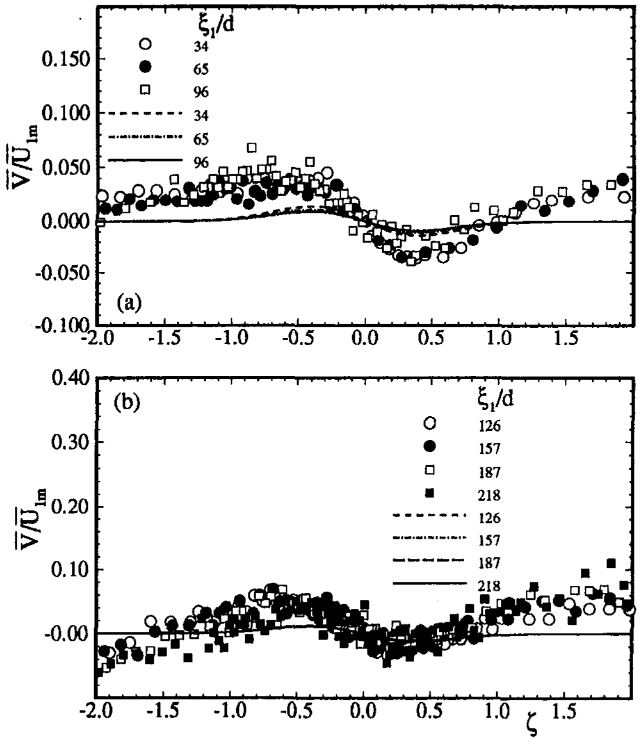

Fig. 12 Mean lateral velocity distribution in curved channel with ξ_1/d as parameter, comparison of theory (lines) and experiment (symbols)

theoretical results are represented by symbols respectively lines. As shown, the velocity distribution exhibits a strong asymmetric character with higher velocities at the positive side of ξ_2, corresponding to the locations closer to the convex wall with $\xi_2 = 0$ as the geometric location of the wake center. The wake velocity defect decreases, resulting in a continuous increase of the wake width with downstream location. The individual velocity profiles are characterized by a highly dissipative vortical core inside the wake region surrounded by external potential flow region. A comparison with the theory developed shows a detailed prediction of this behavior over the entire velocity range. The excellent agreement between theory and measurements confirms the validity of assumptions made including the validity of the derived approximation for potential flow velocity in the vicinity of the wake center, i.e., $U_p = U_{p0}(1 - \xi_2/R)$.

The distribution of the nondimensionalized lateral velocity component $\bar{V}/\bar{U}_{1m}$ for various longitudinal locations is presented in Fig. 12. The experimental results reveal an asymmetric behavior with a minimum at $\zeta > 0$, a maximum at $\zeta < 0$, and zero velocity at the center with nonzero values at the edges. Compared to the $\bar{V}/\bar{U}_{1m}$ distribution for straight wake approaching zero at the edges, the nonzero values at the edges of curved wake are a result of asymmetric velocity behavior discussed earlier. The lines represent the theoretical results for the lateral velocity distribution obtained from continuity equation in conjunction with the equation of motion. Although the theoretical results exhibit the same tendency, they deviate slightly from the experimental results. The main reason for this deviation is that the lateral velocity component is in general very small compared to the longitudinal component. Considering the transformation of the velocity components from the probe coordinate system into the wake eigencoordinate system (see Eqs. (40)–(43)), the deviation is within the accuracy tolerance of the probe associated with inevitable scatter in the measurement. In this connection, it should be noted that many relevant papers on wakes, including the ones dealing with symmetric wakes, have not reported the lateral velocity distribution, probably due to very high scatter in experimental data.

Reynolds Stresses. The experimental results (symbols) for Reynolds shear stress distribution at various longitudinal locations are presented in Fig. 13 and are compared with the theory (lines) developed in section 2. The Reynolds shear stress is nondimensionalized by the square of the maximum velocity defect. As shown

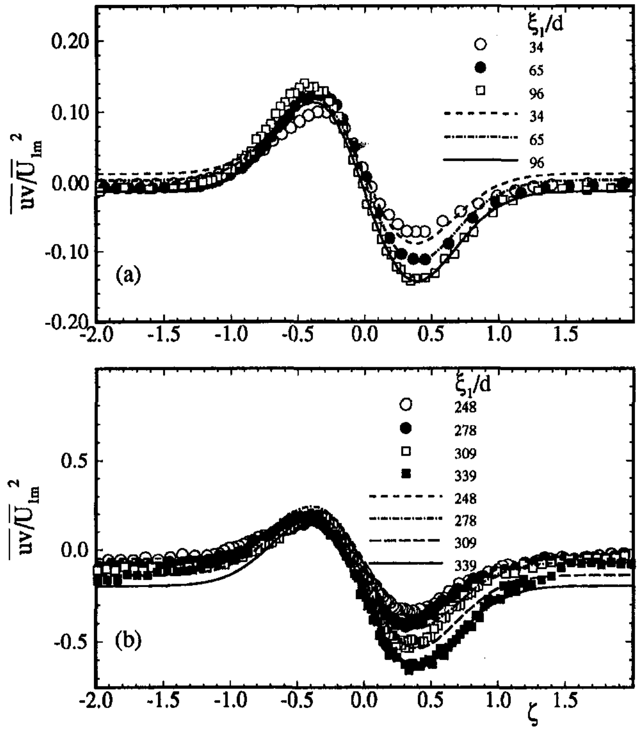

Fig. 13 Nondimensional Reynolds shear stress distribution in curved channel with ξ_1/d as parameter, comparison of theory (lines) and experiment (symbols)

in Fig. 13, unlike the straight channel case (Fig. 17), the curved channel shear stress is nonzero at the wake center because of the curvature effect that causes a pressure gradient in lateral direction resulting in a highly asymmetric distribution of shear stress profiles. Lakshminarayana and Raj (1973) also observed nonzero value of Reynolds shear stress at the wake center. In their investigation, Lakshminarayana and Raj found that the point where $\partial \bar{U}/\partial y = 0$ (the wake center) need not to be the same where the Reynolds stress is zero. They concluded that the mixing length hypothesis is not valid for predicting the mean and turbulent quantities in such a region.

The Reynolds shear stress in the hypothetical potential flow outside the wake is not exactly equal to zero due to the turbulence existing in that region. Measurements at selected longitudinal locations without the wake showed a lateral gradient of $\overline{uv}$ with a negative value near the concave wall and a positive value near the convex wall. The radial position where $\overline{uv} = 0$ was located between convex wall and mean radius of the channel. For example, at the longitudinal position $\theta = 0$ deg, $\overline{uv}$ was zero at $r - r_i = 120$ mm. Similar distribution of Reynolds shear stress has been observed in turbulent flows in curved channels as reported by Wattendorf (1935) and Eskinazi and Yeh (1956). The normalized Reynolds shear stress distributions in Fig. 13 have nonzero values outside the wake. Also the $\overline{uv}$ outside the wake has higher absolute value near the concave side of the wall ($\xi_2 < 0$).

The experimentally determined shear stress distributions shown in Fig. 13(*a, b*) are compared with the developed theory. As shown in section 2, the shear stress was calculated as the difference of the total impulse and the partial impulse $\overline{uv} = \overline{UV} - \bar{U}\bar{V}$ by integrating the conservation equations. The integration constants in the corresponding expressions were evaluated from experimental measurements corresponding to the values at the wake center. As can be seen from Fig. 13(*a, b*), the excellent agreement between the theory and the measurement over the entire range, particularly the precise prediction of the asymmetric pattern, proves the validity of the assumptions necessary in developing the theoretical framework.

The lateral distribution of the nondimensionalized Reynolds normal stresses is presented in Figs. 14 and 15. The Reynolds normal stresses are normalized with respect to their values at the wake center. These values are listed in Table 1 for different longitudinal locations. The Reynolds stress component in the longitudinal direction is shown in Fig. 14. They exhibit a pronounced asymmetric pattern with respect to the wake center with one maximum on each side of the wake center and a minimum at the wake center. A similar pattern is reported by Koyama (1983) and Nakayama (1987). It is observed that the asymmetry of the longitudinal component of Reynolds stress increases with the downstream location. The measurement of the lateral component of Reynolds normal stress (see Fig. 15) reveals a similar pattern, as discussed above. It is worth noting that in case of straight wakes, this Reynolds stress component has a fully symmetric pattern with two identical maxima and one minimum at the wake center. (see Reichardt, 1950; Eifler, 1975; Pfeil and Eifler, 1975a, b).

It should be pointed out that the Reynolds normal stresses are not directly calculated. However, based on experimental results for curved and straight wakes and following the hypothesis of Prandtl (1942) concerning the local dependency of turbulence quantities, it was assumed that the longitudinal and lateral Reynolds stress components are functions of ζ only, resulting in functional relationships that describe $u^2/u_0^2 = f_1(R, \zeta)\varphi_1$ and $v^2/v_0^2 = f_2(R, \zeta)\varphi_1$. Using a second-order polynomial ansatz for the longitudinal Reynolds stress component and calculating the coefficients from the experimental results shown in Fig. 14, the following correlations were derived for a curved channel:

$$\frac{\overline{u^2}}{\overline{u_0^2}} = \frac{R}{R + \xi_2}\left(1 + \frac{b}{R}\zeta + 1.5\zeta^2\right)e^{-\zeta^2} \qquad (50)$$

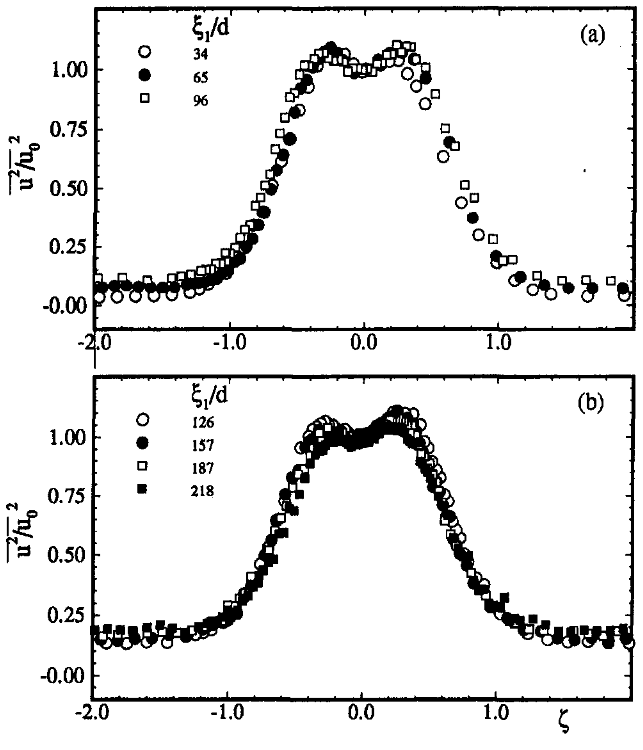

Fig. 14 Nondimensional mean longitudinal turbulent fluctuation impulse distribution in curved channel with ξ_1/d as parameter

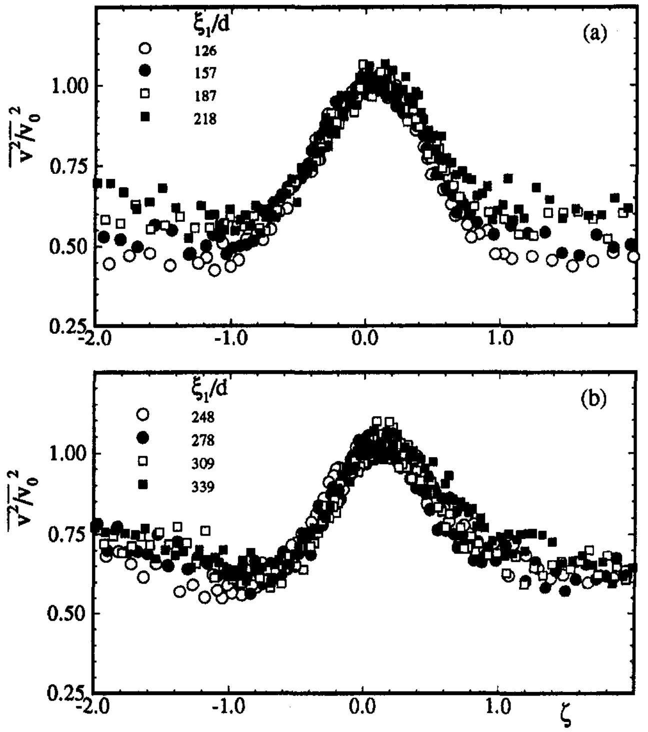

Fig. 15 Nondimensional mean lateral turbulent fluctuation impulse distribution in curved channel with ξ_1/d as parameter

and for a straight channel:

$$\frac{\overline{u^2}}{u_0^2} = (1 + 2.668\zeta^2)e^{-\zeta^2} \qquad (51)$$

Since these relations are purely empirical correlations, they are

Table 1 Values of selected quantities of the steady wake at zero streamwise pressure gradient

θ deg	ξ_1/d	$\bar{U}_{1m}$ (m/s)	b (mm)	$\bar{U}_{po}$ (m/s)	$\overline{u_o^2}$ (m²/s²)	$\overline{v_o^2}$ (m²/s²)	$\bar{V}_{in}$ (m/s)
0	34	2.598	7.44	20.02	1.862	2.004	19.31
5	65	1.734	11.27	20.07	0.880	0.727	19.29
10	96	1.392	13.78	20.12	0.629	0.476	19.30
15	126	1.217	16.76	20.51	0.531	0.401	19.35
20	157	1.084	19.88	20.57	0.470	0.357	19.32
25	187	0.905	22.88	20.60	0.419	0.343	19.32
30	218	0.846	26.13	20.38	0.375	0.322	19.33
35	248	0.686	27.34	18.77	0.300	0.280	19.37
40	278	0.611	33.88	19.11	0.273	0.299	19.34
45	309	0.540	36.92	19.11	0.263	0.289	19.33
50	339	0.494	33.96	19.49	0.253	0.305	19.32
55	370	0.491	39.87	20.03	0.245	0.326	19.33
60	400	0.469	45.91	19.59	0.225	0.326	19.31
65	431	0.445	49.21	20.26	0.229	0.350	19.37
70	461	0.453	47.70	20.31	0.218	0.352	19.39

not plotted in Fig. 14 to avoid any possible confusion with the theoretical results presented in this paper.

5.2 Straight Channel Wake Flow. The straight channel wake flow has been treated by theory as a special case of curved channel wake flow, where the radius of curvature approaches infinity. To demonstrate the general validity of the theoretical framework developed in section 2 with radius of curvature approaching infinity, it was found necessary to compare the theoretical results with the available experimental data from the literature. For this purpose, the experimental work by Eifler (1975) was chosen because it is probably the most comprehensive research work in this area and entails all the detailed information necessary for a theoretical evaluation and comparison. Eifler carried out an experimental study of cylinder wake characteristics for a wide range of longitudinal locations and also for different diameters of cylinders in a straight channel.

Comparisons of theory and experiment of mean wake velocity defect function for several cylinder diameters at different longitudinal locations were carried out, from which only Fig. 16 with $d = 2$ mm is presented here. According to this comparison, wake development in the longitudinal direction depends primarily upon the ratio x/d (ξ_1/d for curved wake) regardless of the separate variation of the parameters involved in this ratio. The excellent agreement of theory verifies the validity of the expression $\varphi_1 = e^{-\zeta^2}$. The same expression was found to predict both cases of straight and curved channel wake flows, provided that the wake velocity defect is defined properly.

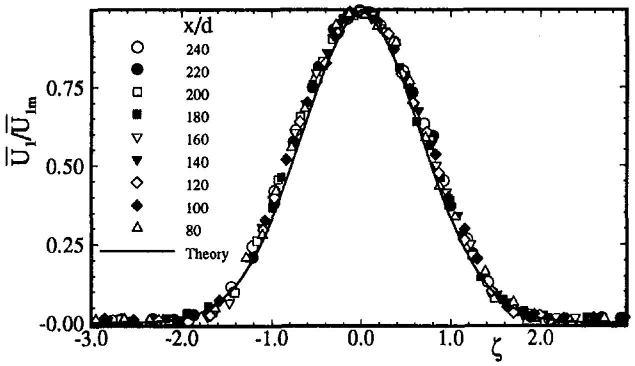

Fig. 16 Nondimensional mean velocity defect distribution in straight channel, theory (solid lines) compared with experimental data (symbols) from Eifler (1975), $d = 2$ mm

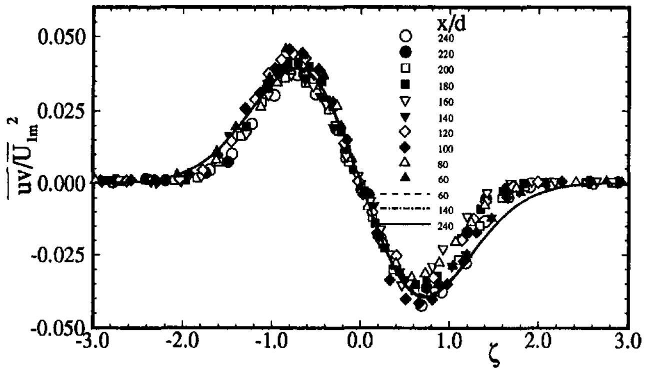

Fig. 17 Nondimensional Reynolds shear stress distribution in straight channel, theory (lines) compared with experimental data (symbols) from Eifler (1975), $d = 2$ mm

Reynolds shear stress distributions for a cylinder diameter $d = 2$ mm at different longitudinal locations are shown in Fig. 17. The shear stress distribution is found to be symmetric about the wake center with a value of zero at the wake center. Thus, the integration constant in the expression for shear stress derived in section 2 vanishes. From the comparison, it is obvious that theory is in excellent agreement with measurement with the peaks being predicted quite reasonably.

6 Conclusions

The development of a wake flow downstream of a cylindrical rod within a curved channel under zero longitudinal pressure gradient is theoretically and experimentally investigated. The theoretical framework generally describes the wake flow through two-dimensional curvilinear channels. It also describes the wake development through two-dimensional straight channel as a special case, for which the curvature radius approaches infinity. Detailed experimental results are presented and compared with the developed theory. Mean and turbulence quantities were measured and were transformed from the probe coordinate system into the curvilinear wake eigencoordinate system. In contrast to the straight wake flow, the mean quantities of the curved wake including the longitudinal and lateral velocity components displayed an asymmetric pattern throughout the flow regime. The introduction of the velocity defect function and the wake width b as a single length scale resulted in a fully symmetric distribution of the nondimensionalized velocity defect $\varphi_1 = \bar{U}_1/\bar{U}_{1m} = f(\zeta = \xi_2/b)$. For the zero pressure gradient curved wake as well as straight wake, the experimental results have proved that the wake defect can be described by the function $\varphi_1 = e^{-\zeta^2}$. This function was implemented in the theory developed to calculate the total impulse $\overline{UV}$, the partial impulse $\bar{U}\bar{V}$, and the resulting shear stress $\overline{uv} = \overline{UV} - \bar{U}\bar{V}$. The experimental results were compared with the theory developed in section 2 of this study. It was shown that the new theoretical framework developed is capable of predicting the zero-pressure gradient wake flow for both curved and straight channel boundary conditions. For further validation of the theory, efforts are under way to prove the general validity of the theory using nonzero pressure gradient cases within the absolute frame of reference.

Dedication

The principal author would like to dedicate this paper to Prof.-Dr.-Ing. Horst Pfeil, with whom he had a very fruitful cooperation at the Technical University Darmstadt, for more than ten years. Prof. Pfeil showed consistently great interest in this research. Two years ago, Prof. Pfeil unfortunately died due to serious illness.

Acknowledgments

The principal investigator and his students would like to express their sincere thanks and appreciations to Dr. R. Simoneau, Chief Heat Transfer Branch, and Mrs. B. Lucci and the administration of the NASA Lewis Research Center for the continuous cooperation and support of this project.

References

Eifler, J., 1975, ''Zur Frage der freien turbulenten Strömungen, insbesondere hinter ruhenden und bewegten Zylindern,'' Dissertation D-17, Technische Hochschule Darmstadt, Germany.

Ermshaus, R., 1970, ''*Eigenümlichketen turbulenter Nachlaufströmungen*,'' Mitt. a.d. Max-Planck-Inst. für Strömungsforschung No. 46. Göttingen.

Eskinazi, S., and Yeh, H., 1956, ''An Investigation on Fully Developed Turbulent Flows in a Curved Channel,'' *Journal of the Aeronautical Sciences*, Vol. 23, pp. 23–34.

John, J., and Schobeiri, T., 1993, ''A Simple and Accurate Method for Calibrating X-Probes,'' ASME *Journal of Fluids Engineering*, Vol. 115.

Kiok, R., 1973, ''Einfluß des Turbulenzgrads auf die aerodynamischen Eigenschaften von ebenen Verzögerungsgittern,'' *Forsch. Ing.-Wes.*, Vol. 39, No. 1.

Koyama, H., 1983, ''Effect of Streamline Curvature on Laminar and Turbulent Wakes,'' *Proc. Fourth Symp. on Turbulent Shear Flows*, University of Karlsruhe, Karlsruhe, Germany, pp. 141–155.

Lakshminarayana, B., and Raj, R., 1973, ''Characteristics of the Wake Behind a Cascade of Airfoils,'' *Journal of Fluid Mechanics*, Vol. 81, part 4, pp. 707–730.

Lakshminarayana, B., and Raj, R., 1976, ''Three-Dimensional Characteristics of Turbulent Wakes Behind Rotors of Axial Flow Turbomachinery,'' ASME *Journal of Engineering for Power*, Vol. 98, pp. 218–228.

Nakayama, A., 1987, ''Curvature and Pressure-Gradient Effects on a Small-Defect Wake,'' *Journal of Fluid Mechanics*, Vol. 175, pp. 215–246.

Pfeil, H., and Eifler, J., 1975a, ''Zur Frage der Schubspannungsverteilung für die ebenen freien turbulenten Strömungen,'' *Forschung, Ing.-Wes.*, Vol. 41, No. 4, pp. 105–112.

Pfeil, H., and Eifler, J., 1975b, ''Messungen im turbulenten Nachlauf des Einzelzylinders,'' *Forschung. Ind.-Wes.*, Vol. 41, No. 5, pp. 137–145.

Prandtl, L., 1942, ''Bemerkungen zur Theorie der freien Turbulenz,'' *Z. angew. Math. Mech. (ZAMM)*, Vol. 22, No. 5, pp. 241–254.

Reichardt, H., 1950, ''Gesetzmäßigkeiten der freien Turbulenz,'' *VDI-Forsch.-Heft*, Vol. 414, No. 2. Auflage Düsseldorf, VDI-Verlag.

Roshko, A., 1953, ''On the Development of Turbulent Wakes From Vortex Streets,'' NACA Technical Note 2913.

Savill, A. M., 1983, ''The Turbulent Structure of a Highly Curved Two-Dimensional Wake,'' in: *IUTAM Symposium on Complex Turbulent Flows*. R. Dumas and F. Fulachier, eds., Marseille, Springer: Berlin–Heidelberg–New York, pp. 185–197.

Schlichting, H., 1930, ''Über das ebene Windschattenproblem,'' *Ing.-Arch.*, Vol. 1, pp. 533–571.

Schobeiri, T., 1976, ''Näherungslösung der Navier-Stokes'schen Differentialgleichung für eine zweidimensionale stationäre Laminarströmung konstanter Viskosität in konvexen und konkaven Diffusoren und Düsen,'' *Zeitschrift für angewandte Mathematik und Physik*, Vol. 27, Fasc. 1.

Schobeiri, T., 1979, ''Theoretische und experimentelle Untersuchungen laminarer und turbulenter Strömungen in Diffusoren,'' Dissertation D-17, Technische Hochschule Darmstadt, Germany.

Schobeiri, T., 1988, ''Establishment of a Research Facility for Investigating the Effects of Unsteady Inlet Flow Condition, Pressure Gradient and Curvature on Boundary Layer Transition and Heat Transfer,'' Internal Report, Texas A&M University, Turbomachinery Laboratory.

Schobeiri, T., 1990, ''The Influence of Curvature and Pressure Gradient on the Flow Temperature and Velocity Distribution,'' *International Journal of Mechanical Sciences*, Vol. 32, pp. 851–861.

Schobeiri, T., and Pardivala, D., 1992, ''Development of a Subsonic Flow Research Facility for Simulating the Turbomachinery Flow and Investigating Its Effects on Boundary Layer Transition, Wake Development and Heat Transfer,'' *Fourth International Symposium on Transport Phenomena and Dynamics of Rotating Machinery*, pp. 98–114.

Schobeiri, T., and Pappu, K., 1994, ''Prediction of Characteristics of Two-Dimensional Turbulent Wakes Under the Influence of Streamline Curvature and Zero, Positive, and Negative Pressure Gradients,'' Final Contract Report, Part I, NAG3-1256, NASA Lewis Research Center.

Schobeiri, T., and John, J., 1994, ''A Study of the Development of Steady and Periodic Unsteady Turbulent Wakes Through Curved Channels at Positive, Zero, and Negative Streamwise Pressure Gradients,'' Final Contract Report, Part II, NAG3-1256, NASA Lewis Research Center.

Townsend, A. A., 1947, ''Measurements in the Turbulent Wake of a Cylinder,'' *Proceedings of the Royal Society*, London, Series A, Vol. 190, pp. 551–561.

Trost, N., 1975, ''Einfluß der Zuströmturbulenz auf die Strömung in Axialgittern,'' Dissertation an der Technischen Hochschule Darmsadt, Germany D 17.

Wattendorf, F. L., 1935, ''A Study of the Effect of Curvature on Fully Developed Turbulent Flow,'' *Proceedings of the Royal Society*, London, Vol. 148, pp. 565–598.

C. Kapteijn

J. Amecke

Institut für Strömungsmechanik,
Deutsche Forschungsanstalt
für Luft-und Raumfahrt e.V.,
Göttingen, Federal Republic of Germany

V. Michelassi

Department of Energetics,
University of Florence,
Florence, Italy

Aerodynamic Performance of a Transonic Turbine Guide Vane With Trailing Edge Coolant Ejection: Part I—Experimental Approach

Inlet guide vanes (IGV) of high-temperature gas turbines require an effective trailing edge cooling. But this cooling significantly influences the aerodynamic performance caused by the unavoidable thickening of the trailing edge and the interference of the cooling flow with the main flow. As part of a comprehensive research program, an inlet guide vane was designed and manufactured with two different trailing edge shapes. The results from the cascade tests show that the flow behavior upstream of the trailing edge remains unchanged. The homogeneous values downstream show higher turning and higher losses for the cut-back blade, especially in the supersonic range. Additional tests were conducted with carbon dioxide ejection, in order to analyze the mixing process downstream of the cascade.

Introduction

Efforts to reduce the specific fuel consumption and the specific weight of jet propulsion engines have resulted in a continuous increase of combustion chamber temperatures. A direct consequence is the rise of the turbine inlet temperature. To this purpose turbine blades are cooled. The second main objective of cooled blades is to avoid negative effects of the coolant ejection on the main turbine parameters, for example on the energy loss coefficient.

A detailed investigation of a single blade configuration, with a slot in the trailing edge, was presented by Sieverding [10]. The considerably enlarged trailing edge enabled detailed pressure measurements on both sides close to the slot. An empirical function for the back pressure was evaluated from these tests. Kost and Holmes [8] compared trailing edge ejection with ejection through holes on pressure (and partly on suction) side, where the stagger angle and the pitch-to-chord ratio differed for both configurations. Köllen and Koschel [7] tested a large number of coolant ejection configurations, all consisting of rows of holes. In their configuration with pressure side coolant ejection (type C) coolant is probably ejected upstream of the throat in contrary to the present study. The data presented by Köllen and Koschel were restricted to subsonic flow.

Therefore the performances of two basically identical internally cooled stator blades with different configurations of the coolant flow exit were compared during experiments carried out in an ambient flow suction type cascade tunnel (EGG Göttingen). These experiments were conduced in the framework of a BRITE/EURAM-project. The participating members were: SNECMA, Alfa Romeo Avio, MTU, VKI, DLR, and the University of Florence.

Aerodesign of the Cascade

The overall design characteristics of the IGV were chosen to be representative for an advanced aero-engine and the mean blade section was optimized following actual design practice. Two different blade configurations were considered:

- Coolant ejection through the trailing edge (called TE ejection blade)
- Coolant ejection from the pressure side near the trailing edge (called PS ejection blade)

It appeared advantageous that, for the comparison of the wake mixing downstream of the cascade, the velocity distribution and the shape should be the same over most of the blades. Hence an optimal blade section with provision for TE coolant ejection was designed and modified for PS coolant ejection. The design conditions for the cascade were defined as follows:

Isentropic outlet Mach No.	$M_{2,is} = 1.05$
Outlet flow angle	$\alpha_2 = 70...75$ deg
Pitch-to-chord ratio	$g/c = 0.75$
Chord length	$c = 72.00$ mm
Axial chord length	$c_{ax} = 43.10$ mm
Throat width TE blade	$b_{th} = 14.98$ mm
Throat width PS blade	$b_{th} = 15.30$ mm
Stagger angle	$\gamma = 51.9$ deg
Trailing edge thickness	$te = 1.70$ mm
Trailing edge wedge angle	$\delta = 6.4$ deg

The cascade geometry is presented in Fig. 1.

Description of the Straight Cascade Test Facility and the Measuring Systems

The wind tunnel for straight cascades at DLR Göttingen [5] is of the blow-down type with atmospheric inlet. The general arrangement is shown in Fig. 2.

The ambient air first enters a silicagel dryer, subsequently passes the inlet line equipped with a butterfly valve, two screens, and a honeycomb flow straightener, and enters the cascade downstream of the contraction. The test section is installed in a spacious walkable plenum chamber.

Downstream of the cascade, the flow passes the adjustable diffuser and the main butterfly valve and enters at last the large

---

Contributed by the International Gas Turbine Institute and presented at the 39th International Gas Turbine and Aeroengine Congress and Exposition, The Hague, The Netherlands, June 13–16, 1994. Manuscript received by the International Gas Turbine Institute February 25, 1994. Paper No. 94-GT-288. Associate Technical Editor: E. M. Greitzer.

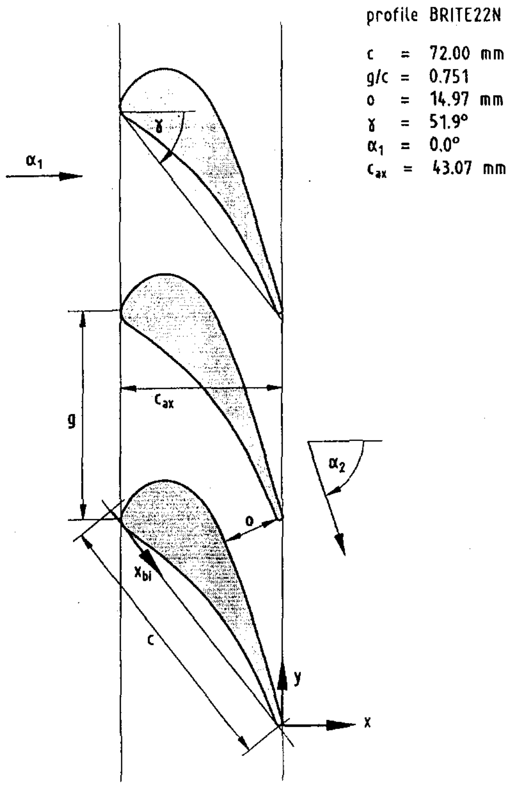

Fig. 1 Blade geometry

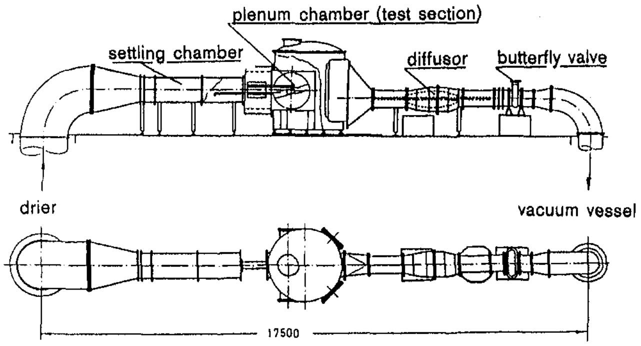

Fig. 2 Wind tunnel for straight cascades

vacuum vessel (10,000 m^3). This vessel is evacuated by two sets of sliding-vane vacuum pumps.

The inlet total pressure of the cascade is equal to the ambient pressure. The Reynolds number cannot be varied, but is in a limited range a function of the Mach number.

Every cascade is mounted with fixed geometric parameters (stagger angle, pitch-chord ratio) in a support frame, which is installed in the test section (Fig. 3), between two circular disks establishing the side walls of the flow channel. The inlet angle is adjusted by turning this assembly. The test section dimensions were 380 mm × 125 mm, allowing the cascade to consist of 8 blades. The four blades in the center of the cascade were equipped with coolant slots.

Near the centerline of the flow channel, the cascade support is equipped with exchangeable panes in which typically four blades (depending on the pitch-chord ratio) are fixed. In general, with respect to schlieren observations, mineral glass panes are installed in this location, but for special purposes (e.g., pressure distribution blades) steel panes are also in use.

The flow downstream of the cascade is not guided. Flow angle and Mach number are only adjusted in mutual dependency by the plenum pressure (i.e., setting of the diffuser).

For the development of high-pressure turbines, the investigation and optimization of cooled blades is of particular interest. Ejection of air or carbon dioxide (CO_2), to simulate the aerodynamic aspects from the blades mounted in the above-mentioned exchangeable panes, is enabled.

For tests with air ejection, the fluid is provided by the central high-pressure system. The air passes a standard measuring orifice (DIN 2071) and a remote-controlled valve for adjusting the desired mass flow rate. Finally the air is distributed by a manifold to both ends of the four blades equipped with ejection slots.

For the tests with CO_2 ejection, the fluid is provided by an isolated, mobile storage tank containing approximately 2000 kg CO_2 in liquid state. Normally enough of the CO_2 evaporates under ambient temperature conditions, and for higher flow rates this process is supported by an electrical heater. But due to the heat required for the vaporation together with the Joule-Thomson effect, the temperature of the CO_2 gas drops. Therefore a heat exchanger consisting of a pipe bundle (leading the CO_2 gas) in a water tank is installed downstream of the storage tank. The water is maintained at the desired gas temperature, which is asymptotically reached by the gas.

Further, the gaseous CO_2 is guided to test blades via the same installation as described above for the air ejection.

Upstream Flow Conditions

The total temperature T_{01} and the inlet total pressure P_{01} are measured in the settling chamber at very low velocities. The inlet static pressure p_1 is determined by 47 pressure taps on the side wall of the channel parallel to the inlet plane of the cascade. The measured inlet Mach numbers for both blade types are

Nomenclature

b_{th} = throat width
c = chord
C_b = base pressure coefficient
C_p = base pressure coefficient
g = pitch of the cascade
M = Mach number
M = molecular mass
p = pressure
T = temperature
Tu = turbulence degree
te = trailing edge thickness
v = velocity
x = coordinate normal to cascade plane
y = coordinate parallel to cascade plane
α = angle between flow direction and normal to the cascade plane
δ = trailing edge wedge angle
γ = stagger angle
ζ = energy loss coefficient
ϑ_v = volume fraction of carbon dioxide
ϑ_m = probability density
ξ = mass fraction of carbon dioxide
ρ = density
σ = standard deviation

Subscripts

0 = total (pressure, density, or temperature)
1 = homogeneous flow upstream
2 = homogeneous flow downstream
2y = measuring plane downstream
a = fluid a
ax = axial
b = fluid b
is = isentropic
m = mass
th = throat
v = volume

Superscripts

* = critical state

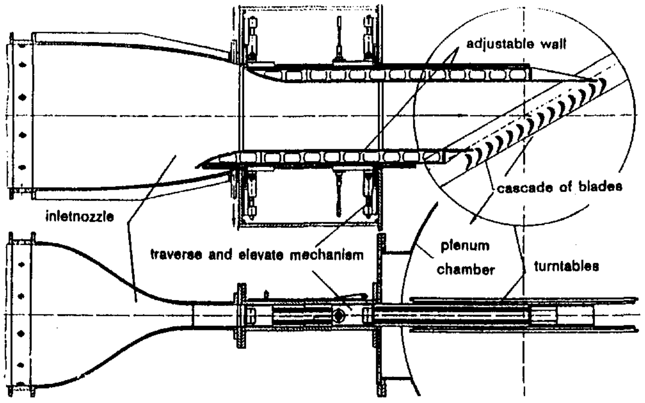

Fig. 3 Test section

presented in Fig. 4 as a function of the downstream Mach number for different ejection rates. All curves show the typical behavior of monotonous increase until approaching choking conditions. No significant difference is recognizable between the TE and the PS blade, although the geometric throat area of the latter is about 2 percent larger. The theoretical choking Mach number calculated from geometric throat width is additionally entered in the figures. The difference between the measured and the calculated choking Mach number is caused by the thick boundary layer at the end of the inlet channel and the reduction of this boundary layer thickness up to the throat on account of the acceleration (Gieß [4]). The observed equal choking Mach numbers for both blade types indicate that the cut-back area of the PS blade does not influence the passage flow seriously, because, when there is coolant ejection, the ejection flow fills up the cut-back area; when there is no coolant injection, a separation area exists at the cut-back area. Only under no-choking conditions and without ejection does the cut-back area affect the passage flow and slightly increase the inlet Mach number.

Tests With Air Ejection

The downstream isentropic Mach number ranged from 0.7 to 1.2 with a Mach number increment of 0.1, whereas the design Mach number 1.05 was included as well. Coolant flow rates were adjusted to 0, 2, 3 percent, i.e., the design coolant flow rate, and 4 percent.

Schlieren Pictures. The four center blades were to this purpose mounted in glass plates instead of the usually applied steel plates. Only for the cascade with PS blades is the effect of coolant ejection on the shock pattern significant; see Fig. 5. The two entirely visible blades in the photos are the two central blades of the four equipped with coolant slots. The presence of the step in the blade surface at the pressure side generates an additional shock as long as coolant ejection is absent. This shock disappears at a coolant mass flow rate c_m equal to or larger than 2 percent, due to displacement effects.

The gradually growing pattern from leading to trailing edge on the suction side is not to be interpreted as a boundary layer in the center of the cascade, as it is caused by dirt on the glass windows in which the blades are mounted. The wake behind the blades is clearly distinguishable in both pictures. The shock generated at the pressure side near the trailing edge reaches the suction side of the next blade and is reflected, inducing boundary layer separation from the blade. The reflected shock reaches the wake of the blade from which it was generated and is reflected again partially. The shock generated at the suction side is reflected by the wake of the blade mounted above and by the free-stream boundary layer, which can be seen in the upper right corner of the pictures.

Pressure Distribution. The local Mach number along the blade profile is based on the ratio of the pressure measured at the blade surface through the pressure tap and the inlet total pressure in front of the cascade. The position of the 39 pressure taps on the surface of the TE blade is demonstrated by Fig. 8, whereas Fig. 9 shows the 38 taps of the PS blade. The number of pressure taps in the vicinity of the trailing edge could not be further increased for mechanical reasons. After instrumentation of the TE ejection blade, it became clear that pressure taps No. 11 and 35 could not be used as the mounted tubes were squeezed flat. The position of tap No. 35 on the pressure side is not critical and, as the pressure rise on the suction side proved to be continuous until point 12, the measurements were accepted in this form.

Figure 6 shows the Mach number distribution at $M_{2,is} = 1.05$ along the blade with coolant slot in the trailing edge at 4 coolant mass flow rates $c_m = 0$, 2, 3, and 4 percent, with air as coolant. Near the position $x/c = 0.4$ on the suction side of the blade, the influence of the incident compression wave, which propagates from the trailing edge of the neighboring blade, becomes noticeable, which results in the origin of a boundary layer separation bubble. At about $x/c = 0.55$ the boundary layer probably reattaches. At $x/c > 0.55$ the Mach number rises continuously farther downstream along the blade. The effect of coolant ejection on the Mach number distribution is rather small, reducing the local maxima and minima in the Mach number distribution on the suction side.

Figure 7 contains the corresponding data for the blade with pressure side coolant ejection. In comparison with the already mentioned blade configuration, the same phenomena are recognizable in the Mach number distribution in the case of pressure side ejection. However, the onset of the boundary layer separation is at approximately $x/c = 0.3$ and reattachment takes place at about $x/c = 0.45$. The fact that the coolant ejection slot and, coupled to that, the throat between the blades are shifted over 7 mm in the upstream direction probably are responsible for this translation. The deviations in the area of boundary layer separation between Mach number distributions for flow with

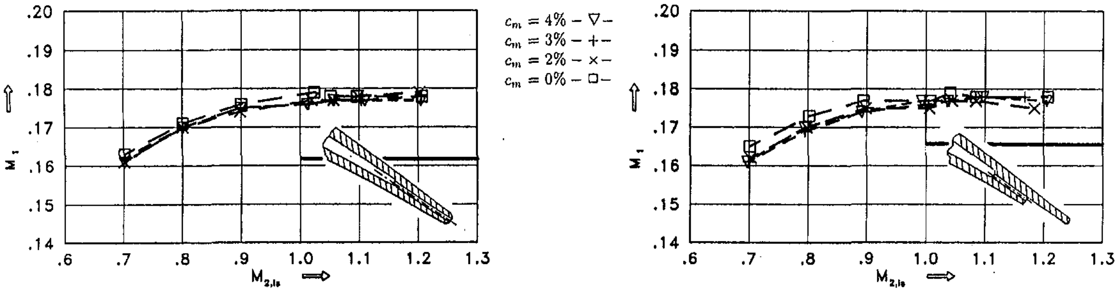

Fig. 4 Mach number in the rectangular inlet section. The horizontal line indicates the theoretically expected inlet Mach number at choking conditions.

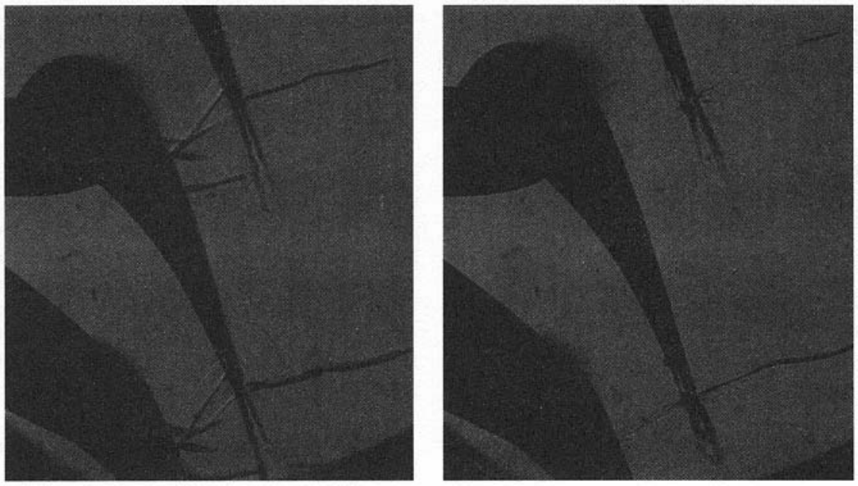

Fig. 5 Schlieren pictures of PS blades at $M_{2,is}$ = 1.05 and c_m = 0 percent (left), c_m = 3 percent (right)

and without coolant ejection are remarkable. Especially the high Mach number values in the area of boundary layer separation in the case of zero coolant ejection are striking.

For both blade types, the velocity distribution for the case of open coolant slots, but without coolant ejection, has been compared with the distribution for a cascade with closed slots. The purpose of this comparison was the elucidation of three-dimensional effects in the flow through the cascade on the internal flow in the cavities of the blades.

The blade surface Mach number distribution at $M_{2,is} = 1.05$ for the blade with coolant slot in the trailing edge, see Fig. 8, shows only very small differences between open and closed coolant slots. The differences are of the order of magnitude of the measurement errors. In Fig. 9 the corresponding Mach number distribution for the PS ejection blades is drawn. Discrepancies are visible at the pressure side of the blade at the position of the coolant slot and at the trailing edge. At both points, especially at the coolant ejection slot, the measured pressure is smaller in case of a closed slot. At the suction side of the blade, a deviation is measured at the position where the compression shock from the trailing edge of the above-mounted blade reaches the boundary layer.

A comparison of the Mach number curves in Figs. 7 and 9 proves that the suction side of the curve in Fig. 7 almost behaves as the closed slot curve in Fig. 9. The reason for this discrepancy is that a tiny deviation in the shock angle (or position) causes the attachment point on the suction side of the next blade to shift from just downstream of pressure tap No. 15 to an upstream position. Therefore, the differences between the curves in this area are of less importance. The conclusion is that, based on the present restricted set of measurements, i.e., without wake measurements at different blade height positions, the coolant slots have minimal three-dimensional effects. The only influence remains at the coolant slot of the PS blade (tap No. 26).

Base Pressure Coefficients. The pressure tap for measuring the base pressure P_b on the TE ejection blade is positioned in one of the struts in the coolant ejection slot (No. 25 in Fig. 8). This implies that the measurement point is not at midblade height. The blade with PS ejection offers two possibilities to measure P_b: (1) in the suction side trailing edge (No. 25 in Fig. 9), and (2) in the edge of the pressure side at the coolant ejection slot (No. 26 in Fig. 9).

Various base pressure coefficients may be deduced from the pressure measurements along the blade described in the previous section:

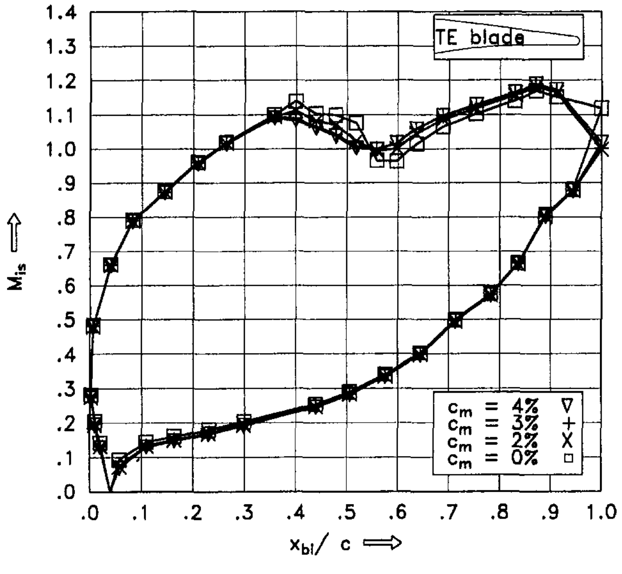

Fig. 6 Mach number distribution over the TE blade at $M_{2,is}$ = 1.05

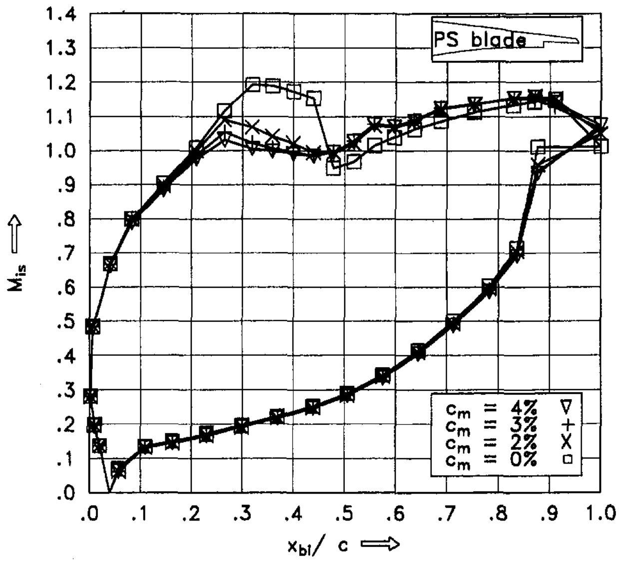

Fig. 7 Mach number distribution over the PS blade at $M_{2,is}$ = 1.05

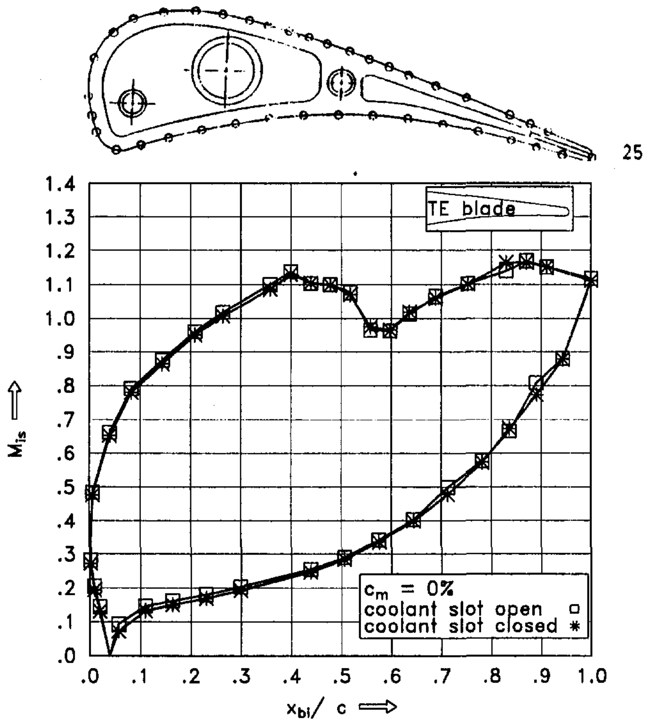

Fig. 8 Pressure taps (SNECMA) and Mach number distribution over the TE blade without coolant ejection at $M_{2,is} = 1.05$ with open (□) and closed (✱) slots

$$C_b = \frac{P_b - P_2}{P_{01}} \tag{1}$$

$$C_p = \frac{P_b - P_2}{\frac{\rho_2}{2} \cdot v_2^2} \tag{2}$$

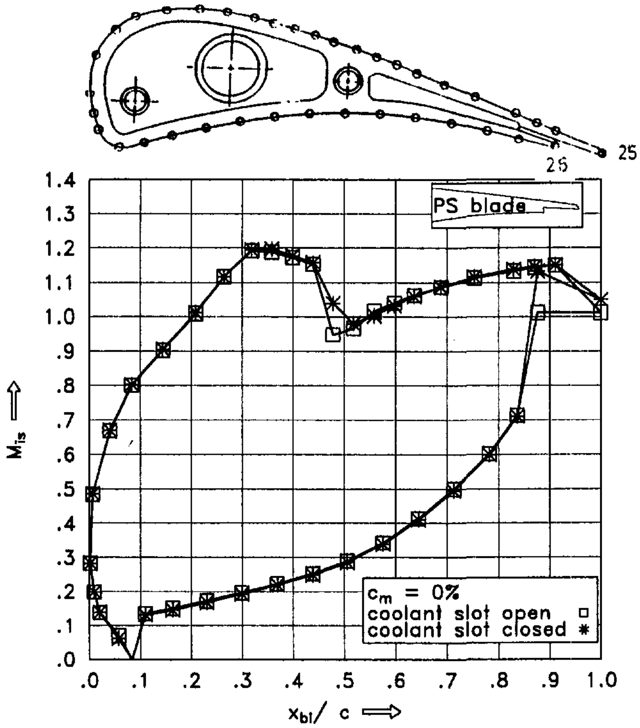

Fig. 9 Pressure taps (SNECMA) and Mach number distribution over the PS blade without coolant ejection at $M_{2,is} = 1.05$ with open (□) and closed (✱) slots

C_p graphs according to Eq. (2) are presented in Fig. 10 for both blade configurations:

$$C_{p*} = \frac{P_b - P_b^*}{\frac{\rho_2}{2} \cdot v_2^2} \tag{3}$$

P_b^* is the base pressure at the same downstream isentropic Mach number without coolant ejection and with closed ejection slot. Figure 11 shows C_{p*} values according to Eq. (3), for the blades with TE and PS ejection, respectively.

At the trailing edge itself, both types of blade show similar tendencies for the variation of C_p (or C_b) with Mach number; i.e., a maximum near $M_{2,is} = 1.0$ and a minimum at $M_{2,is} = 1.1$. The strong decrease in C_b from $M_{2,is} = 1.0$ to $M_{2,is} = 1.1$ can be explained by the shock movement from a position in front of the trailing edge to a position behind the trailing edge.

In contrast to this, the base pressure behind the step of the PS ejection blade exhibits a steady increase with Mach number.

As expected, coolant ejection increases the base pressure, because coolant is diluted in the wake.

The coefficient C_{p*} gives the difference between the base pressure with coolant, to the datum base pressure without coolant. The abscissa p_{0c} is the total pressure of the coolant in the ejection slot. This total pressure increases monotonically with coolant flow rate. Accordingly the curves in Fig. 11 show the

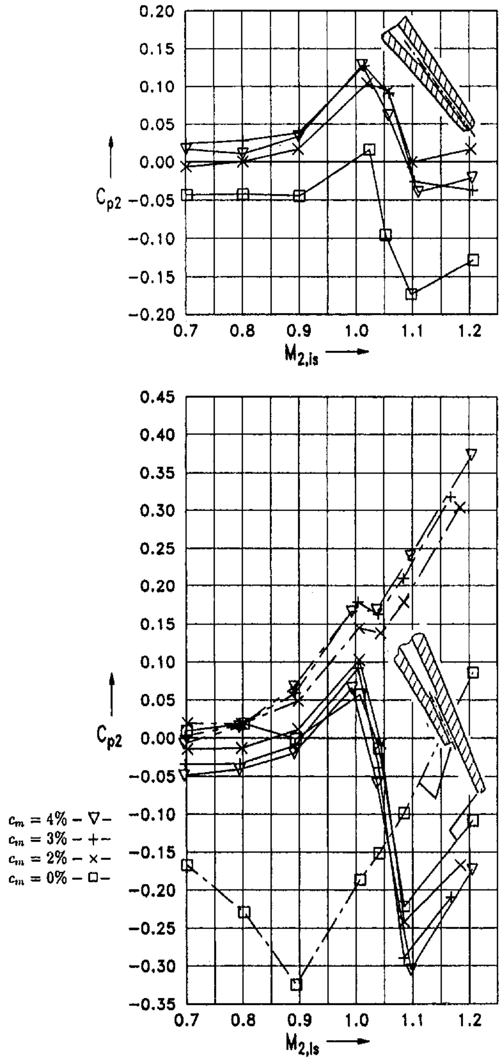

Fig. 10 C_p For TE and PS blades

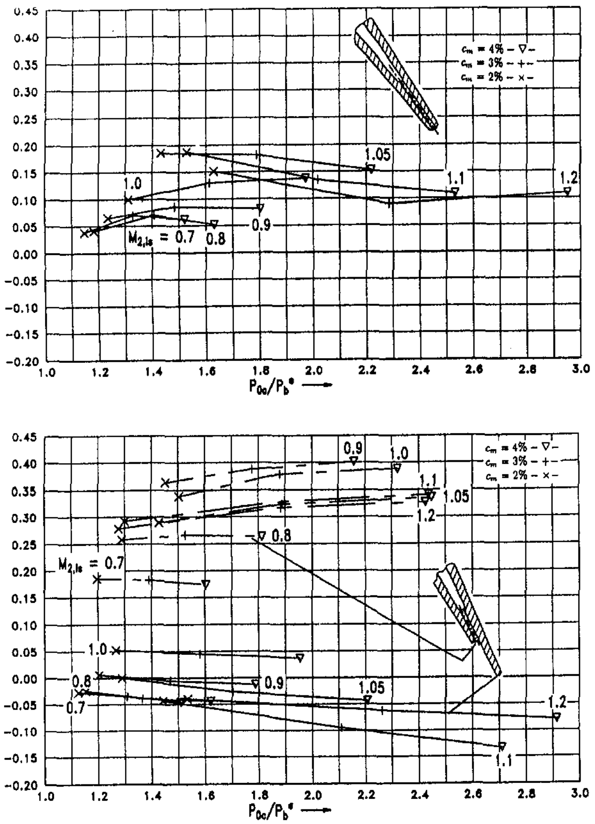

Fig. 11 C_{p^*} for TE and PS blades

influence of cooling flow rate on the base pressure. These curves do not show a strong dependency upon total pressure of the coolant.

When interpreting these graphs, one should bear in mind that these C_{p^*} values should all go to zero at P_{0c}/P_b^* equal to 1.0. The difference between the base pressure coefficient at small coolant mass flow rate and this point without coolant flow demonstrates that there is in fact an effect of coolant flow ejection, which is more or less confined to small coolant flow rates.

Wake Measurements. The measurements of total pressure, static pressure, and flow angle in the wake of the cascade were carried out with a wedge type probe at an axial distance of 35 mm to the cascade exit plane, i.e., at $x/c_{ax} = 0.813$. The length of the traverse parallel to the cascade exit plane was approximately 200 mm, which corresponds to nearly four pitches (g = 54.01 mm) downstream of the four center blades in the cascade equipped with coolant slots. Data were recorded every 1.5 mm. The graphs in this section present the homogeneous flow data belonging to the pitch in which the wake of the second cooled blade, counted in the cascade from bottom to top, is contained. The flow angle of the homogeneous downstream flow (α_2) and the energy loss coefficient (ζ) are plotted as a function of the isentropic downstream Mach number ($M_{2,is}$), with the coolant flow ratio as parameter for both blade types in Figs. 12 and 13.

According to Fig. 12, the deflection of the flow reaches its maximum near $M_{2,is} = 1.0$, for both blade configurations. The influence of coolant ejection on the flow deflection α_2 differs for both blade types: For the TE blade, α_2 decreases with increasing coolant flow rate c_m. Ejection of coolant through the PS blade on the other hand enhances the flow deflection except for the maximum Mach number, i.e., $M_{2,is} = 1.2$.

The energy loss coefficient ζ is based on the energy difference across the cascade, without taking into account the energy input as a result of the coolant ejection. ζ in Fig. 13 is almost constant in the Mach number region up to $M_{2,is} = 1.0$. At higher Mach numbers the losses rapidly rise. At design conditions, i.e., $M_{2,is}$ = 1.05, ζ has already clearly risen. Generally the losses of the PS blade are higher than for the TE blade, with the exception of the design point, where they happen to be equal. Coolant ejection for the lower Mach numbers reduces the losses. This tendency is reversed for the highest Mach number.

Wake measurement data, i.e., total pressure ratio, flow angle, and static- to total-pressure ratio, are drawn in Fig. 14 for the TE, as well as for the PS configuration at $M_{2,is} = 1.05$, with air ejection at a rate c_m = 3 percent.

In Fig. 15 the experimentally obtained energy loss coefficient, in the case of the PS blade, is compared with calculated loss data at two coolant flow rates (c_m = 0 percent, c_m = 3 percent). The numerical loss is approximately equal to the measured loss at $M_{2,is} = 0.8$. At $M_{2,is} = 1.05$, a discrepancy exists between experiment and calculation, especially without coolant ejection. At $M_{2,is} = 1.2$, the differences have sharply fallen again.

Turbulence Measurements. Turbulence measurements were carried out in the settling chamber and in the rectangular inlet section upstream of the cascade. The measurements were made with a hot-wire probe and a hot-film probe. For reasons of mechanical probe stability, downstream of the cascade only the hot-film probe was used. During the measurements in the inlet section, $M_{2,is}$ was held at 0.8. Typical corresponding flow velocities are 6 m/s in the circular inlet duct and 60 m/s in the rectangular inlet section.

The velocity component u is assumed to be in the direction of the time mean velocity. Upstream of the cascade, u is therefore

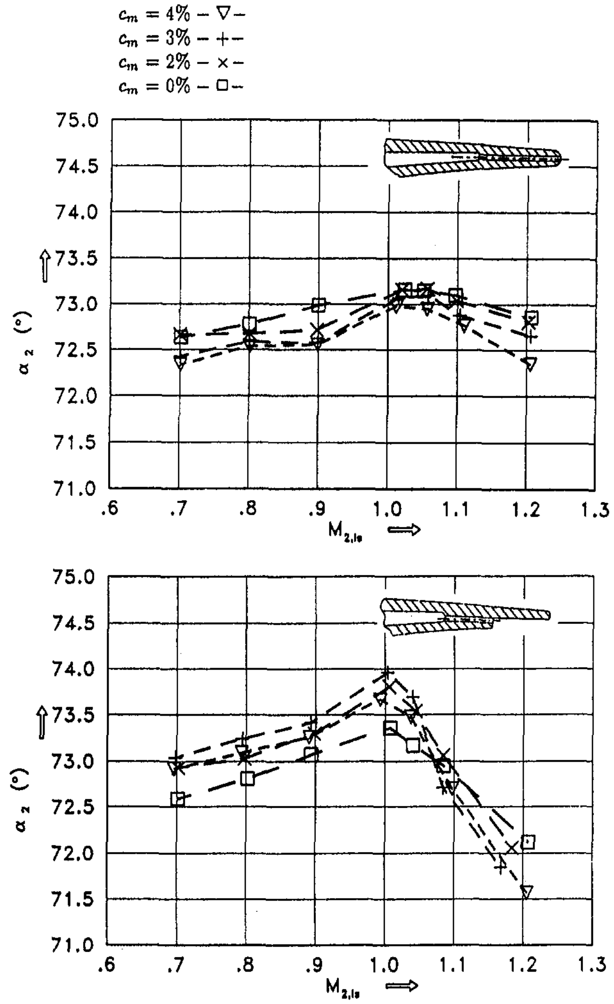

Fig. 12 Flow angle for the homogeneous flow

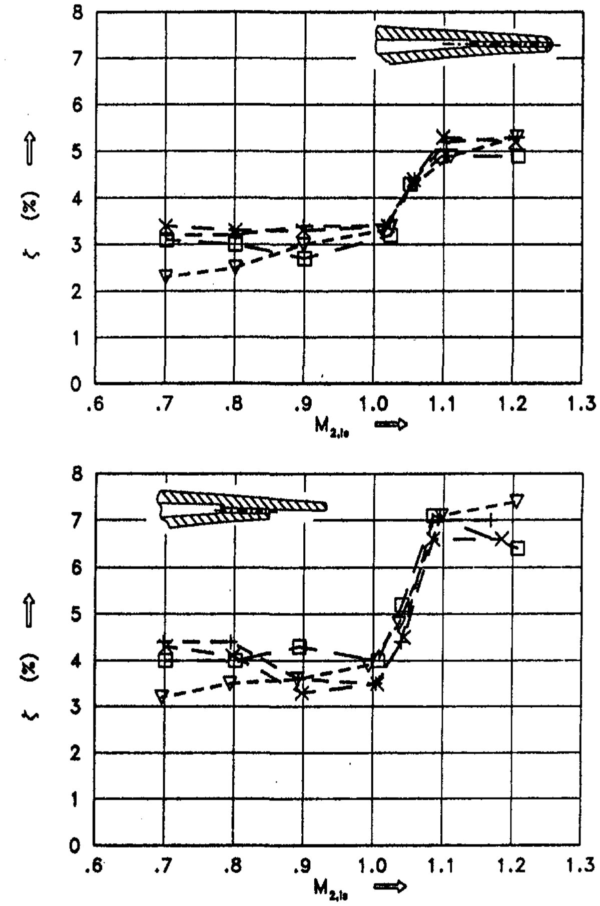

Fig. 13 Energy loss coefficient for the homogeneous flow

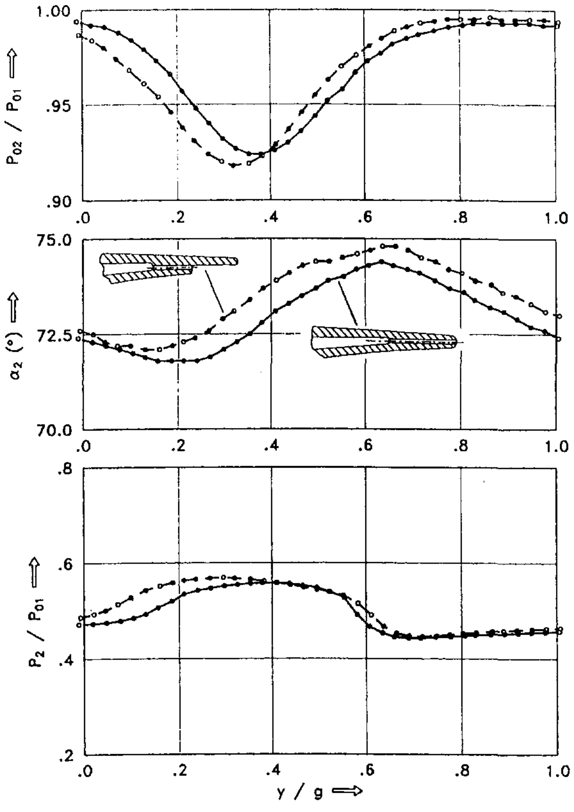

Fig. 14 Wake traverse at $M_{2,is}$ = 1.05

usually in axial direction; however, downstream of the cascade, this no longer holds. The three velocity components are split into their time mean values ($\bar u$, $\bar v$, $\bar w$) and fluctuations in time (u', v', w'), with $\bar v = \bar w = 0$. Further, it is assumed that the rms values of the velocity fluctuations in all three directions are identical. The evaluation of the data was carried out in accordance with the procedure described by Höhler and Baumgarten [6]. In case of isothermal, incompressible flow, King's law is reduced to the following equation:

$$\frac{\bar e^2 - \bar e_0^2}{\Delta T} = B\bar u^{1/n} \qquad (4)$$

where ΔT is the overheat temperature of the wire or film with respect to the flow, $\bar u$ is the time mean velocity, $\bar e$ denotes the anemometer output voltage, $\bar e_0$ is the output voltage when the flow velocity is zero. B and n are calibration constants, $n \simeq 2$. The velocity fluctuations are assumed to be small, leading to the approximation:

$$\frac{\bar u}{u_\infty} = \left(\frac{\bar e^2 - \bar e_0^2}{\bar e_\infty^2 - \bar e_0^2}\right)^n \qquad (5)$$

The turbulence degree Tu may then be written as

$$Tu = \frac{\sqrt{\overline{u'^2}}}{u_\infty} = \sqrt{\overline{e'^2}}\, 2n\bar e \frac{\bar e^2 - \bar e_0^2}{(\bar e_\infty^2 - \bar e_0^2)^2} \qquad (6)$$

where u_∞ represents the mean velocity undisturbed by a boundary or a wake.

After the contraction to the rectangular inlet section, the turbulence degree amounts to 0.5 percent for the hot wire and 0.4 percent for the hot film, as shown in Fig. 16. A possible reason for the discrepancy between the results of the two measurement systems might be the smaller frequency range of the hot-film probes, whose maximum detectable frequency is lower.

Downstream of the cascade, the interpretation of the measurement data is restricted to a qualitative interpretation. The influence of coolant ejection is clearly distinguishable in the wake at $x/c_{ax} = 0.813$ for $M_{2,is} = 0.80$. In case of choked flow in the cascade, on the other hand, an effect of coolant ejection in a distinct direction is only scarcely visible.

Tests With Carbon Dioxide Ejection

Data Reduction of Wake Flow Measurements. The standard data reduction system for the evaluation of cascade wake measurements takes into account the compressible flow field of

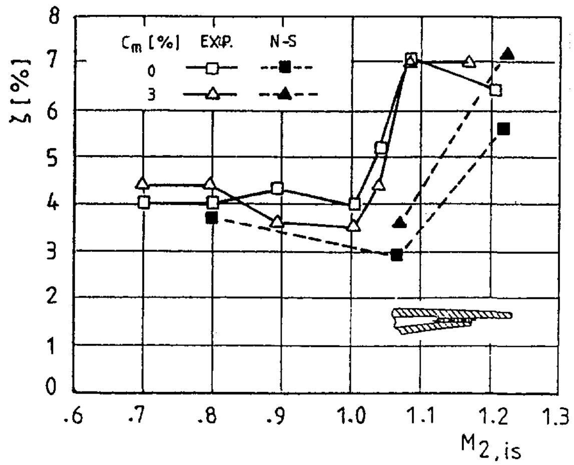

Fig. 15 Comparison of measured and calculated energy loss

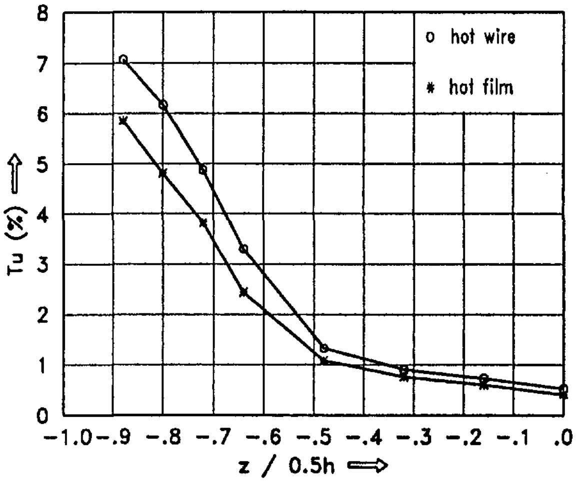

Fig. 16 Turbulence level in the rectangular inlet section

a homogeneous perfect gas with constant specific heat. It is based on the conservation laws for mass, momentum, and energy and is described in detail in [1, 2].

Usually, the total temperature in the entire flow field is assumed to be constant. To comply with this assumption for the present test series, the total temperature of the coolant flow is adjusted exactly to the total temperature of the main flow. This resolution avoids measuring the temperature in the wake flow field, which is generally burdened with strong errors. Nevertheless, the evaluation of tests with a variable (measured) total temperature is possible by application of the extended data reduction system from Oldfield et al. [9].

In the actual research program, additional tests were performed with the ejection of carbon dioxide (CO_2) in order to study the wake mixing process. Therefore, the gas concentration was measured in the wake in addition to the standard aerodynamic values (p_0, p, α) and consequently the data reduction system has to be extended to gas mixtures.

The applied analyzer yields the concentration of CO_2 as volume fraction (ϑ_v), which can be transformed into the mass fraction of the gas component (ϑ_m) with help of the molecular mass M of the components:

$$\vartheta_m = \frac{\vartheta_v M_{CO_2}}{(1 - \vartheta_v) M_{AIR} + \vartheta_v M_{CO_2}} \tag{7}$$

The comparison of the integrated CO_2 mass flow rate in the wake with the CO_2 mass flow rate measured in the supply line allows control of the accuracy of the wake flow measurement.

Wake Mixing Profiles. Tests with carbon dioxide ejection were carried out to elucidate the mixing process of the main flow and the coolant gas downstream of the cascade. This required wake traverses with a Pitot tube, a vacuum pump, and a CO_2 analyzer at more than one distance to the cascade exit plane, as is usual for the standard wake measurements. Therefore the gas concentration of carbon dioxide was determined during seven traverses at axial distances of 1, 2, 4, 7, 12, 20, and 35 mm from the plane containing the trailing edges of the blades (see Fig. 17). The distance between adjacent measurement positions ranged from 1.5 mm in the traverse at 35 mm distance to 0.1 mm in part of the traverse at 1 mm distance. The traverses at 7 mm and further downstream were attended with measurements of the flow angle and the total and static pressure by the wedge type pressure probe as in the usual wake traverses. Closer to the trailing edges of the blades, this probe could not be used any more for dimensional reasons. Instead of this, the concentration measurements at 1, 2, and 4 mm were accompanied with total pressure measurements by a Pitot tube. These experiments were carried out for 2 Mach numbers, i.e., $M_{2,is} = 0.80$ and $M_{2,is} = 1.05$, at a coolant mass flow rate of $c_m = 3$ percent.

The Gaussian curve gives a theoretical probability density distribution, the normal distribution function defined by:

$$\vartheta(y) = \frac{1}{\sqrt{2\pi}\,\sigma} \exp\left(-\frac{(y - \bar{y})^2}{2\sigma^2}\right) \tag{8}$$

where $\vartheta(y)$ is the probability for the variable to take the value y, $\bar{y}$ being the average value of y and σ the standard deviation. In the present case y is the pitchwise direction, $\vartheta(y)$ is the CO_2 concentration. Plotting σ in function of the axial distance quantifies the axial evolution of the concentration.

A better fit can be obtained taking two Gaussians: one for the pressure side and one for the suction side of the wake.

Integrating the normal function between $-\infty$ and $+\infty$ will result in 1. To fit a wake profile, $\vartheta(y)$ has to be multiplied by A, the area under the curve $f(y) = \vartheta$. The distribution functions are then:

$$\vartheta_{t,ps} = \frac{A_{ps}}{\sqrt{2\pi}\,\sigma_{ps}} \exp\left(-\frac{(y - \bar{y})^2}{2\sigma_{ps}^2}\right) \tag{9}$$

and

$$\vartheta_{t,ss} = \frac{A_{ss}}{\sqrt{2\pi}\,\sigma_{ss}} \exp\left(-\frac{(y - \bar{y})^2}{2\sigma_{ss}^2}\right) \tag{10}$$

for pressure side and suction side of the wake, respectively.

The abscissa of the curves is parallel to the cascade and not, as would seem obvious, normal to the flow downstream of

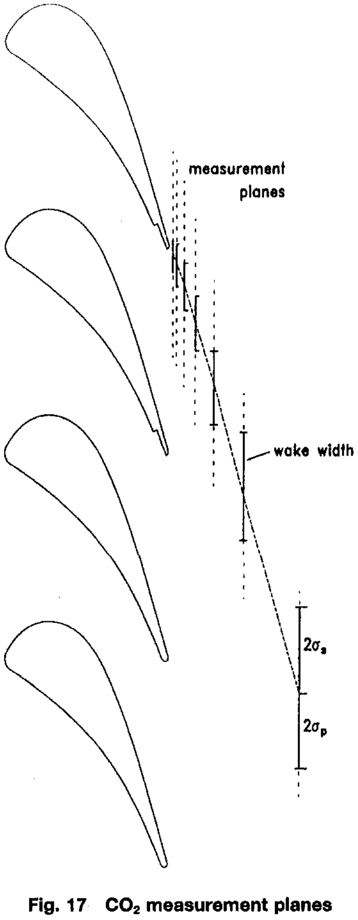

Fig. 17 CO_2 measurement planes

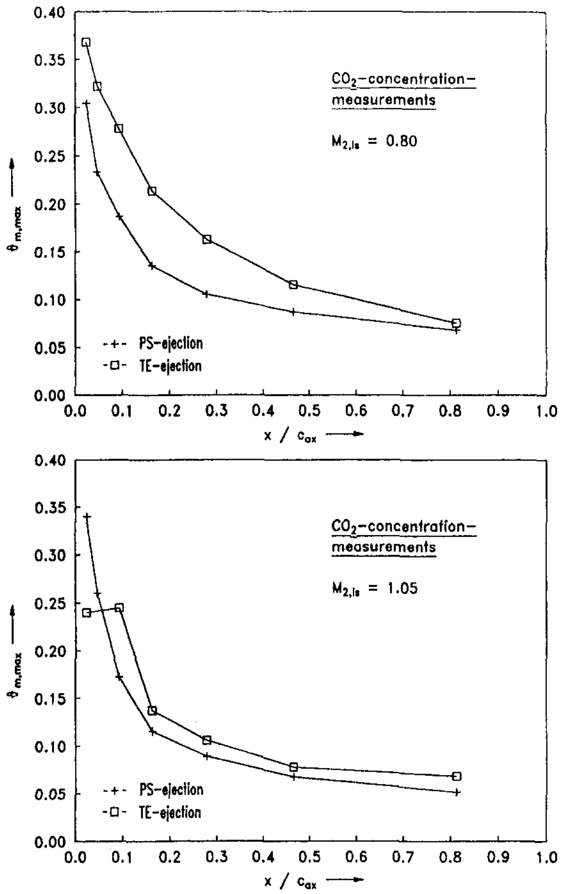

Fig. 18 Maximum CO_2 mass fraction

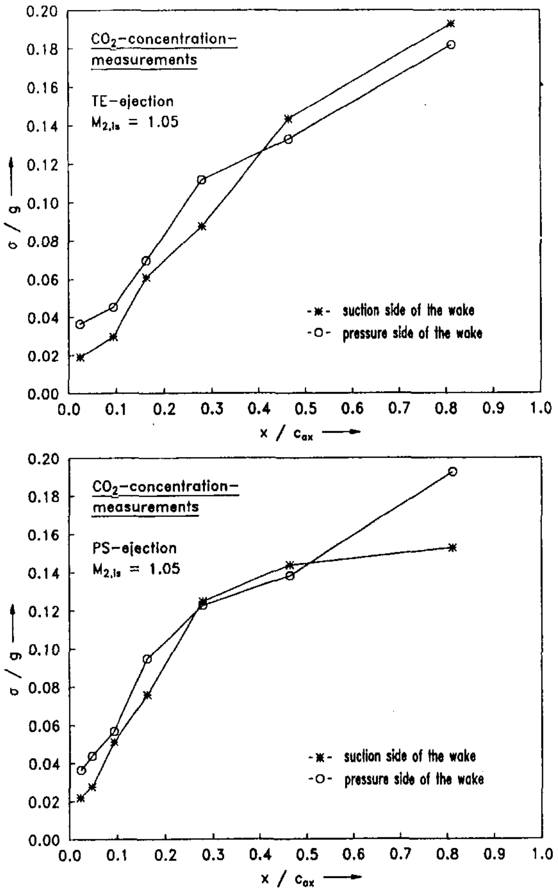

Fig. 19 Width of the CO_2 distribution

the blade. The transformation required to obtain the preferable orientation would have resulted in loss of information due to the large angle of rotation and the restricted number of measurement curves. The Gaussian curves fit reasonably well to the experimental data at axial distances from the cascade exit plane equal to or larger than 12 mm, i.e., $x/c_{ax} \geq 0.279$.

Figure 18 shows the maximum carbon dioxide concentration $\vartheta_{m,\max}$ for $M_{2,is} = 0.80$, and $M_{2,is} = 1.05$. The odd value of $\vartheta_{m,\max}$ at $x/c_{ax} = 0.023$ in Fig. 18 at $M_{2,is} = 1.05$ is caused by the analyzing system, which was operated at the limit of its momentary possibilities, especially due to a comparatively large pressure difference between the wake area just behind the blade at $M_{2,is} = 1.05$ and the atmosphere. The limitations are due to the capacity of the vacuum pump and the compromise between the dimensions of the gas sample probe, which has to be small so as not to disturb the flow, and the required gas sample time to get reliable measurement data.

The width of the wake, indicated by σ_{ps}/c and σ_{ss}/c, is displayed for $M_{2,is} = 1.05$ in Fig. 19, which demonstrates the continuous spread of carbon dioxide in the lateral direction with increasing distance to the trailing edge. This process is accompanied by a reduction of the maximum concentration, shown in Fig. 18.

The fact that the ejection slot of the blade with PS ejection is shifted in the upstream direction with respect to the slot position of the TE blade configuration (the difference amounts to $x/c_{ax} = 0.049$), leads to the expectation that at an identical probe position the mixing process might have further progressed in case of pressure side ejection. The maximum concentration curves in Fig. 18 confirm this assumption, although the support from the side of the σ curves is questionable.

A procedure similar to that on the concentration measurements was carried out on the measurements of the total pressure in the wake.

The total pressure ratio at $M_{2,is} = 1.05$, as measured with the wedge type probe at distances $x/c_{ax} \geq 0.049$ and as measured with a Pitot tube at smaller distances, is presented in Fig. 20 for the blade with PS ejection.

The best fitting asymmetric Gaussian curves through these measured data resulted in a maximum of the total pressure loss and wake width on the suction- and the pressure-side for every measurement plane. Figure 21 shows the maximum total pressure loss for $M_{2,is} = 0.80$ and for $M_{2,is} = 1.05$.

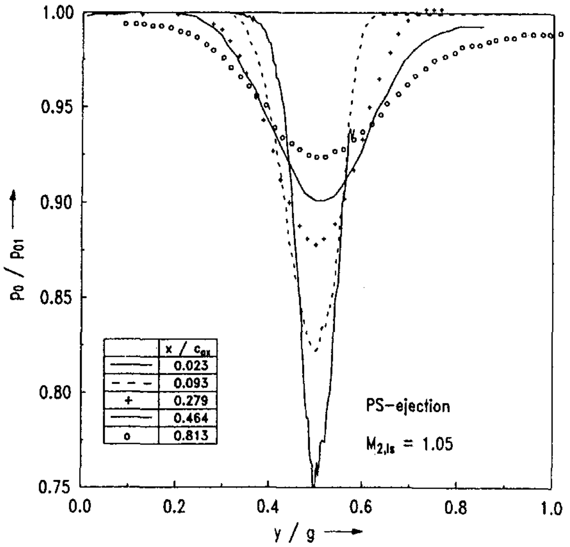

Fig. 20 P_0 distribution in the wake

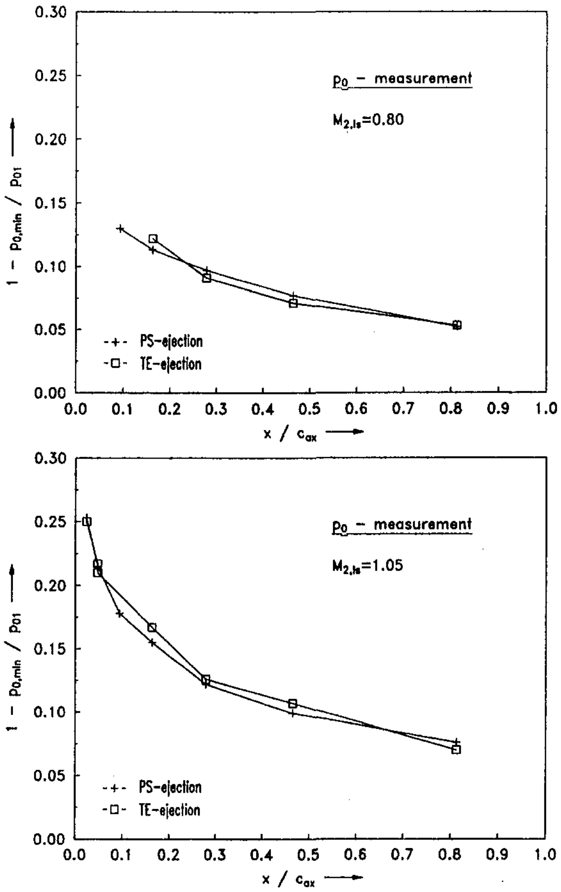

Fig. 21 Evolution of P_0 loss

Experimental Uncertainty

A detailed analysis of measurement errors and pitchwise variation was given by Baines et al. [3]. In general the measurement accuracy of ±0.003 for Mach numbers, ±0.4 deg for flow angles, and ±0.001 for energy loss coefficients at $M_{2,is} = 0.95$, as mentioned in [3], is still valid. The deviations between nominal and real profile on the other hand, of the order of 0.1 mm for this cascade, was large. Especially at the top and bottom sections of the cascade, where blades with and without coolant slots meet, the pitchwise variation rises. In the center part of the cascade with TE coolant ejection the variation in throat dimensions was $b_{th} = 14.97 \pm 0.07$ mm.

Conclusion

Two trailing edge designs for high-temperature gas turbine inlet guide vanes with coolant ejection were comparatively investigated in a cascade wind tunnel. The results are as follows:

- Ejection on the pressure side close to the trailing edge effects higher turning, but also higher losses than ejection through the (thicker) trailing edge.
- The evaluation of the wake mixing profiles indicates, that in subsonic flow the mixing for pressure side ejection takes place much faster than for trailing edge ejection. In supersonic flow no significant difference is observed.

Acknowledgments

The authors are grateful to the European Community for support of this research under contract BRITE/AERO 001.

References

1 Amecke, J., "Anwendung der transsonischen Ähnlichkeitsregel auf die Strömung durch ebene Schaufelgitter," *VDI-Forschungsheft*, No. 540, 1970.

2 Amecke, J., "Data Reduction of Wake Flow Measurements With Plane Cascades," DLR-Report IB 222-90 A 06, 1990.

3 Baines, N. C., Kiock, R., Lehthaus, F., and Sieverding, C. H., "A Comparison of Aerodynamic Measurements of the Transonic Flow Through a Plane Turbine Cascade in Four European Wind Tunnels," presented at the 8th Symposium on Measuring Techniques for Transonic and Supersonic Flow in Cascades and Turbomachines, Genoa, Italy, 1985.

4 Gieß, P.-A., "Berechnung der Abströmwinkel und Verluste bei sub- und transsonisch durchströmten Turbinengittern," *VDI-Forschungsheft*, No. 657, 1999.

5 Heinemann, H.-J., "The Test-Facility for Rectilinear Cascades (EGG) of the DFVLR," DFVLR-Report IB 222-83 A 14, 1983.

6 Höhler, G., and Baumgarten, D., "Boundary Layer and Turbulence Measurements in Test-Rig-ETW," DFVLR-Report IB 222-81 A 20, 1981.

7 Köllen, O., and Koschel, W., "Effect of Film Cooling on the Aerodynamic Performance of a Turbine Cascade," AGARD-CP-390, *Heat Transfer and Cooling in Gas Turbines*, 65th PEP Symposium, Bergen, 1999.

8 Kost, F. H., and Holmes, A. T., "Aerodynamic Effect of Coolant Ejection in the Rear Part of Transonic Rotor Blades," AGARD-CP-390, *Heat Transfer and Cooling in Gas Turbines*, 65th PEP Symposium, Bergen, 1999.

9 Oldfield, M. L. G., Schultz, D. L., and Nicholson, J. H., "Loss Measurements Using a Fast Traverse in an ILPT Transient Cascade," presented at: 6th Meeting on Measuring Techniques in Transonic and Supersonic Flows in Cascades and Turbomachines, Lyon, Oct. 15–16, 1981.

10 Sieverding, C. H., "The Influence of Trailing Edge Ejection on the Base Pressure in Transonic Turbine Cascades," ASME *Journal of Engineering for Power*, Vol. 105, 1983, pp. 215–222.

P. W. Giel

J. R. Sirbaugh

NYMA, Inc.,
NASA Lewis Research Center,
Brook Park, OH 44142

I. Lopez

U.S. Army Research Laboratory,
Vehicle Propulsion Directorate,
Lewis Research Center,
Cleveland, OH 44135

G. J. Van Fossen

NASA Lewis Research Center,
Internal Fluid Mechanics Division,
Cleveland, OH 44135

Three-Dimensional Navier–Stokes Analysis and Redesign of an Imbedded Bellmouth Nozzle in a Turbine Cascade Inlet Section

Experimental measurements in the inlet of a transonic turbine blade cascade showed unacceptable pitchwise flow nonuniformity. A three-dimensional, Navier–Stokes computational fluid dynamics (CFD) analysis of the imbedded bellmouth inlet in the facility was performed to identify and eliminate the source of the flow nonuniformity. The blockage and acceleration effects of the blades were accounted for by specifying a periodic static pressure exit condition interpolated from a separate three-dimensional Navier–Stokes CFD solution of flow around a single blade in an infinite cascade. Calculations of the original inlet geometry showed total pressure loss regions consistent in strength and location to experimental measurements. The results indicate that the distortions were caused by a pair of streamwise vortices that originated as a result of the interaction of the flow with the imbedded bellmouth. Computations were performed for an inlet geometry that eliminated the imbedded bellmouth by bridging the region between it and the upstream wall. This analysis indicated that eliminating the imbedded bellmouth nozzle also eliminates the pair of vortices, resulting in a flow with much greater pitchwise uniformity. Measurements taken with an installed redesigned inlet verify that the flow nonuniformity has indeed been eliminated.

1 Introduction

As the dependence on computational fluid dynamics and heat transfer increases in the design and analysis of turbomachinery, the need for detailed, benchmark quality experimental data also increases. These data are required for validation of codes and models as well as for determination of model functions and constants. As such, one requirement of a benchmark experiment is that more uniform, better documented, and generally higher quality inlet flow is needed. The results of a CFD calculation can be only as good as the boundary conditions, particularly the inlet conditions, that are applied to it. The importance of the inlet geometry and inlet conditions was pointed out in an experimental study by Kiock et al. (1985) where the same blade shape was examined in four wind tunnels and it was shown that only two of the tunnels exhibited two-dimensional inlet flow. An AGARD report on test cases for computation of internal flows in aero engine components (see Fottner, 1990) also stresses the importance of clearly defined upstream flow conditions.

A new Transonic Turbine Blade Cascade Facility was designed and built at the NASA Lewis Research Center to study the flow and heat transfer characteristics of advanced turbine blades. The intent of the cascade is to provide benchmark quality data for CFD code and model verification. Initial measurements of the flow upstream of the cascade, however, indicated that uniform inlet flow had not been achieved.

CFD was itself a tool available to help determine the source of the nonuniformity and then to help eliminate it. The details of several calculations and the results obtained from those calculations will be described. The first calculation was run as an analysis of the original geometry to determine the source of the non-uniform flow. As the results will show, the cavity formed by an imbedded bellmouth inlet appeared to be the source. The next calculation was performed to determine if bridging the region between the bellmouth and the upstream wall would eliminate the problem. A third and final calculation was performed to ensure that the upstream region of the facility did not contribute an additional source of flow nonuniformity. Each of these three computations are described separately below. Finally, experimental measurements taken with the modified inlet geometry will be presented and compared to the calculations.

The analysis was not performed during the initial design for several reasons. As is the case of the design of any new facility, the bellmouth inlet was just one of several potential problems—all others appear to have turned out well. In the course of the initial design, an inlet analysis with the degree of intensiveness that will be shown to be necessary would have been difficult to justify. Also, the inlet design was based somewhat on another turbine cascade facility with a shorter inlet section that performed well (see Stabe and Kline, 1974, and Kline et al., 1983). Other similar inlet geometries can be found in the literature (see Meauze, 1979).

2 Description of Facility

The design of new experimental research facilities involves compromises and the use of novel, but often untested designs. A new Transonic Turbine Blade Cascade Facility was designed and built at the NASA Lewis Research Center to study the flow and heat transfer characteristics of advanced turbine blades. Some noteworthy features of the facility are its ability to achieve transonic Mach numbers, its high blade count for periodicity, and its large scale, which facilitates detailed flow and heat trans-

---

Contributed by the International Gas Turbine Institute and presented at the 39th International Gas Turbine and Aeroengine Congress and Exposition, The Hague, The Netherlands, June 13–16, 1994. Manuscript received by the International Gas Turbine Institute February 11, 1994. Paper No. 94-GT-237. Associate Technical Editor: E. M. Greitzer.

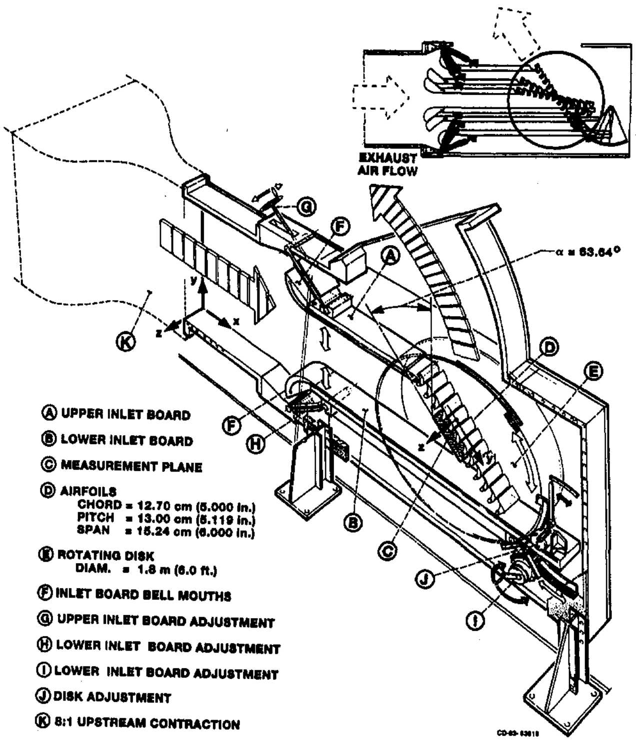

Fig. 1 Overall view of transonic turbine blade cascade test section

fer measurements. Also, because of its large scale and transonic flow conditions, realistic engine Reynolds numbers are achieved with an inlet pressure near one atmosphere. An overall view of the cascade facility is shown in Fig. 1. Dimensions relevant to the work presented here are included in the figure, but a more detailed description is given by Verhoff et al. (1992).

The blade shape is typical of a high-pressure turbine rotor. A highly three-dimensional flow field was sought in the blade passages, characteristic of an actual gas turbine environment. To obtain this highly three-dimensional flow field, a thick inlet boundary layer was desired at the face of the blade row. A 4.5-m-long inlet section was used to develop this thick inlet boundary layer. At the same time, the capability to examine off-design incidence angle variations or to allow for blades of different inlet incidence was desired. The incidence can vary over a range of +15 deg to −30 deg from the design condition (note that Fig. 1 shows the blade row set at the design inlet flow angle, α = 63.64 deg). This incidence variation capability was achieved by allowing the blade row, mounted on a circular disk, to rotate about its center passage. As the blade row is rotated for off-design incidence angles, its upper end is hinged to the upper inlet board, and its lower end slides along the lower inlet board, thus changing the vertical and horizontal positions of the downstream ends of both boards. The upstream ends of the inlet boards are then adjusted vertically, so that the boards remain parallel to each other, and horizontally, so that the inlet board leading edges are at equal x locations. To satisfy all of these desired capabilities, a compromise was reached with the inlet boards, allowing their leading edges to form imbedded bellmouth nozzles.

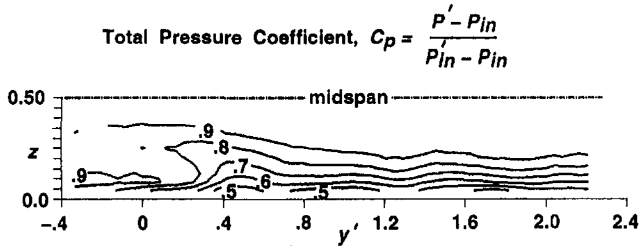

Fig. 2 Experimental measurements of total pressure coefficient in the original geometry

The idea of a bellmouth nozzle with moveable inlet boards was borrowed from another turbine cascade rig at NASA Lewis (see Stabe and Kline, 1974; and Kline et al., 1983). The bellmouth nozzle described in these reports also formed cavities like those of the present study shown in Fig. 1. However, that cascade had a very short inlet section compared to the one in the present study and its inlet was open to the atmosphere. Other similar geometries can also be found in the literature; see, for example, Meauze (1979). The bellmouth nozzle and cavity geometry is also very common in solid rocket nozzles, except that their geometry is typically axisymmetric. The bellmouth nozzle created cavities in the inlet of the present study that were somewhat questionable, but the previous experiences mentioned above indicated that they should not have a detrimental effect.

The most critical requirement of any cascade inlet section is that it should provide pitchwise periodic, two-dimensional flow upstream of at least three of the center blade passages. To verify the inlet periodicity experimentally, total pressure measurements were taken in a plane 2.2 cm (0.18 C_x) upstream of the blade's leading edges, traversing slightly more than three blade passages (the measurement plane is shown in Fig. 1). Because a five-hole probe was used for the measurements, the first data point in the spanwise direction was taken 0.635 cm (0.250 in.) from the endwall. Flat-plate boundary-layer correlations indicated that the full boundary-layer thickness, δ, should be approximately 4.25 cm ($\simeq$0.28 × span) in this region. The experimental measurements of total pressure coefficient are shown below in Fig. 2. The measurements clearly show that periodic flow had not been achieved. The objective of the present work was to identify the source of the flow nonuniformity and then to propose a design change that would eliminate it.

Nomenclature

C_x = blade axial chord = 12.70 cm (5.000 in.)
C_p = total pressure coefficient = $(P' - P_{in})/(P'_{in} - P_{in})$
M = Mach number
P = pressure
Re_x = Reynolds number = $\rho u_{in} x/\mu$
s = blade and inlet section span = 15.24 cm (6.000 in.)
T = temperature
u = velocity in x direction
v = velocity in y direction
w = velocity in z direction
x = axial direction, nondimensionalized by span, s
y = pitchwise direction, nondimensionalized by span, s
y' = pitchwise direction parallel to blade leading edges, nondimensionalized by span, s
y^+ = normalized distance in inner coordinates
z = spanwise direction, nondimensionalized by span, s
α = inlet flow angle to blade row
δ = boundary layer thickness
μ = dynamic viscosity
ρ = density
ω = nondimensional vorticity

Subscripts

in = free-stream inlet value
ex = free-stream exit value

Superscripts

$'$ = total conditions

A computational analysis was chosen for several reasons. First, physical accessibility to the inlet section was limited, making flow measurements more than a few chords upstream of the blade's leading edges very difficult. The computational analysis also allows for a better understanding of the physics than a set of discrete measurements might because the flow properties can be analyzed throughout the entire domain. This understanding can give great insight when proposing design changes. The computational approach also enables design changes to be examined cheaper and more quickly than an experimental approach would.

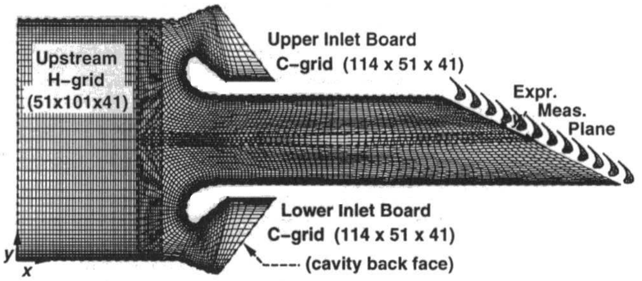

Fig. 3 Computational grids used for calculations of original geometry

3 Computational Methods and Models

3.1 Code Description. The PARC CFD code that was used in this study solves the Reynolds-averaged Navier–Stokes equations formulated in the strong conservation law form for a curvilinear coordinate system according to the method described in "PARC Code: Theory and Usage" (Cooper and Sirbaugh, 1989). The viscous flux terms are handled explicitly on the right-hand side of the equations. The inviscid flux terms are time-linearized, resulting in an explicit flux term on the right-hand side and an additional left-hand side term. Second-order accurate central differencing is used to calculate the inviscid fluxes. Since the flux terms are modeled using central differences, artificial dissipation is added both to the right- and left-hand sides of the equations. To make the solution process economical, the left-hand side flux Jacobian terms are diagonalized, forming a set of scalar pentadiagonal equations that is solved by a backward Euler, alternating direction implicit procedure as developed by Pulliam (1984). The PARC code has the capability to calculate flow in a multiple-block domain. That capability was used extensively in the current study.

The algebraic turbulence model developed by Baldwin and Lomax (1978) was used in the present study. The model was applied globally, and no type of laminar-to-turbulent transition model was used, i.e., the flow was assumed to be fully turbulent everywhere. The search for the maximum of the Baldwin–Lomax model function "F" was stopped at a grid index approximately corresponding to the boundary-layer edge. The unit Reynolds number at the cascade face was 7.8×10^6 m^{-1}.

3.2 Computational Domain and Grids. The location of the computational domain had to be decided upon before proceeding with the calculations. The computational inlet was chosen to be a plane just downstream of an 8:1 streamwise contraction (referring to Fig. 1, a y–z plane at $x = 0$). Because of the strong acceleration caused by the contraction, boundary-layer growth was suppressed, so the flow was assumed to be uniform and one-dimensional over this plane. The computational exit was chosen to be a plane 2.2 cm (0.18 C_x) upstream of the blade leading edges, coincident with the measurement plane shown in Fig. 2, but extending to both inlet boards. This plane was chosen because endwall static pressure measurements were available to specify an exit flow condition as needed by the code. Some implications of this exit plane choice will be discussed with the computational results. Note that in Fig. 1 the spanwise thickness is uniform in the chosen computational domain and thus the geometry is symmetric about a plane through midspan. This fact was exploited to allow modeling of just half of the span.

With the computational boundaries chosen, the domain was discretized with grids that would allow for resolution of the necessary flow physics. The computational grid that was used for calculation of the original geometry is shown in Fig. 3. This grid will be discussed here as an example; subsequent calculations of modified geometries used similar grids. Grid dimensions were chosen to be large enough to resolve the pertinent physics. Three separate grid blocks were chosen to cover the computational domain. The first two blocks are C-grids surrounding the upper and lower inlet boards. The C-grids were chosen to give good resolution of the inlet board's leading edges, which were suspected to be a possible source of the flow nonuniformity. An H-grid was used in the region between the C-grids and the computational inlet, overlapping the C-grids by several points. The dimensions of the three grids are shown in Fig. 3, with dimensions listed as the number of points streamwise, pitchwise, and spanwise. The total number of grid points for this calculation was 688,000, but because the PARC code computes each grid block independently, computer memory requirements are dictated by the size of the largest single grid block. Less than 8.0 M-words of core memory were required on a Cray Y-MP.

The fact that the computational domain was of constant spanwise cross section simplified the grid generation process; two-dimensional grids were generated and then were stacked in the spanwise direction with a hyperbolic tangent stretching function. Fine grid spacing was used near all solid walls to resolve viscous layers. The location of the point adjacent to solid walls was specified such that $y^+ \lesssim 10$.

3.3 Boundary Conditions. Total conditions $P'_{in} = 96.94$ kPa (14.06 psi) and $T'_{in} = 294$ K (530 R) were specified at the computational inlet, and velocity components v and w were set to zero. Static conditions and the u-velocity component were then determined from characteristic information extrapolated from inside the domain. The symmetry plane was treated as an inviscid wall with no flux in the z-direction. All solid walls were treated as no-slip, adiabatic boundaries except the boundaries on the back face of the cavity. Resolving viscous layers on the back faces was not felt to be necessary because the flow in this region is nearly stagnant and thus more detailed modeling of the back faces would not affect the flow in the main passage. The cavity back faces were then treated as inviscid walls with zero flux. Because the exit flow is subsonic for all of the cases examined here, static pressure was specified at the exit and all other flow variables were extrapolated. More details of the exit flow condition will be discussed with the computational results.

4 Discussion of Results

4.1 Calculation of Original Inlet Geometry. The grid shown in Fig. 3 was used for calculations of this case. Initially, a uniform exit static pressure, P_{ex}, was specified at the computational exit. The value of P_{ex} was obtained by averaging the measurements of endwall static pressure taps that were located in the same plane as the computational exit. Because this plane was located only 0.18 C_x upstream of the blade's leading edges, the pressure varied periodically between the blades. Using the average of the measurements was felt to be adequate for the current calculation because it would set up the correct mass flow and because whatever was creating the distortion had to have been generated sufficiently far upstream of the exit plane. The average value of pressure was specified to be $P_{ex}/P'_{in} = 0.904$, which resulted in a total mass flow through the facility of 13.4 kg/s (29.5 lb/s). This was within 1 percent of the experimentally measured mass flow. The inlet free-stream ve-

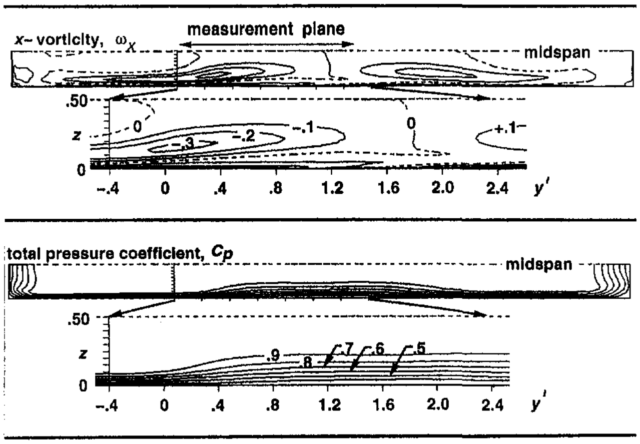

Fig. 4 Results of calculations of original geometry with uniform exit static pressure

locity and Mach number were $u_{in} = 44.7$ m/s and $M_{in} = 0.130$; computed exit values were $u_{ex} = 130.5$ m/s and $M_{ex} = 0.385$.

Starting the computational solution process proved to be difficult for this case. Originally, a uniform flow field of $M = 0.1$ was specified as an initial condition. The solution could not be advanced more than a few iterations before becoming numerically unstable. Therefore, a two-dimensional, midspan solution was obtained in an $x-y$ plane and was stacked spanwise for use as an initial condition for the three-dimensional calculations.

Convergence of the solution was slow for this case, probably due to the relatively low Mach number flow regions and the flow recirculation in the cavities. The code was run in steps of 200 iterations, each run taking about one hour of CPU time. After 5000 iterations, the L_2 norm of the residuals leveled out after decreasing only by about 1.5 orders of magnitude. No evidence of total pressure distortions in the center of the passage was seen after 5000 steps, but the flow field still appeared to be changing. It appeared to stop changing after about 7500 steps but was run out to 8700 steps for added assurance. The overall inlet-to-exit mass flux error was less than 1 percent. Figure 4 shows results on the exit plane (looking downstream) obtained after 8700 steps. The contour plot of vorticity in that figure clearly shows a pair of streamwise vortices near $y' = 0.1$ inside the measurement plane and near $y' = 3.2$ outside the measurement plane. The total pressure contour plot shows, however, that while the vortices clearly distorted the flow, they were not strong enough to affect the flow adversely to the degree that was measured and shown in Fig. 2. The 0.8 and 0.9 contour lines did not turn over on themselves as the experimental data showed.

Recall that the computational exit plane was specified to be just 2.2 cm (0.18 C_x) upstream of the blade's leading edge plane. The effect of the blades is to provide an inlet flow blockage, accelerating the flow in the passages and decelerating it near the leading edges. This local acceleration could be expected to have a significant effect on the pair of vortices in the center of the passage. Accelerating flow stretches and strengthens streamwise vorticity, which would logically produce a higher degree of total pressure distortions. A more realistic exit static pressure distribution was therefore needed to account for blade blockage effects.

Endwall static pressure measurements were available on the computational exit plane, but the data were spatially quite coarse, with most blade passages having only one pressure tap. Fortunately, a three-dimensional Navier–Stokes CFD solution had previously been obtained for flow around a single blade in an infinite cascade. These results were obtained with the RVC3D code described by Chima (1992) and Chima and Yokota (1990). The single-blade calculations were run at the design inlet flow angle, $\alpha_{in} = 63.64$ deg, a Reynolds number of $\mathrm{Re}_{C_x'} = 0.497 \times 10^6$, and a subsonic exit Mach number of $M_{\mathrm{exit}} = 0.9$. The inlet Mach number of 0.385, however, matches the exit Mach number that was used for calculations of the inlet geometry. A comparison of computational and experimental blade static pressure loading data is shown in Fig. 5. The calculations were made of the full blade span and assume asymmetric inlet boundary layer thicknesses on the hub and tip endwalls. The comparison shows that the static pressure field is quite insensitive to the inlet boundary layer thickness and that the agreement between calculations and experiments is excellent. Given this excellent loading agreement, no inlet problem would have been suspected if not for the full pitchwise and spanwise inlet total pressure surveys. The loading diagrams also show that the flow in the blade passages is highly three-dimensional.

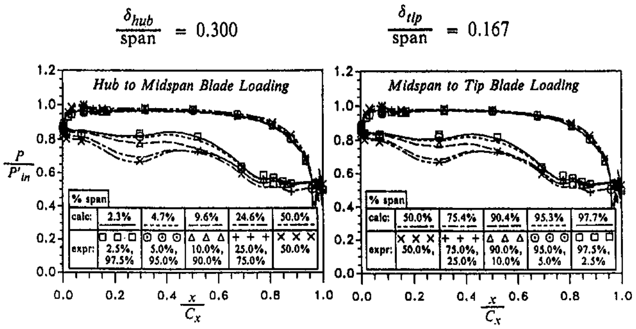

Fig. 5 Blade static pressure loading

With the computational and experimental data giving confidence in the single blade calculations, computed static pressure values upstream of the blade row were interpolated onto a $y'-z$ plane at a distance upstream of the blade's leading edges corresponding to the outflow plane of the inlet calculation. This single-blade interpolated field was then repeated 11 times to cover the entire computational exit plane. Finally, this pressure field had to be interpolated onto the outflow boundary grid of the present calculations. Figure 6 shows the exit static pressure distribution at various stages of interpolation. Note from this figure that the exit grid is rather coarse near the middle of the inlet section, which degrades the interpolation accuracy. For the purposes of determining the cause of the flow nonuniformity, however, this degree of accuracy was assumed to be sufficient.

Figure 7 shows results of the calculations with the nonuniform exit static pressure distribution. As expected, the blade blockage locally accelerated the flow, which strengthened the streamwise vortices. In comparing the total pressure measure-

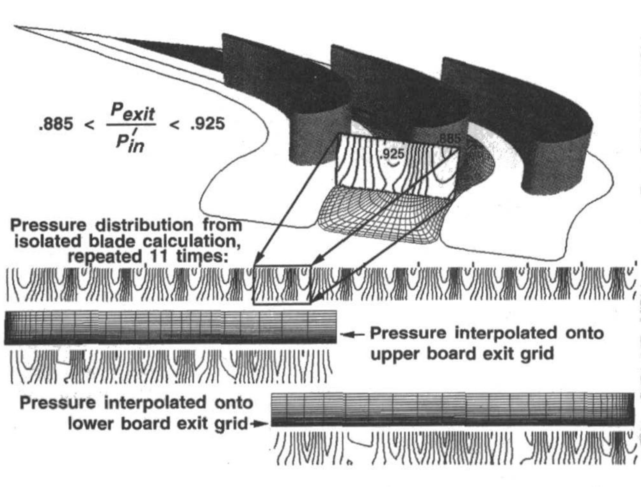

Fig. 6 Nonuniform static pressure distribution used for exit condition

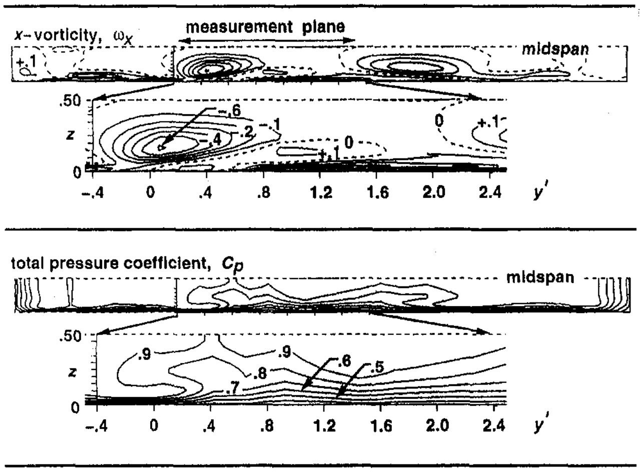

Fig. 7 Results of calculations of original geometry with nonuniform exit static pressure distribution

ments in Fig. 2 with the corresponding calculated results in Figs. 4 and 7, it is shown that this strengthening resulted in total pressure distortions consistent in strength and location to experimental measurements. The vortices are strong enough and sufficiently close to the endwall to cause cross-stream separation, resulting in rapid growth of the low total pressure regions. The behavior and effects of the streamwise vorticity on the total pressure profiles were similar to those observed by Harvey and Perry (1971), who experimentally studied the effects of trailing vortices in the vicinity of the ground. Ideal vortical flow theory (see, for example, Acheson, 1990) can be used to show that the vortices move slowly toward each other and lift off the endwall as they proceed downstream.

4.2 Analysis of Computed Flow. With excellent agreement at the measurement plane, the task was now to identify the upstream source of undesirable streamwise vortices and to determine how to eliminate them. The solution was analyzed to determine the source of the vortices by releasing "particles" into the computed flow field. Some of these particle traces, along with total pressure coefficient contours, are shown in Fig. 8. The following discussion focuses on the lower inlet board cavity, but similar arguments apply for the upper one. As flow enters the inlet section, a low-momentum boundary layer develops on the endwall because of the endwall viscous effects. Flow above the endwall boundary layer has significantly more momentum, allowing it to enter the cavity, thus forcing flow to exit the cavity near the endwall. With flow therefore passing over both sides of the inlet board's blunt leading edge, a horseshoe vortex forms near the leading edge/endwall junction. The passage side (as opposed to the cavity side) leg of this vortex is then convected in the y direction by flow exiting the cavity near the endwall. With the primary flow in this area being essentially axial, the vortex is strengthened by strong z-directional shear caused by viscous effects of the endwall. The main flow then drives the vortex axially, directing it down the center of the passage, where it causes the total pressure distortions described above. Other interesting vortical flow phenomena are evident in Figs. 7 and 8, but will not be examined here as they are beyond the scope of this investigation.

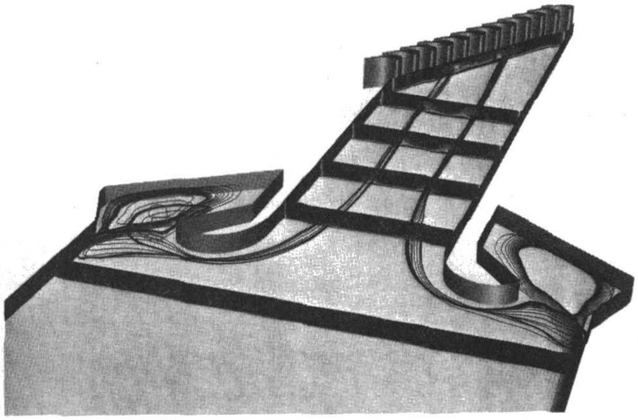

Fig. 8 Particle traces and total pressure coefficient contours

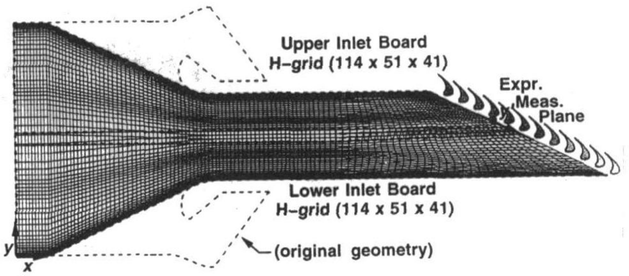

Fig. 9 Computational grids used for calculations of modified geometry

4.3 Calculation of Modified Inlet Geometry. With the first objective of identifying the source of the flow nonuniformity met, the task of proposing a design change that would eliminate it was undertaken. A related experimental study of a vortex formed in the cavity of a two-dimensional submerged inlet was performed by Fleeger (1971). The strength of the cavity vortex was measured by paddle-type vortex meters and the effects of several geometric parameters were examined. The flow was modified in numerous ways: by inserting blocks to reduce the cavity width and height, by placing honeycomb material in the cavity, by adding corner fillets to the cavity, and by bleeding off the incoming boundary layers. The results showed that inserting honeycomb material or decreasing the depth of the cavity decreased the vortex formation. Rivir (1992) recommended eliminating the cavity and keeping the angle between the back face and the free-stream velocity vector less than 70 to 80 deg to eliminate the vortex.

Another design change that was considered was to bleed air from the backs of the cavities to prevent any flow from exiting through their front face. This would, however, still allow horseshoe vortices to be set up in front of the inlet board's blunt leading edges as y-directional vortex lines wrap around them. The more acceptable design change was felt to be one in which the cavities, and thus the imbedded bellmouth nozzle, were completely eliminated.

The proposed new geometry and computational grids are shown in Fig. 9. For comparison, an outline of the original geometry is included. The imbedded bellmouths were eliminated by bridging the cavities with straight boards attached to the upstream walls and to the original bellmouth nozzles. Two H-grid blocks were used for this calculation, each having 114 streamwise points, 51 points between the inlet boards, and 41 spanwise points, for a total of 477,000 grid points. The grids between the inlet boards and near the computational exit are identical to those used for the original geometry. Inlet and exit flow conditions and boundary conditions are identical as well. The nonuniform exit static pressure boundary condition was used.

Perhaps an early indicator of improved flow, it was found to be possible to start this solution with a uniform initial condition of M = 0.1, and a stacked two-dimensional solution was not necessary. Numerical convergence also proved to be more satisfactory for this case, with the L_2 residual norm decreasing by three orders of magnitude, although taking nearly 12,000 steps.

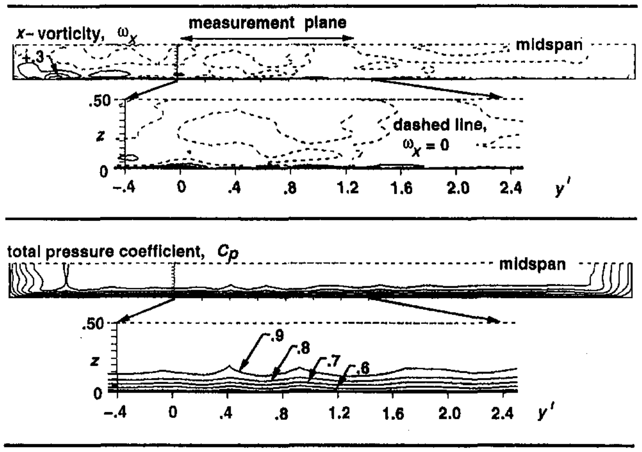

Fig. 10 Results of calculations of modified geometry with nonuniform exit static pressure distribution

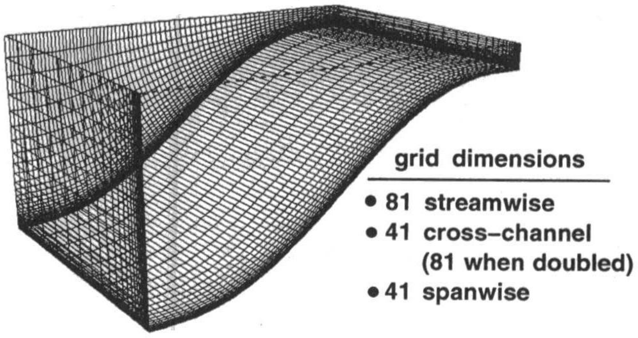

Fig. 11 Computational grid used for calculation of upstream 8:1 contraction section

About 350 steps were possible in each one CPU hour run. The overall inlet-to-exit mass flux error was less than 0.5 percent.

The vorticity and total pressure coefficient contour plots in Fig. 10 show greatly improved flow conditions. Only small, weak vortices are seen near the corners, and they are of the opposite sense to those of the original geometry. As such, the vortices have no adverse effects on the flow near the center of the passage. This analysis clearly indicates that eliminating the imbedded bellmouth eliminates the pair of vortices, resulting in a flow with much greater pitchwise uniformity. Some small peaks of total pressure are seen in Fig. 10, but they are caused by the relatively coarse grid near the center of the passage and the resulting interpolation of the exit static pressure distribution.

4.4 Calculation of Modified Inlet Geometry With Upstream 8:1 Contraction. The original problem of pitchwise nonperiodic flow was clearly traced to the cavities formed by the imbedded bellmouth nozzles. Elimination of the cavities resulted in the elimination of the flow nonuniformity. Recall, however, that a rectangular-to-rectangular, 8:1 converging duct exists upstream of the constant span section (item K in Fig. 1). The 90 deg corners in this converging duct can be expected to produce some streamwise vorticity that may have an adverse effect on the downstream flow. Any vortices that were generated in corners of the contraction section with the original configuration probably would have been masked by the vortices generated in the cavities. However, with the cavities eliminated, these corner vortices could cause flow distortions.

Initially, calculations were run of the 8:1 contraction section isolated from the remainder of the modified inlet section. Because of symmetry in the y and z directions, only one quarter of the contraction had to be modeled. The geometry and grid for this calculation are shown in Fig. 11. The same inlet conditions that were used for the other calculations were specified at the inlet of the contraction. In order to match the overall mass flux, the exit static pressure was specified to be $P_{ex}/P'_{in} = 0.989$, giving $M_{in} = 0.016$ and $M_{ex} = 0.125$. Despite the low Mach number conditions, convergence of the solution was good, with the L_2 residual norm dropping more than four orders of magnitude, and the inlet-to-exit mass flux error dropping to less than 0.05 percent, although taking 14,000 time steps to do so.

Contours of streamwise vorticity and total pressure ratio are shown in Fig. 12. The figure shows that streamwise vortices are generated in the corner, but that their impact on the total pressure field is minimal. Note, however, that the sense of the vortex is the same as the sense of the vortex that was generated in the cavity of the original geometry. To ensure that these vortices would not migrate to the center of the inlet, the contraction geometry was coupled to the modified inlet geometry and the flow was recalculated. The results at the exit plane of this calculation are the same as those shown in Fig. 10, and will thus not be repeated. Although streamwise vortices are indeed generated in the corners of the contraction, they are not convected to the center of the inlet and thus they have no detrimental effect on the flow at the cascade face.

4.5 Experimental Measurements of the Modified Inlet Geometry. With reasonable confidence that the distortion could be eliminated, the experimental hardware was modified to match the geometry shown in Fig. 9. A drawing of the actual hardware is shown in Fig. 13. Note that the hardware is somewhat more complex than the original geometry shown in Fig. 1. Hinges were added between the original, horizontal inlet boards and the new inlet board sections to accommodate disk rotation. The hinges create a forward-facing step, but were designed and fabricated with a step height less than 1.0 mm (0.040 in.). Also, two new hinged lead screws were added to the new inlet board sections near the upstream attachment points.

Total pressure measurements were taken upstream of the blade's leading edges, on the same $y'-z$ plane that was shown in Figs. 2, 4, 7, and 10. The results of the measurements from the modified geometry are presented in Fig. 14. The measurements show good agreement with the calculations shown in Fig. 10. Most importantly, the measurements clearly show that the inlet flow distortion has been eliminated and that the flow upstream of the blades is pitchwise periodic and two dimensional, as was initially desired.

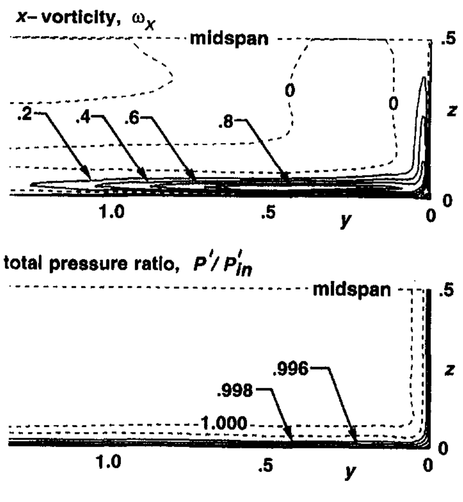

Fig. 12 Results of calculations of upstream 8:1 contraction section

5 Summary and Conclusions

The results indicate that the CFD analysis was quite successful in aiding in the redesign of the cascade inlet. Calculations of the original geometry showed total pressure loss regions consistent in strength and location to the experimental measurements. The calculations further showed that these loss regions were caused by a pair of streamwise vortices that originated as a result of the interaction of the flow with cavities formed by the bellmouth inlet. With the origin of the distortions well understood, calculations were performed on a geometry that eliminated the cavities by bridging the region between the bellmouth inlet and the upstream wall. These calculations showed that eliminating the cavities successfully eliminated the flow distortions at the cascade face. Additional calculations showed that streamwise vortices generated in the corners of the upstream 8:1 contraction section have no detrimental effect on the flow uniformity at the cascade face.

This study exemplifies the use of CFD as a diagnostic and a design tool. It also exemplifies the inherent coupling of computational, analytical, and experimental fluid dynamics and heat transfer. Moreover, the study shows that a detailed analysis of an entire facility may be necessary in order to obtain benchmark quality data. That data can then, in turn, be used more reliably to aid in the improvement of CFD models and codes.

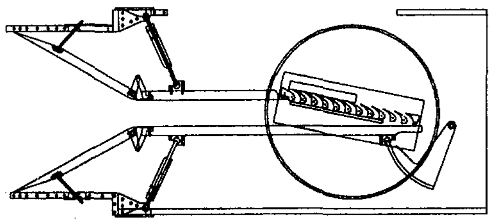

α = 78.64° (+ 15° off-design)

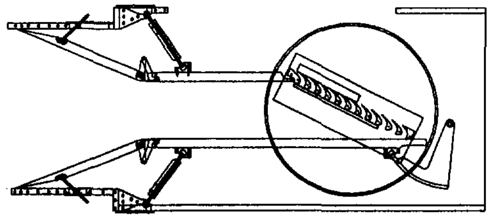

α = 63.64° (design)

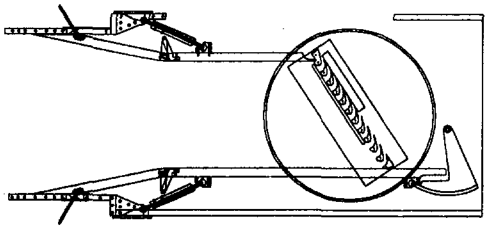

α = 33.64° (− 30° off-design)

Fig. 13 Transonic turbine blade cascade—modified inlet geometry

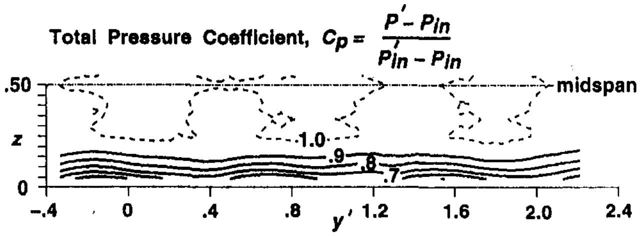

Fig. 14 Experimental measurements of total pressure coefficient in the modified geometry

Acknowledgments

This work was supported by the NASA Lewis Research Center under contract NAS3-25266 with Sverdrup Technology, Inc. and contract NAS3-27186 with NYMA, Inc., both with Mr. Robert J. Boyle as monitor.

References

Acheson, D. J., 1990, *Elementary Fluid Dynamics,* Clarendon Press, Oxford, United Kingdom, pp. 128–129, 177–178.

Baldwin, B. S., and Lomax, H., 1978, "Thin-Layer Approximation and Algebraic Model for Separated Turbulent Flows," AIAA Paper No. 78-257.

Chima, R. V., and Yokota, J. W., 1990, "Numerical Analysis of Three-Dimensional Viscous Internal Flows," *AIAA J.,* Vol. 28, No. 5, pp. 798–806.

Chima, R. V., 1992, "Viscous Three-Dimensional Calculations of Transonic Fan Performance," in: *CFD Techniques for Propulsion Applications,* AGARD Conference Proceedings No. CP-510, AGARD, Neuilly-Sur-Seine, France, pp. 21-1 to 21-19.

Cooper, G. K., and Sirbaugh, J. R., 1989, "PARC Code: Theory and Usage," AEDC-TR-89-15.

Fleeger, D. W., 1971, "Investigation of a Vortex in the Inlet of a Submerged Nozzle," M.S. Thesis, Air Force Institute of Technology, Wright-Patterson Air Force Base, OH.

Fottner, L., ed., 1990, "Test Cases for Computation of Internal Flow in Aero Engine Components," prepared by the Propulsion and Energetics Panel Working Group 18, AGARD Advisory Report No. 275.

Harvey, J. K., and Perry, F. J., 1971, "Flowfield Produced by Trailing Vortices in the Vicinity of the Ground," *AIAA J.,* Vol. 9, No. 8, pp. 1659–1660.

Kiock, R., Lehthaus, F., Baines, N. C., and Sieverding, C. H., 1985, "The Transonic Flow Through a Plane Turbine Cascade as Measured in Four European Wind Tunnels," ASME Paper No. 85-IGT-44.

Kline, J. F., Moffitt, T. P., and Stabe, R. G., 1983, "Incidence Loss for Fan Turbine Rotor Blade in Two-Dimensional Cascade," NASA TP-2188.

Meauze, G., 1979, "Transonic Boundary Layer on Compressor Stator Blades as Calculated and Measured in Wind Tunnel," presented at the 44th International Symposium on Air Breathing Engines, ISABE, Orlando, FL, Apr. 1–6.

Pulliam, T. H., 1984, "Euler and Thin Layer Navier–Stokes Codes: ARC2D, ARC3D," in: *Notes for Computational Fluid Dynamics User's Workshop,* The University of Tennessee Space Institute, Tullahoma, TN, UTSI Publication E02-4005-023-84, Mar. 12–16, pp. 15.1–15.85.

Rivir, R. B., 1992, private communication.

Stabe, R. G., and Kline, J. F., 1974, "Incidence Loss for a Core Turbine Rotor Blade in a Two-Dimensional Cascade," NASA TM-X-3047.

Verhoff, V. G., Camperchioli, W. P., and Lopez, I., 1992, "Transonic Turbine Blade Cascade Testing Facility," AIAA Paper No. 92-4034, NASA TM-105646.

Suppression of Secondary Flows in a Mixed-Flow Pump Impeller by Application of Three-Dimensional Inverse Design Method: Part 1—Design and Numerical Validation

M. Zangeneh
Department of Mechanical Engineering,
University College of London,
London, United Kingdom

A. Goto

T. Takemura

Ebara Research Company, Limited,
Fujisawa-shi, Japan

This paper describes the design of the blade geometry of a medium specific speed mixed flow pump impeller by using a three-dimensional inverse design method in which the blade circulation (or rV_θ) is specified. The design objective is the reduction of impeller exit flow nonuniformity by reducing the secondary flows on the blade suction surface. The paper describes in detail the aerodynamic criteria used for the suppression of secondary flows with reference to the loading distribution and blade stacking condition used in the design. The flow through the designed impeller is computed by Dawes' viscous code, which indicates that the secondary flows are well suppressed on the suction surface. Comparison between the predicted exit flow field of the inverse designed impeller and a corresponding conventional impeller indicates that the suppression of secondary flows has resulted in substantial improvement in the exit flow field. Experimental comparison of the flow fields inside and at exit from the conventional and the inverse designed impeller is made in Part 2 of the paper.

Introduction

The efficiency and stability of mixed and radial flow turbomachines are adversely affected by the presence of impeller exit flow nonuniformity. In recent years, as a result of improvements in experimental techniques and numerical methods, it has been possible to obtain a better understanding of the basic mechanism behind this phenomenon; see Eckardt (1976, 1980), Zangeneh et al. (1988), and Goto (1992a). It is now a well-established fact that the flow in these impellers is dominated by secondary flows, which tend to move low-momentum fluids present on the blade surface and endwall boundary layers toward the location of minimum reduced pressure (or relative Mach number in compressible flow) on the shroud suction surface corner.

The generation of secondary flows in the impeller can be explained by reference to the following equation derived from classical secondary flow theory (see Zangeneh et al., 1988):

$$\mathbf{W}\cdot\nabla(\mathbf{W}\cdot\boldsymbol{\Omega}) = 2\boldsymbol{\Omega}\cdot(\mathbf{W}\cdot\nabla)\mathbf{W} + \boldsymbol{\Omega}\cdot(2\boldsymbol{\omega}\times\mathbf{W}) \quad (1)$$

where $(\mathbf{W}\cdot\boldsymbol{\Omega})$ represents the streamwise component of absolute vorticity. According to this equation streamwise components of vorticity (and therefore secondary flows) are generated when there is a component of acceleration (streamline curvature or Coriolis) in the direction of the absolute vorticity. As a result there are two types of secondary flow in the impellers of mixed flow and radial turbomachines. A blade-to-blade secondary flow (moving low-momentum fluid from pressure to suction surface) is mainly due to the tangential component of Coriolis acceleration ($2\omega W_r$), which is in the direction of vorticity generated by endwall boundary layers. In the case of compressors and pumps, this secondary flow can be minimized by using backsweep (now commonly used), which reduces the tangential component of Corriolis acceleration (and therefore the blade loading). The meridional component of secondary flow, which is mainly due to the combined action of radial component of Corriolis acceleration ($2\omega W_\theta$) and streamline curvature on the blade surface boundary layers, can be observed on both the pressure and suction surfaces; see Goto (1992a) and Casey et al. (1992). The control and possible suppression of this meridional component of secondary flow, however, are more difficult as it requires careful design of the complicated three-dimensional blade geometry of the impeller.

In this paper, the design of the blade geometry of a mixed flow pump impeller is described in which meridional secondary flows have been suppressed. To suppress secondary flows, the impeller blades were designed by using a three-dimensional inverse design method, in which the blade circulation (or loading) distribution is specified; see Zangeneh (1991). In Part 1 of the paper we shall consider in detail the approach used to suppress the secondary flows on the blades by reference to the inputs of the design method. We shall also compare the flow field in the inverse designed impeller with a conventional impeller by using the incompressible version of Dawes' code (1988). In Part 2 of the paper results of detailed experimental measurements for the conventional and inverse designed impeller will be presented.

Inverse Design Method

In this design method the blades are represented by sheets of vorticity whose strength is determined by a specified distribution of circumferentially averaged swirl velocity, or $r\bar{V}_\theta$ (directly related to the bound circulation $2\pi r\bar{V}_\theta$ and the blade loading) defined as:

Contributed by the International Gas Turbine Institute and presented at the 39th International Gas Turbine and Aeroengine Congress and Exposition, The Hague, The Netherlands, June 13–16, 1994. Manuscript received by the International Gas Turbine Institute February 4, 1994. Paper No. 94-GT-45. Associate Technical Editor: E. M. Greitzer.

$$r\bar{V}_\theta = \frac{B}{2\pi}\int_0^{2\pi/B} rV_\theta d\theta,$$

where B is the number of blades. To simplify the problem the blades are represented by a single sheet of vorticity, representing the mean camber line of the blades. The blade blockage effects are then accounted for by using a mean streamsurface thickness parameter in the continuity equation of the mean flow. It is therefore possible to express the bound vorticity on the blades by

$$\mathbf{\Omega}_b = \nabla \times \mathbf{V} = (\nabla r\bar{V}_\theta \times \nabla\alpha)\delta_p(\alpha), \tag{2}$$

where

$$\alpha = \theta - f(r, z) = n\frac{2\pi}{B}, \tag{3}$$

represents the blade surfaces, θ is the tangential coordinate of a cylindrical polar coordinate system, and $f(r, z)$ is the angular coordinate of the point on the thin blade surface, or the mean camber angle (wrap angle in turbocharger terminology). In Eq. (3), B denotes the number of blades and n is an integer, which takes values between 1 and B. $\delta_p(\alpha)$ is the periodic delta function, whose pitchwise mean is unity, so that the tangentially mean bound vorticity is given by

$$\bar{\mathbf{\Omega}} = \nabla \times \bar{\mathbf{V}} = (\nabla r\bar{V}_\theta \times \nabla\alpha). \tag{4}$$

The method starts by using one-dimensional estimates of the meridional velocity obtained from the specified mass flow rate and meridional geometry together with the specified mean tangential velocity to compute an initial blade shape. The blade shape is computed by using the inviscid slip condition, which implies that the flow must be aligned to the blade surfaces. This condition can be expressed mathematically as:

$$\mathbf{W}_{bl} \cdot \nabla\alpha = 0. \tag{5}$$

where $\nabla\alpha$ is a vector normal to the blade surface and $\mathbf{W}_{bl}$ is the relative velocity at the blade surface ($\mathbf{W}_{bl} = (\mathbf{W}^+ + \mathbf{W}^-)/2$, where $\mathbf{W}^+$ and $\mathbf{W}^-$ are the velocities on the upper and lower surface of the blades). Expanding Eq. (5) we obtain

$$V_{zbl}\frac{\partial f}{\partial z} + V_{rbl}\frac{\partial f}{\partial r} = \frac{rV_{\theta bl}}{r^2} - \omega \tag{6}$$

where f is the wrap angle and ω is the rotational speed. Equation (6) is a first-order hyperbolic partial differential equation, which has to be integrated along the meridional projections of streamlines on the blade surface in order to find the blade shape. The integration, as in the case of other initial value problems, cannot be completed without some initial condition on f. This initial value will be called the *stacking condition of the blade.* In this method the stacking condition is implemented by giving as input, the values of blade wrap angle f along a quasi-orthogonal, for example at the leading edge. The effect of different stacking conditions on the flow is discussed in detail by Zangeneh (1992) and will be discussed further later on in this paper.

Table 1 Design specification

	Hub/Mid-span/Shroud	Design flow rate: 9.2 m^3/min
r_1 (mm)	58.0/102.3/132.5	Design Pump head: 6.5 mH$_2$O
r_2 (mm)	142.5/157.8/171.7	Rotational Speed: 800 rpm

Once a value for the blade shape has been obtained, it is then possible to use Eqs. (2) and (3) to determine the vorticity throughout the blade region. This in turn can be used to compute the velocity field throughout the flow; see Hawthorne et al. (1984) and Zangeneh (1991). The flow field is decomposed into tangentially mean and periodic components. A governing equation for the mean flow is obtained by using the Stokes stream function together with tangential component of Eq. (4). The governing equation of the periodic flow is obtained by applying the continuity equation of the periodic flow to the Clebsch formulation for the velocity.

The flow field is computed by solving the governing equations of the mean and periodic flow (two-dimensional and three-dimensional Poisson's partial differential equations, respectively). For the solution of the governing equation of the periodic flow it is possible to express all three-dimensional flow variables in terms of a Fourier series in the tangential direction. As a result the three-dimensional Poisson's equation is reduced to a two-dimensional Helmholtz equation, which is then solved for each hamonic of the Fourier coefficients in the frequency domain. The use of a Fourier expansion in the tangential direction results in substantial savings in computational time and memory as the three-dimensional flow field is solved without the need for a grid in the tangential direction.

The partial differential equations for the flow field are solved numerically by using a finite difference approximation on a body-fitted coordinate system; see Zangeneh (1991) for more detail. Equation (6) is also solved numerically by using a Crank–Nicholson type finite difference discretization.

Once a new estimate for the velocity field has been obtained, it is then possible to compute the new blade shape by using Eq. (6). This iterative process is then repeated until changes in blade shapes between two iterations fall below a certain given tolerance, usually taken as 10^{-5} radians.

Impeller Design

The design conditions used for the design of the mixed flow pump were based on the medium specific speed impeller, which has been studied extensively by Goto (1992a, b). The basic design conditions for the impeller are presented in Table 1. This impeller was designed by using conventional techniques involving the use of curve fits to connect the blade angles smoothly between the leading and trailing edges.

Nomenclature

B = number of blades
f = blade wrap angle (θ value at the blade)
r = radius
(r, θ, z) = cylindrical-polar coordinate system
$S(\alpha)$ = sawtooth function
$\mathbf{v}$ = periodic velocity
$\mathbf{V}$ = velocity
$\mathbf{W}$ = relative velocity
α = angular coordinate of blade surfaces (Eq. (3))
$\delta_p(a)$ = periodic delta function
ω = rotational speed
Ω = vorticity

Subscripts

bl = at the blade
r = radial component
z = axial component (three-dimensional)
θ = tangential component

Superscripts

$^-$ = pitchwise mean value
$+$ = relative to upper blade surface; suction surface in pump
$-$ = relative to lower blade surface; pressure surface in pump

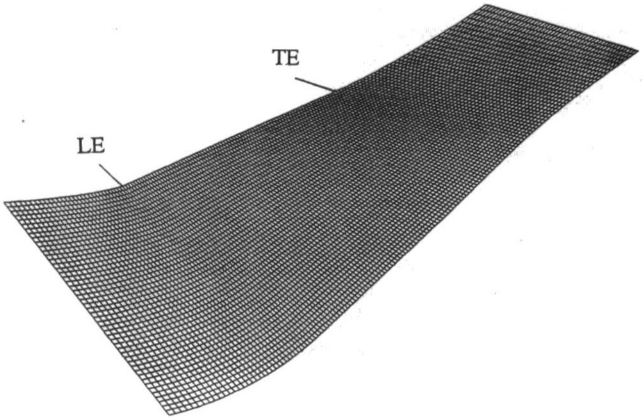

Fig. 1 Computational grid on meridional plane; grid size: 145 × 49

The computational mesh used to represent the meridional geometry of the pump impeller is presented in Fig. 1. This grid consists of 145 quasi-orthogonals and 49 uniformly spaced quasi-streamlines, with 30 quasi-orthogonals in the upstream region and 81 quasi-orthogonals inside the blade region. The meridional geometry of the impeller is the same as the conventional impeller, apart from the curved leading edge, which in this case has been replaced by a straight line connecting the hub and shroud. As the tangential variations in flow variables are represented by a Fourier series, no blade-to-blade grid is required. For the thickness distribution, the normal thickness of the conventional impeller was specified.

Specified Circulation Distribution. The specified circulation (or $r\bar{V}_\theta$) distribution is presented in Fig. 2. A number of important criteria were used to arrive at this $r\bar{V}_\theta$ distribution. The basic approach used is to select an optimum distribution of $r\bar{V}_\theta$ at the hub and shroud and then interpolate linearly between these values to obtain the overall distribution of $r\bar{V}_\theta$ on the meridional plane. The values of $r\bar{V}_\theta$ at the leading and trailing edges are obtained from Euler's pump equation. In this case the nondimensional (by $r_m U_m$) exit value of $r\bar{V}_\theta$ was set to 0.437 while the inlet $r\bar{V}_\theta$ was set to zero. Since the jump in pressure across the blades is given by:

$$p^+ - p^- = \frac{2\pi}{B}(\mathbf{W}_{bl} \cdot \nabla r\bar{V}_\theta) \tag{7}$$

the derivative of $r\bar{V}_\theta$ in the meridional direction, at the leading and trailing edges, must be set to zero in order to satisfy the no-incidence and the Kutta conditions. Equation (7) also indicates that the pressure distribution on the blades is directly related to the meridional derivative of $r\bar{V}_\theta$ (or loading distribution) and by using a smooth loading distribution we should be able to ensure a smooth pressure distribution.

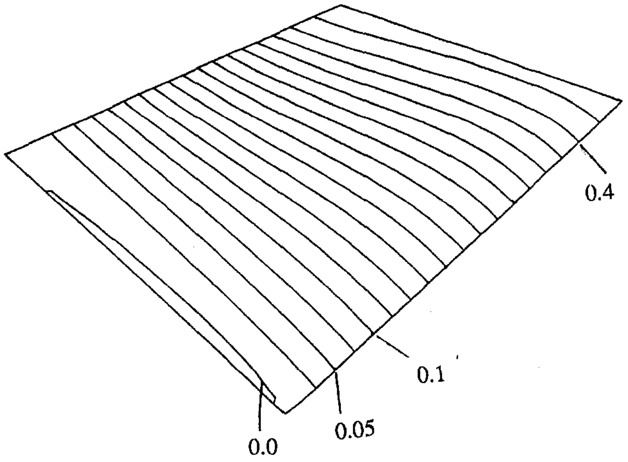

Fig. 2 Specified $r\bar{V}_\theta$ distribution (contour interval = 0.05, normalized by $r_{2m}U_{2m}$)

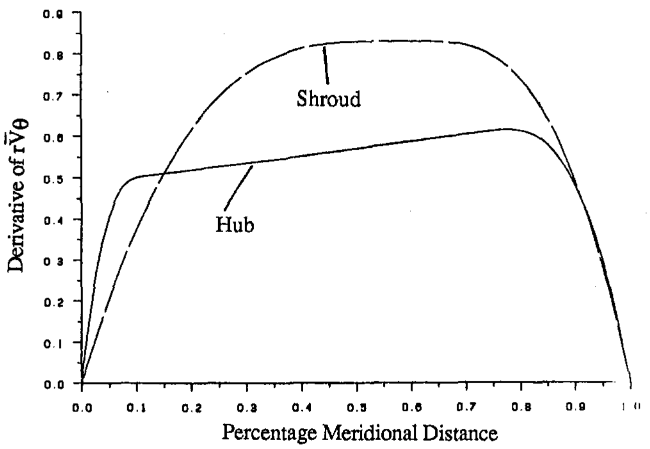

Fig. 3 Meridional derivative of $r\bar{V}_\theta$

The easiest way to satisfy all these criteria is to specify the loading distribution rather than the $r\bar{V}_\theta$ distribution. This is done by assuming the following distribution for the meridional derivative of $r\bar{V}_\theta$:

rVθ :

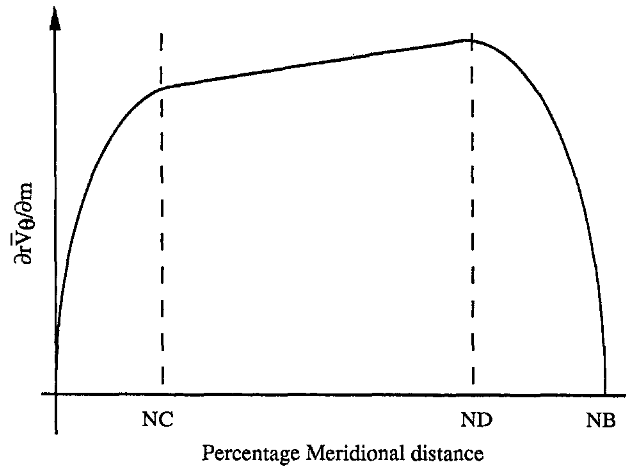

where the distribution is parabolic up to point NC, then a linear variation between point NC and ND with a specified slope, followed by another parabolic distribution, which reduces the loading to zero at the trailing edge (point NB) in order to satisfy the Kutta condition. The $r\bar{V}_\theta$ distribution is then found by integrating these values of $d(r\bar{V}_\theta)/dm$. The specified loading distribution used for the design is presented in Fig. 3. In this case, the location of maximum loading at the hub and shroud was moved away from the leading edge in order to minimize possible cavitation problems.

Stacking Condition. Apart from the loading (or $r\bar{V}_\theta$) distribution, there is one other input specification, which has a very important effect on the flow field. This is the stacking condition mentioned earlier. To obtain radial stacking, the values of f (or mean camber angle) can be set to a constant value (e.g., zero) on the stacking quasi-orthogonal. However, it is also possible to specify a nonzero value for f in which the values of f at the stacking quasi-orthogonal vary from hub to shroud. This type of

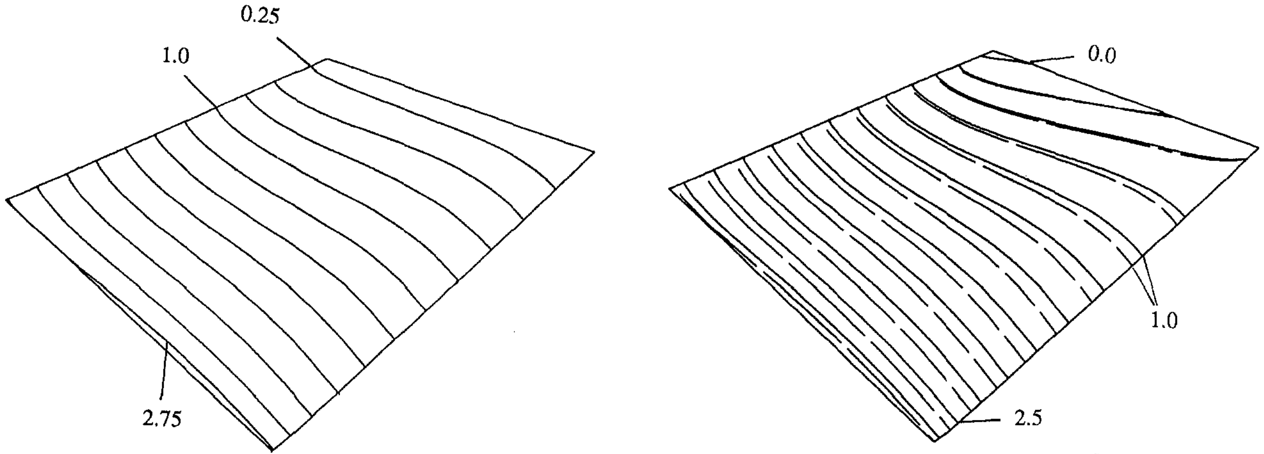

(a) **Impeller A**

(b) **Solid Line - Impeller C**
Dashed Line - Impeller CII

Fig. 4 Contours of wrap angle $-f$ (contour interval = 0.25 rad)

stacking condition is equivalent to lean in axial turbomachinery terminology, which results in a spanwise force that affects the spanwise pressure distribution along the blade surfaces.

It is a well-known fact that secondary flows move low-momentum fluids toward the location of minimum reduced static pressure (see Johnson, 1978). As a result of this fact the presence of meridional secondary flows can be directly correlated with spanwise gradients of reduced static pressure (or relative Mach number); see Zangeneh et al. (1988). Therefore, to minimize meridional secondary flows, particularly on the suction surface, where most of the low-momentum fluids are generated, our main objective was to reduce the spanwise gradients of reduced static pressure. As the choice of loading distribution was to some extent limited by the cavitation reduction criteria, we decided to use the stacking condition in order to control the spanwise gradients of reduced static pressure.

In order to investigate the effect of the stacking conditions on the impeller flow field two different impellers with the same loading distribution (as in Fig. 3) but different stacking conditions were designed. In the first impeller design (to be designated impeller A) the stacking quasi-orthogonal was set at the trailing edge. The stacking values of f were set to vary linearly from 0 rad at the hub to 0.15 rad at the tip. In the second impeller design (to be designated impeller C) the stacking condition was specified at quasi-orthogonal 78 (approximately 96 percent of meridional chord) rather than the trailing edge. In this case the stacking values of f were set to vary linearly from 0.5 rad at the hub to 0 rad at the tip. To achieve further reduction in secondary flows, both impellers were designed with seven blades as opposed to the five blades used on the conventional impeller. The computed distributions of f for both impellers A and C are presented in Fig. 4. The absolute difference between blade angles for the inverse designed impellers and the conventional impeller at a few chordwise locations are presented in Table 2. From the results in Table 2 we can see clearly that the geometry of the inverse designed impellers (particularly impeller C) is radically different from the conventional impeller.

Table 2 Absolute difference in blade angles = $|\beta_{\text{inverse design}} - \beta_{\text{Conventional}}|$

Impeller	8% Chord Shroud/Hub	50%-Chord Shroud/Hub	92%-Chord Shroud/Hub
A	1.4/2.5	7.2/3.3	5.1/8.1
C	1.3/2.6	7.9/0.4	10.7/11.7
CII	1.7/2.4	7.3/1.6	10.3/17.8

(degree)

The effect of the stacking condition used to design impeller A is to produce a spanwise force, which increases the blade loading at the tip (as compared to the corresponding radial stacking condition) at the expense of the loading at the hub; while the effect of the stacking condition used for impeller C is to reduce the blade loading at the tip (near the trailing edge) and increase the loading at the hub. The effect of these different stacking conditions on the pressure distribution can be seen clearly in Fig. 5, which compares the reduced pressure distribution on the hub and shroud for impellers A (Fig. 5(a)) and C (Fig. 5(b)), as predicted by the inverse design method. By comparing the reduced pressure distributions on the suction surface of impellers A and C, it is possible to see that hub to shroud difference in reduced pressure (and therefore the spanwise gradients of reduced pressure) on the suction surface have been reduced considerably in impeller C as opposed to that on impeller A. The corresponding reduced static pressure distribution for the conventional impeller is presented in Fig. 5(c). The pressure distribution on the conventional impeller was computed by using a three-dimensional finite element potential method; see Daiguji (1982). The hub-to-shroud difference in reduced pressure (and therefore the spanwise gradients of reduced pressure) on the suction surface in this case are considerably higher than that in impellers A and C, particularly near the trailing edge. This is partly due to the fact that this impeller has five blades rather than seven blades used on the inverse design impellers. However, and perhaps more importantly, the blade angle distribution used to design this impeller has resulted in a leaned geometry near the trailing edge in the opposite direction to that used to design impeller C—see Fig. 9 and Fig. 2 of Goto et al. (1994)—thereby increasing the spanwise gradients of reduced static pressure.

To confirm that the reduction in spanwise pressure gradients in the case of impeller C as compared to the conventional impeller does in fact help to diminish (or perhaps even eliminate) secondary flows, the flow through the inverse designed impellers A and C was computed by using a three-dimensional viscous method.

Viscous Predictions

The flow fields in the two inverse designed impellers were analyzed by the incompressible version of three-dimensional Navier–Stokes solver developed by Dawes (1988) and Walker and Dawes (1990). For both calculations a computational mesh consisting of 29 pitchwise, 129 streamwise (with 21 points upstream of the blade and 97 points inside the blade region) and 29 spanwise grid points were used. The mesh points near the blade surfaces and endwalls were clustered in order to resolve the shear layers. Analysis of the flow field inside the conventional impeller has already been reported in some detail by Goto (1992a). The results reported by Goto (1992a) indicate clearly that the N–S method can predict the Euler head quite accurately, although the actual head predicted by the method is considerably higher than the measured head as the method underestimates the amount of mixing inside and at the exit from the impeller. The results also indicate that the method can provide a good qualitative picture of the flow field at the exit from the impeller. For easy comparison with the inverse designed impellers, the flow field in the conventional impeller was also analyzed by using a similar 29 × 129 × 29 computational mesh. All computations were performed for zero tip clearance.

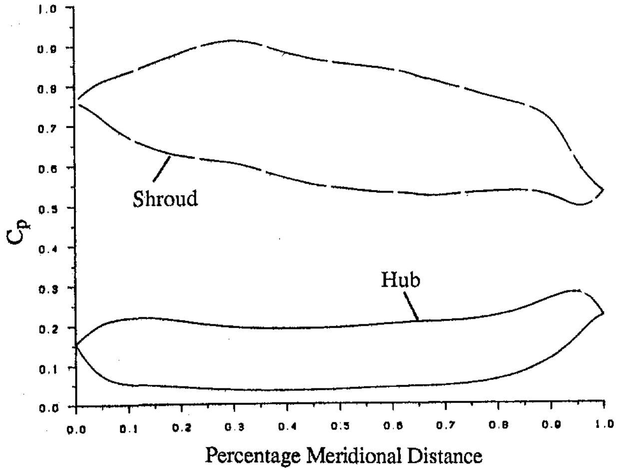

(a) Impeller A

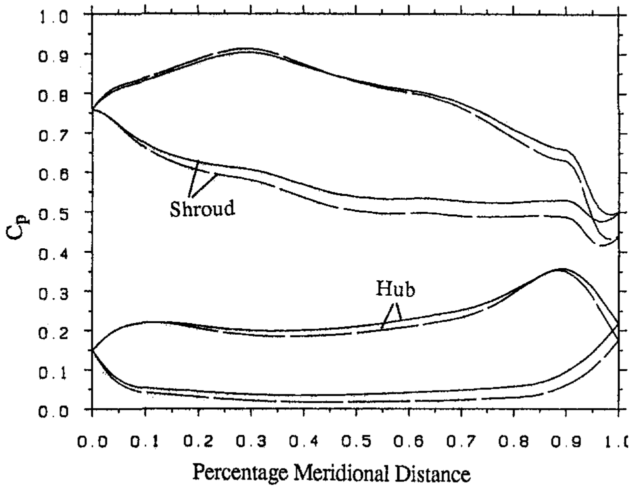

(b) Solid Line - Impeller C
Dashed Line - Impeller CII

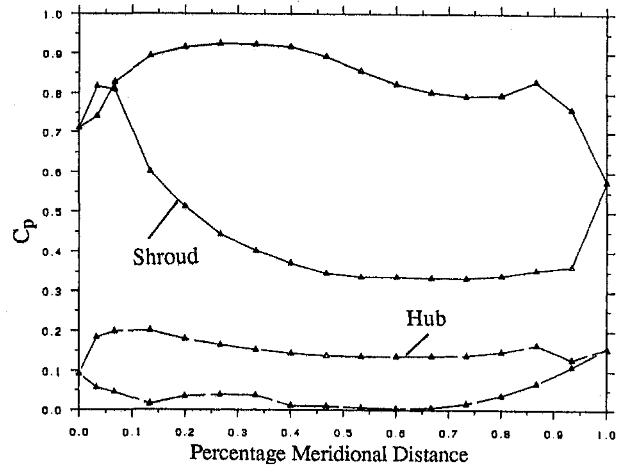

(c) Conventional Impeller

Fig. 5 Reduced static pressure distribution (C_p = (Rothalpy - Reduced static pressure)/$0.5\rho U_{2m}^2$)

Table 3 Predicted performance by Dawes code

Impeller	Euler Head	Efficiency Difference %
Conventional	0.447	0.0
A (7 blades)	0.355	-6.9
C (7 blades)	0.359	-7.1
CII (7blades)	0.401	-3.9
CII (5 blades)	0.392	-0.8
CIII (7 blades)	0.413	-2.2

Overall Performance. A summary of the overall performance predictions for all three impellers is presented in Table 3. The predicted Euler head for both inverse designed impellers is about 18 percent lower than the specified Euler head of 0.437 used to design the impellers. At the time and due to budgetary time constraints, the investigation of the likely causes of the lower Euler head was not possible and therefore to account to some extent for the lower Euler head a new impeller was designed with the same loading distribution and stacking condition as impeller *C*, but with a higher nondimensional design Euler head of 0.485. This was the impeller (to be called impeller *CII*) that was manufactured and used for the experimental study reported in Part 2 of the paper. The wrap angle distribution for impeller *CII* is presented (by the dashed line) in Fig. 4(*b*) and the corresponding reduced pressure distribution is presented in Fig. 5(*b*). The flow through this impeller was also computed by using the viscous code using the same computational mesh as that used for impellers *A* and *C*. The overall performance predictions for impeller *CII* are also presented in Table 3.

The efficiency presented in Table 3 was calculated by dividing the mass-averaged head by the mass-averaged Euler head at the *trailing edge plane* of each impeller and therefore does not include the effect of mixing losses occurring behind the impeller trailing edge. The predicted efficiency for impellers *A* and *C* is about 7 percent less than that of the conventional impeller, while the efficiency of impeller *CII* is only 4 percent less than the conventional. The main cause of the lower predicted efficiency of the inverse designed impellers was found to be due to two main reasons. First, the inverse designed impellers were designed with seven blades rather than five for the conventional impeller (which later work showed to be the optimum blade number for this configuration). Second, the inverse designed impellers were designed with the same normal thickness as that used for the conventional impeller. Due to the difference in blade angles between the conventional and inverse designed impellers, the specification of the normal thickness resulted in higher tangential thickness particularly at the tip of the inverse designed impeller (see Fig. 8). The combined effect of higher blade number and tangential thickness is to increase the relative velocity in the blade passage and therefore losses. The higher losses may also be attributed to the lower predicted Euler head in the inverse designed impellers. The lower Euler head implies slower rate of diffusion through the impeller and therefore higher relative velocity (and as a result losses) at corresponding points in the impellers. The 3 percent improvement in efficiency of impeller *CII* over that predicted for impeller *C* is mainly due to the effect of increased diffusion rate in impeller *CII*. The flow through impeller *CII* was also computed using five blades instead of the seven that the impeller was designed for and the results in Table 3 indicate clearly the improvement in efficiency as a result of using five blades. The results of flow analysis for impeller *CII* with five blades are discussed in detail in Part 2 of the paper (Goto et al., 1994).

In order to investigate the causes of the lower predicted Euler head for the inverse designed impellers, a number of studies were undertaken. At first glance, the effect of hydrodynamic blockage on the impeller flow field was thought to be insignificant, as the boundary layers are thin (because of higher Reynolds numbers as compared to centrifugal compressors) and the flow is not separated. So in order to establish the likely cause of the lower Euler head, the flow through impeller *CII* was computed by using Denton's (1983) inviscid time marching code. As the convergence of this code slows down at low Mach numbers the computation was performed at 10,000 rpm, with scaled velocity triangles. The computed mass-averaged exit $r\bar{V}_\theta$ was found to be 0.4993, which is slightly higher than the specified value. As this computation was performed at a higher rotational speed, the density increases toward the trailing edge as a result of the compressibility effects. The effect of increase in density on the predicted Euler head has been investigated by using the compressible and incompressible version of Dawes code, thereby relating the ratio of compressible Euler head over incompressible Euler head to the density ratios between the trailing edge and the inlet. In this case the density ratio was 1.086, which indicated that the ratio of Euler heads should be about 1.029. Dividing the predicted Euler head (0.4993) by this ratio (to allow for the change in volume flow rate) will give *0.485,* which is the exact value specified to design impeller *CII*. From this result we *can therefore conclude that the predicted lower Euler head is due to the hydrodynamic blockage effect,* which was not accounted for in the design.

In order to investigate the effect of hydrodynamic blockage on the blade shape, a hydrodynamic blockage distribution was assumed. This distribution was arrived at by assuming a linear variation in blockage from zero at the leading edge to 15 percent at the trailing edge and then linearly dropping to zero at the far downstream boundary. The same blockage distribution was applied in the spanwise direction. Using this distribution impeller *C* was redesigned. The flow through this impeller (to be designated impeller *CIII*) was computed by using the viscous code and the results of the overall performance predictions are presented in Table 3. The results indicate clearly that by assuming this aerodynamic blockage distribution the exit Euler head has now increased to 0.413 (from 0.359) and the predicted efficiency has increased by 5 percent. It must, however, be emphasized that the above-mentioned distribution of aerodynamic blockage is based on empiricism and a more systematic approach is required in order to account for the blockage effects. A viscous/inviscid interaction method such as that described by Zangeneh (1994) should provide a more accurate means of accounting for viscous effects in the impeller.

Internal Flow Predictions. The predicted velocity vectors on the pressure and suction surfaces of the conventional impeller and impellers *A*, *C*, and *CII* are presented in Figs. 6 and 7. Strong secondary flows can be observed on both the pressure and suction surfaces of the conventional impeller, with the spanwise movement of low-momentum fluids starting at about 25 percent of meridional chord on both surfaces. As a result of the secondary flows low-momentum fluid is accumulated on the shroud, creating the recirculation region, which can be clearly observed there, downstream of the trailing edge. In the case of impeller *A*, a relatively strong secondary flow can be seen on the pressure surface, but the intensity of the secondary velocities on the suction surface has been markedly reduced as compared to the conventional impeller. In the case of impeller *C*, the secondary flow on the pressure surface is very similar to that observed for impeller *A*. On the suction surface, however, very little secondary flow can be observed. The secondary flows on impeller *CII* are identical to that observed for impeller *C*. The results presented here provide further confirmation of the close correlation between gradients of reduced static pressure and the presence of meridional secondary flows, as pointed out earlier in the paper.

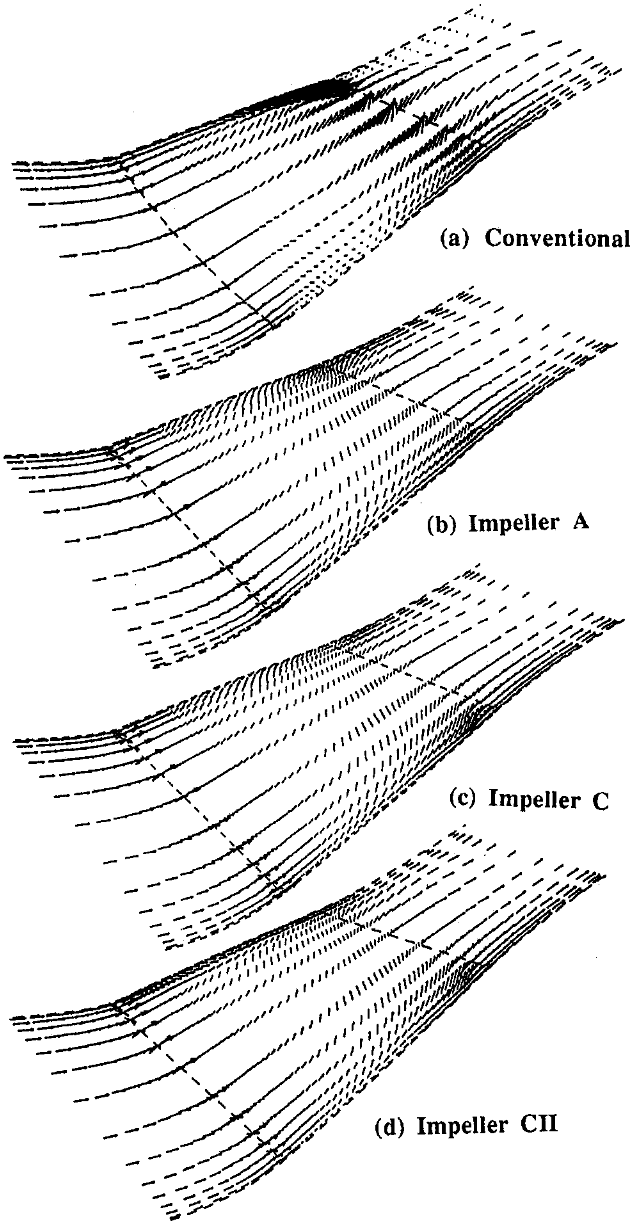
(a) Conventional

(b) Impeller A

(c) Impeller C

(d) Impeller CII

Fig. 6 Velocity vectors predicted by Dawes code near the pressure surface

The development of the relative velocity field in the three impellers is compared in Figs. 8 and 9. Figure 8 presents the relative velocity contours at 50 percent chord. At this stage no distinct wake region can be observed in any of the impellers. One interesting feature of the results is the higher values of relative velocity predicted for impellers *A* and *C* and to a lesser extent *CII*. As explained above this is mainly due to the combined effect of higher blade numbers and tangential thickness.

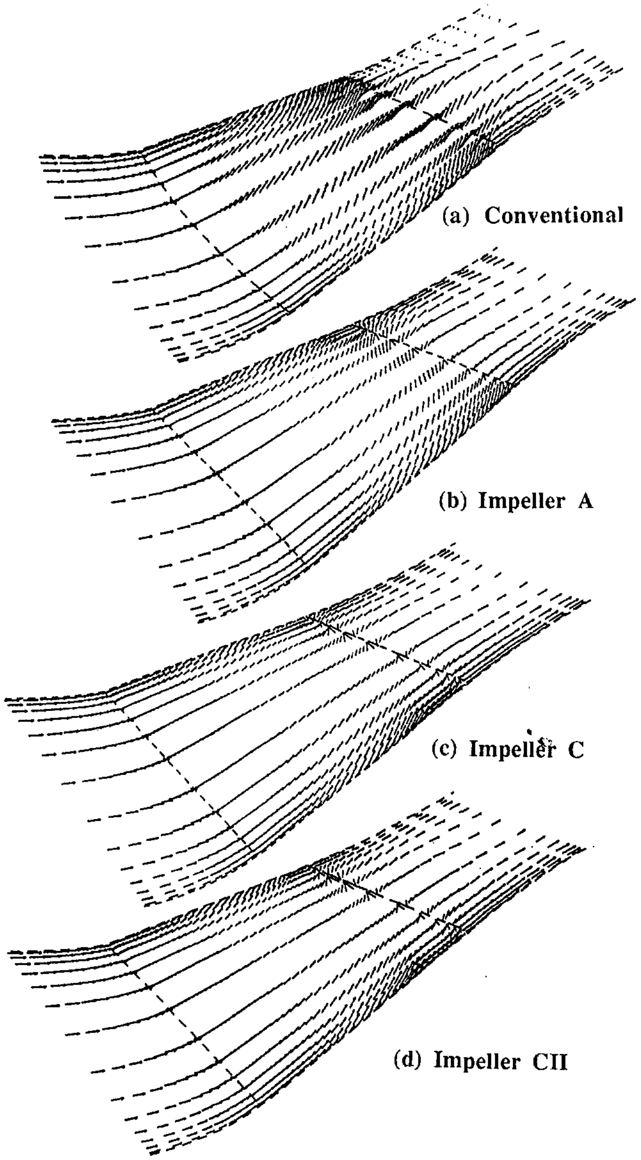

Fig. 7 Velocity vectors predicted by Dawes code near the suction surface

As a result of the higher overall relative velocity more low-momentum fluid has been generated on the suction surface of the three inverse designed impellers. The resulting relative velocity distributions at the exit of the three impellers are compared in Fig. 9. In the case of the conventional impeller a distinct wake region can be observed at the shroud. The exit flow from impeller *CII*, however, shows very little accumulation of low-momentum fluids despite the presence of higher amount of low-momentum fluid on the suction surface. This shows clearly that the suppression of secondary flows on the suction surface of the inverse designed impeller *CII* has resulted in marked improvement in the uniformity of the impeller exit flow.

Conclusion

The impeller geometry of a medium specific speed mixed flow pump was designed by using the three-dimensional inverse design method of Zangeneh (1991), in which the circulation distribution is specified. The main objective of the design was to suppress secondary flows in order to obtain a uniform exit flow field from the impeller. Two different impellers were designed using the inverse design method with the same circulation distribution, but different stacking condition. The flow through the inverse designed impellers was computed by using a three-dimensional viscous code. The viscous predictions showed clearly that it is possible to control meridional secondary flows particularly on the suction surface, where most of the low-momentum fluid in the impeller is generated, by suitable choice of the inputs to the inverse design program. In particular it was shown that the choice of stacking condition and its location can have a very significant effect on the blade reduced static pressure, whose spanwise gradients are directly correlated to meridional secondary flows in the impeller. It was also shown that the suppression of secondary flows on the suction surface results in a uniform exit flow field from the impeller, which should help to improve the stability range of the pump as well as the performance of the diffuser downstream of the impeller.

The performance predictions indicated that it is necessary to account for hydrodynamic blockage effects in the impeller in order to achieve the specified Euler head when the inverse

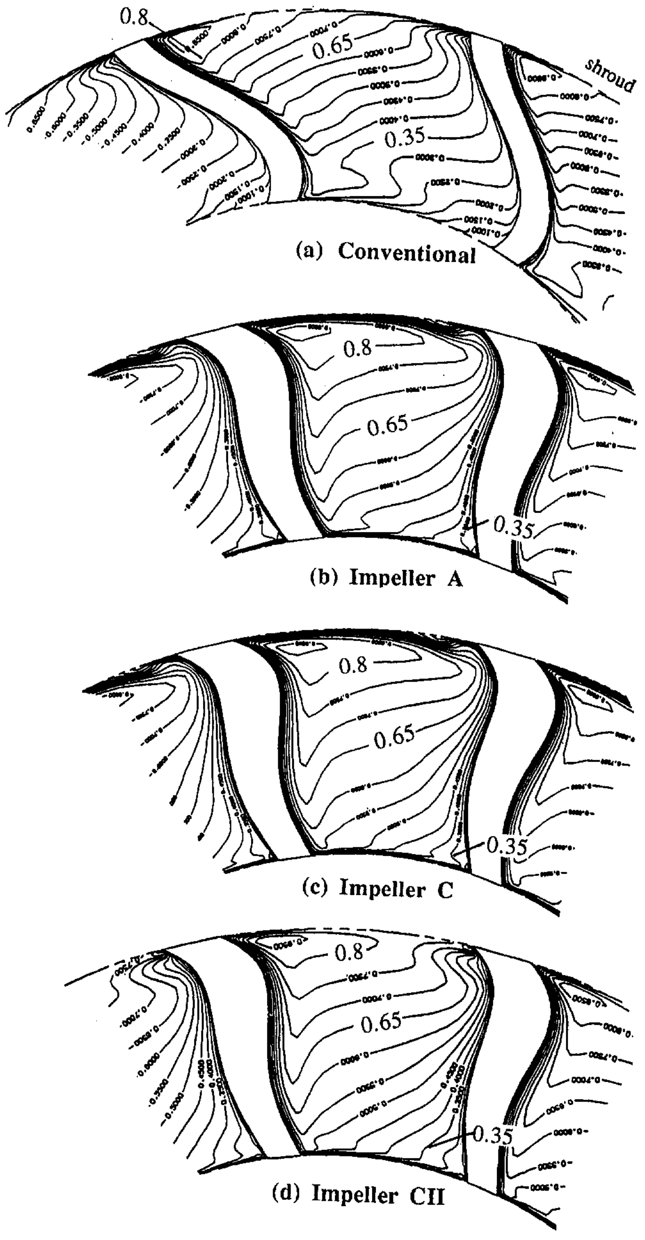

Fig. 8 Relative velocity contours—50 percent chord (contour interval = 0.05, normalized by U_{2m})

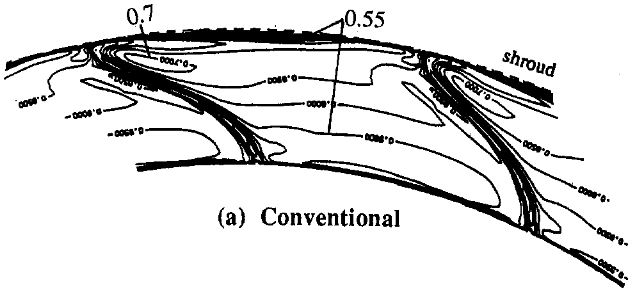

(a) Conventional

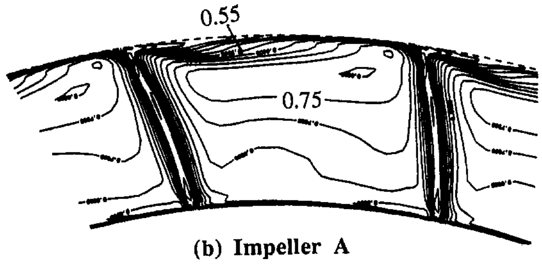

(b) Impeller A

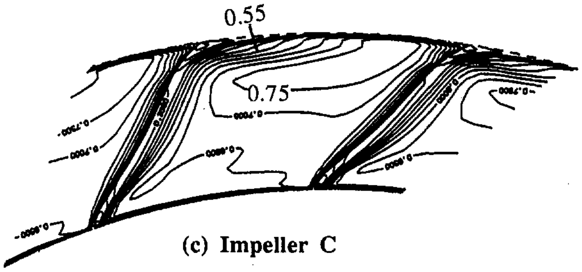

(c) Impeller C

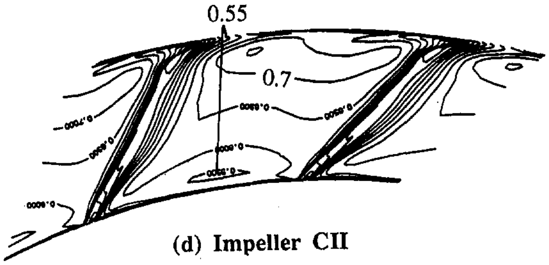

(d) Impeller CII

Fig. 9 Relative velocity contours—trailing edge (contour interval = 0.05, normalized by U_{2m})

design method is applied to incompressible turbomachines such as pumps. A systematic way of accounting for viscous effects in the impeller is to use the viscous/inviscid interaction approach reported by Zangeneh (1993). Work is currently under way to extend this method to incompressible flow.

Acknowledgments

The authors would like to thank Ebara Research Co. Ltd. for permission to publish this paper.

References

Casey, M. V., Dalbert, P., and Roth, P., 1992, "The Use of 3D Viscous Flow Calculations in the Design and Analysis of Industrial Centrifugal Compressors," ASME JOURNAL OF TURBOMACHINERY, Vol. 114, pp. 27–37.

Daiguji, H., 1982, "A Finite Element Method for Analysing the 3D Flow in Turbomachinery," *Proc. 4th International Symposium on Finite Element Methods in Flow Problems,* University of Tokyo Press, pp. 751–758.

Dawes, W. N., 1988, "The Development of a 3D Navier–Stokes Solver for Application to all Types of Turbomachinery," ASME Paper No. 88-GT-70.

Denton, J. D., 1983, "An Improved Time Marching Method for Turbomachinery Flow Calculations," ASME *Journal of Engineering for Power,* Vol. 105, p. 514.

Eckardt, D., 1976, "Detailed Flow Investigation Within a High Speed Centrifugal Compressor Impeller," ASME *Journal of Fluids Engineering,* Vol. 98, pp. 390–402.

Eckardt, D., 1980, "Flow Field Analysis of Radial and Backswept Centrifugal Compressor Impellers—Part I. Flow Measurements Using a Laser Velocimeter," *Performance Prediction of Centrifugal Pumps and Compressors,* Gopalakrishnan, ed., ASME, New York, pp. 77–86.

Goto, A., 1992a, "Study of Internal Flow in a Mixed Flow Pump Impeller at Various Tip Clearances Using 3D Viscous Flow Calculations," ASME JOURNAL OF TURBOMACHINERY, Vol. 114, pp. 373–382.

Goto, A., 1992b, "The Effect of Tip Leakage Flow on Part-Load Performance of a Mixed-Flow Pump Impeller," ASME JOURNAL OF TURBOMACHINERY, Vol. 114, pp. 383–391.

Goto, A., Takemura, T., and Zangeneh, M., 1994, "Suppression of Secondary Flows in a Mixed Flow Pump Impeller by Application of Three-Dimensional Inverse Design Method: Part 2—Experimental Validation," ASME Paper No. 94-GT-46: ASME JOURNAL OF TURBOMACHINERY, Vol. 118, 1996, this issue, pp. 544–551.

Johnson, M. W., 1978, "Secondary Flows in Rotating Bends," ASME *Journal of Engineering for Power,* Vol. 100, pp. 553–560.

Walker, P. J., and Dawes, W. N., 1990, "The Extension and Application of Three-Dimensional Time-Marching Analysis to Incompressible Turbomachinery Flows," ASME JOURNAL OF TURBOMACHINERY, Vol. 112, pp. 385–390.

Zangeneh, M., Dawes, W. N., and Hawthorne, W. R., 1988, "Three-Dimensional Flow in Radial-Inflow Turbines," ASME Paper No. 88-GT-103.

Zangeneh, M., 1991, "A Compressible Three Dimensional Blade Design Method for Radial and Mixed Flow Turbomachinery Blades," *Int. J. Numerical Methods in Fluids,* Vol. 13, pp. 599–624.

Zangeneh, M., 1992, "An Inverse Design Method for Radial Turbomachines," VKI Lecture series, Radial Turbines, 1992-5, Belgium.

Zangeneh, M., 1994, "Inviscid/Viscous Interaction Method for Three-Dimensional Inverse Design of Centrifugal Impellers," ASME JOURNAL OF TURBOMACHINERY, Vol. 116, pp. 280–291.

A. Goto

T. Takemura

Ebara Research Company, Limited,
Fujisawa-shi, Japan

M. Zangeneh

Department of Mechanical Engineering,
University College of London,
London, United Kingdom

Suppression of Secondary Flows in a Mixed-Flow Pump Impeller by Application of Three-Dimensional Inverse Design Method: Part 2—Experimental Validation

In Part 1 of this paper, a mixed-flow pump impeller was designed by a fully three-dimensional inverse design method, aimed at suppressing the secondary flows on the blade suction surface. In this part, the internal flow fields of the impeller are investigated experimentally, using flow visualization and phase-locked measurements of the impeller exit flow, in order to validate the effects of secondary flow suppression. The flow fields are compared with those of a conventional impeller, and it is confirmed that the secondary flows on the blade suction surface are well suppressed and the uniformity of the exit flow fields is improved substantially, in both circumferential and spanwise directions. The effects of tip clearance and the number of blades for the inverse designed impeller are also investigated experimentally and numerically.

Introduction

It is well acknowledged that secondary flows have a dominating effect in establishing exit flow nonuniformity in centrifugal and mixed-flow turbomachinery impellers. The secondary flow pattern inside the impeller affects not only the performance and the stability of the impeller itself, but also the performance of the downstream diffuser, which accepts the impeller discharge flow. Goto (1992a) studied the process of the jet-wake flow formation by secondary flows, inside an isolated mixed-flow pump impeller at various tip clearances, based on experimental observations and numerical computations. The link between the jet-wake flow pattern and the onset of the positively sloped head-flow characteristics (stall onset) was also investigated by Goto (1992b), and it was found that impellers stalled at higher flow rates when the wake regions located closer to the casing-suction surface corner.

In Part 1 of this paper (Zangeneh et al., 1996), a mixed-flow pump impeller was designed by a fully three-dimensional inverse design method, aimed at suppressing the secondary flows on the blade suction surface. Numerical computation by the Dawes Navier–Stokes code predicted well-suppressed secondary flows on the blade suction surface, and substantial improvements in the exit flow field were achieved compared to the predicted flow fields of a corresponding conventional impeller.

In the present paper, the internal flow fields of the impeller are investigated experimentally in order to validate the effectiveness of the three-dimensional inverse design method. The flow fields are compared with those of a conventional impeller, and the secondary flow suppression and the uniformity of the exit flow fields are discussed. The effects of tip clearance and the number of blades for the inverse designed impeller are also discussed.

Experimental Apparatus and Method

Test Loop. Figure 1 schematically shows the cross section of a mixed-flow pump stage used for performance tests and flow field measurements. The inlets of the diffuser blades were moved downstream, away from the trailing edge of the impeller, in order to measure the impeller exit flows at Station B under the isolated impeller configuration. Experiments were carried out on both the inverse designed impeller and the corresponding conventional impeller. The design specific speed of the pump was $\Omega \cdot \sqrt{Q}/(gH)^{3/4} = 1.34$, i.e., 550 $(\text{rpm} \cdot \text{m}^3/\text{min} \cdot \text{m})$. Water was used as the test fluid and the pump stage was placed in a closed flow loop consisting of a 440-mm-dia suction pipe, a 350-mm-dia delivery pipe, a 10.3-m^3 reservoir tank, and a return line with venturi tubes and throttles. Performance tests were conducted according to ISO standards. The impeller speed was 800 rpm giving a Reynolds number of $\text{Re} = W_1 l_m/\nu = 1.33 \times 10^6$ at the design point.

Model Impellers. Each blade of the inverse designed impeller was manufactured from a block of bronze material by a five-axis numerically controlled milling machine, and thus manufactured seven blades were stacked into a hub to form a seven-bladed impeller. The impeller was also tested under a five-bladed configuration by replacing the hub. The front shroud was removable and so the effects of the tip leakage flow were also examined experimentally. The blade tip clearance was 0.5 mm in all unshrouded cases including the conventional impeller case. The design criteria and specifications were described in detail in Part 1 of this paper (Zangeneh et al., 1996). In contrast, the corresponding conventional impeller was designed as a five-bladed impeller by simply connecting the inlet and the exit blade angles with a smooth monotonic curve on each stream surface. The conventional impeller was made by casting and the blade surface finish was applied to make the flow passage hydrodynamically smooth. The unshrouded conventional impeller was made by removing the front shroud by machining. The meridional geometries of the inverse designed and conventional impellers were identical, apart from the curved leading edge in

---

Contributed by the International Gas Turbine Institute and presented at the 39th International Gas Turbine and Aeroengine Congress and Exposition, The Hague, The Netherlands, June 13–16, 1994. Manuscript received by the International Gas Turbine Institute February 4, 1994. Paper No. 94-GT-46. Associate Technical Editor: E. M. Greitzer.

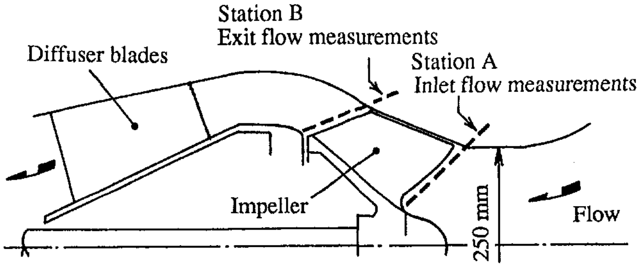

Fig. 1 Cross section of mixed-flow pump stage

Table 1 Design specification

	hub / midspan / shroud	Design flow rate : 9.2 m^3 / min
r_1 (mm)	58.0 / 102.3 / 132.5	Design pump head : 6.5 mH_2O
r_2 (mm)	142.5 / 157.8 / 171.7	Rotational speed : 800 rev / min

Table 2 Test cases

Test Case	Blade Number	Performance Tests	Flow Visualization	Exit Flow Measurements
O-s5	5	X		
O-u5	5	X	X	X
CII-s7	7	X	X	X
CII-u7	7	X	X	X
CII-u5	5	X		X

O: Conventional Design CII: Inverse Design
s: Shrouded u: Unshrouded

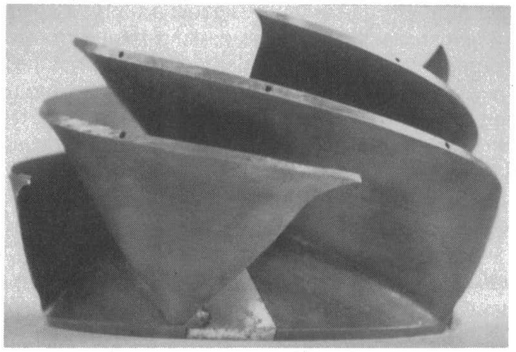

(a) Inverse designed impeller CII-u5

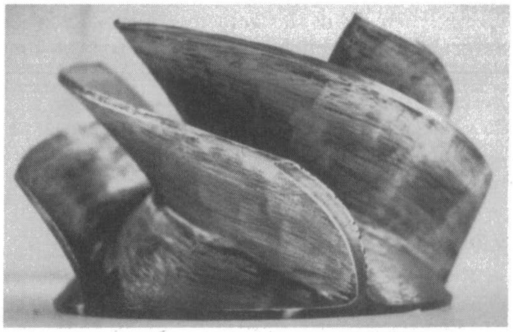

(b) Conventional impeller O-u5

Fig. 2 Comparison of impeller configuration

Table 3 Absolute difference in blade angles

$= |\beta_{\text{CII}} - \beta_{\text{Conventional}}|$

Location	Shroud	Hub
8%-chord	1.7	2.4
50%-chord	7.3	1.6
92%-chord	10.3	17.8

(degree)

the conventional impeller, which was replaced by a straight line connecting the hub and shroud in the inverse design. The meridional geometry and design conditions are given in Table 1, and the test cases are summarized in Table 2. Here, suffix "*u*" represents the unshrouded case, "*s*" the shrouded case, "5" the five-bladed case, and "7" the seven-bladed case.

Figure 2 compares the geometry of the inverse designed impeller (CII-u5) with that of the conventional impeller (O-u5) under five-bladed unshrouded configuration. The trailing edge of the inverse designed impeller is inclined in the counterrotating direction toward the tip, and the effect of the stacking condition adapted in this particular design is clearly observed. As was discussed in Part 1 of the paper, the spanwise gradients of reduced static pressure are well correlated with the presence of meridional secondary flows (also see Cumpsty, 1989). The blade lean of CII impeller reduced the blade loading near the tip and increased the loading at the hub. Because of this, the spanwise gradients of reduced static pressure were reduced and it was possible to suppress the spanwise secondary flows on the blade suction surface. On the other hand, the blade lean of the conventional impeller is in the opposite direction, although there is no clear hydrodynamic background in this case. Table 3 shows the absolute difference in blade angles between these two impellers at three different locations. The difference in blade angle is quite substantial, and it is easily understood that such blade shape can never be reached by conventional design hypothesis.

Flow Field Measurements and Flow Visualization. Besides the performance tests, inlet and exit flow measurements of the impeller were carried out using two types of pressure probe. The inlet flow was measured by an ordinary three-hole Pitot probe at Station A, and the relative exit flow was measured by a two-hole Pitot probe with high-frequency response at Station B (Fig. 1), 8 mm downstream of the trailing edge. In the latter probe, two diffusion-type semiconductor pressure transducers were placed in the stem tube. The resonance frequency

Nomenclature

H = head, m
l = meridional blade chord length
LE = impeller leading edge
Q = flow rate, m^3/s
Q^* = flow rate ratio = $Q/(Q$ at design point)
r = radius
TE = impeller trailing edge
U = peripheral blade speed
W = relative velocity
β = blade angle measured from circumferential direction
Ω = angular rotation frequency, rad/s

Subscripts

1 = inlet
2 = exit
m = midspan
t = blade tip

of the pressure sensing system was about 5.6 kHz and was high enough compared with the blade passing frequency of 67 Hz at 800 rpm. Three-dimensional relative flow fields at the impeller exit were measured by the phase-locked multisampling and averaging technique (for details on the measuring system, the data reduction method, and the accuracy of measurements, see Goto, 1988).

In order to assess the magnitude of the secondary flows within the impellers, flow visualization of the wall streamlines was carried out using an oil-film technique. The viscosity of the oil was carefully adjusted, depending on the local velocity on the flow passage walls, to get clear pictures of the flow pattern.

Accuracy of Measurements. The probable uncertainty in the data reduction process and the measuring system of the two-hole pitot probe has been evaluated by Goto (1988) using a calibration test rig. The accuracy is ±2.5 percent in the static pressure, ±1.3 percent in the velocity, ±0.3 deg in the yaw angle, and ±1 deg in the pitch angle. It has also been confirmed that the steady-state calibration curves are correctly applicable to the present unsteady flow.

The flow rates obtained by the integration of measured velocity fields agreed with those obtained by the venturi tubes at an accuracy of ±5 percent in all cases presented in this paper.

Discussion on Numerical Results

In Part 1 of this paper, the inverse designed impeller CII was designed as a seven-bladed shrouded impeller (CII-s7). In the following experimental investigations, impeller CII was tested with and without the shroud, and under seven and five-bladed configuration in order to see the effects of the tip clearance and the difference in blade numbers. In the present section, the effects of the tip clearance and the reduction in the blade number are numerically investigated beforehand, based on the computations by an incompressible version of the Dawes three-dimensional Navier–Stokes code (Walker and Dawes, 1990) at the design operating condition. Goto (1992a) applied the Dawes code to the present conventional impeller O at various tip clearances, including the shrouded case, and compared the predicted jet-wake flow pattern with that in experiments at the exit of the impeller. The results show that the Dawes code can capture the characteristic feature of the difference in the secondary flow pattern and the resulting jet-wake flow development inside the impeller.

Effects of Tip Clearance. The present three-dimensional inverse design method does not take into account the effects of tip clearance. However, both shrouded and unshrouded impellers are widely used, and there are also a number of studies that show the dominating influence of the tip leakage flow on the three-dimensional flow pattern, such as a jet-wake flow formation pattern.

The Dawes code was applied to compare the secondary flow pattern between the unshrouded CII impeller (CII-u7) and the unshrouded conventional impeller O-u5. Figure 3 shows the computational grid for CII-u7 with a tip clearance of 0.5 mm. The grid points were clustered near the endwalls and blade surfaces, and the blade tip was rounded off in the simulation. There were only two meshes in the clearance, but this should be enough to capture the global effects of the tip leakage flow. The grid size of 29 × 125 × 29 (pitchwise × streamwise × spanwise) required about 10 hours of CPU time on a single processor of a Convex C220 computer (100MFlops).

Figure 4 compares the secondary flow pattern between CII-u7 and O-u5 impellers on the meridional plane close to the blade suction surface. The relative velocity contours at two different streamwise locations, on quasi-orthogonal planes at 50 percent chord and the trailing edge, are also presented. The secondary flows, on the blade suction surface of CII, were better suppressed than those of the unshrouded conventional impeller (Fig. 4(*c*)), and the exit flow was fairly uniform in the spanwise direction. In the case of O-u5, the nonuniformity of the exit flow fields was not as unfavorable as that of the shrouded case O-s5, presented in Part 1 of this paper. This was considered to be caused by the positive effects of the tip leakage flow. However, the nonuniformity of the exit flow fields still existed near the casing, and this may adversely affect not only the efficiency and the stability of the impeller but also the performance of the downstream diffuser, which accepts the impeller exit flow. At 50 percent chord location (Fig. 4(*a*)), there appeared low relative velocity region close to the casing due to the tip leakage vortex in both CII-u7 and O-u5. However, at the trailing edge plane (Fig. 4(*b*)), the casing viscous region is thinner in CII-u7. This is considered to be the effects of secondary flow suppression in CII-u7. Overall, the present computations show very little effects by the tip leakage vortex on the suppression of secondary flows on the blade suction surface.

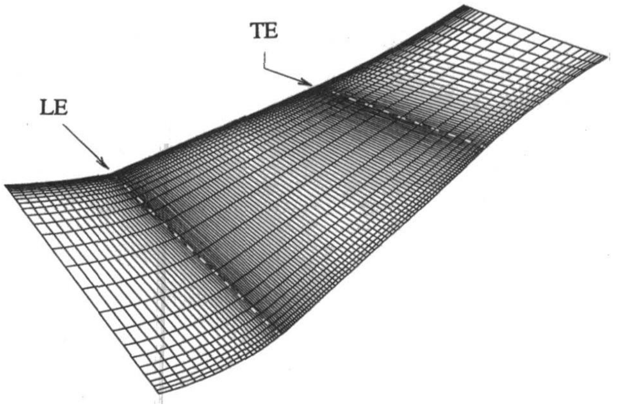

Fig. 3 Computational grid on meridional plane (case CII-u7, grid size = 29 × 125 × 29)

Effects of Blade Number. Figure 4(*b*) shows much thicker blade boundary layer in CII-u7, between 25 percent span and the blade tip. The inverse designed impeller had seven blades and the blade angle was much lower than that of the conventional impeller in the tip region. These two factors made the effective passage area of CII-u7 very narrow. In addition to this, the blade length was longer in CII at the tip due to the small blade angle. Because of this, more friction losses could be generated in CII-u7, and made the blade boundary layer thicker toward the blade tip. It was felt unfair to compare the internal flows between the seven-bladed inverse designed impeller and those of the conventional impeller, originally designed under the five-bladed configuration. So, it was decided to do additional experiments for CII with reduced blade number of five, although this could have deteriorated the secondary flow suppression effects. In this paragraph, the effect of the reduction in blade number is discussed based on numerical predictions.

Figure 5 compares the relative velocity contours between CII-s7 and CII-s5 at two different streamwise locations, on quasi-orthogonal planes at 50 percent chord and the trailing edge. The secondary flow pattern on the meridional plane close to the blade suction surface is also presented. The boundary layer thickness, relative to the pitch length, was reduced in CII-s5 because of the lower blockage effects of the blade thickness. The meridional secondary flow is similar between CII-s7 and CII-s5, and their magnitude is still much weaker than that in the conventional impeller (see impeller O-u5 case in Fig. 4(*c*), for example), and a uniform exit flow is achieved. In impeller CII-s5 case (Fig. 5(*b*), right), the low relative velocity region emerged to the midpitch location along the casing, compared to the case of CII-s7 (Fig. 5(*b*), left) where it stayed closer to the blade, suggesting a slight increase in the suction surface secondary flows.

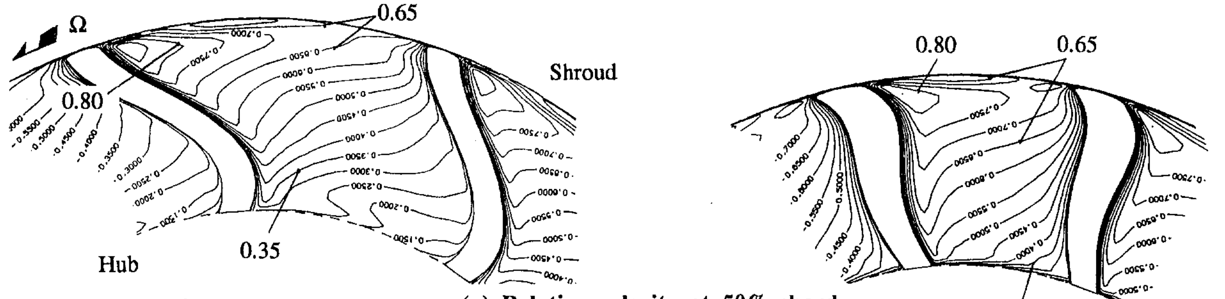

(a) Relative velocity at 50%-chord
(Quasi-orthogonal plane, J=61)

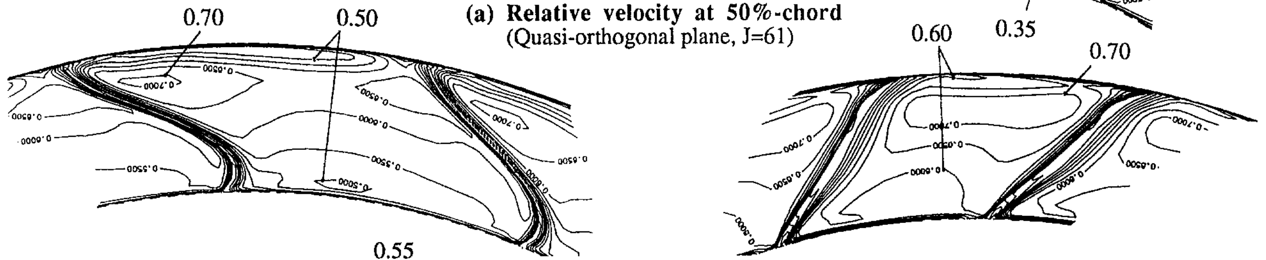

(b) Relative velocity at TE
(Quasi-orthogonal plane, J=100)

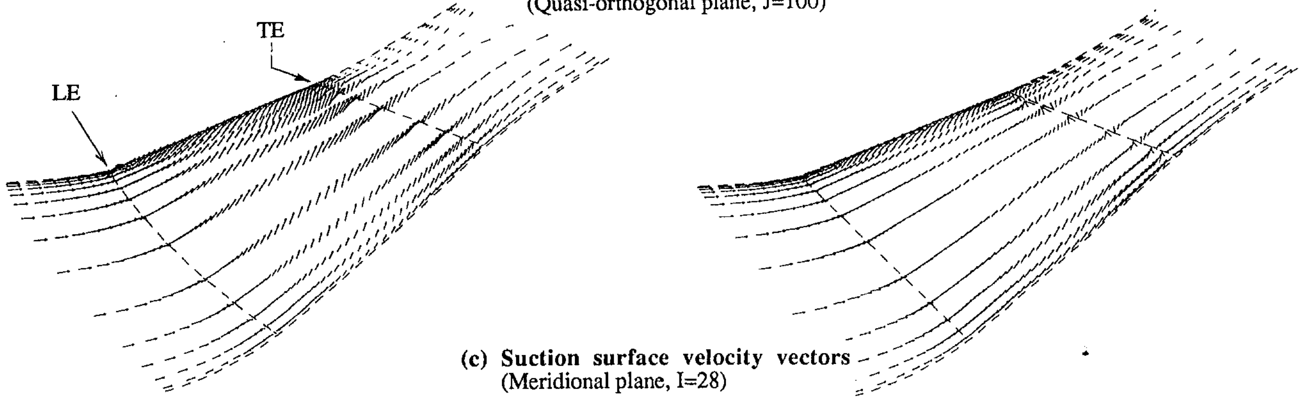

(c) Suction surface velocity vectors
(Meridional plane, I=28)

O-u5 impeller **CII-u7 impeller**

Fig. 4 Comparison of predicted flow patterns for unshoruded cases CII-u7 and O-u5 (contour interval = 0.05, normarized by U_{2m})

The boundary layer of CII-s5 (Fig. 5(*b*), right) is still thicker than that of O-s5 (see Fig. 10 of Part 1). There are probably two main causes. One is the small blade angle and the longer blade chord length at the tip of CII impeller. The blade length at the tip of CII is 1.5 times longer than that of the conventional impeller. Also the small blade angle made the effective flow passage fairly narrow, and the relative velocity was increased especially in the tip region. The other possible cause is the underestimated hydrodynamic blockage in the present inverse design (see discussion in ''Overall Performance'' of Part 1). Since the blockage effects were underestimated, the relative flow was accelerated in reality toward the exit and generated substantial amount of friction losses. The thick blade boundary layers may affect the impeller and the pump stage performances adversely, although the overall exit flow nonuniformity was improved in the CII impeller.

Discussion on Experimental Results

Overall Characteristics. The overall performance of the pump stage with the inverse designed CII-s7 (shrouded seven-bladed) impeller was compared with that of a conventional impeller. Since the overall performance of O-s7, having the same number of blades, had not been measured, the performance of O-s5 was selected for reference and compared with that of CII-s7 (Fig. 6). The pump head and the shaft power were normalized by the values for O-s5 at the design point.

The pump stage with the inverse designed impeller CII-s7 showed substantially lower pump head than that of the conventional impeller O-s5 by about 15 percent. In the present cases, the shaft power is directly related to the impeller work input or Euler head, as the disk friction and the mechanical losses were fairly small. So, Fig. 6 clearly shows that the lower head was caused by the lower impeller work input or lower Euler head of CII-s7. As was discussed in Part 1 of this paper, the main cause of this discrepancy is considered to be the blockage effects by the viscous region, developing along the flow passage walls. Since the viscous blockage effects were underestimated in the present inverse design, the relative flow inside the inverse designed impeller was accelerated in reality and the slip velocity was increased, giving lower swirl velocity inside and at the exit of the impeller. The percentage of the head reduction was larger than that of the shaft power, and so the hydraulic efficiency was also lower in the case of CII-s7. The excessive friction loss, discussed in the previous chapter, is considered to be responsible for this poor efficiency.

The stall, positively sloped head-flow characteristics, occurred late at the lower flow rate for CII-s7, and the stall margin was extended by 17 points (from $Q^* = 0.837$ to 0.665). This is possibly because of the secondary flow suppression on the suction surfaces of CII-s7 impeller blades, predicted by the numerical computations. However, since CII-s7 was lightly loaded, giving lower Euler head, the difference in the flow fields should be compared experimentally in detail in order to confirm

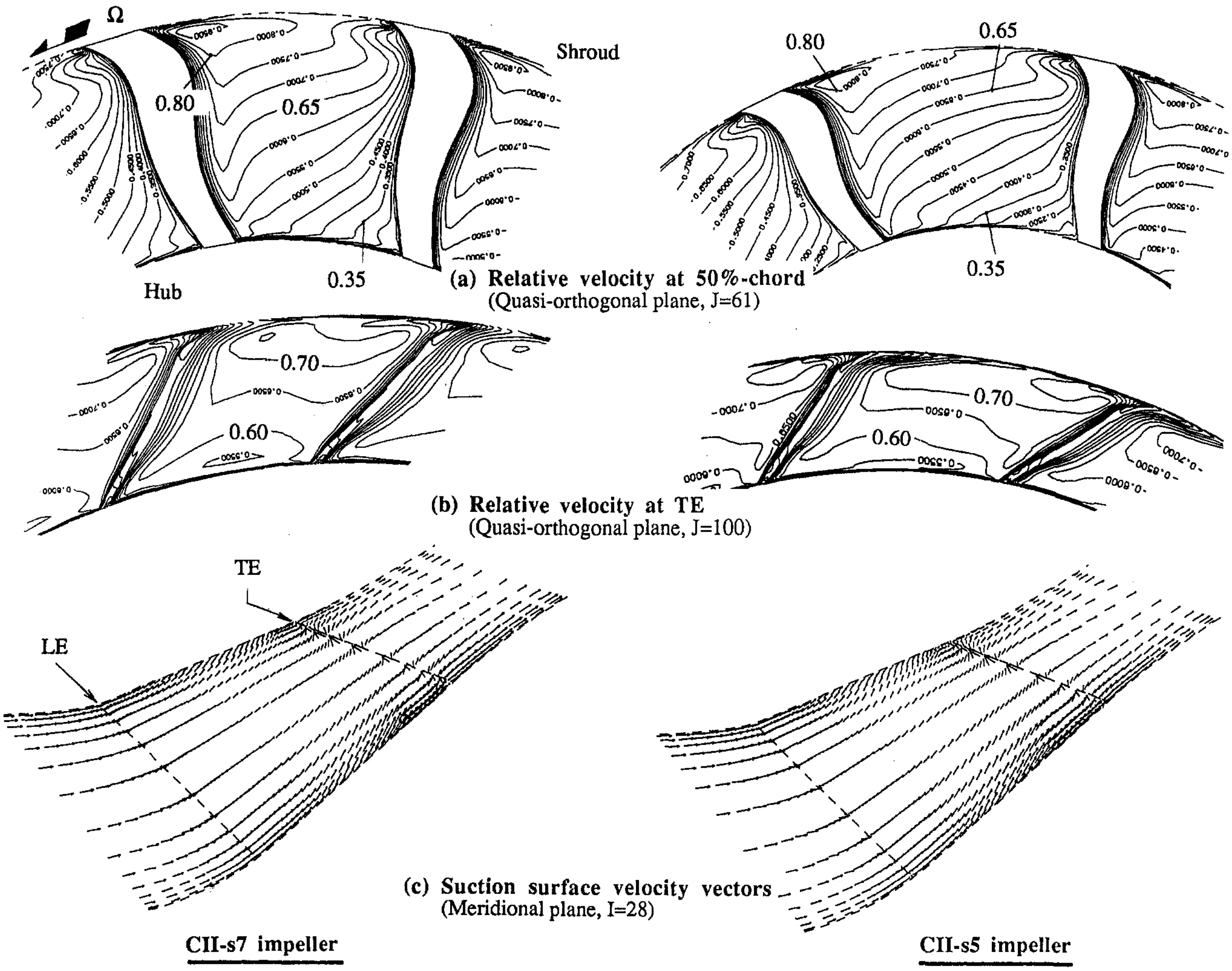

(a) Relative velocity at 50%-chord
(Quasi-orthogonal plane, J=61)

(b) Relative velocity at TE
(Quasi-orthogonal plane, J=100)

(c) Suction surface velocity vectors
(Meridional plane, I=28)

CII-s7 impeller

CII-s5 impeller

Fig. 5 Comparison of predicted flow patterns for CII with different blade number (contour interval = 0.05, normarized by U_{2m})

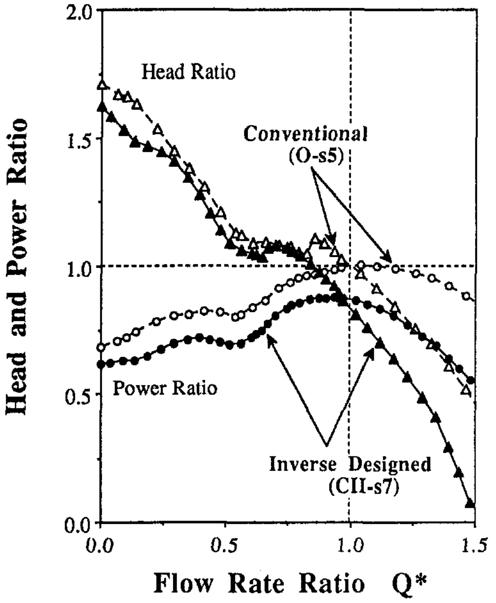

Fig. 6 Comparison of measured overall performances between CII-s7 and O-s5

the actual capability of the inverse design for secondary flow suppression.

Flow Visualization. In order to confirm the effects of secondary flow suppression, flow visualization was carried out for three impellers: O-u5, CII-s7, and CII-u7. Figure 7 shows the oil-film flow pattern on the blade suction surfaces at the design point. In the cases of the CII impeller, one blade among the seven blades was taken off the hub to make the flow pattern more visible. The streak of the oil-film flow pattern, which reached the tip of the each trailing edge, was traced in the upstream direction and the starting point at the leading edge was marked with a solid circle. The streak line reached around the root of the leading edge in case O-u5, while it reached around the 40 percent span location in both CII-s7 and CII-u7 cases. So, the secondary flows on the blade suction surfaces in cases CII-s7 and CII-u7 were relatively weak and were suppressed successfully, compared to the conventional design case O-u5.

The numerical computations for CII-s7 and CII-u7 (Fig. 4(*c*), right, and Fig. 5(*c*), left) predicted fairly suppressed suction surface secondary flows compared to the case of O-u5 (Fig. 4(*c*), left), showing good qualitative agreement with the measured oil-film flow pattern (Fig. 7). The numerical predictions, for inverse designed impellers, show increased secondary flows close to the hub surfaces between 45 and 75 percent chord. This flow pattern was also observed in Fig. 7(*a*, *b*). Around the midspan of the inverse designed impellers, the oil-

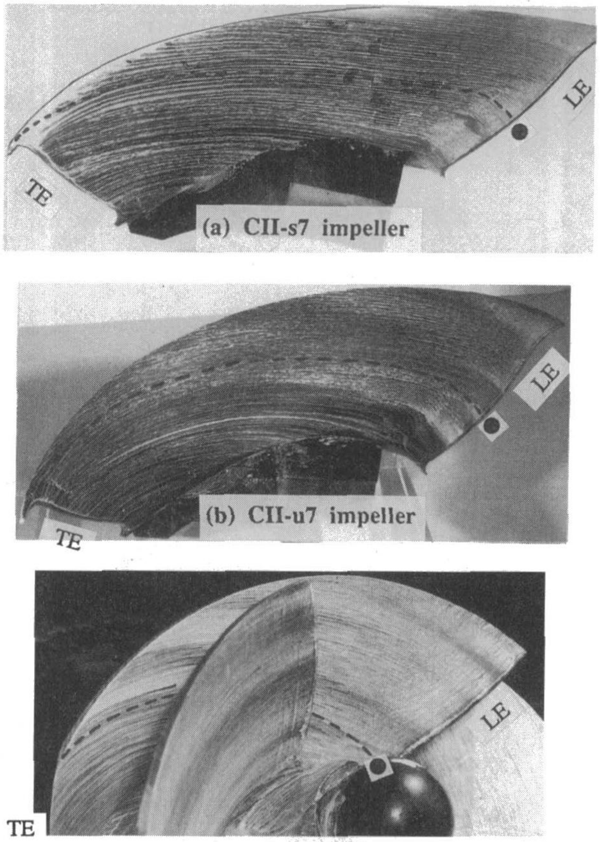

(c) O-u5 impeller

Fig. 7 Comparison of oil-film flow pattern on suction surface

film flow pattern shows almost no secondary flow motion in the fore part region, while it was convected radially outward toward exit, which was not predicted by numerical computations. This is considered to be partly because of the centrifugal force acting on the oil film due to the slight difference in specific gravity between oil and water.

The numerical computations predicted minor effects of the tip leakage flow on the suction surface secondary flows, and this was also confirmed experimentally by flow visualization. However, an apparent difference was observed on the pressure surface close to the casing. Figure 8 compares the oil-film flow pattern on the pressure surfaces between CII-s7 and CII-u7. The secondary flow pattern of CII-u7, predicted by a numerical computation, is also presented. The tip leakage vortex of CII-u7 crossed over the pitch along the casing and reached to the adjacent pressure surface, showing downward movement of the oil-film flow pattern around the blade tip. The numerical computation failed to predict this phenomenon possibly because of the insufficient grid number in the tip region. The predicted secondary flows were much stronger on the pressure surface than on the suction surface, and this was confirmed by flow visualization.

Circumferentially Averaged Exit Flow. The impeller exit relative flow fields, measured by the two-hole unsteady Pitot probe, were compared among the CII-s7, CII-u7, CII-u5, and O-u5 impellers in order to see the effects of the tip clearance and the blade number. The flow loss is defined as the rothalpy difference between the measuring plane and the upstream plane of the impeller, where the flow is considered to be uniform. It was assumed that there is no inlet prerotation, and the inlet flow measurements showed that this assumption was correct at both $Q^* = 1.0$ and 0.85 discussed here. The inlet recirculation was not observed at Station A until the onset of the positively sloped head-flow characteristics.

Figure 9(*a*) shows the spanwise distribution of the flow losses, mass averaged circumferentially, at the design point. The flow loss was extremely high in CII-s7 toward the shroud because of high friction loss in this region, as was discussed in the previous section. However, the loss was reduced substantially when there was a tip clearance (CII-u7). The tip clearance of 0.5 mm corresponds to only 0.8 percent of the exit blade span height, and so a small amount of leakage flow at the tip had large effect over the whole flow fields. The loss distributions between the 65 and 20 percent span are identical between CII-s7 and CII-u7. The reduction of the blade number from seven (CII-u7) to five (CII-u5) further reduced the flow losses between the casing and the 30 percent span location. The high generation of friction losses of CII-u7 had great influence over the whole flow fields. The flow loss of CII-u5 is lower than that of the conventional impeller O-u5, especially in the outer region between 60 and 90 percent span. However, the loss of CII-u5 tends to increase closer to the casing, possibly because of less effective suppression of the blade surface secondary flows, due to the reduced blade number and the resulting migration of the high loss fluid in the tip region, as was discussed in Fig. 5.

Figure 9(*b*) shows the distributions at an 85 percent flow rate of the design point ($Q^* = 0.85$). The trend is similar to

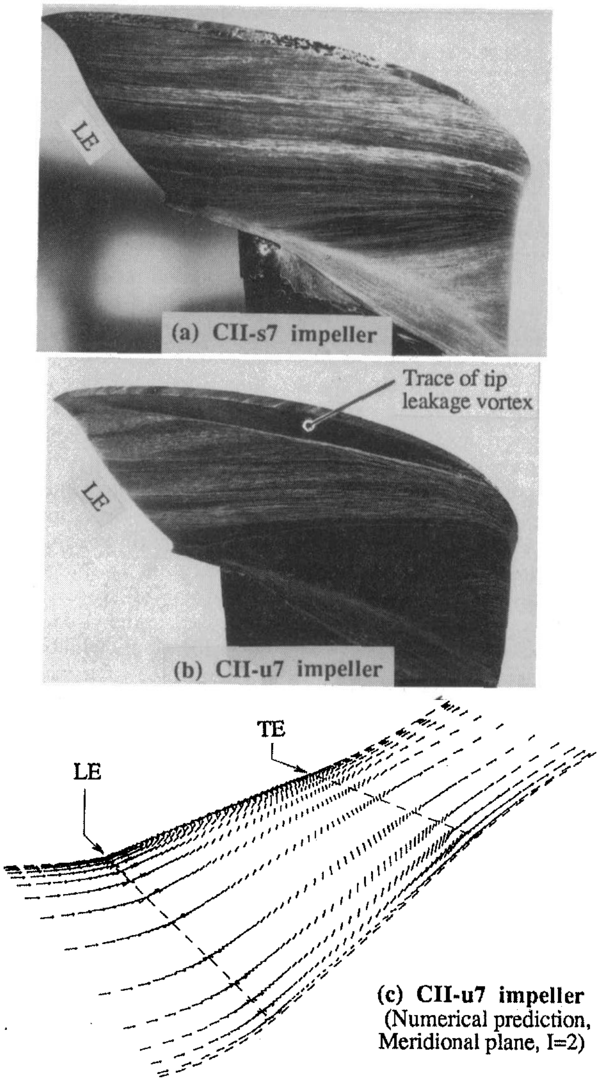

(c) CII-u7 impeller
(Numerical prediction,
Meridional plane, I=2)

Fig. 8 Comparison of secondary flow pattern on pressure surface

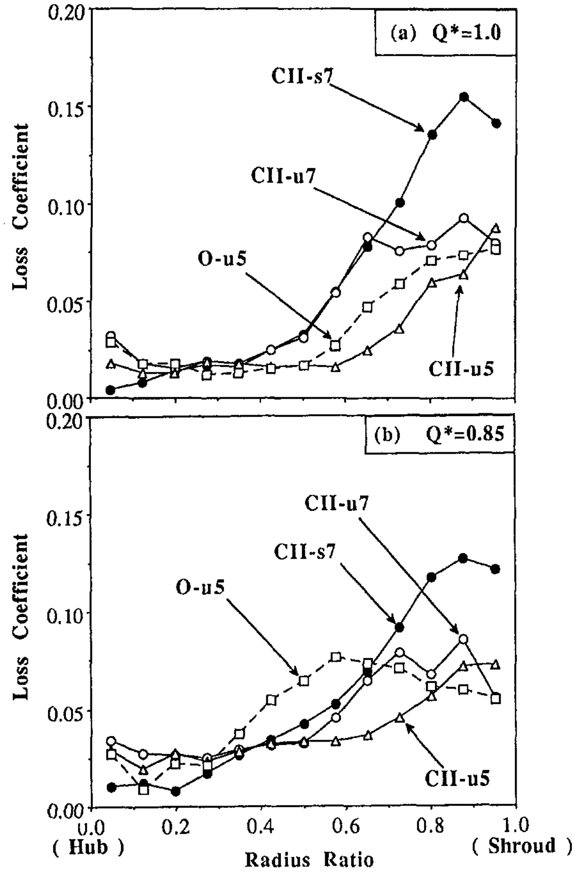

Fig. 9 Measured spanwise loss distribution (at Station B, mass-averaged circumferentially)

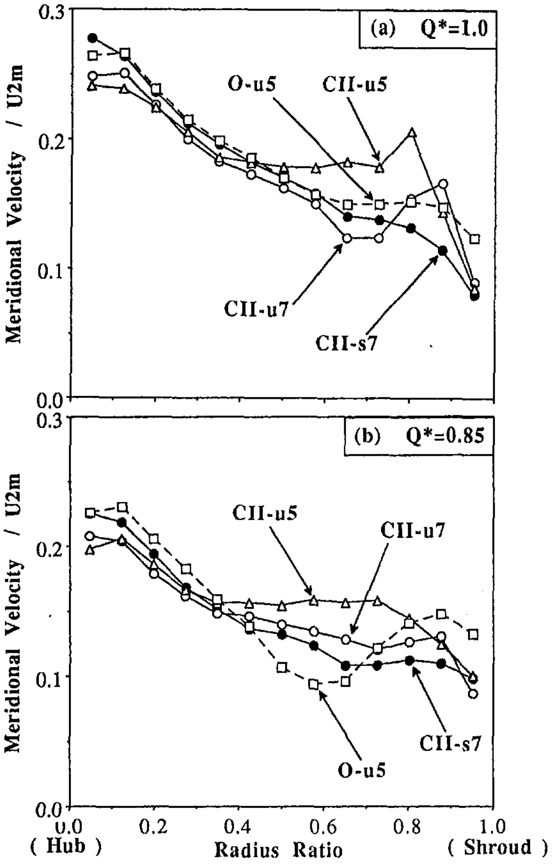

Fig. 10 Measured spanwise meridional velocity distribution (at Station B, area-averaged circumferentially)

that of the design point, but the flow losses were much less in CII-u5 than those in O-u5 between the 30 and 80 percent span locations. The peak value of the loss in CII-s7 is lower than that of the design point (Fig. 9(*a*)), since the friction loss is reduced due to the reduced flow rate and the relative velocity.

Figure 10 compares the spanwise distribution of the meridional velocity. Here, the radial and the axial components of the velocity were area-averaged in the circumferential direction. At the design point, Fig. 10(*a*), the meridional velocity distribution of CII-u5 is more uniform compared to that of the O-u5 impeller between the hub and the 80 percent span location. However, the meridional velocity close to the tip becomes low in CII impellers due to high loss generation in this region. When the flow rate was reduced to $Q^* = 0.85$ (Fig. 10(*b*)), meridional velocity deficit clearly increased in the O-u5 impeller between its 40 and 80 percent span locations, which corresponds to the high loss region in Fig. 10(*b*). The observed lower loss and more uniform meridional velocity distributions in the inverse designed impeller CII-u5 are related to the difference in secondary flow pattern inside the impeller, and this will be discussed in detail in the next paragraph.

Exit Jet-Wake Flow Pattern. Figures 11 and 12 compare the measured relative velocity contours on the quasi-orthogonal planes at the exit of the impeller (Station B, Fig. 1). The approximate locations of the blade trailing edges are mentioned with broken lines. The low relative velocity region of CII-s7 was extremely wide because of the excessive friction loss generated in the shroud region. When the shroud was removed (CII-u7), the flow fields near the casing were significantly improved, and further improvements were achieved when the blade number was reduced to five (CII-u5).

In the case of unshrouded impellers, the high loss fluid, conveyed by the suction surface secondary flows toward the tip,

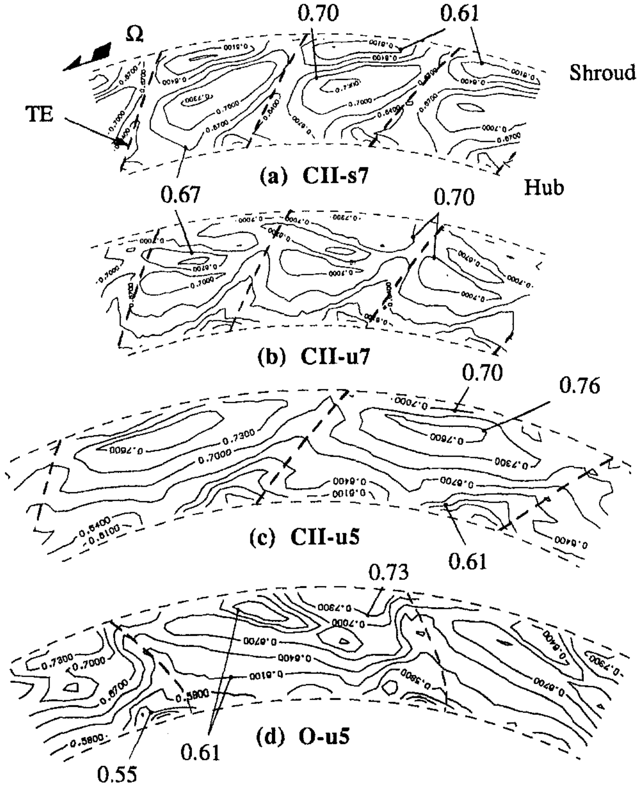

Fig. 11 Measured relative exit velocity contours at $Q^* = 1.0$ (Station B, contour interval = 0.03, normalized by U_{2m})

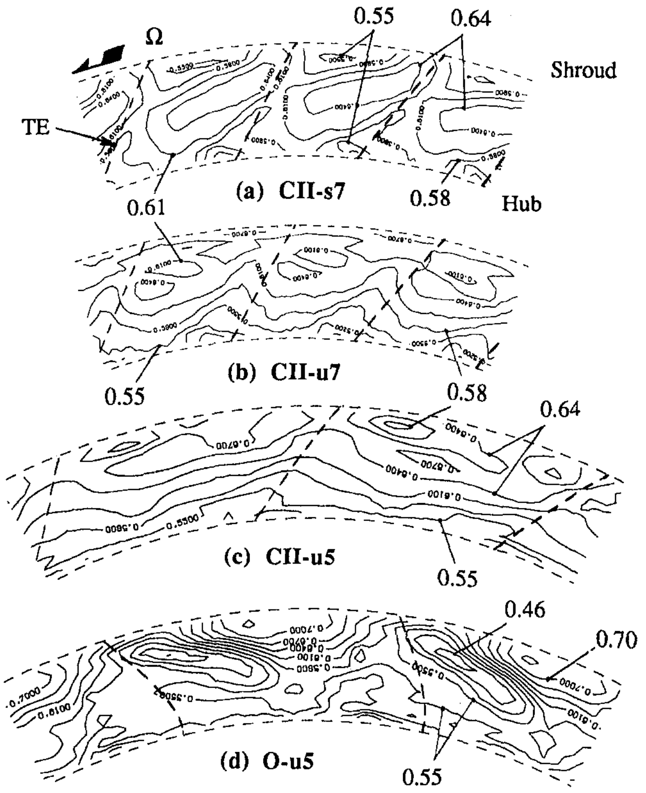

Fig. 12 Measured relative exit velocity contours at $Q^* = 0.85$ (Station B, contour interval = 0.03, normalized by U_{2m})

rolled into the tip leakage vortex. On the other hand, there was a fairly strong passage vortex around the pressure side of the passage (secondary flows from the pressure surface to the suction surface of the blade along the casing), due to the large pressure gradient generated by the Coriolis force. The wake flow, low relative velocity region, formed in the interaction region between these two vortex motions, and tended to be rolled up away from the casing (see Goto, 1992a). The flow fields of O-u5 were highly nonuniform due to thus formed jet-wake flow pattern. The region where high loss was observed in Fig. 9 corresponds to the wake flow regions in Figs. 11 and 12. As the flow rate was reduced, the flow fields in O-u5 became extremely nonuniform in both spanwise and pitchwise directions (Fig. 12(*d*)). The strength of the suction surface secondary flows, the tip leakage vortex, and the passage vortex were all intensified at partial flow rates; the wake flow was formed further away from the casing. This is the reason for the high loss and the low meridional velocity existing between the 40 and 80 percent span locations in the conventional impeller O-u5 (see Figs. 9(*b*) and 10(*b*)).

On the other hand, the flow fields of CII-u5 (Fig. 11(*c*)) were fairly uniform in both spanwise and pitchwise directions, suggesting much weaker secondary flows on the suction surface of CII impellers. No accumulation of low relative velocity fluids was observed here. When the flow rate was reduced to $Q^* = 0.85$ (Fig. 12(*d*)), there appeared a small amount of accumulation in the casing region, but the flow fields of CII-u5 still remained fairly uniform, compared to the appreciable growth in the wake flow region in the conventional O-u5 impeller.

The blade wake flows, predicted by numerical computations (Figs. 4(*b*) and 5(*b*)) at the trailing edge planes, have already mixed out and cannot be observed in Fig. 11. Although the numerical computations succeeded in predicting secondary flow pattern on blade surfaces, they failed to predict the characteristic feature of the flow fields at the exit of the impellers, such as the low relative velocity region existing widely along the casing for CII-s7, the flow field improvement in the casing region by introducing tip clearance (compare Fig. 11(*a*, *b*) with Figs. 5(*b*) and 4(*b*)) and the rolling up of the wake flow in O-u5 impeller caused by the strong interaction between the tip leakage and the passage vortices.

Concluding Remarks

In Part 1 of this paper, a medium specific speed mixed-flow pump impeller was designed by a fully three-dimensional inverse design method. The objective of the design was the suppression of the secondary flows on the blade suction surface, which could be the cause of exit flow nonuniformity and the instability of the impeller. Predictions by the Dawes three-dimensional Navier–Stokes code showed well-suppressed blade suction surface secondary flows and fairly uniform impeller exit flow fields compared to those of the conventional impeller.

In this part, the internal flow fields of the inverse designed impeller were investigated experimentally to confirm the capability of the present three-dimensional inverse design method, especially in terms of suppression of secondary flows on the blade suction surface. The flow fields were compared with those of a corresponding conventional impeller, and it was confirmed that the secondary flows on the blade suction surface were well suppressed and the uniformity of the exit flow fields was improved substantially in both circumferential and spanwise directions.

It is well acknowledged that secondary flows play a very important role to produce the exit flow nonuniformity such as the jet-wake flow pattern at the exit of centrifugal and mixed-flow turbomachines. This phenomenon often deteriorates the performance and the stability of the downstream diffuser and the stage. A substantial amount of efforts have been devoted to control secondary flows by applying a variety of empiricism, experience, and more recently the iterative use of advanced CFD (computational fluid dynamics) techniques, with the expense of time and cost. The present paper showed that it is possible to control secondary flows within the impeller in a more theoretical way by the application of the three-dimensional inverse design method. It is also possible to minimize the loss generation by the careful choice of the input specification in the inverse design method, such as optimum blade number, appropriate hydrodynamic blockage, and the loading distribution.

Acknowledgments

The author would like to express his deepest appreciation to Mr. T. Katsumata for his assistance in setting up the experimental apparatus and conducting the measurements. The author also would like to thank Ebara Research Co., Ltd., for permission to publish this paper.

References

Cumpsty, N. A., 1989, *Compressor Aerodynamics*, Longman Scientific & Technical, pp. 230–232.

Dawes, W. N., 1988, "Development of a 3D Navier–Stokes Solver for Application to All Types of Turbomachinery," ASME Paper No. 88-GT-70.

Goto, A., 1988, "Phase-Locked Measurements of Three-Dimensional Periodic Flow from an Impeller Using a Two-Hole Pitot Probe," *Proc. 2nd International Symposium on Fluid Control and Measurements (FLUCOME '88)*, Sheffield, United Kingdom, Sept. 5–9.

Goto, A., 1992a, "Study of Internal Flows in Mixed-Flow Pump Impellers With Various Tip Clearances using Three-Dimensional Viscous Flow Computations," ASME JOURNAL OF TURBOMACHINERY, Vol. 114, pp. 373–382.

Goto, A., 1992b, "The Effect of Tip Leakage Flow on Part-Load Performance of a Mixed-Flow Pump Impeller," ASME JOURNAL OF TURBOMACHINERY, Vol. 114, pp. 383–391.

Walker, P. J., and Dawes, W. N., 1990, "The Extension and Application of Three-Dimensional Time-Marching Analyses to Incompressible Turbomachinery Flows," ASME JOURNAL OF TURBOMACHINERY, Vol. 112, pp. 385–390.

Zangeneh, M., Goto, A., and Takemura, T., 1996, "Suppression of Secondary Flows in a Mixed Flow Pump Impeller by Application of Three-Dimensional Inverse Design Method: Part 1—Design and Numerical Validation," ASME JOURNAL OF TURBOMACHINERY, Vol. 118, this issue, pp. 536–543.

Experimental and Numerical Study of Three-Dimensional Flows in a Mixed-Flow Pump Stage

T. Takemura

A. Goto

Ebara Research Company, Limited,
Fujisawa-shi, Japan

Internal flows of a low-specific-speed pump stage, having a mixed-flow impeller and a vaned bowl diffuser combination, have been investigated experimentally and numerically. Air was used as the test fluid, and the internal flows were measured at various locations and under various capacities. Flow calculations were made, for both the isolated impeller case and the complete stage case, using Denton viscous codes LOSS3D and MULTSTAGE14, by which the three-dimensional steady flow through multiple blade rows can be calculated using the interrow mixing process. Experimental results showed the effects of the interaction between the impeller and the reverse flow, originating in the downstream diffuser, even at the design point capacity. While an impeller exit reverse flow occurred at the shroud side in the isolated impeller calculation, it was observed at the hub side in the complete stage case, showing good agreement with the experimental results. Although the flow in the diffuser was highly distorted due to a strong swirl flow, patterns of total pressure distribution could be predicted well by the complete stage calculation.

Introduction

The application of Computational Fluid Dynamics (CFD) techniques is becoming important in the research and development process of various turbomachines. Although CFD codes developed by Dawes (1988), Moore and Moore (1980), Hah et al. (1988), etc., are widely used now, it is required to verify their accuracy in more detail, especially in their use for radial and mixed flow turbomachines. For centrifugal compressors, the pioneering work by Eckardt (1976), and Krain and Hoffman (1989), is widely used for numerical code assessment. More recently, Hathaway et al. (1992, 1993) and Joslyn et al. (1991) started a centrifugal compressor research program with detailed measurements, particularly for CFD code assessment. For mixed flow pumps, Goto (1992) presented a comparison between measured and computed exit flow fields of a mixed flow impeller with various tip clearances, including the shrouded case. Schamann and Gülich (1992) measured the inlet and the exit flow fields of a centrifugal pump impeller, using laser anemometry over a wide operating range, and compared numerical predictions by three different CFD codes. However, most of the experiments were carried out for isolated impeller configurations and therefore may not represent the actual flow field around an impeller with a stage configuration that features upstream and/or downstream blade row interaction. This is especially true when blade rows are placed relatively close to each other and at off-design operating points. In such cases, the blade rows in the stage strongly interact with each other, and the flow fields will be very different from those of an isolated blade row case. Based on this view, flow field measurements under a stage configuration are very valuable, both for the investigation of the flow interaction between adjacent blade rows and for the assessment of stage calculation methods.

The flow fields in a turbomachinery stage are inherently unsteady due to relative motion between the rotating impeller blades and stationary diffuser counterparts. A cost-effective full Navier–Stokes solver, simulating three-dimensional viscous unsteady flow fields, is under development by Dawes (1993). However, computations on the unsteady turbomachinery flow by such a flow solver will not become practical for routine design work in near future, as this will require a huge computer power and design criteria including unsteady effects have not been established yet. As an alternate method for calculating the unsteady flow for multiple blade rows, Denton (1992) extended the LOSS3D code to the MULTSTAGE14 code to calculate the steady three-dimensional viscous flow through multistage turbomachines, i.e., by introducing an interrow mixing process between adjacent blade rows.

In the present paper, the time-averaged internal flow fields of a low-specific-speed pump stage, having a mixed-flow impeller and a vaned bowl diffuser combination, are measured in detail, including off-design operating conditions. The measurements are then compared with the steady-state solutions obtained by the Denton MULTSTAGE14 code in order to assess the correctness of the present practical stage calculation method. The flow fields within the isolated impeller configuration are also predicted by the Denton viscous code LOSS3D to highlight the effects of impeller–diffuser interaction. The characteristic features of the low-specific-speed pump stage are investigated in detail based on the experimental observations and the numerical calculations.

Experimental Apparatus and Methods

Test Facility and Model Pump Stage. Figure 1 shows the cross section of the pump stage test facility, which was operated as an open loop using air as the test fluid. Air was drawn into a facility room through air filters having the area of 5.1 m^2, installed on the wall to protect various types of probes from dust contained in the air. The flow passed through an inlet suction duct, via an inlet suction bellmouth with a 4:1 area contraction ratio, then entered the model pump stage. The exhaust air was led to the exterior of the facility room through a throttle valve placed at the end of the discharge duct. In addition to the model pump stage, a calibration wind tunnel was also

---

Contributed by the International Gas Turbine Institue and presented at the 39th International Gas Turbine and Aeroengine Congress and Exposition, The Hague, The Netherlands, June 13–16, 1994. Manuscript received by the International Gas Turbine Institute February 4, 1994. Paper No. 94-GT-44. Associate Technical Editor: E. M. Greitzer.

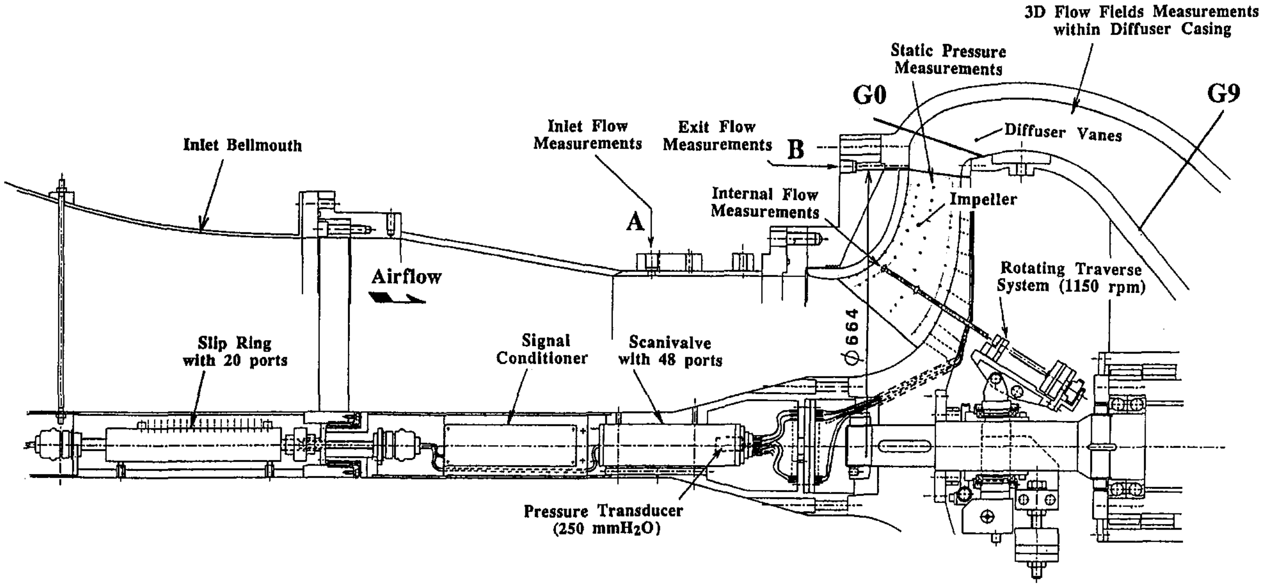

Fig. 1 Cross section of pump stage test facility

Table 1 Design parameters

Number of the impeller blades	6
Number of the bowl diffuser vanes	7
Design flow rate	36.6 m3/min
Design pump head	72.5 m
Rotation speed	1150 rev./min
r_{1m}	154.7 mm
r_{1o}	202 mm
r_{2m}	328 mm

placed in the facility room. A barometer, a thermometer, and a hygrometer were set and used to monitor the inlet air conditions.

The model pump stage consisted of a low-specific-speed mixed-flow shrouded impeller and a vaned bowl diffuser. The design specific speed of the pump stage was $\Omega\sqrt{Q}/(gH)^{3/4} = 0.68$. The model size was twice as large as that of ordinary water model pump stages, having an impeller exit mean diameter of 656 mm, in order to obtain high space resolution in measurements and a Reynolds number similar to that of the water model. All the experiments were carried out at the impeller speed of 1150 rpm giving a Reynolds number of $\mathrm{Re} = U_{2m}2r_{2m}/\nu = 1.73 \times 10^6$. Table 1 shows design parameters for the model pump stage. There are very small clearances of $0.1 \sim 0.2$ mm between the diffuser blade tip and the casing, and the circumferential locations of the diffuser blades are movable relative to the outer casing, where a traverse unit was set. Accordingly, the blade-to-blade flows in the bowl diffuser were easily measured, without having to move the circumferential position of the traverse unit. The flow rate of the tip leakage, i.e., through the clearance, was estimated to be less than 0.8 percent of the total flow rate and was considered to have little effect on the main feature of the flow fields. The impeller was driven by a 3.7 kW electronic motor through a flexible coupling and a right angle gear. The operation of the test facility, three-dimensional calibration of various types of probes, and the flow field measurements were fully controlled by a SUN-EWS-based system.

Inlet Flow Conditions. An axisymmetric uniform inflow condition is very important for the CFD code assessment. Accordingly, preliminary measurements of inlet flow fields were carried out at Station A in Fig. 1. The velocities were calculated from data on dynamic pressure measured by a Pitot total pressure tube (1-mm outer diameter) and eight equally spaced wall static pressure taps (1.6-mm-dia) at Station A. Figure 2 shows the inlet velocity profiles, normalized by their average velocities, measured at four different circumferential locations. The effects of the changing flow rate are also presented in Fig. 2 by overlapping the measured profiles. These results suggest that a sufficiently axisymmetric uniform inflow was obtained throughout the operating range discussed in the present study.

Flow Rate Measurements. Conventional flow rate measuring devices, such as a venturi tube or an orifice plate, were not used in the present test facility to avoid excessive duct

Nomenclature

Cp = static pressure rise coefficient = static pressure rise/$\rho U_{2m}{}^2$
Cpt = total pressure rise coefficient = total pressure rise/$\rho U_{2m}{}^2$
Q = volumetric flow rate, m^3/min
Q^* = flow rate ratio = $Q/(Q$ at design point)
H = pump head, m
Hth = Euler head coefficient = Euler head/$\rho U_{2m}{}^2$
(I, J, K) = grid coordinates (blade-to-blade, streamwise, spanwise)
M = Mach number
PS = pressure surface
r = radius, mm
SS = suction surface
U = peripheral blade speed, m/s
V = velocity, m/s
ρ = density, kg/m^3
Ω = angular rotation frequency, rad/s

Subscripts

1 = impeller inlet
2 = impeller exit
fs = free stream
m = midspan
o = outer
r = radial component
t = tangential component
x = axial component

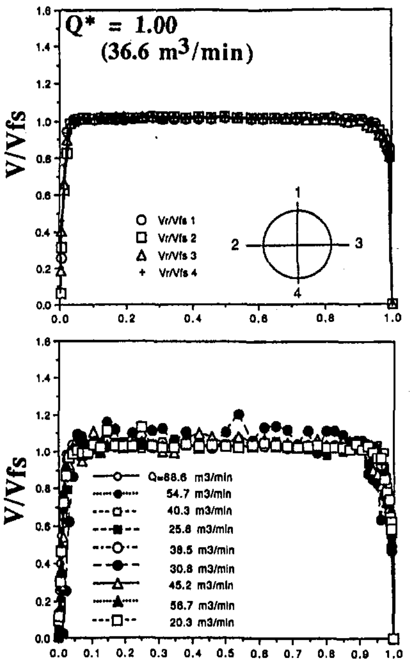

Fig. 2 Uniformity of inlet flow field (at station A in Fig. 1)

resistance and shorten the total length of the test loop. The flow rate through the pump stage was determined from a calibration curve of the correlation between the pressure drop, through the inlet suction bellmouth and the inlet duct, and the actual flow rate. The pressure drop was measured from both the wall static pressure at Station A and the static pressure in the facility room. The actual flow rate was calculated from the measured inlet velocity profiles of Fig. 2, assuming an axisymmetric flow. The flow rate is controlled by moving the throttle at the exit of the test loop, and the throttle was automatically adjusted to meet the specified experimental condition by monitoring the pressure drop.

Instrumentation and Accuracy of Measurements. The facility instrumentation includes a torque meter, a tachometer, a variety of probes for flow field measurements, and a wall static pressure measuring system. The work input, measured by a torque meter, included a substantial amount of windage loss due to pressure tubing on the back of the impeller, so the aerodynamic efficiency of the impeller could not be measured directly. A five-hole pressure probe was used for surveying flow velocity vectors and pressure at impeller exit Station B in Fig. 1. A Kiel-type total pressure probe was also used for surveying the total pressure distribution. This probe, insensitive to the flow direction, could sense accurate total pressures of up to 40 deg in relative angle difference, i.e., for both yaw and pitch directions. This was especially advantageous for the measurements of highly three-dimensional flows within the bowl diffuser. A hot-wire anemometry system was also available for the phase-locked measurements of the impeller exit flow. These probes were calibrated in the calibration wind tunnel. The accuracy of the pressure probes, including data reduction process, was estimated by measuring the flow in a calibration wind tunnel having known flow properties. Uncertainties estimated for the present measurements are listed in Table 2 with the accuracy of the wall static pressure measurements.

To measure wall static pressures, 88 pressure taps were provided on the walls both in the impeller and diffuser flow passages. On the pressure and suction surfaces of the impeller and diffuser blades, eleven taps were placed on each stream surface at 25, 50, and 75 percent span height locations. Another eleven taps were also provided on both hub and shroud surfaces at the midpitch location. In the rotating impeller, pressure tubes were routed out of the front of the impeller hub and connected to a 48 port Scanivalve (48J9) actuated by a Solenoid drive. The pressure was fed to a pressure transducer (PDCR 23D), and the amplified electric signals were transferred to a stationary frame through a 20-port slip ring (Meridian Laboratory MX-20). The Scanivalve, the pressure transducer, and the signal conditioner, specially designed for the present application, were set in a hollow shaft rotating with the impeller.

In the near future, an automatic traverse unit will be installed on the rotating impeller to survey the blade-to-blade flow fields in the impeller. This unit will enable a probe to move in the spanwise and pitchwise directions.

Computational Method

LOSS3D and MULTSTAGE14 Codes. Flow calculations were carried out for both the isolated impeller case and the stage configuration case. The former calculation was carried out using the Denton LOSS3D code, the latter using the Denton MULTSTAGE14 code. The basic Euler solver, commonly used for these codes and described in detail by Denton (1983), is a time-marching explicit finite volume method. Denton (1986, 1992) modified the solver to include viscous effects, essential for predicting realistic jet-wake flow patterns at the exit of centrifugal and mixed-flow impellers, by introducing a viscous body force term in the momentum equations. Among a range of methods to approximate viscous body force, a simplified eddy viscosity model was used for the present calculations. The modeling of the viscous effects in this way is strictly speaking valid only for thin attached boundary layers.

The extension in calculating the flow through multiple blade rows in MULTSTAGE14 code was carried out by Denton (1992) using an interrow mixing model between adjacent blade rows, in order to avoid calculating unsteady flow due to the relative motion between rotating and stationary blade rows. However, simple circumferential averaging of flow quantities, setting circumferentially uniform boundary conditions at the mixing plane, may give unrealistic predictions when the mixing plane is located close to the leading and/or trailing edges of the blades. The problem was resolved in MULTSTAGE14 code by using extrapolated boundary conditions at the mixing plane, allowing the circumferential variation of fluxes while keeping overall conservation of the fluxes across the mixing plane.

Computational Grids. Figure 3 shows the computational grids on the meridional planes for the isolated impeller and stage configuration cases. The grid points were clustered near the endwalls and blade surfaces. Relatively coarse grids of (19, 69, 19) = (pitchwise, streamwise, spanwise mesh) in the isolated impeller case and (19, 197, 19) in the stage case were applied. Both grids were contracted toward the exit boundary to ensure the convergence stability of the calculation especially at partial flow rates. A series of preliminary computations to confirm the mesh independence for a mixed-flow impeller, hav-

Table 2 Measurement uncertainties

Primary measurement	Nominal value	Uncertainty
Pressure	200 mmH2O	1.0 mmH2O
Yaw angle	20 deg	1.0 deg
Pitch angle	20 deg	1.0 deg
Calculated measurement	**Nominal value**	**Uncertainty**
Velocity	33 m/s	1.7 m/s
Volume flow rate	37 m3/min	1.1 m3/min

(a) Isolated impeller case

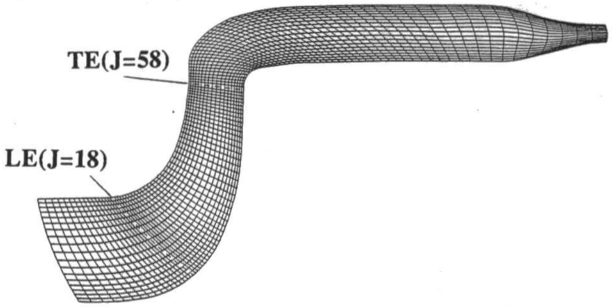

(b) Stage case

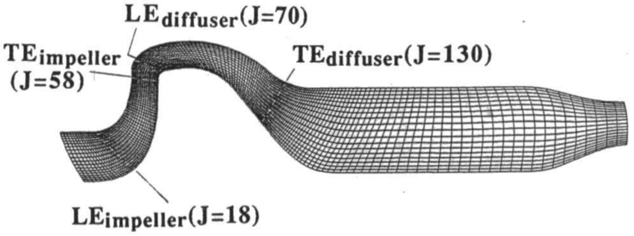

Fig. 3 Computational grid on the meridional planes

ing the design specific speed of $\Omega\sqrt{Q}/(gH)^{3/4} = 0.49$, showed that the grids used here were sufficient to capture the important flow features such as secondary flows on the blade surfaces and the jet-wake flow formation. On the other hand, these mesh sizes are the maximum to be accepted in the routine design process under the computer environment based on a CONVEX C220 (100MFLOPS). One of the objectives of the present study was to assess the accuracy of the numerical predictions obtained on rather coarse grids from the practical point of view of designers. The convergence of the calculation was slow because of the low inlet Mach number, and a typical 19 × 197 × 19 grid requires 6000 time steps and about 5 hours of CPU time on a single processor of a CONVEX C220 computer.

Boundary Conditions. At the inlet, the total pressure, the yaw and pitch angles of the flow were specified and fixed. In every case, the inlet endwall boundary layer thickness was assumed to be zero, a usual option in the design process. The actual measured inlet boundary layer thickness is shown in Fig. 2. At the exit boundary, the hub static pressure was specified and fixed, and its radial variation was derived from a simple radial equilibrium equation.

Effects of Increased Inlet Mach Number. All the experiments were carried out at the impeller speed of 1150 rpm, and the Mach number was too low to obtain any converged solutions by Denton codes developed for compressible flow calculation. Because of this, the impeller speed was increased to 3450 rpm in the present calculations to improve the convergence, and the typical value of the inlet relative Mach number was 0.22. The effects of increased impeller speed were investigated here.

Walker and Dawes (1990) investigated the numerical problems associated with time-marching algorithms at low Mach numbers, and introduced Chorin's method of artificial compressibility to extend Denton's Euler and Dawes' Navier–Stokes solvers to predict incompressible flows. As the incompressible version of Denton viscous code is not available, Dawes code BTOB3D and its incompressible version MACH0 were used for the present investigation. The details of BTOB3D were described by Dawes (1988).

Figure 4 compares the predicted velocity vectors on the suction surface of the isolated impeller blades and the relative velocity contours on the quasi-orthogonal plane at the trailing edge. The operating conditions and the overall impeller performances, Euler head rise and total pressure rise coefficients, are summarized in Table 3. The predictions by BTOB3D code, at the inlet relative Mach numbers of 0.20 and 0.33, show flow patterns similar to those by MACH0 code. However, in the case of lowest inlet Mach number ($M = 0.16$, Fig. 4(*c*)), the location of the wake region and the suction surface secondary flow pattern at the hub inlet are slightly different from those of the incompressible case (Fig. 4(*d*)). This is possibly so because of numerical errors due to the extremely small change in the flow density. Below this Mach number, no converged solution was obtained.

On the other hand, the predicted Euler head and total pressure rise coefficients showed increase as the inlet Mach number became high. The increase in Euler head coefficient was mostly due to the reduced volumetric flow rate (reduced meridional velocity), and not by the change in the internal flow pattern. The increase in total pressure coefficients at high Mach numbers was caused by the increased internal energy due to the fluid compressibility. From the present discussion, the flow pattern of the incompressible flow can be simulated reasonably well by moderately increasing the inlet relative Mach number (to $M = 0.2 \sim 0.3$). However, the effects of the compressibility should be kept in mind for the quantitative discussion of the impeller performances, as they will give 2 ~ 3 percent increase in Euler head and 4 ~ 10 percent increase in total stagnation pressure rise.

Results and Discussions

Experiments and numerical calculations were carried out at three operating conditions, namely $Q^* = 0.7$, 1.0, and 1.3, to reflect the typical flow pattern experienced during the operation. This section introduces predicted flow patterns within the stage, investigated in detail, and then the numerical predictions verified by measured data. Both numerical predictions and experimental data will shed light on the complex three-dimensional flows within a low-specific-speed pump stage, having a mixed-flow impeller and a vaned bowl diffuser combination.

Predicted Flow Pattern. Figure 5 shows the velocity vectors on the meridional planes, predicted by MULTSTAGE14, at three different pitchwise locations for the design point. The very complex three-dimensional flow pattern, especially within the vaned bowl diffuser, can be easily recognized. The prediction, under the isolated impeller configuration, was also carried out and the velocity vectors at the midpitch meridional planes are presented in Fig. 6. Here, the meridional plane at $I = 2$ is close to the impeller pressure surface or the diffuser suction surface, and $I = 18$ close to the impeller suction surface or the diffuser pressure side. Typical secondary flows moving from the hub to the shroud on the impeller blades, due to the strong curvature of the meridional geometry in a low-specific-speed impeller, can be identified very clearly. The development of the flow fields within the impeller is dominated by this secondary flow motion, and the well-known jet-wake flow pattern is established toward the impeller exit as is shown in Fig. 7. In the isolated impeller case at the design point (Fig. 6(*b*)), predicted by LOSS3D, a reverse flow was predicted on the shroud surface at the impeller outlet because of the low-relative-momentum fluid, accumulated in this region (wake flow region) by the secondary flow motion within the impeller (Fig. 7). However, in the stage calculation, a flow separation initiated within the downstream diffuser close to the hub surface due to the overloading of the blade, and a reverse flow appeared in this region (Fig. 5(*b*)). In this case, the reverse flow region on the shroud, which existed in the isolated impeller case, had disappeared because of the blockage effects of the reverse flow in the opposite hub region. The reverse region is not axisymmetric and is more extensive between the midpitch and the pressure side of the diffuser blade.

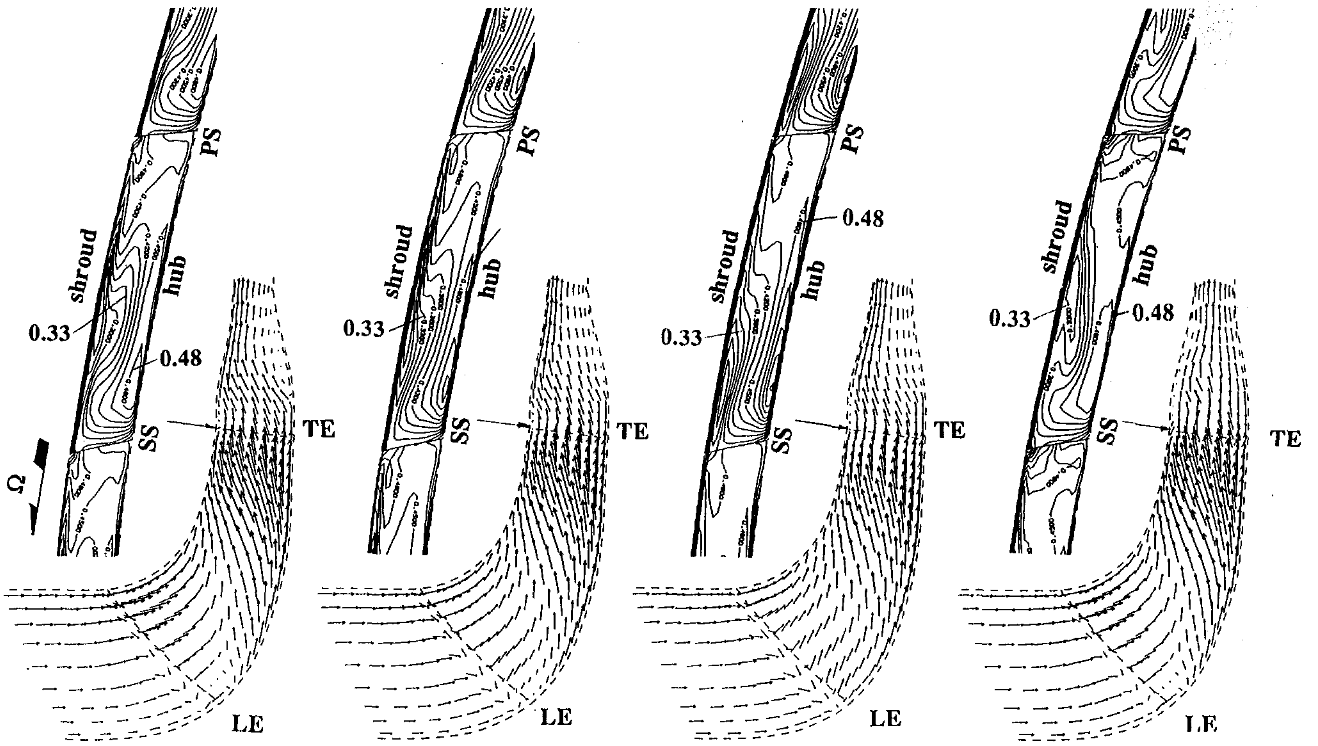

(a) M=0.33 (b) M=0.20 (c) M=0.16 (d) Incompressible case (by using Dawes's code MACH0)

Fig. 4 Effects of inlet Mach number (contour interval = 0.03, normalized by U_{2m})

The midpitch flow fields at off-design conditions, predicted by MULTSTAGE14, are presented in Fig. 8. The reverse flow region in the diffuser hub inlet disappeared at $Q^* = 1.30$ (Fig. 8(*a*)). On the other hand, when the flow rate was reduced to $Q^* = 0.70$ (Fig. 8(*b*)), the reverse flow significantly intensified and reached to the rear part of the impeller blades. Half of the flow passage was blocked by the reverse flow region. On the other hand, a fairly wide region of recirculation appeared in the shroud side of the isolated impeller case (Fig. 6(*c*)). These facts suggest that the flow fields around the impeller cannot be simulated properly without modeling the effects of the downstream diffuser blades, especially at the partial flow rate region. At the inlet of the impeller at $Q^* = 0.70$ (Figs. 6(*c*) and 8(*b*)), both isolated impeller and stage calculations predicted the onset of the inlet recirculation at the shroud side, suggesting little effects of the downstream flow phenomena for the onset of the inlet recirculation in low-specific-speed impellers.

The flow pattern within the bowl diffuser is very complex, because of the inlet shear flow and the large flow passage curvature both on the meridional and blade-to-blade planes. Figure 9(*a*) shows the flow velocity vectors on the stream surface close to the hub at $Q^* = 0.70$. The flow follows the suction surface of the diffuser blade at the inlet, but the flow around the midpitch location started reversing upstream. Just before the blade-to-blade bend, a vortex in the clockwise direction is observed. This vortex is considered to be created by the interaction between two crossflows: one from the suction to the pressure side at the fore part of the passage and the other from the pressure to the suction at the aft part of the passage. Similar vortices were observed by Yoshida et al. (1988) and Kanemoto et al. (1992). As was discussed by Kanemoto (1992), the other

Table 3 Effects of inlet Mach number

Case	Rotational Speed (rpm)	Inlet Relative Mach Number	Stag. Pressure Rise Coefficient	Euler head Coefficient
D	5330	0.33	0.633	0.605
C	3200	0.20	0.584	0.596
B	2500	0.16	0.554	0.588
AA	1600	*	0.563	0.585

*: Incompressible Flow

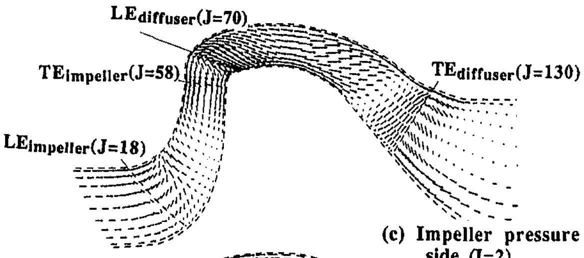

(c) Impeller pressure side (I=2)

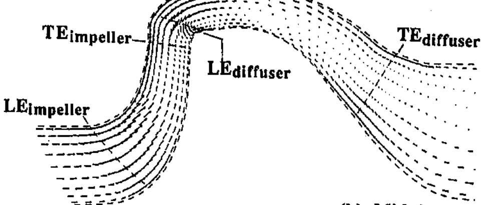

(b) Midpitch location (I=10)

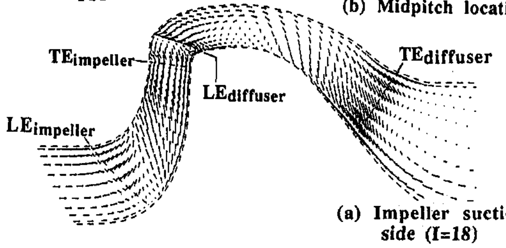

(a) Impeller suction side (I=18)

Fig. 5 Stage flow prediction at $Q^* = 1.0$ on the meridional planes

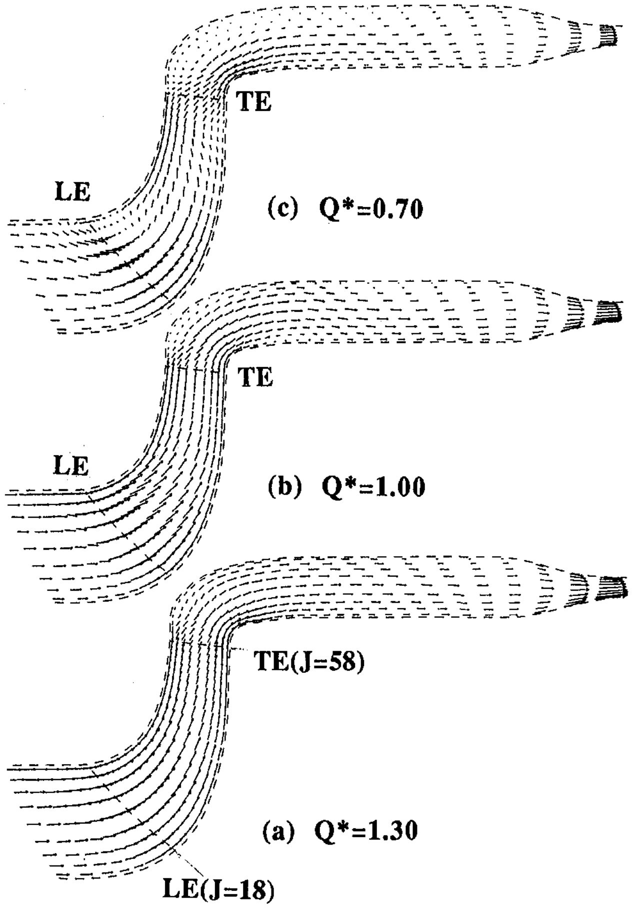

Fig. 6 Prediction for isolated impeller case on the meridional planes (I = 10)

end of the vortex was conveyed by the main flow, and a strong swirl flow, having the same swirl direction with the impeller rotation, was created by its circulation on the downstream cross section (Fig. 9(*b*)). Figure 10 shows the spanwise distribution of the tangential and axial velocity components at the diffuser trailing edge. The magnitude of the swirl velocity is of the same order as the axial velocity. The low total pressure fluids in the inlet reverse flow region, located between the midpitch and the pressure surface of the diffuser blade, moved toward the pressure side during the fore part of the diffuser, and then rolled into the vortex away from the wall toward the core of the swirl flow.

Impeller Surface Pressure Distributions. Figure 11 compares the suction surface pressure distributions on the rotating impeller blade between predictions and experiments on the midspan stream surface. The centrifugal pressure correction was applied to the pressure measured by the pressure transducer, placed at the impeller centerline, in order to obtain the pressure on the blade surface. The abscissa is the normalized meridional distance measured on the stream surface. The numerical predictions by both LOSS3D and MULTSTAGE14 codes in general agreed with the experiments. At the flow rates of $Q^* = 1.0$ and 1.3, the predictions by both codes are similar, but the predictions tend to deviate from experimental results toward the trailing edge. At the flow rate of $Q^* = 0.70$, there was a difference between the predictions by both codes, and also the predictions tend to deviate from experimental results at the inlet region on the suction surface.

Impeller Exit Flow Field. Impeller exit flow fields were measured by a five-hole pressure probe downstream of the impeller exit, at Station B (Fig. 1). The traverse plane B is parallel to the machine axis, and the radial gap between the impeller trailing edge and the probe was 9 mm at midspan, giving the radius ratio of 1.027. As has been discussed previously, there is an interaction between the impeller exit flow and the diffuser blades. Because of this, impeller exit flow measurements were carried out at six different circumferential locations by shifting the position of the diffuser blade relative to the probe. Figure 12 shows the radial velocity of the impeller exit flow. Since the flow fields were different depending on the relative location of the diffuser blades, typical data, measured at three different diffuser locations, are presented here. It is observed that the

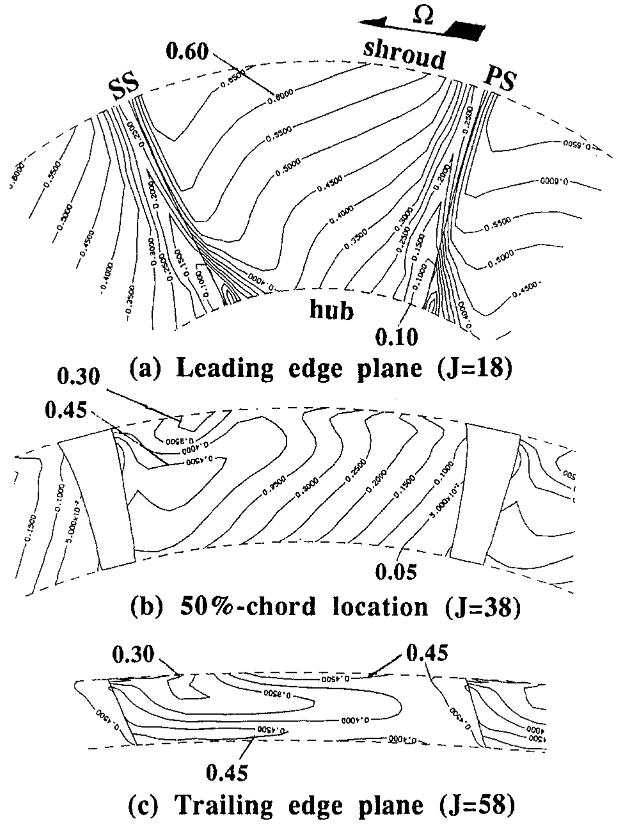

Fig. 7 Relative velocity fields development on the quasi-orthogonal planes (contour interval = 0.05, normalized by U_{2m})

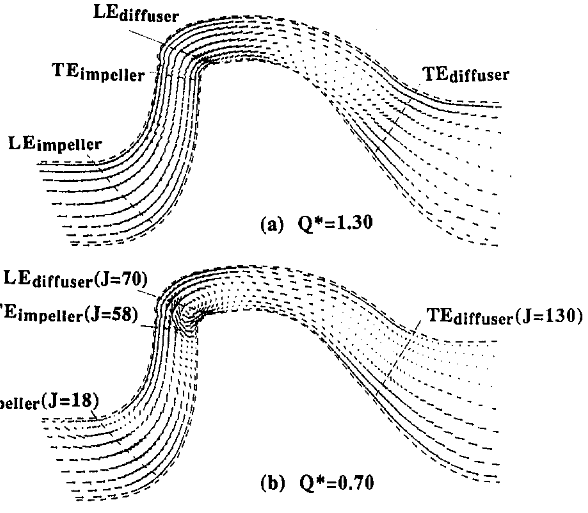

Fig. 8 Stage flow prediction at off-design point on the meridional planes (I = 10)

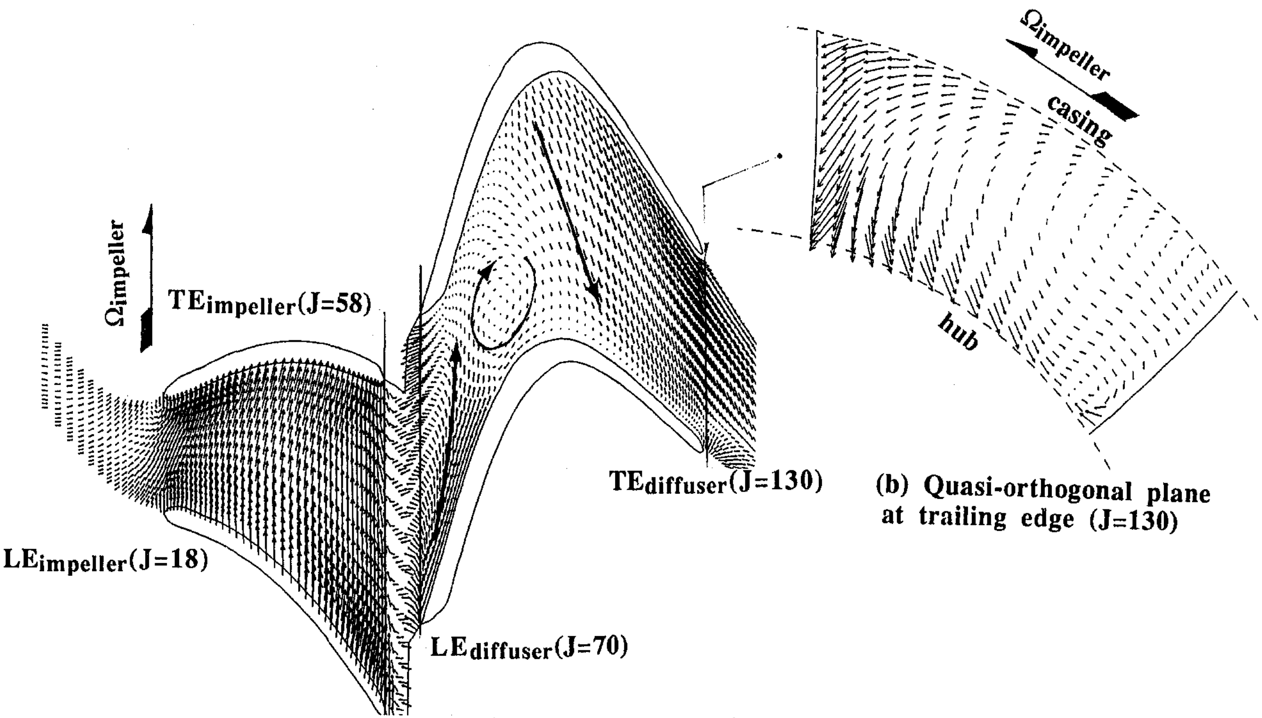

(b) Quasi-orthogonal plane at trailing edge (J=130)

(a) Stream surface near hub (K=2)

Fig. 9 Velocity vectors predicted by stage calculation

interaction between the impeller exit flow and reverse flow at the hub side of the diffuser inlet had already started at the design point capacity. As is shown in Figs. 5 and 8, the MULTSTAGE14 code predicted the reverse flow at the hub side at the impeller outlet. Because of this, the measured pattern of the exit radial velocity distribution (Fig. 12) shows better agreement with the predictions by the MULTSTAGE14 code especially at $Q^* = 0.70$, while LOSS3D calculation for an isolated impeller case failed to predict the flow fields even qualitatively. LOSS3D predicted rather low velocity in the shroud region at $Q^* = 0.70$ (Fig. 6(*c*)), but in reality the flow in this region was accelerated due to the blockage effects in the hub region (Fig. 8(*b*)). A substantial amount of flow loss was generated in this region because of friction due to the high relative velocity and the mixing loss of the recirculating flow.

(a) Axial velocity component

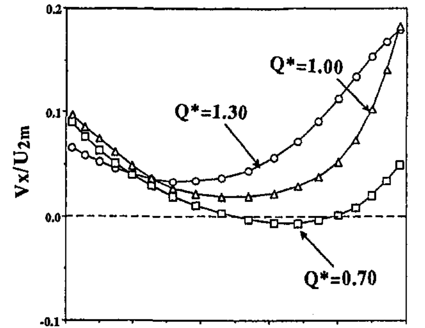

(b) Tangential velocity component

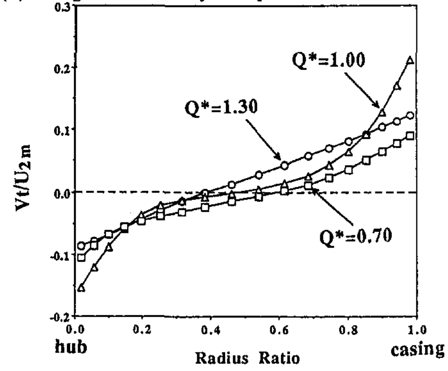

Fig. 10 Diffuser exit flow patterns

Figure 13 shows tangential velocity distributions at the impeller exit. Experimental data at three typical circumferential probe locations were plotted. The distribution is rather uniform in the spanwise direction, compared to the case of radial velocity distribution, and both isolated and complete stage calculation cases predicted experimental results well at $Q^* = 1.0$. Mass-averaged Euler heads are also calculated from this distribution, and the results were listed in Table 4. The predictions by both codes gave 2 ~ 3 percent higher Euler head than experiments. The difference of 2 percent is attributable to the effect of reduced meridional velocity due to the compressibility effects, discussed in the previous section in Table 3, and so the overall input work by the impeller was estimated accurately by both codes. When the flow capacity was reduced to $Q^* = 0.70$, the tangential velocity (Fig. 13(*b*)) decreased near the hub due to the reverse flow from the diffuser (see Fig. 9(*a*)). This effect of the reverse flow was predicted by MULTSTAGE14, although the quantitative agreement was not sufficient.

However, the predicted exit total pressure was substantially greater than measured results. Since the contribution from the compressibility is expected to be around 5 percent, as is listed in Table 3, it is supposed that these overpredictions are due to the poor modeling, of the loss or turbulence, for the flow in the rotating three-dimensionally curved channel. The actual cause of the discrepancy will be clarified in the near future based on the total pressure measurements within the impeller flow passage. The loss model improvement is obviously a very important theme in three-dimensional CFD analysis of turbomachinery.

Flow Fields in Vaned Bowl Diffuser. The total pressure fields in the vaned bowl diffuser of this pump stage were measured by the Kiel-type total pressure probe at six different

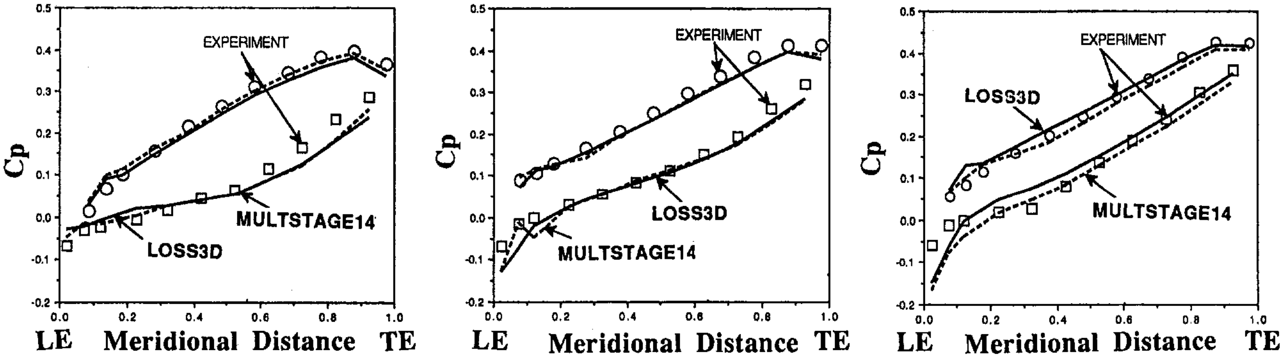

(a) Q*=1.30 (b) Q*=1.00 (c) Q*=0.70

Fig. 11 Blade static pressure rise coefficient *Cp* distribution at midspan

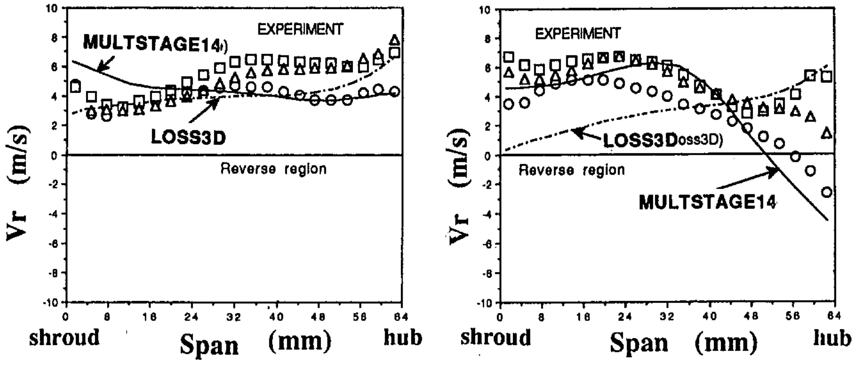

(a) Q*=1.00 (b) Q*=0.70

Fig. 12 Radial velocity at impeller exit (at station B in Fig. 1)

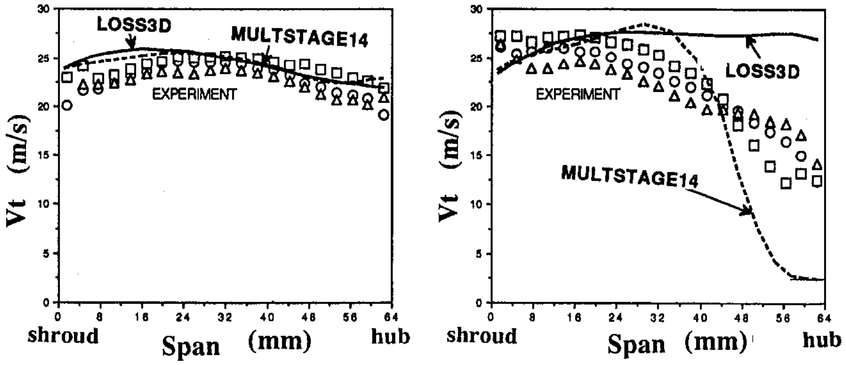

(a) Q*=1.00 (b) Q*=0.70

Fig. 13 Tangential velocity at impeller exit (at station B in Fig. 1)

Table 4 Overall impeller performance

	Experiment	LOSS3D	MULTSTAGE14
Euler's head Hth	0.6042	0.6166	0.6196
Total pressure Cpt	0.4918	0.6007	0.6061

streamwise locations. The surveying cross sections in the vaned bowl diffuser flow path, from Station G1 to G9, are presented in Fig. 1. Figure 14 compares the total pressure contours, on the quasi-orthogonal planes, between measurements and predictions by the MULTSTAGE14 code. The predicted total pressures are higher than those of measurements as the calculations already overpredicted the total pressure at the impeller exit. The contour gradient of the total pressure tends to be more crisp in calculations than experiments from the inlet to the exit of the vaned bowl diffuser. This fact suggests that lower mixing loss will be generated in the numerical computations, rather than in experiments, although the measured mass-averaged total pressure and the overall flow losses are not known yet, as velocity fields have not been measured.

The flow fields in the diffuser are highly distorted due to the strong swirling flow. The low total pressure fluids, initiated at the hub inlet region, were rolled up into the core of the swirling flow toward the exit of the diffuser. This trend of the measured flow pattern of total pressure, at different locations within the bowl diffuser, was fairly well predicted by the MULTSTAGE14 code, as is observed in Fig. 14. Figure 15 compares the flow pattern at the diffuser inlet at off-design operating conditions, showing good qualitative agreement between predictions and calculations. The agreement between the experiments and the numerical predictions by the MULTSTAGE14 code was encouraging considering the simple viscous model used, and it is expected to be a useful tool to optimize the diffuser geometry for minimizing the flow separation, suppressing the excessive swirl and consequent high losses.

Concluding Remarks

Complex three-dimensional flows in a low-specific-speed pump stage, having a mixed-flow impeller and a vaned bowl diffuser combination, were measured in detail using air as the test fluid. The experimental results, even at the design point, showed the effects of the interaction between the impeller and the reverse flow originated in the downstream diffuser. As the flow rate was reduced, the interaction was intensified and the reverse flow reached the impeller exit.

The flow fields were predicted by the well-known Denton viscous code LOSS3D and its multistage version the MULTSTAGE14 code, which can calculate the three-dimensional steady flow through multiple blade rows. The prediction by LOSS3D for the isolated impeller case, without modeling the downstream diffuser blades, showed reverse flow on the shroud side at the impeller outlet. On the other hand, the MULTSTAGE14 code predicted the reverse flow on the opposite hub side, showing a better agreement with the experimental observation. The predicted wall static pressure distributions within the impeller in general showed little differences between the isolated impeller and stage calculation cases, and reasonably agreed with the experimental results. Although the flow fields within the bowl diffuser were highly three dimensional and distorted due to the strong swirling flow, the patterns of the total pressure distribution at various locations in the diffuser were well predicted by stage computations. Overall, the agreement between the experiments and the predictions by the MULTSTAGE14 code was encouraging considering the simplicity of the viscous model (non-Navier–Stokes solver) and the interrow mixing process used to calculate the *steady* flow fields. Such a stage calculation method is expected to be a useful tool for the stage design process.

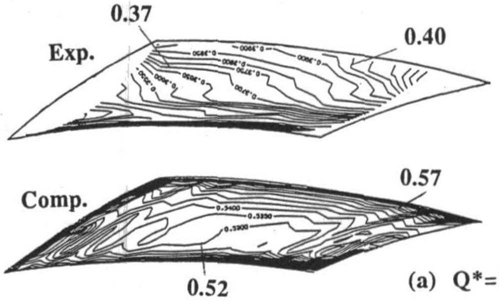

(a) Q*=1.30

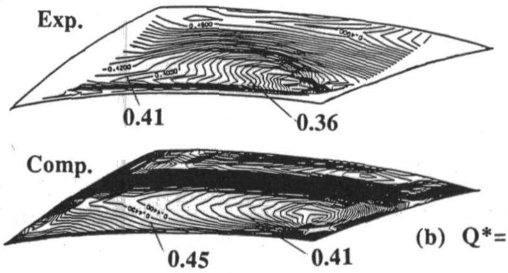

(b) Q*=0.70

Fig. 15 Total pressure rise coefficient *Cpt* distribution at off-design point at leading edge plane (contour interval = 0.005)

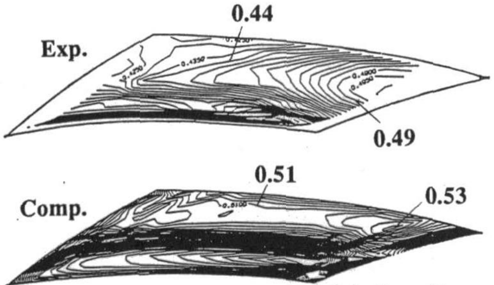

(a) Leading edge

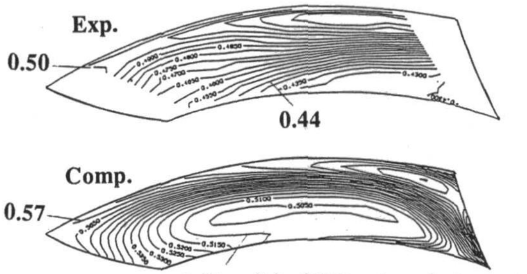

(b) 50%-chord location

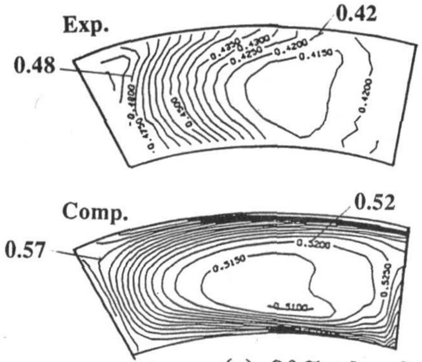

(c) 90%-chord location

Fig. 14 Total pressure rise coefficient *Cpt* distribution within bowl diffuser at Q^* = 1.00 (contour interval = 0.005)

The periodic fluid force acting on the impeller, generated by the strong interaction between the impeller and the reverse flow from the downstream diffuser, could be an important cause of mechanical failure, such as blade breakage and vibration problems, at partial capacity operating conditions. In order to investigate the interaction mechanism, measurements of the unsteady pressure fluctuation on the impeller blades and the traverse of the unsteady flow fields using a hot-wire anemometer are now under progress.

Acknowledgments

The authors would like to thank Ebara Research Co., Ltd., for permission to publish this paper, and Mr. T. Katsumata for his special assistance in assembling facilities and conducting the measurements.

References

Dawes, W. N., 1988, "Development of a 3D Navier–Stokes Solver for Application to All Types of Turbomachinery," ASME Paper No. 88-GT-70.

Dawes, W. N., 1993, "Simulating Unsteady Turbomachinery Flows on Unstructured Meshes Which Adapt Both in Time and Space," ASME Paper No. 93-GT-104.

Denton, J. D., 1983, "An Improved Time Marching Method for Turbomachinery Flows," ASME *Journal of Engineering for Power*, Vol. 105, pp. 514–524.

Denton, J. D., 1986, "The Use of a Distributed Body Force to Simulate Viscous Effects in 3D Flow Calculations," ASME Paper No. 86-GT-144.

Denton, J. D., 1992, "The Calculation of Three-Dimensional Viscous Flow Through Multistage Turbomachines," ASME JOURNAL OF TURBOMACHINERY, Vol. 114, pp. 18–26.

Eckardt, D., 1976, "Detailed Flow Investigations Within a High-Speed Centrifugal Compressor Impeller," ASME *Journal of Fluids Engineering,* Vol. 98, No. 3, pp. 390–402.

Goto, A., 1992, "Study of Internal Flows in a Mixed-Flow Pump Impeller at Various Tip Clearances Using Three-Dimensional Viscous Flow Computations," ASME JOURNAL OF TURBOMACHINERY, Vol. 114, pp. 373–382.

Hah, C., Bryans, A. C., Moussa, Z., and Tomsho, M. E., 1988, "Application of Viscous Flow Computations for the Aerodynamic Performance of a Back-Swept Impeller at Various Operating Conditions," ASME JOURNAL OF TURBOMACHINERY, Vol. 110, pp. 303–310.

Hathaway, M. D., Wood, J. R., and Wasserbauer, C. A., 1992, "NASA Low-Speed Centrifugal Compressor for Three-Dimensional Viscous Code Assessment and Fundamental Flow Physics Research," ASME JOURNAL OF TURBOMACHINERY, Vol. 114, pp. 295–303.

Hathaway, M. D., Chriss, R. M., Wood, J. R., and Strazisar, J., 1993, "Experimental and Computational Investigation of the NASA Low-Speed Centrifugal Compressor Flow Fields," ASME JOURNAL OF TURBOMACHINERY, Vol. 115, pp. 527–542.

Joslyn, H. D., Brasz, J. J., and Dring, R. P., 1991, "Centrifugal Compressor Impeller Aerodynamics: An Experimental Investigation," ASME JOURNAL OF TURBOMACHINERY, Vol. 113, pp. 660–669.

Kanemoto, T., Akamatsu, H., Nishi, M., and Tsukamoto, H., 1992, "Flow Through a Diffuser of a Mixed Flow Pump," *Preprints of the 70th JSME Conference,* Nagano, Vol. C, pp. 210–212.

Krain, H., and Hoffman, W., 1989, "Verification of an Impeller Design by Laser Measurements and 3D-Viscous Calculations," ASME Paper No. 89-GT-159.

Moore, J., and Moore, J. G., 1980, "Calculations of Three-Dimensional, Viscous Flow and Wake Development in a Centrifugal Impeller," in: *Performance Prediction of Centrifugal Pumps and Compressors,* presented at the 25th Annual International Gas Turbine Conference, New Orleans, LA, pp. 185–189.

Schamann, A., and Gülich, J. F., 1992, "Comparison of Three Different Navier–Stokes Codes with LDA-Measurements on a Radial Pump Impeller," Pump Congress, Karlsruhe, Preprint B 7-02.

Walker, P. J., and Dawes, W. N., 1990, "The Extension and Application of Three-Dimensional Time-Marching Analyses to Incompressible Turbomachinery Flows," ASME JOURNAL OF TURBOMACHINERY, Vol. 112, pp. 385–390.

Yoshida, Y., Nakamura, Y., and Nanbu, K., 1988, "Design Method of Curved Diffusers for High Performance Mixed Flow Pumps," *Proc. 12th IAHR Symposium,* Trondheim, pp. 541–552.

Laser Velocimeter Measurements in the Pump of an Automotive Torque Converter: Part I—Average Measurements

J. K. Gruver

R. D. Flack

K. Brun

Department of Mechanical, Aerospace, and
Nuclear Engineering,
ROMAC Laboratories,
University of Virginia,
Charlottesville, VA 22903

A torque converter was tested for two turbine/pump rotational speed ratios, 0.065 and 0.800, and a laser velocimeter was used to measure three components of velocity within the pump. Shaft encoders were used to record the instantaneous pump angular position, which was correlated with the velocities. Average flow velocity profiles were obtained for the pump inlet, mid-, and exit planes. Large separation regions were seen in the mid- and exit planes of the pump for a speed ratio of 0.800. Strong counterclockwise secondary flows were observed in the midplane and strong clockwise secondary flows were seen in the exit plane of the pump for all conditions; vorticities were evaluated and are reported. Velocity data were also used to find the torque distribution. For both speed ratios the torque was approximately evenly distributed between the inlet and exit. Finally, slip factors were evaluated at the mid- and exit planes. At the midplane they were approximately the same as for conventional centrifugal pumps; however, at the exit plane the slip factors are larger than for centrifugal pumps.

Introduction

Torque converters are commonly used in automobiles and other vehicles as a means of smooth torque transmission between the engine and the automatic transmission. The typical torque converter consists of a pump, a turbine, and a stator, and employs oil as the working fluid. Rotational energy from the automobile engine is introduced into the fluid by the pump and extracted by the turbine. The stator is placed between the turbine exit and pump inlet. Its function is ideally to create a zero pump inlet blade incidence angle at some design conditions.

The design of a torque converter is very complex due to a number of conditions. First, the turbomachine should operate efficiently at both on- and off-design conditions. However, the flow field changes drastically over the typical operating range; that is, incidence angles to all of the components change from large positive to large negative values over the operating range. Second, the flow is turned in the passages in two directions. As in any turbomachine, blade slip becomes a problem at off-design conditions and the flow does not follow the blades. The problem is further complicated by the fact that the flow is also turned in the transverse direction in both the pump and turbine, usually in a short distance; that is, flow enters these components in the axial direction, is rapidly turned to the radial direction, and then turned rapidly into the reverse axial direction. Thus, the torque converter pump is a very complex mixed-flow variety of hydraulic turbomachine.

Previous Flow Research in Torque Converters. By and Mahoney (1988) reviewed technology needs for the automotive torque converter. They indicate that the flow is highly three dimensional due to complex three-dimensional geometries with three components rotating at different speeds and that conceptualizing the general flow characteristics is difficult. In addition, the elements operate under an extremely wide range of inlet flow conditions. They concluded that one-dimensional pitch line analyses do not adequately predict flow inside complex mixed-flow turbomachinery such as the torque converter.

Upton (1962) used a large flow table to visualize flows in different two-dimensional blade cascades. This facility was used extensively to develop torque converters through the 1960s. Upton also evaluated torque converter performance characteristics, torque capacity derivations, and gearing effects.

Numazawa et al. (1983) developed an oil film–resin flow visualization technique to trace flow patterns on the blade and end-wall surfaces. They used this technique to study two torque converter flow fields. Crossflow, swirl, reversed flow, and separated flows were shown. Pressure distributions were predicted theoretically and the torus and blade profiles were modified with the aid of these predictions. A smoother flow was obtained, and a higher efficiency torque converter was developed.

Sakamoto et al. (1992) employed a theoretical pressure balance method to improve torque converter performance. The effects of particular design parameters on performance were studied, and an optimal flow path shape that reduced the losses was developed.

Fister and Adrian (1983) and Adrian (1985) published some of the early details of internal torque converter flow. They used a spark-tracer method in a large torque converter with air, and a laser-two-focus (L2F) method in a torque converter with water. The spark-tracer method was used to visualize the entire flow field. The L2F method was used to measure velocity components in the stator blade passages only. They also used multi-holed probes to measure pressures in the gap regions between the elements. Their experimental torque converters, however, were not automotive; they were industrial torque converters with large clearances between the elements. One should also note that industrial torque converters are significantly different in design than the smaller automotive versions with even different placement of the three components.

Browarzik and Grahl (1992) used hot-film anemometry to examine the nonsteady flow field at the inlet and the outlet of a pump and turbine of a torque converter. A frequency spectrum showing the relative magnitudes of velocities at the turbine exit

---

Contributed by the International Gas Turbine Institute and presented at the 39th International Gas Turbine and Aeroengine Congress and Exposition, The Hague, The Netherlands, June 13–16, 1994. Manuscript received by the International Gas Turbine Institute February 4, 1994. Paper No. 94-GT-47. Associate Technical Editor: E. M. Greitzer.

is presented. Relative velocity magnitude as a function of pump and turbine angular position is also shown. Further research was recommended.

Bahr et al. (1990) employed a laser velocimeter (LV) in a Plexiglas torque converter to obtain detailed velocity profiles of five planes in the stator for two speed ratios. Laser velocimetry is the only nonintrusive technique available, whereby three-dimensional details of the flow in small rotating passages can be measured without changing the flow field. In each plane 25 data stations were examined. Separation regions were observed in the pressure side/midchord/core side and suction side/trailing edge/shell side regions of the stator at a speed ratio of 0.800. Using the measured velocities, they also found that the torque and flow rates were poorly distributed from the hub to tip at both speed ratios.

More recently, By and Lakshminarayana (1991, 1993) and By et al. (1993) have studied a torque converter with the same geometry as that of Bahr et al. Steady pressure measurements were taken in both the stator and pump and correlated with both a potential flow analysis and a viscous flow prediction. Good agreement was obtained. The viscous flow prediction was used to show that pump rotation with the radially curved channel precipitated a strong secondary flow.

A number of researchers have successfully used laser velocimetry in turbomachines as reviewed by Bahr et al. (1990), including Miner et al. (1989), Beaudoin et al. (1992), and Flack et al. (1987). Velocity profiles, flow angles, separation regions, and turbulence intensities have all been accurately measured.

Motivations and Objectives of the Current Research. Theoretical analysis of the torque converter has not developed to a level permitting design solely from computational results. Three-dimensional experimental flow data, including velocity distribution, pressures, and turbulence intensities, are required to verify computational results. Although the torque converter has one of the most complex flow fields of any turbomachine, the fluid dynamic aspects of the machine have received little attention. The current understanding of the internal flow field of the torque converter is inadequate.

Three primary incentives motivate research in torque converter pump flow fields. First, the current hydrodynamic design tools need to be upgraded in order to advance torque converter technology significantly. Thus, benchmark velocity data are needed to verify computational methods. Second, the torque converter can be a relatively inefficient machine. Improvement in torque converter efficiency can be obtained by optimizing the internal flow paths through each component. However, before flow passages are modified, an understanding of the fundamental flow behavior is needed so that problem regions can be identified. Third, the pump is the driving mechanism of the torque converter. These pumps are extremely complex mixed-flow turbomachines; that is, the flow is both axial and radial in most regions of the impeller. A basic understanding of mixed-flow behavior is essential for the design process, not only for torque converter pumps but for other mixed-flow pumps as well.

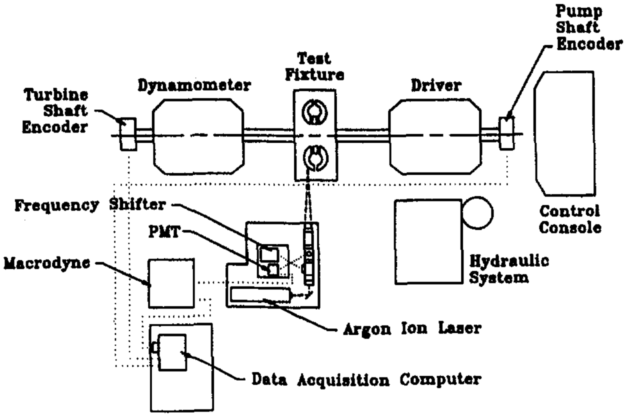

Fig. 1 Schematic of torque converter/LV system

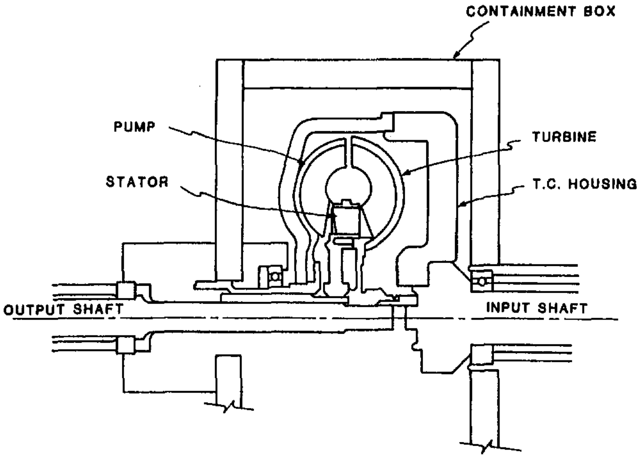

Fig. 2 Cross-sectional view showing containment box

In this paper, a burst-type laser velocimeter was used to measure velocity components in the pump of an automotive torque converter constructed of Plexiglas. Velocities in the pump inlet, mid-, and exit planes were measured. From the velocity data, nonuniformities and in particular separated regions were determined. Also, slip factors at the mid- and exit plane were determined. Secondary flows were seen and vorticities were evaluated. Lastly, the torque distribution was found. The torque converter data presented herein embody the most complete detailed flow data available in the literature for torque converter pumps. With the experimental results as a benchmark, better computational modeling of the internal torque converter flow field can be achieved and the geometries can be optimized to improve the efficiency.

Apparatus

Torque Converter Rig. A schematic of the experimental setup is shown in Fig. 1. It consists of: (1) an input dynomometer to drive the torque converter pump, (2) an eddy current dynomometer to absorb the turbine power, (3) a hydraulic system to cool, pressurize, and lubricate the rig, (4) a control unit to adjust speeds and torques, (5) a laser velocimeter system to measure velocities, and (6) two shaft encoders to correlate the velocity data with the pump and turbine angular positions.

The input dynamometer, which controls the pump, is a 20 kW unit and the rotational speed is controlled to within 1 rpm. The output dynomometer, which controls the turbine, is a 130 kW capacity unit, for which rotational speed is also controlled to within 1 rpm.

The torque converter was constructed entirely of Plexiglas. The index of refraction of Plexiglas is nominally 1.490. To reduce undesired laser beam scattering and bending, the refractive index of the oil and the Plexiglas had to be closely matched. This objective was achieved using Shell-Flex 212 oil, which has an index of refraction of 1.489 at 25°C. The density of Shell-Flex 212 oil at 25°C is 899 kg/m^3 and the viscosity is 1.98×10^{-3} kg/m·s and 1.29×10^{-3} kg/m·s at 25°C and 40°C, respectively. To minimize the effects of wall curvature on the laser velocimetry measurements, the entire torque converter is in an oil-filled Plexiglas containment box as shown in Fig. 2.

The pump and turbine are both of two-piece construction. For both, a solid piece of Plexiglas was milled so that the blades

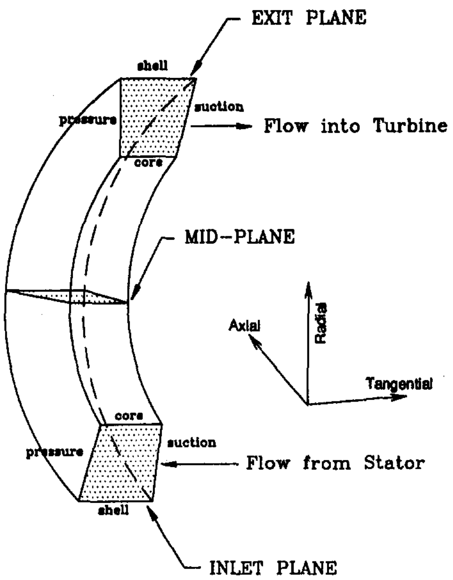

Fig. 3 Pump passage geometry

were an integral part of the core. A shell was then machined and glued to the blades with a solvent. Blades are 1.1 mm thick; the shells are 2.67 mm thick. Twenty-seven, 29, and 19 blades were used for the pump, turbine, and stator, respectively. In Fig. 3 the pump geometry and the three measurement planes are shown. For the remainder of this paper the torque converter cylindrical coordinate system is defined as follows: axial-along the torque converter shaft, tangential-in the torque converter rotational direction, and radial-perpendicular to the shaft. The blade and passage geometries were previously fully documented by By and Lakshminarayana (1993). The performance curves for the torque converter are presented in Fig. 4.

The pump was studied in detail for two-off design speed ratios (0.065 and 0.800); the design speed ratio is 0.600. Torque converter speed ratio is defined as the turbine speed divided by the pump speed. The two operating conditions that were tested are presented in Table 1.

Laser Velocimeter System. The back scatter LV is shown in Fig. 5. The system is a one-directional dual-beam LV. A one-directional system was used because perfect probe volume overlapping with a two-directional three-beam system (for example, used by Miner et al., 1989) was impossible due to the small difference of index of refraction between the oil and Plexiglas and the curvature of the Plexiglas components (shell, core, and blades).

The entire optical assembly (transmitting and receiving optics) was mounted on a mill table to maintain optical alignment throughout the experiments. The probe volume location (measurement point) was moved in the torque converter in all three directions at Cartesian angles by traversing the mill bed. A digital readout on the mill bed was used for precise location of the probe volume. Dial indicators were used initially to align the traverse of the mill bed parallel to the face of the torque converter housing box. The resulting uncertainty in position of the digital readout was 0.005 mm in any direction.

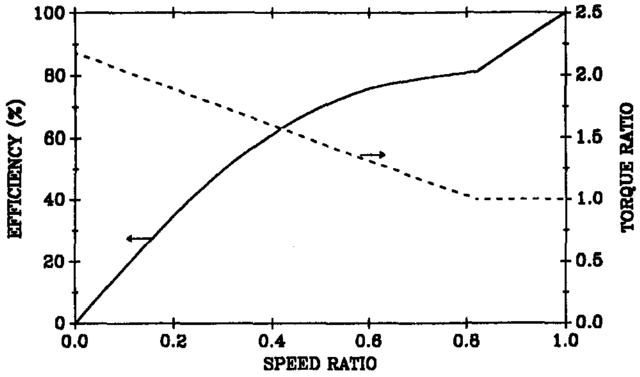

Fig. 4 Torque converter performance curve

Table 1 Test conditions

Condition #1	Condition #2
SR = 0.065	SR = 0.800
Pump Speed = 800	Pump Speed = 1100
Turbine Speed = 52	Turbine Speed = 880
Stator Speed = 0	Stator Speed = 0
Efficiency = 13.0%	Efficiency = 82.0%

A 2 W argon-ion laser was used and the 514.5 nm wavelength was selected. The laser beam was split into two equal intensity components by a beam splitter. Although the LV system was one directional, different velocity components were measured by rotating the beam splitter and realigning the optics for each component. The axial and tangential velocity components were measured by aligning the laser velocimeter beams perpendicular to the torque converter shaft, while for the radial component the beams were aligned parallel to the shaft (Fig. 1 shows the arrangement to measure the axial component and Fig. 5 shows the arrangement to measure the radial component). All three components of velocities were obtained in the inlet, mid-, and exit planes of the pump.

The focusing (and collecting) lens had a focal length of 250.8 mm. A Bragg cell was used to shift the frequency of one beam so that negative velocities were distinguished from positive velocities. A beam spacer and beam expander were used to reduce the probe volume size. The effective probe volume is 72 μm in diameter and 793 μm long. Aluminum coated styrene particles 12 μm in diameter were seeded into the flow; the density of the particles approximated the density of the oil. The light scattered by particles in the flow was focused into a photomultiplier tube (PMT). Output signals of the PMT were amplified, bandpass filtered, and transmitted to a signal processor.

The signal processor is a burst-type processor with a minimum threshold and a $\frac{5}{8}$ peak count comparator to validate the Doppler signal. Noise is eliminated using the minimum threshold. The $\frac{5}{8}$ peak count comparator is used to reject signals from multiple particles in the probe volume. Each valid Doppler signal was recorded with a dedicated microcomputer (Fig. 1).

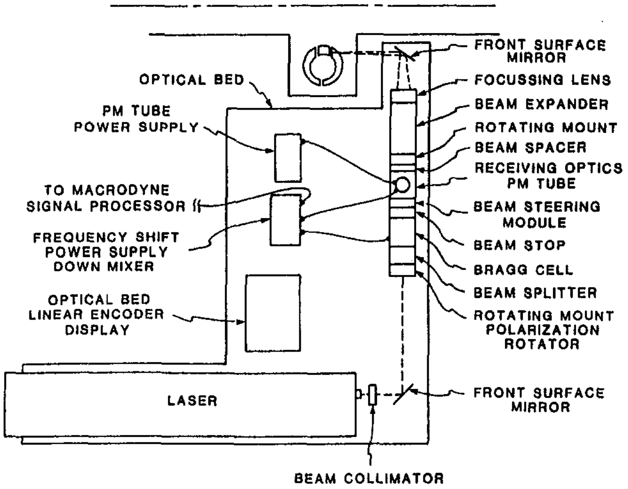

Fig. 5 Schematic of back-scatter laser velocimeter

Typically, 2000 valid signals were recorded for each location in the torque converter.

The instantaneous angular position of the pump and turbine were measured for each valid velocity signal using 9-bit (512 circumferential positions) shaft encoders on the pump and turbine shafts. Thus, for every valid signal, the velocity, instantaneous relative pump position, and instantaneous relative turbine positions were recorded (Fig. 1). Using the angular positions from the shaft encoders, the velocities were then organized to generate the appropriate velocity profiles. Uncertainties in the angular positions of the two rotating components are ± 0.7 deg.

Due to the small difference of index of refraction, the uncertainty of the probe volume position varied depending on the number of interfaces the laser beams traversed. For the pump inlet the beams crossed eight interfaces and the uncertainty of the probe volume location was 0.5 mm in the direction of the length of the probe volume. However, for the pump exit the beams crossed only four interfaces and the uncertainty of the probe volume position was much smaller, 0.2 mm.

Uncertainties in measured velocities are due to the clock in the digital processor, uncertainties in the beam crossing angle, and a finite number of samples used to approximate the true distribution. This uncertainty is typically ±0.05 m/s. Furthermore, uncertainties in translational and angular position translate to uncertainties in the velocity when velocity gradients are present. The positioning uncertainty of the probe volume was approximately 0.3 mm. The total uncertainty due to the combination of these affects is typically 0.07 m/s.

Procedure. Measurement locations were determined by first using reference points in the pump and the known pump dimensions. The probe volume was then moved to the desired measurement locations in the pump with a total accuracy of the absolute position of 0.05 mm in any direction.

For the inlet plane, data were taken in a 1 by 5 (core to shell) equally spaced grid relative to the stator exit. The data for the rotating inlet plane were then resolved into an 18 by 5 measurement grid for the time-averaged flow field for the rotating coordinate system. For the midplane, data were taken in a 9 (core to shell) by 1 grid. In this plane, data were not dependent on the relative stator or turbine position and a resolution of 18 (blade to blade) by 9 (core to shell) was used. For the exit plane data were taken in a 9 (core to shell) by 1 grid. Data were then resolved into a 18 by 9 grid for the time averaged flow field. For 90 percent of the measured grid positions more than 150 valid velocity samples were collected; sufficient samples for a high confidence in the average velocities.

Data Reduction. Average velocities were calculated and organized into blade-to-blade and core-to-shell profiles for the 27 blade passages of the pump. The velocity profiles of all blade passages were shown to be identical within the uncertainties and, hence, could be superimposed and averaged.

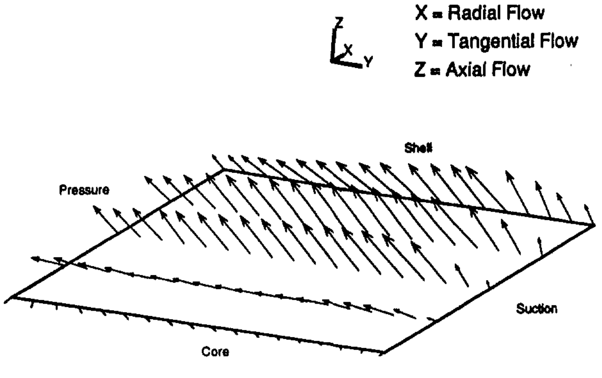

Fig. 6 Average total velocity vector plot at the inlet plane for speed ratio 0.800

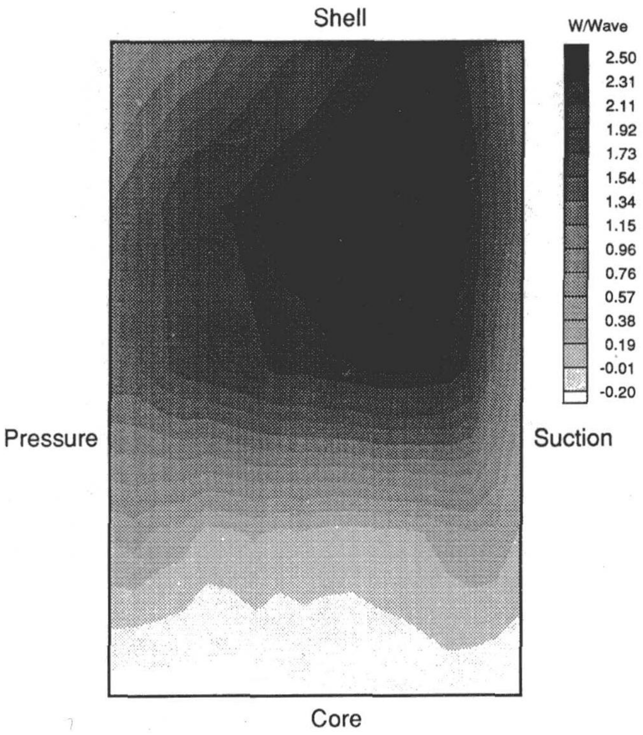

Fig. 7 Average through flow velocity contour plot at the inlet plane for speed ratio 0.800

Blade-to-blade, core-to-shell velocity profiles and vector plots were plotted using commercially available plotting routines. Average flow fields in the inlet, mid-, and exit plane at the two speed ratios are shown in this paper. All through flow velocities are normalized by the average throughflow velocity of the measurement plane.

Results and Discussion

As previously described, data in three pump planes were recorded and analyzed. Time-averaged data are of primary interest and all three velocity components were analyzed. Secondary flows are identified and quantified. All velocities are presented relative to the rotating pump frame. Also, torques are derived from the angular momentum fluxes and slip factors are determined from the relative tangential velocities. All of the above are discussed. Although only average relative velocities are reported herein, Brun et al. (1996) reported unsteady effects for the same apparatus.

Pump Inlet Plane Velocity Fields. Time-averaged (averaged for all relative stator locations) velocity fields were calculated so that general flow trends could be discerned. Typical inlet plane velocity results are shown in Figs. 6, 7, and 8 for a speed ratio of 0.800.

In Fig. 6 a velocity vector plot is presented. In general the velocities are largest near the shell and lowest near the core. In Fig. 7 a contour plot of the throughflow velocity is shown. Throughflow velocity is defined as the velocity component normal to a given measurement plane. From this plot the maximum velocities are observed to be about $\frac{3}{4}$ of the distance between the core and shell and about $\frac{1}{3}$ of the distance between the suction and pressure surfaces. The maximum velocities are approximately 2.5 times the average velocity. Near the core (about 25 percent of the flow area) a separation region is seen as the velocities are very low and sometimes negative. Such a flow separation was also observed for the speed ratio of 0.065. The cause for the flow separation at the core is the sudden area

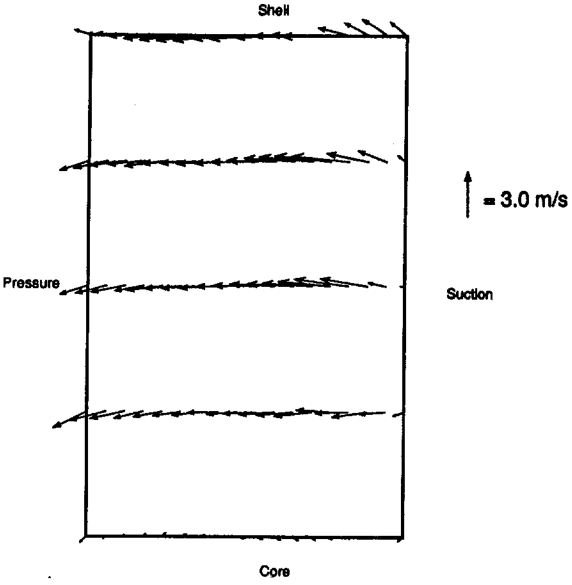

Fig. 8 Average velocities in the plane of the inlet plane for speed ratio 0.800

expansion the flow experiences when leaving the stator exit, shown in Fig. 2.

In Fig. 8 the flow patterns of the relative velocities (with respect to the pump frame) normal to the throughflow component (in the plane) are shown. As can be seen, the general secondary directions of the flows at this speed ratio are nearly uniform from the suction surface to the pressure surface; no circulatory secondary flow patterns are shown. Typical relative velocities normal to the throughflow in this plane are 80 percent of the typical through flow velocities. At a speed ratio of 0.065, the secondary flow was predominantly from the shell to core. Thus, the secondary flow direction depends strongly on the speed ratio; that is, the flow at the exit of the stator is strongly dependent on the speed ratio, which affects the inlet to the pump.

Pump Midplane Velocity Fields. Figures 9 through 13 depict the overall flow field at the pump midplane for both speed ratios. In Fig. 9 a three-dimensional vector plot is shown for the speed ratio of 0.065. The maximum velocities are at the shell side and to a lesser extent toward pressure side. In general velocities decrease smoothly from the shell side toward the core side. For this speed ratio no separation is identifiable in the midplane. Hence, the separation region on the core side from the inlet plane was able to reattach before it reached the midplane.

In Fig. 10 the vector plot of the flow field is presented and in Fig. 11 the contour plot of the throughflows is shown for the speed ratio of 0.800. Both figures show that velocities are very large in the shell/pressure side quadrant and are about three times the average velocity. Furthermore, a large separation region is evident in the core/suction side quadrant. For this speed ratio (lower flow rate) the separation region, which was seen in the inlet plane, has expanded into the midplane and was not able to reattach. Thus, at the lower flow rate, the rapid radial turning from the inlet to midplane manifested the separation. The pressure measurements of By and Lakshminarayana (1993) also indicate a separated region near the core for the speed ratio of 0.800; also, the flow is better behaved near the core for the stall condition.

In Fig. 12 the flow in the plane of interest is shown for the speed ratio of 0.800. As can be seen, secondary flows in the midplane have a strong counterclockwise rotational circulation. Typical relative secondary flow velocities in this plane are 40 percent of the average through flow velocity. Since the fluid is rotating around the shaft of the torque converter and is also being turned from axial to radial and back to axial flow (the curvature of the core and shell), a combined effect of the Coriolis and centrifugal forces as well as shear forces on the fluid

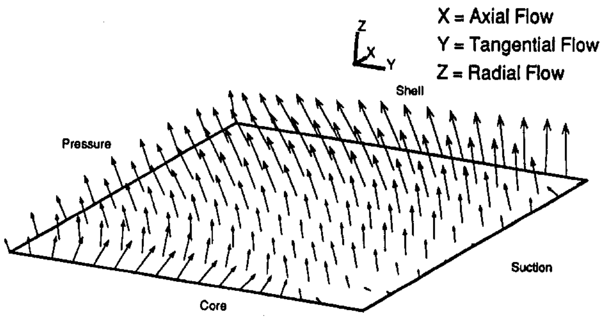

Fig. 9 Average total velocity vector plot at the midplane for speed ratio 0.065

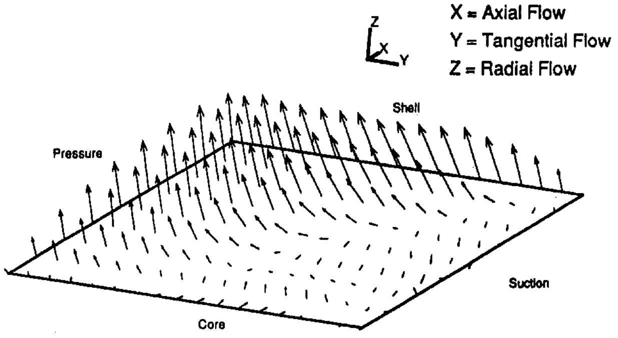

Fig. 10 Average total velocity vector plot at the midplane for speed ratio 0.800

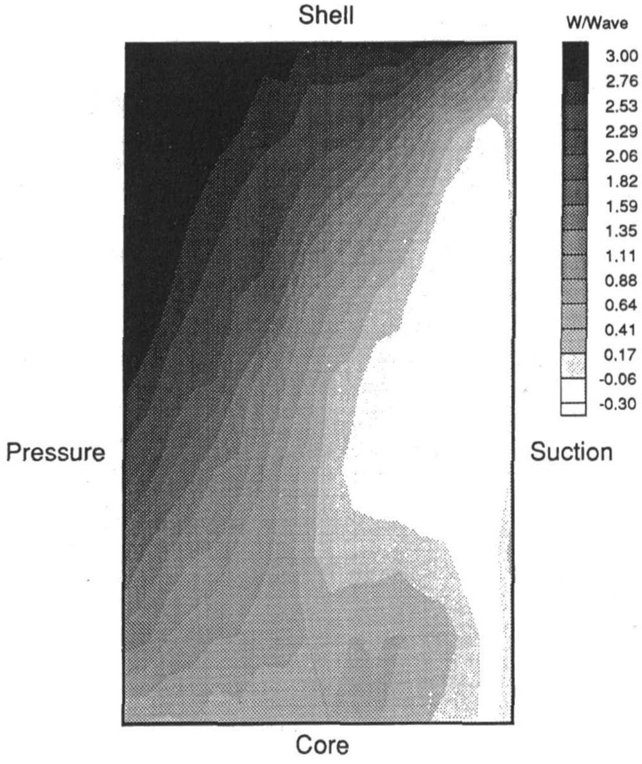

Fig. 11 Average throughflow velocity contour plot at the midplane for speed ratio 0.800

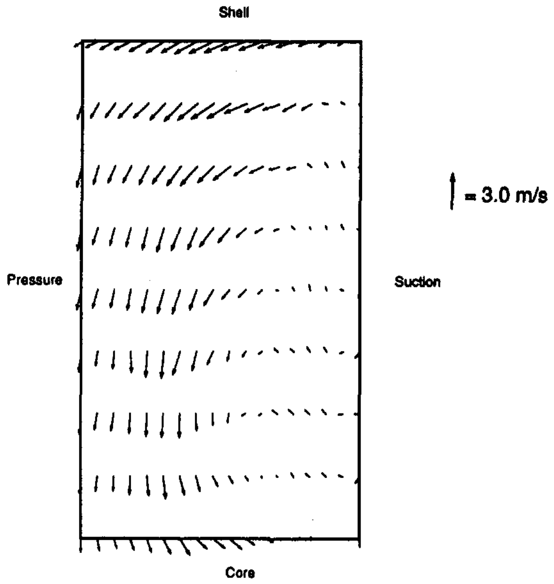

Fig. 12 Average velocities in the plane of the midplane for speed ratio 0.800

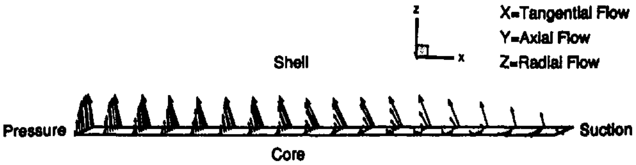

Fig. 13 Average total velocity vector plot at the midplane for speed ratio 0.800 (side view)

are postulated to be responsible for this circulation. Such a circulatory flow was also observed for the 0.065 speed ratio. Figure 13 shows the pump midplane flow field at a side-view angle. This figure demonstrates the pressure-to-suction side velocity profile. More plots of this type can be found in Gruver (1992) for all three pump planes and both speed ratios.

Pump Exit Plane Velocity Fields. Figures 14 through 16 show typical pump exit plane average velocity profiles and are for a speed ratio of 0.800. The vector and contour plots are presented in Figs. 14 and 15, respectively. Largest velocities are seen in the shell side pressure surface quadrant and are 2.9 times the average velocity. A small flow reversal and separation region is visible near the core side/suction surface quadrant. The large separation region from the midplane has decreased in size but was not able to completely reattach. For a speed ratio of 0.065 the largest throughflow velocities again occur at the pressure surface and to a lesser extent shell side of the exit plane. On the other hand no separation was indicated for the lower speed ratio.

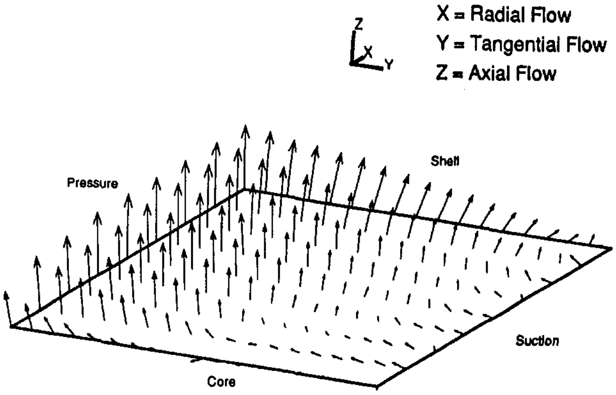

Fig. 14 Average total velocity vector plot at the exit plane for speed ratio 0.800

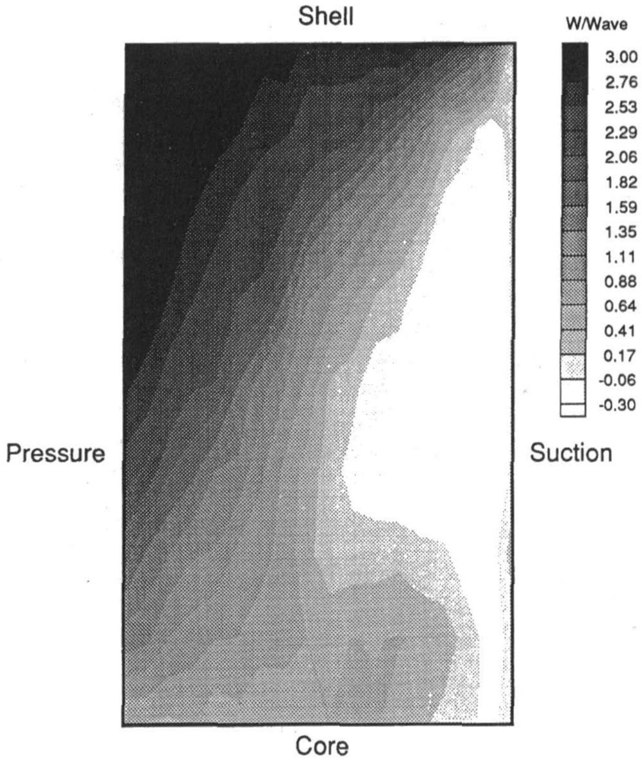

Fig. 15 Average throughflow velocity contour plot at the exit plane for speed ratio 0.800

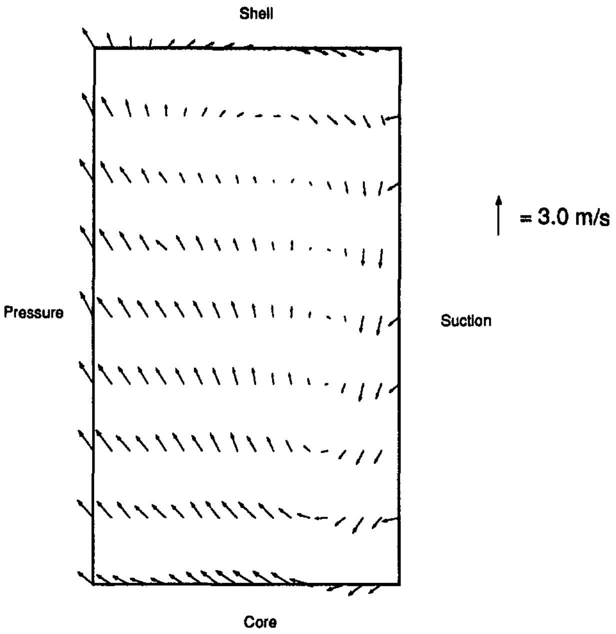

Fig. 16 Average velocities in the plane of the exit for speed ratio 0.800

In Fig. 16 the flow pattern in the plane shows a strong secondary flow in a clockwise circulatory pattern. Typical relative secondary flow velocities in this plane are 25 percent of the average throughflow velocity. One should note that the counter-

Table 2 Mass flows (kg/s) and uncertainties

Speed Ratio	Inlet Plane	Mid–Plane	Exit Plane
0.065	20.1 ± 2.6	20.0 ± 1.0	21.9 ± 2.6
0.800	13.9 ± 2.1	14.0 ± 1.7	14.9 ± 1.7

clockwise circulation from the midplane has reversed between mid- and exit plane. This reversal is attributed to a combination of viscous, centrifugal, and Coriolis forces on the fluid, but needs further research. Again, such a circulatory flow was also observed for the 0.065 speed ratio.

Mass Flow Rates. Mass flow rates for the inlet, mid-, and exit planes were calculated by numerically integrating in two directions the average throughflow velocities across the passages. Small differences between mass flows between the planes were observed. To evaluate the accuracy of the data, an uncertainty analysis of the mass flow rate was performed based on both the uncertainties of the throughflow velocities and the uncertainties of the measurement locations. The mass flow rates of all three planes were found to agree to within the uncertainty limits (Table 2).

Secondary Flow Field Analysis. The relative secondary flows in the mid- as well as the exit planes show strong secondary rotational flow patterns. To quantify the fluid rotational component, the average relative vorticity was calculated using the following equation:

$$\zeta = -\frac{1}{A}\iint (\nabla \times \vec{V})\cdot d\vec{A} = -\frac{1}{A}\iint \left[\frac{\partial v}{\partial x} - \frac{\partial u}{\partial y}\right] dA$$

where x and y are in the plane directions, and u and v are relative secondary flow velocities in the plane of interest. The component u is in the core-to-shell direction and v is in the pressure surface to suction surface direction. Positive is defined from the pressure to the suction side and from the core to the shell side. To integrate the experimental velocity data the expression was rewritten into numerical form.

$$\zeta = -\frac{1}{A}\sum^{N_i}\sum^{N_j}\left[\frac{v_{i+1} - v_i}{\Delta x} - \frac{u_{i+1} - u_i}{\Delta y}\right]\Delta x \Delta y$$

where N_i (pressure-suction) and N_j (core-shell) represent the resolution of the plane. The circulation was obtained by integrating across an entire plane.

Relative vorticity results of the inlet, mid-, and exit plane for both speed ratios are presented in Table 3. The results are consistent with observations of the typical secondary flow plots (Figs. 8, 12, and 15); in the midplane flow is counterclockwise and in the exit plane the flow is clockwise. From Table 3 the relative vorticity is very small at the inlet plane for both speed ratios. Also, one can see that at the midplane the 0.065 speed ratio yields a stronger counterclockwise rotation than the 0.800 speed ratio. In the exit plane the 0.800 speed ratio yields a stronger clockwise rotation than the 0.065 speed ratio.

Pump Torques. The torque generated by the pump was calculated using the angular momentum equation:

$$T_\theta = \iint r V_\theta \rho \vec{V}\cdot d\vec{A}$$

where r is the radius from the shaft center, V_θ is the absolute tangential velocity, $\vec{V}$ is the total velocity, and ρ is the fluid density. This surface integral can be evaluated in the following numerical form for any plane:

$$T_\theta = \sum^{N_i}\sum^{N_j}[\rho r_j V_{\theta_{ij}} w_{ij}]\Delta x \Delta y$$

where w is the through flow component of velocity.

Table 3 Average vorticity (1/s)

Speed Ratio	Inlet Plane	Mid–Plane	Exit Plane
0.065	–1.8	150.1	–71.2
0.800	13.5	117.6	–144.5

Table 4 Pump torques (N·m)

Speed Ratio	Inlet to Mid–Plane	Mid– to Exit Plane	Total
0.065	10.3	8.4	18.7
0.800	12.1	7.9	20.0

The surface integral was evaluated at the inlet, mid-, and exit planes. Thus, the required torque from the inlet to the midplane, from the mid- to the exit plane, and inlet to exit plane (total) were evaluated. Results are presented in Table 4. The total torque required by the pump at the 0.800 speed ratio is 1.3 N·m higher than at the 0.065 speed ratio. For the speed ratio of 0.065, 55 percent of the torque is transmitted to the fluid between the inlet and midplane. For the higher speed ratio (0.800), 61 percent of this transmission occurs between the inlet and midplane. Therefore, the required torque is approximately evenly distributed between the two sections for both speed ratios. Also, more torque is required between the inlet and the midplane for the 0.800 speed ratio than for the 0.065 speed ratio. This can be justified with the high incidence angle of the flow entering the pump at the 0.065 speed ratio. The flow demonstrates large incidence in the direction of the rotation of the pump and thus has high angular momentum in the same direction. Hence, the pump requires less angular momentum change between the inlet and exit and, thus, less torque to accelerate the fluid. Between the mid- and the exit plane the torque required at both speed ratios is within 6 percent.

Pump Mid- and Exit Plane Slip Factors. The slip factor was calculated for the pump mid- and exit planes from the measured velocities using:

$$\mu = \frac{c_\theta}{c'_\theta}$$

where c_θ is the weighted average absolute tangential velocity and c'_θ is the ideal absolute tangential velocity calculated from velocity polygons. The weighted average tangential velocity is obtained by averaging the tangential component across a flow area and weighting the value proportionally to the mass flux across the area.

Since the torque converter pump operates similar to a centrifugal pump, slip factors were quantitatively compared to the slip factor predictions of Stodola (1945) and the graphic slip correlations of Busemann (1928) and Wiesner (1967). Results are presented in Table 5.

Good agreement is found between the pump midplane slip and both Busemann's and Wiesner's correlations, which can be explained by the fact that the torque converter pump section from the inlet to the midplane strongly resembles a conventional

Table 5 Slip factors

	Speed Ratio = 0.065	Speed Ratio = 0.800
Measured Mid–Plane	0.914	0.928
Measured Exit Plane	0.965	0.969
Stodola (1945)	0.884	0.884
Busemann (1928)	0.905	0.905
Wiesner (1967)	0.900	0.900

centrifugal pump. For example, the experimental midplane slip factor at the 0.065 speed ratio was 0.914, while Busemann's correlation gives 0.905. The slip calculated from the exit-plane flow field does not agree with Stodola's, Busemann's, or Wiesner's correlations, and the slip factor is in fact higher. At the 0.065 speed ratio the experimental slip is 0.965, while Busemann's correlation gives 0.905. Thus, the additional guidance (the nominal chord length between inlet and exit planes is 2.2 times longer than the chord length between inlet and midplane) that the flow experiences from the blades between the mid- and exit plane causes flow slip to be significantly smaller (the flow direction is nearly the blade direction) than for centrifugal pump flow.

Conclusions

Laser velocimetry was used to measure the flow field in the inlet, mid-, and exit planes of the pump of an automotive torque converter. Average velocities are presented and analyzed in this paper. Data presented in this paper embody the most detailed velocity measurements in torque converters available. Important conclusions drawn from this investigation are:

1 In all measurement planes, the highest throughflow velocities generally occurred at the pressure and shell sides. For both speed ratios the flow entered the pump inlet plane with a separation region occurring at the core side. The flow was able to reattach at the speed ratio of 0.065 before it reached the midplane, while at the speed ratio of 0.800 (lower flow rate) the flow field demonstrated a large separation region throughout the pump. The rapid radial turning from the inlet to midplane amplified the separation region for this case.

2 The secondary flow in the pump midplane is counterclockwise circulating with vorticities of 150.1 s^{-1} and 117.6 s^{-1} at speed ratios of 0.065 and 0.800, respectively. On the other hand the secondary flow in the pump exit plane is clockwise circulating with vorticities of $-71.2\ s^{-1}$ and $-144.5\ s^{-1}$ at the same two speed ratios. Rotational secondary flows were not observed in the inlet plane.

3 At the 0.065 and 0.800 speed ratios the pump requires 18.7 N·m and 20.0 N·m of torque, respectively. For speed ratios of 0.065 and 0.800, the torque for the inlet section was 55 and 61 percent of the total torque, respectively. Thus, the torque was approximately evenly distributed between the inlet and exit sections.

4 The slip factor was determined at the mid- and exit planes and compared to predicted values for conventional centrifugal pumps. At the midplane the values compared well. However, at the exit plane the values for the torque converter pump were higher than for a centrifugal pump. The added passage length adds to the fluid control, and thus increases the slip factor in the second half of the torque converter pump.

Acknowledgments

This research was sponsored by GM Corporation by the Tech Center-Advanced Engineering and by the Powertrain Division. The authors wish to express their gratitude to R. By and D. Maddock for their many helpful discussions and for their efforts with hardware support. The research was also supported in part by the Rotating Machinery and Controls Laboratory at the University of Virginia.

References

Adrian, F. W., 1985, "Experimental and Analytical Investigation of Flow in Hydrodynamic Torque Converters," Ph.D. Dissertation, The Ruhr University, Bochum, Germany.

Bahr, H. M., Flack, R. D., By, R. R., and Zhang, J. J., 1990, "Laser Velocimeter Measurements in the Stator of a Torque Converter," SAE Paper No. 901769; *SAE 1990 Trans., Journal of Passenger Cars*, Vol. 99, Section 6, pp. 1625–1634.

Beaudoin, R. J., Miner, S. M., and Flack, R. D., 1992, "Laser Velocimeter Measurements in a Centrifugal Pump with an Orbiting Impeller," ASME JOURNAL OF TURBOMACHINERY, Vol. 114, pp. 340–358.

Browarzik, V., and Grahl, K. G., 1992, "Non-Steady Flow Measurements Inside a Hydrodynamic Torque Converter by Hot-Film Anemometry," ASME Paper No. 92-GT-161.

Brun, K., Flack, R. D., and Gruver, J. K., 1996, "Laser Velocimeter Measurements in the Pump of a Torque Converter: Part II—Unsteady Measurements," ASME JOURNAL OF TURBOMACHINERY, Vol. 118, this issue, pp. 570–577.

Busemann, A., 1928, "Das Folderhohen verhaltnis radialer Kreiselpumpen mit Logarithmischapiraligen Schaufeln," *Zeitschrift für Angewandte Mathematik und Mechanik*, Vol. 8, No. 5, pp. 372–384.

By, R. R., and Mahoney, J. E., 1988, "Technology Needs for the Automotive Torque Converter," SAE Paper No. 880482.

By, R. R., and Lakshminarayana, B., 1991, "Static Pressure Measurements in a Torque Converter Stator," SAE Paper No. 911934; *SAE Transactions, Journal of Passenger Cars*, 1992.

By, R. R., and Lakshminarayana, B., 1993, "Measurement and Analysis of Static Pressure Field in a Torque Converter Pump," *Second ASME Pumping Machinery Symposium*, ASME FED-Vol 154, pp. 253–264; to be published in ASME *Journal of Fluids Engineering*.

By, R. R., Kunz, R. F., and Lakshminarayana, B., 1993, "Navier–Stokes Analysis of the Pump of an Automotive Torque Converter," *Second ASME Pumping Machinery Symposium*, ASME FED-Vol 154, pp. 264–274, to be published in ASME *Journal of Fluids Engineering*.

Fister, W., and Adrian, F. W., 1983, "Experimental Researches of Flow in Hydrodynamic Torque Converters," *Proc. 7th Conference on Fluid Machinery*, Budapest, Hungary, Vol. 1.

Flack, R. D., Miner, S. W., and Beaudoin, R. J., 1992, "Turbulence Measurements in a Centrifugal Pump With a Synchronous Orbiting Impeller," ASME JOURNAL OF TURBOMACHINERY, Vol. 114, pp. 350–359.

Gruver, J. K., 1992, "Laser Velocimetry Measurements in the Pump of an Automotive Torque Converter," Master's Thesis, University of Virginia, Aug.

Miner, S. M., Beaudoin, R. J., and Flack, R. D., 1989, "Laser Velocimetry Measurements in a Centrifugal Flow Pump," ASME JOURNAL OF TURBOMACHINERY, Vol. 111, pp. 295–212.

Numazawa, A., Ushijima, F., Kagenoni, G. J., and Ishihara, T., 1983, "An Experimental Analysis of Fluid Flow in a Torque Converter," SAE Paper No. 830571.

Sakamoto, H., Suyama, K., and Saka, T., 1992, "Study on Torque Converter Circuit Profile," SAE Paper No. 920765.

Stodola, A., 1945, *Steam and Gas Turbines*, Peter Smith Publisher, Gloucester, MA.

Upton, E. W., 1962, "Applications of Hydrodynamic Drive Units to Passenger Car Automatic Transmissions," *SAE Design Practices—Passenger Car Automatic Transmissions*, Vol. 1.

Wiesner, F. J., 1967, "A Review of Slip Factors for Centrifugal Impellers," ASME *Journal of Engineering for Power*, Vol. 89, pp. 558–572.

Laser Velocimeter Measurements in the Pump of an Automotive Torque Converter: Part II—Unsteady Measurements

K. Brun

R. D. Flack

J. K. Gruver

Department of Mechanical, Aerospace,
and Nuclear Engineering,
ROMAC Laboratories,
University of Virginia,
Charlottesville, VA 22903

The unsteady velocity field found in the pump of an automotive torque converter was measured using laser velocimetry. Velocities in the inlet, mid-, and exit planes of the pump were investigated at two significantly different operating conditions: turbine/pump rotational speed ratios of 0.065 and 0.800. A data organization method was developed to visualize the three-dimensional, periodic unsteady velocity field in the rotating frame. For this method, the acquired data are assumed to be periodic at synchronous and blade interaction frequencies. Two shaft encoders were employed to obtain the instantaneous angular position of the torque converter pump and turbine at the instant of laser velocimeter data acquisition. By proper "registration" of the data, visualizing the transient interaction effects between the stator and the pump, and between the pump and the turbine, was possible. Results showed strong cyclic velocity fluctuations in the pump inlet plane as a function of the relative stator-pump position. Typical percent periodic fluctuations in the through flow velocity were 70 percent of the average throughflow velocity. The upstream propagation influence of the turbine on the pump exit plane flow field was seen to be smaller. Percent periodic fluctuations of the throughflow velocity were typically 30 percent. The effect of the stator and turbine on the midplane flow field was seen to be negligible. The incidence angle at the pump inlet fluctuated by 27 and 14 deg for the 0.065 and 0.800 speed ratios, respectively. Typical slip factors at the exit were 0.965 and fluctuated by less than 1 percent.

Introduction

The standard torque converter is a recirculating hydrodynamic turbomachine with three independent elements that determine the internal flow field. These three elements are the pump, which adds energy to the flow, the turbine, which extracts energy from the flow, and the stator, which redirects the flow from the turbine into the pump to create ideally zero incidence into the pump inlet at a particular design turbine/pump speed ratio. The pump and the turbine are rotating at different speeds, while the stator is either locked or allowed to float freely, depending on the design.

Due to the interaction between the three independent elements, the internal flow field is highly unsteady and three dimensional. Especially at the element interfaces, stator–pump, pump–turbine, and turbine–stator, the flow field experiences strong fluctuations. These fluctuations can have a significant influence on the performance characteristics of the torque converter. For example, fluctuations of the inlet incidence angle and exit slip factor will directly affect the pump efficiency. Thus, to fully understand and reliably predict the internal flow field of a torque converter, one cannot rely solely on average velocity measurements; one must also visualize the unsteady effects generated by the element interactions.

The only nonintrusive measurement technique that has been successfully used to measure velocities accurately in turbomachines is burst laser velocimetry. Unfortunately, a burst laser velocimeter is a discrete sampling type instrument, which is often only employed to measure steady-state flow phenomena. But the flow field in the torque converter is periodically unsteady and is solely dependent on the instantaneous angular positions of the pump, turbine, and stator. Thus, to visualize the unsteady flow field in the torque converter, a method needs to be employed to correlate discrete laser velocimeter data samples that were collected over many cycles of the torque converter, to the relative angular positions of the pump, turbine, and stator.

Previous Research on Unsteady Flows in Turbomachines. A method was described by Brun and Flack (1993) to analyze the periodic unsteady flow in the turbine inlet of a torque converter. The instantaneous angular position of the torque converter pump and turbine were measured using two shaft encoders. Velocities were measured for a turbine/pump speed ratio of 0.800. A strong influence of the pump on the turbine inlet flow field, with a jet/wake region migrating through the turbine inlet at the blade interaction frequency, was demonstrated.

Other researchers have visualized unsteady velocity fields in single element turbomachine geometries in which data analysis is simpler. For example, Hamkins and Flack (1987) used a laser velocimeter to measure blade-to-blade profiles in a four-bladed impeller centrifugal pump. For these measurements, data repeated periodically at a frequency of four times per impeller revolution. On the other hand, a synchronous fluctuation was not present in these data. The authors identified steady flow reversals in the impeller for low flow rates. Later Beaudoin et

---

Contributed by the International Gas Turbine Institute and presented at the 39th International Gas Turbine and Aeroengine Congress and Exposition, The Hague, The Netherlands, June 13–16, 1994. Manuscript received by the International Gas Turbine Institute February 4, 1994. Paper No. 94-GT-48. Associate Technical Editor: E. M. Greitzer.

al. (1992) used the same experimental facility to measure blade-to-blade profiles in a four-bladed impeller centrifugal pump, in which the impeller synchronously orbited with a fixed orbit size. For these measurements data repeated periodically one time per revolution. Conversely, a precise 4× synchronous (or blade pass) variation was not present in this data. For this case unsteady separation regions were identified for low flow rates.

Eckardt (1979) and Krain (1981) utilized a laser-2-focus system and a shaft timer to investigate the flows in several radial compressor impellers. For one of the impellers, velocities at the exit were fairly uniform. A single-component laser velocimeter and a slotted disk on the shaft for timing was used by Kannemans (1980) to study the velocities in a pump impeller. At design, experimental results agreed well with potential theory predictions. Sideris and Van de Braembussche (1987) used the same rig, and velocity measurements were coupled with pressure measurements to show the influence of the volute on the flow field.

A number of studies on the unsteady flow field in axial flow turbomachines have been completed at NASA-Lewis. Powell et al. (1981) utilized a backscatter laser velocimeter to measure velocities in a compressor rotor. Shaft encoder information was used to develop blade-to-blade velocity profiles. Strazisar (1985) used a laser velocimeter and a variable clock that was phase locked to the shaft to investigate the flow field between the blades in a transonic fan. An oscillating shock was seen. Suder et al. (1987) employed a laser velocimeter to measure the unsteady flow field within the stator row of a fan. Unsteady flow field features were resolved, and both rotor-wake-generated and random unsteadiness were identified.

Previous Studies of Torque Converter Internal Flows. By and Lakshminarayana (1991, 1993) measured average static pressures on the blades of an automotive torque converter stator and pump, respectively. Their results showed that the static pressure distribution is generally poor at the blade core section, that centrifugal force has a dominant effect on the static pressure rise in the pump, and that potential flow theory can approximately predict the static pressure distribution at the blade midspan, but not at the core and shell sections. Later, By et al. (1993) developed a three-dimensional, incompressible, viscous flow code to predict the flow field of a torque converter pump. Results showed that the pump rotation has a major effect on the secondary flow field and that the inlet velocity profiles have a profound effect on the mass-averaged total pressure loss.

The average velocity flow field in the stator of an automotive torque converter was described by Bahr et al. (1990). A torque converter was machined entirely from Plexiglas and a laser velocimeter was employed to measure velocities. Detailed velocity profiles for five planes in the stator and for two speed ratios are presented. Separation regions were observed in the pressure side/midchord/core side and suction side/trailing edge/shell side regions of the stator at a speed ratio of 0.800.

Gruver et al. (1996) used the same experimental facility to determine the average flow field in the pump of an automotive torque converter. Blade-to-blade profiles were generated using a laser velocimeter and an angular encoder on the pump shaft. Velocity vector plots for the inlet, mid-, and exit planes were presented for the 0.065 and 0.800 speed ratios. Separation regions were observed at the core-suction side in the pump mid- and exit planes for the 0.065 speed ratio. Circulatory secondary flow was observed for both speed ratios in the mid- and exit planes.

Objectives. For this research the same experimental facility and torque converter as described by Bahr et al. (1990) and by Gruver et al. (1996) were utilized to measure the unsteady flow field in the inlet, mid-, and exit planes of the torque converter pump at the 0.065 and 0.800 turbine/pump speed ratios. A method similar to that described by Brun and Flack (1993) was employed to correlate the velocity data for the automotive torque converter pump. Detailed studies are included herein to demonstrate the unsteady effect the stator has on the pump inlet flow and the unsteady effect the turbine has on the pump exit flow. The influence from both the stator and turbine on the pump midplane flow field is also discussed. Velocity vector plots and blade-to-blade profiles are included to show the dependence of the pump inlet flow field on the relative stator position, and the dependence of the pump exit flow field on the relative turbine position. Unsteady inlet flow incidence angles and pump exit slip factors are also presented. This paper provides the most complete and detailed data of the unsteady flow field in the torque converter pump published to date. Results presented not only offer a basic understanding of the torque converter pump flow field, but also serve as a benchmark for unsteady mixed flow turbomachinery computational flow codes.

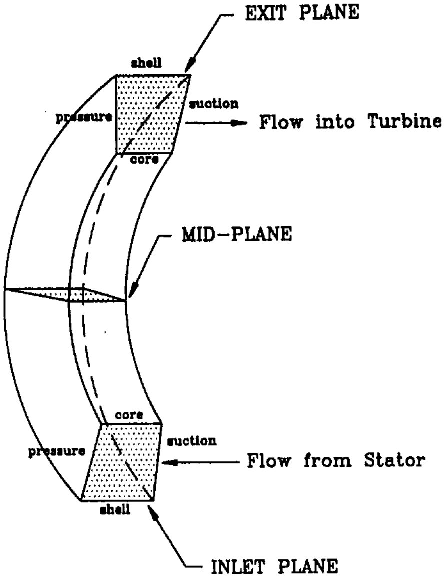

Fig. 1 Pump blade passage geometry

Experimental Facility and Data Acquisition

A one-directional backscatter laser velocimeter was used to measure velocities in the pump of a torque converter. For optical access, the torque converter was entirely machined from Plexiglas. The torque converter pump was driven by an 18 kW motor, with the turbine output power absorbed by a 130 kW capacity eddy current dynamometer. Shellflex 212 oil was the working fluid in the torque converter.

The laser and optics were mounted on a mill table such that the probe volume (measurement location) could be accurately moved in all three directions by traversing the mill table. All three components of the velocities were obtained by accessing the torque converter at Cartesian angles in independent measurements. A counter processor converted analog burst signals from the photomultiplier tube into digital signals. The digital velocity signals were then transmitted to a dedicated microcomputer for further processing. Two 9-bit binary shaft encoders (512 sectors per revolution) measured the instantaneous angular positions of the pump and turbine. Both angular positions were recorded with the instantaneous velocities on the microcomputer.

The torque converter pump consisted of 27 identical blade passages with an angular resolution of 19 sectors apiece. Each blade passage was defined by a pressure, suction, core, and shell side as shown in Fig. 1. Velocities were measured at five core-to-shell side positions for the pump inlet plane, and at nine core-to-shell side positions in the pump mid- and exit planes. Since the stator is not rotating, the laser velocimeter probe

Table 1 Test conditions

Condition 1	Condition 2
Speed Ratio = 0.065	Speed Ratio = 0.800
Pump Speed = 800	Pump Speed = 1100
Turbine Speed = 52	Turbine Speed = 880
Stator Speed = 0	Stator Speed = 0
Efficiency = 13.0%	Efficiency = 82%
Mass Flow = 20.1 kg/s	Mass Flow = 13.9 kg/s

volume was also traversed to circumferential positions in the cylindrical coordinate system relative to the stator to access nine pump–stator relative positions. All measurement locations necessary to obtain blade-to-blade profiles for nine different instantaneous pump–stator relative positions were, thus, accessed. The result was a 9 × 5 measurement grid for the rotating pump inlet plane. As the pump rotated by the stationary laser velocimeter, all blade-to-blade positions were accessed at each measurement location. Measurements were taken at each position for the 0.065 and the 0.800 speed ratios. For the remainder of this manuscript, the speed ratio is defined as the turbine angular speed divided by the pump angular speed. Table 1 indicates the operating conditions of the torque converter for both speed ratios. The entire experimental facility and data acquisition procedure were described by Bahr et al. (1990) and Gruver et al. (1996). The detailed dimensions of the torque converter and passage geometries were given by By and Lakshminarayana (1993). Thus, the measurement geometry and test conditions can be reconstructed from the references given above.

Data Organization Method

Measurement Principles. In a multi-element turbomachine, such as a torque converter, the velocities at any location in the fluid path can be dependent on the angular position of all independently rotating elements. To obtain complete knowledge of the velocities at one measurement location, one must collect velocity samples for all possible angular position combinations of the independent elements in the torque converter. For example, the velocity field in the torque converter pump exit can depend on the relative angular position between the pump and the stator, the pump and the turbine, and the stator and the turbine. Consequently, velocity samples for all possible angular position combinations between the pump, turbine, and stator should be collected for each measurement location. The relative angular position is defined as the difference between the absolute angular positions in the stationary frame.

In a torque converter, the flow field is not only synchronously periodic, but can also be assumed to be periodic over the cycle of a blade passage within the elements. This simplifying assumption holds for most turbomachines where the blade passages are geometrically identical and where the orbit of the element is centered around the turbomachine's centerline. Thus, velocity samples from all blade passages within an element can be superimposed and averaged to obtain one representative blade passage. Velocity samples need not be collected for all relative position combinations between the entire elements, but only for all relative position combinations between the blade passages.

Data Organization Procedure. The pump inlet plane velocity samples must be organized by their pump blade passage angular position and by the relative position between the pump and stator blade passages (pump–stator relative position). Four of the nine possible pump–stator relative positions are shown in Fig. 2. Velocity samples at each of the nine inlet plane measurement locations relative to the stator were first organized into profiles of velocity versus the pump passage angular positions (as the pump blades traversed the stationary probe volume). These profiles do not represent a true "snapshot" of the blade-to-blade profiles one would experience if one measured in the pump rotating reference frame; they are not yet organized by the relative positions between the pump and the stator. Now, from each of the nine profiles, one velocity was selectively picked so that a "snapshot" blade-to-blade profile for one relative pump-stator position was generated. By using these selected velocities, the pump inlet plane resolution was effectively reduced to six pressure-to-suction side locations. This procedure was repeated for nine pump–stator relative positions (0, 11, 22, 33, 44, 56, 67, 78, and 89 percent). The "snapshot" profiles represent the flow field in the pump inlet for different relative angular positions between the pump and the stator. A grid of six pressure-to-suction and five core-to-shell side measurement locations was thus obtained in the pump inlet for nine different pump–stator relative positions.

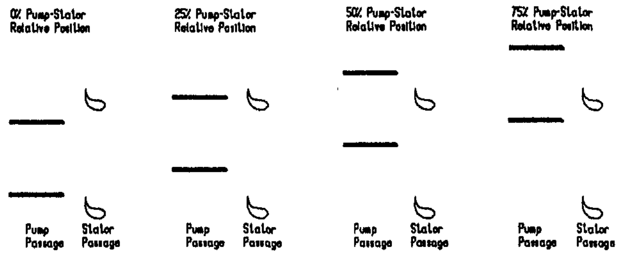

Fig. 2 Four of the nine possible pump–stator relative position combinations

A similar procedure was followed for the pump exit. Velocities taken for the pump exit plane were organized into subgroups by their pump blade passage angular position, and by the relative position between the pump and turbine blade passages (pump–turbine relative position). Figure 3 shows four of the six possible pump–turbine relative positions. Velocity samples in the subgroups were then averaged to obtain a group mean velocity for each instantaneous angular position combination between the pump and the turbine. A resolution of six pressure-to-suction and nine core-to-shell side positions was obtained for the pump exit plane for six pump–turbine relative positions.

Unsteady Velocity Results

As previously described, velocity data in the pump inlet, mid- and exit planes were recorded and analyzed for the 0.065 and the 0.800 speed ratios. The unsteady flow field in the pump inlet and exit planes are of primary interest for pump performance analysis and hence are discussed in greater detail. Also, pump incidence angles and exit slip factors were determined as a function of the relative position of the turbine and stator. All velocity values are normalized by the average throughflow velocity in the plane and all velocity fluctuations are given as the difference between normalized velocities. Throughflow velocity is defined as the velocity component normal to a given measure plane.

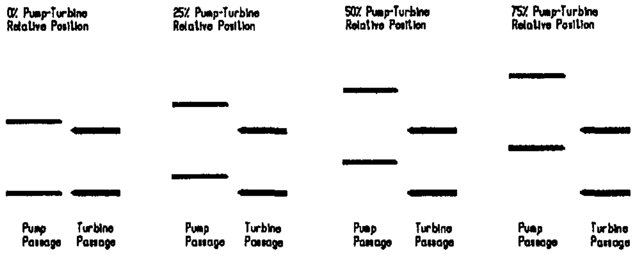

Fig. 3 Four of the six possible pump–turbine relative position combinations

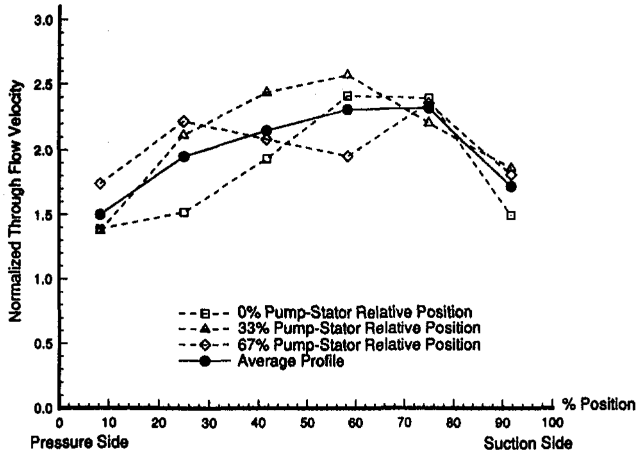

Fig. 4 Pump inlet blade-to-blade velocity profiles for the 0.800 speed ratio at the 50 percent core-to-shell side location

Pump Inlet Plane–Stator Influence. The stator is located directly upstream of the pump inlet plane and hence has a strong influence on the inlet flow field. To demonstrate the influence, the pump inlet plane velocities were organized into groups for nine pump–stator relative positions. For each pump–stator relative position a resolution of six core-to-shell and nine pressure-to-suction side positions were obtained. Results for both speed ratios are presented in Figs. 4–8.

Figure 4 shows throughflow blade-to-blade profiles at the 50 percent core-to-shell side position in the pump inlet for the 0.800 speed ratios. The blade-to-blade profiles are presented for three relative angular position combinations between the stator and the pump: The stator blade is perfectly aligned with pump inlet (0 percent pump–stator relative position), the stator blade is 33.3 percent between pump suction to pressure sides (33 percent pump-stator relative position), and the stator blade is 66.6 percent between pump suction and pressure sides. The plot for the 100 percent pump–stator relative position is identical to the 0 percent pump–stator relative position plot. An average blade-to-blade profile is also included. Velocity profiles are highly nonuniform. A peak average throughflow velocity is located 75 percent between the pressure and suction sides. Lowest average throughflow velocities are seen near the pressure and suction surfaces. A significant influence of the stator on the pump inlet flow field can be observed. Typical throughflow velocity fluctuations between different pump–stator relative positions are 0.5. The maximum fluctuations are 0.8. For the remainder of this manuscript maximum fluctuations are defined as the difference between the highest and lowest normalized velocities that occur at some pressure to suction side location over a complete blade pass cycle. For example, for this case the maximum fluctuations occur at the 25 percent pressure-to-suction side location.

Vector plots of the three-dimensional flow field for this case are presented in Figs. 5(*a*), 5(*b*), and 5(*c*) for the 0, 33, and 67 percent pump–stator relative positions. As the relative positions move from 0 to 37 to 67 percent and back to 0 percent one complete cycle of a pump blade passage is traversed by a stator blade. In general, a high-velocity region is located at the shell side, and a low-velocity region at the core side. The qualitative changes of the flow field in the plane can be analyzed by comparing two or more vector plots for different pump–stator relative positions. Close to the shell the velocity fluctuations are strong, while at the core side almost no unsteadiness is observed. The unsteadiness at the midstream location is seen to be moderate. More three-dimensional plots of this type and vector plots with different viewing perspectives, such as side views and top views, can be found from Gruver (1992). Since

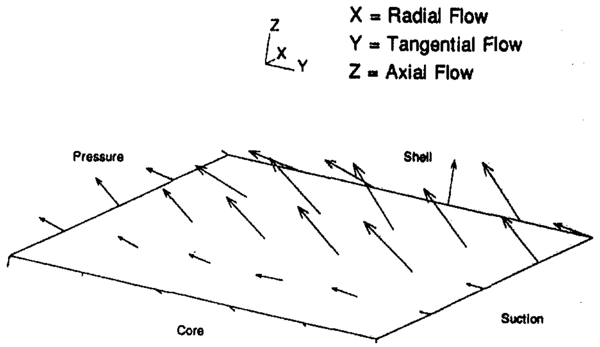

Fig. 5(*a*) Pump inlet velocity field for 0 percent pump–stator relative position at the 0.800 speed ratio

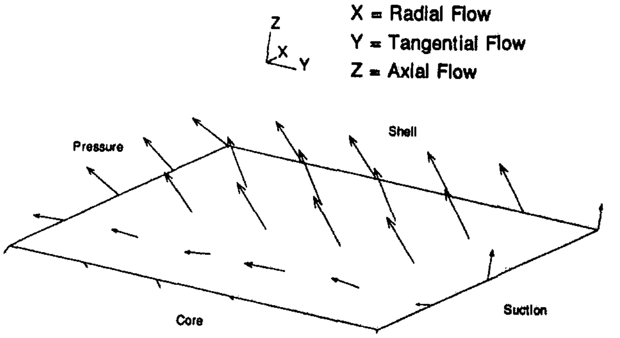

Fig. 5(*b*) Pump inlet velocity field for 33 percent pump–stator relative position at the 0.800 speed ratio

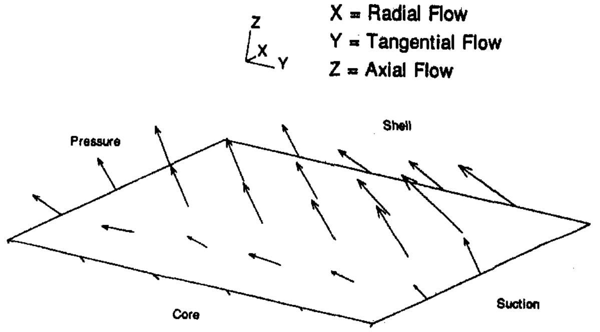

Fig. 5(*c*) Pump inlet velocity field for 67 percent pump-stator relative position at the 0.800 speed ratio

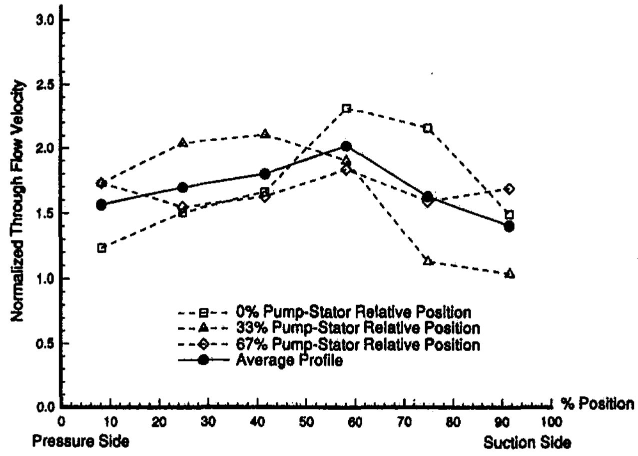

Fig. 6 Pump inlet blade-to-blade velocity profiles for the 0.065 speed ratio at the 50 percent core-to-shell side location

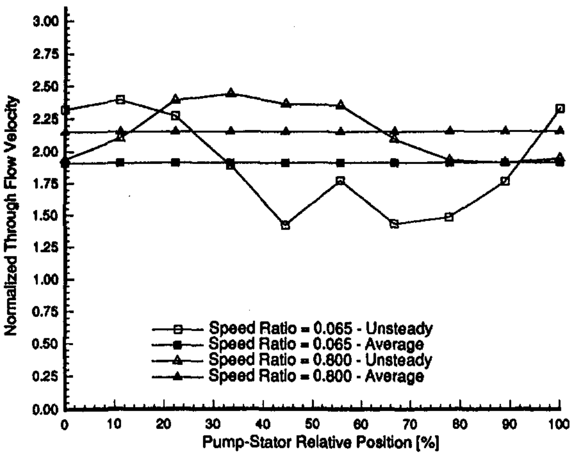

Fig. 7 Dependence of throughflow velocity at pump inlet geometric center on pump–stator relative position for 0.065 and 0.800 speed ratios

these plots do not add much qualitative insight into the flow field, they are not included in this paper.

Measurements by Bahr et al. (1990) showed high throughflow velocity gradients between the pressure and shell sides at the stator exit shell side, and low velocity gradients at the stator exit core side. These stationary velocity gradients are propagated into the pump inlet and appear as unsteadiness as the pump rotates by these gradients. This corresponds to the earlier observation of high unsteadiness at shell side and low unsteadiness at the core side of the pump inlet. Consequently, the unsteadiness in the pump inlet plane is directly related to the nonuniformity of the stator exit flow field.

Similar results were obtained for the 0.065 speed ratio. Figure 6 presents blade-to-blade profiles for the 50 percent core-to-shell side position. Blade-to-blade profiles for the 0, 33, and 67 percent pump–stator relative positions and for the average are shown. The average throughflow velocity profile is nonuniform with a peak velocity at the 60 percent pressure-to-suction side position and minimum velocities at the blades. For this case the highest normalized velocity fluctuations are 1.2 and typical fluctuations are 0.7. Thus, the fluctuations at this location are stronger for the 0.065 speed ratio than for the 0.800 speed ratio.

Figure 7 depicts the throughflow velocity at the geometric center location of the pump inlet plane (50 percent core to shell sides, 50 percent pressure to suction sides) as a function of the pump–stator relative position. This plot quantitatively demonstrates the influence of the stator on one location in the pump inlet for both speed ratios. One complete blade passage cycle (pump–stator relative positions 0–100 percent) and both speed ratios are presented. The average throughflow velocity is also included for both speed ratios. As a pump passage rotates by a stator blade, the throughflow velocity can be seen to vary significantly. The velocities fluctuate by 1.0 for the 0.065 speed ratio and by 0.6 for the 0.800 speed ratios. A direct comparison shows that the influence of the stator on the center of the pump inlet plane flow field is seen to be stronger for the 0.065 speed ratio than for the 0.800 speed ratio. This observation is generally true for all other pump inlet plane measurement positions.

Knowledge of the flow incidence angle into the pump inlet is essential for a one-dimensional flow analysis. Thus, the plane-average incidence flow angles into the pump were calculated from the tangential and axial velocity components. Results are plotted versus the pump–stator relative position for both speed ratios in Fig. 8. One complete blade passages cycle is presented. The pump incidence angle fluctuates between −51 and −24 deg for the 0.065 speed ratio, and between 12 and 27 deg for the 0.800 speed ratio. Thus, the incidence angle varies by 27 and 14 deg for the 0.065 and 0.800 speed ratios, respectively. The total plane average incidence angles of all pump–stator relative positions are −36.5 deg for the 0.065 speed ratio and −29.2 deg for the 0.800 speed ratios. A stronger influence of the stator on the pump inlet is seen for the 0.065 than for the 0.800 speed ratio.

Pump Inlet Plane—Turbine Influence. The pump inlet plane was also studied for a turbine influence. The throughflow velocity in the pump inlet was compared for different pump–turbine relative positions at one fixed pump–stator relative position. Results showed an influence of the turbine on the throughflow velocities of less than 0.004. Hence, the turbine effects do not propagate far enough upstream (or downstream) to be observed in the pump inlet.

Pump Midplane. The pump midplane was analyzed for a stator and a turbine influence. To examine the stator influence, the pump midplane throughflow velocity was measured and compared for different pump–stator relative positions. For this test the turbine influence was eliminated by collecting data for only one fixed pump–turbine relative position. Maximum throughflow velocity fluctuations were less than 0.01. Thus, the strong velocity fluctuations observed in the pump inlet plane were damped out before the flow reached the pump midplane.

Similarly, to analyze the turbine influence, the pump midplane through flow velocities were compared for different pump–turbine relative positions. The stator influence was eliminated by collecting data for only one pump-stator relative position. Negligible fluctuations (less than 0.005) were observed. Thus, the influence of the turbine and stator on the pump midplane flow field can be considered negligible; the flow field is steady.

Pump Exit Plane—Turbine Influence. The torque converter turbine is located directly downstream of the pump exit plane and is rotating at a lower angular speed than the pump. Consequently, the turbine has an upstream influence on the pump exit flow field. To visualize this influence, the pump exit plane velocities were organized into groups for six pump–turbine relative positions. Thus, for each pump–turbine relative position a resolution of nine core-to-shell side and six pressure-to-suction side positions were obtained. Results for both speed ratios are presented in Figs. 9–13.

Figure 9 shows the throughflow blade-to-blade profiles at the 50 percent core-to-shell side position in the pump exit plane for the 0.800 speed ratio. Three relative angular position combinations between the pump and the turbine are presented: 0, 33, and 67 percent. An average blade-to-blade profile is also included. The profiles are highly nonuniform with peak veloci-

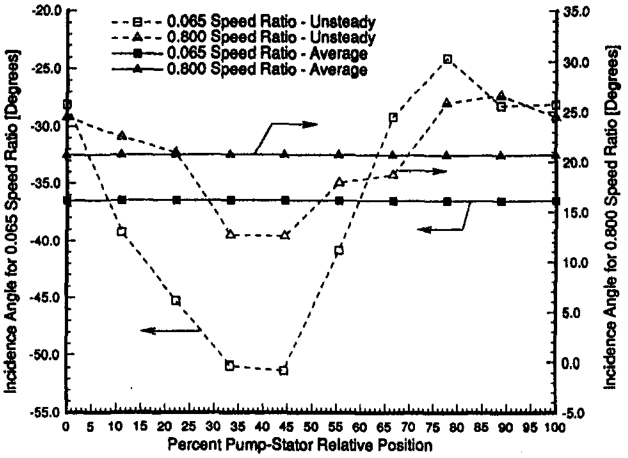

Fig. 8 Plane-average pump incidence flow angle for 0.065 and 0.800 speed ratios

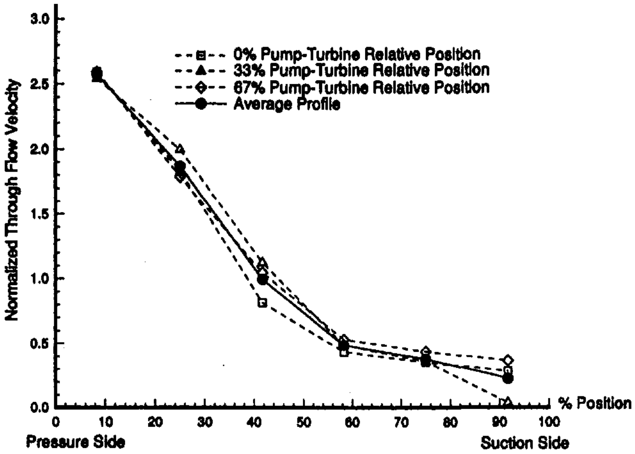

Fig. 9 Pump exit blade-to-blade velocity profiles for the 0.800 speed ratio at the 50 percent core to shell side location; 0, 33, and 67 percent pump–turbine relative positions are shown

ties at the pressure side and minimum velocities at the suction side. Throughflow velocity fluctuations of 0.4 and 0.05 can be seen at the suction and pressure sides, respectively.

Figures 10(*a*)–10(*c*) are vector plots of the 0.800 speed ratio pump exit flow field for three representative relative angular position combinations between the pump and the turbine: 0, 33, and 67 percent. A low-velocity wake region can be observed at the core and suction sides. Velocity fluctuations are higher at the shell side than at the core side. The overall pump exit flow field shows less unsteadiness than the pump inlet flow field. This can be explained by the fact that the influence of the turbine on the pump exit is a flow disturbance that travels upstream against the flow direction, while the stator influence on the pump inlet is a disturbance that is carried downstream with the flow. The upstream traveling disturbance has to overcome a longer relative distance in the fluid than the downstream traveling disturbance and thus experiences more dissipation.

Similar results were obtained for the 0.065 speed ratio in the pump exit plane. Figure 11 shows the throughflow blade-to-blade profiles at the 50 percent core to shell side for the 0.065 speed ratio and three pump–turbine relative positions. Highest throughflow velocities can be observed at the pressure side and lowest velocities are at the suction side. Typical velocity fluctuations are 0.2.

In Fig. 12 the throughflow velocity at the geometric center location of the pump exit plane is shown as a function of the pump–turbine relative position. This plot demonstrates the influence the turbine has on the throughflow velocity at one location in the pump exit. The throughflow velocity fluctuates by 0.3 for the 0.065 speed ratio and by 0.4 for the 0.800 speed ratio. Thus, the influence of the turbine on the pump exit flow field is seen to be higher for the 0.800 speed ratio than for the 0.065 speed ratio.

An important performance parameter for pumps is the slip factor. The slip factor, μ, is calculated from

$$\mu = \frac{c_\theta}{c'_\theta}$$

where c_θ is the measured absolute tangential velocity component in the pump exit, and c'_θ is the ideal tangential velocity calculated from velocity polygons. Figure 13 shows pump exit slip factors as a function of the pump-turbine relative position for both speed ratios. One complete blade passages cycle is presented. The average slip factors of all pump–turbine relative positions combined are also included. Slip factors fluctuate between 0.961 and 0.969 for the 0.065 speed ratio, and between 0.967 and 0.972 for the 0.800 speed ratio. Thus, the exit slip factor is relatively steady for both speed ratios.

Pump Exit Plane—Stator Influence. The pump exit was tested for a stator influence. The influence of the stator on the pump exit through flow velocities was measured and compared for different pump–stator relative positions. Less than 0.004 unsteadiness was observed. Thus, the pump exit flow field is not affected by the stator.

Summary and Conclusions

The unsteady velocity field found in the pump of a torque converter was measured for the 0.065 and 0.800 turbine/pump rotational speed ratios. Velocities in three planes in the torque converter pump were studied: inlet, mid-, and exit planes. Analysis of the flow field indicates the following:

1 Significantly more unsteadiness is seen in the pump inlet than in the pump exit. The unsteadiness in the pump inlet is a

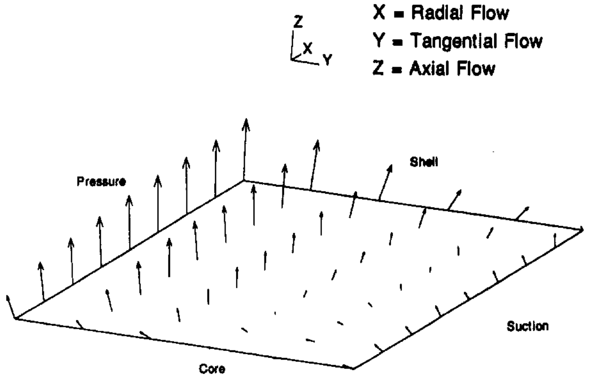

Fig. 10(*a*) Pump exit velocity field for 0 percent pump–turbine relative position at the 0.800 speed ratio

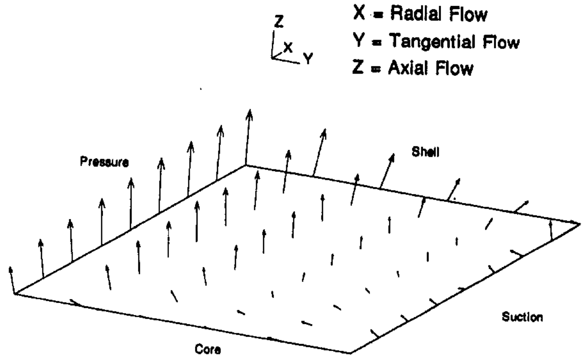

Fig. 10(*b*) Pump exit velocity field for 33 percent pump–turbine relative position at the 0.800 speed ratio

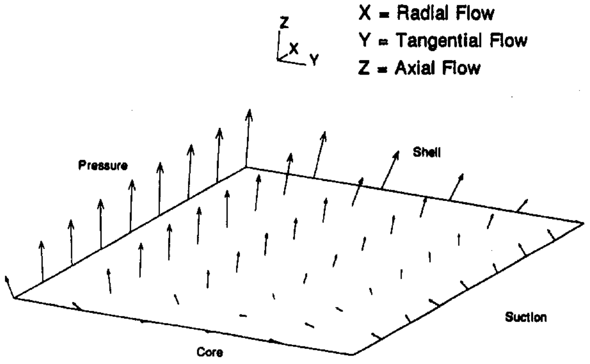

Fig. 10(*c*) Pump exit velocity field for 67 percent pump–turbine relative position at the 0.800 speed ratio downstream effect of the stator blades, while the unsteadiness seen in the pump exit is generated by the turbine blades. Peak normalized throughflow velocity fluctuations in the pump inlet are 1.2 for the 0.065 speed ratio and 0.8 for the 0.800 speed ratio, while peak fluctuations in the pump exit are 0.4 and 0.3 for the 0.065 and 0.800 speed ratio, respectively.

2 The flow disturbances from the stator–pump interaction are damped out by the time they reach the pump midplane and the pump–turbine interaction unsteadiness does not propagate as far upstream as the pump midplane. Pump–stator and pump–turbine interactions account for maximum fluctuations of 0.01 and 0.005 in the pump midplane, respectively. Hence, the pump midplane flow field is relatively steady.

3 The flow field in the pump inlet plane is not dependent on the turbine position. An influence of less than 0.004 was measured.

4 Most unsteadiness in the pump inlet plane is observed at the shell side, and almost no unsteadiness is seen at the core. This corresponds to observations of a very nonuniform flow region at the shell side of the stator exit, and a low-velocity wake region at the core side.

5 More unsteadiness is seen in the pump inlet for the 0.065 than for the 0.800 speed ratio. Typical fluctuations are 0.7 and 0.5 for the 0.065 and 0.800 speed ratio, respectively.

6 The average pump incidence flow angle varies by 27 deg for the 0.065 speed ratio and by 14 deg for the 0.800 speed ratio. These are significant variations considering the blades are designed for a steady value.

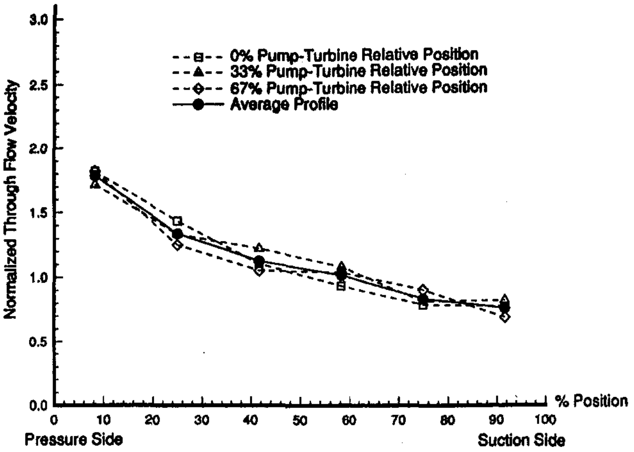

Fig. 11 Pump exit blade-to-blade profiles for the 0.065 speed ratio at the 50 percent core-to-shell side location; 0, 33, and 67 percent pump-turbine relative positions are shown

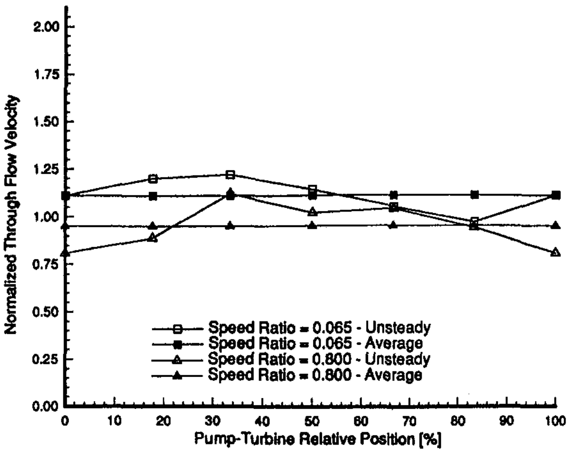

Fig. 12 Dependence of throughflow velocity at pump exit center location on pump–turbine relative position for 0.065 and 0.800 speed ratios

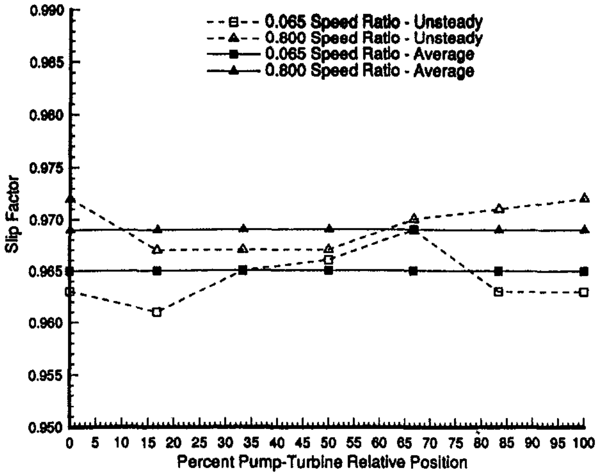

Fig. 13 Pump exit slip factors for 0.065 and 0.800 speed ratios

7 The flow field in the pump exit plane is strongly dependent on the relative angular position between the pump and the turbine. Typical velocity fluctuations are 0.2 for the 0.065 speed ratio and 0.3 for the 0.800 speed ratio.

8 The flow field in the pump exit is not dependent on the stator position. An influence of less than 0.004 was observed.

9 The turbine influence on the pump exit is stronger for the 0.800 speed ratio than for the 0.065 speed ratio. Peak velocity fluctuations are 0.3 and 0.4 for the 0.065 and 0.800 speed ratios, respectively.

10 Average pump exit slip factors are 0.965 and 0.969 for the 0.065 and 0.800 speed ratios, respectively. The slip factor fluctuates by 0.008 for the 0.065 speed ratio and by 0.005 for the 0.800 speed ratio. Thus, the slip factor is relatively steady.

Acknowledgments

This research was sponsored in part by General Motors Corporation NAO Engineering Center in Warren, MI, the GM Powertrain Division in Ypsilante, MI, and Rotating Machinery and Controls (ROMAC) Industrial Research Program at the University of Virginia. The authors wish to express their gratitude to Robert By and Don Maddock for their support and involvement.

References

Bahr, H. M., Flack, R. D., By, R. R., and Zhang, J. J., 1990, "Laser Velocimeter Measurements in the Stator of a Torque Converter," SAE Paper No. 901769, *SAE 1990 Transactions, Journal of Passenger Cars,* Vol. 99, Section 6, pp. 1625–1634.

Beaudoin, R. J., Miner, S. M., and Flack, R. D., 1992, "Laser Velocimeter Measurements in a Centrifugal Pump with an Orbiting Impeller," ASME JOURNAL OF TURBOMACHINERY, Vol. 114, pp. 340–358.

Brun, K., and Flack, R. D., 1993, "Transient Velocity Measurements in a Turbomachine With Independently Rotating Components," *Fifth International Conference on Laser Anemometry,* SPIE Conference Proceedings, Vol. 2052, pp. 419–426.

By, R. R., and Lakshminarayana, B., 1991, "Static Pressure Measurements in a Torque Converter Stator," SAE Paper No. 911934, *SAE 1992 Transactions, Journal of Passenger Cars.*

By, R. R., and Lakshminarayana, B., 1993, "Measurement and Analysis of the Static Pressure Field in a Torque Converter Pump," *2nd ASME Pumping Machinery Symposium,* ASME FED-Vol. 154, pp. 253–264, to be published in ASME *Journal of Fluids Engineering.*

By, R. R., Kunz, R. F., and Lakshminarayana, B., 1993, "Navier–Stokes Analysis of the Pump Flow Field of an Automotive Torque Converter," *2nd ASME Pumping Machinery Symposium,* ASME FED-Vol. 154, pp. 264–274, to be published in ASME *Journal of Fluids Engineering.*

Eckardt, D., 1979, "Flow Field Analysis of Radial and Backswept Centrifugal Compressor Impellers, Part 1: Flow Measurements Using a Laser Velocimeter," *Performance Prediction of Centrifugal Pumps and Compressors,* ASME, New York, pp. 77–86.

Gruver, J. K., 1992, "Laser Velocimetry Measurements in the Pump of an Automotive Torque Converter," Master's Thesis, University of Virginia, Aug.

Gruver, J. K., Flack, R. D., and Brun, K., 1996, "Laser Velocimeter Measurements in the Pump of a Torque Converter: Part I—Average Measurements," ASME JOURNAL OF TURBOMACHINERY, Vol. 118, this issue, pp. 562–569.

Hamkins, C. P., and Flack, R. D., 1987, "Laser Velocimeter Measurements in Shrouded and Unshrouded Radial Flow Pump Impellers," ASME JOURNAL OF TURBOMACHINERY, Vol. 109, pp. 70–78.

Kannemans, H., 1980, "Radial Pump Impeller Measurements Using a Laser Doppler Velocimeter," ASME Paper No. 80-GT-94.

Krain, H., 1981, "A Study on Centrifugal Impeller and Diffuser Flow," ASME *Journal of Engineering for Power,* Vol. 103, pp. 688–697.

Powell, J. A., Strazisar, A. J., and Seasholtz, R. G., 1981, "Efficient Laser Anemometer for Intra-rotor Flow Mapping in Turbo Machinery," ASME JOURNAL OF TURBOMACHINERY, Vol. 103, pp. 424–429.

Sideris, M. T., and Van den Braembussche, R. A., 1987, "Influence of a Circumferential Exit Pressure Distortion on the Flow in an Impeller Diffuser," ASME JOURNAL OF TURBOMACHINERY, Vol. 109, pp. 48–54.

Strazisar, A. J., 1985, "Investigation of Flow Phenomena in a Transonic Fan Rotor Using Laser Velocimetry," ASME *Journal of Engineering for Power,* Vol. 107, pp. 427–435.

Suder, K. L., Hathaway, M. D., Okiishi, T. H., Strazisar, A. J., and Adamczyk, J., 1987, "Measurement of the Unsteady Flow Field Within the Stator Row of a Transonic Axial-Flow Fan," ASME Paper No. 87-GT-226.

Calculation of Three-Dimensional Viscous Flow in Hydrodynamic Torque Converters

H. Schulz

R. Greim

W. Volgmann

Lehrstuhl für Fluidenergiemaschinen,
Ruhr-Universität Bochum,
Bochum, Federal Republic of Germany

A numerical method for calculating three-dimensional, steady or unsteady, incompressible, viscous flow is described. The conservation equations for mass and momentum and the equations of the $k-\epsilon$ turbulence model are solved with a finite volume method on nonorthogonal boundary-fitted grids. The method employs cell-centered variable arrangement and Cartesian velocity components. The SIMPLE algorithm is used to calculate the pressure and to enforce mass conservation. The computer code is vectorizable as far as possible to achieve an optimal performance on modern vector computers. Results of steady flow calculations in the guide vane, the pump rotor, and the turbine rotor and of the unsteady interaction simulation of the pump and the turbine of a one-stage one-phase non-automotive hydrodynamic torque converter are presented.

Introduction

Methods usually applied for the design of hydrodynamic torque converters are based on onedimensional streamline theory. Flow losses are calculated employing empirical setups obtained from the data of previously built torque converters. Thus, one is able to predict the overall performance of geometrically similar torque converters. If the geometry is varied to a greater extent, these methods fail to make a sufficiently accurate prediction about the torque converter performance. For the further improvement of hydrodynamic torque converters, knowledge about the internal flow field is needed. Modern measuring techniques as well as complex numerical methods can be used to obtain internal flow data. In recent years, researchers have begun to apply numerical methods to hydrodynamic torque converters. However, in spite of permanent improvement of the computational techniques and the increasing performance of modern supercomputers, at present an exact flow calculation within a complete torque converter is not possible as the flow is very complex. The flow is three dimensional, unsteady, viscous, and turbulent. It may be two phase due to partial filling and cavitation.

Ziegs (1987) and Thiele (1990) developed a finite volume code with an explicit time marching procedure based on solution methods published by Hirt et al. (1974, 1975). They calculated the three-dimensional turbulent flow in the stator and the pump of a torque converter that has been experimentally investigated by Adrian (1985). Fujitani et al. (1988) solved the Navier–Stokes equations for the pump, turbine, and stator of an automotive torque converter. They coupled the three elements so that they could evaluate the torque converter performance without any empirical parameters or measured data. Abe et al. (1991) also performed Navier–Stokes calculations in an automotive torque converter and found strong secondary flow in each element. They also applied a coupling algorithm. By et al. (1993) modified a Navier–Stokes code (Kwak et al., 1986) for torque converter flow field computations and applied it to the pump of an automotive torque converter. They found that the total pressure loss strongly depends on the inlet velocity profile and that the pump rotation has a major effect on the secondary flow field.

This paper presents flow computations with a new Navier–Stokes code that is based on a finite volume algorithm published by Perić (1985). The algorithm is programed in a way that allows optimal vectorization. Furthermore, periodic boundary conditions, system rotation, coupling algorithms, and unsteady flow simulation are implemented. Results of steady flow calculations in the guide vane, the pump rotor, and the turbine rotor of a hydrodynamic torque converter are given. Furthermore, results of the unsteady pump/turbine interaction are presented.

Governing Equations

The unsteady, three-dimensional, incompressible, viscous flow is governed by the transport equations for mass and momentum. In general this set of equations cannot be solved analytically. For a numerical solution Reynolds averaging and an eddy viscosity model is adopted. The calculations presented in this paper were carried out using the standard $k-\epsilon$ turbulence model to determine the eddy viscosity ν_t. Thus, the complete set of equations to be solved in a rotating frame of reference may be written as follows:

Conservation of mass:

$$\frac{\partial w_j}{\partial x_j} = 0 \qquad (1)$$

Conservation of momentum:

$$\frac{Dw_i}{Dt} = -\frac{1}{\rho}\frac{\partial p}{\partial x_i} + \frac{\partial}{\partial x_j}\left(\nu_{\text{eff}}\left(\frac{\partial w_i}{\partial x_j} + \frac{\partial w_j}{\partial x_i}\right)\right) - 2\epsilon_{ijk}\omega_j w_k + (\delta_{jl}\delta_{km} - \delta_{jm}\delta_{kl})\omega_j\omega_m x_k \qquad (2)$$

Transport equation for turbulent kinetic energy:

$$\frac{Dk}{Dt} = \frac{\partial w_i}{\partial x_j}\nu_t\left(\frac{\partial w_i}{\partial x_j} + \frac{\partial w_j}{\partial x_i}\right) + \frac{1}{\sigma_k}\frac{\partial}{\partial x_j}\left(\nu_t\frac{\partial k}{\partial x_j}\right) - \epsilon \qquad (3)$$

Transport equation for turbulent dissipation:

Contributed by the International Gas Turbine Institute and presented at the 39th International Gas Turbine and Aeroengine Congress and Exposition, The Hague, The Netherlands, June 13–16, 1994. Manuscript received by the International Gas Turbine Institute February 18, 1994. Paper No. 94-GT-208. Associate Technical Editor: E. M. Greitzer.

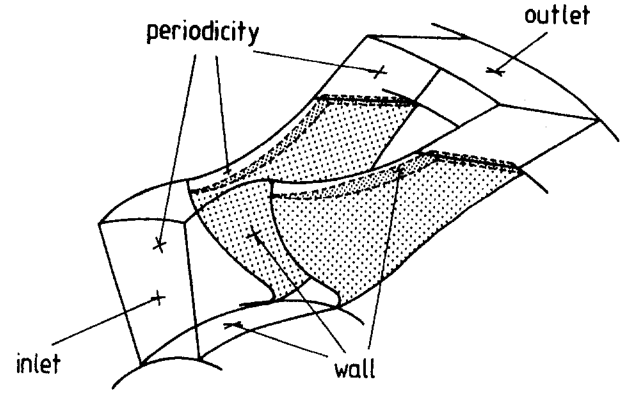

Fig. 1 Boundary conditions

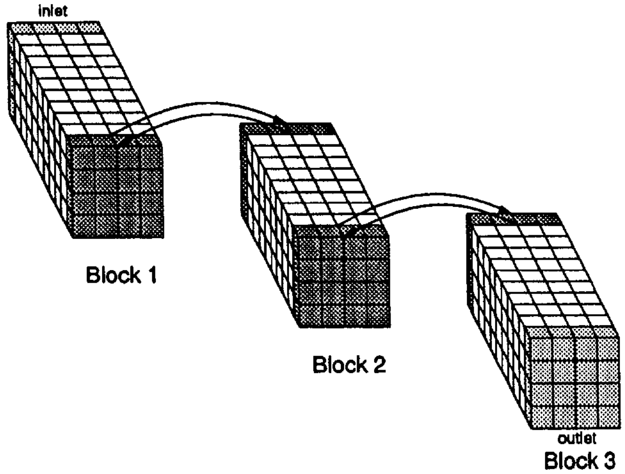

Fig. 2 Coupling of three domains

$$\frac{D\epsilon}{Dt} = \frac{\partial w_i}{\partial x_j}\nu_t\left(\frac{\partial w_i}{\partial x_j}+\frac{\partial w_j}{\partial x_i}\right)c_{1\epsilon}\frac{\epsilon}{k} + \frac{1}{\sigma_\epsilon}\frac{\partial}{\partial x_j}\left(\nu_t\frac{\partial \epsilon}{\partial x_j}\right) - c_{2\epsilon}\frac{\epsilon^2}{k} \qquad (4)$$

Kolmogorov–Prandtl relation:

$$\nu_t = c_\mu \frac{k^2}{\epsilon} \qquad (5)$$

D/Dt represents the substantial derivative, which consists of a local part $\partial/\partial t$ and a convective part. For steady calculations, the time derivation $\partial/\partial t$ is neglected. $\nu_{\text{eff}} = \nu + \nu_t$ represents the effective kinematic viscosity. Calculating turbomachinery flow, a coordinate system rotating with speed ω_3 about the x_3 axis is considered; ω_1 and ω_2 are set to zero.

Numerical Calculation Procedure

Basic Algorithm. A finite volume method was chosen as solution algorithm. For the most part the discretization and the solution procedure published by Perić (1985) were adopted. Since hydrodynamic torque converters have a very complex geometry, nonorthogonal curvilinear boundary-conforming coordinates are used. The solution domain is divided into a network of arbitrarily shaped, hexahedral finite volumes. The method employs a collocated variable arrangement where the Cartesian velocity components, the static pressure, and the turbulence quantities are assigned to the center of the control volume. The differential equations are integrated over each control volume. Approximation of the integrals by sums and linearization yields a set of algebraic equations. The equation system (6) with a seven-diagonal coefficient matrix $[A]$ can be solved efficiently with Stone's strongly implicit procedure (Stone, 1968):

$$[A]\cdot\{\Phi\} = \{S\} \qquad (6)$$

Φ may be replaced by any of the unknown variables. The convective fluxes are discretized using a blend of central and first-order upwind differences. The cross-diffusion fluxes, centrifugal, and Coriolis forces are treated explicitly and added to the source $\{S\}$. For unsteady flow calculations the time derivation is discretized second-order fully implicit:

$$\left.\frac{\partial \Phi}{\partial t}\right|_{n+1} = \frac{1}{2\Delta t}\left(3\Phi^{n+1} - 4\Phi^{n} + \Phi^{n-1}\right) \qquad (7)$$

Due to the nonlinearity and coupling of the differential equations the algebraic equation systems for velocity components and turbulent quantities are solved alternately and the coefficients of $[A]$ are updated consecutively. In general, the calculated velocity field will not satisfy the continuity equation. In order to enforce mass conservation, after each iteration step for the velocity components, the SIMPLE algorithm (Patankar and Spalding, 1972) is used to match pressure and velocities. Pressure and cell-face velocities are linked by a pressure correction equation derived from the momentum and continuity equations. The collocated variable arrangement requires a special interpolation technique for the evaluation of the cell-face velocities

Nomenclature

c = absolute velocity
c_μ = constant of the $k-\epsilon$ model
$c_{1\epsilon}$ = constant of the $k-\epsilon$ model
$c_{2\epsilon}$ = constant of the $k-\epsilon$ model
d = diameter
k = turbulent kinetic energy
n = speed of rotation
p = static pressure
p_t = total pressure
t = time
T = period
T = torque
$\bar{u}$ = velocity component parallel to the wall
u_τ = shear stress velocity
w = relative velocity
w_i = Cartesian velocity component
x_i = Cartesian coordinate
z = blade number
δ_{ij} = Kronecker delta
ϵ = dissipation rate of turbulent kinetic energy
ϵ_{ijk} = permutation tensor
η = efficiency
λ = nondimensional pump power
μ = torque ratio
ν = kinematic viscosity
ν = speed ratio
ν_t = eddy viscosity
ρ = fluid density
σ_k = constant of the $k-\epsilon$ model
σ_ϵ = constant of the $k-\epsilon$ model
τ_w = wall shear stress
Φ = scalar quantity
ω = total pressure loss
ω_i = angular velocity

Subscripts

c = cell
m = meridional component
P = pump
r = radial component
S = stator
T = turbine
u = circumferential component

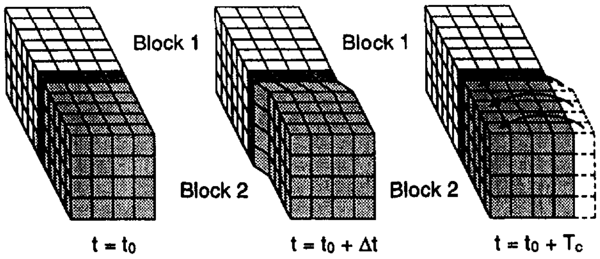

Fig. 3 Coupling with relative movement

from the cell centered values to avoid a checkerboard splitting of the pressure field (Rhie and Chow, 1983).

Boundary Conditions. Various boundary conditions have to be imposed for turbomachinery flow calculations (Fig. 1).

At the inlet measured or estimated values of the velocities and turbulence quantities must be prescribed (Dirichlet boundary condition). The inlet velocity profiles for the calculations in this paper were obtained from experimental data. Since no experimental data were available for the turbulent quantities, the turbulent kinetic energy was set to 0.5 percent of the kinetic energy of the mean flow and the turbulent dissipation was calculated to

$$\epsilon = \frac{k^{3/2}}{l} \tag{8}$$

with a turbulent length scale

$$l = \min(2.5 \cdot y, 0.1 \cdot d_h) \tag{9}$$

where y is the wall distance and d_h is the hydraulic diameter (Perić, 1991). At the outlet the Dirichlet or Neumann gradient condition can be used. On solid surfaces the velocities are set to the wall velocities. Near the wall the turbulence quantities are computed from the universal law of the wall. Newton's shear stress formula with linear approximation of the velocity gradient

$$\tau_w = \rho \cdot \nu_{\text{eff}} \cdot \frac{\bar{u}}{y} \tag{10}$$

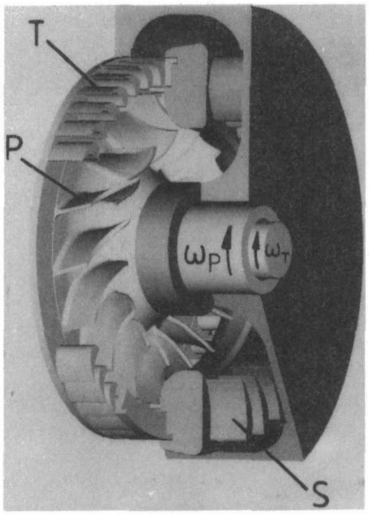

Fig. 4 Hydrodynamic torque converter

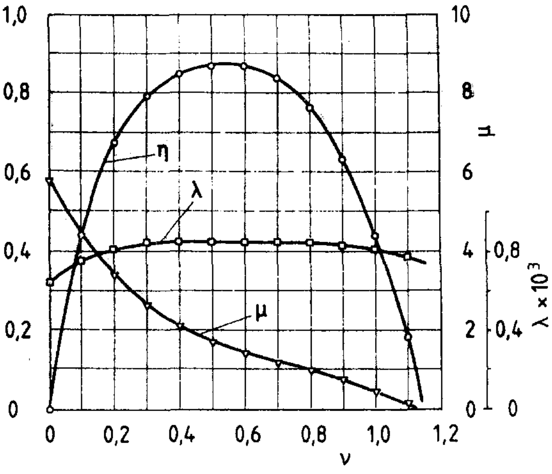

Fig. 5 Nondimensional characteristics

gives

$$\nu_{\text{eff}} = \left(\frac{\overline{\text{Re}}}{\bar{U}}\right)^2 \cdot \frac{\nu}{\overline{\text{Re}}} \tag{11}$$

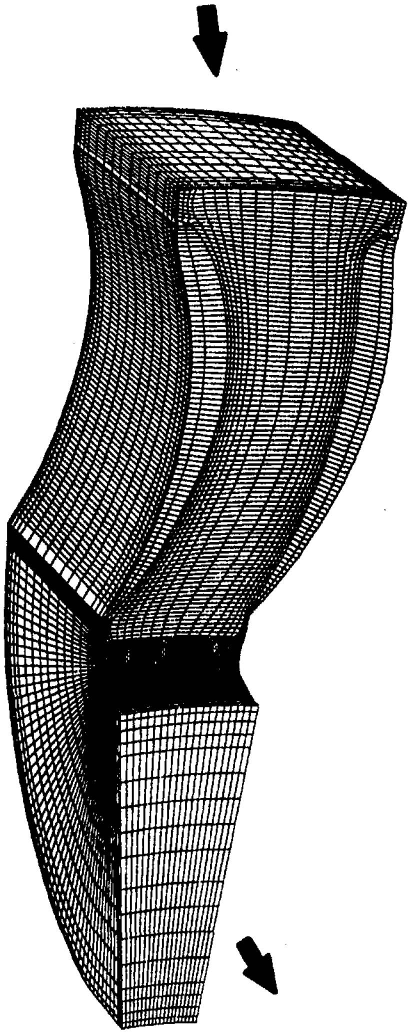

Fig. 6 Stator grid

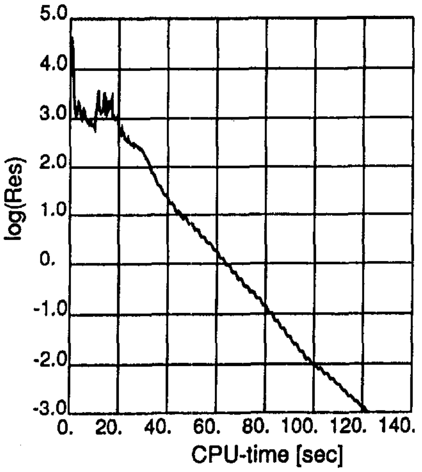

Fig. 7 Convergence history

where

$$\bar{\mathrm{Re}} = \frac{\bar{u}\cdot y}{\nu},\ \bar{U} = \frac{\bar{u}}{u_\tau},\ u_\tau = \sqrt{\frac{\tau_w}{\rho}}.$$

Boundary values for k and ϵ are calculated from

$$k = k^+\cdot\left(\frac{\bar{\mathrm{Re}}}{\bar{U}}\right)^2\cdot\frac{\nu^2}{y^2} \tag{12}$$

$$\epsilon = \epsilon^+\cdot\left(\frac{\bar{\mathrm{Re}}}{\bar{U}}\right)^4\cdot\frac{\nu^3}{y^4} \tag{13}$$

The unknown variables are $\bar{U}$, k^+, and ϵ^+. Nikuradse's (1932) measurements of $\bar{U}$ in the log law region and the buffer layer and Reichardt's (1940) measurements in the viscous sublayer in hydraulic smooth pipes yield the universal law of the velocity distribution (Schlichting, 1965). Modeling of the data yields:

$$\bar{U}^2 = \begin{cases} \bar{\mathrm{Re}} & (14a) \\ [9.63\cdot\arctan\,(0.03293\cdot\bar{\mathrm{Re}}^{0.75}) + 1.85]^2 & (14b) \\ [2.19\cdot\ln\,(\bar{\mathrm{Re}}) + 0.7]^2 & (14c) \end{cases}$$

where (14a) is valid for $0 \le \bar{\mathrm{Re}} \le 65.7891$, (14$b$) for $65.7891 < \bar{\mathrm{Re}} \le 429.3607$, and (14$c$) for $429.3607 < \bar{\mathrm{Re}}$. Now ν_{eff} can be calculated from Eq. (11). The nondimensional wall distance can be calculated to:

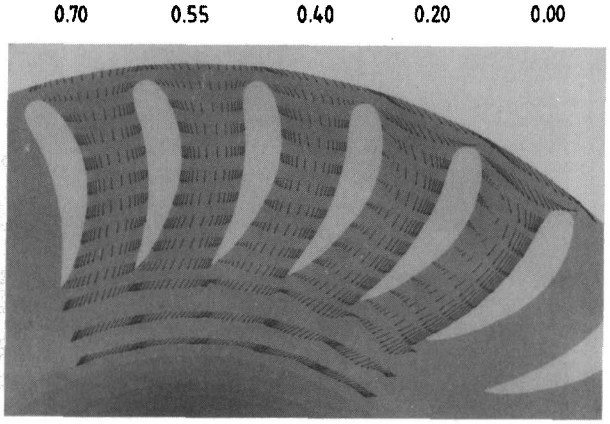

Fig. 8 Velocity profiles

$$y^+ = \frac{\bar{\mathrm{Re}}}{\bar{U}} \tag{15}$$

Scheuerer (1983) collected measured data (Coles, 1978; El Telbany and Reynolds, 1981) of the turbulent normal stresses in channel flows and presented a distribution of the nondimensional turbulent kinetic energy k^+ in the region of the universal velocity distribution law. Modeling of the data yields:

$$k^+ = \begin{cases} 0.05{y^+}^2 \\ 2.83\,|y^+ - 7.85|^{0.35} - 1.29\,|y^+ - 6.30|^{0.56} + 3.335 \\ 5.20\,\arctan\,(y^+) + 1.10[0.0001123{y^+}^{2.75}]^{-1} - 4.72 \end{cases} \tag{16}$$

Scheuerer (1983) collected measured data (Laufer, 1954) of the nondimensional turbulent dissipation in the region of the universal velocity distribution law. Modeling of the data yields:

$$\epsilon^+ = \begin{cases} 0.10[1 + 0.025{y^+}^2 - 0.015\exp(0.88(y^+ - 4))] \\ 2.4576{y^+}^{-1} - 0.8[0.001 + |y^+ - 3.33|^{1.3}]^{-1} + 0.011 \\ 2.4576{y^+}^{-1} \end{cases} \tag{17}$$

Now k^+ and ϵ^+ for the viscous sublayer, the buffer layer or the

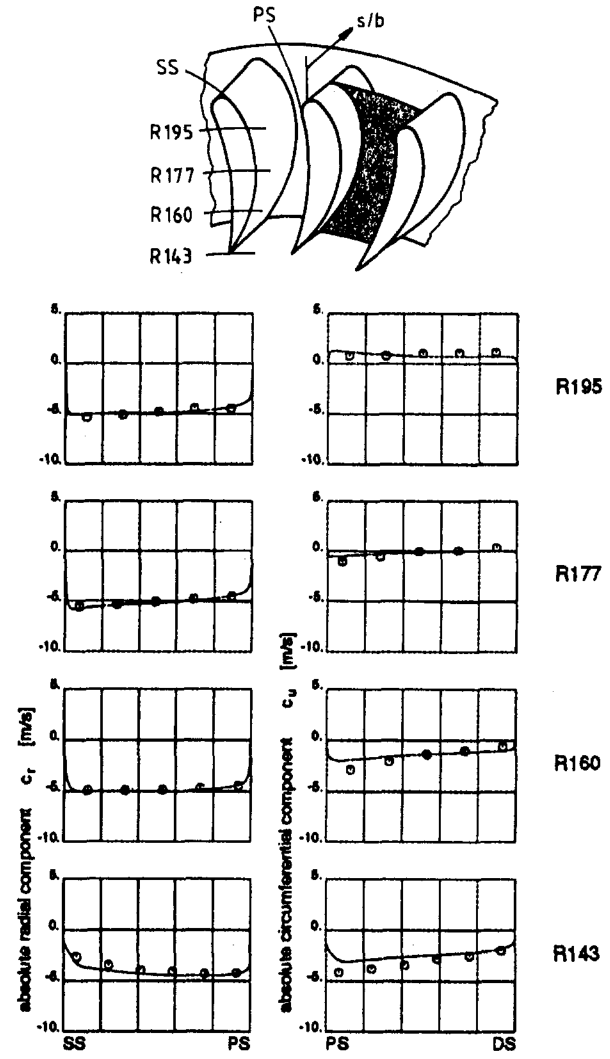

Fig. 9 Velocity comparison: ○ measurement, — calculation

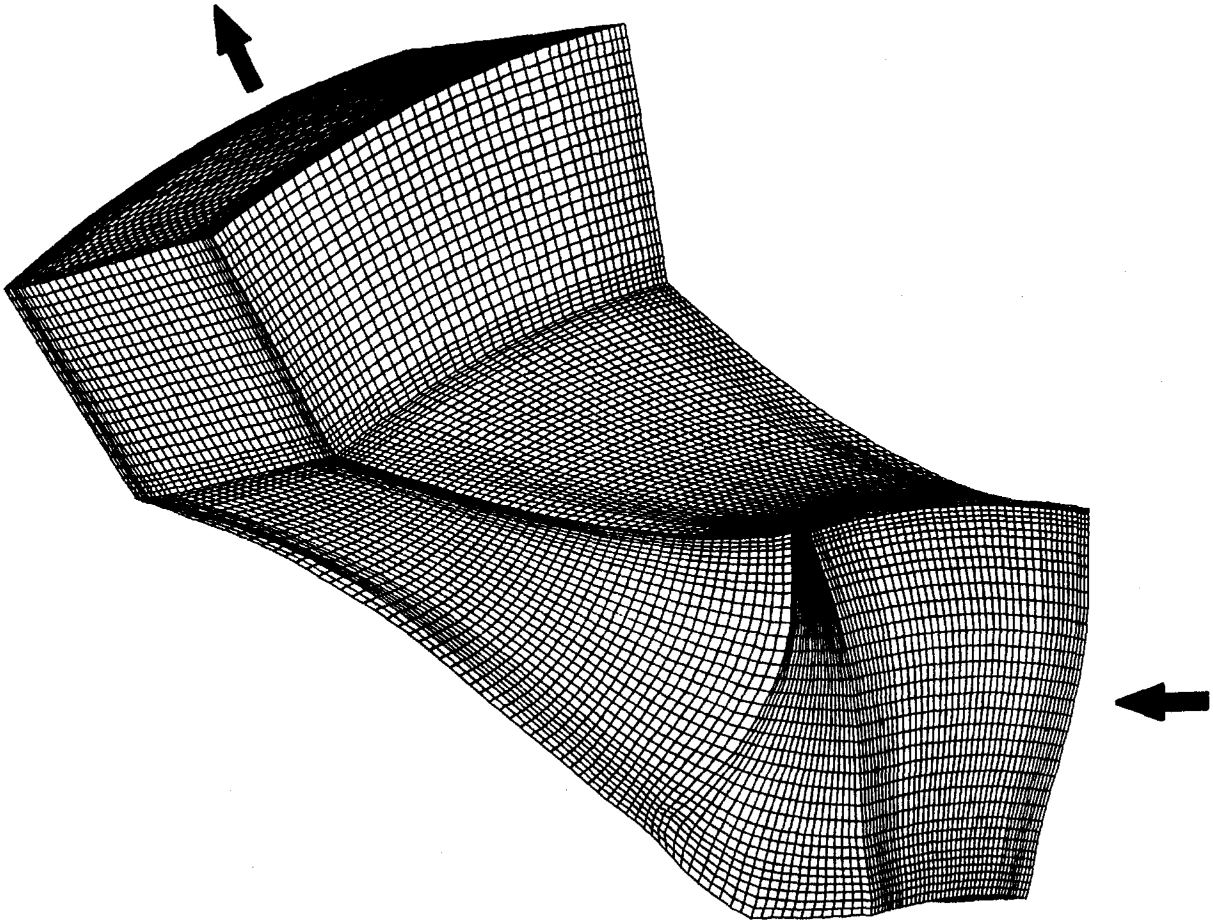

Fig. 10 Pump grid

log law region can be calculated from Eq. (16) and Eq. (17) and k and ϵ from Eqs. (12) and (13).

The pressure on boundary nodes is extrapolated from the interior. Thus, no extra boundary values for the pressure are needed, but global mass conservation must be ensured. If the flow is periodic in the circumferential direction, the computational domain is reduced to a few blade channels and periodic boundary conditions are enforced upstream and downstream of the blade rows and in the clearance between the blades and the casing. This is realized by rotating the velocity vetors from one periodic boundary node to the opposite. Since the SIP solver is limited to seven diagonal matrices, the periodic boundary conditions are treated explicitly. For unsteady calculations initial conditions must be prescribed, which can be obtained from measurements or steady calculations, for example.

Solution Algorithm. The equation systems (6) are solved alternately. While one SIP iteration sweep is sufficient for velocities and turbulence quantities, a few have to be carried out for the pressure corrections to achieve convergence. Underrelaxation of the changes in Φ is necessary in order to enhance the stability of the solution procedure. The sum of the absolute residuals, which are defined as the difference of the left-hand and right-hand sides of Eq. (6), are normalized by the appro-

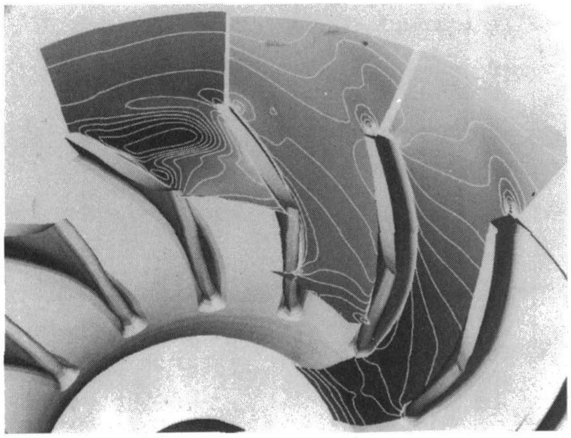

Fig. 11 Pump rotor velocity distribution

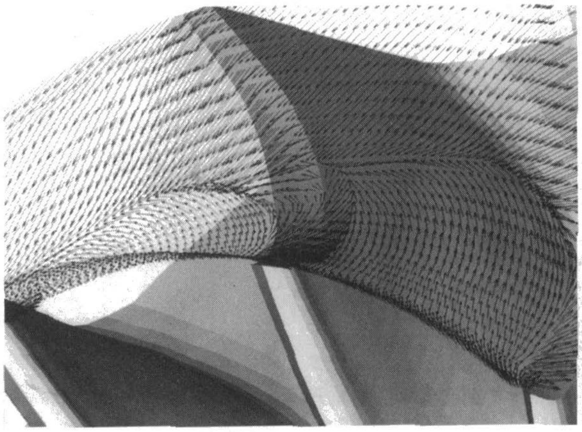

Fig. 12 Velocity vectors near the shroud

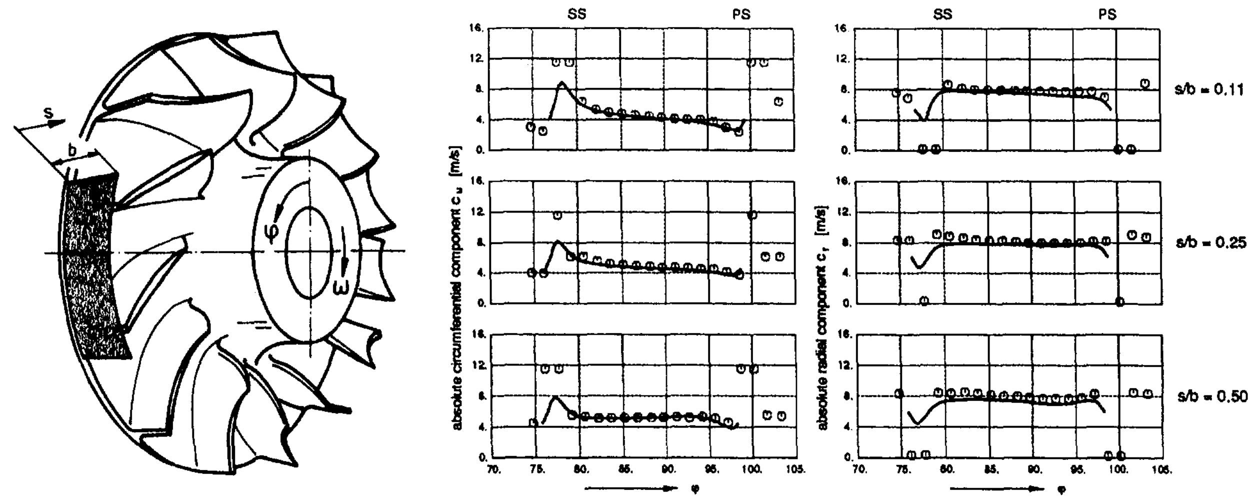

Fig. 13 Velocity comparison: ○ measurement, — calculation

priate inlet fluxes. The calculation is declared converged when all normalized residual sums fall below a prescribed value, typically 10^{-3}.

The FORTRAN computer code is vectorizable to a major extend. Onedimensional arrays are used to avoid nested do-loops. In the main calculation loops flow control statements (e.g., IF statement) are replaced by arithmetic operations. A new version of the SIP solver is implemented. It is programmed as described by Leister and Perić (1994). This implementation allows vector processing in spite of the recursive structure of the SIP. The speed up was factor 15 in some test cases. The required computing time for flow calculations in curved ducts is as low as reported by Majumdar et al. (1992), who used a similar algorithm. The calculations were carried out on the high-performance vector computer Fujitsu S600/20 of the RWTH Aachen, which has 5 GFlops peak performance.

Coupling Algorithms. Since the elements of torque converters are close to one another, interaction effects have to be taken into account. If the flow is calculated in single elements, the boundary values have to supply the information on the upstream and downstream elements. If no measured boundary values are available, several computational domains with different angular velocities have to be coupled. Figure 2 shows schematically the coupling of three domains. The blocks may symbolize pump, turbine, and stator, for example. Two neighboring blocks overlap with one cell size. The flow in each block is calculated with the basic algorithm as described before enforcing Dirichlet boundary conditions at the intersection boundaries. There, the coupling of the blocks is achieved by interchanging data of the neighboring blocks, considering the respective frame of reference. For example, the three-dimensional flow profiles at the inlet of block 2 are calculated from the flow data of block 1 as follows:

$$w_{1,\mathrm{block2}} = w_{1,\mathrm{block1}} + x_2 \cdot (\omega_{3,\mathrm{block2}} - \omega_{3,\mathrm{block1}})$$

$$w_{2,\mathrm{block2}} = w_{2,\mathrm{block1}} - x_1 \cdot (\omega_{3,\mathrm{block2}} - \omega_{3,\mathrm{block1}})$$

$$w_{3,\mathrm{block2}} = w_{3,\mathrm{block1}}$$

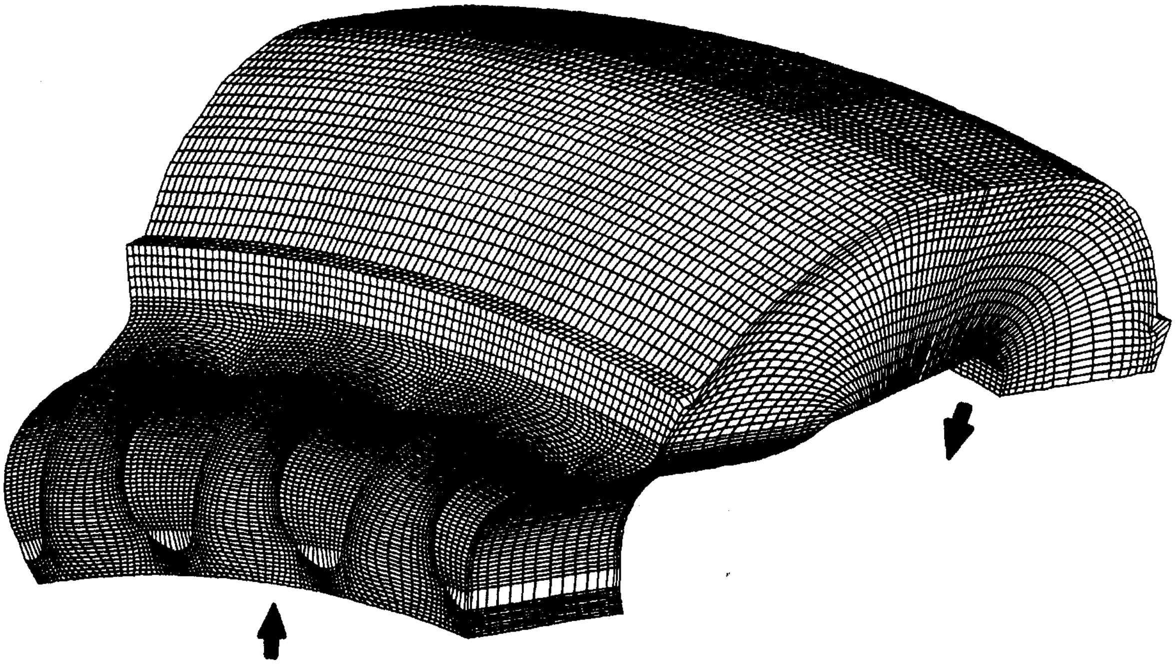

Fig. 14 Turbine and deflection channel grid

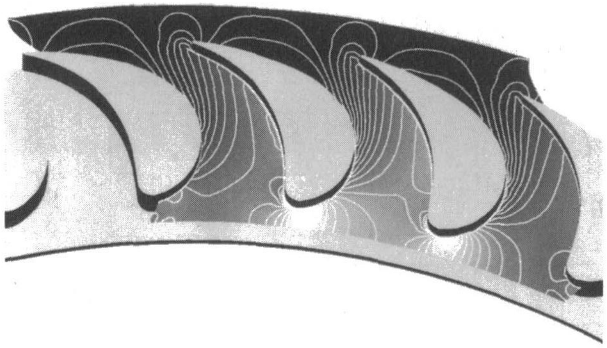

Fig. 15 Static pressure contours

$$k_{\text{block2}} = k_{\text{block1}}$$

$$\epsilon_{\text{block2}} = \epsilon_{\text{block1}} \qquad (18)$$

The velocity data may be scaled to keep the mass flow constant. Because of the limited capacity of the available computers, it is not possible to store all blocks that are necessary for a flow calculation in a torque converter in the main memory. The blocks are loaded into the main memory alternately. After a certain number of iterations the block is changed and the boundary data are transmitted to the neighboring blocks. For calculations in hydrodynamic circuits, like torque converters, the first and the last block are coupled, too.

This algorithm is suitable for steady flow calculations. Since unsteady flow calculations are inherently very time consuming, they cannot be carried out with a permanent change of the main memory content. Therefore, unsteady flow calculations are limited to two blocks, which can be held in the main memory. Furthermore, the computational time is reduced, solving the equations for the complete solution domain and not for single blocks alternately. In addition to steady calculations, the respective relative movement of the blade rows and the numerical grids has to be simulated. The relative movement of the grids leads to a distortion of the cells at the intersection. The shearing of the cells is kept low by periodic transposition (Fig. 3).

Both the coupling algorithms have been tested with an explicit time marching procedure (Greim and Volgmann, 1992; Schulz and Volgmann, 1992). These works have been terminated because of the slow convergence of the explicit procedure.

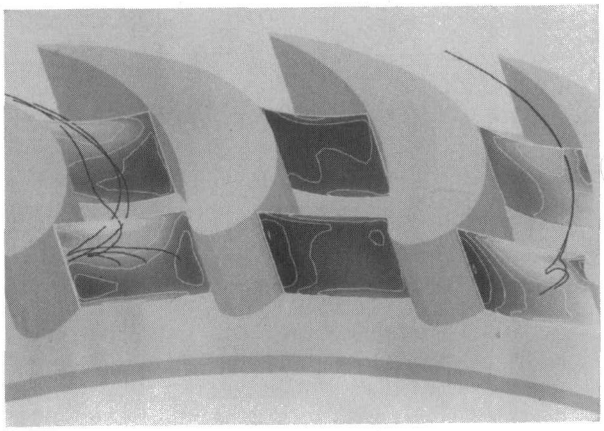

Fig. 16 Total pressure loss, particle paths

Numerical Grids. Structured H-grids are used. They are generated with elliptical (Thompson et al., 1977) and algebraic grid generators.

Computational Results

In this section the results of flow calculations in a one-stage one-phase torque converter are presented. Figure 4 shows a model of the investigated machine. This research torque converter can be equipped with a pump impeller P with a diameter of $d_P = 340$ mm and a pump blade number $z_P = 13$ or $z_P = 16$, a turbine impeller T with a diameter $d_T = 416$ mm and a turbine blade number $z_T = 32$ or $z_T = 40$ and a stator S with a diameter $d_S = 424$ mm and a stator blade number $z_S = 32$. The operating fluid is water.

Adrian (1985) experimentally investigated this torque converter with 13 pump blades and 40 turbine blades at a constant pump speed $n_P = 750$ min^{-1} so that flow data are available that

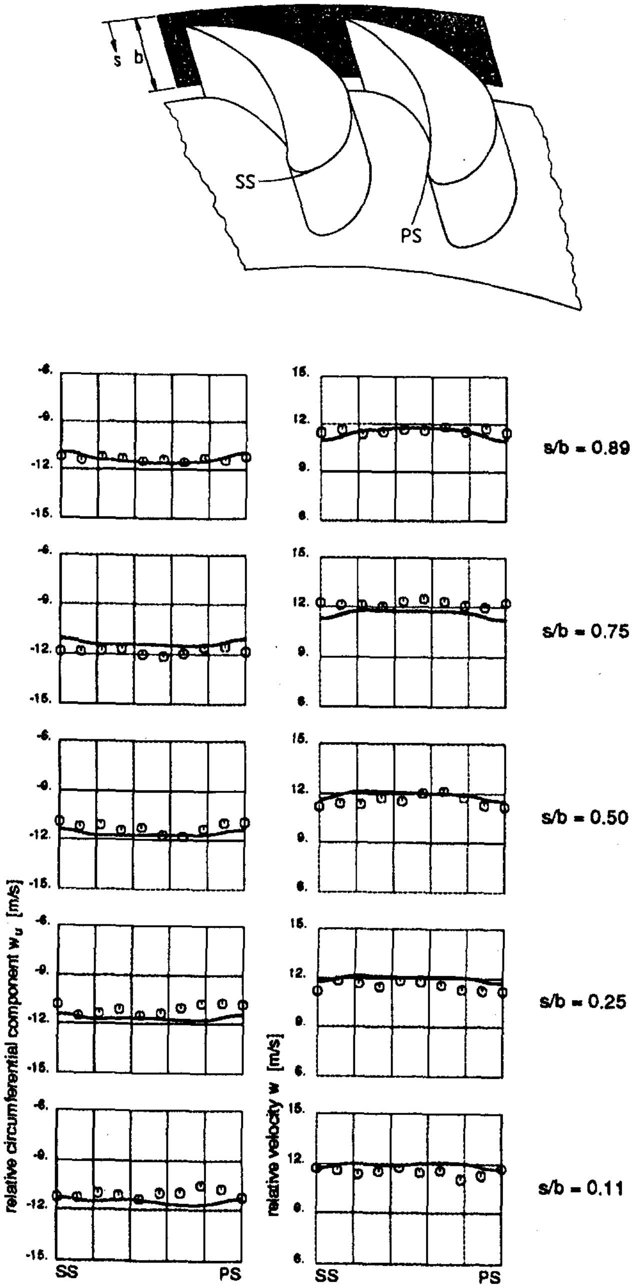

Fig. 17 Velocity comparison: ○ measurement, — calculation

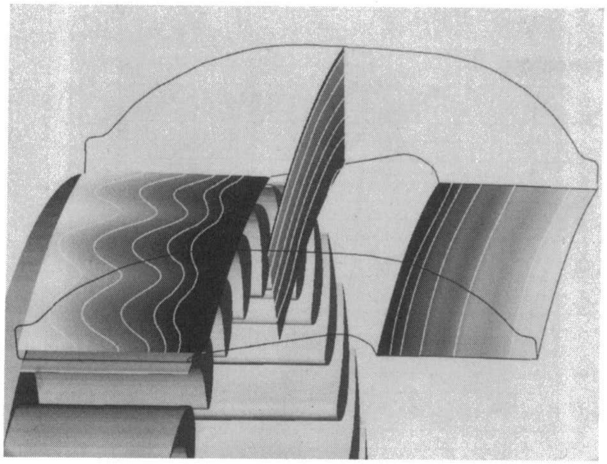

Fig. 18 Static pressure contours

can be set as boundary values and used to verify the calculated data. The Reynolds number is $\mathrm{Re}_u = d_P^2 \pi n_p / \nu = 3.8 \times 10^6$. The measured nondimensional characteristics are given in Fig. 5. The torque ratio $\mu = T_T/T_P$, the efficiency $\eta = (n_T T_T)/(n_P T_P)$, and the nondimensional pump power $\lambda = T_P/(\rho \omega_P^2 d_P^5)$ are plotted as a function of the speed ratio $\nu = n_T/n_P$.

Stator—Steady Single Block Calculation. The guide vane flow in the research torque converter with $z_P = 13$, $z_T = 40$, and $n_P = 750$ min^{-1} was calculated for five different operating points, which are characterized by the speed ratio ν. For $\nu = 0.55$ the torque converter operates at its design condition.

Grid. The solution domain was discretized with 149 grid points in the mean flow direction, 18 grid points in spanwise direction and 21 grid points in the circumferential direction (Fig. 6). It consists of one stator blade channel and the following 90 deg deflection channel. The latter was discretized to ensure that the outlet boundary condition does not affect the stator flow.

Boundary Conditions. As inlet boundary condition a flow field interpolated from measured data (Adrian, 1985) was prescribed. Turbulent inlet quantities were estimated as described before. At the outlet Neumann boundary conditions were used. As the inlet flow is periodic relative to one stator pitch, one stator blade channel was calculated using periodic boundary conditions.

Results. For $\nu = 0.55$ e.g. about 2 minutes CPU time on a Fujitsu S600/20 and 350 iterations were required to reduce the maximum residual below 10^{-3} (Fig. 7).

Figure 8 shows velocity profiles in a midspan plane for the five operating points $\nu = 0.70, 0.55, 0.40, 0.20, 0.00$. Due to the changing speed of the turbine, the incidence angle at the stator, which is defined as the difference between the inlet flow angle and the physical blade inlet angle, changes from negative values for $\nu = 0.70$ to positive values for $\nu \leq 0.40$. At design condition $\nu = 0.55$ the incidence angle is close to zero. It can be seen that the differences in the flow direction of the inlet flow are nearly equalized within half the length of the duct, which is important to ensure similar pump inlet flow conditions. The different inlet velocity profiles effect increasing velocity values from suction side to pressure side for $\nu \leq 0.40$ and from pressure side to suction side for $\nu = 0.70$ in the second half of the duct. For $\nu = 0.00$ and $\nu = 0.20$ flow separation at the

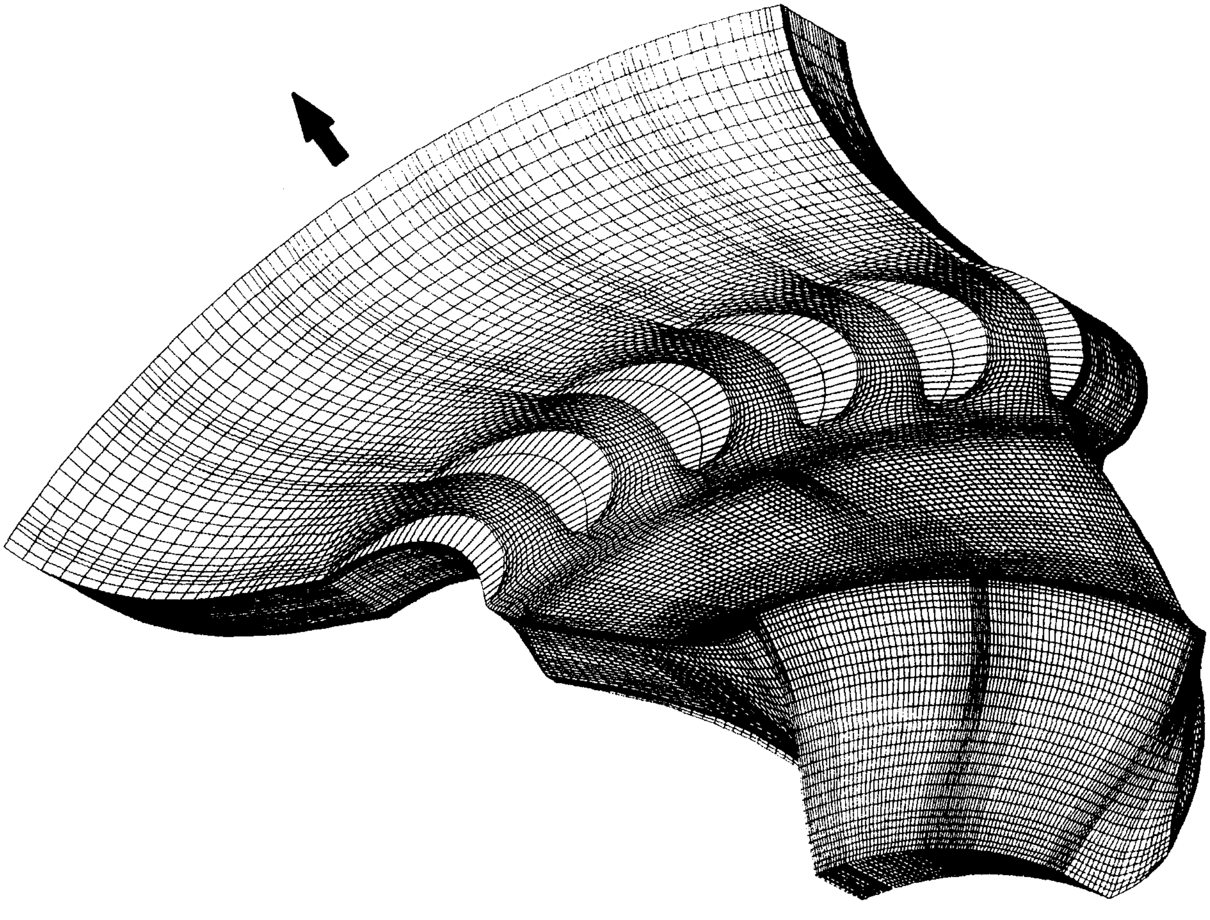

Fig. 19 Pump and turbine grid

suction side was detected. These results are confirmed by measurement (Adrian, 1985) and calculation (Ziegs, 1987).

Calculated and measured data have been compared for $\nu = 0.40$, 0.55, and 0.70 at different locations inside the blade channel. Figure 9 shows, e.g., the distribution of the radial and circumferential velocity component in the guide vane at design condition in a midspan plane. Radial components are well predicted. Deviations appear for circumferential components, but the tendencies are captured.

Pump Rotor—Steady Single Block Calculation. For a first numerical investigation of the pump rotor flow the influence of the turbine was neglected. The problem was reduced to the calculation of one single pump blade channel removing the turbine rotor from the circuit. Thus, a configuration was examined with $z_P = 16$, $z_S = 32$, and $n_P = 750\ \text{min}^{-1}$.

Grid. The solution domain was discretized with 96 grid points in the mean flow direction, 36 grid points in the spanwise direction, and 43 grid points in the circumferential direction (Fig. 10). The tip clearance was discretized with two cells in the spanwise direction.

Boundary Conditions. As inlet boundary condition a flow field interpolated from measured data (Thiele, 1990) was prescribed. Turbulent inlet quantities were estimated as described before. At the outlet Neumann boundary conditions were used. As the blade numbers ensure a periodic pump flow, only one pump blade channel was calculated using periodic boundary conditions. For the calculation in the rotating relative system, the velocities at the core wall surface were set to negative circumferential velocity.

Results. The calculation of the pump flow required about 8 minutes CPU time and 460 iterations.

Figure 11 shows the calculated relative velocity distribution for three different channel heights. The relative flow is accelerated from inlet to outlet. One can see clearly the rotor wakes at the trailing edge of the blades. Furthermore, there is a jet-wake area near the shroud.

The tip clearance flow was also computed. Figure 12 shows the relative velocity field in a plane near the shroud and through the tip gap (only every second vector is drawn). Except at the inlet the flow is directed from the pressure side to the suction side. There is a large reverse flow area at the far region of the blade channel. No distinct vortices due to the tip clearance flow have been found in planes from hub to shroud. These results are confirmed by Thiele's (1990) calculations.

Calculated and measured velocity components of the absolute velocity are compared in a plane 4 mm behind the blades (Fig. 13). Measurement and calculation show a slight decrease of the radial and circumferential components from the suction side SS to the pressure side PS with good agreement. The wake effects are better predicted by Thiele (1990). In the region near the core the highly turbulent flow prevented laser-2-focus measurements.

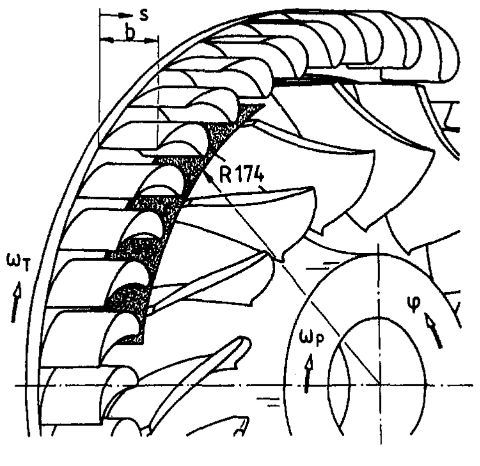

Fig. 20 Measurement plane

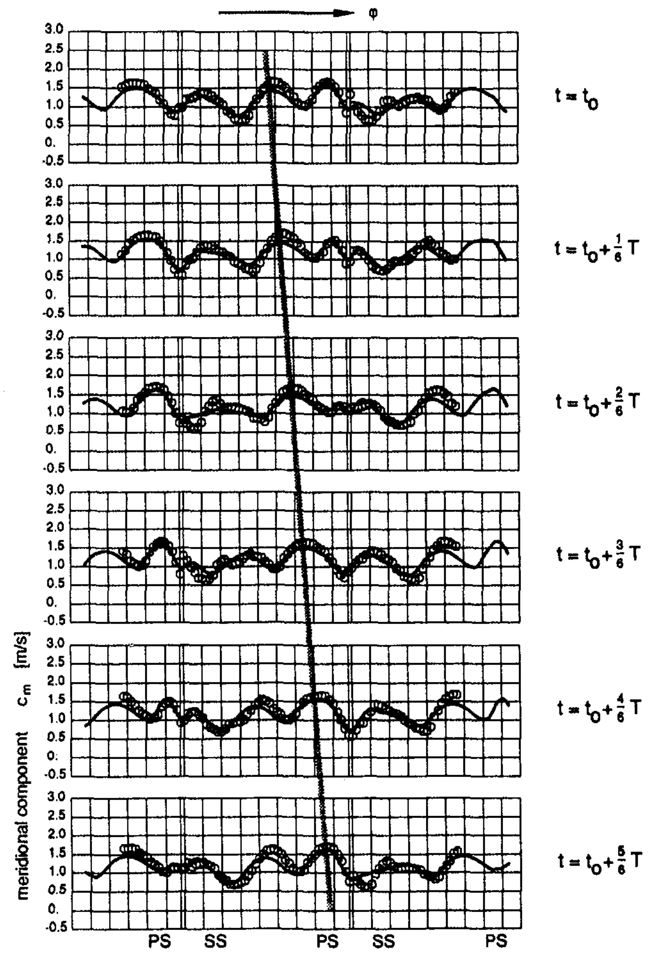

Fig. 21 Velocity comparison: ○ measurement, — calculation

Turbine Rotor—Steady Coupled Calculation. For the investigation of the turbine rotor flow a configuration with $z_P = 13$, $z_T = 40$, and $n_P = 750\ \text{min}^{-1}$ was examined. The speed ratio ν was 0.4. This corresponds to a turbine speed $n_T = 300\ \text{min}^{-1}$.

Grid. The 180 deg deflection channel has an influence on the turbine flow. Therefore, a coupled calculation with two blocks was performed. The first block contains three turbine blade channels; the second block consists of the deflection channel. Each block was discretized with 76 grid points in the mean flow direction, 18 grid points in the spanwise direction, and 85 grid points in the circumferential direction (Fig. 14).

Boundary Conditions. As inlet boundary condition, a flow field interpolated from measured data (Adrian, 1985) was prescribed. At periodic boundaries the inlet velocity profile was set periodic. Due to the blade numbers, the measured profile was approximately periodic over three turbine pitches. Turbulent inlet quantities were estimated as described before. At the outlet of the deflection channel Neumann boundary conditions were used. At the intersection boundaries flow data were interchanged as described before. The blades inside the solution domain were treated as obstacles with wall boundary conditions.

Results. Figure 15 shows static pressure contours in a mid-height plane, which are representative for the whole duct. The stagnation point is shifted toward the suction side due to a negative incidence angle. At the outer profiles the stagnation point is not very distinct. This is a result of the pump rotor wakes. The turbine reduces the static pressure by 100,000 Pa, approximately.

Plots of the total pressure loss are given in Fig. 16 for six different planes. The total pressure loss is defined by:

$$\omega = \frac{p_{t,in} - p_t}{\frac{\rho}{2} \cdot w_{in}^2} \tag{19}$$

where $p_{t,in}$ is the average total pressure at the inlet and w_{in} is the average relative velocity at the inlet. Bright colors represent a high total pressure loss. The middle channel shows a smooth distribution while there are greater differences in the outer channels. This is also a result of the flow differences at the inlet of the blade channels. High pressure losses indicate flow phenomena like vortices for example. The influence of the secondary

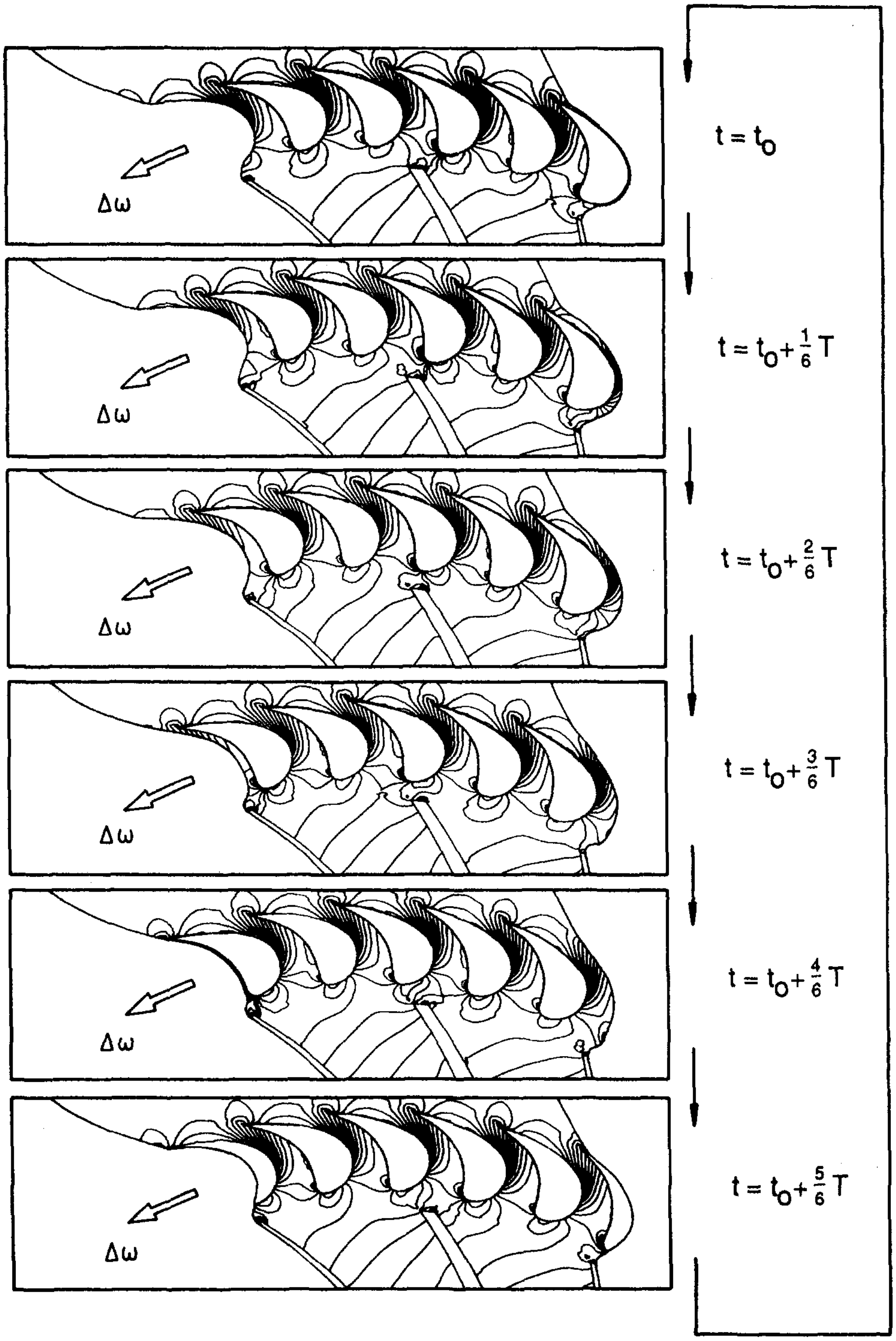

Fig. 22 Static pressure contours

flow is shown by particle paths through areas of high pressure loss. The particles spiral around the core of a vortex. In the far region the influence of the mean flow is dominant.

In Fig. 17 measured and calculated velocities in a plane 9 mm behind the turbine outlet are compared for different relative channel heights s/b from core to shell. The measured data represent an average of all pitches since the laser-2-focus anemometer was triggered over one turbine pitch. Thus, for a comparison the calculated values were averaged over the three pitches. The calculated velocities reach the level of the measured values. The turbine rotor wake is nearly mixed out at this location.

Figure 18 shows static pressure contours in the deflection channel that follows the turbine. In the plane behind the turbine rotor blades, the influence of the rotor wakes can be seen. At the outlet of the deflection channel, the flow is periodic in circumferential direction. Hence, there is no unsteady interaction between turbine and stator provided that the upstream influence of the stator is small.

Pump/Turbine Interaction—Steady and Unsteady Coupling. A configuration with $z_P = 16$, $z_T = 40$, $z_S = 32$, $n_P = 200 \text{ min}^{-1}$, and $\nu = 0.55$ was considered.

Grid. Due to the blade numbers, the flow is periodic over two pump pitches and five turbine pitches. The pump block and the turbine block were discretized with 31 grid points in the spanwise direction, 91 grid points in the circumferential direction, and 72 and 61 grid points in the mean flow direction, respectively (Fig. 19). The pump tip clearance was discretized with two cells in the spanwise direction.

Boundary Conditions. Since no measured data were available in the pump inlet plane for $n_P = 200 \text{ min}^{-1}$, a steady three-dimensional velocity profile obtained from Navier–Stokes calculations was prescribed. For this purpose a steady coupled calculation of stator and pump was performed. For that calculation the inlet boundary condition was derived scaling a velocity profile for $\nu = 0.55$ and $n_P = 750 \text{ min}^{-1}$ with the measured mass flow rate (Browarzik, 1994) for $n_P = 200 \text{ min}^{-1}$. Several steady coupled calculations for the pump and the turbine showed that the circumferential position of the stator wake does not affect the interaction of pump and turbine. Therefore, at the pump inlet a steady velocity profile was used as boundary condition. At the turbine outlet the solution domain was artificially extended to apply the Neumann boundary condition. For the calculation in the rotating relative system of the pump, the velocities at the core wall surface were set to negative circumferential velocity. The blades inside the solution domain were treated as obstacles with wall boundary conditions. At the intersection boundaries flow data were interchanged as described before. As initial condition a calculated steady flow field was prescribed. The time step was 9×10^{-4} s.

Results. The steady calculation of the initial flow field required 29 CPU minutes and 1100 iterations. The unsteady calculation required 150 CPU minutes and about 60 iterations per time step to reach a periodic unsteady solution. Three periods were required to establish a solution that was periodic in time. One period T is the time one pump blade needs to pass one turbine pitch.

For the investigated configuration and operation point measured unsteady flow data on a radial plane R = 174 mm (Fig. 20) are available (Browarzik, 1994). Exemplarily, in Fig. 21 the meridional velocity components in the midspan line $s/b = 0.5$ are shown for six different times of a period T. Relative to the pump, the turbine moves in the φ direction, which is defined in Fig. 20. In Fig. 21 the relative movement of one turbine pitch is illustrated by the oblique line. Altogether, six moving turbine pitches can be registered. Furthermore, there are two fixed wakes of the pump blades noticeable. If a turbine pitch crosses a pump wake, the wake is neutralized. These phenomena occur both in the measurement and the calculation. Good agreement of calculated and measured data appear for all lines of constant s/b. For $s/b < 0.6$ the velocity distribution is similar to Fig. 21; for $s/b > 0.7$ the distinct pump wake area near the shroud causes a drop in the meridional velocity distribution.

Fig. 23 Deviation steady/unsteady flow

Figure 22 shows contours of the static pressure in the interaction region of the midspan plane for the same chronological order as in Fig. 21. The turbine rotates relative to the pump with the relative speed $\Delta\omega = \omega_T - \omega_P$. The isobars are rather smooth and continuous across the block boundary used in the calculation. Slight discontinuities mark areas of strongly distorted cells but do not affect the solution essentially. One can clearly distinguish pressure and suction sides of the pump and the turbine blades as well as the wakes of the pump blades and the stagnation points of the turbine profiles. As an effect of interaction the turbine stagnation point is shifted toward the suction side when a pump blade passes by, but this does not lead to flow separation.

For a relative position of pump and turbine at $t = t_0 + \frac{5}{6}\mathrm{T}$ the unsteady flow field is compared with the steady solution. Figure 23 shows the percent deviation of the meridional velocity component. The highest differences of steady and unsteady results occur in areas of blade wakes and stagnation points. The deviation is up to 30 percent in the interaction region of a pump blade wake with a turbine stagnation point. The interaction affects the flow field both upstream and downstream. In the pump region and behind the turbine unsteady effects are small, so that steady calculations are sufficient, but in the interaction region and in the first half of the turbine blade channel the unsteady effects have to be taken into account for a correct description of the flow.

Conclusion

A finite volume method was presented for calculating three-dimensional, incompressible turbulent flow. Steady test calculations in the guide vane, pump rotor, and turbine rotor and a calculation of the unsteady pump/turbine interaction of a hydrodynamic torque converter have proved that the method is an efficient tool for the investigation of turbomachinery flow. However, the capturing of viscous effects and the turbulence modeling have to be improved.

The calculations show uniform flow conditions at the stator outlet for a wide operating range. The unsteady interaction of the stator with the pump or turbine is neglibile. In the interaction region between pump and turbine unsteady effects are in order of magnitude 30 percent in a midspan plane.

In the future it is planned to calculate the steady flow in a torque converter coupling pump, turbine, and stator. For the calculation of an entire hydrodynamic circuit, no measured data are needed as boundary conditions, as proved by Fujitani et al. (1988).

The investigations concerning the unsteady interaction of the pump and the turbine rotor are continued. These works are connected with an experimental project on nonsteady flow measurements inside hydrodynamic torque converters (Browarzik, 1994).

Acknowledgments

The work described in this paper is a part of the special research program SFB 278 "Hydrodynamic Power Transmission" at the Ruhr-Universität Bochum and is sponsored by the Deutsche Forschungsgemeinschaft. The authors also would like to thank Prof. M. Perić (Universität Hamburg) for the preprint of the paper concerning the vectorizable SIP and Dr. H. Vollmers (DLR Göttingen) for the flow analysis program COMADI.

References

Abe, K., Kondoh, T., Fukumura, K., and Kojima, M., 1991, "Three-Dimensional Simulation of the Flow in a Torque Converter," SAE Paper No. 910800.

Adrian, F.-W., 1985, "Strömungsuntersuchungen und -analyse in Kreisläufen hydrodynamischer Wandler," Dissertation, Ruhr-Universität Bochum, Germany.

Browarzik, V., and Grahl, K. G., 1992, "Non-steady Flow Measurements Inside a Hydrodynamic Torque Converter by Hot-Film Anemometry," ASME Paper No. 92-GT-161.

Browarzik, V., 1994, "Experimental Investigation of Rotor/Rotor Interaction in a Hydrodynamic Torque Converter Using Hot-Film Anemometry," ASME Paper No. 94-GT-246.

By, R. R., Kunz, R. F., and Lakshminarayana, B., 1993, "Navier–Stokes Analysis of the Pump Flow Field of an Automotive Torque Converter," *Pumping Machinery,* ASME FED-Vol. 154, pp. 265–274.

Coles, D., 1978, "A Model for Flow in the Viscous Sublayer," Workshop on Coherent Structure of Turbulent Boundary Layers, Lehigh University, Bethlehem, PA.

El Telbany, M. M. M., and Reynolds, A. J., 1981, "Turbulence in Plane Channel Flows," *Journal of Fluid Mechanics,* Vol. 111, pp. 183–318.

Fujitani, K., Himeno, R., and Takagi, M., 1988, "Computational Study on Flow Through a Torque Converter," SAE Paper No. 881746.

Greim, R., and Volgmann, W., 1992, "Instationäre Berechnung der Strömung in hydrodynamischen Wandlern," Report SFB 278, Ruhr-Universität Bochum, Germany.

Greim, R., Schulz, H., Thiele, M., and Grahl, K. G., 1992, "Berechnung der dreidimensionalen reibungsbehafteten Strömung in Pumpenlaufrädern," Preprint No. B 6-08, Pump Congress Karlsruhe, Germany.

Hirt, C. W., Amsden, A. A., and Cook, J. C., 1974, "An Arbitrary Lagrangian–Eulerian Computing Method for All Flow Speeds," *Journal of Computational Physics,* Vol. 14, pp. 227–253.

Hirt, C. W., Nichols, B. D., and Romero, N. L., 1975, "SOLA—A Numerical Solution for Transient Fluid Flows," Los Alamos Scientific Laboratory, LA-5852.

Kwak, D., Chang, J. L. C., Shanks, S. P., and Chakravarthy, S., 1986, "A Three-Dimensional Incompressible Navier–Stokes Flow Solver Using Primitive Variables," *AIAA Journal,* Vol. 24, No. 3, pp. 390–396.

Laufer, J., 1954, "The Structure of Turbulence in Fully Developed Pipe Flow," NACA Rep. 1174.

Leister, H.-J., and Perić, M., 1994, "Vectorized Strongly Implicit Solving Procedure for Seven-Diagonal Coefficient Matrix," *International Journal for Numerical Methods in Heat and Fluid Flow,* Vol. 4, pp. 159–172.

Majumdar, S., Rodi, W., and Zhu, J., 1992, "Three-Dimensional Finite-Volume Method for Incompressible Flows With Complex Boundaries," *Journal of Fluids Engineering,* Vol. 114, pp. 496–503.

Nikuradse, J., 1932, "Gesetzmäßigkeit der turbulenten Strömung in glatten Rohren," *Forsch. Arb. Ing.-Wes.,* Vol. 356.

Patankar, S. V., and Spalding, D. B., 1972, "A Calculation Procedure for Heat, Mass and Momentum Transfer in Three-Dimensional Parabolic Flows," *International Journal of Heat and Mass Transfer,* Vol. 15, pp. 1778–1806.

Perić, M., 1985, "A Finite Volume Method for the Prediction of Three-Dimensional Fluid Flow in Complex Ducts," PhD Thesis, University of London.

Perić, M., 1991, "Randbedingungen und deren Implementierung in Finite-Volumen-Berechnungsverfahren," presented at NUMET 1991, Erlangen, Germany.

Reichardt, H., 1940, "Die Wärmeübertragung in turbulenten Reibungsschichten," *ZAMM,* Vol. 40, pp. 297–328.

Rhie, C. M., and Chow, W. L., 1981, "A Numerical Study of the Turbulent Flow Past an Isolated Airfoil With Trailing Edge Separation," *AIAA Journal,* Vol. 21, pp. 1525–1532.

Scheuerer, G., 1983, "Entwicklung eines Verfahrens zur Berechnung zweidimensionaler Grenzschichten an Gasturbinenschaufeln," Dissertation, Universität Karlsruhe, Germany, pp. 28–33.

Schlichting, H., 1965, *Grenzschichttheorie,* Verlag G. Braun, pp. 556–564.

Schulz, H., and Volgmann, W., 1992, "Stationäre Berechnung der räumlichen Strömung in hydrodynamischen Wandlern," Report SFB 278, Ruhr-Universität Bochum, Germany.

Stone, H. L., 1968, "Iterative Solution of Implicit Approximations of Multidimensional Partial Differential Equations," *SIAM Journal on Numerical Analysis,* Vol. 5, pp. 530–558.

Thiele, M., Ziegs, K.-U., Volgmann, W., and Grahl, K. G., 1989, "Calculation of the Three-Dimensional Flow in Hydrodynamic Torque Converters," *Notes on Numerical Fluid Mechanics,* Vieweg Verlag, Germany.

Thiele, M., 1990, "Entwicklung eines Finite-Volumen-Verfahrens zur dreidimensionalen Berechnung von inkompressiblen, reibungsbehafteten Strömungen in Laufrädern von Turbomaschinen," Dissertation, Ruhr-Universiät Bochum, Germany.

Thompson, J. F., Thames, F. C., and Mastin, C. W., 1977, "Boundary Fitted Curvilinear Coordinate Systems for Solutions of Partial Differential Equations on Fields Containing Any Number of Arbitrary Two-Dimensional Bodies," NASA CR-2729.

Ziegs, K.-U., 1987, "Berechnung dreidimensionaler, reibungsbehafteter, inkompressibler Innenströmungen am Beispiel des Leitrades eines hydrodynamischen Wandlers," Dissertation, Ruhr-Universität Bochum, Germany.

LDA Investigation of the Flow Development Through Rotating U-Ducts

S. C. Cheah

H. Iacovides

D. C. Jackson

H. Ji

B. E. Launder

Department of Mechanical Engineering,
UMIST,
Manchester, United Kingdom

This paper reports results from the use of laser-Doppler anemometry (LDA) to measure the mean and fluctuating flow field in a U-bend of strong curvature, Rc/D = 0.65, that is either stationary or rotating in orthogonal mode (the axis of rotation being parallel to the axis of curvature). The data acquisition system enables a stationary optical fiber probe to collect flow data from a rotating U-bend sweeping past it. Three cases have been examined, all concerning a flow Reynolds number of 100,000; a stationary case, a case of positive rotation (the pressure side of the duct coincides with the outer side of the U-bend) at a rotational number ($\Omega D/U_m$) *of 0.2, and a case of negative rotation at a rotational number of −0.2. Measurements have been obtained along the symmetry plane of the duct and also along a plane near the top wall. The most important influence on the development of the mean and turbulence flow fields is exerted by the streamwise pressure gradients that occur over the entry and exit regions of the U-bend. In the stationary case a three-dimensional separation bubble is formed along the inner wall at the 90 deg location and it extends to about two diameters downstream of the bend, causing the generation of high-turbulence levels. Along the outer side, opposite the separation bubble, turbulence levels are suppressed due to streamwise flow acceleration. For the rotation numbers examined, the Coriolis force also has a significant effect on the flow development. Positive rotation doubles the length of the separation bubble and generally suppresses turbulence levels. Negative rotation causes an extra separation bubble at the bend entry, raises turbulence levels within and downstream of the bend, increases velocity fluctuations in the cross-duct direction within the bend, and generates strong secondary motion after the bend exit. It is hoped that the detailed information produced in this study will assist in the development of turbulence models suitable for the numerical computation of flow and heat transfer inside blade-cooling passages.*

1 Introduction

In modern gas turbines, internal cooling plays an important role in maintaining the operating temperature of turbine blades at safe levels. Relatively cool air, extracted from the compressor stages of the engine, is circulated through internal cooling passages inside the turbine rotor blades. Flow and heat transfer inside the cooling channels of turbine rotor blades are affected by the presence of sharp U-bends, the use of heat transfer enhancing ribs, and also by Coriolis and rotational buoyancy forces generated by the rotation of the blades.

The engine designer needs to be able to develop efficient cooling systems that can produce the required cooling rates with the minimum of amount of coolant flow. In order to do so, the designer needs to have a clear understanding of the main features of the flow and thermal behavior inside the cooling passages and also access to reliable numerical procedures that can produce quantitatively accurate flow and heat transfer predictions. Progress in either of these areas depends on the availability of detailed flow and heat transfer measurements that show the effects of strong curvature, Coriolis forces, rotational buoyancy, and rib roughness on the hydrodynamic and thermal development.

The effect of Coriolis forces and curvature on the development of *two*-dimensional boundary layers has been known for many years (Bradshaw, 1973; Johnston et al., 1972), the extra strain associated with either producing an effect on the turbulent stresses at least an order of magnitude greater than the modification to the strain field itself. As remarked by Bradshaw, this feature effectively means that eddy viscosity turbulence models (in which the percentage change in stress equals that in strain) cannot capture the effects of either Coriolis force or streamline curvature adequately without introducing flow-specific modifications to the modeling.

Of course, in the practical flows of interest here, the duct is not two dimensional and the confining end walls (enforcing gradients in the third direction) induce severe secondary motions either in a straight rotating duct (e.g., Moon, 1964; Moore, 1967) or in a curved passage (Chang et al., 1983; Taylor et al., 1982). Paradoxically, this greatly increased flow complexity can sometimes simplify the task of turbulence modeling since these are effects directly on the *mean* velocity components whereas the influences discussed in the preceding paragraph act only on the turbulence. Now, the types of flow arising in blade-cooling systems entail the *combined* complexities of curved *and* rotating ducts. Moreover, space constraints dictate that the U-bend must be so tight that flow separation occurs, certainly downstream of the bend and possibly at entry also. These flows are, therefore, very much more complex than the unseparated flows in ducts with *either* curvature *or* Coriolis effects present that have been the subject of previous hydrodynamic studies.

An impression of the flow complexity can be inferred from the wall heat transfer data obtained by Guidez (1989), and more recently and extensively by Wagner et al. (1991a, b). These investigations were of major significance, since for the first time they provided heat transfer data for rotating passages that were directly of relevance to the engine designer and which

---

Contributed by the International Gas Turbine Institute and presented at the 39th International Gas Turbine and Aeroengine Congress and Exposition, The Hague, The Netherlands, June 13–16, 1994. Manuscript received by the International Gas Turbine Institute February 15, 1994. Paper No. 94-GT-226. Associate Technical Editor: E. M. Greitzer.

could also be used for judging whether the turbulence models employed in numerical computation of these flows produced realistic predictions. Nevertheless, both for design and also for turbulence modeling purposes, there remains a strong need to advance our knowledge of these flows to a more fundamental level, at which the detailed flow and thermal processes that determine the overall heat transfer behavior are clearly understood. In order to develop such a comprehensive understanding of these flows, it is essential to have detailed measurements of the mean and the fluctuating flow fields to complement and provide a basis for understanding mapped distributions of local heat transfer coefficient. These are the data the present study attempts to provide.

Here we report the results of a mapping of the mean and the fluctuating motions, using laser-Doppler anemometry (LDA), in flows through a smooth U-bend of strong curvature that rotates in an orthogonal mode. The objective is to reveal how the combination of the Coriolis force and strong curvature influence the development of the mean and of the turbulent flow field inside blade cooling passages.

2 Experimental Apparatus and Procedure

2.1 Test Facility. In order to be able to match engine levels of Reynolds and rotation numbers at large scale with a rig rotating at a sufficiently modest rate not to cause stress problems, it became clear that water was the desired working fluid. Moreover, using water removed several of the LDA problems that would have been present if air had been used.

The test rig consists essentially of a motor-driven turntable mounted in a 1.22-m-dia water tank. A U-bend of square cross section 0.05 by 0.05 m, and curvature ratio $Rc/D = 0.65$ shown in Figs. 1(*a*) and 1(*b*) is mounted on a turntable, so that the curvature axis of the duct is parallel to the axis of rotation. Most turbine coolant passages have their axis of rotation normal to their curvature axis. The present mode of rotation was, however, chosen at this initial stage of our investigation because, with this arrangement, the geometric plane of symmetry of the U-bend remains a hydrodynamic symmetry plane. Numerical computations, aiming to assess how well turbulence models reproduce the combined effects of Coriolis and strong curvature, can consequently consider only one half of this three-dimensional flow domain, thereby making it easier to produce solutions that are free of numerical error. The axial throughflow to the test rig is fed into the square duct through a passage that is built into the rotating turntable and the outflow is exhausted into the open water tank. A combination of fine wire meshes and a honeycomb section are located downstream of the flow entrance to the duct to ensure a uniform and symmetric flow into the U-bend section. Figure 1(*c*) shows velocity profiles along the horizontal and vertical duct centerlines at a distance of three diameters upstream of the bend entry, which for the stationary case demonstrate the degree of uniformity and symmetry produced by the entry arrangements. The test section is made of 0.01-m-thick perspex for optical access by LDA laser beams.

The rotor/turntable can be driven at any required speed up to 250 rpm in both directions. A feedback control circuit utilizes the input signals from a shaft rotary encoder to control precisely the rotational speed.

2.2 LDA Measurements. The LDA employed was a TSI two-channel, four-beam fiber-optic system with frequency shifting on both the blue and the green channels. A 4-watt argon-ion laser was used to power the system and two counterprocessors (TSI 1980B) were used for signal validation. Subsequent data processing was done through a Zech data acquisition card on an Opus PC.

LDA measurements were collected along two planes normal to the axis of rotation; the symmetry plane and a plane at a distance of 0.125 D away from the duct top wall. The fiber-optic probe, of focal length 135 mm, was mounted in a stationary position above the rotating turntable, as seen in Fig. 1(*b*). The laser beams entered the top wall of the duct, with the LDA measurements being taken as the rotating duct swept across the beams. Simultaneous two-component velocity measurements were taken, with a coincidence window of 20 μs, at several selected radial locations. The position of each data point in the flow was indexed by an incremental rotary encoder mounted on the rotating drive shaft. Measurements from each discrete angular location were then stored in separate data bins. The stationary probe was thus able to collect data along an entire circumferential traverse line of the rotating duct, as shown in Fig. 2. Sufficiently detailed flow mapping of the duct flow was obtained by employing a $\frac{1}{8}$-deg resolution of 2880 data bins. With artificial seeding of the flow, a total 60,000–80,000 data points was gathered in each traverse over a period of 3–4 hours. The maximum circumferential length of a single data bin, along the circumferential traverse line of the largest radius, was 0.6 mm. Within the straight sections, where the radius of the traverse lines was smaller, several adjacent bins of the data were combined to obtain the ensemble average results of a sample of up to 1000 data points for each angular position. The total circumferential length of the combined data bins did not exceed 0.8 mm. To obtain the velocity distribution along a straight traverse line across the rotating duct, three circumferential traverses were performed along three slightly different radii so as to envelope the required cross-duct plane (Fig. 2(*a*). The corresponding cross-duct distribution was subsequently obtained by interpolating the data of the enveloping circumferential traverses. Measurements within the U-bend were obtained along eleven equispaced radial traverses, as shown in Fig. 2(*b*). Bilinear interpolation was then used to construct profiles along radial lines.

Similar two-component LDA measurements of the same duct flow without rotation were also taken at various locations to provide a reference set for comparison. For all the tests, the fluid temperature was maintained at a steady level within 0.2°C by cold water injection into the flow. The flow through the duct was monitored by an orifice run preceding the U-bend. The bulk velocity U_m was measured by a U-tube waster manometer to an uncertainty of less than ±0.25 percent.

The overall estimated uncertainties for the nondimensionalized mean velocities in the streamwise and cross-duct directions U_z and U_x respectively, and of the corresponding turbulence quantities are:

Nomenclature

D = duct hydraulic diameter
Rc = radius of curvature of U-bend
Re = flow Reynolds number $\equiv U_m D/\nu$
Ro = rotation number $\equiv \Omega D/U_m$
U_m = bulk velocity
U_x = mean velocity component in the cross-duct direction
u_x = fluctuating velocity in the cross-duct direction
U_z = mean velocity component in the streamwise direction
u_z = fluctuating velocity in the streamwise direction
x = cross-duct direction
y = direction normal to duct symmetry plane
z = streamwise direction
ν = fluid kinematic viscosity
Ω = angular velocity of rotation

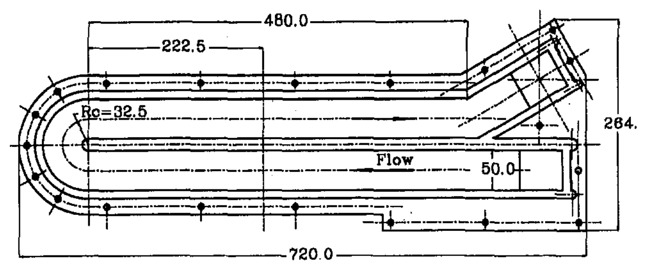

(a) Plan view

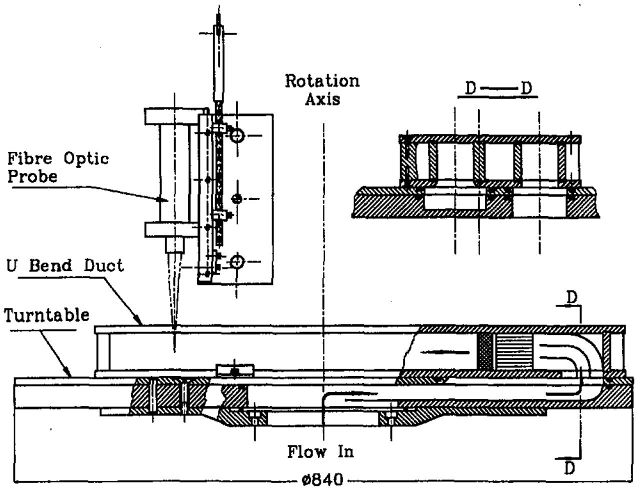

(b) Side view

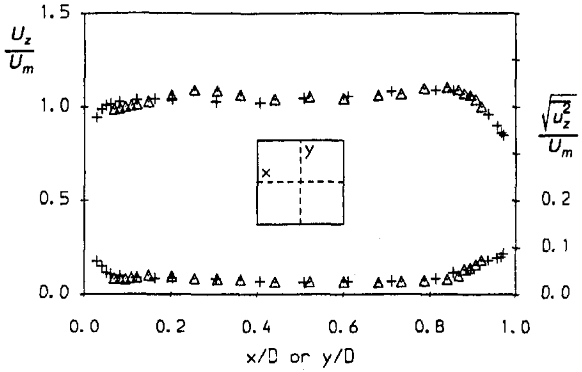

(c) Flowfield at 3 diameters upstream of the bend entry for stationary case.
△ : Vertical Traverse   + : Horizontal Traverse

Fig. 1 Experimental apparatus and entry conditions

$$U_z \le 0.02U_m \sqrt{\overline{u_z^2}} \le 0.02U_m$$

$$U_x \le 0.03U_m \overline{u_x^3} \le 0.09U_m^3$$

In arriving at these figures several effects were considered; the uncertainty of the rotor speed, phase uncertainty of the Doppler signal, uncertainty on wavelength and beam angle, velocity gradient broadening, velocity bias and flow-rate uncertainty associated with the orifice plate.

3 Presentation and Discussion of Results

Measurements have been obtained along the symmetry plane ($y/D = 0$) and along a plane near the top wall ($2y/D = 0.75$), with Y denoting the vertical distance from the duct symmetry plane. A number of cross-duct traverses have been obtained covering a region from three hydraulic diameters (D) upstream of the bend entry to $8D$ downstream of its exit. LDA traverses yielded measurements of the mean velocity components in the streamwise and cross-duct directions z and x, respectively, measurements of the two turbulence intensities along these two directions and also of the related turbulent shear stress $\overline{u_z u_x}$. The four triple correlations associated with these directions have also been obtained.

Three cases have been investigated, all at a flow Reynolds number ($\mathrm{Re} = U_m D/\nu$) of 100,000; a stationary U-bend case, a case with the U-bend rotating positively at a rotation number ($Ro = \Omega D/U_m$) of 0.2 and a case with negative rotation at $Ro = -0.2$. A positive rotation direction, as shown in Fig. 2, is defined as one in which the duct trailing (pressure) side coincides with the outer side of the U-bend. Due to space limitations only a selection of the available measurements can be included.

The mean velocity measurements are summarized in the vector plots of Fig. 3, which provide a picture of the overall flow development through the U-bend for the stationary and also for the two rotating conditions. The stationary U-bend results, Fig. 3(a), indicate that in the upstream tangent, a reasonably symmetric developing flow approaches the bend entry. At the bend entry there is a strong flow acceleration along the inner wall and flow deceleration along the outer wall, which becomes stronger near the corner between the top and outer walls. As the flow progresses through the bend, the fluid begins to move faster over the outer wall. Along the inner wall, by the 90 deg location the flow has separated near the symmetry plane, while close to the top wall the flow is still attached. This development can be more clearly observed in Fig. 4, which shows the measured profiles of the streamwise velocity. The two sets of velocity vectors at the 90 deg location indicate that, because of the development of secondary motion, the flow has become strongly

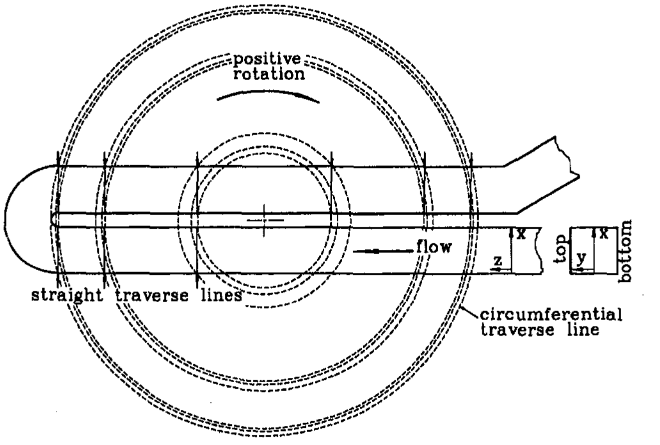

(a) Straight sections

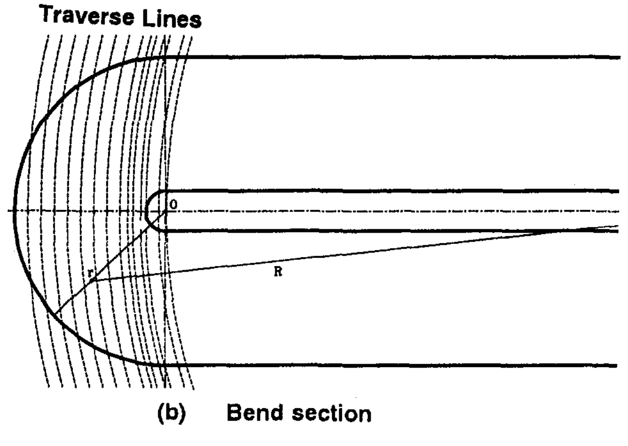

(b) Bend section

Fig. 2 Paths of LDA probe traverse

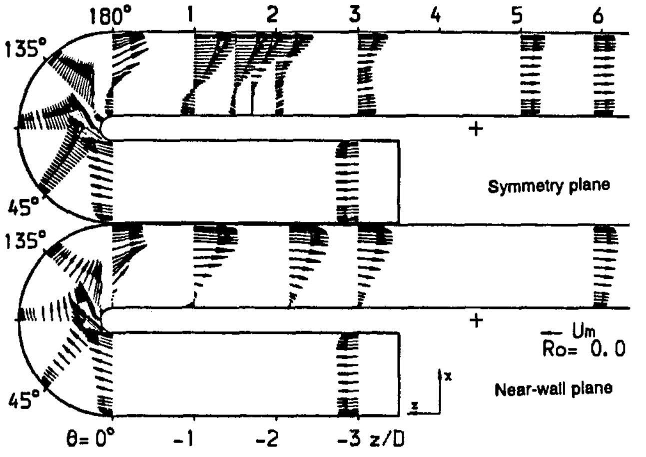

(a) Stationary U-bend

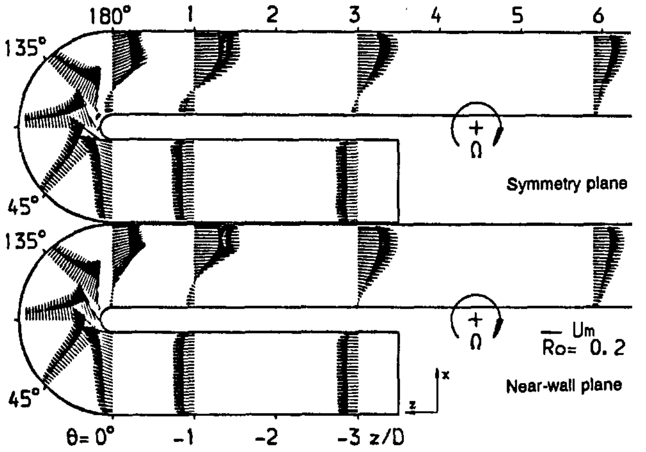

(b) U-bend in positive rotation

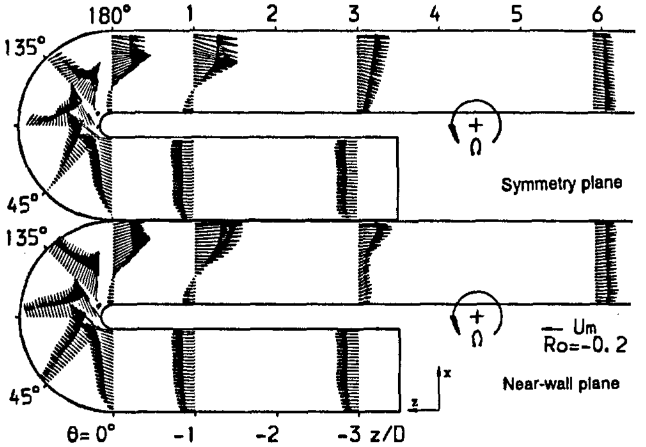

(c) U-bend in negative rotation

Fig. 3 Measured mean velocity field

three-dimensional. The secondary motion transports fluid from the outer to the inner side along the top wall (whereas along the symmetry plane the secondary motion has the opposite direction) and consequently separation is delayed near the top wall. By the 180 deg location (the bend exit), the separation region along the symmetry plane has grown to 35 percent of the duct diameter, while near the top wall the reverse motion is weaker and confined to a narrower region. Both sets of measurements show that the fluid undergoes strong acceleration along the outer wall at the bend exit. Over the downstream region, the stationary U-bend measurements show that even though the reverse motion is stronger near the symmetry plane than near the top wall, reattachment occurs earlier along the symmetry plane. Recovery downstream of the reattachment point is also faster along the symmetry plane than along the top wall. At a distance of six diameters downstream of the bend, the velocity distribution on the symmetry plane is virtually symmetric while near the top wall the velocity is still greater near (what was) the outer wall. A recent numerical investigation of flow through an identical stationary U-bend (Bo and Iacovides, 1993) has shown that the fast recovery along the symmetry plane is caused by the strong secondary motion that persists over the first three downstream diameters.

The effects of positive rotation ($Ro = 0.2$) on the mean flow development are shown in Fig. 3(*b*). In positive-mode of rotation the Coriolis force acts in the same direction as that due to bend curvature. Positive rotation (at $Ro = 0.2$) does not appear to affect the mean flow development significantly upstream of and within the first half of the bend. Downstream of the bend, because the Coriolis-induced secondary motion opposes the return of the high-momentum fluid to the inner side of the duct, the separation region is twice as long as that of the stationary case (Fig. 3(*b*)). Thus flow acceleration along the outer wall is stronger. In contrast to the stationary case, the reverse motion near the top wall is almost as strong as it is along the symmetry plane. However (again contrary to the nonrotating case), the separated flow region in the straight duct tangent is shorter near the upper wall than on the symmetry plane. Farther downstream, the data indicate that the flow starts to approach fully developed flow conditions for a rotating duct. In agreement with earlier numerical studies (Iacovides and Launder, 1991) of flow in rotating straight ducts, the high-momentum fluid accumulates along the trailing side of the rotating duct, which in this case coincides with (what was) the bend outer side.

The mean flow development under negative rotation ($Ro = -0.2$) is shown in Fig. 3(*c*). Under negative rotation, the Coriolis-induced secondary motion transports the low-momentum fluid to the outer side of the duct. As a result, at the bend entry the flow along the outer wall is considerably slower than in the stationary case. Indeed, the results indicate that a small region of flow reversal develops at the symmetry plane. Again, this flow feature is more easily visible in the relevant velocity profile of Fig. 4(*a*) at $\theta = 0$ deg. Along the symmetry plane, the low-momentum region along the outer wall extends over the first half of the U-bend. Near the top wall, the outer side fluid accelerates more rapidly over the first half of the bend. In the downstream region the negative Coriolis force leads to the development of a secondary motion opposite to that caused by the bend curvature. The symmetry plane fluid consequently begins to move across the duct toward the inner side, causing reattachment to occur at around two diameters downstream of the exit. Along the top wall, in contrast to the stationary case, the reverse flow is as strong as it is on the symmetry plane. Immediately after reattachment (3D), the reversal of the secondary flow leads to the accumulation of low-momentum fluid along the inner side near the top wall. By the six-diameter location, the flow again begins to approach fully developed conditions for a rotating duct, in which the high-momentum fluid now moves to what was the inner side of the duct. The axial velocity profiles of Fig. 4 basically present the same mean velocity information, albeit in profile form, which allows a larger scale to be adopted.

Figure 5 shows profiles of the streamwise turbulence intensity. In the first half of the bend, low inlet turbulence levels begin to rise near the outer side where the flow is decelerated. Along the symmetry plane, this initial increase in turbulence levels is stronger in the negative rotation case in which there is a small region of flow separation at the bend entry. At the 90 deg location, a thin region of high turbulence is formed along the inner side, caused by flow separation. As the separation region grows over the second half of the U-bend, the region of high turbulence expands from the inner side toward the duct

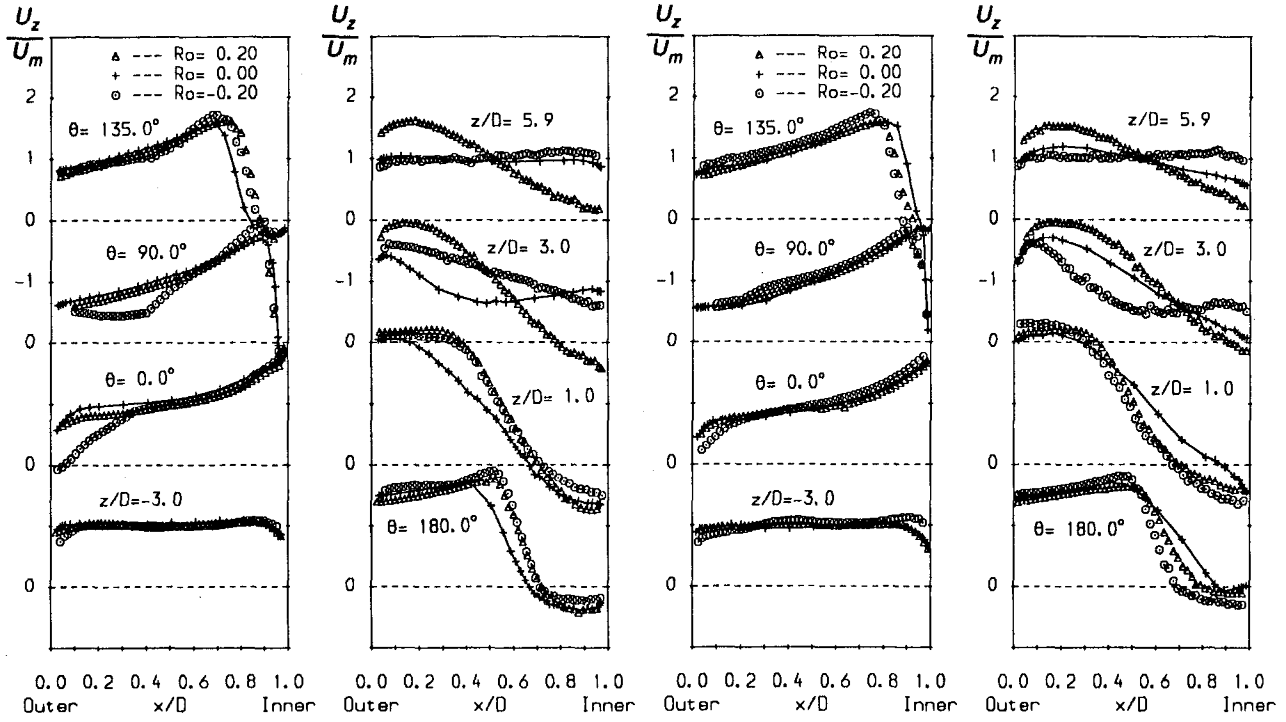

(a) **Symmetry plane 2y/D = 0** **(b)** **Near-wall plane 2y/D = 0.75**

Fig. 4 Streamwise velocity profiles

center. The outer side turbulence levels are suppressed over the second half of the bend probably due to the strong flow acceleration. The one exception to this development is the behavior of the turbulence levels for the negative rotation case along the symmetry plane where the flow acceleration is not as strong. As the flow develops downstream, the measurements show a gradual return to a more uniform distribution of the streamwise turbulence intensities over a length of about six diameters, through an increase in the turbulence levels along the outer side and a corresponding reduction along the inner

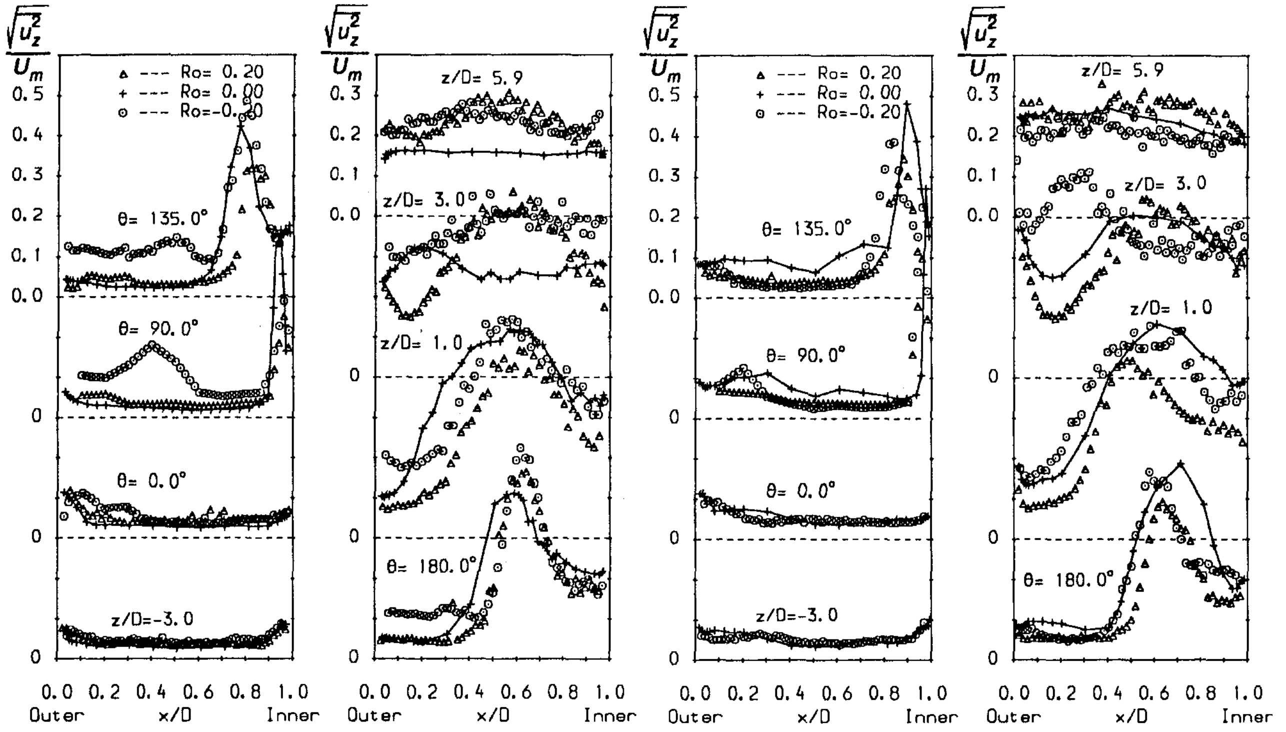

(a) **Symmetry plane 2y/D = 0** **(b)** **Near-wall plane 2y/D = 0.75**

Fig. 5 Profiles of the streamwise component of turbulence intensity

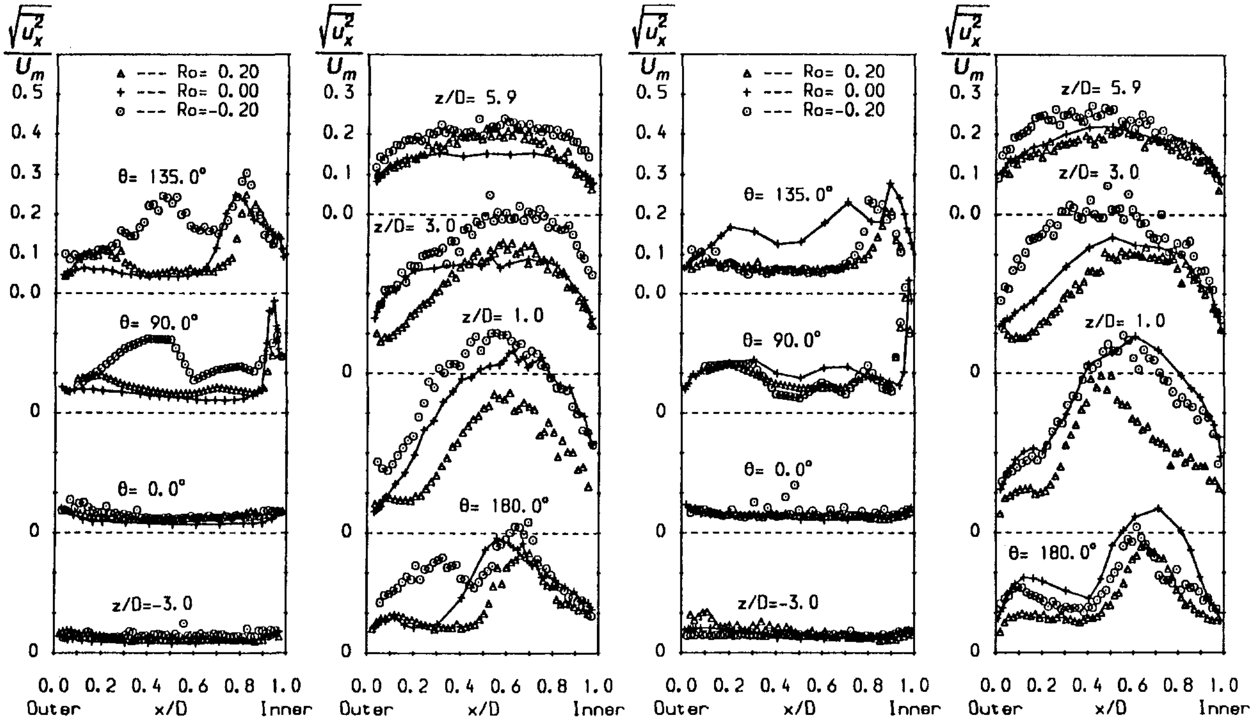

(a) Symmetry plane 2y/D = 0 **(b) Near-wall plane 2y/D = 0.75**

Fig. 6 Profiles of the cross-duct component of turbulence intensity

side. For the positive rotation case, however, the outer side turbulence levels remain suppressed over a longer distance, possibly because positive rotation (as shown in Figs. 3 and 4) causes a stronger flow acceleration along the outer side. Negative rotation leads to a more rapid reduction in the velocity of the outer side fluid downstream of the bend exit. This strong deceleration causes the turbulence levels there to recover more rapidly in the case of negative rotation. For the near-wall plane, by three diameters downstream of the bend, turbulence levels along the outer duct side thus become higher than those of the inner side.

The corresponding development of the turbulence intensities in the cross-duct direction is shown in Fig. 6. Along the symmetry plane, the distribution of $\sqrt{\overline{u_x^2}}/U_m$ is largely similar to the corresponding distribution of streamwise intensities but the levels of the cross-stream intensities are generally lower. In the case of negative rotation, however, over the second half of the U-bend and up to one diameter downstream, the levels of the cross-duct turbulence intensity within the outer half of the duct are similar to or higher than those of the streamwise intensities at the corresponding locations. Near the top wall, the results show that, over the second half of the U-bend, the cross-duct turbulence intensities along the outer side are higher than the corresponding streamwise intensities for all three cases. The strong secondary velocity that develops along the top surface is probably responsible.

The distribution of the turbulent shear stress component within the cross-duct plane $\overline{u_z u_x}$ is shown through the profiles of Fig. 7. Since most of the significant shear stress variation occurs downstream of the bend, the profiles in Fig. 7 begin from the $Z/D = 1.0$ location. These measurements indicate that within the first three downstream diameters, turbulence shear stress levels rise significantly along the symmetry plane, especially for the case of negative rotation. The measurements also indicate that the shear stress distribution is significantly affected by rotation. At the $1D$ location, negative rotation increases the symmetry plane shear stresses while positive rotation has the opposite effect. Farther downstream, the symmetry plane shear stresses are reduced with the reduction occurring more rapidly for the stationary U-bend case. Near the top wall, shear stress levels are generally higher. In the downstream region, the shear stresses near the top wall are higher for the case of negative rotation and considerably lower for the case of positive rotation. In contrast to the symmetry plane development, the decay rate of the shear stresses for the stationary duct case near the top wall is similar to the decay rate for the two rotating cases.

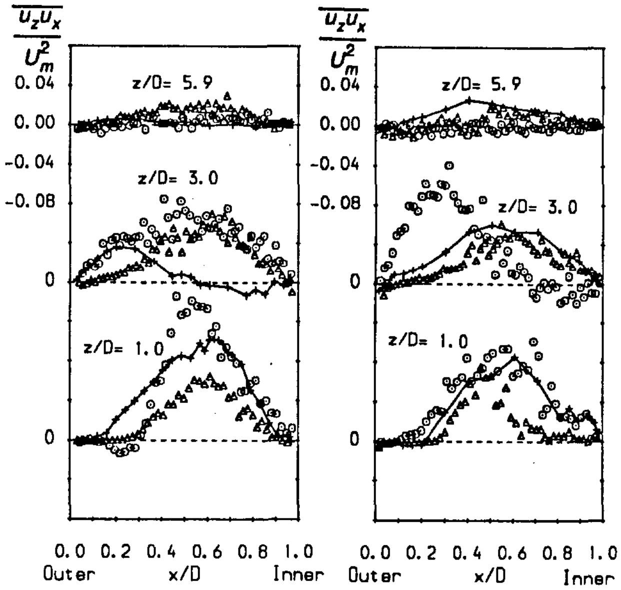

(a) Symmetry plane 2y/D = 0 **(b) Near-wall plane 2y/D = 0.75**

Fig. 7 Profiles the turbulent shear stress $\overline{u_z u_x}$

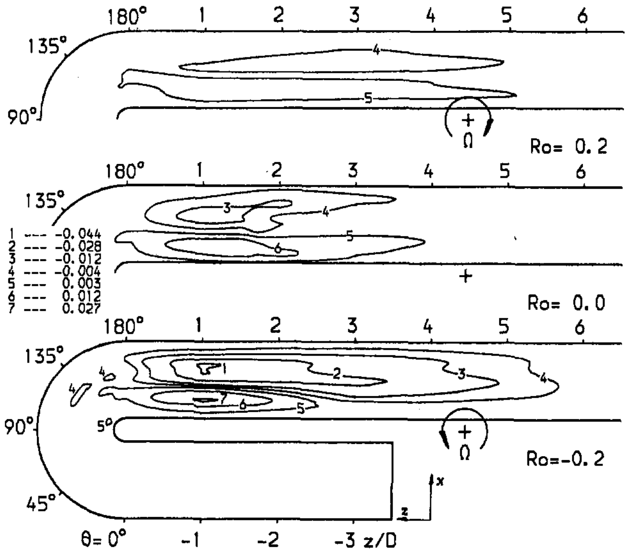

Fig. 8 Contours of the triple moment $\overline{u_x^3}/U_m^3$ along the duct symmetry plane

Finally, the contour plots of Fig. 8 present the variation of the triple moment, $\overline{u_x^3}$, downstream of the 90 deg location. This component is typical of the triple-moment data, which we plan to report more fully in a separate publication. The main feature of interest would appear to be the very strong rise in the level of this quantity downstream of the bend and the considerable differences in the profiles across the duct depending on the sense of rotation; in particular at $1D$ downstream negative rotation produces values of $\overline{u_x^3}$ an order of magnitude greater than for positive rotation with the stationary results lying in between. A negative value of $\partial \overline{u_x^3}/\partial x$ implies a local diffusive gain of fluctuating energy; thus regions close to the inner and outer walls are gaining energy at the expense of the highly turbulent fluid in the core. The difference in the magnitude of the slopes near the wall helps explain why, for negative rotation, fluctuating velocity levels are higher and, for positive rotation, lower than in the stationary case. The decay of the triple product with distance downstream also seems to be consistent with the normal stresses and mean velocity becoming more uniform across the duct.

4 Summary of Results

The present measurements reveal the combined effects of strong curvature and orthogonal rotation (with the axis of rotation parallel to the axis of curvature) on the core flow of a square duct. The *stationary* U-bend flow is dominated by the entry and exit plane streamwise pressure gradients. At the exit, separation raises the inner side turbulence levels and streamwise acceleration suppresses the outer wall turbulence. The reverse flow is stronger along the symmetry plane than near the top wall due to the effects of secondary motion. Reattachment occurs within the first two downstream diameters. Along the symmetry plane the mean velocity distribution rapidly becomes symmetric after reattachment, whereas near the top wall recovery proceeds more slowly. Moreover strong gradients in the variation of triple moments in the downstream region are expected to contribute toward the development of high turbulence by diffusing turbulence energy from the core to the near-wall regions.

Rotation (at $Ro = 0.2$) is found to exert a strong influence in the development of the mean and also of the fluctuating motion. *Positive rotation* almost doubles the length of the separation bubble and also strengthens the reverse motion near the top wall. The laminarizing effect of flow acceleration along the outer side at the bend exit is prolonged by positive rotation, remaining influential over the first three downstream diameters. The triple moments in the downstream region also appeared to be dumped by positive rotation. Turbulence levels downstream of the exit plane are consequently lower for this mode of rotation. *Negative rotation* produces flow separation at the bend entry, which raises the core turbulence levels within the first half of the U-bend. Negative rotation also increases the cross-duct turbulence intensity within the U-bend core relative to the streamwise turbulence intensity. Downstream of the bend exit, this sense of rotation causes the development of strong secondary motion, which has the opposite direction to that of the secondary motion induced by the bend curvature. Along the symmetry plane, the high-momentum fluid along the outer side is convected across the duct to the inner side, thus confining the recirculation bubble to a length of two downstream diameters. Because negative rotation causes a strong deceleration of the downstream flow along the outer side and also increases the triple moments, turbulence levels downstream of the bend exit are generally higher in the presence of negative rotation.

The measurements obtained in this study thus show that at rotational Reynolds numbers relevant to blade cooling applications, rotation can substantially alter the development of the mean and also the fluctuating motion within and downstream of sharp U-bends. This conclusion is consistent with the findings of earlier heat transfer investigations of similar cases. In addition to revealing the details of the flow development, the present measurements also provide test data for the assessment of turbulent models used in the computation of blade cooling flows.

5 Acknowledgments

The research has been supported by the SERC through grant No. GR/F89039. Outstanding technical assistance has been provided by Mr. J. Hosker and Mr. D. Cooper. Authors' names appear alphabetically.

References

Bo, T., and Iacovides, H., 1993, "The Discretization of the Turbulence Transport Equations in the Prediction of Flow and Heat Transfer Through a Sharp U-Bend," presented at the 8th Int. Conf. on Num. Meth. in Lam. and Turb. Flow, Swansea, July.

Bradshaw, P., 1973, "The Effect of Streamline Curvature on Turbulent Flow," AGARDograph, No. 169.

Chang, S. M., Humphrey, J. A. C., and Modavi, A., 1983, "Turbulent Flow in a Strongly Curved U-Bend and Downstream Tangent of Square Cross-Section," *Physico Chemical Hydrodynamics,* Vol. 4, p. 243.

Guidez, J., 1989, "Study of the Convective Heat Transfer in a Rotating Coolant Channel," ASME JOURNAL OF TURBOMACHINERY, Vol. 111, pp. 43–50.

Iacovides, H., and Launder, B. E., 1991, "Parametric and Numerical Study of Fully Developed Flow and Heat Transfer in Rotating Rectangular Ducts," ASME JOURNAL OF TURBOMACHINERY, Vol. 113, pp. 331–338.

Johnston, J. P., Halleen, R. M., and Lezius, D. K., 1972, "Effects of Spanwise Rotation on the Structure of Two-Dimensional, Fully Developed Turbulent Channel Flow," *Journal of Fluid Mechanics,* Vol. 56, pp. 533–557.

Moon, I. M., 1964, "Effects of Coriolis Force on the Turbulent Boundary Layer in Rotating Fluid Machines," MIT Gas-Turbine Laboratory Report No. 74.

Moore, J., 1967, "Effects of Coriolis on Turbulent Flow in Rotating Rectangular Channels," MIT Gas-Turbine Laboratory Report No. 89.

Taylor, A. M. K. P., Whitelaw, J. H., and Yianneskis, M. J., 1982, "Curved Ducts With Strong Secondary Motion: Velocity Measurements of Developing Laminar and Turbulent Flow," ASME *Journal of Fluids Engineering,* Vol. 104, pp. 350–359.

Wagner, J. H., Johnson, B. V., and Hajek, T. J., 1991a, "Heat Transfer in Rotating Passages With Smooth Walls and Radial Outward Flow," ASME JOURNAL OF TURBOMACHINERY, Vol. 113, pp. 42–51.

Wagner, J. H., Johnson, B. V., and Hooper, F. S., 1991b, "Heat Transfer in Rotating Serpentine Passages With Smooth Walls," ASME JOURNAL OF TURBOMACHINERY, Vol. 113, pp. 321–330.

Evaluation and Prediction of Blade-Passing Frequency Noise Generated by a Centrifugal Blower

Y. Ohta

E. Outa

K. Tajima

Department of Mechanical Engineering,
Waseda University,
Tokyo, Japan

The blade-passing frequency noise, abbreviated to BPF noise, of a low-specific-speed centrifugal blower is analyzed by separating the frequency response of the transmission passage and the intensity of the noise source. Frequency response has previously been evaluated by the authors using a one-dimensional linear wave model, and the results have agreed well with the experimental response in a practical range of the blower speed. In the present study, the intensity of the noise source is estimated by introducing the quasi-steady model of the blade wake impingement on the scroll surface. The effective location of the noise source is determined by analyzing the cross-correlation between measured data of the blower suction noise and pressure fluctuation on the scroll surface. Then, the surface density distribution of a dipole noise source is determined from pressure fluctuation expressed in terms of quasi-steady dynamic pressure of the traveling blade wake. Finally, the free-field noise level is predicted by integrating the density spectrum of the noise source over the effective source area. The sound pressure level of the blower suction noise is easily predicted by multiplying the free-field noise level by the frequency-response characteristics of the noise transmission passage.

Introduction

In the case of low-specific-speed centrifugal fans or blowers, the BPF noise could dominate the overall noise level, if sufficient care is not taken. Therefore, many blower noise investigations, such as Weidemann's (1971), Neise's (1975, 1976), Suzuki and Ugai (1977) and Bommes's (1982) have been made with special attention to the prediction of the BPF components. However, complete understanding has not yet been established, since the BPF components depend not only on the source strength but also on the frequency-response characteristics of the noise transmission passage.

In the present study, the experimental evaluation of both contributions was made by sweeping the blower rotational speed with a precise resolution, and the similarity rule developed by Neise (1975, 1976) and Bommes (1982) was utilized for data reduction. The influence of several blower design parameters was discussed for each of the similarity terms constituting the rule.

The frequency response of the noise transmission passage has been described by introducing a one-dimensional linear wave model, in which the key parameter is the number of blade-to-blade passages selectively determined by the noise wavelength. Application of the model, allowing the selection of the inlet duct length, the blower rotational speed, and the number of blades, facilitates reducing the noise level transmitted to the blower exterior without any effect on blower performance (Ohta et al., 1987).

One of the most comprehensive methods to define the noise source extent may be the correlation analysis. Curle (1955), Siddon (1973), Akishita et al. (1978), and Maruta and Kotake (1979a, b) have been made to analyze the aerodynamic noise radiated from flat plates or aerofoils immersed in steady flow. The authors intend to utilize the correlation analysis based on Lighthill's (1952) dipole theory for the BPF component radiated from a centrifugal blower. The extent of the effective source region was determined by measuring the cross correlation between the data of the acoustic pressure and the pressure fluctuation on the scroll surface (Ohta et al., 1991). As usually expected, the location of the effective source was restricted to the vicinity of the scroll cutoff, irrespective of the cutoff geometries. The free-field noise characteristics were then obtained by integrating the surface density spectrum of the dipole source over the effective extent on the scroll surface. A quasi-steady model of blade wake impingement was applied to express surface pressure fluctuation, and dipole strength was calculated by taking the cross-correlation between the pressures measured at two different locations on the scroll surface. The key parameters were the extent of the noise source and the velocity profile of the blade wake diffusing toward the cutoff surface.

The next stage of interest is thus focused on an increase of the BPF noise level in accordance with the decrease of flow rate from the maximum-efficiency operation. A preliminary discussion is made tentatively to predict the off-design noise level by utilizing the present model.

Experimental Facility

Tested Centrifugal Blower. The centrifugal blower and the data acquisition system are shown schematically in Fig. 1. The blower rotational speed is swept every 50 rpm within the range between 1000 and 4500 rpm. The operation point is set by a butterfly valve installed at the end of the outlet duct of 16.7 m length. The blower volume flow rate is measured using an orifice flow meter at the outlet duct. Impeller dimensions and specifications of blower performance are listed in Tables 1 and 2.

The blower external noise is obtained by the sound pressure measurement at the location 1 m apart from the inlet bellmouth. As recognized in previous researches, the cutoff clearance Δr_c,

---

Contributed by the International Gas Turbine Institute and presented at the 39th International Gas Turbine and Aeroengine Congress and Exposition, The Hague, The Netherlands, June 13–16, 1994. Manuscript received by the International Gas Turbine Institute March 2, 1994. Paper No. 94-GT-334. Associate Technical Editor: E. M. Greitzer.

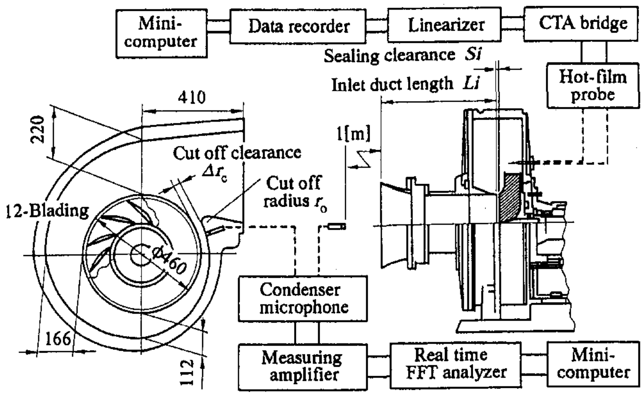

Fig. 1 Experimental apparatus and measuring systems

Table 1 Design performance of tested blower

Rotational speed	N	3000	rpm
Volume flow rate	Q	50.0	m^3/min
Total pressure rise	Pt	300	mmAq
Specific speed	Ns	42.4	rpm,m^3/s, m
Gas horsepower	Lat	3.59	kW

which is the distance between the impeller periphery and the scroll cutoff, as well as the radius of the cutoff r_0, give direct influence on the BPF components. In the present study, therefore, three types of cutoff geometries are analyzed, i.e., (Δr_c = 12 mm, r_0 = 12 mm), (Δr_c = 32 mm, r_0 = 12 mm), and (Δr_c = 12 mm, r_0 = 1.5 mm).

Table 2 Impeller dimensions

Number of blades	Z	12
Inlet diameter	D_1	260 mm
Outlet diameter	D_2	460 mm
Blade shape		NACA-65

Measurement Methods. The blower suction noise *Pam* is measured using a B&K 4133 microphone at a location 1 m apart from the inlet bellmouth. The pressure fluctuation data *Ps* are acquired over the whole surface of the casing wall. Since the vicinity of the scroll cutoff is thought of as the most effective area of the noise source, the precise distribution of the fluctuation is carefully recorded. In the measurement, $\frac{1}{8}$-in. precision microphones of B&K 4138 are used mounting flush to the scroll surface.

Instantaneous flow velocity and angle of the impeller discharge are also measured every 50 rpm by a constant-temperature hot-film anemometer. An X-type nickel-coated quartz-fiber of DANTEC 55R52 is used. The probe is mounted to a rotatable and axially traversable support, and is inserted from the rear casing wall. The X-fibers are placed in the impeller meridional plane in such a manner that the velocity vector lies in the probe plane. Data sampling period is 2×10^5 times per second, and each of the velocity and the flow angle waveforms is averaged 120 times with a pulse trigger train generated every one revolution of the impeller.

Similarity Rule of Blower Noise

The present analyses and discussion are based on a similarity rule of the inlet acoustic pressure *Pam* at the fundamental and the second harmonic frequency of the BPF components, which is expressed as

Nomenclature

$A_2 = \pi D_2^2/4(m^2)$
a = speed of sound, m/s
Csa = cross-correlation function between Ps and Pa
Css = cross-correlation function between Ps_1 and Ps_2
D = surface density spectrum of noise source
D_2 = external diameter of impeller = 460 mm
F_M = frequency-distribution function in Eq. (1)
f = frequency, Hz
G_0 = frequency-response function in Eq. (1)
He = Helmholtz number $= fD_2/a$
K_D = machine constant in Eq. (1)
k = wave number $= 2\pi f/a$
Li = inlet duct length, mm
N = blower rotational speed, rpm
n_b = number of impeller blade-to-blade passages
Pa = sound pressure with ideal transmission, Pa
Pam = sound pressure radiated from blower, Pa
P_0 = reference pressure = 2×10^{-5} Pa
Ps = pressure fluctuation on the scroll surface, Pa
ΔP = amplitude of surface pressure fluctuation, Pa
Ri = distance from blade trailing edge, mm
Rsa = cross-spectral density function between Ps and Pa
$Rsam$ = cross-spectral density function between Ps and Pam
r = distance between noise source and measuring location, mm
r_0 = radius of the scroll cutoff, mm
Δr_c = clearance between impeller and scroll cutoff, mm
S = frequency correction function in Eq. (1)
Sa = power spectral density of Pa
Sam = power spectral density of Pam
S_b = cross-sectional area of a blade-to-blade passage
Si = clearance between impeller and inlet duct, mm
St_D = Strouhal number; St_D = 1: first BPF, St_D = 2: second BPF
S_2 = cross-sectional area of inlet duct
U_2 = impeller tip speed, m/s
Vc = free-stream velocity (absolute flame), m/s
ΔV = amplitude of blade wake (absolute flame), m/s
ΔW = duration of blade wake, ms
x = position vector of noise measuring location
y = position vector of noise source
Z = number of impeller blades
α = impingement angle, deg
θ = angle between surface normal and direction of noise radiation, deg
ρ = density, kg/m^3
σ = nondimensional specific speed = $\phi^{1/2}/\psi^{3/4}$
ϕ = flow coefficient
ψ = pressure coefficient
ω = angular velocity, rad/s

Subscripts

m = effect of noise transmission passage
opt = maximum-efficiency operation

Superscripts

$\bar{\ }$ = time average
$*$ = scroll surface

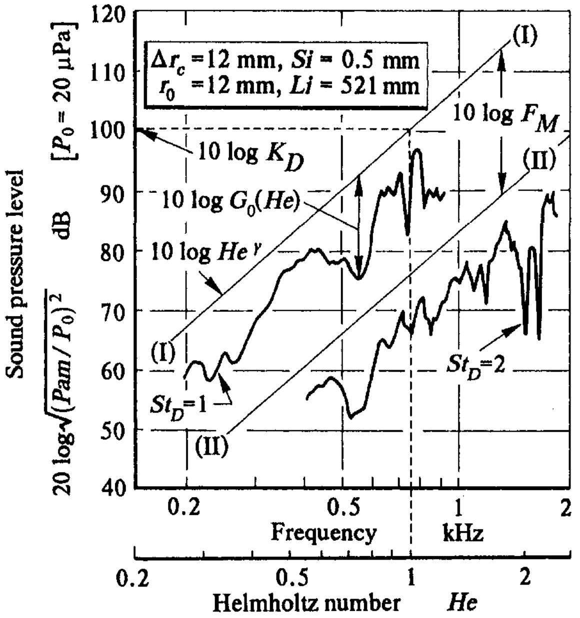

Fig. 2 Loci of BPF components versus blower rotational speed

$$\left(\frac{Pam}{P_0}\right)^2 = \underbrace{k_0\frac{A_2}{4\pi}\left(\frac{\pi}{Z}\right)^{\gamma}}_{K_D}\ \underbrace{\frac{F_0(\mathrm{St}_D)}{\mathrm{St}_D^{\gamma}}}_{F_M}\ \underbrace{G_0(\mathrm{He})\ \mathrm{He}^{\gamma}}_{G_M}\ \underbrace{S(\sigma,\ \mathrm{St}_D;\ \mathrm{He})}_{S_M}. \qquad (1)$$

In the expression, blower rotational speed is normalized by Helmholtz number He and the harmonics of the BPF components are denoted by Strouhal number St_D. The power of the blower inlet noise is expressed as a product of the following four terms:

1 K_D: A machine constant representing the rms level of the free-field characteristics of the first BPF component. The value is indicated in Fig. 2 as the ordinate of the ideal free-field characteristic (I) – (I) at a standard frequency of He = 1. This term takes a constant value particular to each machine, and is related to the so-called specific sound power level.

2 F_M: Amplitude ratios of the higher harmonics to the first BPF component. For the second harmonics, i.e., $\mathrm{St}_D = 2$, the value is denoted in Fig. 2 as a level shift between free-field characteristics (I) – (I) and (II) – (II) of the fundamental and the second harmonics. This term is evaluated at the frequency but not at the operational speed of the impeller. For the tested blower, the third and the higher components are not taken into account, since they slightly exceed the broad-band noise level.

3 G_M: Frequency-dependent product of functions $G_0(\mathrm{He})$ and He^{γ}. The function $G_0(\mathrm{He})$ describes the frequency-response of the noise transmission passage. The second function He^{γ} represents the usual power-law relationship of noise increase versus convection velocity, and in the case of a dipole source γ can be assumed as 6.

4 S_M: A supplementary correction function due to the harmonics of BPF and the deviation σ from the maximum-efficiency operation.

The frequency-response function $G_0(\mathrm{He})$ is overlaid in narrow shaded zones in Fig. 3 for wide varieties of cutoff geometries. By introducing a one-dimensional linear wave model, $G_0(\mathrm{He})$ has been evaluated, as shown by thick and broken lines in Fig. 3. The results agree well with the experimental data, and may be applied for practical use. The effective number n_b of the blade passage where the generated noise is transmitted from the cutoff is selected between 2 and 5, depending on the frequency range. This selection of the effective number n_b by the noise wavelength is considered to characterize the noise transmission mechanism of the blower system (Ohta et al., 1987). The results of lumped impedance models, such as Moreland's (1974) and Yeow's (1974a, b) describe considerably lower frequency phenomena than that of the industrial noise concerned.

The source strength terms K_D and F_M are found to indicate a simple relationship to the distance between the cutoff and the impeller as shown by open circles in Fig. 4. However, quantitative evaluation of these terms requires information about the velocity profile of the impeller discharge flow, the diffusing process of the blade wake, and conversion mechanism to the pressure fluctuation on the scroll surface. The extent of the effective noise source should also be determined for the analysis.

Characteristics of the Noise Source

Procedure of Source Noise Prediction. The procedure to predict the source strength terms K_D and F_M in Eq. (1) has the three steps discussed below. It is necessary in the procedure to determine the velocity distribution of the impeller discharge and the extent of the noise source by experimental measurements.

Step 1: The distribution of the BPF noise source on the scroll surface is determined using a correlation analysis between the acoustic pressure *Pam* at the inlet and the pressure fluctuation *Ps* on the whole surface of the casing wall, referred to as *Rsam* in Fig. 5. In the analysis, dipole noise is assumed. Then, the extent of the effective source distributed on the scroll surface is obtained.

Step 2: The free-field characteristic of the BPF noise is obtained by integrating distributed pressure fluctuations in the source extent on the scroll surface; see *Rss* in Fig. 6. The surface density spectrum of the noise source is calculated by taking a product of power spectral density of the pressure fluctuation and the correlation area, which is determined by integrating the cross-spectral density of the pressure fluctuation data. Then,

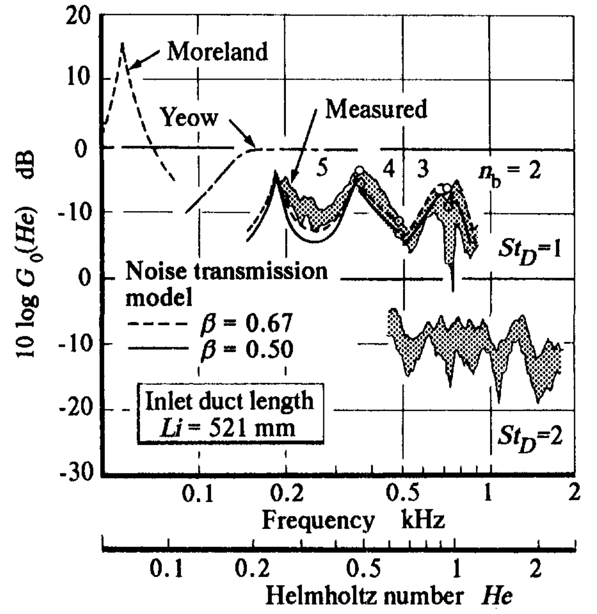

Fig. 3 Frequency-response of the transmission passage determined by experiments and by a wave model

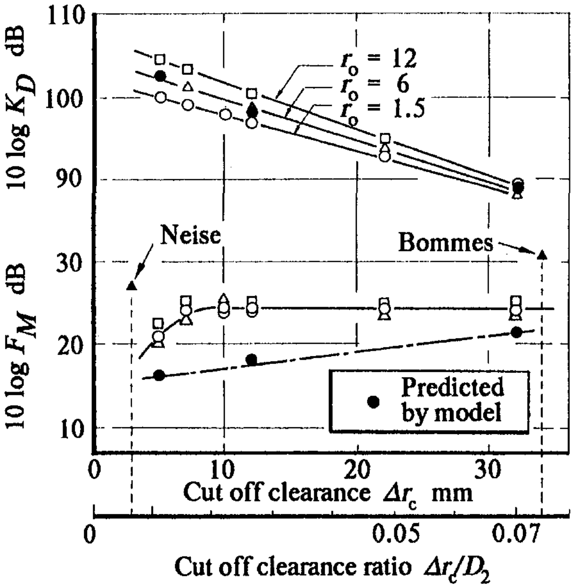

Fig. 4 Source strength terms of the similarity rule determined by experiments and predicted by a quasi-steady flow model

integration of the surface density spectrum over the effective source extent gives the free-field noise.

Step 3: The surface pressure fluctuation is expressed by a model equation in terms of the amplitude and the traversing duration of the impeller blade wake. The free-field characteristics of the noise source are predicted using the modeled pressure fluctuations according to the correlation analysis shown in step 2.

Dipole Strength on the Scroll Surface

Theoretical Background. The relation between the acoustic pressure *Pa* in the free field and the associated surface pressure fluctuation *Ps* is expressed by Curle's (1955) solution of the Lighthill (1952) equation

$$Pa(x,t) = \frac{1}{4\pi a}\int_S \frac{\cos\theta}{r}\left[\frac{\partial}{\partial t}Ps(y,t)\right]_{\hat{t}} dS(y), \qquad (2)$$

where *S* denotes the extent of the noise source distributed on the scroll surface.

Reflection and diffraction of the sound waves within a casing are ignored since the wavelength of the acoustic pressure is large enough in comparison with blower dimensions. The square brackets [ ] denote evaluation at the retarded time of $\hat{t} = t - r/a$.

Both sides of Eq. (2) are multiplied by the acoustic pressure at a new time $t + \tau$, and by taking a time average,

$$\overline{Pa(x,t)Pa(x,t+\tau)} = \frac{1}{4\pi a} \times \overline{\int_S \frac{\cos\theta}{r}\left[\frac{\partial}{\partial t}Ps(y,t)\right]_{\hat{t}} Pa(x,t+\tau)\,dS(y)}. \qquad (3)$$

Using the cross-correlation function *Csa* between *Ps* and *Pa*, Eq. (3) may be written as

$$\overline{Pa(x,t)Pa(x,t+\tau)} = -\frac{1}{4\pi a} \times \int_S \frac{\cos\theta}{r}\frac{\partial}{\partial\tau}[Csa]_{\tau+r/a}dS(y). \qquad (4)$$

Two Fourier transforms are introduced as follows:

$$Sa(x;f) = \int_{-\infty}^{\infty}\overline{Pa(x,t)Pa(x,t+\tau)}\exp(-j2\pi f\tau)d\tau, \qquad (5)$$

$$D(x,y;f) = -\frac{\cos\theta}{4\pi ar} \times \int_{-\infty}^{\infty}\frac{\partial}{\partial\tau}[Csa]_{\tau+r/a}\exp(-j2\pi f\tau)d\tau, \qquad (6)$$

where *Sa* is the power spectral density function of the radiated acoustic pressure *Pa*, and *D* denotes the surface density spectrum of the noise source, i.e., contribution to the total sound pressure spectrum associated with the unit area of the scroll surface.

In terms of the cross-spectral density function *Rsa*, the transform *D* is expressed as

$$D(x,y;f) = -\frac{if\cos\theta}{2ar}\exp\left(\frac{j2\pi fr}{a}\right)Rsa(x,y;f). \qquad (7)$$

Since the acoustic pressure *Pam* measured at the blower inlet has already influenced by the response characteristics $G_0(\mathrm{He})$ of the noise transmission passage, the functions *Sa* and *Rsa* are expressed as

$$Sa(x;f) = Sam(x;f)/G_0(f), \qquad (8)$$

$$Rsa(x,y;f) = Rsam(x,y;f)/\sqrt{G_0(f)}, \qquad (9)$$

where *Sam* is the power spectral density function of the measured acoustic pressure *Pam*, and *Rsam* denotes the cross-spectral density function between *Ps* and *Pam*.

From Eqs. (7), (8), and (9), we obtain the following relations:

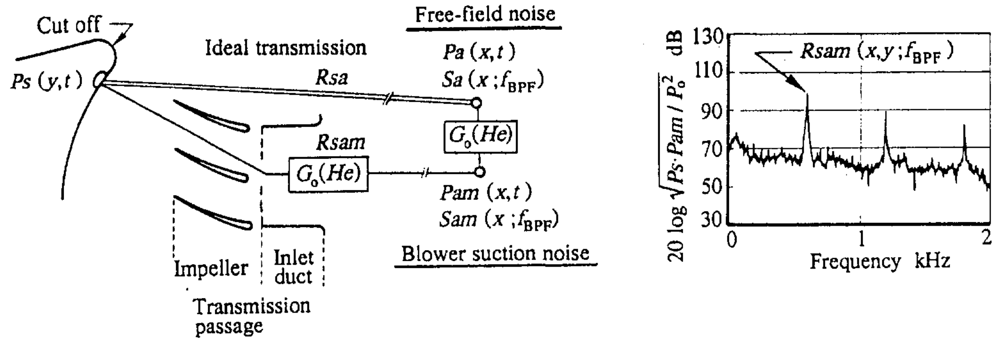

Fig. 5 Correlation analysis for evaluation of noise source extent distributed on the scroll surface

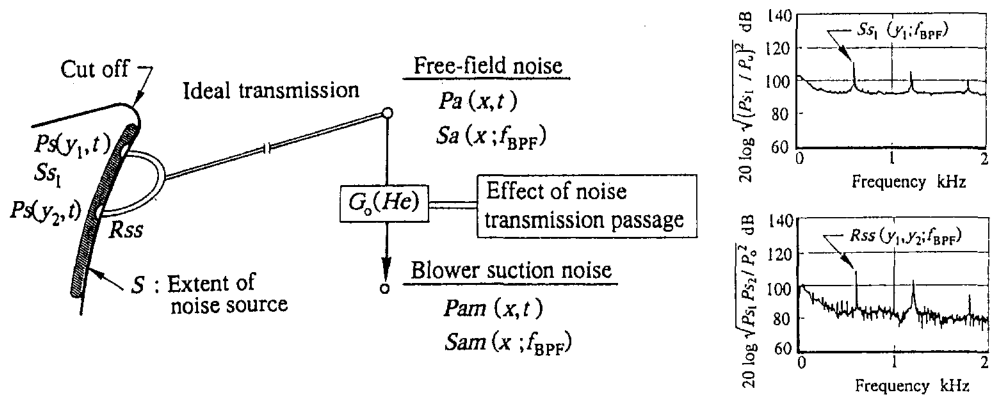

Fig. 6 Correlation analysis for blower noise prediction

$$Sam(x;f) = \int_S D(x,y;f)dS(y). \qquad (10)$$

By means of the precise measurement of *Rsam* at various locations on the scroll surface, distribution of the surface dipole strength, i.e., D, is obtained. Then, the complete power spectrum *Sam* is determined by integrating the surface density spectrum D over the whole extent of the noise source. Since *Sam* is a real and even function, the imaginary part of *Rsam* tends to zero by the integration, and *Sam* must be doubled to obtain the true power spectrum.

Experimental Results and Discussion. Typical distributions of the surface density spectrum D of blade-passing frequency on three kinds of cutoff surfaces are indicated in Fig. 7. In the measurement, both the magnitude and real part of the complex-valued data of *Rsam* in Eq. (9) are obtained. However, the difference is less than 2 dB, and only the magnitude data of *Rsam* are presented in the figure. The distance r appearing in Eq. (7) is determined by the blower geometry as a distance from the scroll surface to the microphone location at the suction side along the passage of the impeller and the duct. The angle θ at the noise source is similarly obtained as an angle between the surface normal and the radiation direction, which is assumed to be in the direction of the impeller axis.

The experimental results indicate the following features of the noise source distribution:

1 In Fig. 7(*a*), the distribution of the surface density spectrum D shows an extremely high level in the meridional plane of the impeller and decreases rapidly with the distance η from the rear casing wall. This tendency is unchangeable, irrespective of the cutoff geometries, and the effective extent of the noise source may be restricted in the vicinity of the impeller meridional plane, as usually accepted. The distribution is largely influenced by the cutoff clearance Δr_c, and the level discrepancy between the cases of $\Delta r_c = 12$ mm and 32 mm is more than 10 dB. However, any significant difference of the radius r_0 of the cutoff is not recognized. Therefore, the amplitude discrepancy of the suction noise between the cases of $\Delta r_c = 12$ mm and 32 mm is caused not by the extent area but by the strength of the noise source.

2 In the direction ξ along the casing scroll, the surface density spectrum D shows the maximum value at the closest point to the impeller on the scroll surface, and gradually decreases to a constant value. The effect of the cutoff radius r_0 is proved to be caused only by the extent of the noise source that faces the impeller exit. The difference in the extent is indicated by a shaded area in Fig. 7. Two cases of extent of the noise source in the ξ direction are utilized in the integration of Eq. (10); i.e., from the cutoff apex to C and D.

The magnitude distribution of the surface density spectrum D is represented by third-order spline functions in both η and ξ directions, and integrated over the extent of the noise source according to Eq. (10). The power spectra *Sam* of the suction noise corresponding to two different extents of the noise source are plotted in Fig. 11. Both data seem to agree well in the decibel scale with the measured sound pressure level shown by a thick trace. The two selections of the extent of the noise source do not lead to any significant difference in the results

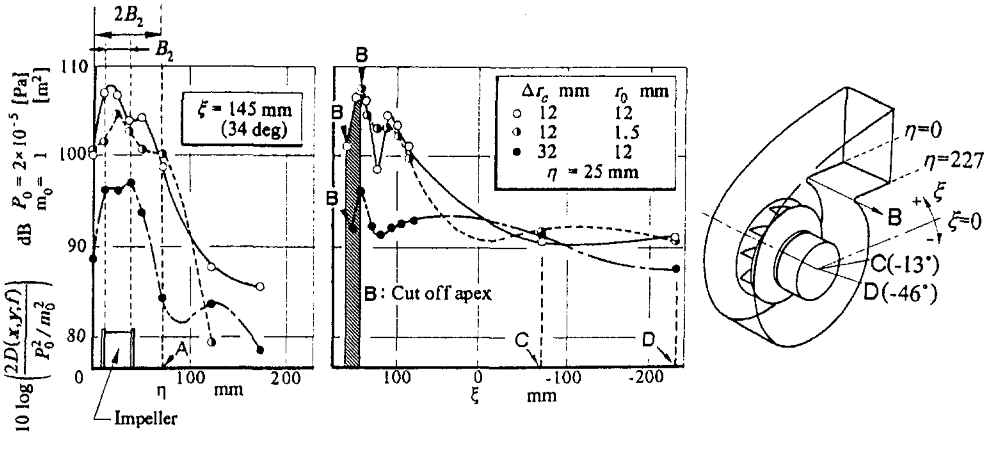

Fig. 7(*a*) η-direction Fig. 7(*b*) ξ-direction Fig. 7(*c*) Scroll coordinates

Fig. 7 Distribution of surface density spectrum on the scroll surface of the integration. The extent of the noise source that contributes to the suction noise essentially lies in the vicinity of the scroll cutoff, and the effects of sources located outside of that vicinity are found to be very slight. In the following analyses, the extent of the noise source is assumed to be between the cutoff apex and C in the ξ direction, and between the rear casing wall and A, at a distance twice the impeller width, in the η direction.

Characteristics of the Free-Field Noise

Theoretical Background. Since the distance r between the measuring location and the surface source is almost unchanged by the locations of the respective sources, Eq. (2) at a time t may be written as

$$Pa(x, t) = \frac{1}{4\pi ar} \int_S \cos\theta \left[\frac{\partial}{\partial t} Ps(y, t) \right]_{\hat{t}} dS(y), \quad (11)$$

and at a new time of $t + \tau$,

$$Pa(x, t + \tau) = \frac{1}{4\pi ar} \int_S \cos\theta \left[\frac{\partial}{\partial t} Ps(y, t + \tau) \right]_{\hat{t}} dS(y). \quad (12)$$

By taking a product of the respective sides of Eq. (11) and Eq. (12), and taking a time average, the result is

$$\overline{Pa(x, t)Pa(x, t + \tau)} = \left(\frac{1}{4\pi ar} \right)^2 \times \int_S \int_S \cos^2\theta \frac{\partial^2}{\partial \tau^2} [Css]_{\tau + (r_1 - r_2)/a} dS(y_2) dS(y_1), \quad (13)$$

where Css is the cross-correlation function between the pressure fluctuations measured at locations y_1 and y_2 in the extent of the noise source.

In terms of a cross-spectral density function Rss, a Fourier transform of Eq. (13) is expressed as

$$Sa(x; f) = \left(\frac{f}{2ar} \right)^2 \int_S \int_S \cos^2\theta \exp\left(j2\pi f \frac{r_1 - r_2}{a} \right) \times Rss(y_1, y_2; f) dS(y_2) dS(y_1). \quad (14)$$

The inner integral of Eq. (14) is replaced by a correlation area Ac_1, which is defined as

$$Ac_1 = \int_S \cos^2\theta \exp\left(j2\pi f \frac{r_1 - r_2}{a} \right) \times \frac{Rss(y_1, y_2; f)}{Ss_1(y_1; f)} dS(y_2), \quad (15)$$

where normalization of Rss refers to the power spectral density Ss_1 at a source location y_1. The correlation area Ac_1 is the extent area where the pressure fluctuation at location y_1 is effectively converted to a part of the free-field noise, and is evaluated in the present case for the component of the blade-passing frequency. Then, by substituting Eq. (15) for Eq. (14), the power spectral density function Sa of the free-field noise is expressed as

$$Sa(x; f) = \left(\frac{f}{2ar} \right)^2 \int_S Ac_1 Ss_1(y_1; f) dS(y_1). \quad (16)$$

Equation (10) derived in the previous section expresses a simpler formula to relate the suction noise and the surface pressure fluctuation, but it is not suitable for prediction purposes. By knowing the surface pressure fluctuation, Eq. (16) enables us to calculate the free-field noise, and the power spectrum Sam at the blower inlet is immediately obtained by multiplying the frequency-response function $G_0(\mathrm{He})$.

Experimental Results of the Free-Field Noise. The correlation area Ac_1 shown in Eq. (15) is determined by integrating the normalized value of cross-spectral density Rss/Ss_1, which is expressed by the third-order spline function in both η and ξ directions.

The free-field noise level Sa is calculated according to Eq. (16) by integrating the product of the power spectrum of the pressure fluctuation and its correlation area. Third-order spline functions are again used to represent the η- and ξ-directional distribution of the products. The integral is taken over an extent consistent with the extent of the noise source determined in the previous section. The results are plotted by open circles in Fig. 11. The data agree well with the presumed free-field noise level indicated by a thin line, which is evaluated by adding the frequency-response function $G_0(\mathrm{He})$ to the measured blower suction noise. The ascending slope is close to 6 and is in accordance with the far-field characteristics of the dipole noise.

Thus, the free-field noise is successfully evaluated from the surface data of the pressure fluctuation applying the correlation analysis. The selection of the extent of the noise source area is found appropriate, and the frequency-response function is proved efficient for noise prediction.

Then, by knowing an expression of the pressure fluctuation on the scroll surface, blower noise prediction becomes possible in terms of the velocity configuration of the impeller discharge. In the following section, characteristics of the discharge velocity and a quasi-steady flow model are presented to describe the pressure fluctuation.

Model of Surface Pressure Fluctuation

Diffusion Characteristics of Blade Wake. The velocity profile of the impeller discharge flow, especially the diffusion characteristics of the blade wake is measured by X hot-film anemometer, since the wake shows large amplitude in the profile of the absolute velocity and is considered to dominate the noise source of the BPF components. The most comprehensive parameters to describe the characteristics of wake profile are wake amplitude ΔV and duration of wake ΔW, which are defined by Shaw and Balombin (1981) for the absolute velocity of the axial blowers. The definitions of ΔV and ΔW are schematically shown in Fig. 8. By changing the distance Ri from the blade trailing edge to the radial direction of the impeller, the characteristics of ΔV and ΔW can be investigated. The results are shown in Fig. 8.

Both wake amplitude ΔV and duration of wake ΔW show a simple relationship to the distance Ri from the blade trailing edge, e.g., ΔV and ΔW are proportional to Ri^{-1} and Ri, respectively. This relationship is valid for almost every measuring location around the impeller, except those locations where the distance between the impeller and the scroll surface is extremely small. In these locations, the wake is suppressed by the scroll surface, and shows the characteristics as represented by the broken lines in Fig. 8. However, the discharge velocities from these locations of the impeller impinge on the lower part of the scroll surface where the surface density spectrum of the noise source shows an extremely low level and slightly influences the BPF noise. Thus, the characteristics of the wake diffusion that contribute to the BPF noise are confirmed by the hot-film measurement, and these relations are utilized for the flow model of the surface pressure fluctuations. The utilized data of ΔV and ΔW for the model are measured at the location from where the discharge velocity impinges directly on the extent of the noise source.

Profile of Pressure Fluctuation on the Scroll Surface. In order to have quantitative evaluations of the source strength terms K_D and F_M, a wave model describing the surface pressure

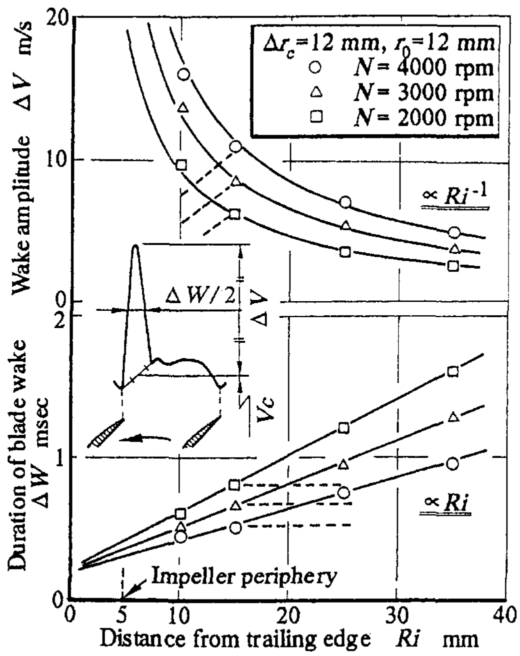

Fig. 8 Diffusion characteristics of blade wake

fluctuation has been utilized. The outline is schematically shown in Fig. 9, and the following assumptions are made:

1 The velocity profile of the blade wake diffuses between the impeller and the cut off according to the characteristics shown in Fig. 8.

2 The amplitude of the pressure fluctuation on the scroll surface is determined from the instantaneous velocity profile of the impeller blade wake. By assuming a formula of pressure distribution on a jet impinging plate, the fluctuation of the pressure is expressed as (Kamoi and Tanaka, 1977):

$$Ps = \Delta P \exp\left\{-0.694\left(\frac{4 \sin \alpha}{\Delta W^*}\,\xi\right)^2\right\} + Pc, \qquad (17)$$

where

$$\Delta P = \tfrac{1}{2}\rho(\Delta V^{*2} + 2Vc^*\Delta V^*) \sin^2 \alpha, \qquad (18)$$

$$Pc = \tfrac{1}{2}\rho Vc^{*2} \sin^2 \alpha. \qquad (19)$$

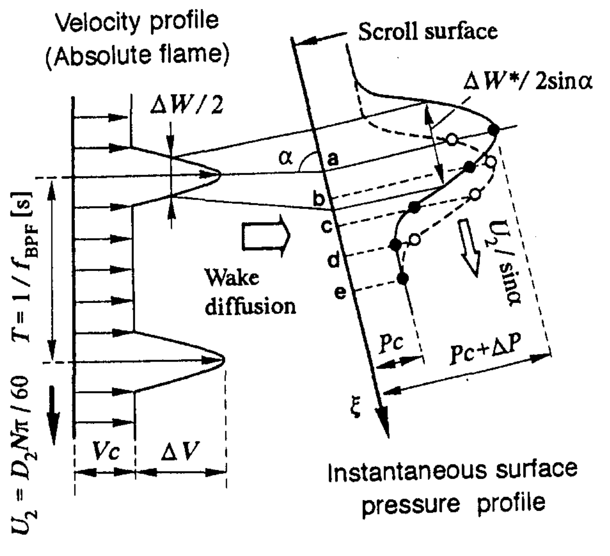

Fig. 9 Flow model for describing pressure fluctuations on the scroll surface

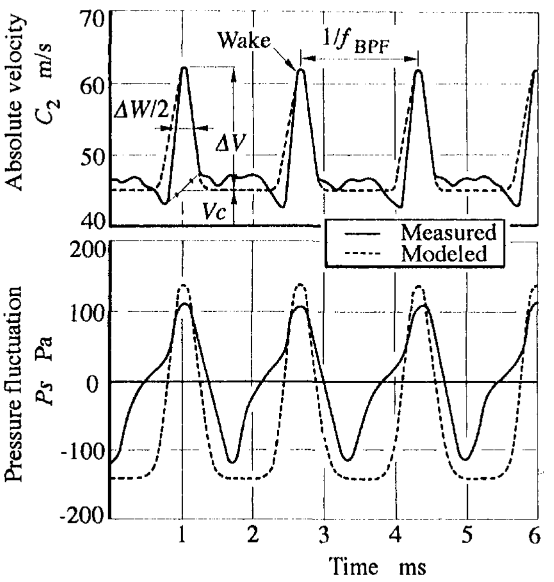

Fig. 10 Modeled waveforms of velocity and pressure fluctuation, compared with measured data

3 The pressure of such profile travels with the impeller tip speed U_2 along the scroll, and forms the fluctuating pressure wave. The frequency coincides with the blade-passing frequency. The impingement angle α between the wake direction and the scroll tangent of the surface are determined by hot-film velocity measurement.

Thus, the time history of the pressure fluctuation is obtained at an arbitrary point on the scroll surface. A typical waveform of the modeled pressure fluctuation is shown in Fig. 10 in comparison with the measured data which were acquired with the scroll-mounted microphone. The modeled waveform of the impeller discharge velocity is also indicated in the upper part of the figure. The present model that utilizes the wake parameters ΔV and ΔW to describe the surface pressure fluctuation makes possible an amplitude prediction of the fundamental frequency component.

In the correlation analysis, such time data at five locations are used; i.e., at points *a* to *e* in Fig. 9. These points correspond to microphone locations in the experiment to evaluate the free-field noise by cross-correlation analysis, and are also located within the assumed noise source extent. In the calculation of the correlation area, uniform distribution of pressure is assumed in the spanwise direction η of the scroll surface. Therefore, the correlation area is expressed as a product of length twice the impeller width and the correlation length in the ξ direction, which is calculated from integrating the modeled pressure fluctuation. The process of calculating the free-field noise is similar to the process stated before in the experimental evaluation.

Prediction of Blower Suction Noise. The free-field noise calculated by the quasi-steady flow model is shown by the closed circles in Fig. 11. The result agrees well with the experimental data indicated by the open circles. The ascending slope in respect to the blower rotational speed is close to 6, which is consistent with the free-field characteristics of the dipole noise. By multiplying the frequency-response function $G_0(\mathrm{He})$, the blower suction noise is obtained as indicated in Fig. 11. The noise level predicted by the present model agrees well with the measured BPF trace within a few decibels. Thus, the present model of traveling wake for describing the pressure fluctuations has been satisfactorily utilized in the noise analysis developed in the present research. The assumed extent of the noise source is also proved sufficient for practical use.

The K_D value obtained by applying the quasi-steady flow model is shown for a variation of the cut off clearance Δr_c in Fig. 4. For different cases of the clearance, the velocity data of the impeller discharge are determined by measurements. However, the diffusion characteristics of the blade wake are not altered from those shown in Fig. 8. Despite the fact that the effect of the cutoff radius r_0 could not be taken into account, the predicted value of K_D agrees well with the experimental data. This result indicates that the K_D value is only affected by the amplitude of the surface pressure fluctuation within the noise source extent in the vicinity of the scroll cutoff. The amplitude is mainly caused by the impingement of the impeller blade wake on the scroll surface. The impinging flow of the blade wake is more diffused as the cutoff clearance is increased, and then the K_D value decreases. This feature is satisfactorily proved in the figure.

The F_M value expressing the amplitude ratio of the second harmonics to the fundamental BPF noise is also shown in Fig. 4. Predicted value of the pressure fluctuation by the present model is seriously low compared with the experimental value. This is an inevitable consequence of the fact that the expression of the pressure fluctuation took account only of the fundamental waveform. As shown in Fig. 10, the waveform of the modeled pressure fluctuation does not correspond with that of the measured data except the amplitude level of the fundamental frequency component. In order to have a quantitative evaluation of the F_M value, in other words the rms level of the higher harmonic components, the effect of other unsteady factors such as vortex shedding and/or scattering pressure waves may be included in the model analysis.

Influence of Off-Designed Blower Operation. The change in the noise level with a change in the blower flow rate is recognized in previous findings where the noise level increases in accordance with the decrease of flow rate from the maximum-efficiency operation. In the similarity rule shown in Eq. (1), blower flow rate is normalized by introducing a nondimensional specific speed σ. Since σ is the parameter that only represents the deviation of the operation point, σ constant does not always mean that the blower is operating under maximum efficiency operation in the case of rotational speed changes. Therefore, in order to confirm the application of the similarity rule to the off-designed operation, the influence of σ on each term of the similarity rule has to be examined. As shown in Fig. 12, measurements have been made at five points between the maximum and half-flow operation where the broad-band noise level is remarkably low and has no influence on the BPF components.

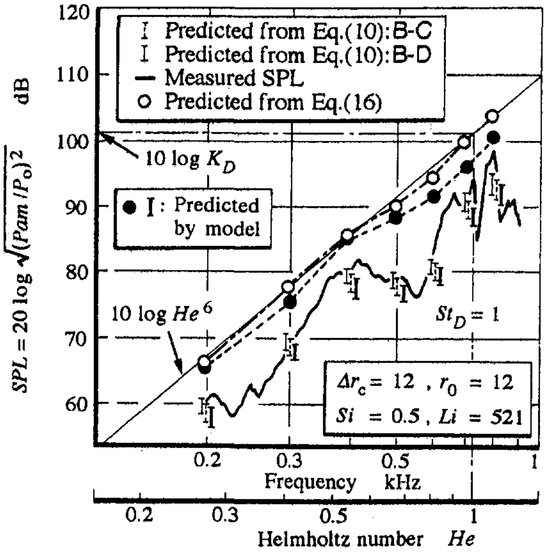

Fig. 11 Characteristics of the BPF components estimated by experiments and by a quasi-steady flow model

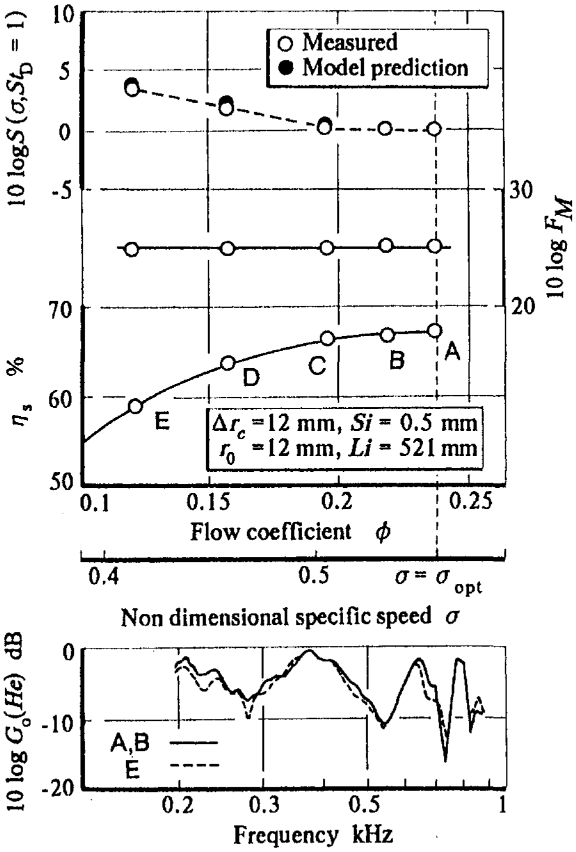

Fig. 12 Influence of off-design operation on similarity rule terms

Neither the frequency-response function $G_0(\mathrm{He})$ nor the amplitude ratio F_M is influenced by the blower flow rate. The effect only appears at the first term of the similarity rule, which represents the rms level of the first BPF components. Therefore, the amplitude growth of the blower suction noise in off-design operation is found to be caused only by the strength of the noise source and not by the response of the transmission passage. The quasi-steady flow model of surface pressure fluctuation presented in the previous section has been utilized in the evaluation of the amplitude growth of the BPF components. The growth is expressed by the correction function S_M in the similarity rule. The results are plotted by closed circles in Fig. 12. The present model of surface pressure fluctuation satisfactorily predicts the strength of the noise source between the maximum and half-flow operation. Therefore, taking account of frequency-response function $G_0(\mathrm{He})$, which is unchangeable with the blower flow rate, blower suction noise level even in the off-designed operation can be predicted by utilizing the present model.

Conclusions

In order to obtain an acoustic and fluid mechanical understanding of centrifugal blower noise, amplitude traces of the blade-passing frequency components versus the blower rotational speed have been discussed by introducing the similarity rule developed by Bommes. The measured data at the blower inlet were decomposed into frequency-response term and source strength terms. Quantitative evaluation of the source strength terms by introducing the correlation analyses and the quasi-steady flow model of surface pressure fluctuation enables us to predict the suction noise level of the blower.

The findings can be summarized as follows:

1 The extent of the noise source was restricted within the vicinity of the scroll cutoff regardless of cutoff geometries. The noise reduction in the case of a large cutoff clearance was mainly caused by the diffusion of the wake profile. The cutoff radius influenced the extent of the noise source.

2 The free-field noise was determined from the pressure fluctuation data within the extent of the noise source by using cross-correlation analyses. The results agreed well with the experimental data, which were influenced by the frequency-response function described by a one-dimensional wave model. The noise level increased to the sixth power of the impeller rotational speed in accordance with dipole noise characteristics.

3 The source strength terms of the similarity rule were determined by presenting a quasi-steady flow model of surface pressure fluctuation. In the model, special attention was paid to introduce the diffusion characteristics of the blade wake between the impeller and the scroll surface. The amplitude of the pressure fluctuation was determined by steady-state dynamic pressure of the blade wake. The evaluated data of sound pressure at blower inlet agreed with the experimental data within an uncertainty range of 5 decibels.

4 The amplitude growth with a change in volume flow rate was satisfactorily evaluated by utilizing the present model between the maximum and half-flow operation.

In the summary, the analysis given here was found to be useful for the purpose of noise prediction. However, the process of analysis is very complicated and cumbersome. Considerable simplification for practical application would be still necessary. Investigation on the superharmonics of the BPF noise is further required.

References

Akishita, S., Morinushi, K., and Umeda, Y., 1978, "The Surface Dipole Strength Correlated With Vortex Shedding Noise: Experiment on Blunt Trailing-edge Airfoil," *Transactions of the JSME,* Vol. 44, No. 387, pp. 3797–3808 [in Japanese].

Bommes, L., 1982, "Analyse und Vorausberechnung des Geräusches von Ventilatoren," *HLH,* No. 7, pp. 245–257.

Curle, N., 1955, "The Influence of Solid Boundaries Upon Aerodynamic Sound," *Proceedings of the Royal Society,* Series A, Vol. 231, pp. 505–514.

Kamoi, A., and Tanaka, H., 1977, "Studies on a Two-Dimensional Impinging Jet Considering Initial Turbulence: 2nd Report, Static Behavior of Boundary Layer in the Stagnation Region," *Transactions of the JSME,* Vol. 43, No. 372, pp. 2957–2973 [in Japanese].

Lighthill, M. J., 1952, "On Sound Generated Aerodynamically: General Theory," *Proceedings of the Royal Society,* Series A, Vol. 211, pp. 564–587.

Maruta, Y., and Kotake, S., 1979a, "Separated-Flow Noise of a Flat Plate: 1st Report, Noise Characteristics and Generation Mechanism," *Transactions of the JSME,* Vol. 46, No. 406, pp. 1055–1064 [in Japanese].

Maruta, Y., and Kotake, S., 1979b, "Separated-Flow Noise of a Flat Plate: 2nd Report, Characteristics of Noise Sources," *Transactions of the JSME,* Vol. 46, No. 408, pp. 1415–1426 [in Japanese].

Moreland, J. B., 1974, "Housing Effects on Centrifugal Blower Noise," *Journal of Sound and Vibration,* Vol. 36, No. 2, pp. 191–205.

Neise, W., 1975, "Application of Similarity Laws to the Blade Passage Sound of Centrifugal Fans," *Journal of Sound and Vibration,* Vol. 43, No. 1, pp. 61–75.

Neise, W., 1976, "Noise Reduction in Centrifugal Fans: A Literature Survey," *Journal of Sound and Vibration,* Vol. 45, No. 3, pp. 375–403.

Ohta, Y., Outa, E., and Tajima, K., 1987, "Blade Passing Frequency Noise Induced by Flow Around Cut-Off of Scroll in a Centrifugal Fan," *Proceedings of the 1987 Tokyo International Gas Turbine Congress,* Vol. 2, pp. 231–238.

Ohta, Y., Outa, E., and Tajima, K., 1991, "An Acoustic Model for Prediction of Centrifugal Blower Noise Induced by Blade Discharge Flow Around the Scroll Cut Off," *Proceedings of the Yokohama International Gas Turbine Congress,* Vol. 2, pp. 101–108.

Shaw, L. M., and Balombin, J. R., 1981, "Rotor Wake Characteristics Relevant to Rotor–Stator Interaction Noise Generation," NASA TM, Vol. 82703, pp. 1–24.

Siddon, T. E., 1973, "Surface Dipole Strength by Cross-Correlation Method," *Journal of the Acoustical Society of America,* Vol. 53, No. 2, pp. 619–633.

Suzuki, S., and Ugai, Y., 1977, "Study on High Specific Speed Airfoil Fans," *Bulletin of the JSME,* Vol. 20, pp. 575–582.

Weidemann, J., 1971, "Analysis of the Relations Between Acoustic and Aerodynamic Parameters for a Series of Dimensionally Similar Centrifugal Fan Rotors," NASA Technical Translation, F-13, pp. 1–102.

Yeow, K. W., 1974a, "Acoustic Modeling of Ducted Centrifugal Rotors, (1) The Experimental Acoustic Characteristics of Ducted Centrifugal Rotors," *Journal of Sound and Vibration,* Vol. 32, No. 1, pp. 143–152.

Yeow, K. W., 1974b, "Acoustic Modeling of Ducted Centrifugal Rotors, (2) The Lumped Impedance Model," *Journal of Sound and Vibration,* Vol. 32, No. 2, pp. 203–226.

H. Hefazi

K. Kaups

Aerospace Engineering Department,
California State University, Long Beach,
Long Beach, CA 90840-8304

R. Murry

Allied Signal Inc.,
Aerospace Systems and Equipment,
Torrance, CA 90504-6094

Ice Accretion on a Radial Inflow Turbine Blade

A computational method for predicting ice accumulation on a radial inflow turbine blade has been developed. The method includes particle trajectory calculations based on a flow field solution, and icing analysis that takes the impinging liquid and formulates a heat balance equation on the surface of the blade. The two-dimensional heat balance model assumes no heat transfer to the surface of the blade. Since there are no known previous calculations or experiments to compare with the prediction of the present method, calculations for several ranges of parameters are performed in order to gain experience. Some qualitative predictions of ice shedding frequencies, types of ice that may be formed, and a design suggestion for reducing ice buildup is also made.

1.0 Introduction

In recent years, a number of research organizations, led by the NASA Lewis Aircraft Icing Research Branch, have launched an effort to develop and validate a series of mutually compatible computer codes to predict the details of ice accretion, and its effect on the aerodynamic performance of aircraft components such as airfoils, wing, and engine inlets [1–3]. These codes, once they are fully validated, can be used for preliminary design studies to ascertain component sensitivity to icing and to predict the performance of proposed ice protection systems. A typical computer program consists of a flow code that determines the velocity components necessary for the particle trajectory calculations and an icing analysis code that takes the impinging liquid and formulates a heat balance equation on the surface of the blades.

Experimental studies conducted by the NASA Lewis Research Center have revealed many key aspects of the icing problems that must be adequately modeled or predicted in any component icing analysis. However, since the details of ice formation and water run-back are not fully understood, the icing model still relies on some empirical data. The usual procedure is to determine the accumulation of ice in one time step and then to recalculate the trajectories in a flowfield that has been altered by the change of shape of the surface of the airfoil due to ice accumulation during the time step. This procedure is then repeated through subsequent time steps.

Application of this approach to geometries other than two-dimensional airfoils has been attempted but with severe restrictions because of the limitations of the two-dimensional heat balance model used. Attention so far has been mostly on external flows such as airfoils, wings, and nacelles. Icing, however, frequently occurs in other aircraft components such as Aircycle machines, used in aircraft environmental control systems. The objective of the present work is to develop a computational method to predict icing on the blade surface as air passes through a radial inflow expansion turbine.

The reverse Brayton cycle (also known as air cycle) is the standard process used in providing refrigeration for pressurized aircraft. The standard Brayton cycle used in the gas turbine adds heat to the compressor discharge flow by means of a combustor. The reverse Brayton cycle removes heat from the compressor discharge flow by means of a ram air heat exchanger. In both cases the flow then expands through the turbine. But whereas the result of expansion in a gas turbine is the shaft power to run the cycle, the result of expansion in an air cycle turbine is cold air for refrigeration. The power to run the cycle comes from a pressurized air source at the front end of the process.

The 100 hp (75 kW) of shaft power generated by the turbine of a typical wide body aircraft air cycle refrigeration pack is split between a compressor that boosts the inlet air pressure and a fan that draws ram air across the heat exchanger.

The classical conditions for blade icing are routinely encountered in the air cycle expansion turbine. The turbine inlet flow is normally at near-ambient temperature and at three times aircraft cabin pressure. Ambient air is at 40 percent relative humidity (RH) at sea level pressure, but increased to 120 percent RH at 3 atm pressure, simply due to the constancy of temperature and the proportionality between moisture pressure and air pressure. The impingement of entrained moisture on a turbine blade operating at a subfreezing temperature results in blade icing.

In the air cycle turbine test cell, blade icing can be detected by monitoring the dynamic response of the rotating assembly. Because the bearings are soft mounted, the unbalanced loads due to ice shedding cause a measurable change in the radial run-out of the rotating assembly. The specific conditions analyzed in this ice accretion study have consistently resulted in the high radial run-outs typical of severe blade icing.

Since the rate of ice formation depends on the intensity of the impinging particles, the quantity to be determined is the so-called collection efficiency, which depends on the trajectory calculations for the water particles. The release points, concentration, and space distribution of particles in this case must be idealized because the upstream flow field is not as well defined as in external flows.

The equations of motion are expressed in a rotating cylindrical polar coordinate system with the velocity field given at discrete points. From a computational standpoint this is an initial value problem for ordinary differential equations. If the given velocity field is adequate and the solutions are stable, realistic prediction of the impingement points for the water particles is expected to occur. Since there are no known previous calculations with which to compare the present method, calculations for a range of conditions should be performed in order to gain experience for icing calculations.

The next section presents the formulation of the particle trajectory calculation method. In section 3.0, calculated trajectories and their impinging points for several conditions are given. Ice accumulation calculations and an analysis of ice shedding is discussed in subsequent sections.

2.0 Particle Trajectory Calculation Method

Expressed in vector form, the equations of motion in a rotating coordinate system are given by

---

Contributed by the Turbomachinery Division for publication in the JOURNAL OF TURBOMACHINERY. Manuscript received at ASME Headquarters October 1994. Associate Technical Editor: N. A. Cumpsty.

$$\bar{F} = m\left[\frac{d^2\bar{R}}{dt^2} + 2\bar{\omega} \times \frac{d\bar{R}}{dt} + \bar{\omega} \times (\bar{\omega} \times \bar{R})\right] \quad (1)$$

where $\bar{F}$ is the external force acting on the particle, m is the mass of the particle, $\bar{R}$ is the position vector of the particle, and $\bar{\omega}$ is the angular velocity vector of the rotating cylindrical coordinate system, x, r, θ. In our case we select x as the rotational axis such that $\bar{\omega} = i\omega$ and express the position vector, $\bar{R}$ as

$$\bar{R} = ix + \hat{t}_r r = ix + r(j\cos\theta + k\sin\theta) \quad (2)$$

Thus

$$\bar{\omega} \times (\bar{\omega} \times \bar{r}) = -\omega^2 r(j\cos\theta + k\sin\theta) \quad (3)$$

and

$$\bar{\omega} \times \frac{d\bar{R}}{dt} = -\omega\left(\frac{dr}{dt}\sin\theta + r\frac{d\theta}{dt}\cos\theta\right)j + \omega\left(\frac{dr}{dt}\cos\theta - r\frac{d\theta}{dt}\sin\theta\right)k \quad (4)$$

$$\frac{d^2\bar{R}}{dt^2} = \frac{d^2x}{dt^2}i + \frac{d^2r}{dt^2}(j\cos\theta + k\sin\theta) + 2\frac{dr}{dt}(-j\sin\theta + k\cos\theta)\frac{d\theta}{dt} + r\frac{d^2\theta}{dt^2}(-j\sin\theta + k\cos\theta) + r\left(\frac{d\theta}{dt}\right)^2(-j\sin\theta - k\cos\theta) \quad (5)$$

Equation (1) is written as a system of first-order differential equations in terms of the coordinates x, r, θ and the corresponding velocity components V_x, V_r, V_θ as

$$\frac{dx}{dt} = V_x, \quad \frac{dr}{dt} = V_r, \quad r\frac{d\theta}{dt} = V_\theta \quad (6)$$

$$F_x = \bar{F}\cdot i = m\left[\frac{dV_x}{dt}\right] \quad (7)$$

$$F_r = \bar{F}\cdot\hat{t}_r = m\left[\frac{dV_r}{dt} - \frac{V_\theta^2}{r} - 2\omega V_\theta - r\omega^2\right] \quad (8)$$

$$F_\theta = \bar{F}\cdot\hat{t}_\theta = m\left[\frac{dV_\theta}{dt} + \frac{2}{r}V_rV_\theta + 2\omega V_r\right] \quad (9)$$

The external forces on the particle consists of the drag force and the gravitational force. Since the drag force is generated by the relative speed difference between the particle and the flow speed, it is expressed as

$$-\bar{D} = C_D\rho\,\frac{(\bar{V}_p - \bar{U})\cdot(\bar{V}_p - \bar{U})}{2}\,\frac{(\bar{V}_p - \bar{U})}{|\bar{V}_p - \bar{U}|}A = \frac{C_D\rho A}{2}|\bar{V}_p - \bar{U}|(\bar{V}_p - \bar{U})$$

where C_D and A are the particle drag coefficient and frontal area, respectively, $\bar{V}_p$ is the velocity vector of the particle, $\bar{U}$ is the velocity vector of the flow field, and ρ is the density of the fluid.

$$\bar{V}_p = V_x i + V_r\hat{t}_r + V_\theta\hat{t}_\theta$$

$$\bar{U} = U_x i + U_r\hat{t}_r + U_\theta\hat{t}_\theta \quad (10)$$

The gravity force vector is given by

$$\bar{G} = -mg\hat{n} \quad (11)$$

where $\hat{n}$ is the fixed vertical direction. In the present study the gravity force is negligible compared to drag. However, it is still maintained in the equations for the sake of completness. The angular position of the particle with respect to the vertical after time t is $\theta + \omega t$. Taking the components of the external force vector $\bar{F}$ and rearranging, Eqs. (7)–(9) can be written as

$$\frac{dV_x}{dt} = k|\bar{V}_p - \bar{U}|(U_x - V_x) \quad (12)$$

$$\frac{dV_x}{dt} = k|\bar{V}_p - \bar{U}|(U_r - V_r) + \frac{V_\theta^2}{r} + 2\omega V_\theta + r\omega^2 - g\cos(\theta + \omega t) \quad (13)$$

$$\frac{dV_r}{dt} = k|\bar{V}_p - \bar{U}|(U_\theta - V_\theta) - 2\frac{V_rV_\theta}{r} - 2\omega V_r + g\sin(\theta + \omega t) \quad (14)$$

We normalize all lengths by R, velocities by $V_o = R|\omega|$, and time by $\tau = tV_o/R$. Hence the normalized variables are:

$$\bar{x} = \frac{x}{R} \quad \bar{r} = \frac{r}{R} \quad \bar{u} = \frac{V_x}{V_o} \quad \bar{v} = \frac{V_r}{V_o} \quad \bar{w} = \frac{V_\theta}{V_o}$$

The system of equations represented by Eqs. (6)–(9) is:

$$\frac{d\bar{x}}{d\tau} = \bar{u} \quad (15)$$

$$\frac{d\bar{r}}{d\tau} = \bar{v} \quad (16)$$

$$\frac{d\theta}{d\tau} = \frac{\bar{w}}{\bar{r}} \quad (17)$$

$$\frac{d\bar{u}}{d\tau} = kV_r(\bar{U}_x - \bar{u}) \quad (18)$$

$$\frac{d\bar{v}}{d\tau} = kV_r(\bar{U}_r - \bar{w}) + \frac{\bar{w}^2}{\bar{r}} - 2\bar{w} + \bar{r} - \frac{\cos(\theta - \tau)}{F^2} \quad (19)$$

Nomenclature

R = inlet tip radius
C_D = drag coefficient of the particles
$\hat{t}_r$, $\hat{t}_\theta$ = unit vectors in r and θ directions
$\bar{u}$, $\bar{v}$, $\bar{w}$ = normalized velocity components in x, r, θ directions
$\bar{U}$ = velocity vectors of the flowfield
V_x, V_r, V_θ = velocity components
$\bar{V}_w$, $\bar{V}_p$ = velocity vector of the particles
x, r = dimensional variables
$\bar{x}$, $\bar{r}$ = normalized variables

$$\frac{d\bar{w}}{d\tau} = kV_r(\bar{U}_\theta - \bar{w}) - 2\frac{\bar{v}\bar{w}}{\bar{r}} + 2\bar{v} + \frac{\sin(\theta - \tau)}{F^2} \quad (20)$$

Here:

$$V_r = |\bar{V}_p - \bar{U}|$$

and

$$F = \left(\frac{V_o^2}{Rg}\right)^{1/2}; \quad k = \frac{3}{4} C_D \frac{\rho_a}{\rho_w} \frac{R}{d_w}$$

where the subscript w refers to the water particle. The particles are assumed to be spheres and the drag coefficient is evaluated from an empirical relation between C_D and Reynolds number, which is valid for rigid spheres with diameters in the range of 10–500 μm. Note that the signs of terms containing ω have been changed because the rotation takes place in the negative sense with respect to the coordinates.

3.0 Trajectory Calculations

The system of differential equations (15)–(20) is solved by the Gear method [4], which is very appropriate for stiff equations that occur in trajectory calculation problems. It is a higher order accurate method with automatic step size and error control, where the user only specifies a convergence criterion and the initial step size. Since this is an initial value problem, the user also specifies the initial particle location $\bar{x}$, $\bar{r}$, θ, and the particle velocity components $\bar{u}$, $\bar{v}$, $\bar{w}$.

Trajectories of the particles depend strongly on their sizes. In the absence of exact information on the size of the water particles as they enter the turbine, three different representative sizes of 20, 40, and 80 μm are considered in the present study. In aerodynamic applications, 20 μm particles are most common in atmospheric flight conditions. In the present problem, however, with water running at the trailing edge of the guiding vanes, much larger particles are possible. Therefore particles of sizes 40 and 80 μm and even larger are not unrealistic.

Details of the trajectory calculation procedures are presented in [5]. The stream speed and flow properties of various points are interpolated from a flow solution obtained by a stream curvature method with boundary layer correction. The present test case represents flow in a radial turbine with rotor inlet tip radius of 68.45 mm and inlet tip speed of 225 m/s. The turbine has 20 blades and the height of the blade at inlet is 9.14 mm. The rotor outlet tip radius is 44.45 mm. All particles were released at the first station of the rotor, which is at the blade tip radius. They are assumed to have a purely radial velocity equal to 99 percent of that of the flow at the release point, which is typically 73 m/s.

Case 1—20 μm Particles. All of the particles passed through without impinging on any surfaces.

Case 2—40 μm Particles. Figure 1(*a*) shows the top view of rectangular blade-channel cross section between the pressure (bottom) and suction (top) surfaces and the hub (left) and casing (right) walls. The release points are equally distanced in the axial direction but have different incremental angular distances of 1, 1, 1, 0.9, 0.8, 0.7, and 0.5 deg, respectively, from the pressure surface. The open circles represent release locations of those particles that impinge on the pressure surface of the blade. All other particles passed through without impinging on any surface, and their release locations are not shown. Figure 1(*b*) shows the corresponding impinging points on the pressure surface of the blade for this case. The five rows of seven impingement locations denoted by open circles in Fig. 1(*b*) correspond to the five rows of seven release locations in Fig. 1(*a*), with the first row of impingement locations (closest to inlet), corresponding to the first row of release locations (closest to PS), etc. The meridional view and three-dimensional view of a typical trajectory of a particle released at $X = 3.55$ mm, $\theta = 5$ deg, and $r = 68$ mm are shown in Figs. 2(*a–b*). The release location and impingement point of this particle are marked with filled circles in Figs. 1(*a–b*). In Fig. 2(*b*), as well as subsequent Figs. 4(*b*) and 5(*b*), the trailing edge of every second blade (right) is cut back.

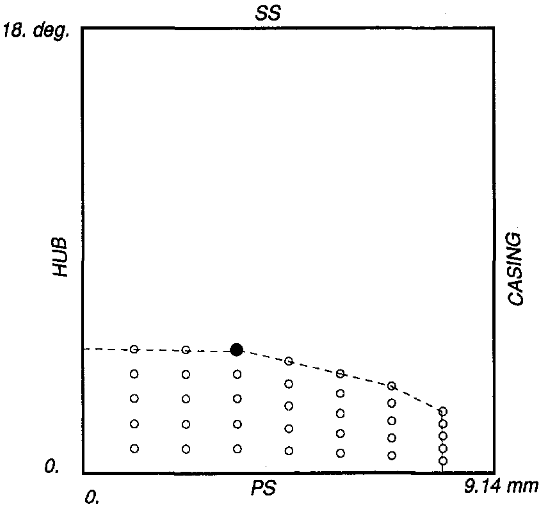

Fig. 1(*a*) Location of release points of 40 μm particles at the inlet plane to the impeller. Only those locations are shown for which impact with the wall occurred.

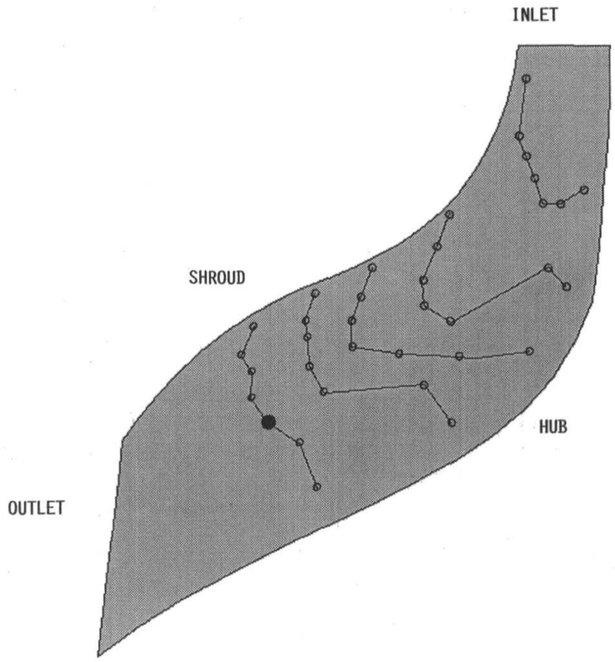

Fig. 1(*b*) Location of impact points on the pressure surface of the impeller for 40 μm droplets released at positions shown with open circles in Fig. 1(*a*)

From Fig. 1(*a*), the portion of entrance area (enclosed by dotted lines) where particles that are released there impinge on the blade, varies from 5 to 2.5 deg away from the pressure surface, and represents about 20 percent of the inlet rectangle. Assuming a uniform particle flow over the inlet, these impinging particles represent a similar percentage of liquid water particles of the size that can form ice on the blade surface. Therefore, this condition is expected to result in relatively small to moderate ice accretion on the pressure surface of the blade.

Case 3—80 μm Particles. Figure 3(*a*) shows the location of the particles released in this case. As before, only points representing the release location of particles that hit a surface

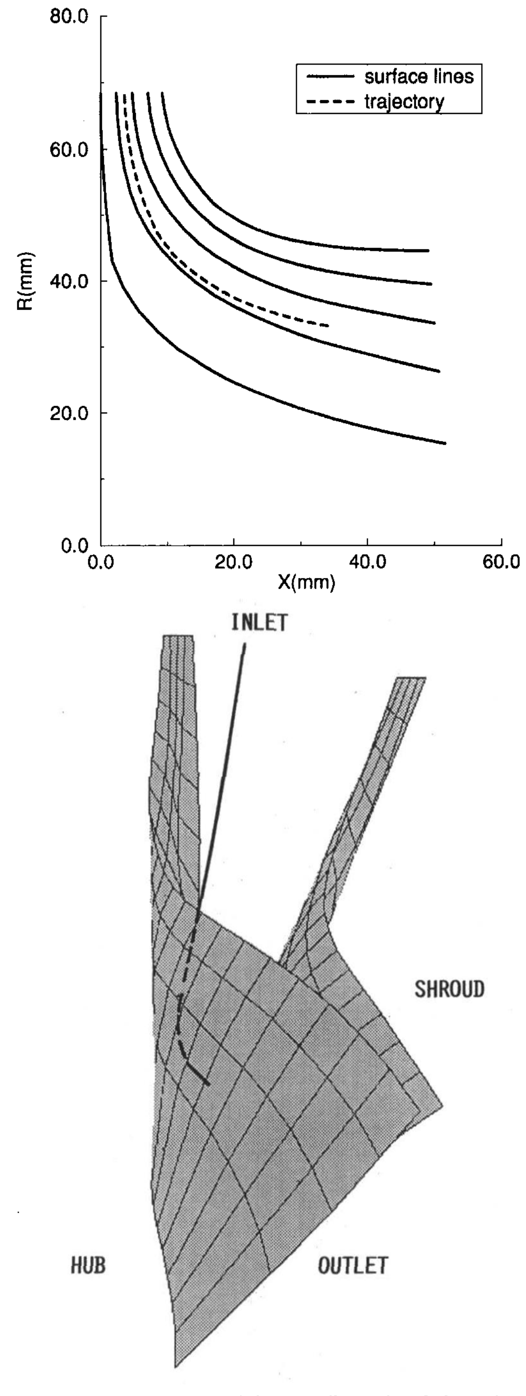

Fig. 2 (*a*) Meridional view and (*b*) three-dimensional view of trajectory of the 40 μm particle for which release and impingement locations are denoted by ● in Figs. 1(*a–b*); X = 3.55 mm, θ = 5 deg

are shown. Release points are equally distanced in the x direction, but the incremental angular distances from the pressure side varies in some cases, in order to have better distribution of release points. The angular distance from the pressure surface for the last row of impinging particles varies from 17 to 9 deg.

The impinging particles in this case could be divided into two groups. The first group, indicated by ⊗, escape the gap between the two blades and hit the casing. The rest of these particles impinge on the pressure surface of the blade. Impingement locations on the pressure surface of the impeller corresponding to Fig. 3(*a*) are shown in Fig. 3(*b*). As before the first row of four impingement locations in Fig. 1(*b*) (closest to inlet) corresponds to the first row of four release locations (closest to PS) in Fig. 1(*a*), etc.

The ejection of the larger particles to the outside of the blade passage could be expected in regions where the release velocities are relatively small and where they are overcome by centrifugal forces. Figures 4(*a–b*) show the meridional view and three-dimensional computer-generated view of the trajectory of a particle released at X = 7.11 mm, θ = 4.9 deg, and r = 68 mm. As it can be seen in these figures, the particle escapes the gap between the two blades and hits the casing. The release location of this particle is marked with filled circle in Fig. 3(*a*). On the other hand, Figs. 5(*a–b*) show the meridional view and three-dimensional view of the trajectory of a particle released at X = 3.55 mm, θ = 16 deg, and r = 68 mm that impinges on the pressure surface of the blade. The release location and impingement point of this particle are marked with the symbol ⊗ in Figs. 3(*a–b*).

For the calculation of ice in the present study, we will only consider the pressure surface of the blade. Compared to the previous case, a much larger number of particles hit the blade than before. From Fig. 3(*a*) (area enclosed by dotted lines) it

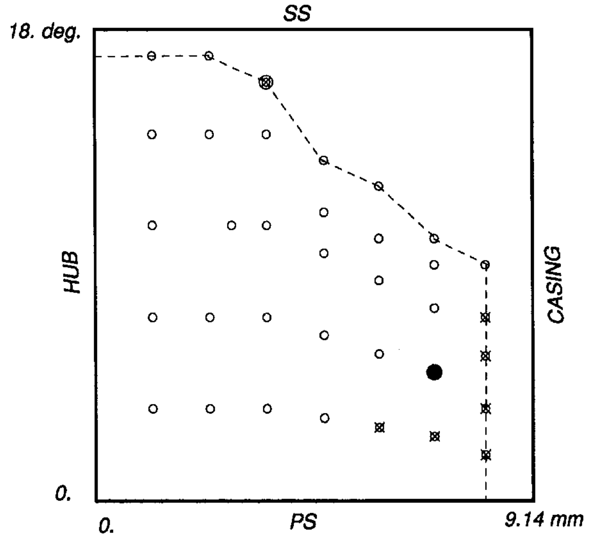

Fig. 3(*a*) Location of release points of 80 μm particles at the inlet plane to the impeller. ○ denote particles for which impact with the wall occurred. ⊗ denotes particles that escaped the gap between the two blades and hit the casing.

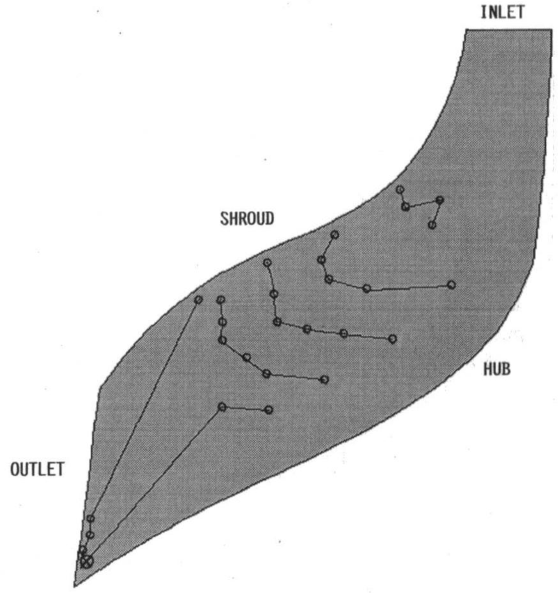

Fig. 3(*b*) Location of impact points on the pressure surface of the impeller for 80 μm particles released at positions shown with ○ in Fig. 3(*a*)

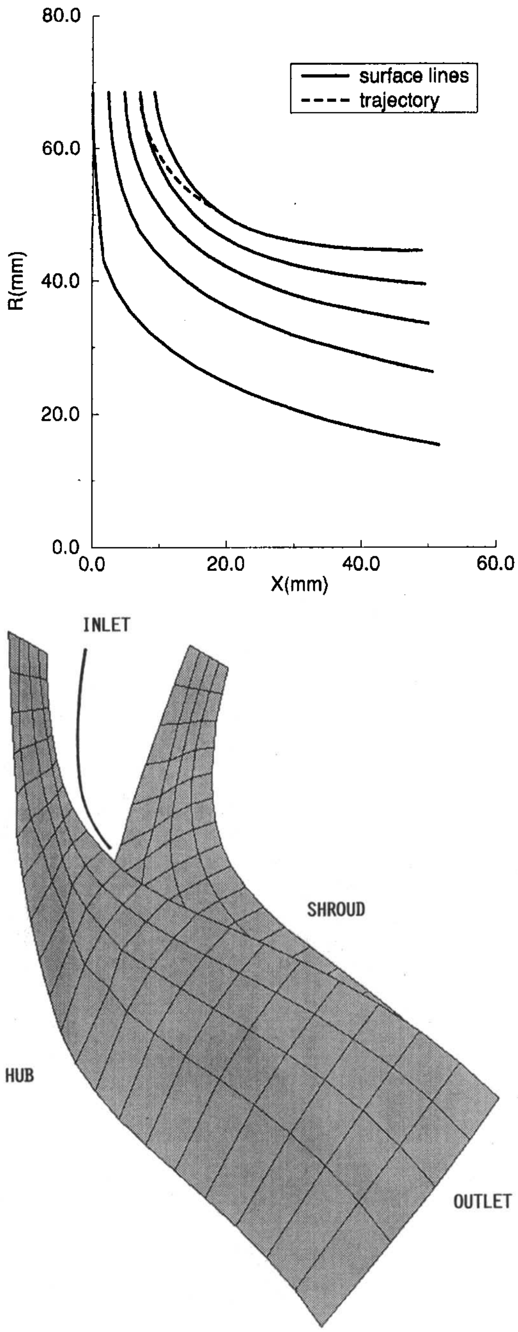

Fig. 4 (*a*) Meridional view and (*b*) three-dimensional view of trajectory of an 80 μm particle which escapes the gap between the two blades. $X = 7.11$ mm, $\theta = 4.9$ deg. Release location for this particle is denoted by ● in Fig. 3(*a*).

is seen that approximately 50–60 percent of particles of this size impinge on the pressure surface. Furthermore, the affected area on the blade is smaller than for the previous case. Therefore, it is expected that this condition results in a more severe ice build-up.

4.0 Ice Accumulation Calculation

In the Lewice code, ice growth on the surface is calculated from the mass and energy balance in a control volume. The basic unknowns are the freezing fraction and the air–ice interface temperature; heat transfer through the ice layer is ignored. The freezing fraction gives the fraction of the net water flow into the control volume that freezes; this determines the rate of ice growth. Since the Lewice code was developed for two-dimensional flows, its application to other situations depends on the particular circumstances. The principal restriction is that the energy and mass flow in the lateral direction must be small or negligible if the calculation in the strip-theory sense has any hope of giving realistic results. The main cause for the deviation of the mass flow is the runback water on the surface, which may not flow in the desired direction and would require an additional equation to describe its path. But as long as most of the flow is almost two dimensional, say in the external stream-

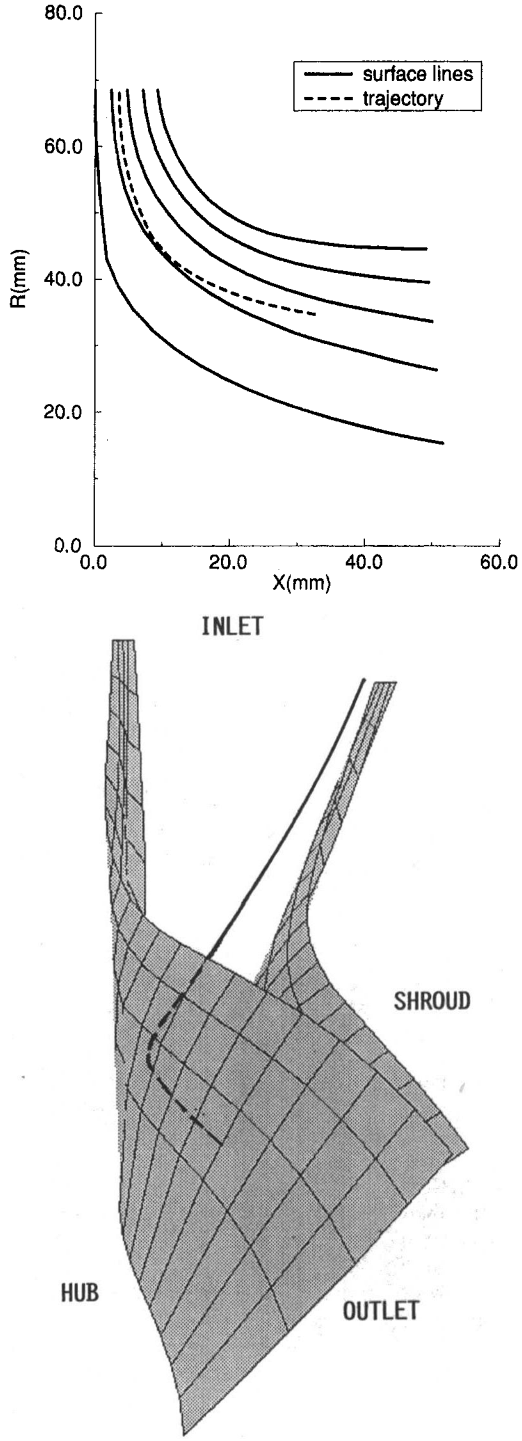

Fig. 5 (*a*) Meridional view and (*b*) three-dimensional view of trajectory of an 80 μm particle that impinges on the pressure surface of the impeller. $X = 3.55$, $\theta = 16$ deg. Release and impingement locations are denoted by ⊗ in Figs. 3(*a–b*).

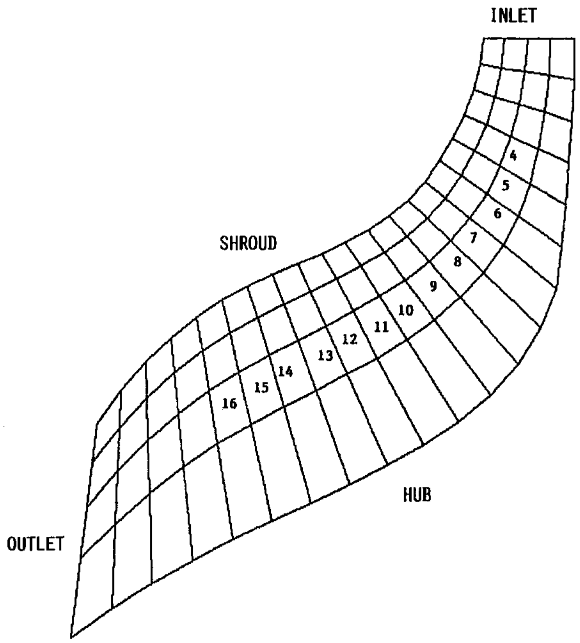

Fig. 6 Location of ice calculation segments on the pressure surface of the blade

line direction, the approximation is reasonable. It is obvious that the runback water on the surface of a rotating blade would be subject to centrifugal forces and deviate from the inviscid streamlines. However, there is one situation that eliminates this problem, and that is when the freezing fraction is such that all water entering a control volume freezes. This condition is characteristic for the low temperatures encountered in the present turbine application and was confirmed by the calculated freezing fractions. The conclusion is that the two-dimensional analysis is valid along strips formed by inviscid surface streamlines on the blades as long as the temperature is low enough for all impinging water to freeze.

One of the problems encountered when computing trajectories and heat balance is to determine the correct water particle sizes and their initial speeds. It is likely that some of the particles are small and well dispersed in the air stream while others are formed as the runback water on the inlet vanes leaves the surface. Very little is known about their probable sizes and speeds, but if they are relatively large and slow, their impingement points could be on the suction surface. On the other hand, in the off-design condition the flow near the leading edge on the suction side is separated, and the calculation of trajectories without a detailed knowledge of the flow field becomes rather arbitrary.

In the present study, we consider the formation of ice on the second strip (from the hub) of the pressure surface shown in Fig. 6. For case 2, with a particle size of 40 μm, collection efficiencies are calculated from Fig. 1(*b*) for "segments" 5–15, where impinging data are available. These coefficients are obtained using weighted average values based on areas. Furthermore, the conditions of the icing were assumed as follows:

Reference velocity at exit of inlet vanes	73.15 m/s
Liquid water content	2 g/m^3
Ambient temperature (static)	249 K
Relative humidity	100 percent
Ambient pressure (static)	127,406 Pa
Surface roughness	0.000122 m

Here ambient pressure and temperature are defined as the pressure and temperature of air as it leaves the inlet vanes. Furthermore, it is assumed that there is no heat transfer from the blade surface.

Table 1 Ice accretion results for 40 μm particle size after 100 seconds

Segment	Collection efficiency	Ice thickness, mm	Freezing fraction	Ice surface temperature
5	0.0336	0.54	1.0	246.5
6	0.0353	0.57	1.0	245.5
7	0.0353	0.57	1.0	244.3
8	0.0346	0.56	1.0	243.2
9	0.0337	0.55	1.0	242.2
10	0.0418	0.67	1.0	242.8
11	0.0501	0.81	1.0	242.9
12	0.0497	0.78	1.0	241.7
13	0.0430	0.69	1.0	239.9
14	0.0433	0.70	1.0	239.3
15	0.0423	0.69	1.0	238.6

As mentioned earlier, the ice code calculates the rate of growth of ice at the center of the segments being considered. Table 1 summarizes the ice accretion results for segments 5–15 after 100 seconds.

It is important to note that as a result of the very low temperature encountered in the present application, the freezing fraction is equal to one, so that there is no runback water on the blade surface.

The maximum ice thickness occurs at segment 11 where the collection efficiency is also maximum. It is also interesting to note that the ice surface temperatures for all segments are a few degrees higher than their respective static surface temperatures. This is due to the assumption by the ice code that impinging water particles are at the ambient temperature. The possibility of a particle's temperature being different from ambient has implications on both ice growth and ice type and is commented on in the next section.

Similar calculations were performed for 80 μm particles. The icing condition considered was the same as previous case. The results are summarized in Table 2.

While the freezing fraction and ice surface temperature have the same behavior as in the previous case, the ice growth rate is much larger, and the maximum ice build-up occurs further downstream. The larger ice accretion rate could be expected since particle sizes and collection efficiencies are much larger in this case.

5.0 Ice Shedding

The principal reason for ice departing the blade surface after initial ice build-up is the presence of centrifugal forces, which are typical in rotating machinery and therefore cause periodic de-icing. In the present case the largest component of the centrifugal force acts nearly parallel to the blade surface, subjecting ice to shear forces, but the component normal to the surface may be important if the hub is considered. Since calculations indicate that the majority of particles impinge on the blades, we will consider data pertaining to the ability of ice to resist shear. Here one has to consider adhesive shear stresses (the

Table 2 Ice accretion results for 80 μm particles after 100 seconds

Segment	Collection efficiency	Ice thickness, mm	Freezing fraction	Ice surface temperature
8	0.1429	2.27	1.0	256.6
9	0.1424	2.27	1.0	256.3
10	0.1209	1.93	1.0	253.5
11	0.0914	1.45	1.0	248.5
12	0.0910	1.45	1.0	246.9
13	0.1227	1.96	1.0	249.3
14	0.2363	3.77	1.0	257.8
15	0.1887	3.01	1.0	253.9

binding forces between ice and the surface) and the cohesive shear stresses that bind ice particles together. In reviewing the available experimental data on the subject, one finds a wide range of force data for seemingly identical test conditions. Additional tests are in order. Results from [6] are comprehensive and up-to-date. In addition, the range of test variables such as flow velocity, temperature, and liquid water content roughly cover those of interest in the present investigation. Despite careful and systematic experiments the results showed considerable scatter; this may be indicative of the statistical nature of the problem.

There is no clear evidence regarding the type of ice that is formed in the case considered here. Because of low temperatures in the turbine preliminary indications are that rime ice is the preferred mode in ice formation. However, there is another point to be considered in the ice accumulation process that relates to the temperatures of the particles as they traverse the turbine. The present analysis assumes that water particles remain at their initial temperature, which is the free-stream temperature, along their trajectories. In the turbine application this may no longer be true because the air temperature in the inlet scroll is about 277 K and decreases to around 222 K in the turbine. Hence, it is doubtful that particles remain at their equilibrium temperatures despite their short residence time in the colder region. One can visualize the impinging particles as being at various temperatures depending on their sizes, and producing ice that is not clearly definable as rime or glaze ice.

The main conclusion of [6] pertaining to our case is that the average limiting holding stress for all test data at about 277 K is 60 psi.

To find the maximum ice thickness for the adhesive failure we simply balance the tangential centrifugal force with the holding force

$$F = PA = \rho_i \frac{V\omega^2}{r \sin \gamma}$$

Here P is the maximum holding stress, A is the contact area element, ρ_i is the density of ice, V the volume of ice above A, ω the rotational speed, r the distance from the rotational axis, and γ the angle between the surface normal and the direction of the centrifugal force. For the examples calculated taking $\rho_i = 0.917$ g/cm^3, $\omega = 3288.7$ rad/s, p in psia, and r in inches, the maximum accumulated height h of ice in millimeters is:

$$h = 0.02735 \frac{\text{psi}}{r \sin \gamma}$$

For example, selecting psi $= 60$ and $\gamma \sim \pi/2$, which is reasonable for the present case, we get for the maximum ice thickness at 2 in. and 1 in. radii to be 0.82 and 1.64 mm, respectively. Since the trajectory of the loosened ice will depend on the size and shape of the individual pieces, both clear passage and impingement on the outer casing can be expected. Another possibility for which there are no quantitative data available is that rime ice will fail cohesively and produce a somewhat different efflux. From the calculated thickness of ice after 100 seconds and maximum possible thickness of ice before departing from the blade, the frequency of ice shedding can be calculated. For the case of 40 μm particles, estimated frequencies vary between 0.006 and 0.04 Hz. A more sophisticated statistical analysis could be applied to determine the spectrum of ice shedding frequencies.

6.0 Conclusion

Depending on water particle size, moderate to severe icing conditions on the blade of a turbine are expected.

The predictions for ice accretion and the maximum ice thickness suggest ice shedding frequencies of 0.006–0.04 Hz for each of the ten turbine exducer blades. This is in qualitative agreement with rotor dynamic response data obtained when operating under these conditions.

As a design suggestion, from trajectory studies, it appears that in order to reduce icing, the inlet vanes should be shaped to concentrate the water droplets shedding to their casing-side end, because near-casing droplets are much less likely to hit the blade surface.

Improvements in the present investigations are needed if greater details of ice accumulation are to be obtained. In particular, the effect of initial relative particle velocity and size on the trajectories and collection efficiency needs a systematic study that considers particles shedding from the runback water on the inlet vanes. Furthermore, the heat balance equation needs modification because the stream enthalpy is variable and the particle temperature does not remain constant during its traverse through the system before impingement.

7.0 Acknowledgments

This work was supported by two grants to the first two authors from the Allied Signal Inc., Aerospace Systems and Equipment. This support is gratefully acknowledged. The authors would also like to thank Mr. Kim Linnett from Allied Signal for very useful discussions.

References

1 Cebeci, T., 1989, "Calculation of Flow Over Iced Airfoils," *AIAA J.*, Vol. 27, p. 853.

2 Cebeci, T., Chen, H. H., and Alemdaroglu, N., 1990, "Fortified Lewice With Viscous Effects," AIAA Paper No. 90-0754.

3 Ruff, G. A., and Barkowitz, B. M., 1990, "User Manual for the NASA Lewice Accretion Prediction Code," NASA CR-185129.

4 Gear, C. W., 1971, *Numerical Initial Value Problems in Ordinary Differential Equations*, Prentice Hall, Englewood Cliffs, NJ.

5 Hefazi, H., and Kaups, K., 1992, "Ice Accretion in a Radial Inflow Expansion Turbine," Report AE-92-3, Aerospace Engineering Department, California State University, Long Beach.

6 Chu, M. C., and Scaruzzo, R. J., 1991, "Adhesive Shear Strength of Impact Ice," *AIAA Journal*, Vol. 29, No. 11, Nov.